Structural Design Verification by using Failure Criteria and More

- scientific knowhow gained over a long practical working life -

Prof. Dr.-Ing. habil. Ralf Cuntze VDI, Ralf_Cuntze@t-online.de

Retired from industry MAN-Technologie (2004) and from Composites United (2021)

The document incorporates results of the author's never funded, non-supported personal research work performed in his vacant time at industry and as retired person.
The work aims to further impart a wealth of experience and messages to structural engineers in the areas of modeling, analysis and testing.

The author assumes no liability for damages resulting from application.

Considering prior editions here the research elaborations have been partially revised and reorganized according to the author's understanding as a designing engineer from industry.

Practical Initiation for this work was:
The author had revisited an important earlier document by Richard M. Christensen and where the author now believes he has found some answers to the questions posed in Christensen's document „Failure Criteria.com", publication of the Stanford University, 2013.
Furthermore, see the contact in 1999 on the next side, please.

Several mottos that have accompanied me in *'Strength was my life'*

"Anyone who stops learning is old,
whether at twenty or (far) beyond eighty.
Anyone who keeps learning stays young.
The greatest thing in life is to keep your mind young"
[Henry Ford]

"Quid quid agis, prudenter agas, et respice finem" (slogan of my school class)
"Whatever you do, do it wisely and remember where it leads".
from [Gesta Romanorum]

"It were good for both the dicsciplines mechanical and civil engineering to act side-by-side such as croco and hippo document below.
[my surprising picture, Sambia 2011.]

Since I had to work in several disciplines, I hope that at least my GLOSSARY, edited 2019, has contributed a little to a better common 'language', understanding and collaboration.

"Si enim alicui placet mea devotio, gaudebo. Si autem nulli placet, memet ipsam tamen iuvat quod feci"
[*A letter from Hrotsvita, nun of Gandersheim, 950 anno domini*]
If my work pleases anyone, I will be happy, but if it pleases no one, it will nevertheless be good that I did it.

If I had known beforehand how much time this work would take, I probably would not have done it.

MAN Technologie AG
Postfach 13 47 · 85751 Karlsfeld

FAX:

Datum/Date: 23.02.99

Seitenanzahl/No. of pages: 1

An/To: **Prof. Dr. R. M. Christensen**
University of California
L-355, Livermore
Fax: **001-925-424-4737**

Von/From: **Prof. Dr.-Ing. habil. R. Cuntze**
Dept. RA
Telefon: **+8131-89-1783**
Fax: **+8131-89-1939**

Kopie/Copy:

Betreff/Ref.:

Dear colleague,

at the beach of the Emirates I eventually got time to thoroughly read your paper on „The Numbers of Elastic Properties and Failure Parameters for Fiber Composites".

I think we are on the same track, however, with different engines in our vehicles to generate strength criteria. Nevertheless, when reading above title I became happy for having found a co-fighter for an improved mechanics-based generation of failure conditions.
Of-course, there are still differing views in detail and therefore I would like to know more about your test-data fitting.

My experience from fitting of test data is the tackling of the following number of failure parameters:

- In case *isotropic dense* materials
  ductile behaviour (shear failure, no friction): 1
  brittle behaviour (normal + shear failure, no friction): 2
  brittle behaviour (normal + shear failure, friction): 2 + 1
- In case of *isotropic porous* materials
  Similar to the dense case
- In case of *dense transversally-isotropic* materials
  brittle behaviour (normal + shear failure, friction): 7 .
  If neclecting the bulge in the (negative σ_2, τ_{21})-domain or if modeling (σ_2, τ_{21}) the same as (σ_3, τ_{21}) (that means disregarding the different action planes of σ_2 and σ_3 with respect to τ_{21}), and if neclecting friction I end up with 5 parameters. Then, all 5 failure (curve) parameters can be determined from the 5 basic strengths which always have to be known in a proper proof of design.
  My experience covers the stress combinations (σ_2, τ_{21}), (σ_3, τ_{21}), (σ_2, σ_1), (τ_{21}, σ_1).

The rounding-off in the transition (interaction) domains of adjacent modes I do probabilistics-based. Therefore I do not mathematically couple uncoupled modes as Stephen Tsai is doing. I avoid by this the shortcomings of the usual 'Single surface failure descriptions'.

In order not to become punished by my wife, I have to close now.
A comprehensive edition of my actual view with applications to a few materials I am going to get ready in a couple of weeks. This I will send you for further discussions.

Waiting for your next response.

Best regards

Ralf Cuntze

P.S.: Hopefully Rajapakse will appreciate *your* work.
I did never get any response from him, and thereby, I have to say, he is disregarding our various German activities. From these activities my 'Concept' is a completely private homework, the others are partly funded.

With my
Failure Mode Concept
(FMC)
it is a little similar to the
experiences
of the outstanding scientist
Max Planck,
who said:

"It is one of the most painful experiences of my life that I have never succeeded in bringing a new assertion, for the correctness of which could provide a compelling theoretical proof, to general recognition.
New scientific work prevails after the extinction of the opponents".

Where are the discussions
on my meanwhile
'30 years old' FMC
in our contact-simple
'digital time'?

0 Introduction 9
0.1 Ralf Cuntze CV in short 9
Abstrac 23
0.2 Technical Terms with some Definitions and Abbreviations 24
0.3 Focus: Structural Parts and Structural Materials 31
0.3.1 Structural Parts and Brittleness Grade 31
0.3.2 Structural Composite Materials 32
0.3.3 Special Views of the Author concerning Structural Mechanics and Design Dimensioning 33
0.3.4 Comments on Properties to be used in Analysis 35
0.4 Stress-Strain Relationships of Isotropic materials, of UD and Orthotropic materials 35
0.4.1 Isotropic materials 35
0.4.2 Transversely-isotropic UD-material 36
0.4.3 Orthotropic materials 37
0.5 Invariants of Isotropic materials, of UD and Orthotropic materials 38
0.5.1 Isotropic materials 38
0.5.2 Transversely-isotropic UD-material 40
0.5.3 Orthotropic Materials 41

1 Special Features with Isotropic and UD Materials to consider in Design 42
1.1 Facts and Effects of the Various Materials 42
1.1.1 Pores and crack-like flaws ('defects'), multi-site damage failure 42
1.1.2 Mixed (fracture) Failure versus Multi-fold Failure of isotropic and UD-materials 43
1.1.3 Multi-fold failure effects of isotropic brittle and UD brittle materials 43
1.1.4 Effect of High Failure Probability Domains – Size Effects 44
1.1.5 Redundancy effects (healing, benign behavior) 45
1.1.6 Residual stresses (Eigenspannungen) and Pre-stresses (Vorspannungen) 45
1.1.7 In-situ behavior of an embedded UD lamina 45
1.1.8 Thickness effect, example UD 46
1.1.9 Viewing a material's behavior 46
1.1.10 2ndTg shift effect, preview 46
1.2 Fracture Failure Types and Behavior of the Various Materials 46
1.2.1 Isotropic dense materials 47
1.2.2 Isotropic porous materials 48
1.2.3 Transversely-isotropic dense UD materials 50
1.2.4 For Pre-understanding a Visualization of an isotropic Failure Body with Associated Stresses 51

2 Design Dimensioning 54
2.1 General on Quasi-Static Design 54
2.1.1 Modelling Materials 54
2.1.2 Industrial Tasks when performing strength design verifications 54
2.1.3 Preview on Strength Failure Conditions (SFC) and on Designing 55
2.2 Design Verification Procedure Scheme with usual Requirements to achieve Structural Integrity 59
2.2.1 Urgent need to move to 3D Analysis and to use Eff in order to understand stress states 60
2.2.2 Linear and non-linear structural analyses 60
2.3 Structural Integrity, Design principles and Loading Processing 61
2.3.1 Survey in 'Dynamic/Cyclic' Design 61
2.3.2 The two different design principles (philosophies) "Safe Life" and "Damage Tolerance" 62
2.3.3 Structural Modelling and Boundaries 62
2.3.4 Design and Loading processing 64

3 Safety Concepts in Structural Engineering Disciplines and Reserve Factor 65
3.1 Safety Concepts 65
3.2 Former *forbidden* Safety Concept of Allowable Stresses 66
3.3 Lumped (global) Design Factor of Safety Concept on Loading ('deterministic format') 66
3.3.1 Different loading (action) FoS in aircraft and space engineering? 67
3.3.2 The resistances strengths and bearable loads at joints etc 68
3.3.3 Lumped Safety Factor Concept versus Partial Safety Factor Concept 69
3.3.4 Robust Design Requirements 70
3.4 Determination of a UD material Reserve Factor 71
3.5 Probabilistic Assessment of a Deterministic Margin of Safety 71
3.5.1 Theoretical Background: The Multi-stochastic parameter Problem 72
3.5.2 Probabilistic Design Procedure, example composite 74
3.5.3 Design advantages found with the Ariane Booster design, when using a probabilistic tool 74

3.6 Reliability: Failure State versus Failure Rate 75

4 Cuntze's Failure Mode Concept (FMC) for Structural Materials 78

4.1 'Global' Strength Failure Conditions (SFCs) and failure mode-linked 'Modal' SFCs 78
4.2 Mohr's SFCs for completion 81
4.3 Basics of the Invariant-based FMC for generating 'Modal' SFCs 81
4.4 Material stressing effort *Eff* (Werkstoff-Anstrengung) 83
4.5 Direct use of a Friction Value μ in the SFCs of Isotropic and UD materials, preview 84

5 Material Symmetry- driven 'Generic' Material Properties Number 86

5.1 General with Material Symmetry View 86
5.2 Generic Number (material inherent?) 86
5.2.1 Isotropic Material 87
5.2.2 Transversely-Isotropic UD-Materials 87
5.2.3 Orthotropic Material 87

6 Interaction of Stresses versus Interaction of Failure Modes 89

6.1 Modal equivalent stress σ_{eq} and Modal Material stressing effort *Eff* 89
6.2 Interaction of Stresses 89
6.3 Interaction of Failure Modes 90

7 Novelties 'Normal Yielding' (NY) and 'Compressive Fracture Toughness' 91

7.1 Crazing-caused Normal Yielding NY of Plexiglass (non-convex failure surface !) 91
7.2 Compression-caused Shear Fracture Toughness $K_{IIcr}^{(c)}$ of Brittle Isotropic materials 92
7.3 Fracture Toughness Properties of transversely-isotropic UD lamina materials 93

8 Evidencing 120°-symm. Failure Bodies of Brittle, Ductile Isotropic Materials 94

8.1 General 94
8.2 Brittle Isotropic Materials (Metals, Glass, Ceramics, Concrete, Soil, ..) 94
8.3 Ductile isotropic Material's Proof of 120°-rotational axial symmetry in tensile domain 96

9 Derivation of Constant Fatigue Life curves considering Mean Stress Effect and Residual Strength 99

9.1 General 99
9.2 Fatigue Micro-Damage Drivers of Ductile and Brittle behaving Materials 99
9.3 Haigh diagram with its Mapping Challenge of the decisive Stress Ratio Transition Zone 100
9.4 Pre-dominantly Brittle Materials: Estimation of the cyclic Micro-damage Portions 102
9.5 Automatic Establishment of Constant Fatigue Life Curves 102
9.6 Lifetime Estimation 102
9.7 Design Verification of a critically cycled UD lamina within a chosen laminate 105
9.8 Novel Determination of the Residual Strength R_{res} 106
9.8.1 Design Verification in Projects of a not yet cracked Part 106
9.8.2 Classical way to determine Rres, with rendering 107
9.8.3 Probabilistic determination of a 90%- R_{res} -value using distributions with convolution integral 108
9.8.4 Residual Strength R_{res} of a pre-cracked Part 110
9.9 Determination of a Load Spectrum-equivalent SN curve 110

10 Nonlinear isotropic Stress-Strain relationships and Models 112

10.1 General on Stress-Strain curves *σ(ε),* Strengths *R* and Poisson's Ratio *ν* 112
10.2 Uniaxial Rod Tensile Test Aspects 113
10.3 Derivation of an accurate Average Stress-strain curve, example UD 115
10.3.1 Test data recording 116
10.3.2 Statistical evaluation of a bundle of test curves 116
10.4 Ramberg-Osgood (R-O) Mapping of the average stress-strain curve 117
10.5 Mapping of a measured stress-strain curve by the Ramberg-Osgood Model 119
10.6 Presentation of Engineering and of True Stress and Strain Quantities 119
10.7 Variation of Poisson's ratio ν up to Rupture level 120
10.8 Estimation of the 'Onset-of-ductile Cracking' Strength R_{odc} 124
10.9 Beltrami's Potential Surfaces in Elastic-plastic Regime, Idea for the Plastic Porous Regime 125
10.9.1 Elastic-plastic transition regime 125
10.9.2 Plastic porosity affected regime, an anticipation 125
10.10 Post-Necking, a 'measurable parameters-based Extended-Mises' Model replacing 'Gurson' 127
10.10.1 History of the 'Gurson-replacing' Idea 128
10.10.2 Bridgman-3D Correction of the true σ-ε-Curve employing 'Mises' 130
10.10.3 Porosity-improved Bridgman 3D-corrected True σ-ε-Curve employing 'Extended Mises' 134

10.10.4 Measurement of Tensile Rod failure stresses and Estimation of Failure Body Vertex 135
10.10.5 Proposal of the Two Parameter 'Extended Mises' Yield function in the Porosity domain 137
10.10.6 Visualization of a specific 'Gurson'-model versus the 'Extended Mises'-model 137
10.10.7 Visualization of the Bridgman–corrected true curve with consideration of porosity 140
10.11 Specific Potential Surfaces representing Strength Failure Criteria 141

11 Engineering Note on Continuum (micro-) Damage Mechanics (CDM) 144
11.1 Static Behavior 144
11.1.1 Micro-damage formulations 144
11.1.2 Material behavior-caused Slip and Failure angles preview of Isotropic and UD materials 146
11.2 Cyclic Behavior of Ductile Metals applying Micro-scale Material Modelling 147
11.3 Application of Continuum (micro)-Damage Mechanics (CDM) in Static Strength 149
11.3.1 Note on Stressing effort Eff versus micro-damage development D 149
11.3.2 Stress Man's Assessment of CDM applications 150
11.4 Macroscopic SN-curve with Relation Material Stressing Effort *Eff* ↔ Micro-damage *D* 151
11.4.1 General application 151
11.4.2 Transfer from classical Fatigue Damage to the (micro-)Damage Mechanics view 151
11.5 Multiscale Modelling approach of Infinite Life and Endurance limit of Metals 153

12 Note on Multi-scale Structural with Material Modelling and Analysis 155
12.1 Structural Modelling and Analyses over the Scales 155
12.2 'Meso'–Material Modelling of the Example UD material 156
12.3 Material Mixture Rules: Example Micro-mechanical Formulas of UD laminas (ply) 156

13 Some Notes on Structural and Material Testing with Evaluation of Results 159
13.1 General 159
13.2 Structural Testing, primarily based on the Ariane launcher development 159
13.3 Some practical Hints for Applications on *Design Process and Modelling* 161
13.3.1 Stability Loading processing 161
13.3.2 Validation of the analytical model 162
13.3.3 Stability Proof testing considering analysis and test 163
13.3.4 Test Data Evaluation of a Qualification Pressure Tank (deterministic and probabilistic) 163
13.4 Pre-Assessment of UD-Material Testing Data Input primarily based on WWFE-I and -II 164

14 Replacing fictitious Model Parameters by Measurable Friction Values 167
14.1 Brittle Isotropic Materials 167
14.1.1 Visualization of the Friction Value μ by the linear Mohr-Coulomb relation 167
14.1.2 Derivation of the relationship Friction Parameter with Friction Value μ 167
14.2 Transversely-isotropic UD Materials 169
14.2.1 Derivation of the relationship Friction Parameter $a_{\perp\perp}$ with Friction Value $\mu_{\perp\perp}$ ($\theta_{fp}{}^{c}$) 169
14.2.2 Derivation of a relationship Friction Parameter $a_{\perp\parallel}$ with Friction Value $\mu_{\perp\parallel}$ 169
14.3 Evaluation of UD Friction Values $\mu_{\perp\perp}, \mu_{\perp\parallel}$ from test results 171

15 Ductile Isotropic Materials' Strength Failure Criteria 173
15.1 Onset-of-yielding: 'Mises' (Hencky-Mises-Huber) or Tresca Yield Hypothesis 173
15.2 Failure Determination using Mises with Tresca and regarding Prior Test data 173
15.3 Failure Determination using novel 120°-rotational symmetry documenting test data (see §8) 175
15.4 SFC-Application to Semi-brittle isotropic Matrix WWFE-II Data, for Hydrogen Tanks 177

16 Brittle Isotropic Materials' Strength Fracture Failure Criteria 180
16.1 3D-SFC Fracture Failure Formulations with Interaction Formula 180
16.1.1 Used Stresses and Invariants 180
16.1.2 Strength Failure Criteria (SFC), Eff-linked 180
16.2 Isotropic Materials, some Brittle Fracture Envelopes and Fracture Bodies 182
16.2.1 Mapping (Visualization) of Normal Concrete 3D compression test data 183
16.2.2 Mapping of UltraHighPerformanceConcrete (UHPC) 3D compression test data 187
16.2.3 Mapping of Grey-cast Iron Test Data 189
16.2.4 Mapping of Glass C 90 Test Data (window pane of ISS) 191
16.2.5 Mapping of Porous Foam Rohacell 71 IG Test Data 192
16.3 Mapping 3D Test Results of UHPC and Rocks obtained on the Meridians TM and CM 198
16.4 Mapping of 3D Ultra-High-Performance-Concrete UHPC (relatively dense) Test Data 200
16.5 Mapping specific Sandstone Test Data 206
16.6 Do we accurately apply accurate isotropic SFCs? Example Normal Concrete test data 210

16.6.1 Comparison with Drucker-Prager's global SFC a rotationally-symmetric conical fracture body 210
16.6.2 Cuntze's modal SFCs, rotationally-symmetric body version 211

17 'Brittle' Transversely-isotropic UD Materials 213
17.1 Proposal of a 2D Yield Condition SY 213
17.2 3D-SFCs of Dense UD Materials 213
17.3 3D-SFCs of Porous UD Materials 216
17.4 'Proportional Stressing' versus 'Design Driving Stress' concept and "Failure Index 217
17.5 Comparison of 2D-UD-Strength Failure criteria: Which one should I take? 218
17.5.1 SFC Hashin, 4 failure modes 218
17.5.2 SFC Tsai-Wu, global SFC 219
17.5.3 SFC Puck, failure mode-based, IFF conditions interacted by Master Fracture Body approach 219
17.5.4 Comparison of the mapped four different SFC Failure Envelopes 223
17.6 Computation of a SFC-linked Reserve Factor 225
17.7 On Modelling General Laminates 225

18 Brittle Orthotropic Materials 227
18.1 Fabric Properties Specifics 227
18.2 3D-SFCs of Orthotropic Fabrics 228
18.3 2D-Mapping of shear stress-normal stress τ_{WF} (σ_W) with Test Data Evaluation 228

19 World-Wide Failure Exercise Contribution with Evaluation of Test data 232
19.1 General 232
19.2 Mapping of some UD-material World-Wide-Failure-Exercises-I and -II Test Cases (TC) 234
19.2.1 Failure Stress state $\tau_{21}(\sigma_2)$ 234
19.2.2 Failure Stress state $\tau_{21}(\sigma_1)$ 235
19.2.3 Failure Stress state $\sigma_2(\sigma_1)$ 236
19.2.4 WWFE-II, UD lamina 237
19.3 Gaps and Shortfalls in the experimental data sets of the WWFE-II TCs 237
19.3.1 '2ndTg-effect' in the various ultrahigh-compressed TCs 237
19.3.2 Some Conclusions from the necessary effortful evaluation of the WWFEs 238
19.3.3 Some final remarks with Lessons Learned 239
19.3.4 Open or closed failure surface? A recurring question in WWFE-II 240
19.4 WWFE-II, ranking and the citation" *Cuntze's SFC-set needs 75 parameters*" [*Kad13*] 241
19.5 WWFE-provided Mechanical Properties of the UD laminas 242

20 Laminate 2D-Design with Tsai's 'Omni Failure Envelopes' 243
20.1 Tsai's indirect Determination of the 2D 'Omni principal FPF strain failure envelope' 243
20.2 Cuntze's Determination of the 2D 'Omni Envelope' 244
20.3 Pre-design Example using the 'Omni Non-FPF area' and Determination of Reserve Factors 245

21 Investigation on Criticality of Carbon Fiber Micro-Fragments and Dusts 249
21.1 General 249
21.2 Carbon Fiber Production 249
21.3 WHO-'Fiber' hazard criticality 250
21.4 Fact & Idea to sort out Application-carefree Fibers 252

22 Derivation of Mohr-Coulomb Curve and Cohesive Shear Strength Values 254
22.1 Improved Mohr-Coulomb Curve and Cohesive shear Strength R^{τ} of Isotropic materials 254
22.1.1 General 254
22.1.2 Assumption of Otto Mohr 254
22.1.3 Note on the Mohr-Coulomb (M-C) criterion (also see § 26.1) 255
22.1.4 3D-SFCs regarding material-inherent 120°-rotational symmetry of isotropic fracture bodies 255
22.1.5 Improved Mapping of Failure Stress data to obtain a more realistic $\theta_{fp}°(\vartheta)$ 257
22.2 R^{C}-extrapolation-based estimation of cohesive strength R^{τ}, M-C curve $\tau_n(\sigma_n)$ and angle $\theta_{fp}°$ 259
22.3 Accurate Mode-interactive determination of R^{τ}, M-C curve, fracture angle $\theta_{fp}° > \theta_{fpc}°$ 260
22.4 Application to Normal Concrete - computation data input 261
22.5 Results: Extrapolation Solution Path Variants $\Theta_{fp}°(F^{\tau})$ 261
22.6 Results: Accurate Mode interaction Solution Path $\Theta_{fp}°(F\tau, F\sigma)$ 263
22.7 Results: Guessing a Cohesive Strength value R^{τ} considering $f\sigma$ 264
22.8 Full UD-Mohr Envelope $\tau_{nt}(\sigma_n)$, Derivation of $\Theta_{fp}(\sigma_n)$ and of Cohesive shear Strength 266
22.8.1 Relations for a Transformation from a Test Fracture Curve $\sigma_3(\sigma_2)$ to Mohr's $\tau_{nt}(\sigma_n)$ 267

22.8.2 Accuracy Problem of the IFF2-model in the transition zone IFF2 (SF) - IFF1 (NF) 267
22.8.3 Improvement of the IFF2 Criterion in the Transition Zone, Figs.22-8 and 22-9 268
22.8.4 Determination of Cohesive shear Strength R_{23}^{τ} 271

23 Nonlinear Design Verification regarding MoS_{yield}, MoS_{ult} for Ductile Materials 273
23.1 Inelasticity topics of ductile and brittle materials 273
23.2 Thoughts before performing Linear Analysis and Non-linear analysis 274
23.3 General on the Stress-strain Curves to be used 275
23.4 Notes on Dimensioning and Verification concerning Stress and Deformation 279

24 Finite Fracture Mechanics (FFM) for Investigating Statically-loaded Notches 283
24.1 List of Symbols 286
24.2 Analysis using the Crack Growth Resistance curve = 'R-curve' 287
24.2.1 General on Fracture Mechanics quantities and R-curve Concept 287
24.2.2 Models for R-curve (resistance) and for Stress Intensity Factor (SIF)-curve 288
24.2.3 Conditions to Determine the unknown critical quantities σ_c , a_{ce} 289
24.2.4 Solution of the Equation set to Predict the Unknowns 290
24.3 Analysis using Finite Fracture Mechanics (FFM) 292
24.3.1 General 292
24.3.2 Introduction 293
24.3.3 FFM-model focusing isotropic dense material 294
24.4 Design Verification of a 'Through center cracked Open hole Panel' 295
24.4.1 Application of FM, R-curve, concerning 'Open hole panel fracture', pre-crack a_0 296
24.4.2 Application of FFM, concerning 'Onset-of-Cracking' at a non-cracked Open Hole edge 298
24.5 Application of the FFM to a Test Data-based HSB-example 302
24.6 Some Conclusions 305
24.7 Annexes 306

25 Influence of low Cross-sectional Shear Rigidity and Rotatory Inertia on the Critical Speeds of Shafts 310
25.1 Introduction to this Gas-Ultra-Centrifuge-driven Elaboration 310
25.2 Theoretical Relations , Shaft with Uniformly Distributed Mass 310
25.3 Range and Limit Value considerations 312
25.4 Results 312
25.4.1 General information on the evaluation of results 312
25.4.2 Presentation of the Correction Coefficient curves 313
25.5 Numerical Example 316

26 Note on Application of Shell-Tensor-Analysis to Filament Winding 319
26.1 Introduction 319
26.2 Tensorial Derivation of Clairaut's Condition for Geodesic Lines on bodies of revolution 319
26.3 Filament Wound Pressure Vessels and some Practice at MAN Technologie (> 1971) 321
26.4 Application of winding technology, re-calculation of a Kevlar tank 324

27 References, Papers, Presentations & MAN reports 327
27.1 References 327
27.2 Some further works, presentations of the author and MAN reports 334

Acknowledgement (see details in [CUN25]*) 339

Other Works of the author (*see* also: Carbon-connected.de/Group/Prof.Ralf.Cuntze)

If one might be interested one can find information on the following subjects in the author's compilation [*CUN22-23*], especially on various projects at MAN the author was involved.

18 Structural Vibration and Work Cases 586

18.1 General on Oscillation/Vibration 586

18.2 Damping and Damped Vibrations 591

18.3 The Influence of Dead Mass and Elastic Clamping on the Bending frequency of a slender Tower with linearly reducing Thickness (1969) 594

18.4 Natural Frequencies of Thin Inclined Isotropic Plates (*Cuntze, 1969*) 598

18.5 Natural Frequencies (eigenfrequencies) of Orthotropic Deep Beams (Dissertation, 1968) 603

18.6 The Influence of Cross-sectional Shear Flexibility and Rotatory Inertia on the Natural Frequencies of Beams with Uniformly Distributed Mass (1983) 616

18.7 Analysis of the Natural Frequencies of Laminated Beams of low 'Shear-rigidity' 624

18.8 Influence of low Cross-sectional Shear Rigidity and Rotatory Inertia on the Critical Speeds of Shafts with Uniformly Distributed Mass *(1984)* 627

18.9 Natural Frequencies of a Cracked Beam for Production Quality-testing of Rotor blades 637

18.10 Equivalent Sinusoidal Acceleration corresponding to an Excitation by Random Vibration 641

19 Some Flywheels and Rotors 643

19.1 Metallic Energy storage Flywheel for the floating crane ship Swartow (1982) 643

19.2 A New concept of a Composite Flywheel due to novel fiber-reinforced materials (1988) 649

19.3 An Axial Energy Storage Rotor, the 'EnWheel' (2015) 653

19.4 Increasing the Limit of Usability of CFRP Tubes by Built-in-Stresses (1993) 664

19.5 The Large Windmill GroWiAn GROWIAN (1977-1982), development and build 678

19.6 Design of a Fiber-reinforced Gas-Ultra-Centrifuge Cylinder, GUZ (1971-1986) 696

20 Some Winding Theory of Filament Wound Pressure Vessels 702

20.1 Introduction 702

20.2 Geometry of the Rotation Shell with Bottom Equilibrium Equations 704

20.3 General Fiber Net-shell 707

20.4 Meridian Shape (contour) of the Vessel Bottom under Internal Pressure 710

20.5 Contour of the Fiber Net-shell Bottom under Centrifugal Loading *(Fig.3f)* 715

20.6 Theoretically Possible and practically Feasible Winding Contours 718

20.7 Winding Patterns 723

20.8 Applications of Winding Theory at MAN Technologie 725

Life-Work *Cuntze* - a compilation Living Document edition 29mar23 12

20.9 Application of winding technology, re-calculation of above AFRP tank (1975) 729

*The kernel of the present document bases on a reworked content of the [*CUN25*, CV Ralf Cuntze].

*From the compilation 'Life-Work Cuntze' [*CUN22*-23] a uranium centrifuge-caused rotor dynamics work and a pressure vessel production dedicated filament winding-linked elaboration were added as last sections.

0 Introduction

0.1 Ralf Cuntze CV in short

1939 born Sept 8 in Erfurt, Thuringia. Thankful for surviving bombing at the city Erfurt and a head-narrow machine gun fire at the war's end, when the US troops captured his home village

1964: Dipl.-Ing. Civil Engineering CE (construction, ***TU Hannover***). 1968: I was promoted Dr.-Ing. in Structural Dynamics (CE) on 'Structural Vibrations of deep beams'. 1978: I have habilitated from industry Dr.-Ing. habil. Venia Legendi in Mechanics of Lightweight Structures (CE, TU-Munich)

1980-1983: Lecturer at *Universität der Bundeswehr München*: on 'Fracture Mechanics' in the construction faculty and 1990-2002 on 'Composite Lightweight Design' in the aerospace faculty

1987: Full professorship 'Lightweight Construction', *not started in favor of interesting industry tasks*

1998: Honorary professorship at Universität der Bundeswehr München.

1968-1970: Finite Element Analysis-programming (***DFVLR*** at the airport Essen/Mühlheim)

1970-2004: to ***MAN - Neue Technologie*** (München, Augsburg) instead of being ***DLR***-Postdoc at Stanford University. Headed the Main Department 'Structural and Thermal Analysis'. Thereby facing 50 years of life with Fibers: CarbonF, AramidF, GlassF, BF (bor), Bs(basalt)F.

*Theoretical fields of work: structural dynamics, finite element analysis, rotor dynamics, structural reliability, partial/deterministic safety concepts, material modeling and model validation, fatigue, fracture mechanics, design development 'philosophy' & design verification

*Mechanical Engineering applications at ***MAN****:* ARIANE 1-5 launcher family (design of different parts of the launcher stages, inclusively Booster), propellant motor cases MAGE, IRIS, Cryogenic Tanks, High Pressure Vessels, Heat Exchanger in Solar Towers (GAST Almeria) and Solar Field, Wind Energy Rotors (GROWIAN Ø103 m, WKA 60, AEROMAN. MAN-bus SR 240, Wendelstein VII. Probably the first world-wide wind energy conferences organized in 1979 and 1980 together with Dr. Windheim, PLR Jülich). Space Antennas, IRAM antenna, SOFIA telescope (2003), Automated Transfer Vehicle (Jules Verne, supplying the space station ISS), Crew Rescue Vehicle (CMC application) for ISS, Carbon and Steel Gas-Ultra-Centrifuges for Uranium enrichment. Filament winding theory, Structural Material Databank etc.

*Civil Engineering applications, private: Supermarket statics, armoring plans, pile foundation, 5th German climbing garden (1980 designed, concreted and natural stone-bricked)

1971-2010*:* Co-author in ASMIEG-WG of ***ESA/ESTEC***-Structural Materials Handbook, Co-author and first convener of the ESA-Buckling Handbook and co-author in ECSS-Engineering standard systems Working Groups (WGs) for 'Structural Analysis', 'High Pressure Vessels' (metals and composites) and 'Safety Factors'

1972–2015, ***IASB-member***: WG of Luftfahrt-Technisches Handbuch HSB '*Fundamentals and Methods for Aeronautical Design and Analyses'*. Author and Co-author of numerous HSB sheets and about 2006-2008 co-transfer with co-translation of the HSB aerospace structural handbook into its present English version. That working Group, where I learned most!

1980-2011: **Surveyor/Advisor** for German BMFT (MATFO, MATEC), BMBF (LuFo) and DFG

1980-2006: **VDI Guideline 2014**, co-author of Parts 1 and 2, Beuth Verlag '*Development of Fiber-reinforced Plastic Components'* and of Part 3 *'Analysis*', editor/convener/co-author

1986 and 1889: One week **FRP-lectures** on composite design in Pretoria, SA

2000-2013: World-Wide-Failure-Exercises **WWFE** on Uni-directional fiber-reinforced materials (UD) strength: WWFE-I (*2D stress states)* non-funded winner against institutes of the world, WWFE-II (*3D states*) top-ranked

2009-2021 linked to ***Carbon Composites e.V***. at Augsburg, later ***Composites United CU e.V.*** and to TUDALIT Dresden. Since 2011 working on the light weight material Fiber-reinforced (polymer) Carbon Concrete. **Founded and headed the working groups**: (1) 2009: 'Engineering' linked to the WG Non-Destructive Testing and the WG Connection Technologies, mechanical engineering. (2) 2010: 'Composite Fatigue'. In 2010 the author held an event that was excellently attended by international speakers. (3) 2011: 'Design Dimensioning (*Auslegung, Bemessung*) and Design Verification (*Nachweis*)' mainly for carbon concrete. This working group was the foundation stone for the later specialist network ***CU Construction***, aiming at *"Fiber-based lightweight construction*". (4) 2017: 'Automated fabrication in construction including serial production' *("3D-Print")*. (5) 2020, 2021: Forum 'Carbon concrete for practice' at the well-known 'Ulm Concrete Days'

2010: Founder of the Germany-wide Working Group BeNa to base fatigue life prediction 'embedded lamina-wise' in order to become more general in future fatigue life design

2019: *__GLOSSAR__ "Fachbegriffe für Kompositbauteile - *technical terms for composite parts*". Springer 2019. Edited at suggestion of carbon concrete colleagues to improve mutual understanding

2022: **Life-Work Cuntze - a compilation from the author's papers, presentations, published and non-published design sheets and project works in industry* (850 Pages, more design work-related)

2023 etc: **Design of Composites using Failure-Mode-Concept-based tools - from Failure Model Validation to Design Verification*. Mechanics of Composite Materials, Vol. 59, No. 2, May, 2023, pp. 263-282. **Minimum Test Effort-based Derivation of Constant-Fatigue-Life curves, displayed for the brittle UD composite materials*. Mechanics of Composite Materials, Springer, Advanced Structured Materials, Vol.199, 107–146, draft.

*Cuntze R and Kappel E: *Benefits, applying Tsai's Ideas 'Trace', 'Double-Double' and 'Omni Failure Envelope' to Multiply UD-ply composed Laminates?*

* *UD-Strength Failure criteria: Which one should I take*? * Elaboration on Finite Fracture Mechanics.

The various projects at MAN made it necessary - in addition to the 'personnel work' -
to provide employee support in my department by my taking care of material models.

Pursued strength-related ideas of the authors macro-scopic "Failure Mode Concept":

1. Thinking and Modelling in mutually independent Failure Modes with the use of the mode-linked material stressing effort *Eff*, the German Werkstoffanstrengung
2. An invariants-based generation of associated Strength Failure Criteria considering just measurable SFC-model parameters. This includes the measurable friction value μ, instead of fictitious model parameters
3. Provision of the minimum number of material properties required by material symmetry for the three material families isotropic, transversely-isotropic UD and orthotropic material
4. Viewing material families with dense, porous, ductile and brittle characteristics not a special material, because the same behavior links materials
5. Working with equivalent stresses, $\sigma \Rightarrow \sigma_{eq}$ (the FMC *beginning was with UD!*).

The presented novel scientific ideas invite for discussion.

* such marked p*reprints, drafts are fully open for the public and are downloadable from*
https://www.carbon-connected.de/Group/Prof.Ralf.Cuntze or partly from Research Gate.

Some accompanied essential Technical Projects at MAN-Technologie (1970-2004)

Dr. Zippe's Original Gas Ultracentrifuges for uranium-235 enrichment, single-stage. (secret), see [CUN25]

Wind Energy Rotor GROWIAN, 1980, 51 m blade, Profile NACA 44, 3 MW electric power. GFRP shell with wind speed measurement facility.

CFRP Booster section 2001

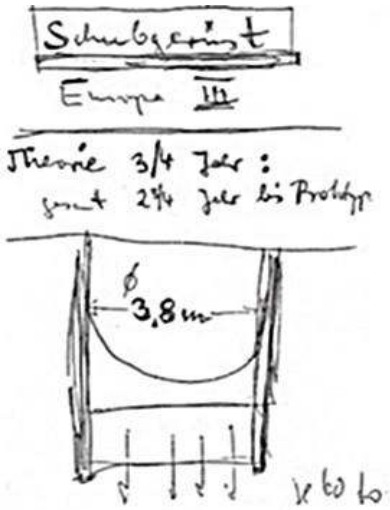

Start of my work at MAN Technologie: Make a design proposal, an offer for a Thrust Structure, please. September 1970

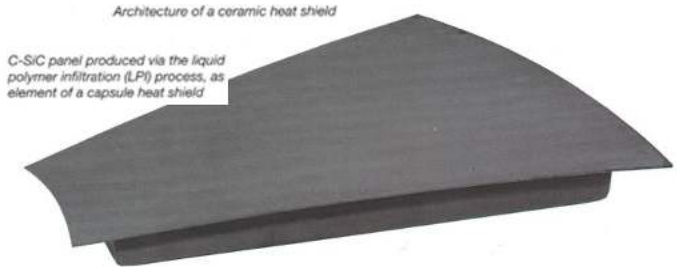

C-SiC panel, part of a re-entry heat shield

Airbus A330/340 drinking water tanks

Ariane Launcher 1-5

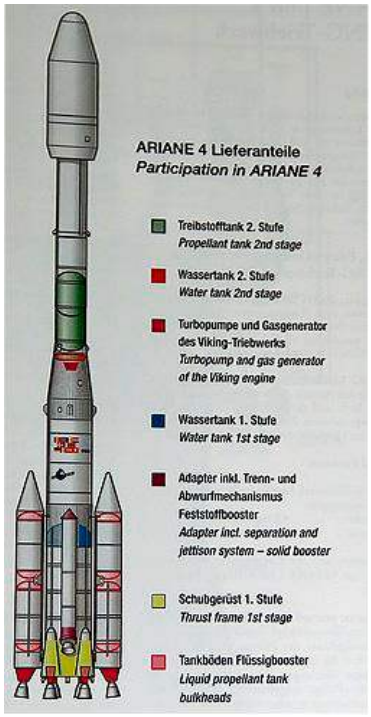

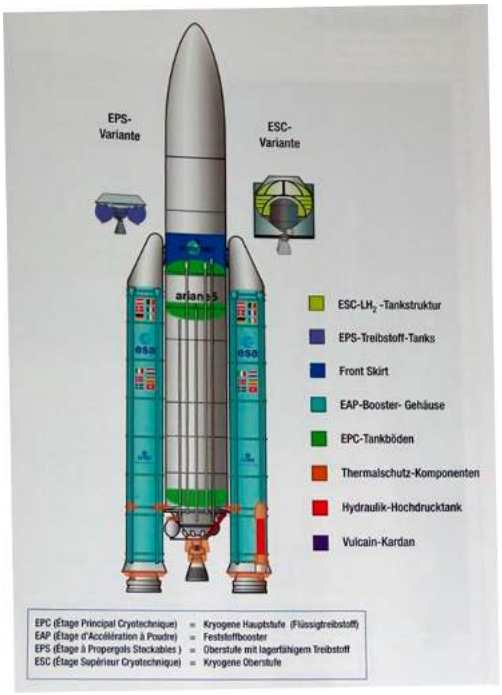

The Civil Engineer (my work in the Mechanical Engineering domain is compiled in [CUN 22]).

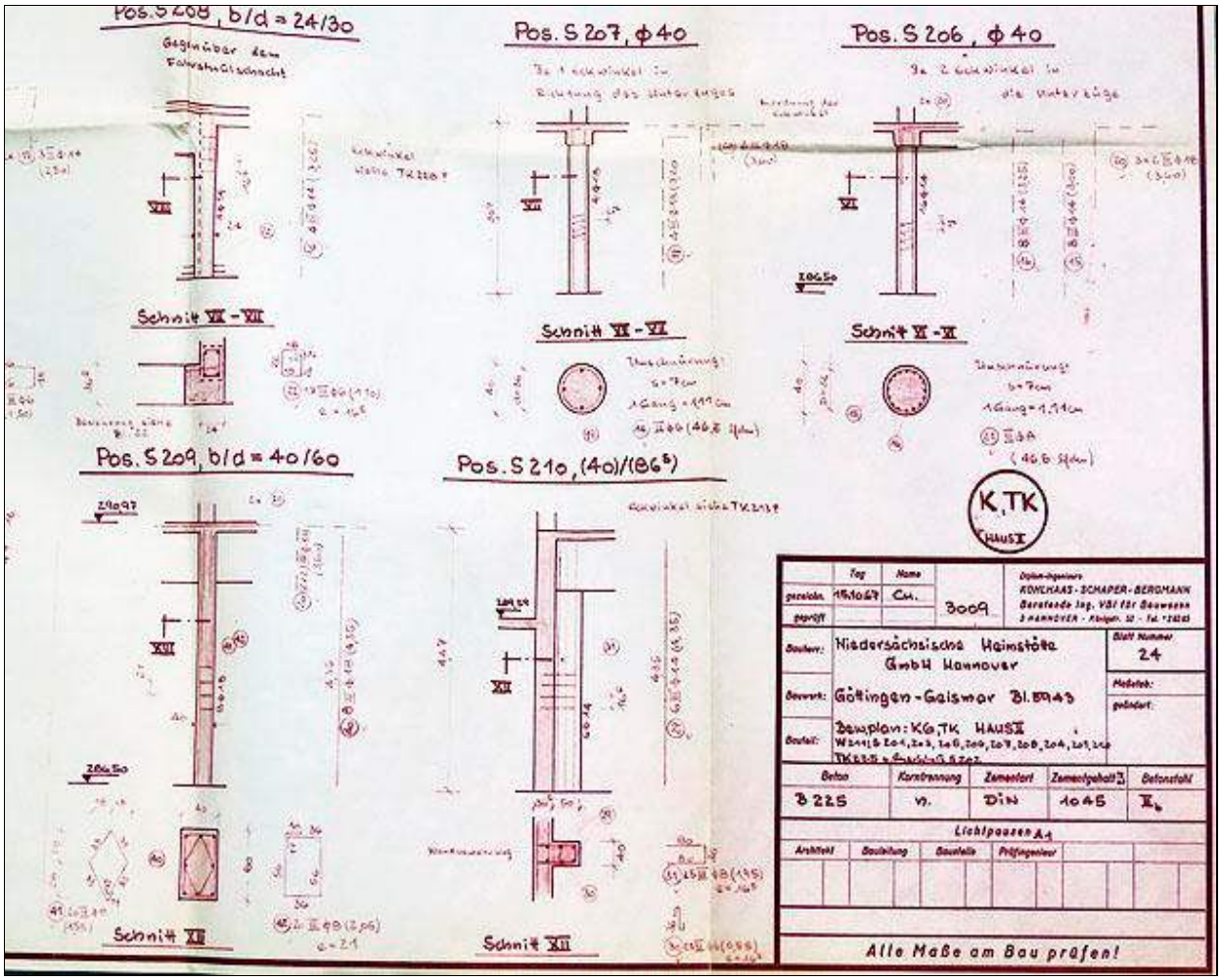

* **Working as a Bricklayer:** 1959, 1960
* **Working as a Structural Engineer** (in German the precise description Tragwerksplaner = a civil engineer with comprehensive knowledge of both the statics of load-bearing structures and the material-specific design (concrete and reinforced concrete construction, timber and steel construction, foundation engineering, etc.)

1964-1968: Freelance worker at the engineering office Kohlhaas-Schaper-Bergmann in Hanover,
1978 onward: Structural engineering, armoring plans.

Working in different disciplines made to become an

application-oriented engineer with a scientific touch for material modelling and with the hope to be some bridge-builder between mechanical and civil engineering ***(****construction).*
*Some construction links below mean 'back to my roots'****.***

Co-working when building his new house in 1976

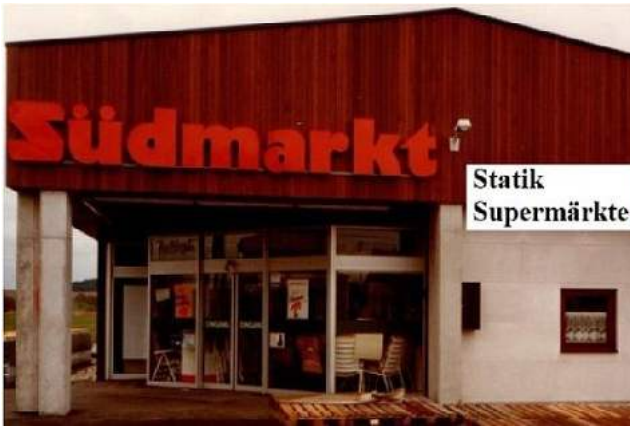

Structural engineering, armoring plans, pile foundation

Example: Südmarkt Pöttmes, with pile foundation.

Late soil investigations made the unexpected driving of piles necessary. However, their installation was not structurally sound, and this had to be reported to the client.

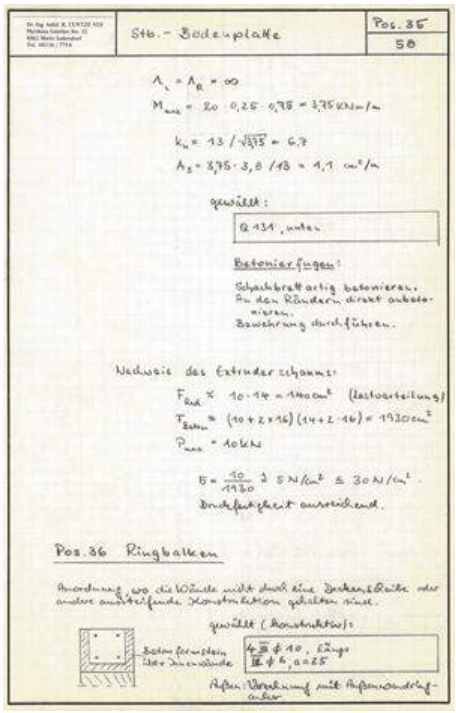

a page from a structural analysis in civil engineering

Lived Working Group (WG) - ‘Hobbies’

HSB
HANDBUCH STRUKTUR BERECHNUNG

General description

Issue E Year 2018
Page 1 of 21

Luftfahrt-Technisches Handbuch (LTH)

HSB

HANDBUCH STRUKTUR BERECHNUNG

Fundamentals and Methods
for
Aeronautical Design and Analyses

issued by

iasb INDUSTRIE-AUSSCHUSS-STRUKTUR-BERECHNUNGSUNTERLAGEN

Prepared:	Checked:	Date:	
Dr. M. Schagerl	Dr. M. Magin	22.11.2018	IASB / IVW

IASB, July 1972-2025:
HSB, “German Aeronautical Handbook” (‘Airbus structural design sheets folder’, Design sheet contributor Co- reworker and Co-translator of the initial HSB into English (2004)

FORTSCHRITT-BERICHTE VDI

R. Cuntze, R. Deska und B. Szelinski, Karlsfeld
R. Jeltsch-Fricker und S. Meckbach, Kassel
D. Huybrechts und J. Kopp, Aachen
L. Kroll, Dresden
S. Gollwitzer und R. Rackwitz, München

Neue Bruchkriterien und Festigkeitsnachweise für unidirektionalen Faserkunststoffverbund unter mehrachsiger Beanspruchung – Modellbildung und Experimente –

Reihe **5**: Grund- und Werkstoffe Nr. **506**

Project leader of the funded Research on
“UD Fracture Criteria,
investigating Puck ‘s Strength Criteria”.
***Issued 1997*“**

View of the
Completion-effort of the VDI guideline 2014
(*meaningful drawing from my deputy S. Schneider in 1989*).

It was the right view:
I edited the guideline in *2006!*
(after alltogether 25 years)

(author is an old VDI member)

Founding of 3 WGs with Carbon Composite e.V. and then with Composites United

Joint meeting of the 3 CCeV WGs:
Engineering, Non-destructive material and component testing, Adhesive and joining technology

CARBON COMPOSITES

Gemeinsame Sitzung der 3er-CCeV-AG
Engineering, Zerstörungsfreie Werkstoff- u. Bauteilprüfung, Kleb- und Verbindungstechnik,

am 9. 3. 2018 beim CCeV, Am Technologiezentrum 5, D 86159 Augsburg
CCeV-Kontakt Bernhard Jahn (Bernhard.Jahn@carbon-composites.eu).

Agenda (Folien deutsch oder englisch, 25 + 5 min)

9:00	**Begrüßung**
9:15	Vortragstitel. *NN, LCC, München (Kümmerer Dr. Hartmann)*
9:30	**Betrachtungen zur Betriebsfestigkeit von CFK-Triaxialgeflechten.** *F.Herrla, Institut für Leichtbau, UniBw, Neubiberg*
10:00	**Novel Lifetime Prediction for UD-materials.** *R. Cuntze, CCeV Augsburg*
10:30	*Kaffeepause*
11:00	**Schwingfestigkeit von Klebverbindungen unter multiaxialer Schwellbelastung.** *C. Nagel, IFAM Bremen*
11:30	**Festigkeitssimulation in Klebverbindungen.** *R. Sachse, DLR Stuttgart*
12:00	**Einbeziehung geklebter Fensterbänder und Glasfronten in die Festigkeit von Schiffen.** *O. Klapp, IFAM Bremen*
12:30	*Mittagspause*
13:30	**Carbon Fiber Armored Polymer – a novel economic process?** *R. Müller, Kube GmbH Ingenieurbüro, Plochingen*
14:00	**Konzentrierte Lasteinleitung in CFK-Strukturen unter Anwendung der lokalen Metall-hybridisierung.** *E.Petersen, DLR Braunschweig*
14:30	**Faseroptische Prüfmethoden zur Inspektion von CFK-Komponenten.** *D. Samiek, Polytec GmbH*
15:00	*Kaffeepause*
15:30	**Koppelmittelfreie Prüfung von CFK und CFK-Metall-Klebeverbindungen mit Hilfe von Luftultraschall.** *R. Steinhausen, Forschungszentrum Ultraschall*
16:00	**Einsatz des Nichtlinearen Ultraschalls für die Untersuchung geklebter CFK-Strukturen.** *M. Kreutzbruck, Institut für Kunststofftechnik, Uni Stuttgart*
16:15	**Resumee, Abschlussdiskussion**
	Get Together

Wir freuen uns auf eine rege Beteiligung und interessante Vorträge

Ihre Ralf Cuntze (08136-7754), Marc Kreutzbruck und Markus Brede

Hinweise: Sitzungstermine: 16. 11. 2018, gemeinsam mit CC Austria, FH OÖ Campus Wels (Österreich), Dr. R. Hinterhölzl (Leiter Studiengang Leichtbau und Composite-Werkstoffe); 8. 3. 19 UniBw, Neubiberg (Institut für Luft- und Raumfahrt, Prof. H. Rapp)

WG Engineering in mechanical mechanics: Logically unified meetings with the WGs NDI and Joining Technology

"Carbon concrete-Applications in practice - on the construction site and in the precast plant"

BETONTAGE CONCRETE SOLUTIONS

COMPOSITES UNITED BAU

CC Bau-Forum
"Carbonbeton-Anwendungen in der Praxis
- auf der Baustelle und im Fertigteilwerk"
Transformation von praktischem Anwendungswissen.
Zielgruppe: Hersteller, Sanierer, Vertreter der Betonbranche
am 25. Februar, Donnerstag, als Podium integriert bei den Ulmer Betontagen vom 23. - 26.02.2021

25 min Vortrag + 5 min Diskussion. Folien: deutsch oder englisch. Vortrag: falls möglich möglich deutsch

08:30	*Kaffeepause – Networking*
09:00	**Einführende Worte** *Prof. Dr.-Ing. habil. Ralf Cuntze, CU Bau, Augsburg. Composites United e.V. CUeV (formerly CCeV)*
09:15	**Digitale Entwicklung – von der Faser zum textilen Gelege.** *Roy Thyroff, rothycon – Roy Thyroff Consulting, Naila*
09:30	**Carbonbeton: Zwischen Theorie & Praxis.** *Dipl.-Ing. Oliver Heppes, GOLDBECK Bauelemente Bielefeld SE*
12:10	**Größer, stärker, wirtschaftlicher - Carbonbewehrungen in neuen Dimensionen.** *Dipl.-Ing. Stephan Gießer, Solidian, Albstadt*
12:40	***Mittagspause und Besuch der Ausstellung***
14:00	**Tragwerksplanung des C³–Ergebnishauses „CUBE" – Bemessung, Nachweisführung und Zulassung im Einzelfall.** *Dipl.-Ing. Hendrik Ritter, Assmann Beraten und Bauen, Dresden*
14:30	**Modulare Brückenbauwerke aus Carbonbeton** *M.Sc. Sven Bosbach, Lehrstuhl und Institut für Massivbau, RWTH Aachen*
15:00	**Bauen mit CPC-Carbonbetonplatten, einer komplett neuen Bauweise in Beton – Verfahren, Konstruieren, Bemessen.** *Prof. Joseph Kurath, ZHAW Winterthur, Schweiz*
15:30	**Stadtbahnbrücke Stuttgart: CFK-Zugglieder finden Akzeptanz.** *Prof. Dr. Urs Meier, EMPA, Dübendorf, Schweiz*
16:00	**Ausgewählte Ingenieurbauwerke - nachträgliche Bauteilverstärkung mit Carbon-Faser-Kunststoffen „CFK" (geklebte Lamellen).** *Dr.-Ing. Horst Peters, HPTL Carbon GmbH, Ditzingen*

Ihr Ralf Cuntze und der weitere Vorstand des Netzwerks CU Bau

Weitere Termine 2020 / 2021 des Netzweks CU Bau:

- 19.11. 2020: CU Thementag „Richtlinien, bauaufsichtliche Zulassungen und Bauartgenehmigungen für die potenziellen Anwender Architekten, Tragwerksplaner und Bauherrn". Zoom-Konferenz
- 17.03.2021: Thementag aller Arbeitsgruppen des Netzwerks CU BAU mit TU Chemnitz. Zoom-Konferenz?
- 30.03.2021: 4. Thementag der AG „Automatisierte Fertigung im Bauwesen inkl. Serielles Bauen". Zoom-Konferenz?

Das Netzwerk CU Bau, besteht aus 4 Arbeitsgruppen: Bemessung und Nachweis (Prof. Ralf Cuntze), Faserverbundarmierter Beton (Dr. Ingelore Gaitzsch), Faserverstärkte Kunststoffe (Prof. Jens Ridzewski), Automatisierte Fertigung im Bauwesen inkl. Serielles Bauern (Cuntze)

Agenda Carbonbeton-Forum Ulmer Betontage Cuntze 21okt20

WG Engineering in construction and WG '3D-printing'

Purpose of the Glossary:

Borders between engineering disciplines are disappearing, more and more. It can also be noticed that in the different fields of the fiber-using industry there are different "speeches" and that technical terms are sometimes used very differently. Several groups of engineers would therefore have to be connected conceptually so that they understand each other correctly when making decisions. These are 'constructive' engineers from building industry and mechanical engineering and further, engineers from the textile and material range as well as from manufacturing. This glossary focuses especially on carbon fibers CF and concrete matrices. At the beginning it presents a first scheme of order for the different, interconnected disciplines. At the end, a picture gallery illustrates technological details and applications. This gallery just includes carbon applications from construction industry.

"Scientists would rather use someone else's toothbrush than someone else's terminology" (*Nobel laureate Murray Gell-Mann****)***

As the ESA-appointed organizer of the right handbook, I had the opportunity to integrate existing, extremely valuable stability test results, because it was still possible to invite retired former officials to participate in the working group.

⇒ A successful preservation of expensive test data knowledge.

ECSS-E-HB-32-24A
24 March 2010

EUROPEAN COOPERATION
ECSS
FOR SPACE STANDARDIZATION

Space engineering

Buckling of structures

ECSS Secretariat
ESA-ESTEC
Requirements & Standards Division
Noordwijk, The Netherlands

This Handbook has been authored and agreed
J. Arbocz, TU Delft
C. Bisagni, Politecnico di Milano
A. Calvi, ESA-ESTEC (Convenor)
E. Carrera, Politecnico di Torino
R. Cuntze, formerly MAN-Technologie
R. Degenhardt, DLR Braunschweig and PFH
N. Gualtieri, Thales Alenia Space
H. Haller, Intales
N. Impollonia, Università di Catania
M. Jacquesson, CNES
E. Jansen, TU Delft
H.R. Meyer-Piening, ETH Zuerich
H. Oery, RWTH Aachen
A. Rittweger, Astrium EADS
R. Rolfes, Leibniz Universitaet Hannover
G. Schullerer, MT Aerospace
G. Turzo, CNES
T. Weller, Technion, Haifa
J. Wijker, Dutch Space
The valuable contributions of the following per
C. Huehne, DLR Braunschweig; D. Petry, A
H. G. Reimerdes, RWTH Aachen; K. Rohwe
R. Zimmermann, DLR Braunschweig.

The ECSS-E-HB-32-24 has been prepared by merging the volunteer contributions of the
Comments concerning the technical content of this handbook will be welcomed by the E
Cooperation for Space Standardization, Noordwijk, the Netherlands, www.ecss.nl.

Affiliations

> 50 years VDI
(Association of German engineers)

> 40 years DGLR
(German Association for Aircraft and Spacecraft)

10 years ‘L’Ordre des Coteaux de Champagne’
For enjoyment!

30 years ‘Chaine de Rotisseurs’
For enjoyment!

The author after the yearly ‘pilgrimage’

Kloster Indersdorf (home) ↔ Kloster Scheyern
to and back , 44 km (26 miles):
9 h, 9 min, 9 s ?.
2025, September
Being able to make this hike was a thankful 86 year’s birthday present for me.

My empowering side, not to forget**: Gardener, Globetrotter and Photographer**

Cabin: 80cm x 80cm x 210cm

The relative narrowness of a ROTEL sleeping cabin helped the author to explore the wide world of nature

Daily ROTEL bus cleaning job

DAV = German Alpine Club > 50 Years

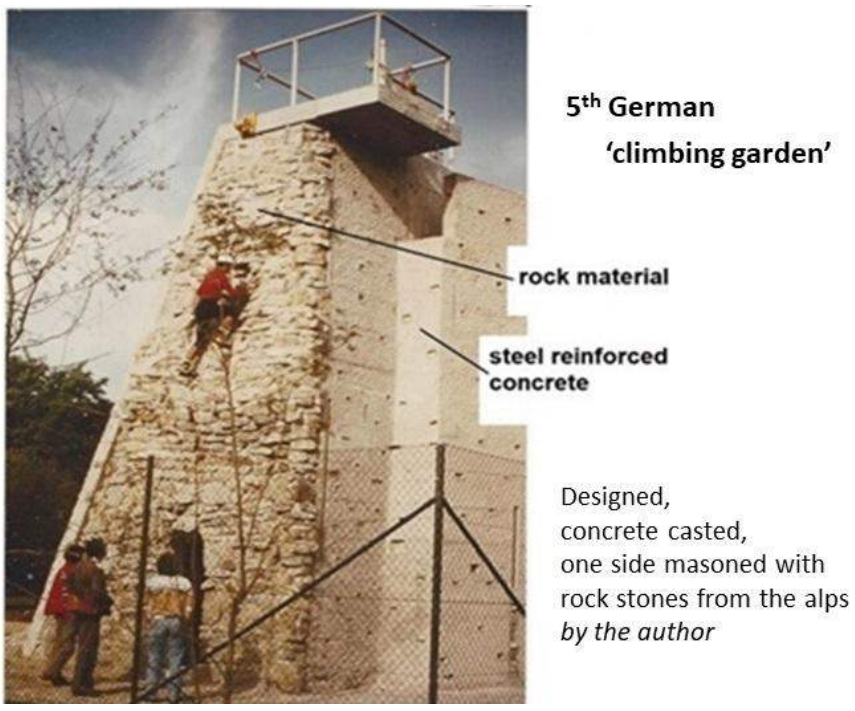

Our local Alpine club ‚My rock', built 1979

Hiking tour with the club ⇒

The Hobby Photographer**: some special Pictures from home and vicinity**

breeder of winter Alpine lillies

beautyful Gentiana: > 40 years old flower!!

anemone

Edelweiss flower on November 30, 2024, i in snow. 8 months too early!
The gardening engineer, July 2025 ►

dragonfly on floating leaf

← dragonfly on a Nuphar Lutea

a nice young frog couple in love (a year later by chance I saw when she ran away from him!)

If the amphibian became too intrusive, *he* was quickly swept away with a butterfly-caterpillar's tail hit

my amphibians at the wedding dance

my cat MAUSI, relaxing

← hummingbird hawk-moth

March: a weary hare

common buzzard

robin

Doesn't that deer look great?

Altogether there were 13 deer on our standard walk within our village

the very rare goldcrest
in front of our kitchen window

dovetail in the garden

family discussion

Feeding sparrow mum: Stuff in

ringdove

Interested mouse

great tit

blue tit

star

marsh tit

wasp spider

midday flower

magpie

sparrow with star

swallow

wild bee

wasp nest

black swans in our little river Glonn

Kiebitz Sperber Turmfalke

bumblebee approaching

A few Pictures from afar

Invited for a vulcanic exploration in beautiful Kamchatka

Beautiful dragonfly

Oman:1 dromedar + 1 bush

Mind the moon

If of interest? Much more referring pictures can be found in the country picture annexes of the [CV Ralf Cuntze]

Tiger Nest in Bhutan,

high up

Yemen, festivity

North-Korean border

Novel simulation-driven product development shifts the role of physical testing to virtual testing. This requires High Fidelity concerning structural and material models used. First and usual assumption for the material models is an ideally homogeneous material. Deviations are specifically taken into account.

Abstract

* Design Dimensioning Aspects, Design Verification and Safety Concepts: Enough Strength resistance must be generally demonstrated by a positive Margin of Safety MoS or a Reserve Factor *RF* = *MoS* - 1 > 1 in order to achieve Structural Integrity for the envisaged Design Limit State! For the 3D-Demonstration of Strength - nowadays a must regarding the usual 3D FEA stress output - principally so-called 3D strength criteria or 3D failure bodies are required to firstly perform Design Dimensioning and to finally achieve Design Verification. AND all this requires a clear terminology, which could be obtained with great effort!

* Failure-Mode-Concept (FMC): In the case of brittle materials the failure body is a fracture (failure) body. The surface of such a failure body is determined by the points of all those stress states that lead to failure. It is mathematically defined by a Failure function *F* which becomes 1 at Onset-of-Failure. Usually these *F*s are written as Strength Failure Conditions (SFC) *F* = 1, however are unfortunately termed Criterion. The SFC models consider - *following Beltrami, Hencky-Mises-Huber (ν =0.5) and Mohr-Coulomb (friction μ >0)* – that the solid material element may experience, generated from different energy portions: a shape change (HMH), a volume change and friction. The SFCs in this paper have been generated on above FMC.

* The FMC incorporates a rigorous thinking in failure modes and can be briefly described by the features: Failure mode-wise mapping, stress invariant-based *F*-formulation, equivalent stress generation for each material family σeq (isotropic, UD, orthotropic), each failure mode is governed by one strength R^{mode}, all SFC model parameters are measurable entities!

* This involves a novel direct use of the friction value μ in the case of compressed brittle materials where the fictitious model parameter for friction in the SFC can be replaced by the measured, merely scattering μ. To make this possible, the very challenging task to transform a SFC in structural stresses into a SFC in Mohr stresses had to be executed.

* The difference between a so-called 'Global' SFC and a '(failure mode-linked) Modal' SFC, such as with 'Mises Yielding', when mapping failure test data is pointed out. Further, terms such as mixed failure mode (mode interaction), multiple failure mode action and multi-axial strength are presented and discussed.

* During the derivation of the FMC a closer look at material symmetry facts was taken whereby the question arose: "Does a material symmetry–linked Generic Number exist with a number 2 for isotropic and 5 for UD materials? This looks to be proven by the novelties Normal Yielding NY of plexi-glass PMMA and compressive fracture toughness K_{cr}^{c} for ideally brittle materials. ►Such a Generic Number limits the test data amount!

* 'Modal' SFCs: If several failure modes are activated by the stress state then the application of the *material stressing effort Eff* (Werkstoffanstrengung) is very helpful because the full *Eff* consists of the mode portions Eff^{mode}. The contribution of each single Eff^{mode} informs the designing engineer about the importance of the single portions in the SFC and therby about the critical failure driving mode. Whereas the structural engineer is more familiar with the equivalent stress the material engineer prefers above 'material stressing effort' *Eff* . These terms are linked by $\sigma_{eq}^{mode} = Eff^{mode} \cdot R^{mode}$.

* 'Modal' SFCs are enlisted for a large variety of isotropic brittle structural materials such as porous Concrete Stone, Normal Concrete, UHPC sandstone, monolithic ceramics and for the transversely-isotropic fiber-reinforced polymers Lamina (ply, lamella) and Fabrics. Orthotropic fabrics inclusively fabric ceramics are further included. Associated fracture bodies are displayed with distinct cross–sections of them: Principal stress plane, octahedral stress plane and tensile and meridian planes.

* Various links or interrelationships between the materials are outlined. Different but similar behaving materials can be basically treated with the same SFC.

* Special attention is paid not only to the porous materials like grey cast iron, concrete, foam which possess a *convex* fracture failure surface, but also to the normal yielding experiencing plexiglass which possesses a *concave* fracture failure surface part in the principal tension stress domain!

* Novel automatic generation of Constant Fatigue Life curves considering Mean Stress Effect on basis of just a few tested Master SN curves together with a physically based model, namely Kawai's 'Modified fatigue strength ratio' Ψ . This procedure is applicable tor materials like UD plies and isotropic concrete as well.

* Evidencing 120°-symmetrical Failure Bodies of Brittle and Ductile Isotropic Materials.

* Thoughts about the non-criticality of Standard Fiber (T 300 grade) Micro-Fragments of CFR-Plastic/CFR-Concrete.

* Enabling a correct understanding of the often used diffuse cohesive strength value R^{τ}, a bi-axial fracture failure stress.

* Nonlinear isotropic Stress-Strain relationships and a proposal for a 'measurable parameter-based Extended Mises Model' to replace a multi-fictive, simulation-determined parameter 'Gurson model' parameter set.

* A first test data-based comparison of Cuntze's modal SFCs with the global isotropic Drucker-Prager SFC model and with the transversely-isotropic UD-SFCs namely the global Tsai-Wu, modal Hashin and modal Puck.

* A test-validated application of the novel Finite Fracture Mechanics to predict statically loaded open holes is presented

* Terminology, which shows no more contradictions between materials and the engineering disciplines construction, mechanical engineering!

The author asks for forgiveness in advance for inaccuracies, due to missing proofreaders.

0.2 Technical Terms with some Definitions and Abbreviations

Indexing is a chaos in the disciplines: It seems to be that the author could find (some years ago for the planned novel ESA –Material Handbook) a physically clear indexing system for the 3 material family models isotropic, transversely-isotropic UD and orthotropic materials (fabrics etc.). This indexing captures all material properties and allows a switching between. The author's Glossar 'Technical Terms' (Springer) together with the VDI 2014 guideline (*he was editor*) will hopefully generate some clarity.

- Automatic Fabrication AF an Additive ~~Manufacturing~~ process = Digitized process to make parts from 3D-model data. (1) Real 3D-print process: analogous to book printing the fabrication of pre-defoned single full cross section wide pretty thin (< mm) layers, openings are included in such a powder bed process. (2) Extruded strand deposit (~~3D print~~): Caterpillars, beads are deposited in a pre-defined path-oriented manner (> mm) to finally produce the full cross-section of the structural part.
- Allowable stress: $j \cdot$ allowable stress = strength design allowable
- Analysis: computation that uses fixed model parameters, such as those of the final design
- Closed and Open failure surfaces: Brittle dense isotropic materials under hydrostic pressure p_{hyd} do not fracture and thereby have an open failure surface. Porous isotropic materials fracture like the UD materials due to Poisson's ratio FF1-fracture under a very high p_{hyd} beyond some 1000 bar
- Design Principle: design of a structure is the result of the design principle chosen. Such design principles are 'fail safe', 'safe life', 'damage tolerant'
- Drucker-Prager SFC: $\sqrt{J_2} = c_1 + I_1 \cdot c_2$, $c_1 = (2 \cdot R^c \cdot R^t / \sqrt{3} \cdot (R^c + R^t), c_2 = (R^t - R^c) / \sqrt{3} \cdot (R^c + R^t)$
- Ductile-brittle transition: possible by (1) multi-axial tensile stress state and (2) temperature
- Cohesive Strength: **bi**-axial fracture failure stress (≠ *fictitious technical uniaxial strength*). Limits: (iso) $\tau_n^{Tp} + \mu \cdot \sigma_n^{Tp} > R^\tau = \tau_n(\sigma_n = 0) > R^t$; (UD) $\tau_n^{Tp} + \mu_{\perp\perp} \cdot \sigma_n^{Tp} > R_{23}^\tau = \tau_{nt}(\sigma_n = 0) > R_\perp^t$.
  Often called S_{23}, but never clearly defined nor tested. ^{Tp} Touch point of the Mohr-Coulomb curve
- Connection: physical device (bolts, plates, welds)
- Delamination: separation of material layers within a laminate or also in a textile reinforced concrete.
- Ductile-brittle transition temperature: temperature point at which the behavior changes
- Epoxy resin (thermoset, Duromer, Duroplast): A reactive resin that, through polyaddition with curing agents, transitions into a solid, infusible state. Empa researchers have developed an epoxy resin that can be repaired and recycled, and is also flame-retardant and mechanically resistant!
- Equivalent stress: author's double interpretation,considering ductile and brittle materials
  (1) Equivalent (*in German, gleichwertig dem vorliegenden Spannungszustand*) to a multi-axial stress state combining the effects of those stresses that are active in a distinct failure mode. Examples: Von Mises Equivalent Stress $\sigma_{eq}^{Mises} = \sqrt{3J_2(\{\sigma\})}$ in case of the associated 'shear yielding' failure mode; or Maximum Principal Stress $\sigma_1(\{\sigma\})$ in case of Rankine's brittle 'tensile fracture' failure mode NF.
  (2) The uni-axial scalar σ_{eq}-value (*in German termed 'Vergleichsspannung' = vergleichbar mit Festigkeit f)* is comparable to the mode-'reigning' associated uni-axial 'basic' strength *R* or *f* of the activated failure mode. A σ_{eq} is not given for Global SFCs which incorporate more than one mode
- Fabrics: 2D-woven textile semi-finished products (interlocking of fibers, Gewebe) and 2D-non-woven ones (Non-Crimped Fabrics NCF, Gelege)
- (design) Factor of Safety (FoS *j)*: load-increasing factor to capture design uncertainties
- Failure: Yield failure (ductile) or fracture failure (brittle).
- Failure condition: condition on which a failure becomes effective, meaning $F = 1$ for one limit state
- Failure criterion: distinctive feature defined as a condition for one of the 3 states F < = > 1

- Failure Function (F), i.e. $F^{\text{Mises}} = \sqrt{3 \cdot J_2} \,/\, R_{0.2}$ and Failure Index (FI): $FI = |F|$
- Failure Mode Concept (FMC)**:** invariant, failure mode-based general concept to generate strength failure conditions (SFCs) for single modes. It is a 'modal' formulation in contrast to 'global' concepts where all failure modes are mathematically linked and a concept for materials that can be homogenized (smeared). Applicability of SFC ends if homogenization as modeling pre-requisite is violated
- Failure stress: means failure indicated by a SFC and does not principally mean 'breaking into pieces'
- Fatigue: Failure danger, stemming from static loading (Static Fatigue, in German Zeitstandfestigkeit) and Cyclic loading (Cyclic Fatigue, *in German Zeitfestigkeit mit Dauer(schwing)festigkeit*)
- Fiber-Reinforced-Polymer (FRP) (Faserverstärkter Kunststoff, auch Faser-Kunststoff-Verbund nicht ~~Faserverbundkunststoff~~), Carbon Fiber-Reinforced-Concrete CFRC: usually UD-reinforced matrix:
- Filament: Single endless fiber with a diameter of typically 5 µm (see roving, thread)
- Finite Fracture Mechanics: a 'coupled stress and energy criterion' [*Leguillon, 2002*]
- Fracture body: smoothed surface of the ends of the multi-axial failure stress vectors
- First-Ply-Failure (FPF): usually First Inter-Fiber-Failure IFF in a lamina of the laminate. FPF failure envelopes are searched by the SFCs. This means determination of 'Onset-of-(micro)damage' and includes both Inter Fiber Failure (IFF) and Fiber Failure (FF)
- 'Global' SFC: criterion, which interacts not only failure stresses but also failure modes
- Isotropic material: material with identical properties in all directions
- Joint: overall functional zone, where forces are transferred
- Lamella: specific NCF lamina in construction
- Lamina: Designation of the single UD ply as *computational element* of the laminate, used as laminate subset or building block for laminate modeling. It might capture several equal plies
- Laminate: multi-ply-composed structure (ply stack)
- Last-Ply-Failure (LPF) in the laminate: usually requires a non-linear laminate analysis, which can be used to save a design
- Letters: R strength (internationally fixed, not f like we construction engineers partly still do); σ, τ indicate the fracture responsible normal or shear stress acting on the fracture 'plane'. T Thermal, M Moisture; E Young's modulus, ν Poisson's ratio, G shear modulus. $\parallel$ parallel to the fiber, $\perp$ transversal to the fiber direction; W Weft, F Fill of a fabric; m matrix, f fiber
- Material Stressing *Effort* (*Eff*): $\sigma = R \cdot Eff$ (not material utilization in the usual sense of manufacture waste minimization): artificial term, generated in the UD World Wide Failure Exercises in order to get an English term for the meaningful German term Werkstoff-Anstrengung. The SCF is stress-based and not strain –based. In the linear case it is directly valid $f_{\text{Res}} = RF = 1/Eff$. (*in his book Puck originally used the term effort* ε *and further exposure).* $Eff_{\max} = 100\% = 1$. If just one mode acts, then $\sigma_{\text{eq}} = R \cdot Eff$
- Macro-Damage technischer Schaden): i.e. a crack in a structural part, tackled by damage tolerance tools
- Margin-of-Safety (MoS): Reserve Factor - 1
- Material Reserve Factor f_{Res}: $f_{\text{Res}} = \text{strength design allowable / stress at distinct design load level}$
- Matrix: resin system or mortar system, cured or non-cured. Resin system is a mixture of resin, with ingredients such as catalyst, initiator, diluents or additives to influence handling, processing behavior and ultimate properties of the final product
- Micro-Damage (Schädigung, Ungänze): discontinuity in the material, tackled by SFCs
- 'Modal' SFC: criterion, which interacts just stresses within one single failure mode
- Mohr- Coulomb curve *(Mohr envelope):* $\tau_n(\sigma_n = 0)$
- Mohr-Coulomb friction value: μ (for iso); $\mu_{\parallel\perp}$, $\mu_{\perp\perp}$ (for UD)
- Normal Fracture (NF): failure occurring under tensile stress states
- Parameters: usually scattering design parameters including material properties

- Partial Factor of Safety concept γ: concept, which discriminates load model uncertainties considering factors from design uncertainties
- plastic behavior: irreversible deformation of a material when subjected to stress beyond its elastic limit
- Ply, layer: *physical element* of a laminate from a winding, tape-laying process etc
- Poisson's ratio: ν (iso), $\nu_{\perp\|}$ (here the larger UD, analogous to load-indexing logic in VDI 2014, sheet 3).

  Data input can be always checked by *Maxwell-Bett :* $\nu_{\perp\|} \cdot E_{\perp} = \nu_{\|\perp} \cdot E_{\|}$
- Properties: 'agreed' values to achieve a common and comparable design basis. Must be provided with average value and coefficient of variation
- Reserve Factor *RF*: load-defined value $RF_{\text{ult}} = \text{final failure load} \;/\; \text{design ultimate load}\,(DUL)$
- Roving: Bundle of thousands of filaments, such as a 50k roving, meaning, for example, 50,000 filaments in a so-called heavy tow (see also thread, filament)
- Sample (Stichprobe): set of test specimens or of measurements
- Simulation: Process, that consists of several analysis loops and lasts until the system is imitated in the Design Dimensioning process. The model parameters are adjusted hereby to the 'real world'
- Size effect: the geometrical size affects failure behavior, exemplarily considering differently large holes in a tensioned plate
- Shear Fracture (SF): τ-activated micro-damaging under shear stress and compressive stress
- general Strength R: general the strength and the strength design allowable for Design Verification
- average Strength $\bar{R}$: in model validation for mapping tasks, marked by the statistical 'bar over'
- Strength Design Allowables: statistically reduced average values such as A- and B-values or 5% fractiles in civil engineering
- Strength Failure Criteria (SFC): mathematical formulation of the design limit state, here the strength limit state to assess a 'multi-axial failure stress state in a critical location of a structural part
- Strength quantities: $\{R\} = (R_{\|}^{t}, R_{\|}^{c}, R_{\perp}^{t}, R_{\perp}^{c}, R_{\perp\|};\ R_{23})^{\mathrm{T}} \Leftarrow (\mathrm{X}, X', Y, Y', S_{12}; \mathrm{S}_{23})^{\mathrm{T}}$ Tsai
- Strengthening effect of pressure: increases multiaxial 'strength capacity'and not the technical strength. The *Eff*-value remains the same under overloading with p_{hyd}
- Stress-based versus strain-based SFC design:
  - Stress-based: Failure stress-based SFC formulations are not only applicable for solids but to fluids, too. SFCs use as action the present failure stress state and require for design verification as resistance properties the standardized strength design allowables (statistically reduced uni-axial material failure stresses). Stress-based SFCs are compatible with fracture mechanics
  - Strain-based: In the case of relaxation under ε = const no failure would occur
- Stress intensity factor (K): property used to predict the 'stress intensity' near the tip of a crack
- Stress **tensor** components: They should not read 'stress components' (*only a shear stress can be composed of a tensile component jointly acting with a compressive stress component*)
- Technical strength R, standard-measurable: for UD-clarity symbolically indexed $R_{\perp}^{\,c}, R_{\perp\|};\ R^{t}, R^{c}$. A general strength quantity is indexed by numbers like $R_{\perp\perp} \rightarrow R_{23}$
- Thread (Faden): single flexible (slack) strand in textile technology made of fibers and extruded fine mortar-strand deposit in construction (falsely termed 3D–print)
- Transition ductile-brittle: multi-axial tensile stress states, *TrF*-linked. Guess for isotropic material is at $I_{1,\text{tr}} = 3 \cdot R^{t} - R^{c}$
- Triaxiality Factor $TrF = \sigma_{\text{hyd}} / \sigma_{\text{eq}}^{\text{Mises}} = (I_1 / 3) / \sqrt{3 \cdot J_2}$
- Uni-Directional (UD) : fiber-parallely reinforced plastics (FRP), thermoset or thermoplastic matrix
- Vessel risks: (1) associated to energy content of dangerous fluid $\rightarrow$ bar$\cdot\ell$. (2) Leak rate (tightness grade)

- Yielding: design failure mode, normally not catastrophic, unlike the ultimate fracture failure, which is the load-bearing capacity for a given material
- Yield stress (unfortunately termed yield strength, despite of the fact that it is not set as a strength property for Design Verification): material property corresponding to the point at which the material begins to deform plastically (in German Streckgrenze Re), is end of proportionality σ_{prop}
- Proof stress: point at which the material exhibits 0.2% of plastic deformation, known as stress at 0.2% strain- offset and set as yield strength property Rp0.2. (in German Fließgrenze or 0.2% - Dehngrenze)
- (model) Validation**: (**from Latin, validus = strong). Modeller's objective to 'qualify' a created model by well mapping physical test results with the model.
- (design) Verification (from Latin, veritas facere): fulfillment of a set of design requirement data or control whether the design requirements data set in the performance specification is met. *Proof, that the product fulfils the product requirements data, defined in the agreed performance requirements specification (= Pflichtenheft, supplier) = reduzierte ursprüngliche Anforderungsliste, Lastenheft des Kunden, customer). Performed by a computation and/or a physical experiment such as a structural test like with a girder being below a given deformation limit under loading.* Verification may be fulfilled without fulfillment of the validation and vice versa. Solving the right equations
- continuous Carbon Fiber (CF): endless single fiber, usually termed C-filament (*Kohlenstoff-Faser*)
- recycled Carbon Fiber (rCF): maintaining a fiber length distribution such that a loss of strength compared to long fibers results, i.e., degradation has occurred. Furthermore, fatigue and creep strength losses due to the necessary matrix transfer -as a result of short single rCF within the strand - must not be overlooked in the design
- Thermosets versus Theromopastics: Thermosets cannot be reshaped after curing. Thermoplastics can often be thermoformed and welded.

** Material composite (Werkstoffverbund): structural-mechanically a composed 'construction of different materials. Note: A not smearable 'conglomerate' is usually the Fiber-grid-Reinforced-Concrete.

** Composite material (Verbundwerkstoff): combination of materials, different in composition.

**Definition of Lay-ups for UD laminates and orthotropic laminates: It' necessary to provide the material-modeling design engineer and his colleague in production with a clear, distinguishing description of UD-lay-ups, (stitched multi-UD-layer) NonCrimpFabrics and of (crimped) Fabric layers.

*Single UD-layers-deposited stack [0/90], $[0/90]_S = [0/90/90/0]$ lay-up

(a wavy bracket for each deposited UD layer is neither handable nor necessary)

* Semi-finished product, stitched NCF: $\{0/90\} + \{90/0\}$ symmetrically stacked

now also deliverable 'building blocks' $\{0/45/\text{-}45/90\}, \{\varphi/\text{-}\psi/\text{-}\varphi/\psi\}, \{0/60/\text{-}60\}$, etc.

DoubleDouble, two NCFs stacked = „*Bi – Ax*" $[\{75/-75\}/\{-15/15\}]_{r\ (epeated)}$

* Semi-finished product, woven Fabric: $\begin{bmatrix}0\\90\end{bmatrix}, \begin{bmatrix}0\\90\end{bmatrix}_S = \begin{bmatrix}0\\90\end{bmatrix}_2, \begin{bmatrix}45\\-45\end{bmatrix}$

⇒ Combinations: $[\begin{bmatrix}45\\-45\end{bmatrix}/\{75/-75/-15/15\}]_3/[0/90/90/0]/\begin{bmatrix}0\\90\end{bmatrix}_2$

* Design Sheet (author's definition): Worksheet that can be used to carry out dimensioning (based on his experience with previously used design documents in construction, for example for calculating concrete slabs) and the Design Handbook HSB

* pressure vessel: 100 bar = 10 MPa = 10 N/mm^2; 1 N = 1 kg·m/s^2. 1 J= 1 Nm, 1W = 1 Nm/s

Table of self-explaining notations for structural properties and of property numbers of the materials

9	**general orthotropic**	R_1^t	R_2^t	R_3^t	R_1^c	R_2^c	R_3^c	R_{12}	R_{23}	R_{13}
5	**UD, ≅ non-crimp fabrics**	$R_{\parallel}^t$ NF	$R_{\perp}^t$ NF	$R_{\perp}^t$ NF	$R_{\parallel}^c$ SF	$R_{\perp}^c$ SF	$R_{\perp}^c$ SF	$R_{\parallel\perp}$ SF	$R_{\perp\perp}$ NF	$R_{\parallel\perp}$ SF
6	**fabrics**	R_W^t	R_F^t	R_3^t	R_W^c	R_F^c	R_3^c	R_{WF}	R_{F3}	R_{W3}
9	**fabrics general**	R_W^t	R_F^t	R_3^t	R_W^c	R_F^c	R_3^c	R_{WF}	R_{F3}	R_{W3}
5	**mat**	R_{1M}^t	R_{1M}^t	R_{3M}^t	R_M^c	R_{1M}^c	R_{3M}^c	R_M^τ	R_M^τ	R_M^τ
2	*ductile* **isotropic** *brittle*	R_m SF	R_m SF	R_m SF	*deformation-limited*			R_m^τ	R_m^τ	R_m^τ
		R_m NF	R_m NF	R_m NF	R_m^c SF	R_m^c SF	R_m^c SF	R_m^σ NF	R_m^σ NF	R_m^σ NF

9	*general orthotr.*	E_1	E_2	E_3	G_{12}	G_{23}	G_{13}	ν_{12}	ν_{23}	ν_{13}	**comments**
5	*UD, ≅ non-crimp fabrics*	$E_{\parallel}$	$E_\perp$	$E_\perp$	$G_{\parallel\perp}$	$G_{\perp\perp}$	$G_{\parallel\perp}$	$\nu_{\parallel\perp}$	$\nu_{\perp\perp}$	$\nu_{\parallel\perp}$	$G_{\perp\perp} = E_\perp/(2+2\nu_{\perp\perp})$ $\nu_{\perp\parallel} = \nu_{\perp\parallel} E_\perp / E_\parallel$ *1 is perpendicular to quasi-isotropic 2-3-plane*
6	*fabrics*	E_W	E_F	E_3	G_{WF}	G_{W3}	G_{W3}	ν_{WF}	ν_{W3}	ν_{W3}	*Warp = Fill*
9	*fabrics general*	E_W	E_F	E_3	G_{WF}	G_{W3}	G_{F3}	ν_{WF}	ν_{F3}	ν_{W3}	*Warp ≠ Fill*
5	*mat*	E_M	E_M	E_3	G_M	G_{M3}	G_{M3}	ν_M	ν_{M3}	ν_{M3}	$G_M = E_M/(2+2\nu_M)$ *1 is perpendicular to quasi-isotropic mat plane*
2	*isotropic*	E	E	E	G	G	G	ν	ν	ν	$G=E/(2+2\nu)$

9	general orthotropic	α_{T1}	α_{T2}	α_{T3}	α_{M1}	α_{M2}	α_{M3}
5	UD ≅ non-crimp fabrics	$\alpha_{T\parallel}$	$\alpha_{T\perp}$	$\alpha_{T\perp}$	$\alpha_{M\parallel}$	$\alpha_{M\perp}$	$\alpha_{M\perp}$
6	fabrics	α_{TW}	α_{TW}	α_{T3}	α_{MW}	α_{MW}	α_{M3}
9	fabrics general	α_W	α_F	α_F	α_{MW}	α_{MF}	α_{M3}
5	mat	α_{TM}	α_{TM}	α_{TM3}	α_{MM}	α_{MM}	α_{MM3}
2	isotropic for comparison	α_T	α_T	α_T	α_M	α_M	α_M

Table of structural properties

Below from the author's Glossar „Technical terms for composite parts" in mechanical and civil engineering.
171 pages, Springer- Vieweg, Wiesbaden (2019). Pre-print downloadable*

Mapping of courses of test data points by SFC models with visualization:

- All used model parameters are statistically means, which should be always indicated by a bar over like the strength $\bar{R}$. The applied so-called physical model parameters, like μor ν, are mean values
- In the case of modal SFCs the model parameters are determined in the pure mode domain
- Transitions between parts of the complete failure body must show no gap. For instance for a porous concrete fracture failure body with its closed ends these domains must fit:

  Cap - NF : chosen cap model with given SFC model for NF (effortful extra work)
  NF – SF : performed by the mode interaction formula
  SF – Bottom : chosen bottom model with given SFC model for SF (effortful extra work).

Lightweight construction is a primary focus of this document:

Its focus is on mass reduction, material savings, and functional requirements. It is therefore an interdisciplinary field. During the design dimensioning phase, lightweight construction employs several principles: (1) Material-based lightweight construction, which is based on replacing the original material of a component with another material offering improved properties. (2) Structural lightweight construction, which aims to achieve the lightweight design goal through design measures. (3) System-based lightweight construction, which considers the entire load-bearing system and achieves a system-wide lightweight design goal through functional integration.

Since loads are generally the most uncertain model parameters, they must be critically examined: Precise requirements in the specifications (the German *Lastenheft*) and subsequent functional specifications (the German *Pflichtenheft*) lead to lighter structures. Dimensioning load cases and their associated loading combinations typically do not occur simultaneously in a load-bearing component. In civil engineering, when combining individual scattering actions such as permanent actions G and variable actions Q·ψ, the latter are corrected by a combination factor ψ <1 which takes into account the frequency of occurrence.

Mind in the context above, please:

- ✓ An additional requirement is Design-to-Minimum Waste beside Design-to-Cost!
- ✓ And, there is no sustainability without durability.
- ✓ Fully following NAFEMS as former WG member: We have to build products and to set up processes, which are robust and resilient. Uncertainty quantification is a key to that.

Some symbols

f, m	fiber, matrix
R	stress ratio (*straight letter*), defined as minσ/maxσ *(mind signs)*
R	resistance, strength design allowable *(skew letter, statistically reduced strength)*
$\bar{R}$	average (‘mean’) or typical strength *(utilized for test data mapping)*
$\bar{x}, s$	mean value, standard deviation of a sample
x, y, z	structural COS (Cartesian), laminate COS
x_1, x_2, x_3	lamina CoS
α	fiber orientation angle of the lamina (*positive from* fiber parallel ||-axis *x to* x_1)
μ	Mohr-Coulomb material friction value (*practically* $0 < \mu < 0.3$)
μ, σ	mean value, standard deviation of the Basic Normal Distribution derived from the statistical population of the i samples, characterized by $\bar{x}_i, s_i$; $\cos_\mu = \sigma / \mu$
γ	partial design factor of safety in civil engineering, shear angle
ν	Poisson’s ratio
σ, τ	stresses in engineering notation.

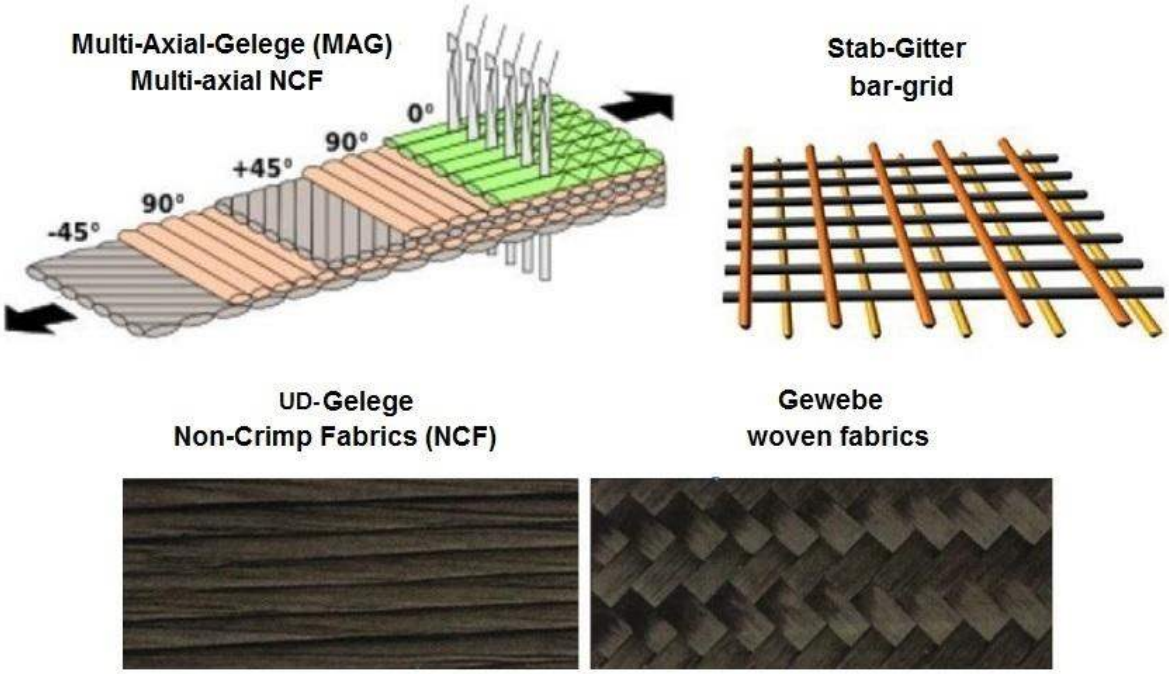

Some essential notions for reinforcement materials with straight fibers, excluding textile fiber grids.

(left up) Non-crimp fabric NCF composed of tapes, (right up) Rebar grid composed of pultruded bars (industrially laid bars ≡ bar lattice mat) [after Wikipedia, Delcotex].
(left down) Lamella in civil engineering ≡ UD-tape or a multi-axial NCF, (right bottom) weave.
Einige wesentliche Bewehrungsmaterial-Begriffe bei gerade ausgerichteten Fasern, ohne textile Gitter.
(links oben) Multi-Axial Gelege MAG aus Tapes, (rechts oben) Stabgitter aus pultrudierten Stäben.
(limks unten) Lamelle ≡ UD-Gelege- oder auch MAG-Streifen, (rechts unten) Gewebe [Hänchen]
Schmaler Gelege-Streifen ≡ Lamelle = strip, breites Gelege-Band ≡ 'Sheet' = tape

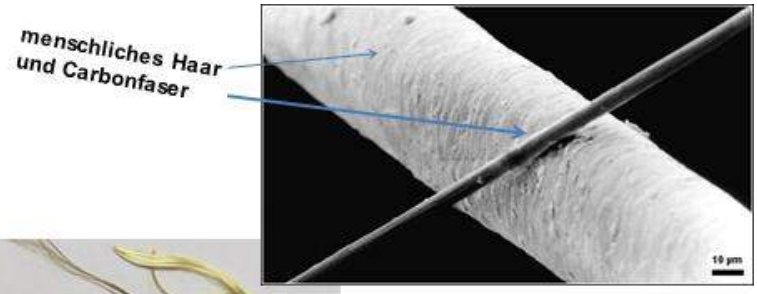

A comparison of a carbon-fiber (Ø 7 μm) versus a hair

Durchmesser-Vergleich Carbonfaser-Haar

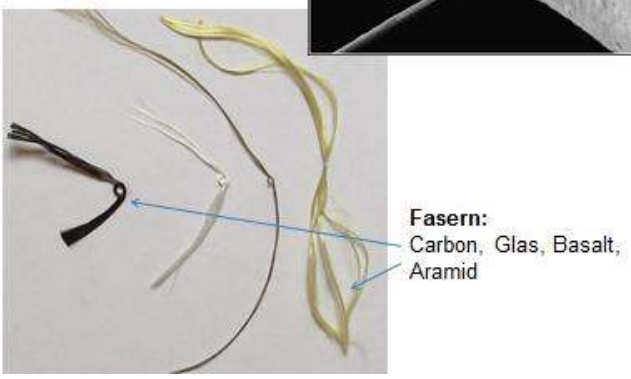

knot test of carbon, glass, basalt and aramid fibers (Knotentest von Fasern)

(left) a test to visualize brittleness grade and fiber bending radius limits of fibers, (i.e. in construction necessary for radius of the reinforcing fiber elements in cages)

The behavior of laminas is different for so-called isolated test specimens and embedded test specimens. Isolated test specimens are unconstrained laminas whereas laminas embedded in the laminate are mutually constrained according to the strain-controlled state. This was decisive when mapping specific test data sets such as in the WorldWideFailureExercise-II, TC3. Isolated test specimens deliver values for the strength = failure stress, which represent the value at the end of the strain-hardening curve. Embedded laminas contribute further to the laminate stiffness and load carrying capacity as long as the microdamage-caused strain-softening curve is active.

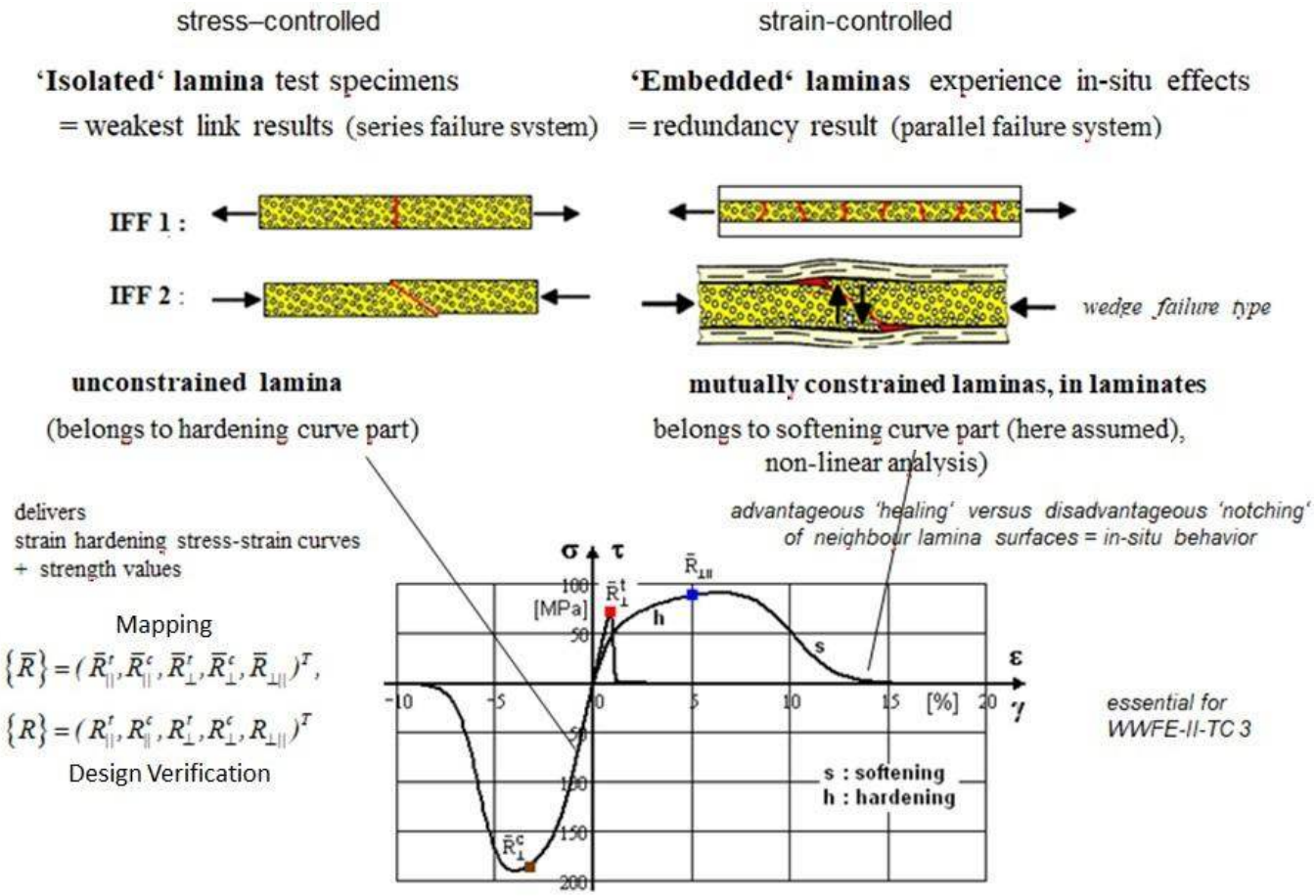

CarbonFiberReinforcedPolymer (CFRP): Strain Hardening and Strain Softening, curve parts of the example UD-material. FF = Fiber Failure, IFF = Inter Fiber Failure.

Mixed-mode crack propagation in concrete support the author's outsmoothing at the peak points and not the usually applied sharp decay, there [*Car93*].

0.3 Focus: Structural Parts and Structural Materials

0.3.1 Structural Parts and Brittleness Grade

Viewing structural parts three types of surfaces are faced by the structure-designing engineer, see below:

Table 0-1: Surfaces of structural parts

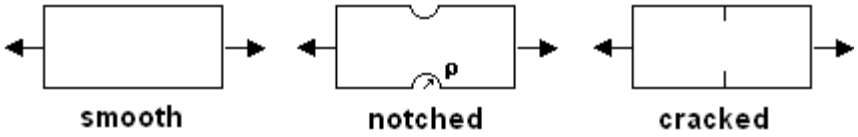

Stress plain, smooth domains Strength Mechanics	Stress concentrations Stress-gradients. Neuber notch mechanics, Finite Fracture Mechanics (FMM)	Stress intensities, high Stress Singularities at crack tips Fracture Mechanics (FM)

and the behavior of the material, whether it is in its extremes ductile or brittle. A widely used information on the ductile-brittle transition is $R^c >\approx 3 \cdot R^t$. Basic focus are the structural parts (*Table 0.1*) of smooth type. Further, the more complex connections are effortful to design. Stress gradient, size effect, rate dependency are not addressed, here. (Connections are the physical devices like bolts, plates, welds. Joints are the overall, functional zone where forces are transferred).

0.3.2 Structural Composite Materials

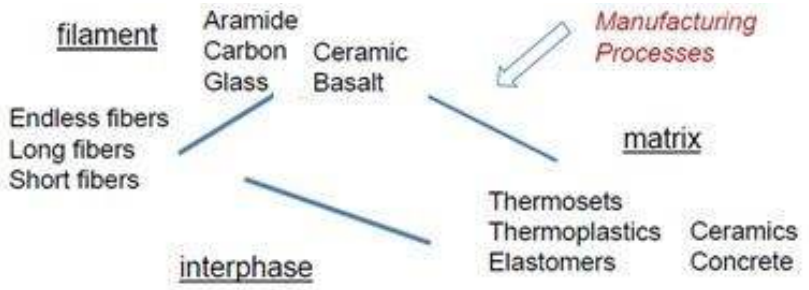

Filaments: glass, aramide, carbon, ceramics, ..

Fibre preforms from ***roving, tape, weave, braid (2D, 3D)***
knit, stitch, or mixed
as in a ***preform hybrid***
non-crimp fabric laminates

PP/glass/aramidePEEK/
glass –filament-yarn

Matrices : thermosets, thermoplastics, ceramics, concrete, ..

Polymers (crystalline and amorphous)		
Plastics		Elastomers
thermo-plastics	thermo-sets	
Acrylic, polycarbonat, polyimide, polypropylene	epoxy, phenolic, polyurethane, silicon	natural rubber, silicone rubber, polyurethan elastomer

polymers are also bonding materials *(3D understanding)*

Manufacturing: pre-pregging, wet winding, Resin Transfer Molding, casting, SMC, shotcrete

Polymers (crystalline and amorphous)		
Plastics		Elastomers
thermo-plastics	thermo-sets	
Acrylic, polycarbonat, polyimide, polypropylene	epoxy, phenolic, polyurethane, silicon	natural rubber, silicone rubber, polyurethan elastomer

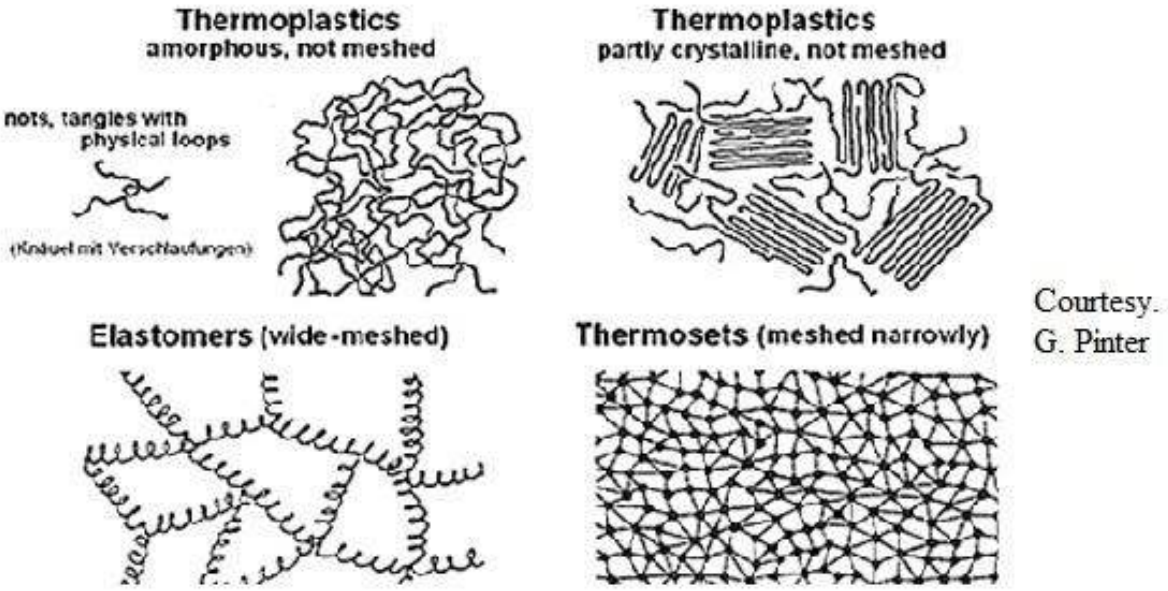

Fig.01: Possible combinations of different constituents with various polymers used
Filaments: bor B, glass G, aramide A, carbon C, ceramics, basalt Bs, ..

The widely quoted ideal strength of isotropic solid materials of $R^t = 0.1 \cdot E$ is orders of magnitude larger than the measured realistic strength and thereby showing the effect of the always given differently sized flaws.

Very essential for this elaboration are the fiber-reinforced leightweight materials with its various combinations including polymer matrix and mineral matrix, see *Fig.0-1, before*. Traditional epoxy resin systems (EP) deliver rigid thermoset structures after curing, excellent properties but recycling of the FRP-composite is pretty difficult. Residual stresses from curing are inherent and can merely lowered by a heat treatment process. Thermo-plastics (TP) can be deformed after curing and are recycling-friendly and suffer not from residual stresses but have distinct shortcomings in the process.

Fig.0-2 various combinations of different constituents building up the final homogenized (*hopefully 'smearing' is possible*) material are possible and to model

Exemplarily as composites preview *Fig. 0-2* presents stresses, strengths and witnessed failure modes:

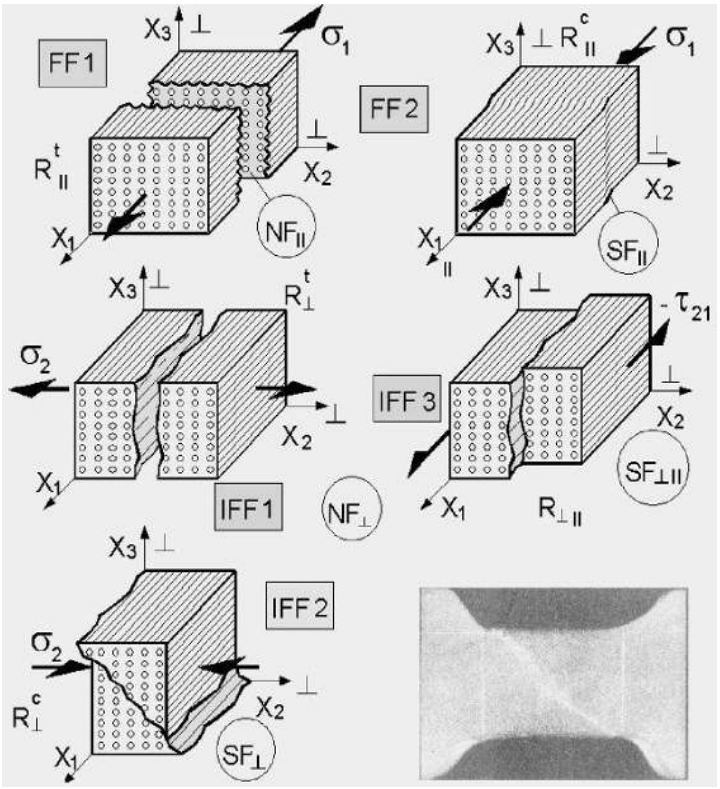

Fig. 0-2: 5 strength quantities and 5 strength failure modes of the transversely-isotropic UD material

Keep in mind, please: Lamina properties used as input for the *embedded* (benign behavior) plies in a laminate analysis are test results from *isolated* UD lamina specimens such as a tensile coupon. They are load-controlled derived and its results are of weakest link type.

0.3.3 Special Views of the Author concerning Structural Mechanics and Design Dimensioning

Capturing all kinds of possible types of failure in a uniform classification scheme is challenging, because the classification can be carried out according to different ways. The author thinks that a material behavior-overarching system delivers a good classification scheme for a macro-mechanics building including 3 definable structural material families. This scheme should be clear and as simple as possible for the dimensioning structural engineer without violating any material-typical facts.
In consequence, the author may conclude from experience:

If one knows from a similar behaving material some material facts,
that knowledge can be transferred to the behavior of the 'new' material, and
then pre-dimensioning with the new material becomes easier and more trusting!

LL:

- *There are coincidences between brittle UD laminas and brittle isotropic materials*

- *With composites: After an initial matrix yielding of the more or less ductile polymer matrix follows a 'Quasi-Yielding' due to diffuse micro-cracking. Increased degradation occurs in the laminate beyond onset of the first Inter-Fiber-Failure IFF*
- *What may be learned from studying the failure conditions? If the shear stress yielding mechanism is still active until fracture its yield failure function remains at least part of the formulation of the fracture failure function F. In other words, the same mathematical form of a failure condition (means interaction of stresses within one mode) may be valid from Onset-of-Yielding SY to Onset-of-Fracture SF if the physical mechanism remains, such as with shear yielding in case of ductile steels*
- *Today's FEA gives 3D FE stress results as output. The evaluation of these 3D stress states therefore requires 3D conditions that predict the onset-of-failure. Unfortunately, due to a lack of 3D test results, the known standard 'global' SFCs – even for isotropic materials – are usually not sufficiently well 3D-validated.*
- *A software analysis model is validated by test, whereas a hardware/structure is qualified by test,*
- *A final design is verified by test.*
- *Software Model Verification means: „Solve the equations right"*
- *Software Model Validation means: „Solve the right equations", which needs testing.*

From above follows an advantage when material symmetry knowledge is applied: Presuming, homogeneity is a valid assessment for the project task-determined model, just a minimum number of properties must be measured, only. This offers significant benefits in Cost and time.

Looking at his Structural Mechanics Building the author sees two missing links or empty rooms, see *Fig.0-3* : Why are there not also 2 yield modes (*as still mentioned*) and 2 'basic' critical stress intensity factors (*fracture toughness entities*)?'

Strength Mechanics		**Fracture Mechanics**
SY	*known*	$K^t_{Icr} \equiv K_{Ic}$, K_{IIc}, K_{IIIc} **(tension, shear)**
Normal Yielding NY		K^c_{IIcr} **(compression)**

*Fig.0-3: Isotropic material, the two searched missing links **NY** and $K_{IIcr}{}^c$*

(1) ***NY :*** Is there Normal Yielding**?**

NY is known for a long time, but not in structural mechanics design. An explanation for the 'Not known' is that a describing yield failure condition F^{NY} was missing. For establishing this missing link in his 'complete system' the author found applicable test data which he evaluated and mapped with his model and visualized in chapter 5. → Proof is given.

(2) $K_{IIcr}{}^c$ **:** Is there a Critical Stress Intensity Factor (SIF) under compression or a fracture toughness under a compression-induced shear, respectively?

Here, the author remembers a two decades old citation of A. Carpinteri that approximately reads: "With homogeneous isotropic brittle materials there are 2 real energy release rates $\mathcal{G}_{Icr}$, $\mathcal{G}_{IIcr}$, one in tension and one in compression. These two $\mathcal{G}s = K^2 \cdot (1-\nu^2) / E$ (*formally, plane strain case*) possess the attribute that the crack plane does not turn and are therefore real (*or 'basic'*) material properties". This forced the author at that time to intensively search $K_{IIcr}{}^c$ as the basic pendant to $K_{Icr}{}^t$, officially indexed K_{Ic} in fracture mechanics FM, and to postulate in the sense of Carpinteri:

"***Only a stable crack growth plane-associated*** *(self-similar crack growth)* ***SIF is a 'basic' FM property"***.

This is valid in the tension domain for the SIF $K_{Ic} \equiv K_{Icr}{}^t$ above and not for the *model-necessary* K_{IIc} and K_{IIIc}. It should be valid in the compression domain, too, that means failure is shear-linked, which requires to write $K_{IIcr}{}^c$. This missing link will be presented by the author in chapter 6. The author admits at this point that this SIF is not relevant for the treatment of common fracture-mechanical tasks in the compression range because it requires an ideal homogeneous

crack-tip situation of a pretty brittle material. However, he believes that the proof of $K_{IIcr}{}^{c}$ is an important theoretical task for achieving the desired 'complete system or building'.

0.3.4 Comments on Properties to be used in Analysis

- Properties are 'agreed' values to achieve a common and comparable design basis
- Properties must be provided with average value and coefficient of variation cov
- Sources of uncertainty should be investigated, because changing a certified material is economically seldom possible
- Model parameters should be measurable, unambiguously properties and physically self-explaining
- Variety of composite properties: Many properties for design and manufacturing are not yet available
- Generally valid for materials: A 3D-stress assessment is not possible on basis of uniaxial strength values alone. Knowledge of material internal friction values, following Mohr-Coulomb, is mandatory in the compression domain (see *Table 1-2a*)
- Suffix of Poisson's ratio: use Maxwell-Betti theorem, check analogously to $\nu_{\perp\|} \cdot E_{\perp} = \nu_{\|\perp} \cdot E_{\|}$
- Usually the strains are based on engineering strain formulation $\gamma_{xy,}$ as with the VDI 2014. However, some authors define thermal shear strains *tensorial* and others *engineering-like* which means a factor 2 is to consider, because $\gamma_{eng} = 2 \cdot \gamma_{tens}$. This has an effect on the input of α_{Txy} . ABAQUS follows VDI.

And the strength properties displayed in a vector format for the 3 families read:

Isotropic: $\{R\} = (R^t, R^c)^T$ with μ , if friction acts

Transversely-isotropic: $\{R\} = (R^t_{\|}, R^c_{\|}, R^t_{\perp}, R^c_{\perp}, R_{\perp\|})^T$ with $\mu_{\perp\|}, \mu_{\perp\perp}$

Orthotropic: $\{R\} = (R^t_W,\ R^c_W,\ R^t_F,\ R^c_F,\ R_{WF},\ R^t_3,\ R^c_3,\ R_{3F},\ R_{3W})^T$ with $\mu_{WF}, \mu_{3W}, \mu_{3F}$.

0.4 Stress-Strain Relationships of Isotropic materials, of UD and Orthotropic materials

0.4.1 Isotropic materials

For a better understanding of the body text the stress-strain relations in structural stresses and principal stresses of the investigated 3 material families are added as fourth-order and second-order compliances

3D: $\{\varepsilon\} = [S] \cdot \{\sigma\}$ with $[S]$ *C*ompliance matrix, $\{\sigma\} = [C] \cdot \{\varepsilon\}$ with $[C]$ *S*tiffness matrix

Table: General elasticity matrices, generalized Hooke's law, tensor-format for compliance S and stiffness C

$$\begin{Bmatrix} \varepsilon_x \\ \varepsilon_y \\ \varepsilon_z \\ \gamma_{yz} \\ \gamma_{xz} \\ \gamma_{xy} \end{Bmatrix} = \begin{bmatrix} \frac{1}{E} & \frac{-\nu}{E} & \frac{-\nu}{E} & 0 & 0 & 0 \\ \frac{-\nu}{E} & \frac{1}{E} & \frac{-\nu}{E} & 0 & 0 & 0 \\ \frac{-\nu}{E} & \frac{-\nu}{E} & \frac{1}{E} & 0 & 0 & 0 \\ & & & \frac{1}{G} & 0 & 0 \\ & (symm.) & & & \frac{1}{G} & 0 \\ & & & & & \frac{1}{G} \end{bmatrix} \cdot \begin{Bmatrix} \sigma_x \\ \sigma_y \\ \sigma_z \\ \tau_{yz} \\ \tau_{xz} \\ \tau_{xy} \end{Bmatrix}, \qquad \begin{Bmatrix} \varepsilon_I \\ \varepsilon_{II} \\ \varepsilon_{III} \end{Bmatrix} = \begin{bmatrix} \frac{1}{E} & \frac{-\nu}{E} & \frac{-\nu}{E} \\ \frac{-\nu}{E} & \frac{1}{E} & \frac{-\nu}{E} \\ \frac{-\nu}{E} & \frac{-\nu}{E} & \frac{1}{E} \end{bmatrix} \cdot \begin{Bmatrix} \sigma_I \\ \sigma_{II} \\ \sigma_{III} \end{Bmatrix}$$

from which spatially follows

$$E \cdot (\varepsilon_x + \varepsilon_y + \varepsilon_z) = -3 \cdot \sigma_{hyd} \cdot (1 - 2 \cdot \nu) \quad \text{or} \quad E \cdot \Delta V / V = \sigma_{hyd} \cdot (3 - 6 \cdot \nu),$$

with the so-called bulk modulus $K = E/(3-6\nu)$.

In typical engineering applications the stiffness elasticity matrix $\{\sigma\} = [C] \cdot \{\varepsilon\}$ reads

$$\begin{Bmatrix} \sigma_x \\ \sigma_y \\ \sigma_z \\ \tau_{yz} \\ \tau_{zy} \\ \tau_{xy} \end{Bmatrix} = \frac{E}{(1+\nu)\cdot(1-\nu)} \begin{bmatrix} 1\text{-}\nu & \nu & \nu & 0 & 0 & 0 \\ \nu & 1\text{-}\nu & \nu & 0 & 0 & 0 \\ \nu & \nu & 1\text{-}\nu & 0 & 0 & 0 \\ 0 & 0 & 0 & 0.5\cdot(1\text{-}2\nu) & 0 & 0 \\ 0 & \textit{symm.} & 0 & 0 & 0.5\cdot(1\text{-}2\nu) & 0 \\ 0 & 0 & 0 & 0 & 0 & 0.5\cdot(1\text{-}2\nu) \end{bmatrix} \cdot \begin{Bmatrix} \varepsilon_x \\ \varepsilon_y \\ \varepsilon_y \\ \gamma_{yz} \\ \gamma_{zy} \\ \gamma_{xy} \end{Bmatrix}$$

and for invariant investigations $\sigma_{ik} = C_{ijkl} \cdot \varepsilon_{kl}$ in matrix presentation (*C is fourth rank tensor*)

$$\begin{Bmatrix} \sigma_{xx} \\ \sigma_{yy} \\ \sigma_{zz} \\ \sigma_{yz} \\ \sigma_{zy} \\ \sigma_{xy} \end{Bmatrix} = \frac{E}{(1+\nu)\cdot(1-\nu)} \begin{bmatrix} 1\text{-}\nu & \nu & \nu & 0 & 0 & 0 \\ \nu & 1\text{-}\nu & \nu & 0 & 0 & 0 \\ \nu & \nu & 1\text{-}\nu & 0 & 0 & 0 \\ 0 & 0 & 0 & 0.5\cdot(1\text{-}2\nu) & 0 & 0 \\ 0 & \textit{symm.} & 0 & 0 & 0.5\cdot(1\text{-}2\nu) & 0 \\ 0 & 0 & 0 & 0 & 0 & 0.5\cdot(1\text{-}2\nu) \end{bmatrix} \cdot \begin{Bmatrix} \varepsilon_{xx} \\ \varepsilon_{yy} \\ \varepsilon_{zz} \\ 2\varepsilon_{yz} \\ 2\varepsilon_{zy} \\ 2\varepsilon_{xy} \end{Bmatrix} .$$

0.4.2 Transversely-isotropic UD-material

From test reasons in typical engineering applications the compliance elasticity matrix [S] is given:

$$\begin{Bmatrix} \varepsilon_1 \\ \varepsilon_2 \\ \varepsilon_3 \\ \gamma_{23} \\ \gamma_{13} \\ \gamma_{12} \end{Bmatrix} = \begin{bmatrix} \frac{1}{E_{\parallel}} & \frac{-\nu_{\parallel\perp}}{E_{\perp}} & \frac{-\nu_{\parallel\perp}}{E_{\perp}} & 0 & 0 & 0 \\ \frac{-\nu_{\perp\parallel}}{E_{\parallel}} & \frac{1}{E_{\perp}} & \frac{-\nu_{\perp\perp}}{E_{\perp}} & 0 & 0 & 0 \\ \frac{-\nu_{\perp\parallel}}{E_{\parallel}} & \frac{-\nu_{\perp\perp}}{E_{\perp}} & \frac{1}{E_{\perp}} & 0 & 0 & 0 \\ & & & \frac{1}{G_{\perp\perp}} & 0 & 0 \\ & (\textit{symm.}) & & & \frac{1}{G_{\parallel\perp}} & 0 \\ & & & & & \frac{1}{G_{\parallel\perp}} \end{bmatrix} \cdot \begin{Bmatrix} \sigma_1 \\ \sigma_2 \\ \sigma_3 \\ \tau_{23} \\ \tau_{13} \\ \tau_{12} \end{Bmatrix}$$

or $\{\varepsilon\} = [S]\,\{\sigma\}$.

$\{E\} = (E_{\parallel}, E_{\perp}, G_{\parallel\perp}, G_{\perp\perp}, \nu_{\parallel\perp})^T$ with $\nu_{\perp\perp}, \nu_{\perp\parallel}$ off-diagonal, and $G_{\perp\perp} = E_{\perp}/(2+2\cdot\nu_{\perp\perp})$.

The spatial UD stiffness elasticity matrix [C] in the column-normalized formulation is complicated and therefore seldom documented. Therefore, S is used instead of C. However, for completion the full C and S relations of UD-composites shall be given:

$$\begin{Bmatrix}\sigma_1\\ \sigma_2\\ \sigma_3\\ \tau_{23}\\ \tau_{13}\\ \tau_{12}\end{Bmatrix} = [C]\cdot\begin{Bmatrix}\varepsilon_1\\ \varepsilon_2\\ \varepsilon_3\\ \gamma_{23}\\ \gamma_{13}\\ \gamma_{12}\end{Bmatrix} = \begin{bmatrix} C_{11} & C_{21} & C_{21} & 0 & 0 & 0\\ C_{12} & C_{22} & C_{32} & 0 & 0 & 0\\ C_{12} & C_{23} & C_{33} & 0 & 0 & 0\\ 0 & 0 & 0 & \dfrac{C_{22}-C_{23}}{2} & 0 & 0\\ 0 & 0 & 0 & 0 & C_{66} & 0\\ 0 & 0 & 0 & 0 & 0 & C_{66}\end{bmatrix}\cdot\begin{Bmatrix}\varepsilon_1\\ \varepsilon_2\\ \varepsilon_3\\ \gamma_{23}\\ \gamma_{13}\\ \gamma_{12}\end{Bmatrix}$$

$$= \begin{bmatrix} S_{22}\cdot S_{33}-S_{32}^2 & S_{12}\cdot(S_{32}-S_{33}) & -S_{12}\cdot(S_{22}-S_{32}) & 0 & 0 & 0\\ S_{12}\cdot(S_{32}-S_{33}) & S_{11}\cdot S_{33}-S_{12}^2 & -S_{11}\cdot S_{32}+S_{12}^2 & 0 & 0 & 0\\ -S_{12}\cdot(S_{22}-S_{32}) & -S_{11}\cdot S_{32}+S_{12}^2 & S_{11}\cdot S_{22}-S_{12}^2 & 0 & 0 & 0\\ 0 & 0 & 0 & G_{23} & 0 & 0\\ (\text{symmetric}) & 0 & 0 & 0 & G_{13} & 0\\ 0 & 0 & 0 & 0 & 0 & G_{12}\end{bmatrix}\cdot\begin{Bmatrix}\varepsilon_1\\ \varepsilon_2\\ \varepsilon_3\\ \gamma_{23}\\ \gamma_{13}\\ \gamma_{12}\end{Bmatrix}$$

with the denominator $N = S_{11}\cdot(S_{22}\cdot S_{33}-S_{32}^2)-S_{12}^2\cdot(S_{33}-2\cdot S_{32}+S_{22})$.

Stresses and strengths can be shortly written vectorlike:

$$3D:\ \{\sigma\}=(\sigma_1,\sigma_2,\sigma_3,\tau_{23},\tau_{31},\tau_{21})^T \quad\rightarrow\quad \left\{\sigma_{eq}^{\text{mode}}\right\}=\left(\sigma_{eq}^{\parallel\sigma},\ \sigma_{eq}^{\parallel\tau},\ \sigma_{eq}^{\perp\sigma},\ \sigma_{eq}^{\perp\tau},\ \sigma_{eq}^{\parallel\perp}\right)^T$$

$$2D:\ \{\sigma\}=(\sigma_1,\sigma_2,-,-,-,\tau_{21})^T \quad \textit{for}\ \ \text{FF and IFF}$$

$$2D:\ \{\sigma\}=(-,\sigma_2,-,-,-,\tau_{21})^T \quad \textit{for}\ \ \text{IFF}$$

$$3D:\ \{R\}=(R_{\parallel}^t,R_{\parallel}^c,R_{\perp}^t,R_{\perp}^c,R_{\perp\parallel})^T \ \text{ with }\ \mu_{\perp\parallel},\mu_{\perp\perp}$$

$$2D:\ \{R\}=(R_{\parallel}^t,R_{\parallel}^c,R_{\perp}^t,R_{\perp}^c,R_{\perp\parallel})^T \ \text{ with }\ \mu_{\perp\parallel},\mu_{\perp\perp}\ \textit{for}\ \text{FF and IFF}$$

$$2D:\ \{R\}=(-,-,R_{\perp}^t,R_{\perp}^c,R_{\perp\parallel})^T \ \text{ with }\ \mu_{\perp\parallel} \quad \textit{for}\ \text{IFF}\ \ .$$

0.4.3 Orthotropic materials

In typical engineering applications the strain-stress relationship *{ε}= [S] {σ}* and the compliance elasticity matrix [S] read:

$$\begin{Bmatrix}\varepsilon_W\\ \varepsilon_F\\ \varepsilon_3\\ \gamma_{F3}\\ \gamma_{W3}\\ \gamma_{WF}\end{Bmatrix} = \begin{bmatrix} \frac{1}{E_W} & \frac{-\nu_{FW}}{E_W} & \frac{-\nu_{W3}}{E_W} & 0 & 0 & 0\\ \frac{-\nu_{WF}}{E_F} & \frac{1}{E_F} & \frac{-\nu_{F3}}{E_F} & 0 & 0 & 0\\ \frac{-\nu_{3W}}{E_3} & \frac{-\nu_{3F}}{E_3} & \frac{1}{E_3} & 0 & 0 & 0\\ & & & \frac{1}{G_{F3}} & 0 & 0\\ & (symm.) & & & \frac{1}{G_{W3}} & 0\\ & & & & & \frac{1}{G_{WF}}\end{bmatrix}\cdot\begin{Bmatrix}\sigma_W\\ \sigma_F\\ \sigma_3\\ \tau_{F3}\\ \tau_{W3}\\ \tau_{WF}\end{Bmatrix},\quad \text{Maxwell-Betti}\ \ \frac{-\nu_{WF}}{E_W}=\frac{-\nu_{FW}}{E_F}$$

Stresses and strengths can be shortly written vectorlike:

$$3D:\ \{\sigma\} = (\sigma_W, \sigma_F, \sigma_3, \tau_{F3}, \tau_{3W}, \tau_{WF})^T \quad \rightarrow \quad \{\sigma_{eq}^{mode}\}$$
$$2D:\ \{\sigma\} = (\sigma_W, \sigma_F, -, -, -, \tau_{WF})^T$$

$$3D:\quad \{R\} = (R_W^t,\ R_W^c,\ R_F^t,\ R_F^c,\ R_{WF},\ R_3^t,\ R_3^c,\ R_{3F},\ R_{3W})^T \quad \text{with} \quad \mu_{WF}, \mu_{3W}, \mu_{3F}$$
$$2D:\quad \{R\} = (R_W^t,\ R_W^c,\ R_F^t,\ R_F^c,\ R_{WF}{}^T) \quad \text{with} \quad \mu_{WF}$$

Five Stress-strain curves are needed if Warp = Fill.

0.5 Invariants of Isotropic materials, of UD and Orthotropic materials

At first, in *Fig.0-4* the different stress types applied in structural mechanics are depicted. Secondly for the three material families the associated stresses and invariants are displayed. The suffixes I, II, III denote principal stresses, ||, ⊥ lamina stresses, W (warp), F (fill, weft) fabric stresses. The stresses in the different CoS can be transferred into each other.

0.5.1 Isotropic materials

In structural mechanics invariants of the stress tensor σ_{ik}, the strain tensor ε_{ik} and of the material stiffness tensor C_{ijkl} or its inverse the compliance tensor S_{ijkl} are employed. Invariants of the stress tensor are used to establish stress-based Strength Failure Criteria (*see the author's FMC for the three material families isotropic, transversely-isotropic and orthotropic*) and also invariants of the strain tensor for strain failure criteria. Strength failure criteria use as action the present stress state and as resistance strength properties (*failure stresses*) whereas strain failure criteria use the present strain state and failure strains as resistance properties. A compilation of some Main Invariants shall be presented here:

$$I_1 = (\sigma_I + \sigma_{II} + \sigma_{III}) = f(\sigma), \quad 6J_2 = (\sigma_I - \sigma_{II})^2 + (\sigma_{II} - \sigma_{III})^2 + (\sigma_{III} - \sigma_I)^2 = f(\tau)$$ 'Mises' invariant

$$27J_3 = (2\sigma_I - \sigma_{II} - \sigma_{III}) \cdot (2\sigma_{II} - \sigma_I - \sigma_{III}) \cdot (2\sigma_{III} - \sigma_I - \sigma_{II}),$$

$$3 \cdot \sigma_{oct} = \sigma_I + \sigma_{II} + \sigma_{III} = \sigma_\ell + \sigma_n + \sigma_t \ ; \ 9 \cdot \tau_{oct}{}^2 = 6J_2 = 4 \cdot (\tau_{III}{}^2 + \tau_I{}^2 + \tau_{II}{}^2), \ \tau_{II} = \max \tau (mathem.)$$

with

$\sigma_I, \sigma_{II}, \sigma_{III}$ the principal stresses. $\sigma_I > \sigma_{II} > \sigma_{III}$ are mathematical stresses (> means more positive) .

If in the brittle isotropic case above the same 'strength fracture mode' multiply occurs, then a 120° rotational symmetry of the fracture body is to face. The invariant J_3 can excellently map this.

A comparison of the stress-based and strain-based invariants brings a more global understanding:

$\boldsymbol{\sigma_{ik}}$:
$$I_1^{\sigma} = I_1 = (\sigma_I + \sigma_{II} + \sigma_{III}), \ I_2^{\sigma} = 0.5 \cdot (\sigma_I \cdot \sigma_{II} + \sigma_{II} \cdot \sigma_{III} + \sigma_I \cdot \sigma_{III})$$
$$J_2^{\sigma} = (I_1^{\sigma})^2/3 - I_2^{\sigma} = [(\sigma_I - \sigma_{II})^2 + (\sigma_{II} - \sigma_{III})^2 + (\sigma_{III} - \sigma_I)^2] / 6 .$$

$\boldsymbol{\varepsilon_{ik}}$:
$$I_1^{\varepsilon} = (\varepsilon_I + \varepsilon_{II} + \varepsilon_{III}) = \varepsilon_{ii} = \varepsilon_{vol}, \ I_2^{\varepsilon} = 0.5 \cdot (\varepsilon_I \cdot \varepsilon_{II} + \varepsilon_{II} \cdot \varepsilon_{III} + \varepsilon_I \cdot \varepsilon_{III}),$$
$$J_2^{\varepsilon} = (I_1^{\varepsilon})^2/3 - I_2^{\varepsilon}.$$

C_{ikjl}: rank four tensor general, C_{ik}: rank two tensor of principal stresses-strains.

Residual stresses are taken into account by adding their values to the Load stresses, $_L$, according to

$$\{\sigma\} = \{\sigma_L\} + \{\sigma_{Res}\} .$$

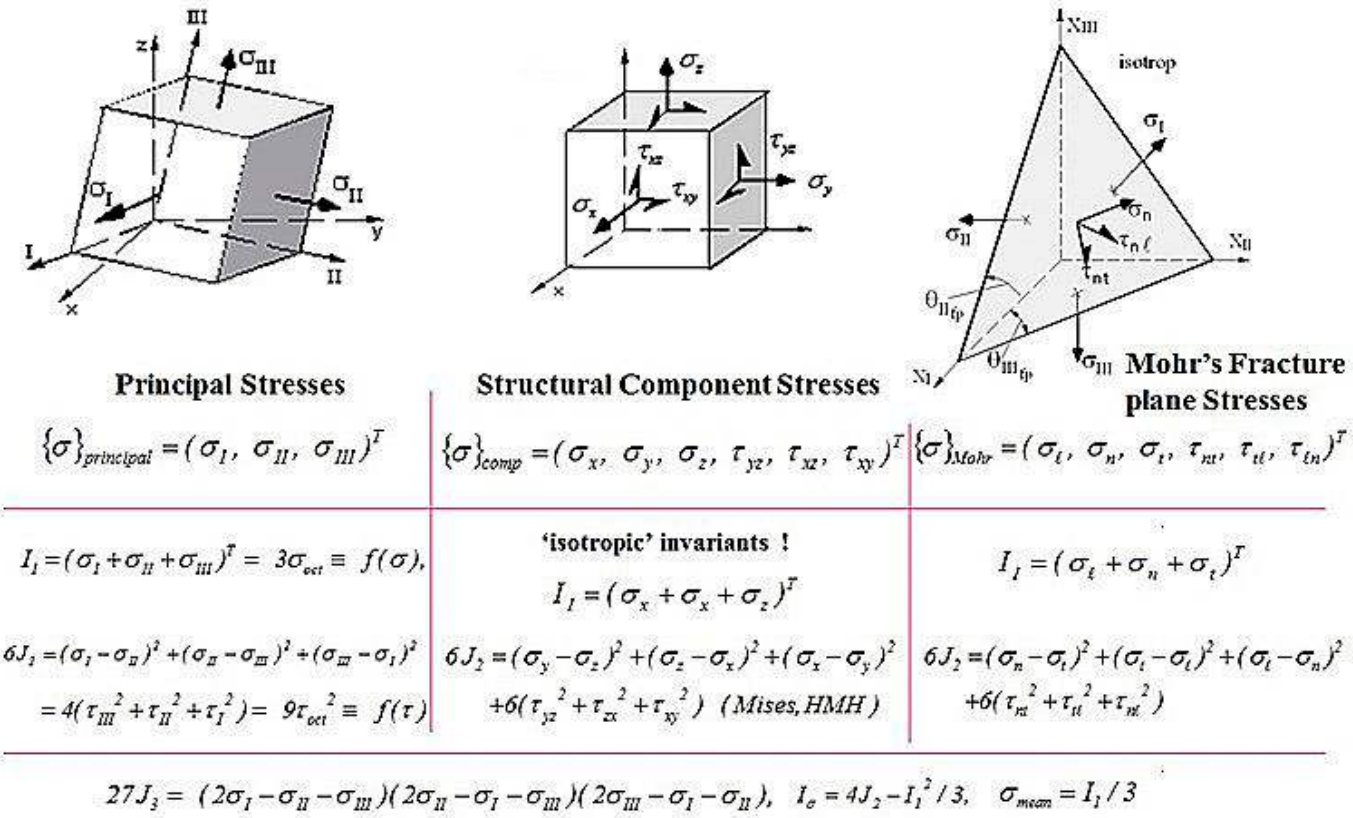

Fig.0-4: Applicable stresses and invariants of isotropic materials. (left) on the material cube's surfaces, (center), structural (component) stresses, and (right) Mohr stresses acting at the associated fracture plane

Table 0-2 finally presents the Mohr (*fracture plane*) stresses which are necessary to derive a relationship between the fictitious friction parameter in the SFC and the more engineer-attractive measurable friction value.

In the transformation of structural stresses into Mohr stresses the advantage of invariants fully comes out: *They do not depend on the coordinate system, one can simply switch between the systems.*

Table 0-2: Structural stresses,invariants and Mohr stresses

Structural Stresses and Invariants, 3D and 2D:

$I_1 = (\sigma_I + \sigma_{II} + \sigma_{III}) = f(\sigma)$, $6J_2 = (\sigma_I - \sigma_{II})^2 + (\sigma_{II} - \sigma_{III})^2 + (\sigma_{III} - \sigma_I)^2 = f(\tau)$ 'Mises invariant'

$27J_3 = (2\sigma_I - \sigma_{II} - \sigma_{III}) \cdot (2\sigma_{II} - \sigma_I - \sigma_{III}) \cdot (2\sigma_{III} - \sigma_I - \sigma_{II})$,

$\sigma_I, \sigma_{II}, \sigma_{III}$ are principal stresses, $\sigma_I > \sigma_{II} > \sigma_{III}$ are mathematical stresses (> *means more positive*).

Mohr Stresses and Invariants, 3D and 2D:

$I_1 = (\sigma_n + \sigma_t + \sigma_\lambda)$, $6J_2 = (\sigma_n - \sigma_t)^2 + (\sigma_t - \sigma_\lambda)^2 + (\sigma_\lambda - \sigma_n)^2 + 6 \cdot \left(\tau_{nt}^2 + \tau_{n\lambda}^2 + \tau_{t\lambda}^2\right)$, isotropic $\tau_{nt} \to \tau_n$

$3 \cdot \sigma_{oct} = \sigma_I + \sigma_{II} + \sigma_{III} = \sigma_\ell + \sigma_n + \sigma_t$; $9 \cdot \tau_{oct}^2 = 6J_2 = 4 \cdot (\tau_{III}^2 + \tau_I^2 + \tau_{II}^2)$, $\tau_{II} = \max \tau$(mathem).

Fig.0-5 presents as complete preview the Main Invariants and the associated structural component stresses, principal stresses of the three material families:

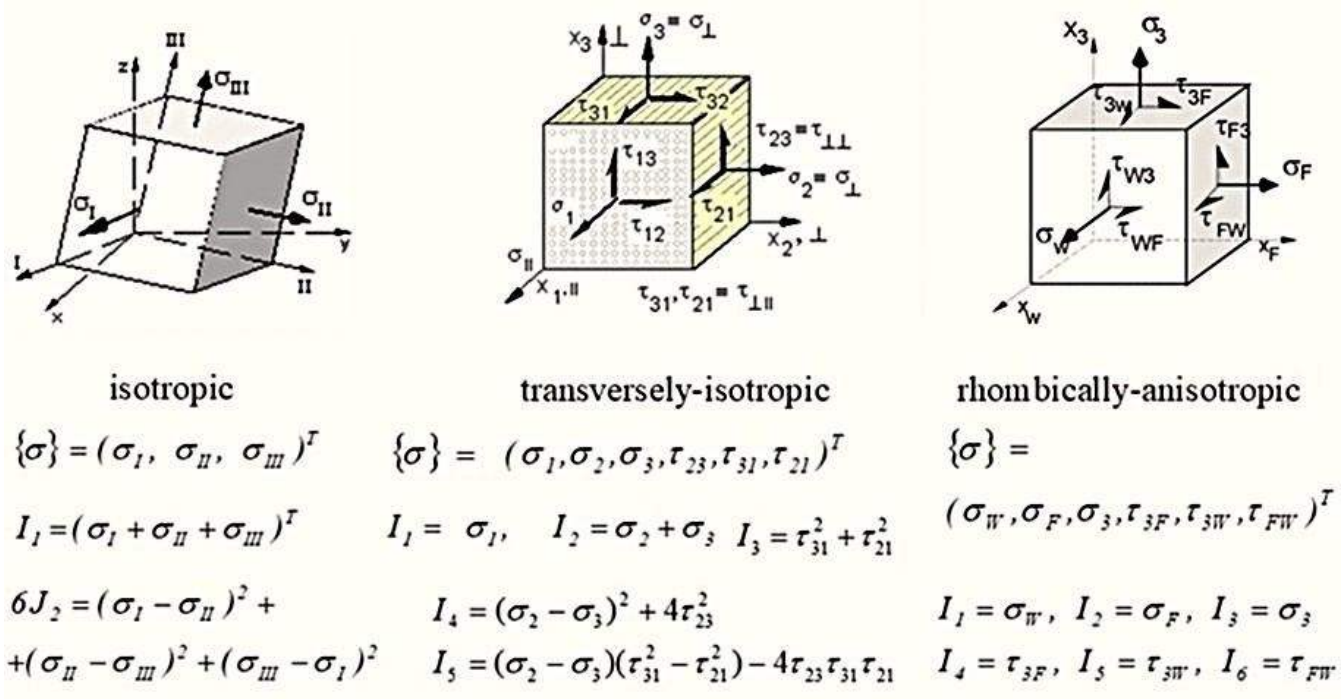

Fig.0-5: Stresses & invariants of isotropic, transversely-isotropic UD and orthotropic materials

0.5.2 Transversely-isotropic UD-material

For UD-lamina-based materials it is valid:

$$I_1 = I_1^{\sigma} = \sigma_1,\ I_2 = \sigma_2 + \sigma_3,\quad I_3 = {\tau_{31}}^2 + {\tau_{21}}^2,\quad I_4 = (\sigma_2 - \sigma_3)^2 + 4\cdot {\tau_{23}}^2,$$

$$I_5 = (\sigma_2 - \sigma_3)\cdot({\tau_{31}}^2 - {\tau_{21}}^2) - 4\cdot\tau_{23}\cdot\tau_{31}\cdot\tau_{21}$$ (from A. Boehler, applied in the FMC) .

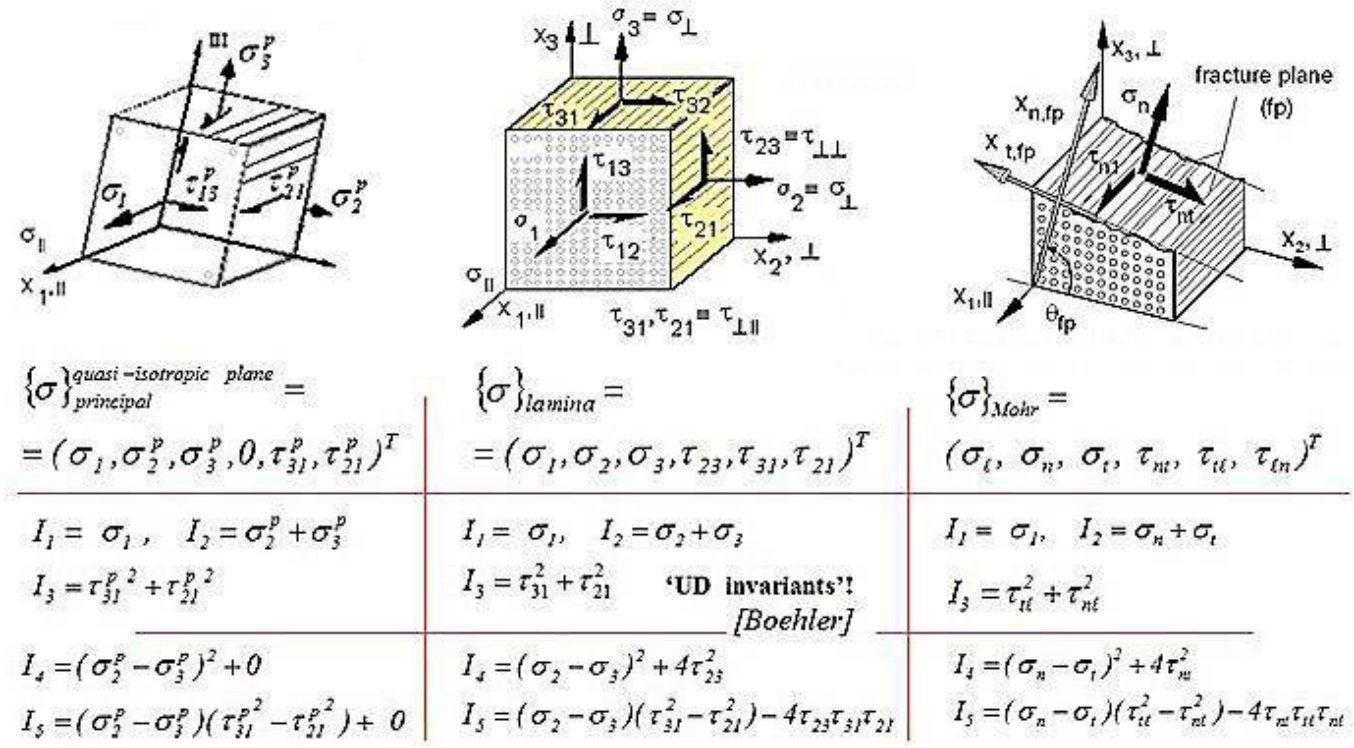

Fig.0-6: Applicable stresses and invariants of transversely-isotropic UD materials

3D: $\{\varepsilon\} = [S] \cdot \{\sigma\}$ with $[S]$ *C*ompliance matrix, $\{\sigma\} = [C] \cdot \{\varepsilon\}$ with $[C]$ *S*tiffness matrix

2D: $\{\varepsilon\} = [S] \cdot \{\sigma\}$ with $[S]$ *C*ompliance matrix, $\{\sigma\} = [Q] \cdot \{\varepsilon\}$ with $[Q]$ *S*tiffness matrix.

0.5.3 Orthotropic Materials

In the case of (rhombically-anisotropic) orthotropic materials much more modes and strengths are present, however simpler invariants are to apply. In the quasi-isotropic 2-3-plane principal stresses may be used.

Eventually for orthotropic materials the related information is to provide.

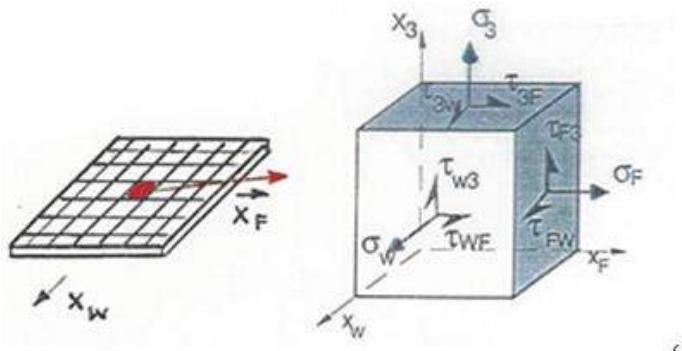

$$\{\sigma\}_{lamina} = (\sigma_W, \sigma_F, \sigma_3, \tau_{3F}, \tau_{3W}, \tau_{FW})^T$$

$$I_1 = \sigma_W, \; I_2 = \sigma_F, \; I_3 = \sigma_3$$
$$I_4 = \tau_{3F}, \; I_5 = \tau_{3W}, \; I_6 = \tau_{FW}$$

$$\{\bar{R}\} = (\bar{R}^t_W, \bar{R}^c_W, \bar{R}^t_F, \bar{R}^c_F, \bar{R}_{WF}, \bar{R}^t_3, \bar{R}^c_3, \bar{R}_{3W}, \bar{R}_{3F})^T$$
$$\{\bar{R}\}_{W-F} = (\bar{R}^t_W, \bar{R}^c_W, \bar{R}_{WF}, \bar{R}^t_3, \bar{R}^c_3, \bar{R}_{3W})^T$$

Fig.0-7: Applicable stresses, strengths and invariants of orthotropic materials

Design Terms, used by an industrial engineer who had to become an 'upper schoolmaster':

1. (model) Validation**: (**from Latin, validus = strong). Modeller's objective to 'qualify' a created model by well mapping physical test results with the model.
2. (structural) Modelling: Term, which practically defines the chosen load-bearing system of the structural system parts joined by the chosen connections. It's not numerical modelling.
3. (numerical) Analys**es** (≠ simulation, NAFEMS takes care of this) in the dimensioning phase
4. Simulation: defined as a process, that consists of several analysis loops and lasts until the system is imitated in the Design Dimensioning process. The model parameters are adjusted hereby to the 'real physical world'
5. Refined sub-model improved Analyses (false, unfortunately also termed Simulation): enables the integration of so-called *virtual tests of sub-models*, for example regarding strength, control, or manufacturing process, and allowing the expected behavior to be pretty well captured virtually. This improves the performance, reliability, and safety still during the development phase. It also reduces the need for costly and time-consuming physical prototype manufacturing. The model parameters are adjusted hereby to the 'virtual world'.
6. Analysis of the final design, (design) Verification (from Latin, veritas facere): fulfillment of a set of design requirement data or control whether the design requirements data set in the performance specification is met. Proof, that the product fulfils the product requirements data, defined in the agreed performance requirements specification *(= Pflichtenheft, supplier = reduzierte ursprüngliche Anforderungsliste, oder Lastenheft des Kunden, customer).* Performed by a computation and/or a physical experiment such as a structural test like with a girder being below a given deformation limit under loading. Verification may be fulfilled without fulfillment of the validation and vice versa. Solving the right equations

1 Special Features with Isotropic and UD Materials to consider in Design

Aim: *Providing the necessary material knowledge, without which proper design is impossible.*

1.1 Facts and Effects of the Various Materials

1.1.1 Pores and crack-like flaws ('defects'), multi-site damage failure

Fig.1-1 serves to complete the understanding of the effect of crack-like flaws, notches, pores and inclusions. It very well characterizes the different effects of 'round' void flaws and crack-like flaws (*from legal reasons avoid the term defect, please*). Under uniaxial tensile stresses, micro-damage depends on the orientation of the crack-like flaws due to the generated different stress intensity at the crack tips. In the case of round micro-pores the micro-damage effect is pretty similar in both the directions due to similar stress concentrations.

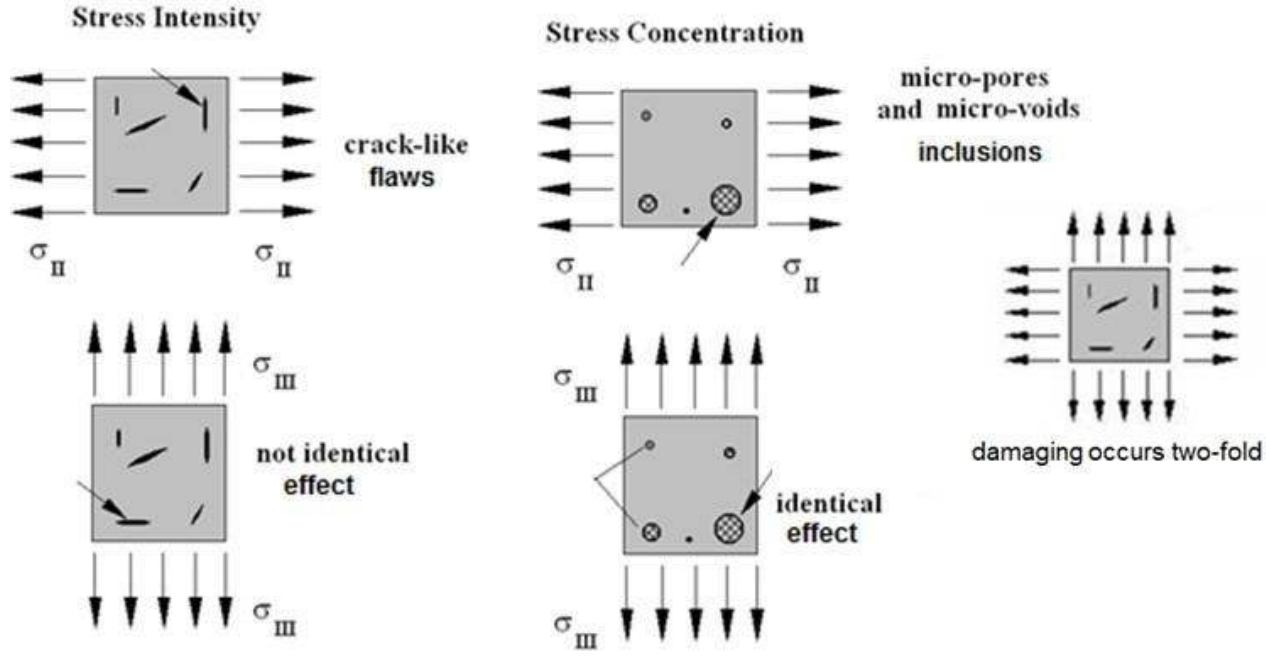

Fig.1-1: Effect of cracks, notches, hard and soft inclusions as originators of fracture. Influence of flaw type, size and orientation

It is to conclude: Failure causing effects are different for round pores and crack-like flaws.

The failure danger usually increases with the grade of the Tri-axiality factor $TrF = \sigma_{hyd} / \sigma_{eq}^{Mises}$. Shear stress drives the yielding process. Therefore the *TrF*-value of a stress state $(\sigma_I, \sigma_{II}, \sigma_{III})$ is a very helpful brittleness measure as is depicted in Table 1-1:

T*able 1-1: Visualization of the tri-axiality factors of several stress states*

Stress state	$\sigma_{hyd} = I_1 / 3$	σ_{eq}^{Mises}	TrF	
(1,0,0)	1/3	1	1D: 1/3	minimum stress brittle
(1,1,0)	2/3	1	2D: 2/3	growing
(1,1,0.5)	0.83	0.5	3D: 5/3	maximum
(1,1,-0.5)	0.5	1.5	3D: 1/3	a compressive stress reduces

Remind, please:

The decision, whether a *strength design verification* must be performed in a critical material location as *strength demonstration* or as a *fracture mechanics design verification* in the structural component,

depends on the size of the flaw. If the size becomes a technical crack, then a fracture mechanics-based macro-damage-based tolerance tool must demonstrate structural integrity.

1.1.2 Mixed (fracture) Failure versus Multi-fold Failure of isotropic and UD-materials

Fig.1-2 displays the difference between Mixed Failure and Multi-fold Failure which can be recognized in the associated domains indicated in the figure. Due to the small tensile strength R^t of many brittle materials the bi-axial tensile strength R^{tt} of them - for instance of concrete - is not of interest but the more its bi-axial compressive strength as will be demonstrated later.

1.1.3 Multi-fold failure effects of isotropic brittle and UD brittle materials

The local existence of twofold and threefold failure effects must be considered:

- A usual SFC just describes a 1-fold occurring failure mode or mechanism !
- A multi-fold occurrence of a failure with its joint probabilistic effects must be additionally considered in the formulas:

  2-fold $\sigma_{II} = \sigma_I$ tension or compression is elegantly captured by using the invariant J_3;

  3-fold $\sigma_{II} = \sigma_I = \sigma_{III}$ hydrostatic compression, by a closing bottom formula part in the case of porous materials.

The later rendered 120°-located inward tension dents and outward compression bulges of the failure body, as the probabilistic result of the *2-fold* acting of the same failure mode. They are described by replacing J_2 by $J_2 \cdot \Theta\,(J_3, J_2)$, which is able to fully maps the non-circularity of the 120° rotationally-symmetric isotropic fracture body.

Eventually *Fig.1-2* displays for UD material multi-fold and mixed mode failure.

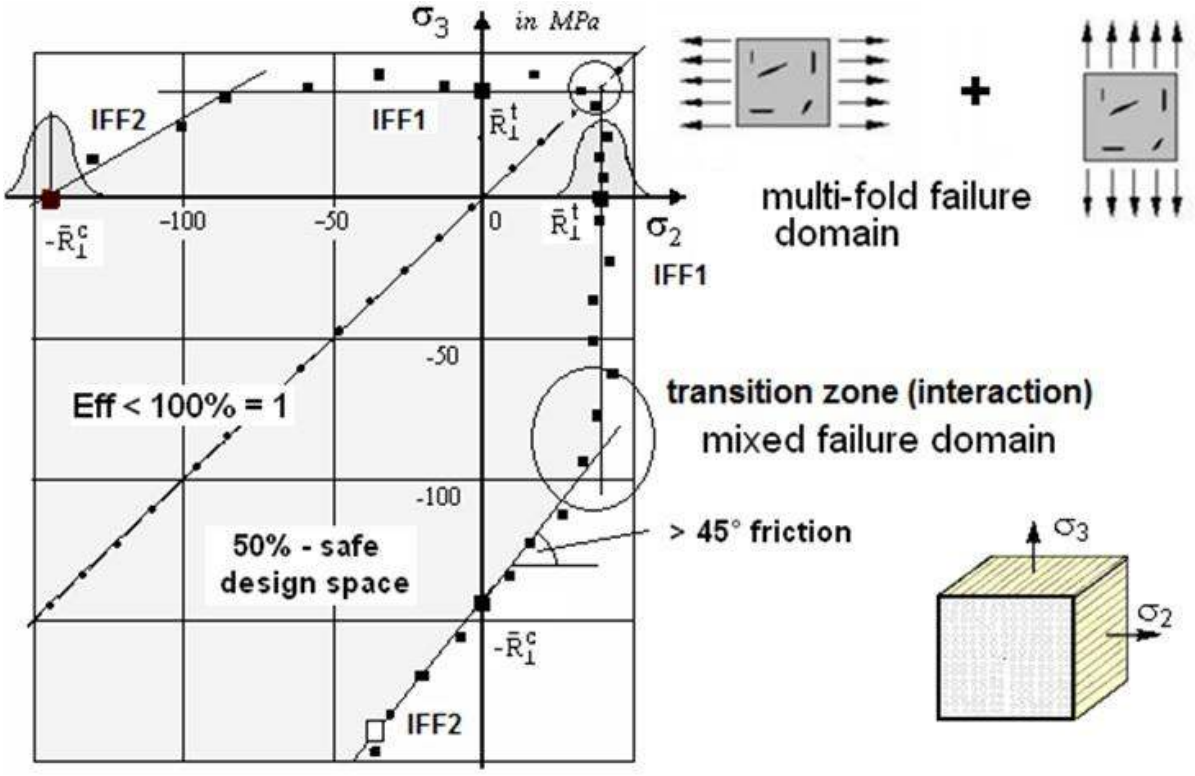

Fig.1-2: Schematic example for a two-fold failure domain and a mixed-failure domain (example UD)

In above context a closer look at materials addressing Shear Stress and Multi-fold Failure is taken in *Fig,1-3*. Principally, shear tests are not uniaxial tests but can be seen to be bi-axial and can be

performed bi-axially. In the isotropic and a quasi-isotropic plane τ can be replaced by $\sigma_I^{pr} = \tau$, $\sigma_I^{pr} = -\tau$. Inserting τ or the two principal stresses = τ-stress components does give the same result, *Fig.1-3*.

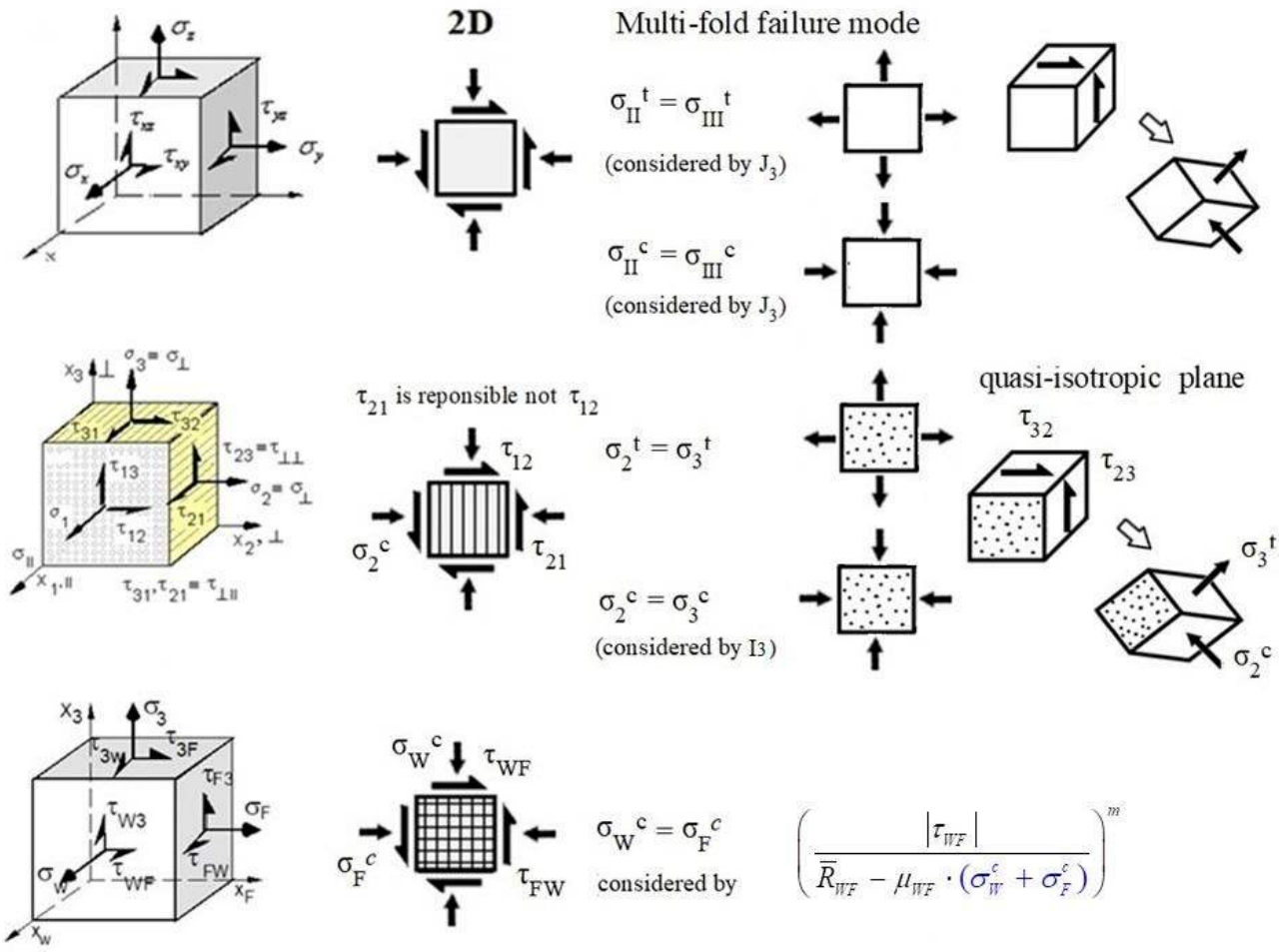

Fig.1-3: Consideration of multi-fold failures with the material families

1.1.4 Effect of High Failure Probability Domains – Size Effects

This effect comes to act where differently large domains of ultimately stressed material parts are given. In the axial load case each material volume is stressed equally high, *Fig.1-4.*

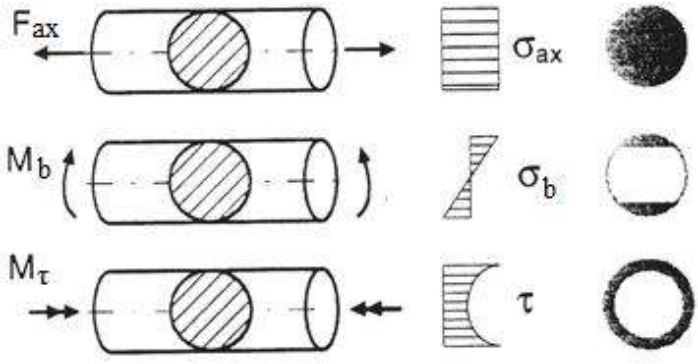

Fig.1-4: Domains of different fracture probabilities for the simple example rod

'Weibull volume effect' and 'Weibull surface effect' are used to estimate the micro-damage effect of an acting tensile stress considering volume and surface. A larger volume leads to lower strength but usually to a lower scattering, which generally makes the statistical reduction to be carried out more favorable. A thick adhesive layer contains more flaws, therefore less cohesive failure danger.

The micro-damage situation at a hole depends on the hole size despite classical mechanics does not say this.

1.1.5 Redundancy effects (healing, benign behavior)

Redundancy effects are usually faced in hydro-static pressure cases. Examples are the materials UD and UHPC (UltraHighPerformanceConcrete). In the UD-case the failure curve consists of the most often weakest-link part and a redundant part under p_{hyd}. This requires a different mapping of the course of test data in the p_{hyd}-dominated IFF2 domain and the IFF3 domain (*see WWFE-II, Test Case 2, later.*). Such redundancy effects are also given for UHPC, being always $R^{cc} > R^{c}$.
Amount, size and orientation of flaws determine whether the generated crack 'plane' becomes an in-plane or out-of-plane failure.

Hydrostatic pressure seems to 'heal' the adverse effect of flaws (*such as micro-cracks, micro-voids*) and delamination by compressing the flaws and increasing the amount of fracture energy necessary for crack growth. However, if fracture nevertheless then begins to act this will happen faster and hence more 'catastrophically', which means fracture occurs in this compressed state in a more brittle manner. Hydrostatic compression and in a minor manner through-thickness compression alone improve both static strength capacity and cyclic strength capacity. This issue is of high importance, e.g. at bearings and joints.

Also, opposite to *redundancy* (a *benign behavior*) the material may experience *weakest link* behavior, and in the case of brittle material becomes valid $R^{tt} < R^{t}$, because flaws are activated by stresses in two orthogonal directions.

1.1.6 Residual stresses (Eigenspannungen) and Pre-stresses (Vorspannungen)

In a lamina of a laminate the curing process of epoxy matrices generates wall thickness-dependent *frozen* residual stresses. These depend on the height of the chemical shrinking (Schwinden) with respect to the physical thermal shrinking (Schrumpfen) due to deformation mismatch, moisture, temperature. Residual stresses are decaying with decreasing stiffness caused by the micro-damage degradation which accompanies increasing non-linearity. In mechanical words: In parallel to the decay of the stiffness the non-linear analysis releases matrix-dominated stresses.

For assessing the temperature-linked height a temperature drop from the difference 'stress free temperature minus room temperature' as effective temperature difference was applied in the WWFE in order to consider the effect of curing stresses as thermal residual stresses of the 1st kind. Moisture was assumed to have a balancing effect of 30°C. Chemical shrinking and thermal curing stresses do not affect the shear stresses. Micro-mechanical curing stresses, being residual stresses of the 2nd kind at filament/matrix level, could not be assessed and considered. They are usually assumed to be respected in the values for the UD-strengths.

Pre-stresses are used to lower for instance the stress state in the low tensile strength polymer matrix at the cost of the fiber, see the procedure given in [*CUN22*]. The same is standard in construction with pretension the mineral matrix concrete at the cost of the steel or of the carbon fiber reinforcement. The size of residual stresses depends on curing and of hygro-thermal stresses on environment.

1.1.7 In-situ behavior of an embedded UD lamina

The in-situ behavior of an embedded UD lamina is deformation-controlled and therefore of redundant type. This fact shows up that a good mapping of the strain-hardening course of 'isolated UD test data' does not involve the full information (*with strain-softening*) necessary for a qualified analysis of laminates which consist of a stack of embedded laminas.

1.1.8 Thickness effect, example UD

Due to being strain-controlled, the material flaws in a *thin* embedded lamina cannot grow freely up to micro-crack size in the thickness direction (*this is sometimes called 'thin layer effect'*), because the neighboring laminas act as micro-crack-stoppers.
Considering fracture mechanics, the strain energy release rate, responsible for the development of damage in the 90° plies from flaws into micro-cracks and larger, increases with increasing ply thickness. Therefore, the actual absolute thickness of a lamina in a laminate is a driving parameter for initiation or onset of micro-cracks, i.e. [*Fla82*]. Investigations on the more expensive but better performing thin layer laminates are present works.

1.1.9 Viewing a material's behavior

Based on his experience the author looks at the material's behavior not whether it is a concrete or a grey cast iron for instance. If such a view is permitted, then the mathematical description of a fracture failure body model of a similarly behaving multi-axially tested material in the past could be used for another material. This transferability idea was stressed for an isotropic example: Given was a good 2D Foam test data basis, the model of which was successfully transferred to a Concrete Stone where a lack of multi-axial failure stress test data had to be faced.

1.1.10 2^{nd}Tg shift effect, preview

Under high hydrostatic pressure, for instance the shear failure curve of a polymer matrix exhibits pretty a non-linearity. This special behaviour of the matrix beyond a certain 'knee' point, see [*Cun13*]**,** is generated because the molecular motion between the cross-links is not frozen anymore. The reason for the occurrence of this knee or kink is attributed to the shift of the point of the so-called second glass transition temperature 2^{nd}Tg up to ambient temperature where many WWFE-tests cases were run. Therefore, this matrix weakening effect has to be considered when the matrix material is subjected to high multi-axial pressure. The influence affects both, modulus and strength. It varies from material to material. Matrix weakening causes a loss in stiffness and an increase of the yield capacity.

1.2 Fracture Failure Types and Behavior of the Various Materials

According to the macroscopic load deformation curve, one can distinguish between deformation-poor and deformation-rich fracture processes. Here, too, the real material plays only a minor role. A mineral material can exhibit the same macroscopic behavior as a carbon fiber material, as a cast material or as a ferritic steel in the low-temperature range. And, a metal and a polymer can show large irreversible deformations up to fracture, although the micro-mechanical deformation mechanisms may be different. The micromechanical failure mechanisms of fracture are material-specific and therefore arbitrarily diverse. This is where (micro-)damage models come in. Some of what appears *similar* at the macro-level (e.g. brittle behavior) may turn out to be completely different on the micro-level.
Examples are: Cleavage fracture in ferritic steels is for instance preceded by local *plastic deformations.* Compression-caused fracture failure of concrete which implies small deformations from damage *mechanisms* on different length scales, micro-damage and macro-damage due to the complex microstructure.

Macroscopic fractures can be classified to span between deformation-rich and deformation-poor (grey cast iron, concrete) fractures, respectively. In tension and compression, the deformation-rich material experiences sliding failure under the influence of the failure-driving shear stress. In the deformation-poor case, the material is plastically non-deformable and at first micro-fractures and then macro-fractures under tension perpendicular to the tensile stress as soon as the normal stress reaches the

separation (tensile) strength R^t. This is accompanied by cleavage fracture designated here as Normal Fracture NF.

A failure usually occurs at a distinct lower scale and has been identified there, thus making the observed level understandable (observed micro-scopic UD kink band versus the fiber-compressed Fiber Failure FF2. Some polymers, which usually fracture in a brittle manner in tension may undergo 'yielding' if tested under hydrostatic pressure p_{hyd}.
Hence, investigating materials failure at all scales is the only basis to obtain a general material understanding.

1.2.1 Isotropic dense materials

Compression of materials normally causes shear failure, because the shear stress is decisive. This includes as well sliding failure of ductile materials under tension and friction-sliding fracture failure of brittle materials under compression, see *Fig.1-5*.

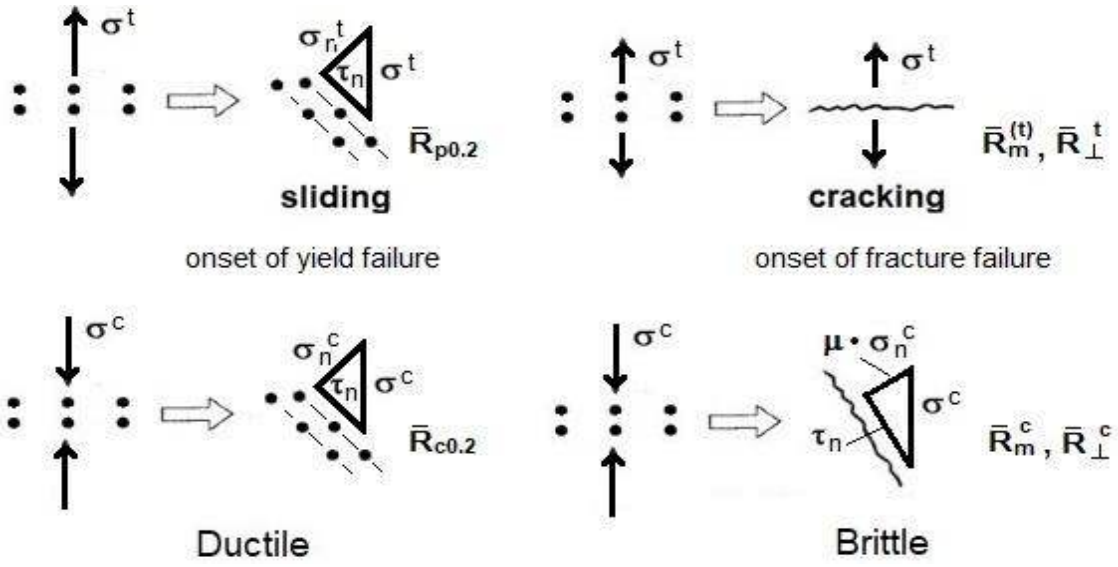

Fig.1-5: Rendering Sliding (micro)Cracking, ductile and brittle and the effect of p_{hyd}

LL:

** Brittle: failure is fracture failure, 2 failure modes, 2 strengths to be measured.*

** Ductile: failure is yield failure, 1 failure mode, 1 strength $\bar{R}^t$ to be measured (= load-controlled value), $\bar{R}^c$ is neither really existing due to barreling of the cylindrical test specimen nor necessary for design → $R_{0.2}$ is the design driving 'strength'.*

**Presumption "SHAPE of the fracture failure body of a material is known". Then, just the SIZE of the body needs to be further determined. This can be always performed by the necessarily known (uniaxial) different tensile and compressive strengths. → Helpful, when designing with pretty novel materials*

** Rock material like e.g. marble yields under high pressure!*

The full failure surface of isotropic materials is not axisymmetric. The surface shapes do not only depend on the two strengths but also in the negative domain $I_1 < 0$ further on the friction value and generally on the existence of a two-fold acting stress failure mode in the positive and the negative domain, causing the 120°-rotational axial symmetry of the failure surface with inward and outward dents.

⇒ Usually applied '*Two properties failure theories for isotropic materials*' cannot map this.

In *Fig.1-6* are depicted:

(left) load situations with associated fracture plane sketches and shear fracture pictures, and
(right) situations of tensioned, differently brittle isotropic materials. Before tensile rupture (*end of so-called 'Gurson domain'*) firstly a diffuse and later a local *necking* with *void growth* occurs associated by a volume change before rupture starts. Dimples are generated under tension.

If brittle, then failure is fracture failure. The normative suffix $_m$ in $R_{(m)} = R^t$ should and can (must) be dropped in order to achieve a simpler and clearer general material designation system.

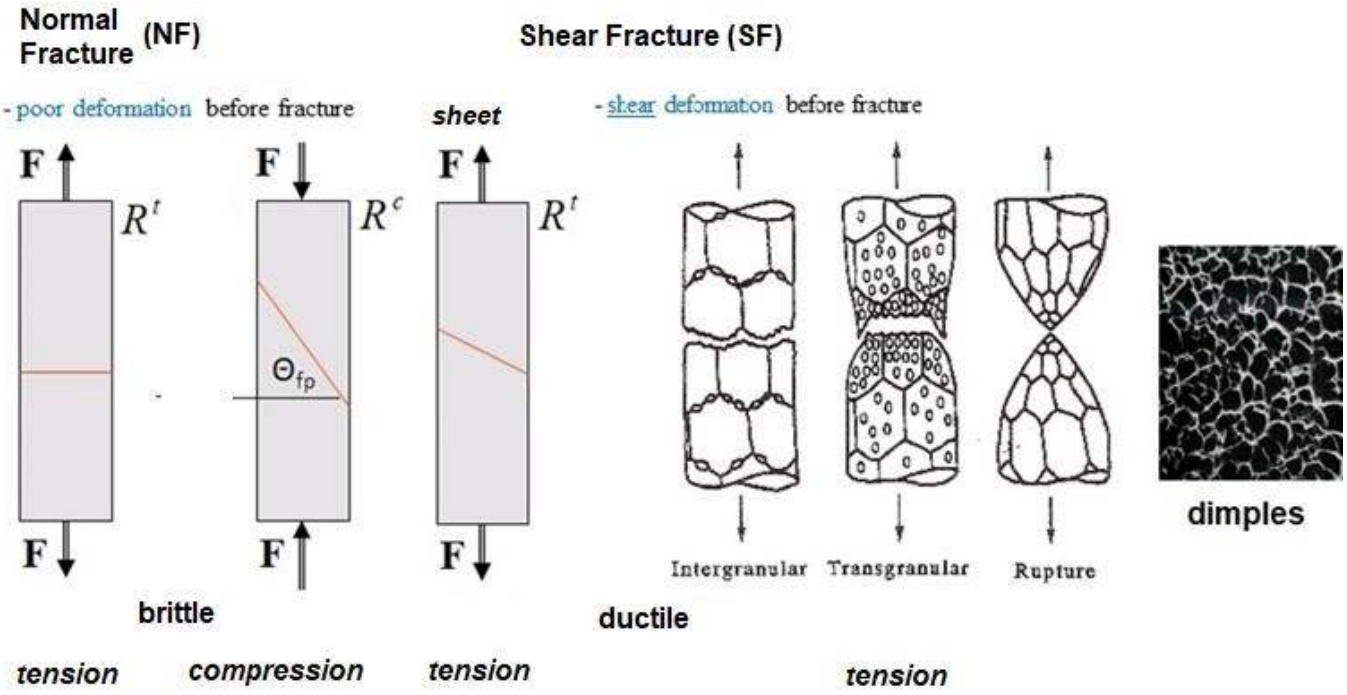

Fig.1-6: Fracture 'plane' sketches of different 'dense' isotropic tensile test specimens (the angle may complementary defined)

1.2.2 Isotropic porous materials

In the case of isotropic brittle porous materials two failure modes are faced above, NF and CrF. This leads over to **Mineral Grain materials,** see *Fig.1-7*. In the case of cracks, in contrast to the strength of intact solid materials, a uniaxial compressive stress causes a tensile stress at the crack tip of an

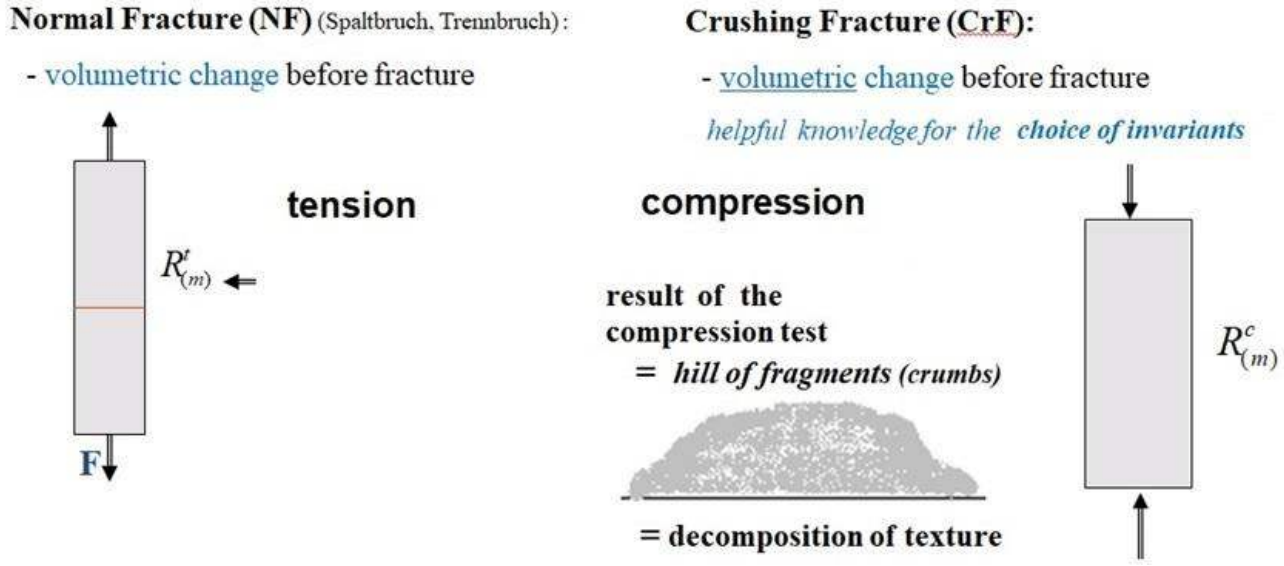

Fig.1-7: Normal Fracture NF and Crushing Fracture CrF of porous isotropic materials

inclined crack. This generates a secondary crack, termed wing (kink) crack, which turns into the direction of the acting compressive stress and may lead to splitting. Principally, this is similar to what happens in the fracture mechanics tension domain to an oblique macro-crack. Under multi-axial stress states the original crack may become instable and kinks with an altering direction of the fracture plane (*strain rate is influencing this behavior*). This problem has attracted much attention and shall be here considered by using a strength failure view.

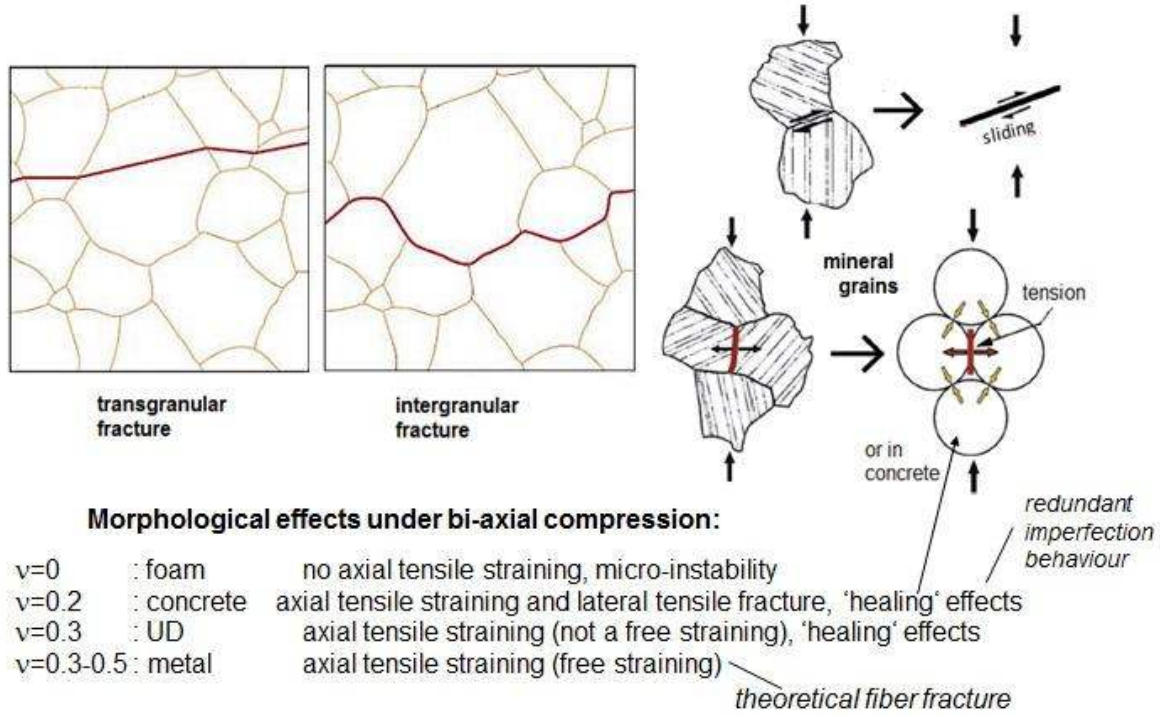

Fig.1-8: (left) Texture influence considering inter-granular and trans-granular fracture under tension; (right) Fracture between the mineral grains under compression due to 3D-tensile stress states

In the 2D compression case one wing branches off from each end of the initial crack, *Fig.1-9*. These wings are generated dynamically. Then the further wing growth proceeds continuously.
In the 3D compression case the generation of the wings causes an additional volume (*cavitation*) which is suppressed under multi-axial compression.

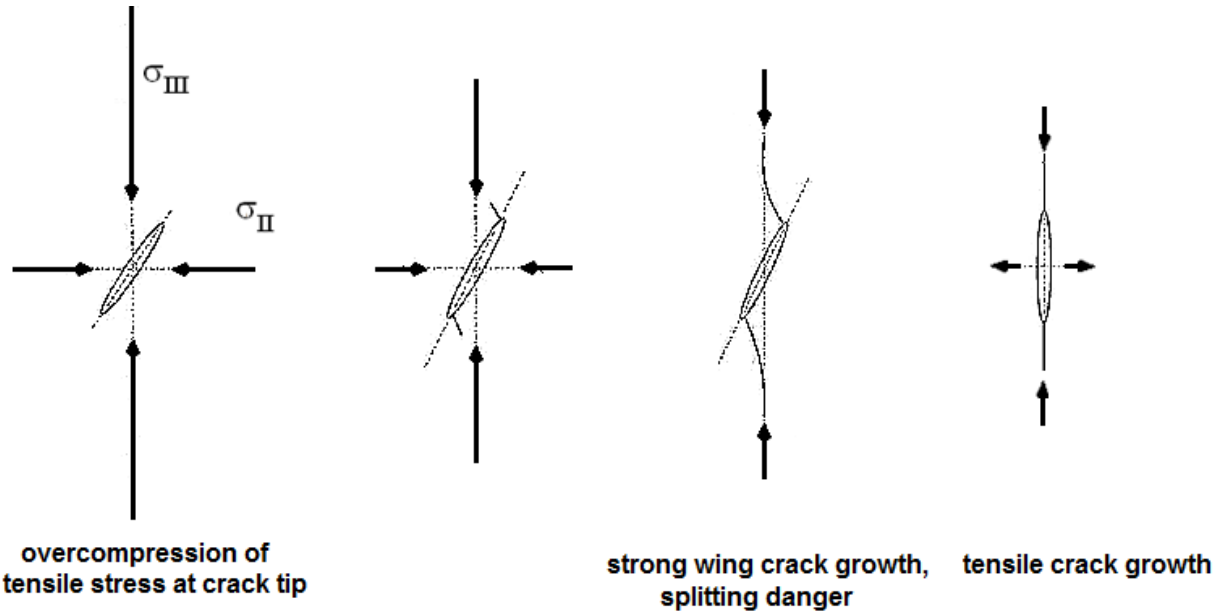

Fig.1-9: Initiation and attenuation of wing cracks (see [Ger94]

For completion, *Fig.1-10* allocates cracks to 2D stress states. Under operational loading open-through crack and closed-through crack situations are to treat.

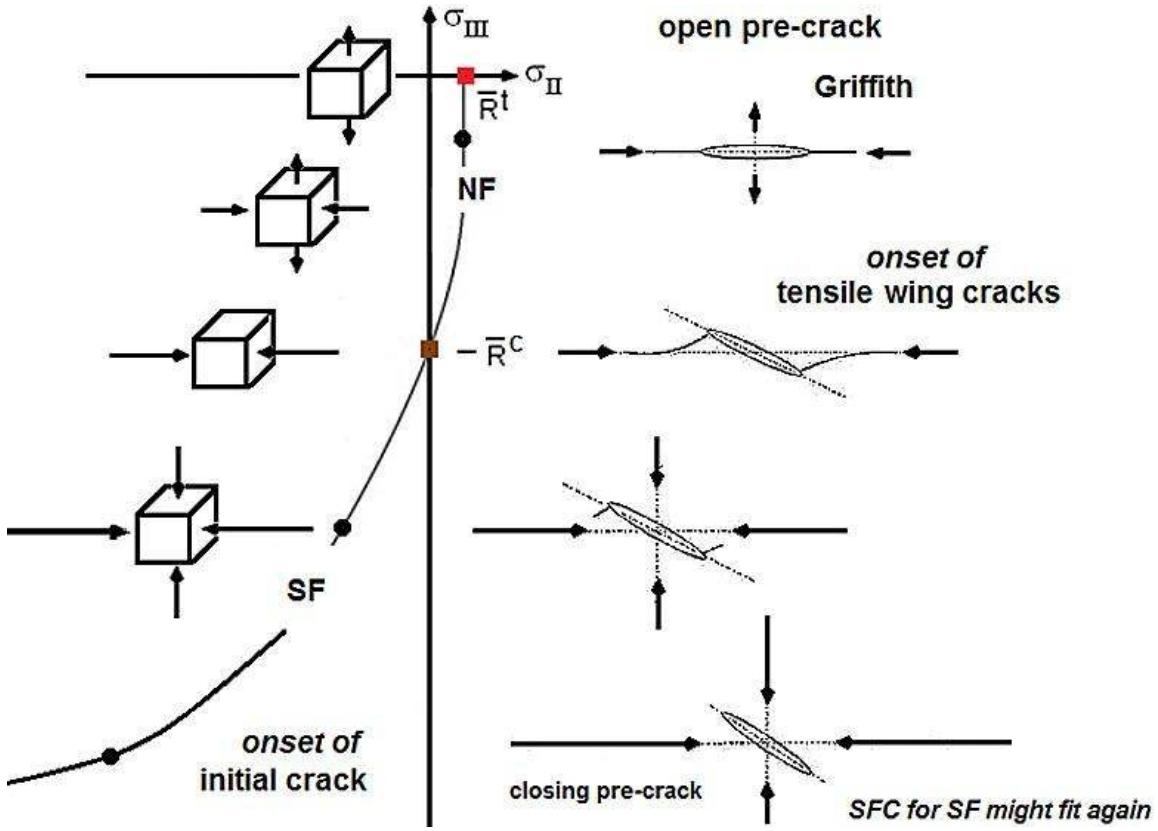

Fig.1-10: Mixed-Mode Compression, isotropic: 2D stress states, Observations w.r.t. failure modes NF and SF and fracture 'planes' in the case of initially crack-free (intact), open-through crack and closed-through crack situations

***LL**:*

2D-models are not sufficient to describe progress of fracture in brittle behaving isotropic [Ger 94] materials such as grey cast iron, rock material, concrete, UD-material etc. 3D-theory and 3D experimental proofs are principally needed.

In the context of this chapter the influence of porosity shall be shortly addressed:

Porosity is composed of all the cavities that are connected to each other and to the environment (*open porosity*) and the unconnected cavities (*closed*). A highly open-pored material is a honeycomb for instance, closed porosity one finds with foams, see [*Dr. J. Macht, Univ.-Doz., Dr. P. Nischer, Forschungsinstitut der VÖZ, Wien*]. Porous materials, such as foams, porous laminates, porous polymer and concrete matrices, mortar, brick and geo-materials have stress-strain curves, which can be divided into 3 sections: (1) Pressure low: the material behaves elastically, pores are preserved, (2) Pressure increased: pores are compressed, (3) Pressure exceeds a certain limit: finally complete compaction with pulverization of the crushed material. Collapse of the pores during crushing drives the compaction behavior of porous materials.

1.2.3 Transversely-isotropic dense UD materials

The *Fig.1-11* presents micro-mechanical fracture of transversely-isotropic UD-material.

The observed fracture types in *Fig.1-11* can be dedicated to the well-known 5 UD fracture failure modes.

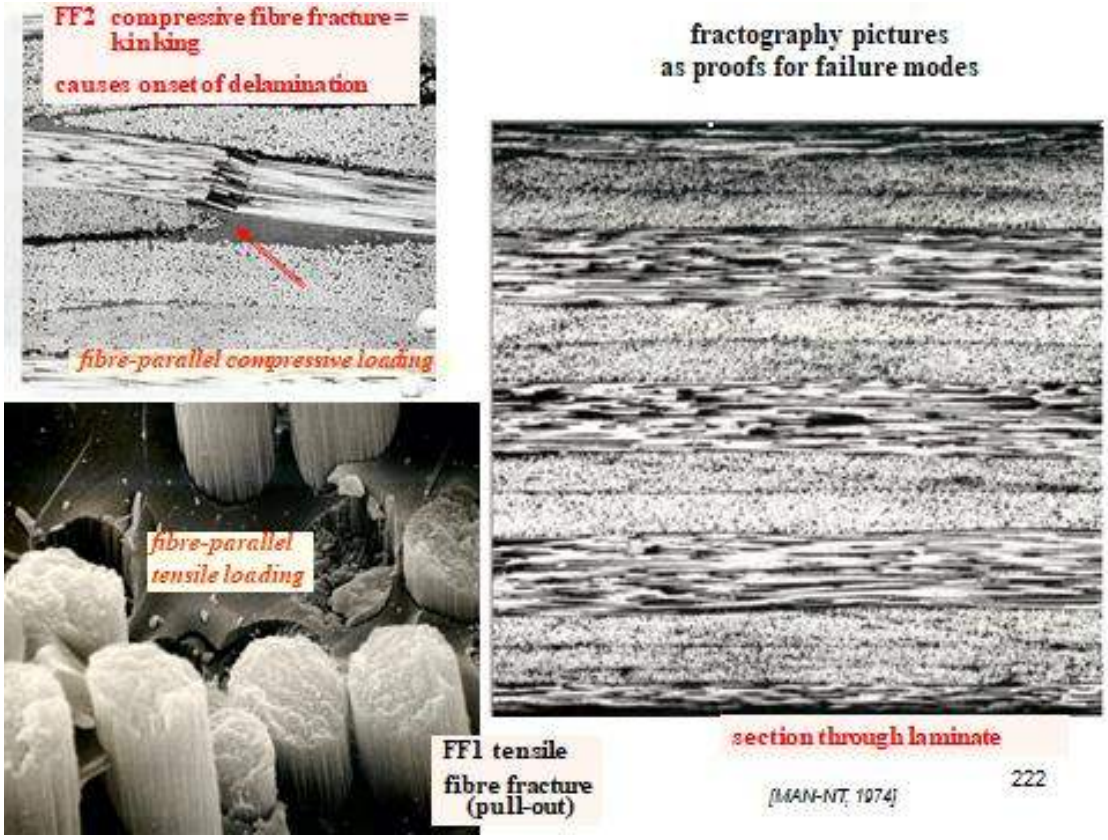

Fig.1-11 Fracture of UD material on micro-level

***LL**:*

- *SFC input: 'In-situ' strength properties are more benign than the inserted 'virgin' properties!*
- *SFCs shall focus failure behavior and not a specific material class*
- *Ductile-brittle transition failure behavior may be faced for the matrix material*
- *UD compressive strength is smaller than the tensile one, because micro-mechanically shear instability (above kinking) prevents the inherent filament strength from being utilized due to misalignment. The use of pultruded rods improves the utilization rate.*

1.2.4 For Pre-understanding a Visualization of an isotropic Failure Body with Associated Stresses

Engineers better learn from meaningful figures than from formulas. Therefore, numerically very effortful visualizations of the generated SFC failure bodies are a strong need, because a failure body shows the designing engineer the '*multiaxial strength capacity'* of a material under general stress states. As a preview this task will be exemplarily performed for an isotropic Normal Concrete material where a 3D test data set was available. *Fig.1-12* outlines the essential quantities for two body cross sections.

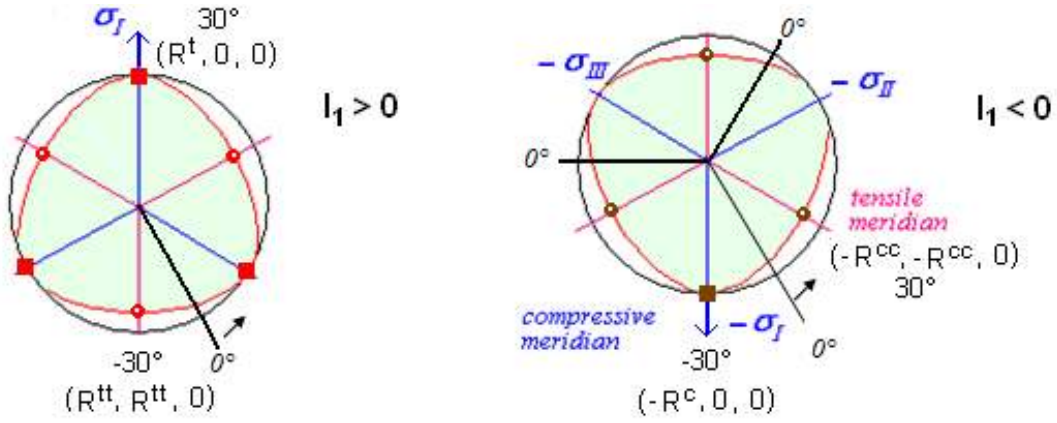

Fig.1-12: Principal stresses, strength points, Mises cylinder shape, dents and Lode angle ϑ° around the 120°-symmetric hoop. Ansatz: sin(3ϑ) with ϑ°=0° at shear meridian was taken

For the tensile meridian the Lode angle is ϑ = +30° and for the compressive meridian -30°. The shear meridian was chosen here as neutral meridian with a Lode angle ϑ = 0.

A failure body is the location of all 1D-, 2D- and 3D-failure stress states. These are all points on the failure surface. As still mentioned, *F* = 1 or *Eff* = 100% mathematically defines the surface of the failure body.

Such an isotropic failure body is rendered here using the Haigh-Westergaard-Lode coordinates with $I_1/\sqrt{3}$ as y-coordinate (axial) and $\sqrt{2 \cdot J_2}$ as x-coordinate (hoop), see below in *Fig.1-13*,the upper left part. This figure confirms that above coordinate choice physically makes sense, because of the equal measurement in all directions.

The part figure, left down, depicts the stress states belonging to a tensile meridian and to a compressive meridian. These are those axial cross–sections of the failure body (right) along most of the compression tests are run. On the fracture failure body the 3 main meridians are outlined.

Some 3D-failure stress states are indicated as fracture body points. Finally, for three essential design quantities the formulas are presented at the right side down.

The mapped test data set demonstrates the 120°-axial symmetry for isotropic materials.

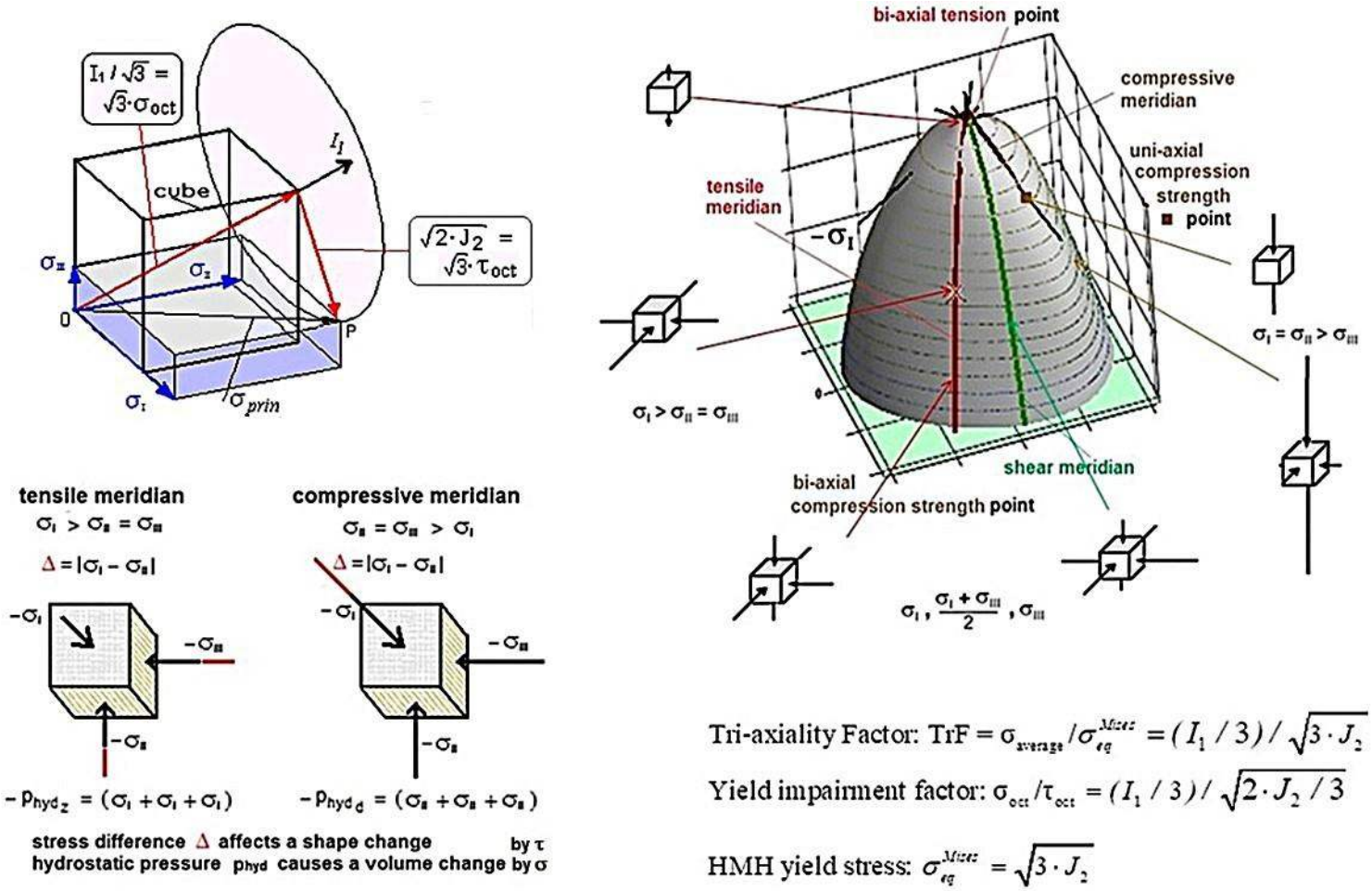

Fig.1-13, visualization of a failure body with associated quantities:

Haigh-Westergaard Lode-coordinates $I_1/\sqrt{3}$, $\sqrt{2\cdot J_2}$ *, coordinates of the main meridians (compression, shear and tension) and various multi-axial stress states. Squares ■ ■ indicate strength values (strengths are defined as uniaxial failure stresses) and crosses mark bi-axial points (bi-axial failure stresses)*

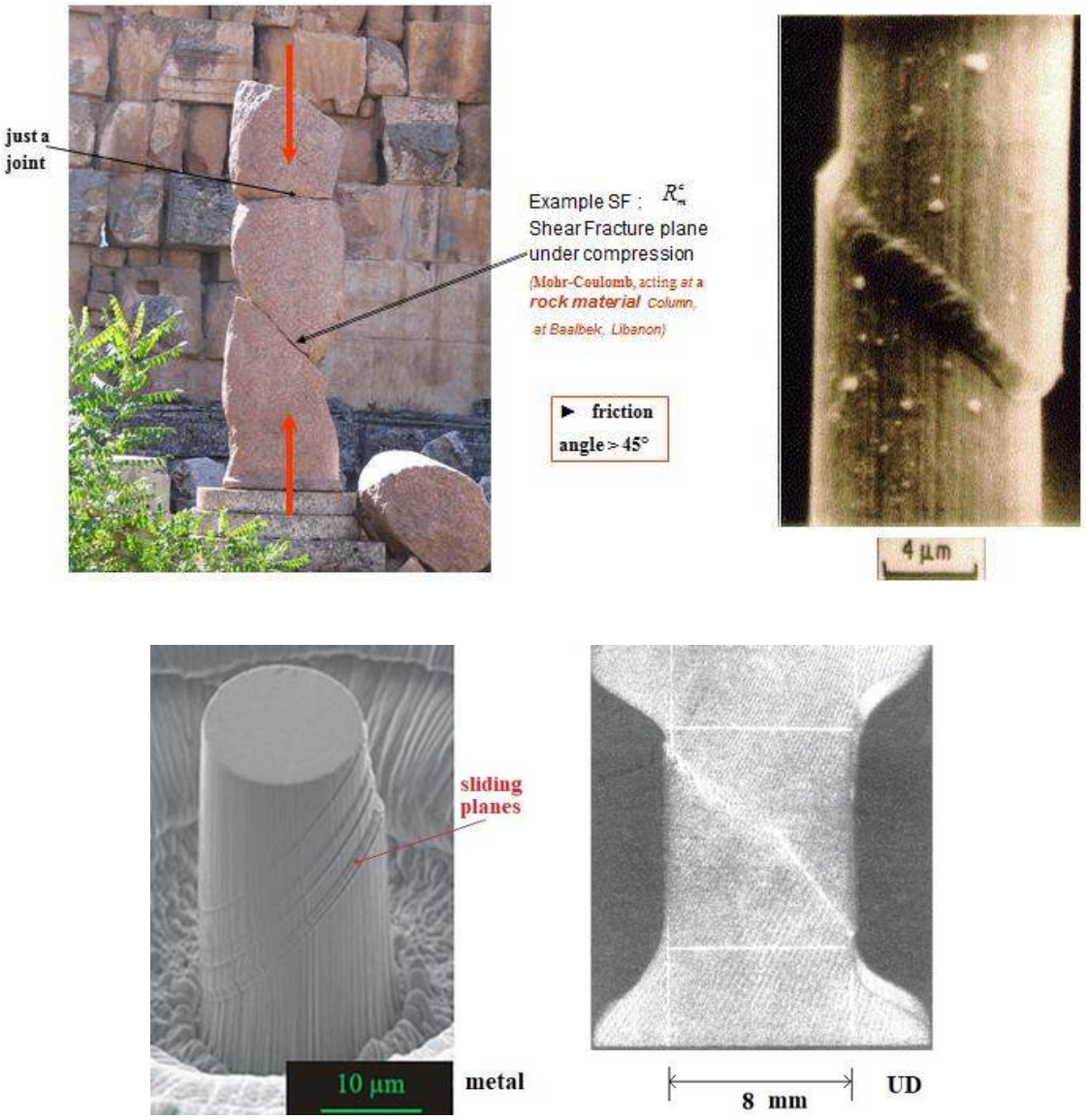

Fig.1-14, Shear failure planes at extreme length scales:

Facture angles of the brittle materials Rock material, Carbon fiber [K. Schulte, TU Hamburg-Harburg], Ductile metal compression cut from a single crystal (deformed pillar after compression testing. Monnet, G. & Pouchon, M. A. (2013), Determination of the so-called critical resolved shear stress and the friction stress in austenitic stainless steels by compression of pillars extracted from single grains', Mater. Letters 98, 128-130) and laterally compressed UD-CFRP

Mind, please before designing: $\bar{R}^{tt} > \bar{R}^{t}$!

- Technical strength *R:* 1D-failure stress, defined by standards and cannot be increased considering the same material. Its value for a given material is fixed!
- Test data mapping, using an average strength $\bar{R}$: Results belong to a 50% survival probability expectance value
- Design verification, using *strength design allowable R*: is a distinct statistical survival probability
- Material symmetry: fixes the number of measurable properties. A material model that needs more parameters than measurable properties requires the execution of a simulation process with several analysis loops in order to determine these parameters by numerical fitting. This causes a problem in fulfilling the statistical requirements to be considered in the final (single) Design Verification analysis
- Facing Process-induced Deformation (PID) in thermosetting composites is the unavoidable, often undesired, change in shape (warpage, spring-in, thickness variation) resulting from residual stresses developed during manufacturing. It is primarily caused by mismatches in thermal expansion coefficients between fiber/resin and tool/part, along with chemical shrinkage of the resin during curing.

2 Design Dimensioning

Aim: *Obtaining reliable structural components for the series production, later.*

2.1 General on Quasi-Static Design

2.1.1 Modelling Materials

* Modelling shall use self-explaining terms, as those given in *Table 0-1*
* Then it is to decide which failure types may be faced
* In the third step it is to decide, whether the - *in general* - material conglomerate can be homogenized (smeared) to a still available validated material model like a validated Strength Failure Criterion **(**SFC)
* The choice of the material model always depends on the efficiency a structural task must be and can be solved and further on the required quality of the answer!

2.1.2 Industrial Tasks when performing strength design verifications

More and more, the engineering decisions depend on computational simulations, shifting the role of physical tests from product compliance demonstration to simulation model validation and in context the industry seeks to replace the expensive 'Make and Test' design method by verified and benchmarked predictive tools that engineers could use with confidence, or – in other words - novel simulation-driven product development shifts the role of physical testing to virtual testing, to simulation, respectively. Then, however, the limitations of these predictive tools such as its part ‘strength failure conditions (SFC)’ should be clearly described. The required high fidelity asks for the use of reliable material models. In this context:

- Simulation means imitation of the operation of a real-world process and model adaption due to test information by performing many analyses.
- Basic desire of the usually macro-scopically working structural engineer thereby is a material model linked to an ideally homogeneous material which might be isotropic or anisotropic.

For the 3D-Demonstration of Strength are required - nowadays practically a must regarding the usual 3D FEA stress output – validated 3D Strength Failure Criteria (SFC) rendered by 3D failure bodies to firstly perform Design Dimensioning and to finally achieve Design Verification and thereby proving Structural Integrity.

Table 2-1: Survey on tequired strength design verifications, quasi-static and cyclic (fatigued, cracked)

	Flaws stress					Notches stress concentration		Cracks stress intensity	
	dense	*dense*	*dense*	*dense*	*porous*	*dense*	*porous*	*dense*	*porous*
	SY	NY	SF	NF	CrF	Neuber etc, FFM		damage tolerance tools	
ductile	*x*	*x*	-	*x*	---	*x*	*x*	*x*	---
brittle	*x*	*x*	*x*	*x*	*x*	*x*	*x*	*x*	*x*

Reliable structural designs are searched in design dimensioning on various theoretical levels and bases:

Continuum Mechanics ↔ Continuum (micro-)Damage Mechanics ↔ (macro-)Damage Mechanics,
the latter with its Fracture Mechanics based Damage Tolerance analysis tools is used in the case of cracks.

2.1.3 Preview on Strength Failure Conditions (SFC) and on Designing

The variety of new materials in engineering requires the knowledge of the failure state in order to enable verification of the designed structural part. And this much more since modern lightweight design requires a higher exertion of the material and thereby contributes to sustainable engineering.
Design Verification demands for reliable Reserve Factors *RF* or Margins of Safety *MoS* = *RF* -1 and these – beside a reliable structural analysis - demand for reliable Strength Failure **Conditions** (SFCs), usually termed **Criteria**). Such a condition is the mathematical formulation *F* = 1 of a failure curve or of a failure surface (body). Generally required are a yield strength conditions and a fracture strength conditions. A load-driven growing yield failure surface is terminated by the fracture failure surface.

A yield SFC usually describes just one mode, namely for isotropic materials the classical 'Mises' Shear Yielding (SY). For PMMA, however, there are two yield modes, SY in the compression domain and normal yielding NY in the tension domain. Fracture SFCs usually describe two independent fracture modes, namely Shear Fracture (SF) and Normal Fracture (NF).

Fig.2-1 displays the structural engineer's tasks he is involved when designing a structural part. It is to demonstrate that the static Dimensioning Load Cases as well as the dynamic and cyclic ones, considering lifetime, and others are fulfilled. Addressed are Design Dimensioning (*Auslegung, Bemessung*) and Design Verification (DV, *Nachweis*), sometimes termed Proof. Of special focus thereby

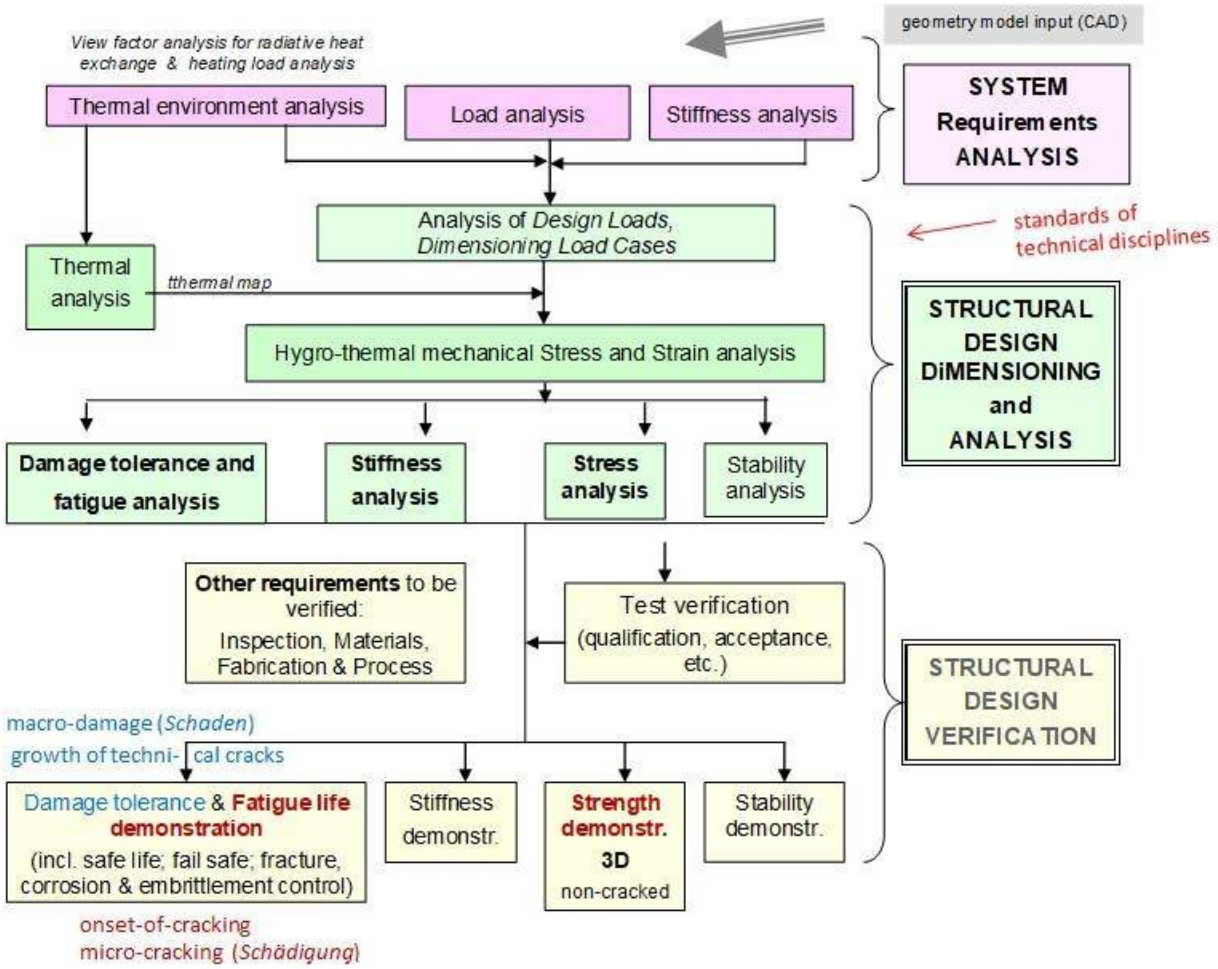

Resistances to be demonstrated by proof of a Reserve Factor RF > 1 or a positive Margin of Safety MoS = RF – 1 in order to achieve Structural Integrity for the Certification Process.

- Mechanical Engineering, proof of *Design Ultimate Load (limit state) DUL, *Design Limit Load (limit state) DLL
- Civil Engineering, proof of * Ultimate Limit State (ULS, GZG) and *Serviceability Limit State (SLS, GZG)

Fig.2-1: Structural engineer's tasks and complete work flow in structural design

is the strength verification of non-cracked structural components (regime micro-crack ≡ micro-damage) and the fracture mechanics verification of cracked components (macro-crack ≡ macro-damage).

Strength verification of non-cracked structural components is demonstrated by the SFCs if "No relevant limit failure state is met *considering* **all dimensioning load cases".**

The size of the (macro-)damage decides whether it is to apply a Strength Failure Condition SFC, $F = 1$, (now most often termed strength criterion, which originally meant $F <= > 1$) for the verification of onset-of-fracture of the un-cracked structural part or a fracture mechanics-based Damage Tolerance Condition in case of a technical crack.

Fig.2-2 gives hints where which verification procedure is to apply or in other words: When must be fracture mechanics used and when strength mechanics? The figure refers to:

(a) Strength Mechanics versus Linear Elastic Fracture Mechanics (LEFM) analysis;

(b) Crack-free versus crack-driven fracture through a_0 being an initial flaw size (surface flaw) or a developed crack (for instance an internal delamination).

Further, *Fig.2-2* depicts in b where the different technical failure types Normal Fracture NF, Shear Fracture SF and Shear Yielding SY are located.

In order to understand the mechanisms of crack growth itself, it is necessary to consider the phenomena at the tip of a crack on a microscopic level. On the modelling-desired macroscopic structural level, however, such an approach is not practical. Therefore, Fracture Mechanics FM works on a macroscopic scale, and tries to determine parameters from structural response results.

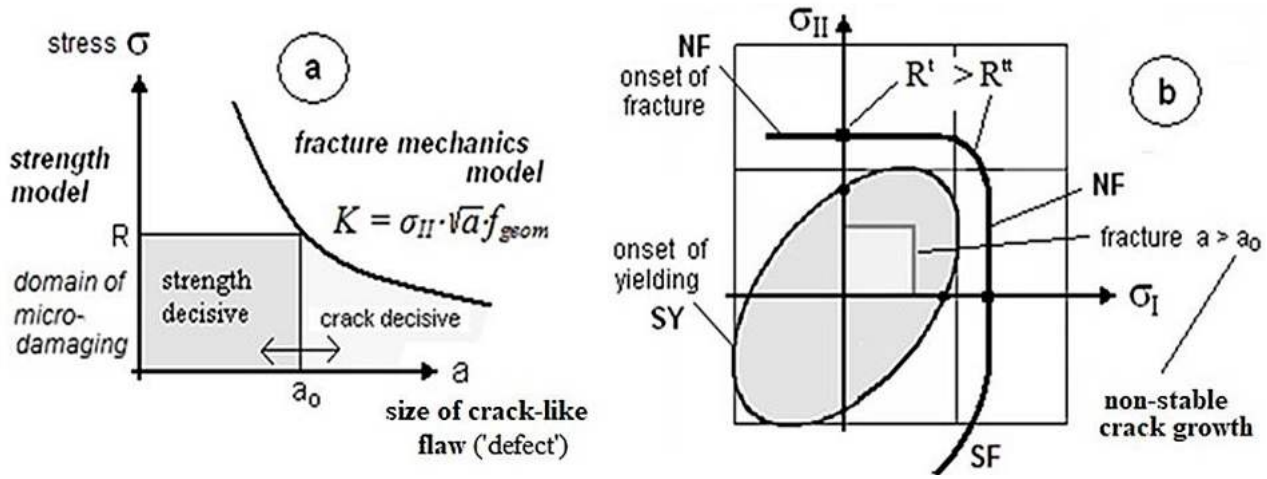

Fig.2-2: (a) Continuum mechanics strength analysis versus fracture mechanics analysis. (b) Crack free fracture onset and crack-driven fracture through f a crack geometry factor, a_0 the initial flaw size (surface flaw, delamination, ..), K is stress intensity factor, a is crack size, NF Normal Fracture, SF Shear Fracture, R is strength value, ^{t} means tensile. σ_{II} is principal stress

'Unclearness' or Fuzziness (in German Unschärfe) is inherent in loadings, strengths, and other design variables such as geometrical parameters, applied engineering models, etc. All these uncertainty sources in design contribute to the overall Structural Risk defined here arbitrarily as

Amount of Costs - *incurred in the case of later failure* –

times the Probability that the distinct Failure occurs in the structural part.

Risk drives the designer to follow *Table 2-1*.

Table 2-1: Design objectives and process

Objective: Reliable Structural Components

Design = compromise of *Design–to-Cost* and *Design-to-Quality*. Robust design helps to 'safely' accept smaller design changes and to 'survive' manufacturing flaws, and this saves money and trouble! Optimization-to-production is mandatory considering (as-built, effects-of–flaws and *Design-to-Non-destructive inspection*). Thereby the two essential requirements

- Functional Requirements (tasks to let the developers know what to build, to let the testers know what tests are to run, to let stakeholders know what they are getting [Wikipedia]) and
- Operational Requirements (needed performance capabilities, lifetime etc.)

have to be fulfilled.

Functional Integration is a basic driver especially with composites when viewing costs.

Aim: Reduction of design uncertainties

Means: Sorting out the weakest links in the development process which involve the highest uncertainties. Most often the loadings are the most uncertain design parameters.

Tight schedule constraints often lead to a so-called Success-oriented Development Logic. This however requires excellent specifications, a consistent design philosophy including safety concept with FoS *j*, nonlinear analyses, true and average (σ,ε)-curves; efficient design methods including strength design allowables and validated failure conditions, mean geometry; a practical risk judging and Simultaneous Engineering..

The next tables present a short survey on loading conditions and Load Cases (LC). To consider are effects such as media, temperature, creeping, aging, relaxing.

Table 2-2 compiles the loading types to be generally considered in design

Table 2-2: Loading types for the design

Static loading: *strength*

Validated 3D strength failure conditions for isotropic (foam, concrete, PMMA,..), transversely-isotropic UD materials, and orthotropic materials (e.g. textiles) to determine 'Onset-of-fracture' and 'Final fracture' in case of benign failure behavior (quasi-ductile).

Standardization of material test procedures, test specimens, test rigs, and test data with raw test data evaluation for a comparably good structural analysis input.

Consideration of manufacturing imperfections (tolerance width of uncertain design variables) in order to achieve a production cost minimum by "Design-to-Imperfections", which includes flaws

Dynamic loading: *hazards, impact, crash loading, blast*

Cyclic loading: *fatigue and crack growth*

$\Rightarrow$ Concern is the development of practical, physically-based lifetime-prediction methods and the generation of SN curve test data for the validation of the prediction models, crack growth models, delamination growth models if laminates.

Table 2-3 presents a survey on design loadings and their possible combinations.

Table 2-3: Design load analysis, loadings, combinations of loadings & Load Cases - Mechanical Engineering and Civil Engineering

Design Loadings:

'Estimation' of all external + internal loadings of the structural component:
- mechanical (static, cyclic, and dynamic) and hygro-thermal,
- acoustical environment as well as of the
- corresponding lifetime requirements (duration, number of cycles)

Loadings are specified by
a Technical Specification from the customer, or an authority or
a common standard (EC codes, DIN, EN, FAA, ESA, automotive, wind energy, ...)

Otherwise a load(ings) analysis is required = Establishment of load events the structure is likely to experience (= load history). Dynamic structural system analyses are performed to estimate the loadings. *Examples: launcher in aerospace, 'old' bridge refurbishment in construction*

Combinations of Loadings: → *structural specifications*

Combinations usually involves a Worst Case scenario, w.r.t. combinations of loadings, temperature and moisture, and undetected damage.

→ Set of Combinations of Loadings, termed Load Cases (LCs). From this usually vast number of Load Cases - if possible - a minimum set should be selected. This

→ Set of (*design driving*) Dimensional Load Cases (DLCs) will make fast project decisions possible in the case of input changes, to by-pass an FEA output evaluation death and to automatically provide the engineer with a better understanding of the structure's behavior**.**

Design Dimensioning and Design Verification are performed on different structural levels, see following *Table 2-4*.

The bold words in the table show the focus viewed in this document.

Table 2-4: Levels of Design Verification with respect to Static Strength

- Structure level : forces & moments (resistance of a truss element *strut*)
- Cross-section level : section forces (stress resultants) & section moments (resistance of a *shell wall*)
- **Material level : stresses** (strength at a material point, basically *envisaged here*).

Structural load-carrying capacity is mainly *locally* determined by the stress state in the critical material locations, such as in:

* **undisturbed areas** (uniform material areas, membrane areas etc.),
* disturbed areas (discontinuities such as joints, notches etc.).

Assessment of stress states at critical locations is to be performed for the material families:

* **isotropic material** (metal, concrete, glass, etc.)
* **transversely-isotropic UD-material** (UD := Uni-Directional)
* **orthotropic material** (textiles etc.).

* The construction (*Bauweise*) of a load-carrying structure must be suitable for the intended task and the materials must then correctly meet the required properties locally
* All designed products should be manufacturable, testable, and maintainable
* Materials used must have known, reliable, and reproducible properties and shall have proven resistance to the environment envisaged.

It has to be shown : by

- Analyses, that the design meets the requirements
- Manufacturing with Quality Assurance, that the structural product meets the requirements
- Structural Testing, that the specific requirement data set is verified.

2.2 Design Verification Procedure Scheme with usual Requirements to achieve Structural Integrity

In *Fig.2-3* the general procedure and a simple static strength verification procedure is visualized for completeness, depicting the levels of possible design verification. The highest level is the load level and the lowest the stress level, where one should better use validated SFCs (***arrow***) instead of dubious interaction formulas below to interact normal and shear stresses, as unfortunately still found in design 'books'.

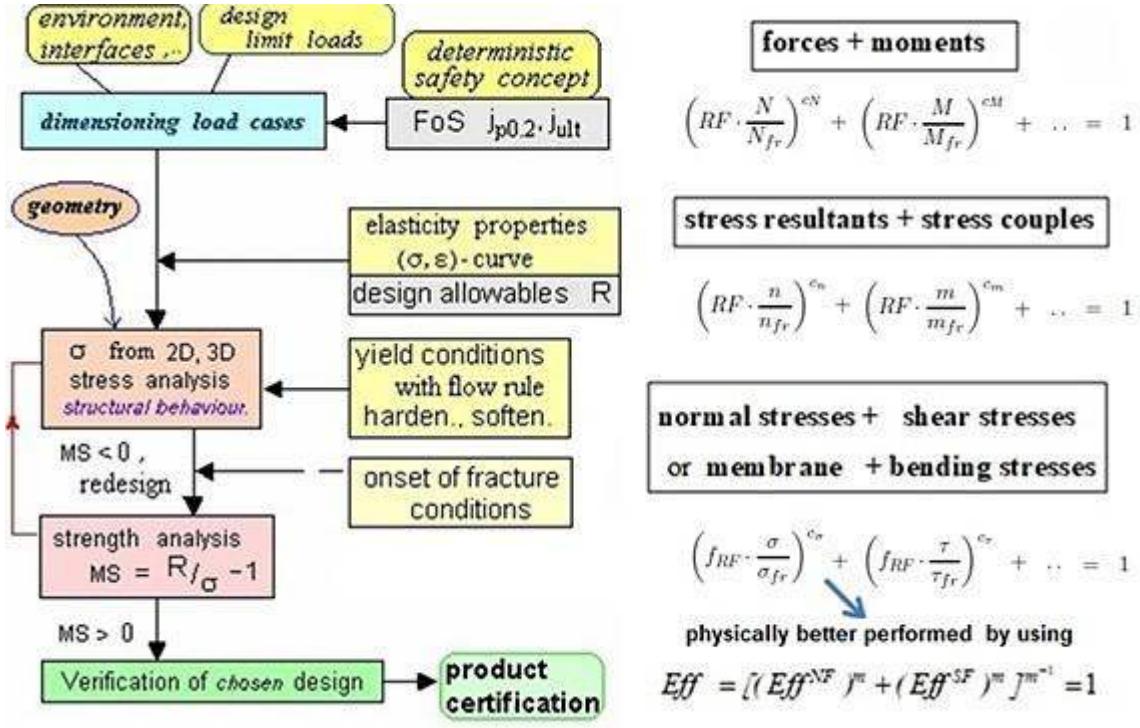

Fig.2-3: Static strength verification procedure. (design) Factor of Safety j, strength R, stress σ. Exponents c from tests, handbooks. λ is a so-called loading multiplier, which corresponds to some extent to RF. MS = M0S

Design Dimensioning and Design Verification are to perform considering different stress situations, see *Table 2-5.*

Table 2-5: Analysis Levels of the structural component – static & cyclic

- Stress, locally at a critical material location ('point'): *using strength mechanics.*
  Micro-damage domain. Verification by uniaxial ('basic') strengths and multi-axial SFCs.
  Applied stresses are local stresses (continuum mechanics, regarding the cyclic growth of an initially most often diffuse and later a localized micro-damage state)
- Stress concentration at a notch (often joints): *using notch mechanics (low singularity).*
  Verification by a notch strength (usually 'Neuber-like', Nuismer, etc.). Applied stress peaks.
  Mind: SN curves (Wöhler curves) of plain material narrow 'notched' SN curves
- Stress 'intensity' = stress intensity factor (*high singularity*) at a crack tip: *using fracture mechanics.*
  Macro-damage. Verification by fracture toughness K_{cr} or a critical energy release rate $\mathcal{G}_{cr}$ (energy–related). Applied stresses are 'far'-field stresses (*far from the crack-tip*).
  Task: Cyclic growth of a detected 'technical (macro-)damage' (i.e. inter-laminar delamination).

Each failure mode contributes to the experienced micro-damage or macro-damage activated by the stress state:

Strength Mechanics:

If all strength failure modes are activated then the SFC, beyond which onset-of-failure will occur, reads $Eff = f(Eff^{modes}) = 1 = 100\%$

with *Eff*, the so-called 'material stressing effort' (artificial English term for the German *Werkstoffanstrengung*).

Fracture Mechanics:

If all fracture mechanics failure modes are activated then the failure condition beyond which the crack will begin to propagate reads $\mathcal{G} / \mathcal{G}_{cr} = 1$ with

$\mathcal{G} = \mathcal{G}_I + \mathcal{G}_{II} + \mathcal{G}_{III}$ and $\mathcal{G}_{cr}$ the critical energy release rate.

For a general stress state the *('tension-related' linear elastic*) fracture mechanics situation is fully similar to strength mechanics.

2.2.1 Urgent need to move to 3D Analysis and to use Eff in order to understand stress states

FEA output delivers 3D stress states if required and these are then to assess. Such stress states are encountered in submarine hulls, bolted and screwed joints, in bearings, in the foot of a hoop-reinforced concrete strut, after impact and ballistics, hazards and in applications like the inner surface of composite high pressure vessels.

In the past, mainly specific and effortful experimental investigations have been performed including 2D and 3D compression (*such as hydrostatic pressure loading p_{hyd}. Thanks for doing it*) and not so much effort was put on analytical investigations. In consequence, there is a strong need to validate failure conditions in the compression domain. 2D models are not sufficient to describe the fracture progress of brittle behaving isotropic materials such as grey cast iron, rock material, concrete, UD-material etc.

For instance an example from 3D tests on Ultra-High-Performance-Concrete proofs that the consideration of a realistic 3D stress state may promise an advantage (*see §4.4*):

a 1D-failure stress state of (-160, 0, 0) MPa *fully corresponds to the*

3D failure stress state one (-224 -6, -6, -6) MPa.

In both the cases is Eff = 100% or is 'Onset-of-Fracture' failure met!

→ Conclusion: A validated 3D failure theory with experimental evidence is required and helpful.

2.2.2 Linear and non-linear structural analyses

Linear and non-linear structural analyses are to perform considering all DLCs and Design Limit States $\mathcal{G}$ which represent all failure modes, see *Table 2-6.*

Often the aim of non-linear analysis is just: „Save a structural design or a still produced structure" by making the hidden load carrying reserves visible. Hidden practically means that less favorable linear analysis was used in design.

Table 2-6: Linear and nonlinear structural analyses for each LC

Linear Analysis**:** action *S* (stress level) < material resistance *R* (strength)
3D-stress state Design Dimensioning or design dimensioning with section quantities which depend on the distribution of the structure's stiffness.
Non-linear Analysis**:** action *E* (*Einwirkung*, load level) < structural resistance *W* (*Widerstand).*

Nevertheless: Standard survival probabilities shall be kept - as usually applied - in the linear case.

LL:

- *Statically in-determinate structures are redundant and must be treated differently to the statically determinate ones (one load path). Principally, in order to avoid either to be too conservative or too un-conservative, a separation of the always needed analysis of the average structural behavior in Design Dimensioning from the following Design Verification of the final design is required.*
- *It must be applied:*
  *(1) An average σ-ε curve and characteristic (= typical, average) design parameters (Example statically indeterminate continuous beam: Determination for Design Dimensioning of the most realistic section quantities with 50% probability of expectation for the following local cross-section proofs (*However, what do codes? Exemplarily, but not only, EuroCode2 lowers stress-strain curve and reduces the Young's modulus of the compressive stress-strain curve of the concrete. No physical reason is given*?).*
  (2) Design values: Consideration of minimum values for strength and min, mean or max as especially project task-required for other properties.
- *In order to live a consistent design philosophy the higher true stresses as outcome of the material non-linear analysis should permitted to be assessed by the higher true strength design allowables!*

2.3 Structural Integrity, Design principles and Loading Processing

2.3.1 Survey in 'Dynamic/Cyclic' Design

The next figure visualizes the design principles in the case of cyclic loading. Depicted are the required A- and B-(strength) Design Allowables to be applied aerospace (civil aircraft) and military aircraft with the statistically higher strength B-values.

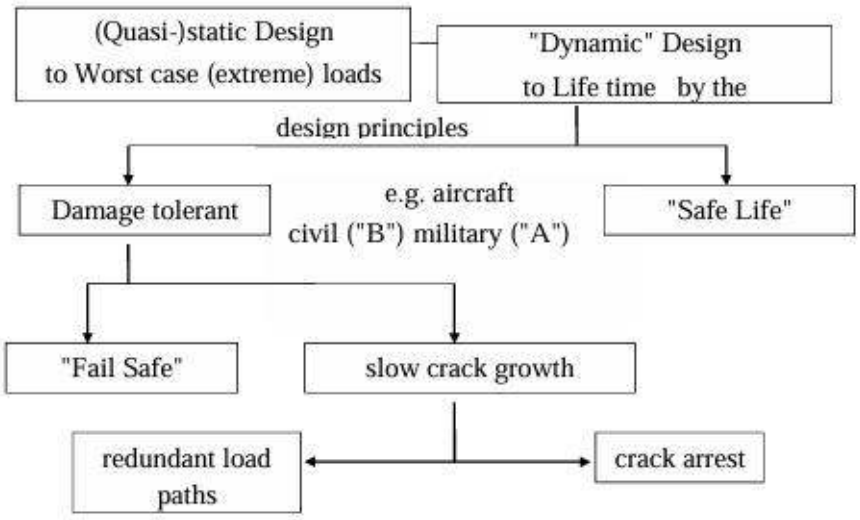

Fig. 2-4: Damage tolerant design principles of a structure

With a design concept in place, all aspects of Structural Integrity need to be assessed in relation to the total life expectancy of the structural part [*from former ESA publications*]. In this context structural integrity control is addressed for the component, the sub-assembly and for the assembled structure or system based on the following issues:

- In what environments is the structural part expected to operate?
- Which are the requirements on structural and material durability?
- Which are the damage tolerance implications for the material? (metal alloys, composites)
- What is the fatigue environment in respect of mechanical, acoustic or thermal loading?
- Should Safe-life or Fail-safe principles be applied? This will influence the *design FoS j*.
- Which are the inspection requirements over the life of the structure and does this influence the design?

2.3.2 The two different design principles (philosophies) "Safe Life" and "Damage Tolerance"

- Safe Life Design Principle:
  By this principle the structure is thought defect-free over lifetime. The principle is applicable to all types of structures, monolithic as well as redundant structural elements.

- Damage Tolerance Design Principle:
  A damage tolerant structure can endure the specified design limit load DLL even in case of a pre-damage caused e.g. by fatigue as long as the macro-damage will be discovered by inspection or malfunction and will be repaired.
  (*This approach differs from the original Fail-Safe philosophy in that it assumes cracks of the smallest allowable size to exist in the structure already at the very first load cycle. Also, a distinction is made between in service-inspectable and non-inspectable structures*).

  The procedure includes the determination of the macro-damage type and its size allowed by the required performance level. Type and size which is not allowed have to be found by inspection. For this reason, the probability of being detected or not detected is important.

In order to achieve structural integrity for composite components, an old but still valid certification procedure, *Fig. 2-5 left*, for 'Composite Materials' shall be depicted. It is for laminates composed of Fiber-Reinforced-Plastic-layers.

2.3.3 Structural Modelling and Boundaries

Modelling in Construction:

For the modeler it is important, whether the applied material or even the structural element built-of is homogenizable = '*smearable'*. A merely smearable 'Material Composite' is for instance a concrete–reinforcing bar-grid or a mat with a large roving distance, see *Fig.2-5 right*.

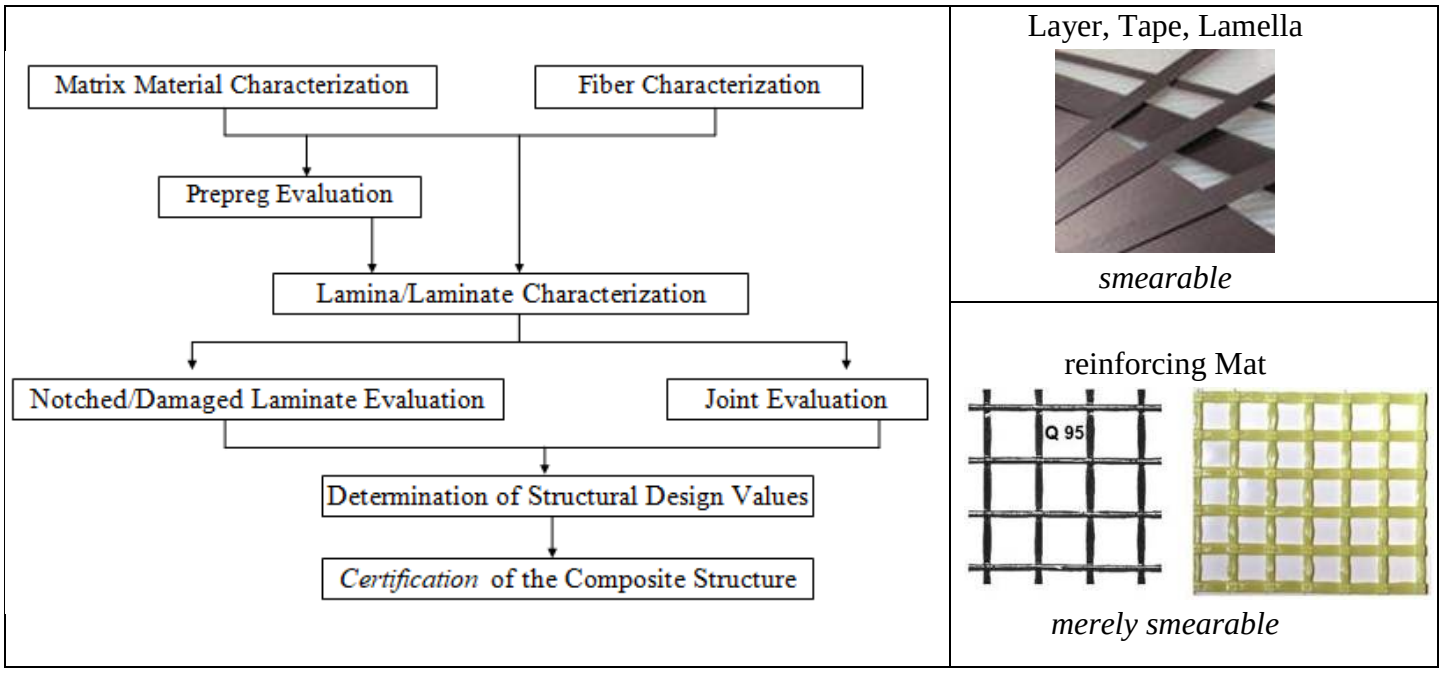

Fig. 2-5: Procedure proposed [MIL-HDBK-17-3C] . Smearable and merely smearable fiber products

This makes to remember the vast field of elements to reinforce structures in construction. In order to unify a little the technical disciplines (mechanical, civil and textile engineers asked me to do) the author proposed in his Glossar an ordering scheme in Fig.2-6. For details see the downloadable draft of the Glossar*.

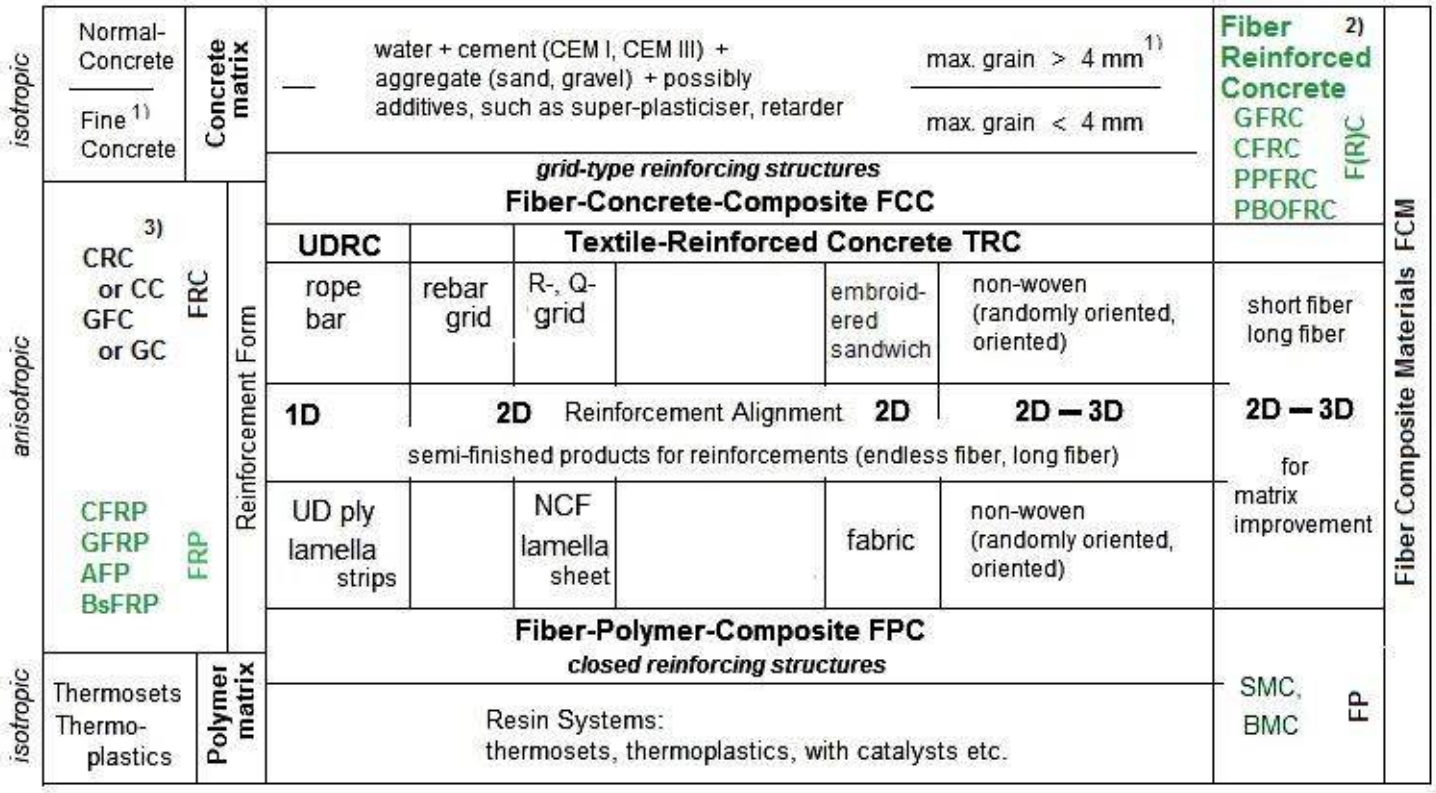

Fig. 2-6, Ordering scheme for vaarious fiber-composite materials FCM: see [Glossar]

Fiber-reinforced polymer FRP, fiber-reinforced concrete FRC, Carbon Concrete C(R)C, CRC:= Carbon–Reinforced Concrete, Bi-Directionally Reinforced Concrete BDRC, UHP-(short)Fiber-Reinforced Concrete UHPFRC.
Green couloured are still fixed notions

Check Boundaries, Specifications, Standards before Designing

These design driving features and limits should always kept in mind.

One vital experience with boundary specifications (limits) was very impressive for me. The 4 m long caiman mother Maria strictly observed the Limit "No trespassing (No pase!)": *Maria stopped at the tape, marked with "No pase"!*
Her behavior was very good for the '*personal health'* of my friend Eddi, who unfortunately fell down 1.5 m in front of her snout while running away.

We engineers should learn from Maria and always rationally observe the limits set by specifications etc. This is good for '*structural health'* (= Integrity) and it further meets application limits of the literature-offered SFCs

2.3.4 Design and Loading processing

Structure design is a balance between mass and safety (*structural reliability*) with an essential goal to be as light as possible (*required not in aerospace only*). The designer must develop a structure which has to meet stiffness, loads, environments, mass requirements, time and costs. Thus, Dimensioning is a complex process: It shall combine the different external and internal loadings acting on the structure of the sources: static, dynamic (impact), cyclic, thermal, environmental, residual stresses. Special concern is on the effect of local loadings due to attachments, joints and so on. This is particularly true in buckling design, when different kinds of loadings act on the same structure and it is to correctly combine mechanical, thermal and local loading. Once the first design is obtained, the resistance against local and global buckling of the structure can be assessed according to the procedures presented above.

Always a series of calculation with different sets of loadings is to perform in order to:

- understand the behavior of the structure with respect to buckling,
- define a reference configuration with a set of imperfections.

The loading to which each structure is submitted can be classified in two categories:

- the destabilizing loads, which create a stress field decreasing the apparent stiffness of the structure leading to its buckling. For instance, for a launcher tank, destabilizing loads are external pressure or compression loads.
- the stabilizing loads, which in the case of the buckling create a field of constraints increasing the apparent stiffness of the structure. In the case of a cylindrical shell, they can be the internal pressure or the tension loads.

A loading combination which does not take into account the distinction between these two types of loads leads to apply the same *FoS* to both loading types *destabilizing* and *stabilizing* and therefore leads to increase these loads simultaneously until the structure breaks down. This way to consider the loads is correct if it is assumed that the stabilizing loads are statistically dependent on the destabilizing loads, which is a priori not always the case. In this last case, the method is optimistic with regard to the critical buckling load and overestimates it. If the two types of loads are statistically independent, the approach to be followed is to apply the *FoS* to the destabilizing loads and to increase them until collapse whereas stabilizing loads are maintained at their specified level (*design limit loads DLL*).

Exemplarily for a shell it is to be accounted for:

(1) Geometric specifica of the structural elements tubes, frames, stiffeners,

(2) Geometrical deviations (i.e. w*eld joints*),

(3) Ovalization effects. Radial buckling and axial buckling may occur.

3 Safety Concepts in Structural Engineering Disciplines and Reserve Factor

***Aim**: Providing basic knowledge for a reliable design, in order to pace the required necessary design verification of the final design of a component.*

For becoming production ready and obtaining structural product certification, a Safety Concept is to apply. It is presented with his various facets in detail below.
Exemplarily the *designer* of a structure (*e.g. aerospace*) has to demonstrate to the *operator* (*airline*) and the *regulator* (*airworthiness authority*) compliance with the design requirements concerning Structural Integrity of flight hardware components such as: Stiffness, strength, vibration, fracture behaviour as well as to material selection, manufacturing process, hardware tests, inspection methods, quality assurance and documentation. This procedure is principally valid for other disciplines like civil engineering, too.
Structural Integrity of Hardware shall be proved by analyses and finally verified by tests under mission environmental conditions considering the complete life history of each item.

3.1 Safety Concepts

Applying a *Safety Concept* means to implement reliability into the structural component by 'capturing' the uncertainty of the design parameters! A Safety Concept can just provide an unknown safety distance between load ('stress' *S*) and load resistance ('strength' *R*). Required Factors of Safety (*FoS)* capture uncertainties, small inaccuracies, and simplifications in analyses w.r.t. manufacturing process, tolerances, loadings, material properties (strength, elasticity etc.), structural analysis, geometry, strength failure conditions. *FoS* do not capture missing accuracies in modeling, analysis, test data generation and test data evaluation!

Fig.3-1 reminds where FoS have to be applied. Fatigue Life and Strength are focused here.

In the *deterministic concepts* or *formats*, respectively, the worst case scenario is usually applied for loadings considering temperature, moisture, undetected damage. Further, a load is to increase by a 'Design *FoS*' and the resistances are to decrease. For the decrease of the strength, statistical distributions are used. If the loading is also based on a statistical distribution, then one speaks about a *semi-probabilistic format*.

Design Development was the basic work of the author in industry. This is why at first the Flow Chart below shall remind of the structural analysis tasks. There are basically four blocks, where – after the material Model Validations - the fulfillment of the Design Requirements has to be demonstrated for obtaining Design Verification as precondition of the final Certification Procedure.

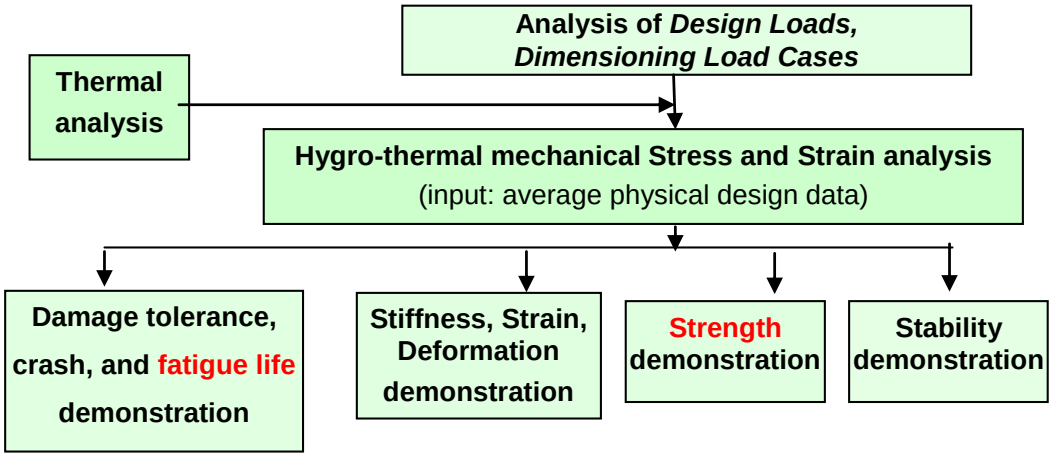

Fig.3-1: Structural Design-Analysis Flow Chart

Essential question of engineers in mechanical and in civil engineering when demonstrating Structural Integrity is:

"*How much could one further increase the loading? Which is the reserve"?*

3.2 Former *forbidden* Safety Concept of Allowable Stresses

At least since 1926 the civil engineer M. Mayer questioned the old safety concept, which used allowable stresses, meaning: the *resistance* strength was reduced by a design safety factor *j*. However, this gives no accurate results in the case of non-linear behavior!
In construction this was replaced since some decades in the deciding standard DIN 1054 by the Partial Safety Factor concept, which applies design safety factors and combination factors for general service loads, live loads, snow, ice loads, and wind loads. Temperature effects are specified in DIN 1055-100.

Material resistance must be generally demonstrated by a positive Margin of Safety *MoS* or a Reserve Factor $RF = MoS + 1 > 1$ in order to achieve Structural Integrity for the envisaged Design Limit State! A *FoS* is given and not to calculate (***as it is too often to read even in FEA code manuals***) like the *MoS* or the *RF*.

Fig.3-2 visualizes the stress-strength (R-S) distribution which outlines that the crossing over will determine the probability of failure p_f . Its value is the area of the p_f-distribution within the overlapping (gusset) of the stress and the strength distribution tails, see for details [CUN22, §16]

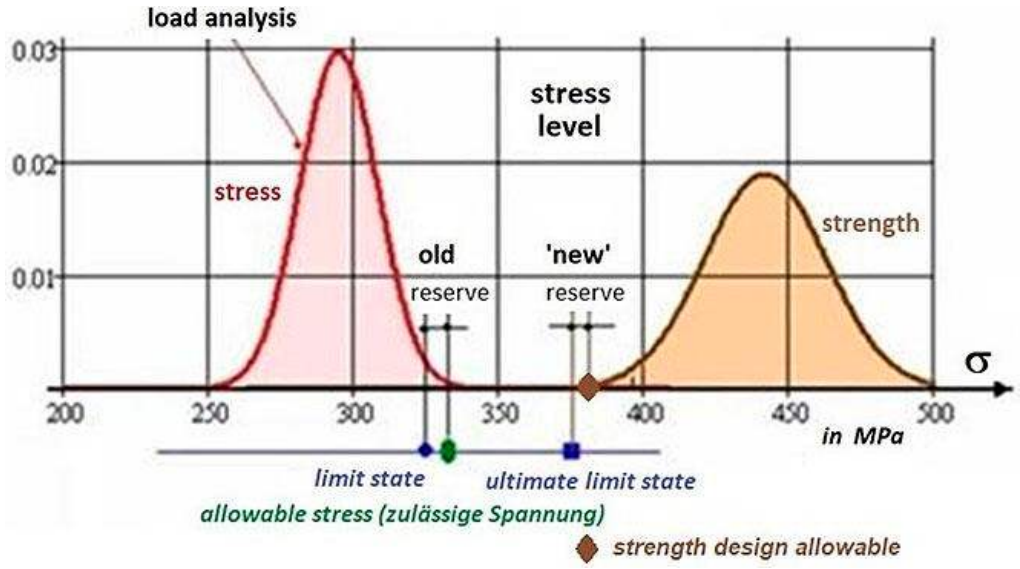

Fig.3-2: Visualization of the required present safety concept in mechanical engineering and the forbidden Safety Concept of Allowable Stresses

***j · allowable stress = strength design allowable** !! (see again the figure above)* !

LL:
The citation of the term 'allowable stress ' is restricted to the former 'Concept of Allowable Stresses' and shall be not applied within present concepts anymore. Why? The usual application of the abbreviating term 'allowable' instead of the accurate term 'strength design allowable' may not confuse, but 'allowable stress' is error-prone.

3.3 Lumped (global) Design Factor of Safety Concept on Loading ('deterministic format')

A concept, that deterministically accounts for design uncertainties in a lumped (global) manner by enlarging the action 'Design Limit Loads' through multiplication with a design Factor of Safety FoS j.

As still mentioned, *FoS* are applied to decrease the chance of failure by capturing the uncertainties of all the given variables outside the control of the designer. In the design process the scatter of individual values and parameters is usually treated by using fixed deterministic *FoS*, which act as load increasing multiplying factors *FoS* and should be called, more correctly, *Design FoS*.

Presently, in mechanical engineering the loading is increased by one lumped (global) FoS *j*, and in civil engineering (above mentioned) the procedure was improved by using several partial Design FoS γ for the uncertain stochastic design variables.
The *FoS* are based on long term minimum risk experience with structural testing. Depending on the risk consequences – analogous to civil engineering - different classes of *FoS* are applied, e.g. in spacecraft for manned space-crafts higher *FoS* are used than for unmanned space-crafts.

The present spacecraft safety concept is an *improved global deterministic format representing the* ***s****implest* Partial Safety Factor concept: It discriminates load model uncertainties considering factors (K_{Model} , $\boldsymbol{K_{Project}}$) from design uncertainties which are considered by one global FoS *j* ! The to be applied values *j* for the *FoS* are risk or task driven.
Facts to consider are:

- As mentioned exemplarily: Different application in cases of manned, un-manned spacecraft
- Design verification by 'Analysis only' (*necessarily this is the usual case in construction*)
- Different risk acceptance attitude of the various industries, i.e. j_{ult}

Example: $DUL = j_{ult} \cdot$ design limit load DLL .

(The virtual design value must be written *DUL*, because *UL* is marking the real test fracture load).

3.3.1 Different loading (action) FoS in aircraft and space engineering?

The first task in aerospace industry is load analysis. In any load analysis there are to establish all load events the structure is likely to experience in later application. This includes as well the estimation of loadings induced by the hygro-thermal, the mechanical *(static, cyclic and impact)* and the acoustical environment of the structure as further the corresponding lifetime requirements (*duration, number of cycles*), specified by an authority or a standard.
Then, the so-called Design Limit Load values are determined, usually derived from mission simulations utilizing the so-called mathematical models of the full structure (*dynamical analyses, at first on basis of the preliminary design*).

After co-working on updating ESA 3 former not-harmonizing Standards for launcher and spacecraft, when preparing a special HSB sheet [*Cun12*] the author sorted out, that there practically is no different risk view between air-craft and space-craft:

* Spacecraft:
using a *d*ynamic *L*imit *L*oad model obtaining a basic load prediction d*LL* considering a load model uncertainty considering factor j_{LM} =1.2. This delivers a Design Limit Load DLL= 1.2 ·d*LL*, and from this follows DUL = d*LL*· j_{LM} ·j_{ult} , with 1.2 ·1.25 = **1.5** ! In spacecraft, the DLL level is applied in fatigue life demonstration.

* Aircraft: Definition of a so-called (design) Limit Load *LL* directly delivering DUL = *LL*·**1.5.**

***LL**:*
****** *Hence, the author could conclude after comparing the ESA/ESTEC aerospace Standards* (the author had to work on them), *that the DUL-value is practically the same value in aircraft and in spacecraft!*

** Loads are most often the parameters of highest uncertainty. Therefore checking the loadings pays off. Otherwise a bad design with a money grave may be faced.*

**** Uncertainty quantification is the basic challenging design task!***

3.3.2 The resistances strengths and bearable loads at joints etc

Dependent on the design requirements the average, the upper or a lower value of the property is used as analysis input for the various properties.
This is in the case of strength verification a statistically reduced value *R*. To achieve a reliable design the so-called 'Strength Design Allowables' have to be applied. It is a value, beyond which at least 99% ("A"-value) or 90% ("B"-value) of the population of values is expected to fall, with a 95% confidence (*on test data achievement*) level, see MIL-HDBK 17. A "B"-value is permitted to use for multi-layered, redundant laminates.
Bearable loads require series tests of the distinctive structural component with statistical evaluation in order to determine the 'Load-resistance Design Allowables'.

Measurement data sets are the result of a Test Agreement (norm or standard), that serve the desire to make a comparability of different test procedure results possible. The Test Agreement consists of test rig, test specification, test specimen and test data evaluation method and the Test Procedure. Therefore, one can only speak about *'exact test results in the frame of the obtained test quality'*. Hence, there are no exact property values available. Test specimens shall be manufactured like the structure ('as-built').

Considering property input: (again) When applying test data from 'isolated lamina' test specimens (*like tensile coupons*) to an embedded lamina of a laminate one should consider that coupon test deliver tests results of 'weakest link' type. An embedded or even an only one-sided constrained lamina, however, possesses redundant behavior → "B"-values permitted.

Formulas for Reserve Factor *RF* and Margin of Safety *MoS*:

Linear analysis is sufficient (presumption): $\sigma \equiv \text{load} \quad \Rightarrow RF \equiv f_{RF} = 1 / Eff$

Material Reserve Factor $$f_{\mathrm{RF},\,ult} = \frac{\text{Strength Design Allowable } R}{\text{Stress at } j_{ult} \cdot \text{Design Limit Load}} > 1,$$

Non-linear analysis required: σ not proportional to load

Reserve Factor (load-defined) $$RF_{ult} = \frac{\text{Predicted Failure Load } \textit{for } \textit{Eff} = 100\%}{j_{ult} \cdot \text{Design Limit Load}} > 1.$$

LL:

- ** A FoS is given and not to calculate such as a MoS or the Reserve Factor RF = MoS + 1.*
- ** A MoS is usually the result of worst case assumptions that does not take care of the joint actions of the stochastic design parameters and thereby cannot take care of the failure probability. This failure probability is a 'joint failure probability' because it considers the probability of joint acting*
- ** A material with a high Coefficient of Variation CoV disqualifies itself, when computing the statistically-based 'strength design allowable' value. Therefore, one must not penalize it further - as performed in some standards in the past - in the case of new materials.*
- ** Both, an increasing mean value and a decreasing standard deviation will lower p_f*
- ** The MoS value does not outline a failure probability. Failure probability p_f does not dramatically increase if MoS turns slightly negative. Check then, whether one may get better information on material and structural data in order to reduce scatter and reduce failure probability and RF. In this context: A local safety measure of MoS = -1 % is no problem in design development if a*

'Think (about) Uncertainties' attitude is developed in order to recognize the main driving design parameters and to reduce the scatter (uncertainty) of them.

* *Nowadays, often non-linear analyses are performed, delivering true quantities, however Design Verification is executed with engineering strength values R. Why do we not use in such a case in verification the true tensile strength, however we cite the material-RF f_{RF} with four numbers 'accuracy'? 'True-in' requires 'True-out' and an assessment by* $true\bar{R}^t$. *Fig.3-3 (right) shows for an al alloy a difference between the mean (material model) strength values* $eng\bar{R}^t \rightarrow true\bar{R}^t$ *of 8%.*

* *Uncertainty (fuzzyness, Ungewißheit, Unsicherheit): unclearniness in loadings, strengths, and other design parameters such as geometrical parameters, applied engineering models etc. (it must be discriminated*

(1) Epistemic uncertainty within technical measurements of geometry, material properties etc., which is improvable by better and more measurements, test data evaluation and additional information.

(2) Aleatoric uncertainty, due to usual measurement tolerances, where 'nothing' can be improved concerning the given test situation).

Fig.3-3 (left) visualizes strength distribution, *Eff as a* micro-damage growth parameter and material reserve factor f_{RF}.

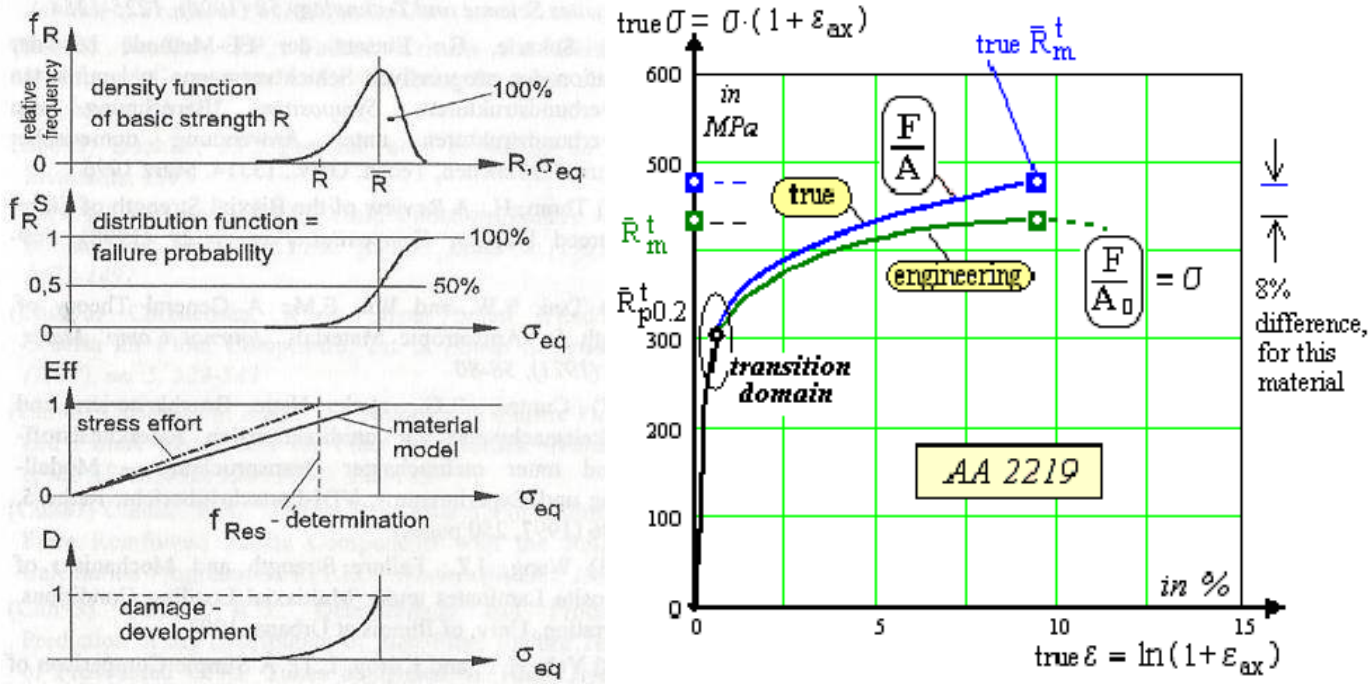

Fig.3-3: (left) Design quantities when approaching failure in Design Verification.
(right) Difference engineering and true tensile strength of AA2219

3.3.3 Lumped Safety Factor Concept versus Partial Safety Factor Concept

A Safety Concept implements the necessary reliability into the structural component, to robustly endure uncertain design parameters (variables). Different formats are available to capture the uncertainties of the design parameters:

* Lumped, Deterministic Safety Factor Concept by *j*

Concept, that deterministically accounts for design uncertainties in a lumped manner through enlarging the 'design limit loads' by multiplication with a design Factor of Safety FoS *j*. This provides an unknown not really deterministically quantifiable 'safety distance' between load and load resistance ('strength') represented by the required positive Margin of Safety (*MoS* = *RF*-1).

* semi-probabilistic Partial Safety Factor Concept by several γ

Concept, that semi-probabilistically bridges the deterministic format and the more complicated probabilistic format. A probabilistic format can model each single design parameter's uncertainty into a stochastic uncertainty described by a probability density function. Accounting for uncertainties informs about the robustness of the design and considers the correlations of the design variables.

On the ultimate design loading side the usual FoS in aircraft and construction i.e. read:

- Aircraft DUL : lumped load factor $j_{ult} = 1.5$
- Construction ULS ≡ DUL : partial load factor, Gewicht $\gamma_{G,\,static} = 1.35$,
  and partial material factor concrete $\gamma_{c,\,static} = 1.5$.

3.3.4 Robust Design Requirements

The goal of any design engineer should be to end up with a robust design. In order to achieve this, the main stochastic design parameters have to be used to outline the robustness of the design against the envisaged actual failure mode by firstly computing the sensitivity measures α and then investigating the reduction of the design's sensitivity to changes of X_j *while* keeping the probability of failure p_f at the prescribed level. This is important for the production tolerances.

Probabilistic design may be used as an assessment of the deterministic design or is necessary as design method if a *reliability* target $\mathfrak{R}$ is assigned instead of a *FoS*. or its complement, the p_f .

A structural reliability analysis in a Hot Spot reveals the influence of each stochastic design parameter on the distinct failure mode by means of the sensitivity measures. Robust designs, which means *robust to later changes of the design parameters* are required with identification of the most sensitive design parameters! For better illustration of the Safety Concepts the *Fig.3-4* is included from *[CUN22, §12]*. It clearly depicts the definition of the failure probability in this two-parameter case.

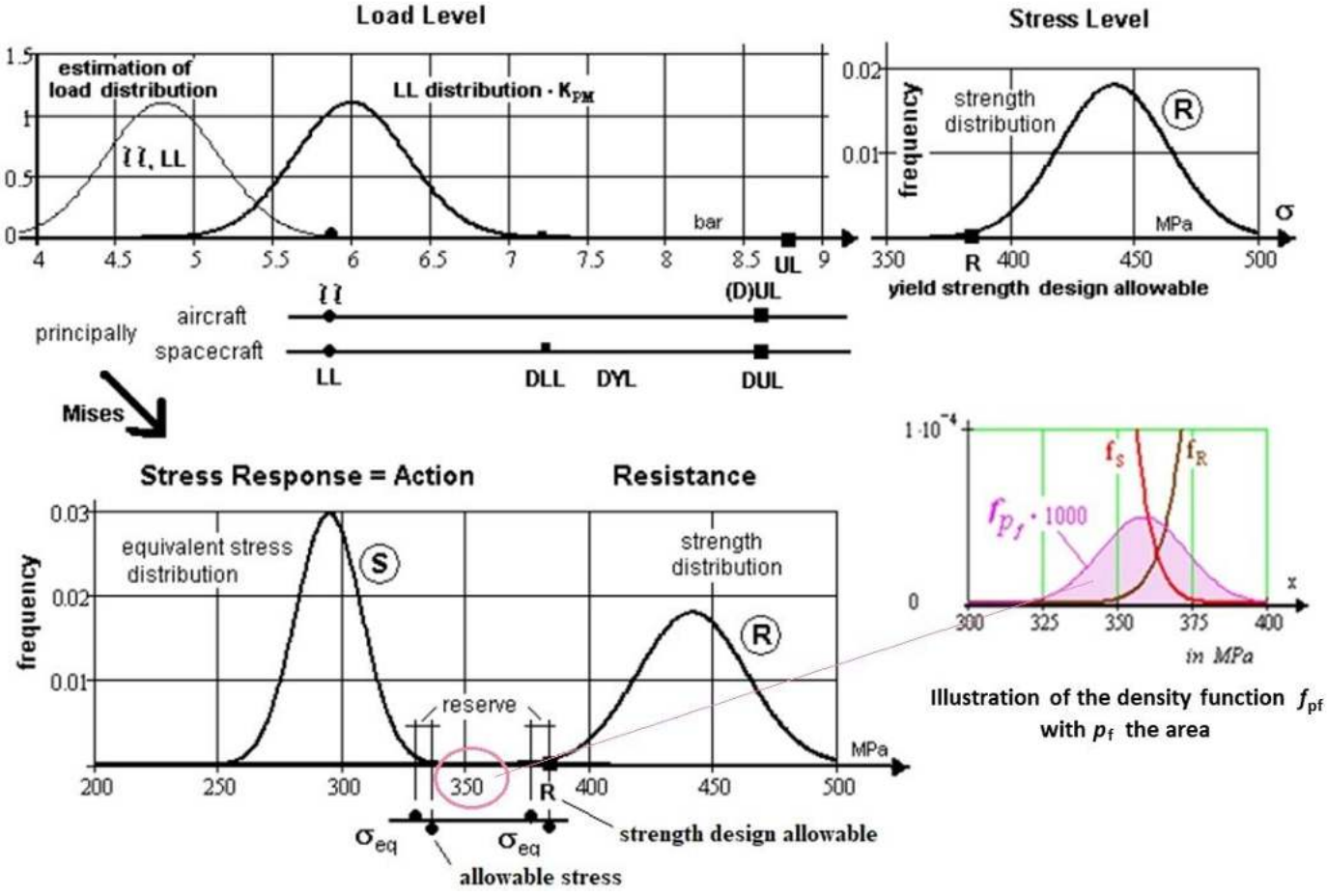

Fig.3-4: Visualization of the difference of the aerospace load terms used in the Strength Design Allowable Safety Concept and of the 'hopefully forgotten' Allowable Stress Safety Concept

3.4 Determination of a UD material Reserve Factor

Fig.3-5 presents a numerical example how exemplarily for the later derived UD material SFC the reserve factor *RF* is to compute.

Asssumption: Linear analysis permitted, design FoS $j_{ult} = 1.25$

* Design loading (*action*): $\{\sigma\}_{design} = \{\sigma\} \cdot j_{ult}$

* 2D-stress state: $\{\sigma\}_{design} = (\sigma_1, \sigma_2, \sigma_3, \tau_{23}, \tau_{31}, \tau_{21})^T \cdot j_{ult} = (0,\ -76,\ 0,\ 0,\ 0,\ 52)^T$ MPa

* Residual stresses: 0 $\left(\textit{effect vanishes with increasing micro-cracking}\right)$

* Strengths (*resistance*): $\{\bar{R}\} = (1378,\ 950,\ 40,\ 125,\ 97)^T$ MPa average from mesurement

statistically reduced $\{R\} = (R_{||}^t, R_{||}^c, R_{\perp}^t, R_{\perp}^c, R_{\perp||})^T = (1050,\ 725,\ 32,\ 112,\ 79)^T$ MPa

* Friction value(s): $\mu_{\perp||} = 0.3,\ (\mu_{\perp\perp} = 0.35)$, Mode interaction exponent: $m = 2.7$

$$\left\{Eff^{\text{mode}}\right\} = \left(Eff^{||\sigma},\ Eff^{||\tau},\ Eff^{\perp\sigma},\ Eff^{\perp\tau},\ Eff^{\perp||}\right)^T = (0.88,\ 0,\ 0,\ 0.21,\ 0.20)^T$$

$$Eff^m = (Eff^{||\sigma})^m + (Eff^{||\tau})^m + (Eff^{\perp\sigma})^m + (Eff^{\perp\tau})^m + (Eff^{\perp||})^m = 100\%\ .$$

The results above deliver the following material reserve factor $f_{RF} = 1/Eff$

* $Eff^{\perp\sigma} = \dfrac{\sigma_2 + |\sigma_2|}{2 \cdot \bar{R}_{\perp}^t} = 0, \quad Eff^{\perp\tau} = \dfrac{-\sigma_2 + |\sigma_2|}{2 \cdot \bar{R}_{\perp}^c} = 0.60, \quad Eff^{\perp||} = \dfrac{|\tau_{21}|}{\bar{R}_{\perp||} - \mu_{\perp||} \cdot \sigma_2} = 0.55$

$$Eff = [(Eff^{\perp\sigma})^m + (Eff^{\perp\tau})^m + (Eff^{\perp||})^m]^{1/m} = 0.80.$$

$\Rightarrow \quad f_{RF} = 1/Eff = 1.25 \rightarrow RF = f_{RF}$ (if linearity permitted) $\rightarrow$ MoS = $RF - 1 = 0.25 > 0$!

Fig.3-5: Computation scheme of a UD material Reserve Factor (see §17.2)

3.5 Probabilistic Assessment of a Deterministic Margin of Safety

"*Is a Costly Re-Design really justified if a slightly negative deterministic MoS is encountered ?*"

was a very essential issue for the author in the Ariane 5 design verification. The following chapter captures the contents of a probabilistic assessment of the *MoS* from the split paper [*Cun05*] and shall contribute to a discussion about the question above, very important in industry:

(1) How safe is a positive Margin of Safety (MoS)= RF -1 ?
(2) What is the real meaning of a slightly negative MoS value ? A MoS value itself does neither outline the size of risk nor specify the probability of failure!
(3) *Is there a possibility to improve the* 'Holy MoS value > 0 standard thinking'*?*

A value of *MoS* = + 4% in the one case may incorporate a higher risk to fail than a *MoS* = –2% in another case. The author's intention is to make those engineers, who are responsible for 'approving and releasing' structural designs, aware of the real sources of risk. There is no compulsory need to reject a design if *a MoS* becomes slightly negative, e.g. –0.5%. No part of the structure will necessarily loose its functionality or will fracture, but an outright rejection could result in high additional Costs as well as in a delay of the whole project due to the re-designing efforts required. A numerical example from the aerospace industry – experienced by the author - is used here to illustrate this topic.

Uncertainties can be found in the area of data input and in the analysis of the whole modelling process. Stages with uncertainties comprise load analysis, testing and test data evaluation, the choice

of the non-linear stress-strain curve, fabrication process, modelling, material properties and safety concept, choice of yield condition and fracture conditions, structural analysis procedure, and finally the determination of the *MoS* value itself. All these sources contribute to the overall structural **risk**, which shall be formulated here again as

Amount of costs *(direct and consequential)* ***incurred in the case of later failure***

times ***the probability that the distinct failure occurs.***

In the *stress* analysis itself as well as in the failure criteria used in the *strength* analysis there are design parameters, which can exhibit relative large uncertainties. The nature of uncertainty of these parameters loads, strength properties, geometry, elasticity properties, etc. is either of *mechanical* one or of *statistical* one (*e.g. the way measurements are performed, lack of accurate information due to insufficient sample size in measurements of a specific design parameter*). Beside this, there is always some uncertainty in the *calculation model* (*e.g. solution procedure, FE mesh, etc.*) as well as in the *results* provided by *testing* and *evaluation* of 'raw test data'. Usually loads are those design parameters with highest uncertainty. Therefore, the design parameter *load* is always to be looked at carefully.

3.5.1 Theoretical Background: The Multi-stochastic parameter Problem

A function $g(X_j) = g(\underline{X}) = 0$ is called limit state function. The vector $\underline{X}$ includes all stochastic design parameters, frequently also denoted as basic random variables. Searched is the *most likely failure point*, the so called *x**-point or *β*-point, see *Fig. 3-6*. This is that point of the limit state that marks the

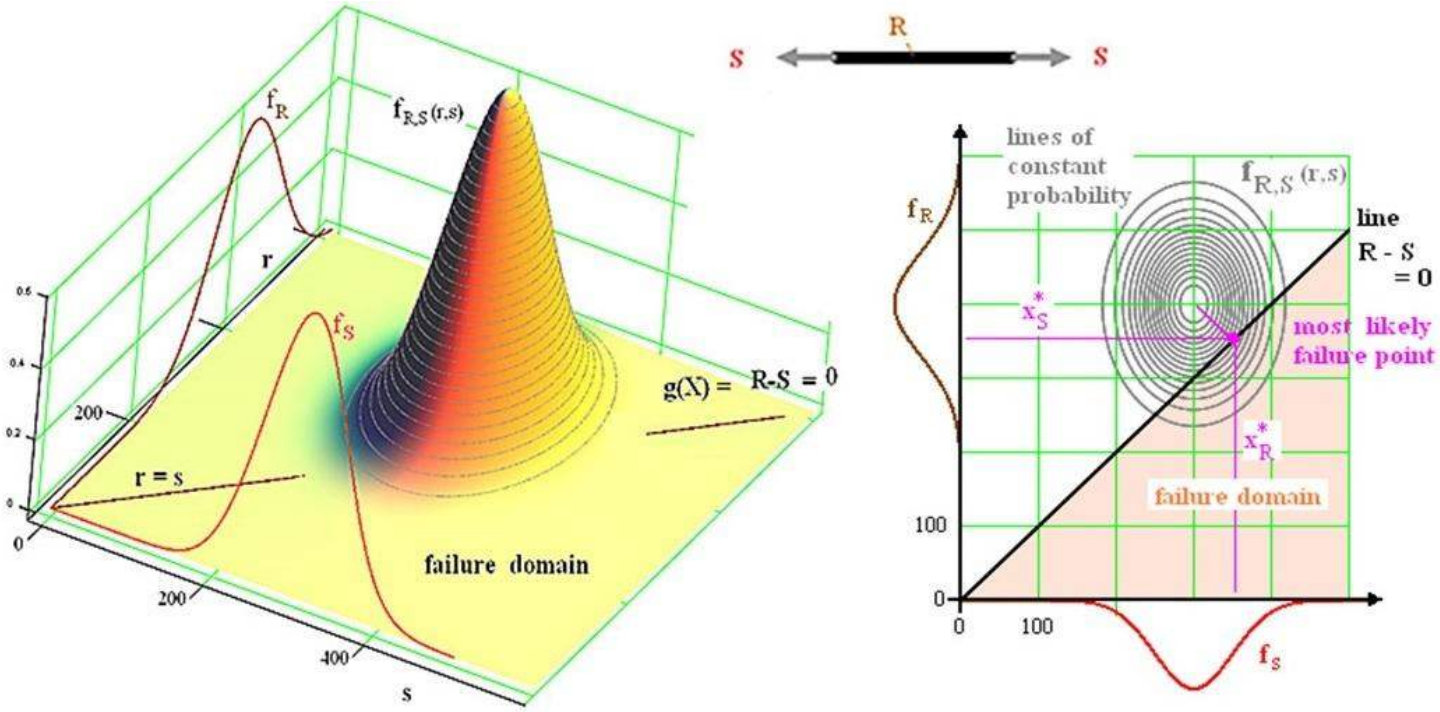

Fig. 3-6, Visualization of the most likely failure point called x-point or β-point:*
(left) Probability hill (joint density function $f_{R,S}(r,s)$) with lines of constant probability density.
Data: $\mu_R = 440$, $\sigma_R = 70$, $\mu_S = 300$, $\sigma_S = 50$; $p_f = 5.2 \cdot 10^{-2}$. (right) horizontally projected lines of constant probability density on the 'probability hill'

minimum distance from the origin in the so-called standard normal space. This minimum distance, termed *β*, is the so-called *reliability index.* It allows to compute probabilities due to

$$p_f = \Phi(-\beta) = 1-\Phi(\beta) \quad \text{and} \quad \Re = 1-p_f = \Phi(\beta)$$

with $\Re$ the survival probability and Φ the tabled Gauss integral.

The influence of the stochastic design parameters, also termed uncertain basic variables, on the failure mode is best shown in terms of the co-called sensitivity measures, the *α-values*. The α_i are derived from the gradient of the limit state function *g* with respect to the uncertain basic variables at the most likely failure point *x**, and may be interpreted as an effective percentage. A positive sign indicates an increase of $\mathfrak{R}$ if the mean value μ of the basic variable is increased and a negative sign (*typically found for load variables*) indicates a negative influence on the risk $\mathfrak{R}$ for increasing mean load value.

The Two-stochastic-parameter Problem or the so-called 'Strength *R* minus Stress *S*' Problem

In case of the most simple limit state, $g(X_j) = 0 = R - S \equiv$ *resistance R – action S* or, if linear analysis is permitted due to *strength R – stress S*, one has to treat just two basic variables one *R* variable and one *S* variable. Assuming a normal distribution for both of these basic variables *R* and *S*, the probabilistic measures β and p_f can be derived by utilizing the formulation

$$\beta = \frac{\mu_R - \mu_S}{\sqrt{\sigma_R{}^2 + \sigma_S{}^2}} = \frac{\mu_Z}{\sigma_Z} \qquad \text{and} \qquad \Phi(-\beta) = \frac{1}{\sqrt{2\pi}} \int_{-\infty}^{\beta} e^{-t^2/2} dt$$

with μ := mean value, σ := standard deviation of the parent distribution.

For this simple '(*R– S)* problem' an approximate comparison of deterministic *MoS* values with probabilistic values of β or p_f is still manually possible.

A MoS can be formulated on load level (defined *reference level*) and on stress level

*The load level formulation reads

$$MoS + 1 = \frac{load\ resistance\ \ 'design\ allowable'}{design\ load} = \frac{daLR}{design\ load}.$$

According to the high measurement costs, a *design allowable Load Resistance daLR* (*prefix da to discriminate load level from the strength design allowable* $R_{p0.2} \equiv R^t_{02}$ *on stress level*) for the load resistance of a structure is barely determined. A test series on pressure vessels may be an exception. Therefore, the 'load resistance design allowable' is defined here to be that load when the associated equivalent stress σ_{eq} in the structure achieves the level of the strength design allowable $R_{p0.2}$ or R_m.

*The stress level formulation may be utilized if a linear structural analysis is permitted:

$$MoS + 1 = \frac{\mu_R - k_R \cdot \sigma_R}{j \cdot (\mu_S + k_S \cdot \sigma_S)} = \frac{strength\ \ 'design\ allowable'}{stress\ at\ design\ load\ \text{DLL}}. \quad R, S \text{ now on stress level.}$$

This simple linear computation is sufficient for instance when high *FoS* are required such as for high pressure vessels in industry.

To achieve a reliable design the statistically based design allowable has to be applied. This is a value, above which at least 99% *("A" value, application of military Safe Life Concept*) or 90% *("B" value, application in case of multiple load paths, redundancy, laminates*) of the population of values is expected to fall, with e.g. a 95% confidence level. The factors k_R and k_S respect this and are to be chosen according to reliability goals set for the individual project, and extracted from statistical tables (see Table 12.9 [CUN22], [Int. Standard ISO 3207-1975 (E): Statistical Interpretation of Data - determination of a statistical tolerance interval. ISO Standards Handbook 3 "Statistical Methods", First edition, 1979]. They further depend on the stochastic model (*Normal Distribution, Weibull distribution, etc.),* the statistical basis (*sample size n, one- or two-sided tolerated),* and the desired confidence level C for the transfer of the sample population to the infinite basic population.

3.5.2 Probabilistic Design Procedure, example composite

A system failure is a problem that causes a system to end its intended function (malfunction). The term 'failure system', used in *Fig.3-7*, shall describe the joint failure action of failure modes which finally might result in a 'system failure'.

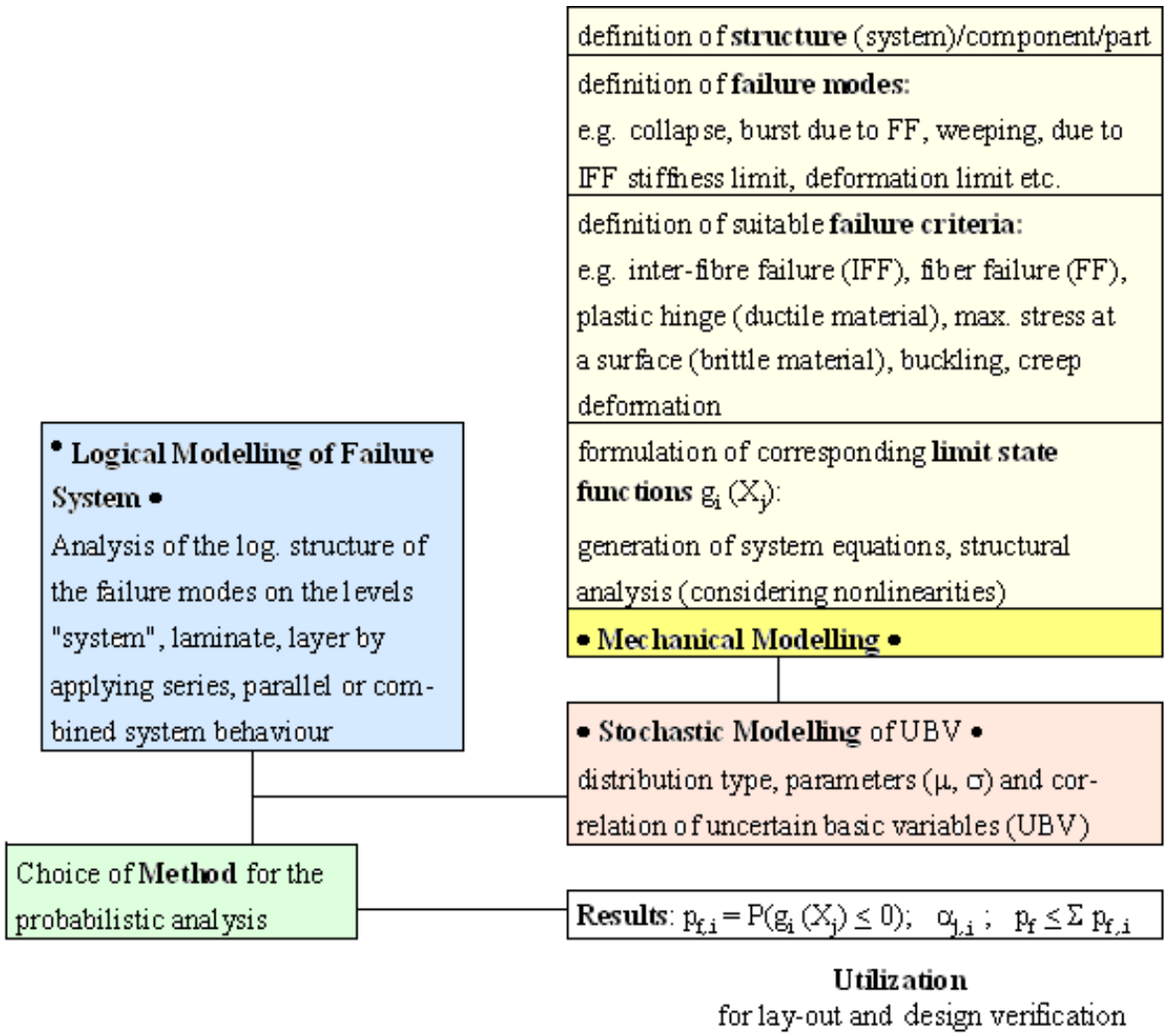

Fig.3-7: Example UD laminate wall

As far as safety is concerned, major efforts have to focus on risk identification, risk assessment and management with the understanding that risk is linked to the probability of loss of human life, loss of equipment and of damage. It is important to define hazard classes and into probability classes considering the product exposition severity times the occurrence frequency. This is similarly done in all technical disciplines. One should always consider the real risk entities and not view just the MoS-value. Essential question with respect to all uncertainties is whether these increase the risk to an un-acceptable level or not. This has to be evaluated and may result in avoiding additional costs.

3.5.3 Design advantages found with the Ariane Booster design, when using a probabilistic tool

Two advantageous applications of the probabilistic tool shall be shortly demonstrated, where probabilistic modelling and computation were successfully applied:

1. A reduced production tolerance width lead to a reduced mass and fuel mass savings.
2. Probabilistic modelling of the geometrical tolerances of bore hole, pin, position (pitch) and strength minimum restrains with minimum residual (mounting) stresses could be achieved..

(1) Booster Wall Thickness tolerance:

Former : t = 8.2 +- 0.20 mm

Improved manufacturing : t = 8.2 +- 0.05 mm !

Reduction in scatter permits, when keeping the same theoretical reliability value $\Re = 1 - p_f = 1 - 5 \cdot 10^{-6}$

a thinner nominal thickness is permitted: ***t = 8.1 +- 0.05***

Less mass!

And much fuel mass savings, in addition

(2) Optimum number of connecting pins of the Booster sections,

Probabilistic modelling of the geometrical tolerances of:

bore hole, pin, position (pitch), strength

in order to support a design decision on

asssembly + fixation of tolerance values.

The pitch was the driving design parameter.

For 180 pins:

Minimum restraints with minimum residual stresses could be achieved

As early as 1985 for our pre-design of the Ariane 5 launcher so-called target survival probabilities $\Re$ were fixed for the several structural parts and of course the MAN parts, too!

3.6 Reliability: Failure State versus Failure Rate

In a European Structural reliability working group we distinguished Failure *Rate* (bathtub failure statistics) people from Failure *State* (strength failure) people.

Both work together in the reliability assessment of an overall system, as we had to do with the Reliability of an Ariane 5 sub-system. Ariane 5 launcher target survival probabilities $\Re = 1 - p_f$ were fixed for the several structural parts, including our MAN parts. The following *Fig.3-8* presents an example of the Ariane launcher for a distinct mixed scenario. The full system is divided into subsystems and these in turn are divided into elements. The individual elements are then assigned a required probability of failure so that the full system can meet the target value of the survival reliability $\Re = 1 - p_f$ of the launcher subsystem. For our different parts we obtained p_f-limit values.

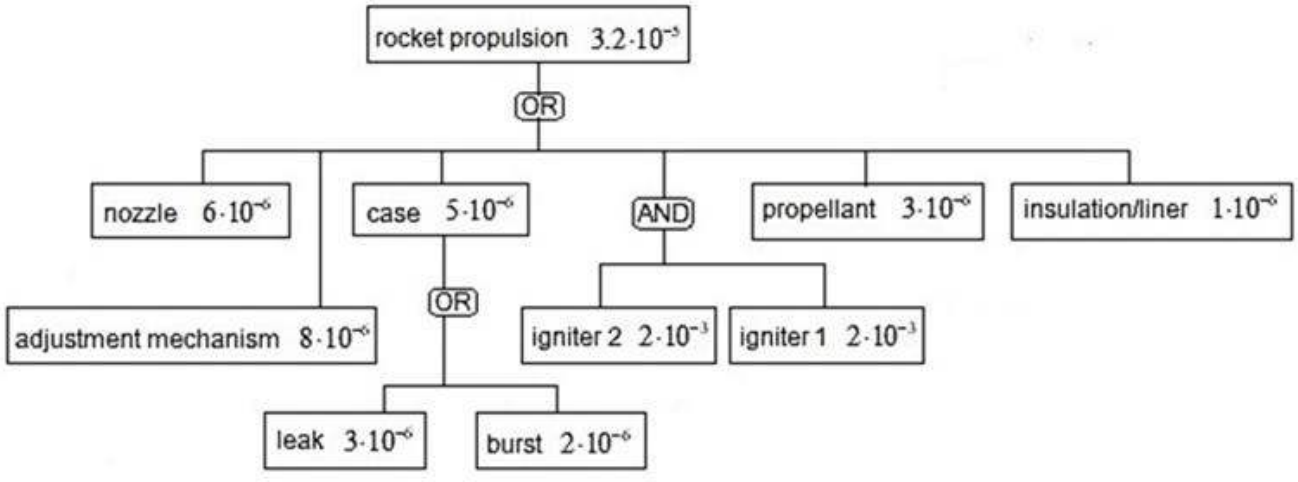

Fig.3-8: Procedure to estimate the reliability of a sub-system of the Ariane launcher.

In reliability analysis, AND and OR define how component failures combine to affect system functionality.

Series failure system:

The reliability of the series system is always smaller than that of the sub-system. The so-called ***or***-link rule applies. The greater the number of sub-systems, the more unreliable the overall system is (breaking of a tension rod and tearing out a bolt at a joint) $\mathfrak{R}_{sys} = \mathfrak{R}_1 \cdot \mathfrak{R}_2 \cdot \mathfrak{R}_3 = 1 - p_f$ with $p_f \leq \sum p_{f,i}$

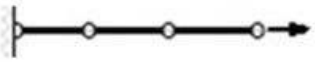

Parallel failure system:

In the parallel system, there is only one combination that describes a system failure, namely that all components fail at the same time. The ***and***-link rule applies. (rivet rows in a connection). $\mathfrak{R} = 1 - [(1-\mathfrak{R}_1)\cdot(1-\mathfrak{R}_2)\cdot(1-\mathfrak{R}_3)] = 1 - p_f$

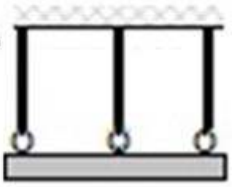

Combination:

The reality more often corresponds to a combination of both the failure systems.

Fig.3-9: Failure systems in reliability

LL:

- ***Lightweight design becomes easier by reducing uncertainties!***
- *We should focus robust products and fabrication processes. Optimum fulfilling of product liability: Secured, validated design procedures + reproducible manufacturing processes*
- *Robust Design: 1 / (uncertainty·complexity). Good design optimization must consider the scatter of the stochastic design variables*
- *Uncertainty quantification opens the door for a successful lightweight dimensioning*
- *Loadings are most often the design variables of highest scatter or uncertainty. Not to get a money grave: Careful checking of loadings, their possible combinations defined in the load cases*
- *The basis for determining reliability is the recording of uncertain parameters*
- *Uncertainty, citing Freudenthal: "The application of probabilistics makes me aware of my risk, since it provides numbers, whereas deterministics does not. You can buy certainty." However, concerning costs: How safe is safe enough?*
- *Random variation (aleatory: dice rolling; physical in nature such as fluctuations in material properties, stress) and Uncertainties (epistemic: knowledge, inference from sample to population of a design parameter, weakness of used models) are to consider*
- *Design Limit Load (NASA: not just Limit Load !!) = Limit Load of load model ·uncertainty factor. DLL is a statistically evaluated value if a distribution is available or (b) value from an engineering judgement following a rationale*
- *Probabilistic Safety Concept , a concept, that maps each single design parameter's uncertainty into a stochastic uncertainty, each described by a probability density function f.*
- *Analogous to the **deterministic lumped safety factor concept** formula, used in mechanical engineering, reading on stress level in the linear case* $RF = R / (\sigma \cdot j)$ *and in construction the **semi-probabilistic partial safety factor concept*** $RF = (R / \gamma_{Resistance}) / (\sigma \cdot \gamma_{Stress})$.
  (see compilation in §12 in [*CUN 22*] on 'Structural Reliability, Factors of Safety and Design Values')
- *RF = 0.97 < 1 does not mean failure, but only that the target failure probability of < 10^{-6} for a 50-year service life decreases by orders of magnitude depending on the variation magnitude. A value RF = 1.03 can, due to the lack of consideration for the probability of combinations of the uncertain design variables, represent a greater risk than RF = 0.97 in another case!*

✓ *One basic goal of probabilistic design is to identify that set of design parameters that will experience minimum impact from the scattering. In deterministic design it is to show for each load case and each failure mode by computation through RF ≥ 1 , that the resistance of a structure is higher than the loading R > S , valid for loads, or cross section loads or stress combinations.*

- ✓ *In probabilistic design, the work is more complex. It's objective is the evaluation of a probability of occurrence of a given failure state demonstrating* p_f < target p_f *(admissible) or of a survival probability ≡ reliability* $\Re = 1 - p_f$ > required $\Re$
- ✓ *Guess for a Strength Design Allowable is* $\overline{x} - 2.3 \cdot \sigma$
- ✓ *With a probabilistic concept the individual failure probabilities* p_{fi} *are determined and from them a failure probability* p_{fsys} *for the full system can be computed. This system information can be not obtained by the deterministic concept.*
- ✓ *Often just lower bound strength design values (A or B) are provided. In order to perform the best prediction of the average structural behavior means are required: a rough estimation may serve for the means of the basic population:* $\mu \approx$ *B-value / (1 - 2·*cov_μ*) and* $\mu \approx$ *A-value / (1 - 3·*cov_μ*) with the coefficient of basic population* cov_μ.

Personal Experience:

A safety distance pays off ".

Komodo dragon ≈ 75 kg

4 Cuntze's Failure Mode Concept (FMC) for Structural Materials

***Aim**: Creating a physically based foundation for building SFCs.*

4.1 'Global' Strength Failure Conditions (SFCs) and failure mode-linked 'Modal' SFCs

***Aim**: Shortly explaining the difference of so-called 'Global' and 'Modal' SFCs.*

There are a lot of possibilities to generate SFCs of different kinds. *Fig.4-1* presents a survey:

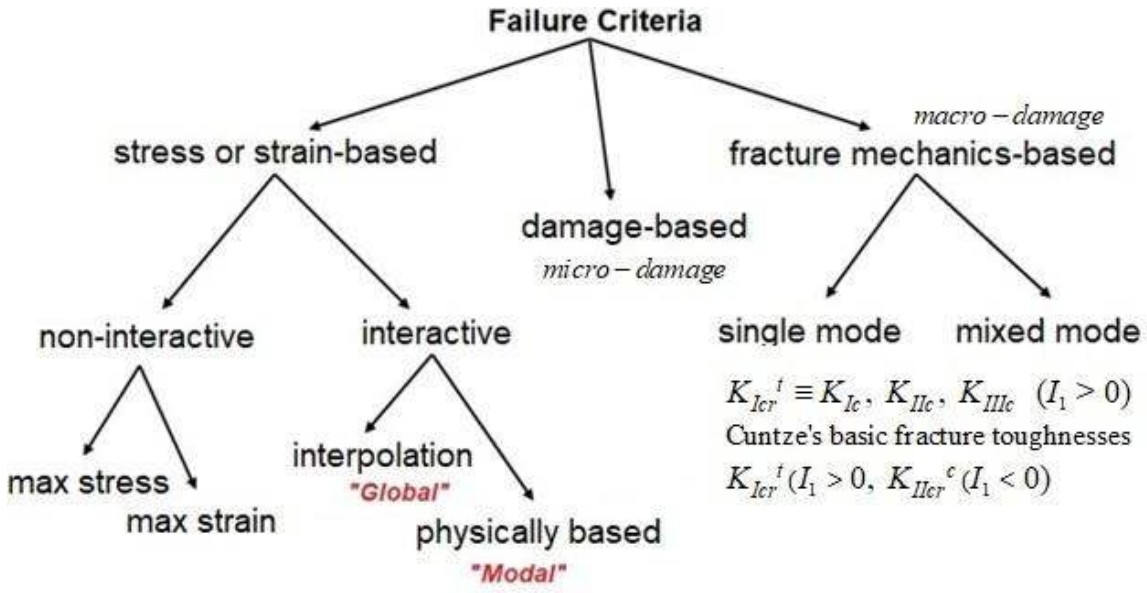

Fig.4-1: Possibilities to generate SFCs following Klaus Rohwer

[Rohwer K.: *Predicting Fiber Composite Damage and Failure*. J. of Composite Materials, http://jcm.sagepub.com/content/early/2014/09/26/0021998314553885]

Presently used, so-called interactive SFCs are a sub-part, which the author separates into two groups, 'global' and 'modal' ones. For instance the HMH yield failure condition is a modal SFC that captures just one failure mode. Further, the author choose the term global as "*play on words*" to modal and to being self-explaining. Global SFCs describe the full failure surface by one single mathematical equation. This means that for instance a change of the UD *tensile* strength $\bar{R}^{t}_{\perp}$ affects the failure curve in the *compression* domain, where no physical impact can be.

Global SFCs (later investigated Drucker-Prager, Ottosen, Tsai-Wu, Tresca, Willam-Warnke, Yu, Altenbach/ Bolchun/Kolupaev etc.) couple physically different failure modes whereas modal SFCs (Mises-yield, Puck, Hashin, Cuntze) describe each single failure mode, by-passing fiddle parameters and therefore will better map the course of test data and not lead to a wrong Reserve Factor in any mode domain:

Table 4-1: Formulation of a global and a modal SFC

1 Global SFC	$F(\{\sigma\},\{R\})=1$	*mathematically 'married' modes*
Set of Modal SFCs	$F(\{\sigma\},\{R^{\mathrm{mode}}\})=1$	*single mode formulations.*

Cuntze's SFCs employ friction directly, only

In the case of modal SFCs (*such as the FMC-based ones*) also equivalent stresses can be computed

as with 'isotropic Mises', namely $\left\{\sigma_{\mathrm{eq}}^{\mathrm{mode}}\right\} = \left(\sigma_{eq}^{\|\sigma},\ \sigma_{eq}^{\|\tau},\ \sigma_{eq}^{\perp\sigma},\ \sigma_{eq}^{\perp\tau},\ \sigma_{eq}^{\|\perp}\right)^{T}$,

and this is advantageous for any *laminate re-design decisions*!

Interactive SFCs can be discriminated. To do that the author choose the term "Global" as a 'play on words' to "modal" and both the terms as being self-explaining names. Here, global and modal have a similar level of abstraction, as in the case of stability the terms 'global' and 'local':

*Global SFCs describe the full failure surface by one single equation capturing all existing failure modes such as Normal Fracture (NF, *under tension or shear*) or Shear Fracture (SF, *under compression*). A specific name used for 'global' is 'Single Failure Surface Description'.

*Modal SFCs describe each failure mode-associated part of the full failure surface by one equation.

Table 4-1: Details Pros (+) and Cons (-) of 'global' and 'modal' SFCs

Global SFCs

(+) Describe the full failure surface by one single mathematical equation

(-) Usual global SFCs do not capture a multi-fold acting failure mode, i.e. $\sigma_I = \sigma_{II}$ or $\sigma_2 = \sigma_3$ or a 3-fold acting failure mode under σ_{hyd} with additional tension or compression stressing.

(-) Re-calculation: In the case of a test data change in a distinct mode domain re-calculation of model parameters is mandatory. Any change in one of the 'forcibly married' modes requires a new global mapping which also changes the failure curve in a physically independent failure domain, see *Fig.4-2*. In consequence, the material reserve factor has to be determined again

(-) The determination of *RF* for multi-axial stress states seems to be questionable for the simple Drucker-Prager model (*conical failure body*), still often used in civil engineering, *§16.6*.

Derivation Global SFC: Formulation of shape functions for the failure body describing (1) hoop cross-section (π-plane $\equiv I_1$ =constant plane regarding the Lode angle ϑ), (2) the axial cross-section = meridian along I_1.

Modal SFCs

(+) Describes each failure mode-associated part of the full failure surface by a single equation. Therefore, modal SFCs are more physically-based than global SFCs

(+) A change within one mode just hits this mode, *see Fig.2-3*. *RF* is just to re-determine in the affected failure mode domain!

(+) Equivalent stresses σ_{eq} are always determinable for isotropic UD materials

(+) Cuntze's SFCs capture multi-fold occurring failure modes by an additional term

(+) Cuntze's SFCs directly use the well to estimate parameter friction value μ

(-) Affords an interaction of the FMC-based SFCs for the activated failure modes.

Fig.4-2 visualizes for a distinct global SFC, used in a German guideline, how dramatically a change of the tensile strength $\bar{R}_{\perp}^{t}$ affects the failure curve in the compression domain, although no physical impact can be!

In order to only use experimentally derivable material quantities, the author directly introduced in his 3D-SFCs for the compression domain, the internal material friction μ as a SFC model parameter. Friction is a well-known physical property in engineering. However, one does not yet find a direct use of μ in the textbooks! Why using Mohr's friction angle φ if μ (φ) exists? The direct introduction of the measurable friction value is possible for the modal shear fracture SFCs. This possibility was achieved after the performance of an effortful *transition of the SFC formulated in structural stresses into a Mohr stresses formulated one (see Section* 22).

Within a ‘global’ SFC formulation all modes are mathematically married. This has a very bad impact: Each change, coming from new test information for any pure mode, has an effect on all other independent failure modes and might include some redesign, see the full change of the ZTL-curve.

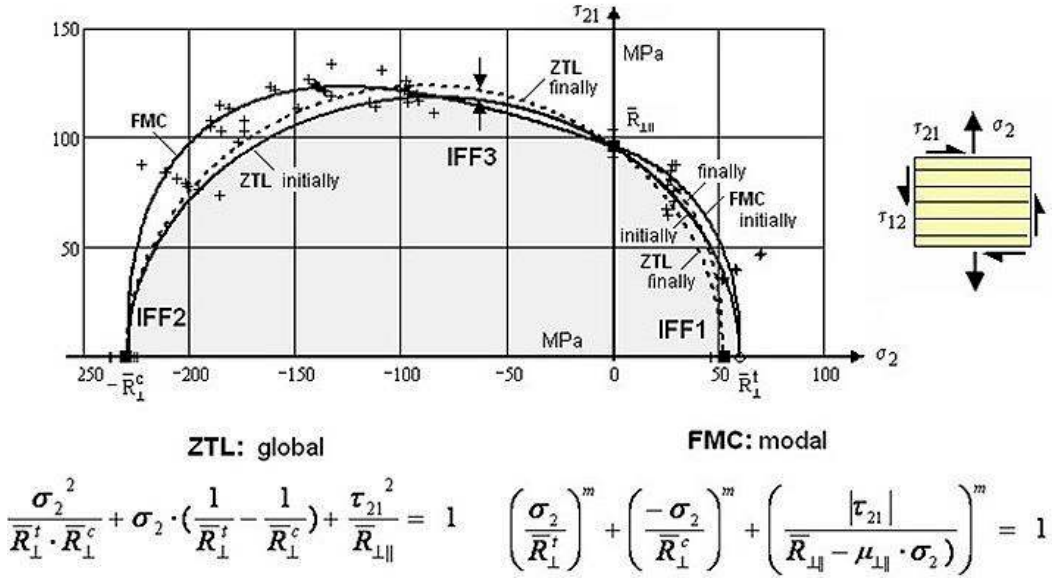

$$\frac{\sigma_2^{\,2}}{\bar{R}_\perp^t \cdot \bar{R}_\perp^c} + \sigma_2 \cdot \left(\frac{1}{\bar{R}_\perp^t} - \frac{1}{\bar{R}_\perp^c}\right) + \frac{\tau_{21}^{\,2}}{\bar{R}_{\perp\parallel}} = 1 \qquad \left(\frac{\sigma_2}{\bar{R}_\perp^t}\right)^m + \left(\frac{-\sigma_2}{\bar{R}_\perp^c}\right)^m + \left(\frac{|\tau_{21}|}{\bar{R}_{\perp\parallel} - \mu_{\perp\parallel} \cdot \sigma_2}\right)^m = 1$$

Fig.4-2: Modelling example, impact of a novel test information in the mode IFF1 considering the global ZTL-SFC, and a modal SFC

Such a bad impact is never faced using a ‘modal’ formulation, like the FMC-based ones. Of course, a modal FMC-approach requires an interaction in all the mode transition zones. This is performed by a probabilistic approach, using a ‘series failure system’ in the transition zone of the adjacent modes NF with SF, which reads as Interaction Equation,

$$Eff = \sqrt[m]{(Eff^{\text{mode }1})^m + (Eff^{\text{mode }2})^m + ...} = 1 = 100\% \qquad for \quad \text{Onset-of-Failure},$$

applying a ‘mode interaction exponent’ *m*, also termed rounding-off exponent, the size of which is high in case of low scatter and vice versa. The value of *m* is obtained by curve fitting of test data in the transition zone of the interacting modes. 30 years of experience delivered that $2.5 < m < 2.9$.

With the FMC-generated SFCs for the three ‘material families’ many available multi-axial fracture test data were mapped by the author to validate the SFCs as mathematical descriptions of the envisaged fracture failure models. Further, for a large variety of materials the associated fracture bodies were displayed in later chapters with distinct cross–sections of them, for instance for the isotropic applications: Principal stress plane, octahedral stress plane and tensile and meridian planes.
Various links or interrelationships between the materials could be outlined.

*Lessons Learned (**LL**):*

- ** So-called Global SFCs couple physically different failure modes whereas the Modal SFCs describe each single failure mode and therefore better map the course of test data and not lead to a wrong RF*
- ** Here, global and modal have a similar level of abstraction, as in the case of stability the terms ‘global’ and ‘local’ have*
- ** Similarities between the materials could be found*
- ** The surface of the failure body reads: F = 1 for a ‘global’ SFC-formulation and Eff = 1 = 100% for a ‘modal’ formulation.*
- ** Often, SFCs employ just strengths. This is physically not accurate: Mohr-Coulomb acts in the* case of compressed brittle materials! Consequence: The computed RF may not be on the safe side.
- *On the interaction equation above, citing Aristoteles: The whole is more (accurate) than the sum of its parts.

4.2 Mohr's SFCs for completion

Mohr's Fracture Stresses (*in later chapters necessarily to be used*) act together at the *same plane*, namely the fracture plane.

Using them for isotropic materials the following two very simple Failure functions can be formulated for isotropic materials:

$F_\sigma = F(\{\sigma^{Mohr}\}, R_\sigma) = 1$ ..... NF

$= \sigma_n/R_\sigma = 1$ (*normal stress hypothesis*)

$F_\tau = F(\{\sigma^{Mohr}\}, R_\tau) = 1$ ... . SF

$= \tau_n/(R_\tau - \mu\sigma_n) = 1$ e.g.(*shear stress hypothesis, Mohr-Coulomb*)

with R_σ: = separating strength (resistance) R_τ: = cohesion (resist.), μ: = Coulomb friction.

This outlines: *one* condition is to be used for *each* fracture mechanism which is dominated by *one fracture resistance* R_σ or R_τ. A resistance (of the fracture plane) corresponds with the basic strength associated if the action plane of a distinct stress comes to be the potential (*load must be high enough, too*) fracture plane: e.g. in the brittle case $\max \sigma = R_\sigma = R^t$ (isotropic) or $R_\perp{}^t$ (transversally-isotropic). R_σ can be measured and R_τ principally remains undeterminable unless the fracture angle θ_{fp} is determined. This is also valid for the *fracture plane stresses* $\{\sigma^{Mohr}\}$.

4.3 Basics of the Invariant-based FMC for generating 'Modal' SFCs

***Aim**: Creation of a physically-based SFC-building as basis for all material families.*

Being since 1970 in the industrial composite business the author tried to firstly sort out in regular discussions with Alfred Puck applicable SFCs for UD materials. Puck developed in 1990 his Hashin-based Action-plane Inter-Failure-Failure SFC, which was included in 2006 into the VDI 2014 guideline, sheet 3 (editor *R. Cuntze*).

Working with practically all material types the author was encouraged to find a Concept for all the material families: isotropic, UD and further the orthotropic ones including dense with porous materials. His finally developed (*about 1995*) so-called Failure-Mode-Concept (FMC) incorporates a rigorous thinking in failure modes and can be briefly described by the FMC features below, which were the basis for the development of Cuntze's micro-mechanics considering macro-mechanical SFCs:

- Each failure mode represents 1 independent failure mechanism and thereby represents 1 piece of the complete failure surface.
- A failure mechanism at the lower micro-scopic mode level shall be considered in the applied desired macro-scopic SFC
- Each failure mechanism or mode is governed by 1 basic strength *R*, only (witnessed!)
- Each failure mode can be represented by 1 SFC

The author's idea was to create physically-dedicated, invariant-based SFCs regarding:

* Failure mode-wise mapping and stress invariant's-based formulation
* Equivalent stress generation
* Each neat failure mode is governed just by one strength R^{mode}, witnessed for ductile and brittle materials
* Just measurable SFC model parameters are permitted, the model should not contain adjustable parameters
* Each SFC represents a failure surface portion

* SFC-models must have a sound physical basis and a good mathematical one, too
* If the mode driving stress becomes zero then also the criterion must become zero, which is stringent for a friction-linked criterion!

In the case of brittle materials the failure surface is the surface of a fracture failure body. Such a surface is determined by the peaks or ends of all failure stress vectors. The surface is mathematically defined by a Failure function *F*, which becomes 1 at 'Onset-of-Failure'.

Usually $F = 1$ is the formulation of a SFC (*mathematically this is a condition*).

The FMC was originally derived for UD materials because there was the big demand at that time. The employed stress invariants shall be presented via isotropic knowledge: Beltrami, Schleicher et al. assumed at initiation of yield that the strain energy (denoted by *W*) in a solid cubic element of a material will consist of two portions:

$$W = \int \{\sigma\}\{\varepsilon\}\, d\{\varepsilon\} = W_{Vol} + W_{shape} \quad \text{with} \quad \{\sigma\} = (\sigma_1, \sigma_2, \sigma_3, \tau_{23}, \tau_{13}, \tau_{12})^T .$$

Including Hooke's law in the case of a ***transversely-isotropic*** (UD solid) the expression will take the form, using s_{ik} := compliance coefficients, E:=elasticity modulus, ν:=Poisson's ratio,

$$W = [s_{11}\cdot\sigma_1^2 + s_{22}\cdot\sigma_2^2 + s_{33}\cdot\sigma_3^2 + s_{44}\cdot\tau_{23}^2 + s_{55}\cdot(\tau_{12}^2 + \tau_{13}^2)] / 2 + s_{12}\cdot(\sigma_1\sigma_2 + \sigma_1\sigma_3) + s_{23}\cdot\sigma_2$$

$$\sigma_3 = \underbrace{\frac{I_1^2}{2\cdot E_{\parallel}}}_{\text{volume}} + \underbrace{\frac{I_2^2\cdot(1-\nu_{\perp\perp})}{4\cdot E_{\perp}}}_{\text{volume}} - \underbrace{\frac{\nu_{\perp\parallel}\cdot I_1\cdot I_2}{E_{\parallel}}}_{\text{volume}} + \underbrace{\frac{I_3}{2\cdot G_{\parallel\perp}}}_{\text{shape}} + \underbrace{\frac{I_4\cdot(1+\nu_{\perp\perp})}{4\cdot E_{\perp}}}_{\text{shape}} .$$

with the invariants $I_1 = \sigma_1$, $I_2 = \sigma_2 + \sigma_3$; $I_3 = \tau_{31}^2 + \tau_{21}^2$; $I_4 = (\sigma_2-\sigma_3)^2 + 4\tau_{23}^2$;

$$I_5 = (\sigma_2 - \sigma_3)(\tau_{31}^2 - \tau_{21}^2) - 4\tau_{23}\tau_{31}\tau_{21}.$$

In the ***isotropic*** case analogously follows, however simpler,

$$W = \underbrace{\left[\frac{1-2\nu}{3} I_1^{iso\,2}\right]}_{\text{volume}} + \underbrace{\left[\frac{2+2\nu}{3} 3J_2^{iso}\right]}_{\text{shape}} / 2E$$

with $I_1^{iso} = \underline{f(\sigma)} = \sigma_I + \sigma_{II} + \sigma_{III}$, $6\cdot J_2^{iso} = \underline{f(\tau)} = (\sigma_I - \sigma_{II})^2 + (\sigma_{II} - \sigma_{III})^2 + (\sigma_{III} - \sigma_I)^2$,

It is known, both portions in the bracket above may be used to formulate a failure function

$$F = \underbrace{c_1 \cdot \frac{(1-2\nu)\cdot I_1^{iso2}}{3\bar{R}^2}}_{\text{volume}} + \underbrace{c_2 \cdot \frac{(2+2\nu)\cdot 3J_2^{iso}}{3\bar{R}^2}}_{\text{shape}} .$$

Fig. 4-3 below displays for the 2 material families a physically-based choice of invariants for isotropic and UD SFCs.

Exemplarily, the isotropic SFC model, spanning up the fracture body in the compression domain, shall be used for demonstration. The complete SFC reads:

$$\text{Shear Fracture SF, } I_1 < 0: \quad F^{SF} = F^{\tau} = c_1 \cdot \frac{3\cdot J_2}{\bar{R}^{c2}} \cdot \Theta^{\tau} + c_2 \cdot \frac{I_1}{\bar{R}^{c}} + c_3 \cdot \left(\frac{I_1}{\bar{R}^{c}}\right)^2 .$$

Herein, the first part of the SFC represents the shape change, the second the friction effect, the third the volume change and the non-circularity parameter Θ^{τ} describing the inherent, nevertheless often not known 120°-symmetry of the failure bodies of isotropic brittle and ductile material, too (*see a later chapter).*

Note, please:

R means strength (resistance) in general and further Strength Design Allowable

$\overline{R}$ means average strength used for modelling, mapping of the course of test data.

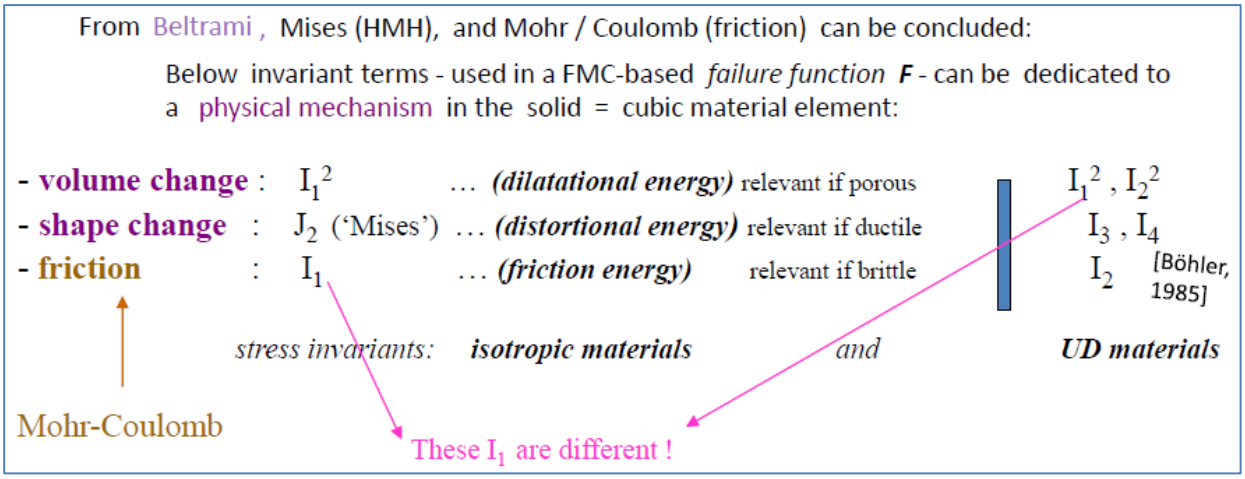

Fig.4-3: Reasons for choosing invariants when creating FMC-based SFCs

Above invariants can be formulated in 3D structural component stresses, in principal stresses and in Mohr stresses, which will become essential when deriving a stress state-caused fracture angle and the friction value occurring in the SFCs.

4.4 Material stressing effort *Eff* (Werkstoff-Anstrengung)

***Aim**: Generation of a physical basis for the interaction of failure modes and for an excellent understanding of a failure body with multi-axial strength (capacity) values. (Eff = 100% describes the failure surface).*

If several failure modes are activated by the stress state then the application of the so-called *material stressing effort Eff* is very helpful (*in German termed Werkstoffanstrengung. The artificial name had to be created in the World Wide Failure Exercise (WWFE) on UD-SFCs, together with its UK-organizers, because an equivalent term to the excellent German term is not known in English).*

The full *Eff* consists of all mode portions Eff^{mode}. It works analogous to 'Mises'

$$Eff^{\text{yield mode}} = \sigma_{eq}^{\text{Mises}} / R_{0.2} \;\rightarrow\; Eff^{\text{fracture mode}} = \sigma_{eq}^{\text{fracture mode}} / R \;.$$

The contribution of each single Eff^{mode} informs the designing engineer about the importance of the single portions in the SFC and thereby about the critical failure driving mode and thereby outlining the design-driving mode.

Whereas the structural engineer is more familiar with the equivalent stress the material engineer prefers above 'material stressing effort' *Eff*. These terms are linked by $\sigma_{\text{eq}}^{\text{mode}} = Eff^{\text{mode}} \cdot R^{\text{mode}}$.

The use of *Eff* supports 'Understanding the multi-axial strength capacity of materials' (s. *Fig.13-4*): For instance, 3D-compression stress states have a higher bearing capacity, but the value of *Eff* nevertheless stays at 100%. Consequently, this has nothing to do with an increase of a (*uniaxial*) technical strength *R* which is a fixed result of a Standard!

The still used fracture test result of a brittle concrete impressively shows how a slight hydrostatic pressure of 6 MPa increases the strength capacity in the longitudinal axis from 160 MPa up to 230 MPa - 6 MPa = 224 MPa. Thereby, the benefit of 3D-SFCs–application could be proven as the fracture stress states below depict both the Effs are 100% :

$$\sigma_{\text{fr}} = (\sigma_I\,,\ \sigma_{II}\,,\ \sigma_{III}\,)_{\text{fr}}^{\ \text{T}} = (-160,\ 0,\ 0)^{\text{T}}\ \text{MPa} \Leftrightarrow (-224-6,\ -6,\ -6)^{\text{T}}\ \text{MPa}\,. \qquad !$$

This can be transferred to the similar loaded quasi-isotropic plane of the transversely-isotropic UD-

materials, $\sigma_2 - \sigma_3$, see [*Cun23c*], and to the orthotropic CMC fabric, when beside shear τ_{WF} the compressive stress σ_W^c acts together with σ_F^c and both activate friction on the sides [*Cun24b*].

LL: *The physically clear-based quantity Eff gives an impressive interpretation of what 100% strength capacity in 1D- 2D- and 3D stress states physically really means.*

Mode interaction does not work with the Failure Function *F* but with *Eff* of each mode. Table 4-2 presents the interaction process.

Table 4-2: Outlining the interaction process of the modal Eff portions

* Normal Fracture NF for $I_1 > 0$ $\Leftarrow$ SFCs $\Rightarrow$ Shear Fracture SF for $I_1 < 0$

$$F^{NF} = \frac{\sqrt{4J_2 - I_1^2/3} + I_1}{2 \cdot \bar{R}^t} = 1 \quad \leftrightarrow \quad F^{SF} = c_1^{SF} \cdot \frac{3J_2}{\bar{R}^{c2}} + c_2^{SF} \cdot \frac{I_1}{\bar{R}^c} = 1$$

after inserting $\sigma = R \cdot Eff$ and dissolving for Eff follow the equations

$$Eff^{NF} = \frac{\sqrt{4J_2 - I_1^2/3} + I_1}{2 \cdot \bar{R}^t} = \frac{\sigma_{eq}^{NF}}{\bar{R}^t} \quad \leftrightarrow \quad Eff^{SF} = \frac{c_2^{SF} \cdot I_1 + \sqrt{(c_2^{SF} \cdot I_1)^2 + 12 \cdot c_1^{SF} \cdot 3J_2}}{2 \cdot R^c} = \frac{\sigma_{eq}^{SF}}{\bar{R}^c}.$$

The complete *Eff* and the always required Reserve Factor *RF* are determined via the interaction equation: $Eff = [(Eff^{NF})^m + (Eff^{SF})^m]^{m^{-1}} \rightarrow f_{RF} = 1/Eff$.

4.5 Direct use of a Friction Value *μ* in the SFCs of Isotropic and UD materials, preview

Aim: *Direct use of the measurable μ instead of applying a μ-hiding friction model parameter.*

Mohr-Coulomb usually acts with brittle materials: Therefore, in the case of compressed brittle materials the effect of friction is to capture, which usually is performed by 'fictitious' friction-linked SFC model parameters. Such a model parameter for friction in the SFC can be replaced by the measurable friction value μ.

An engineer prefers the application of such a measurable and physically understandable value μ, especially, because it does practically not scatter which is essential in design and can be well assumed! However, in order to achieve this, the very challenging task to transform a SFC in structural stresses into a SFC in Mohr stresses at first has to be successfully performed for the isotropic and the UD materials. Exemplarily for isotropic materials this direct relationship is depicted in *Table 4-3*.

Table 4-3, Isotropic materials: Determination of SFC model parameters considering 120°-axial symmetry.

Assumption: Fracture failure body is 120°-rotationally symmetric unlike Mises cylindrical yield failure body.

$$Eff^{NF} = c_\Theta^{NF} \cdot \frac{\sqrt{4J_2 \cdot \Theta^{NF} - I_1^2/3} + I_1}{2 \cdot \bar{R}^t} = \frac{\sigma_{eq}^{NF}}{\bar{R}^t} \leftrightarrow Eff^{SF} = \frac{c_{2\Theta}^{SF} \cdot I_1 + \sqrt{(c_{2\Theta}^{SF} \cdot I_1)^2 + 12 \cdot c_{1\Theta}^{SF} \cdot 3J_2 \cdot \Theta^{SF}}}{2 \cdot \bar{R}^c} = \frac{\sigma_{eq}^{SF}}{\bar{R}^c}.$$

with $c_{2\Theta}^{SF} = c_2^{SF} = (1 + 3 \cdot \mu)/(1 - 3 \cdot \mu)$ from $\mu = \cos(2 \cdot \theta_{fp}^c \circ \cdot \pi / 180)$,

c_Θ^{NF}, see *Table* 16 - 4 ; $c_\Theta^{NF} = 1$, if not of practically interest and because most often the tension dent is too small,

$1 + c_{2\Theta}^{SF} = c_{1\Theta}^{SF} \cdot \Theta^{SF}$ from inserting the compressive strength point $(\bar{R}^c, 0, 0)$. See also *Table* 16 – 4.

Compr. Meridian: $\Theta^{SF} = \sqrt[3]{1 - d^{SF}}$, Tensile Meridian: $\Theta^{SF} = \sqrt[3]{1 + d^{SF}}$, Neutral Meridian: $\Theta^{SF} = 1$

with the non-circularity function Θ including d as non-circularity parameter.

For details about the tedious derivation of the relationship c (μ), see chapter 14.

LL:

* *In the case of friction so-called 2-parameter Failure Theories outline a bottleneck*
* *Often SFCs employ just strengths and no friction value. This is physically not accurate and the undesired consequence in Design Verification is: The RF may be not on the safe side..*
* *In contrast to the usual '(un)doing': Friction must and can now be directly considered by the measured μ*
* *Friction occurs similarly over the scales.*
* *With composites, friction is basically generated by micro-crack closure and opening, With ductile behaving materials by shear straining*
* *As long as the damage mechanism remains unchanged, the corresponding failure condition can always be used. This applies to failure limits, specified as a strain or a deformation in the case of ductile behaviour (→ yield criterion), and to fracture failure in the case of brittle behaviour (→ fracture criteria).*

Similarly behaving materials show the same shape of a fracture body, when using the same SFC!

5 Material Symmetry- driven ‘Generic’ Material Properties Number

Aim: *Targeting at a minimum test amount and a simpler generic’ number- driven Strength Mechanics Building by consideration of the available material knowledge.*

5.1 General with Material Symmetry View

During the derivation of the FMC a closer look at material symmetry facts was taken whereby the question arose: “Does a material symmetry–linked ‘Generic’ Number exist with a number 2 for isotropic and 5 for UD materials?

Under the design-simplifying presumption

“Homogeneity is a permitted assessment for the material concerned”

and regarding the respective material tensors, it follows from material symmetry that the number of strengths equals the number of elasticity properties!

Fracture morphology gives further evidence: Each strength property corresponds to a distinct strength failure mode and to a distinct strength failure type, to Normal Fracture (NF) or to Shear Fracture (SF). This seems to mean, that a characteristic number of quantities is fixed: 2 for isotropic material and 5 for the transversely-isotropic UD lamina (≡ lamellas, used in civil engineering). Hence, the applicability of material sym*metry involves that in general just a minimum number of properties needs to be measured* (benefits: test cost + time) which is helpful when setting up strength test programs.

⇒ Witnessed material symmetry knowledge seems to tell: “There might exist a ‘generic’ (*term was chosen by the author*) material inherent number”. This looks to be proven by the later following investigation of Normal Yielding NY of plexi-glass and (*theoretically*) by a compressive fracture toughness K_{IIcr}^{c} for a brittle material with an ideally homogeneous state at the crack tip.

At first *Fig.5-1* presents the stresses faced with the three material families.

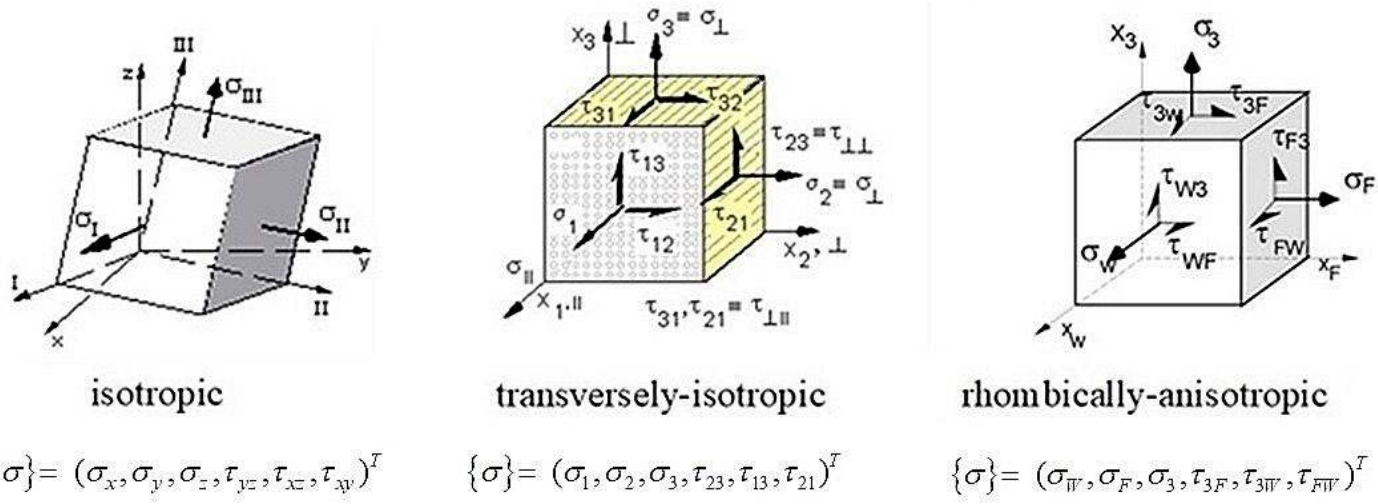

Fig.5-1: Presentation of the stresses faced with the envisaged three material families

5.2 Generic Number (material inherent?)

After 3 decades of searching applicable test results the author came to the conclusion that a material symmetry-based, material inherent Generic Number (*term, chosen by me*) might exist:

2 for isotropic, 5 for transversely–isotropic materials, and 9 (6) for orthotropic material..

The generic number is strictly linked to my Failure Mode Concept, the basis for generating my strength criteria. ‘Generic Number’ means that in general just a minimum number of properties needs to be measured which is helpful when setting up strength test programs, for instance → the minimum test amount is fixed.

5.2.1 Isotropic Material

For isotropic materials the following results can be compiled:

- 2 elastic 'constants' *E, ν and* 2 strengths R^t (tension), R^c (compression); driving 2 strength failure modes: Normal Fracture NF with Shear Fracture SF if brittle, replaced by Crushing Fracture CrF if porous,
- 2 yield strengths $R_{0.2}^t$, $R_{0.2}^c = R_{p0.2}$; driving 2 yield failure modes: Normal Yielding NY (*as I mapped it for the tension-caused crazing plexiglass PMMA, a non-convex failure body!)* with Shear Yielding SY
- 2 fracture mechanics modes (*defined by me as modes, where the original crack planes do not turn in the undisturbed crack-tip ideal elastic homogeneous case*) KIcr (critical, tension), K_{IIcr}^c (compression), a fracture toughness for a brittle material with an ideally homogeneous state at the crack tip. (Although not practically possible, this would theoretically be possible if the shear fracture angle 'plane' was continued under compressive stress). For me: the fracture mechanics terms K_{IIcr} and K_{IIIcr} are necessary valuable quantities to describe the process under a general far stress state of turning a crack into the K_{Icr} – driven direction. According to the usual disturbances at the crack tip K_{IIcr}^c has just a holistic theoretical meaning for me.
- 1 for a so-called 'physical' parameter (such as the coefficient of thermal expansion CTE, the coefficient of moisture expansion CME, and the friction value μ, etc.)

5.2.2 Transversely-Isotropic UD-Materials

Analogously the higher number 5 is now valid for the properties:

- 5 elastic 'constants', 5 strengths, 5 strength failure modes fracture (NFs with SFs),

  5 fracture toughness quantities
- 2 physical parameters (CTE, CME, friction $\mu_{\perp\perp}$, $\mu_{\perp\parallel}$, etc.).

5.2.3 Orthotropic Material

Orthotropic materials are less homogenizable, generally. If yes, the generic number is 9.

LL:

- ✓ *Beside the standard Shear (band) Yielding SY there also exists Normal Yielding NY analogous to the failure modes Shear Fracture SF and Normal Fracture NF* (author assumption proven)
- ✓ *120°-rotational symmetry is inherent to brittle and ductile isotropic materials* (assumption is proven in a following chapter)
- ✓ *Generic number 2, K_{Icr}^t with $K_{IIcr}^c : K_{IIcr}^c$ will be later theoretically proven for the non-real, ideal case of no flaws in front of crack tip*
- ✓ *Also in consequence of above building: Different but similar behaving materials can be basically treated with the same SFC. Examples are: Concrete ↔ foam, different fabrics*
- ✓ *The obtained Strength Mechanics Building matured, became clearer and more complete*.

Note, please:

R. M. Christensen once cited:

"*Virtually all practitioners are comfortable with the simple, traditional, but incorrect Mises and Tresca forms. The best work will survive and prosper and ultimately provide the basis for enlightenment and forward movement*".

In this context my question:

"*Isn't an 'inherent' number - claimed by the author for the three 'homogenizable' material families - not at least a field link, which intends to combine the SFC domain specifics with Fracture Mechanics specifics*"?

In the frame of his material symmetry-driven thoughts the author intended to test-proof some ideas that help to complete his envisaged Strength Mechanics Building by finding missing links and by providing engineering-practical strength criteria (SFCs), the parameters of which are directly measurable.

All this supports the assumption of a 'generic' number for a smeared-modelled material.

Material Symmetry seems to tell:

"In the case of ideally homogeneous materials a generic number is inherent. This is valid for elastic entities, yield modes and fracture modes, for yield strengths R_{02} and fracture strengths R, fracture toughness entities K_{cr} and for the invariants used to generate strength criteria".

One might think*: **"Mother Nature gives Strength Mechanics a mathematical order!"***

In the context above some thoughts of the author on his 3D-SFCs which make future 3D analyses real:

* It is possible to realize an idea without financial resources (funding).

* It is possible to reach relatively high altitudes without suitable mountaineering equipment (sherpas were too late). ⇒

Much is possible if a goal is pursued!

* Is it perhaps also possible to get an idea like the FMC or the Generic Number into more practical use?

Or does it remain true what the author stated in 2000*:*

"It seems to be simpler to launch Ariane 5 than to launch an idea in the scientific community."

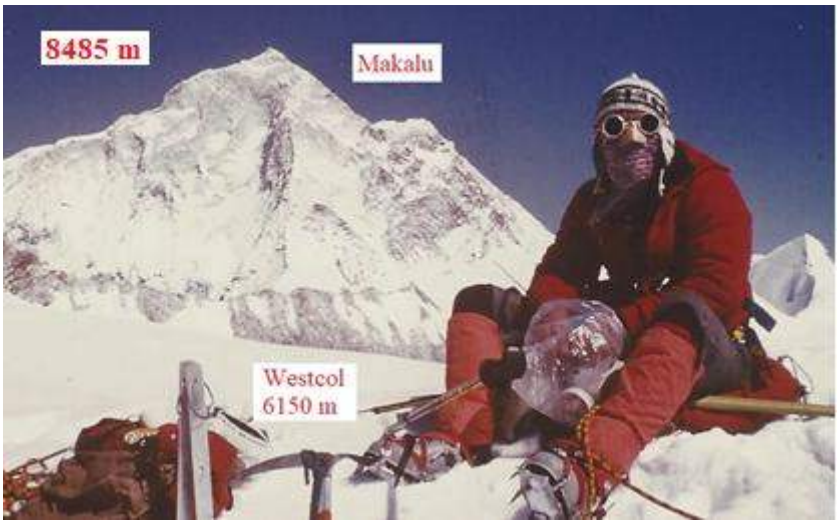

In addition: Being very often invited for giving presentations is nice but where is the feedback with the desired discussions and mails

in order to exploit novel ideas by available knowledge?

6 Interaction of Stresses versus Interaction of Failure Modes

***Aim**: Making aware of the difference of the two interaction-types Stresses and Modes.*

6.1 Modal equivalent stress σ_{eq} and Modal Material stressing effort *Eff*

For the failure mode 'yielding' the HMH hypothesis (in short 'Mises') delivers an equivalent stress and this for all stress situations (normal stress, shear stress, torsion stress) when the mode yielding comes to act, *Fig.6-1*. Fully analogously to the (modal) HMH equivalent *yield* stress the equivalent *fracture* stress is related to the 'material stressing effort' *Eff* (Anstrengung. *Eff* is an artificial term, created with the WWFE originators in the UK, because a similar term does not exist in English).

$$Eff^{Mises} = \sigma_{eq}^{Mises}/R_{po.2} \Rightarrow Eff^{fracture\ mode} = \sigma_{eq}^{fracture\ mode}/R_m\ ,\ Eff^{mode} = \sigma_{eq}^{mode}/\overline{R}^{mode}$$

Above possibility to formulate equivalent stresses caused Cuntze to differentiate Global from Modal strength criteria types. About more details and the Pros and Cons, see [*Cun16c*].

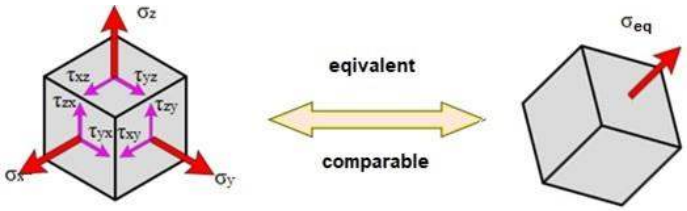

Fig.6-1: multi-axial structural stress state with its representing equivalent stress

Fig.6-1 shows via the equivalent stress the definition of the material stressing effort.

6.2 Interaction of Stresses

***Aim**: Provision of a mode-based 'Modal' stress-interaction and not a mathematically married 'Global' one.*

The derivation of the FMC-based SFCs builds up on the hypotheses of Beltrami, Hencky-Mises-Huber (HMH) and Mohr-Coulomb. Therefore the depicted SFC approaches consider, that the solid material element may experience, generated from different energy portions, a shape change (HMH), a volume change and friction. FMC-based SFCs will be given for a large variety of isotropic brittle structural materials such as porous Concrete Stone, Normal Concrete, UHPC sandstone, monolithic ceramics and for the transversely-isotropic fiber-reinforced polymers Lamina (ply, lamella) and finally orthotropic fabrics inclusively fabric ceramics, see [*CUN22, Cun23a,24b*].

In the development of structural components the application of 3D-validated strength failure conditions SFCs (the function is a condition $F = 1$ and the design request is whether $F < 1$, a 'criterion') is one essential pre-condition for achieving the required fidelity for the user. This includes Yield Failure Conditions (ductile behavior) for the non-linear analysis of the material and the Onset-of-Yield limit verification. It further includes conditions to verify that Onset-of-Fracture does not occur, in the case of brittle and ductile behavior.

Since two decades the author believes in a macroscopically-phenomenological 'complete classification' system, where all strength failure types are included, see the figure below. In his assumed system several relationships may be recognized:

(1) Shear stress yielding (SY), followed by Shear fracture (SF) considering 'dense' materials. For porous materials under compression, the SF for dense materials is replaced by Crushing Fracture (CrF).

(2) In order to complete a mechanical system beside SY also NY should exist. This could be demonstrated by PMMA (plexiglass) with its chain-based texture showing NY due to crazing failure under tension and SY in the compression domain, [see *subsection* 7.1].

The right side of the scheme outlines that a full similarity of the 'simpler' isotropic materials with the transversely-isotropic UD materials exists.

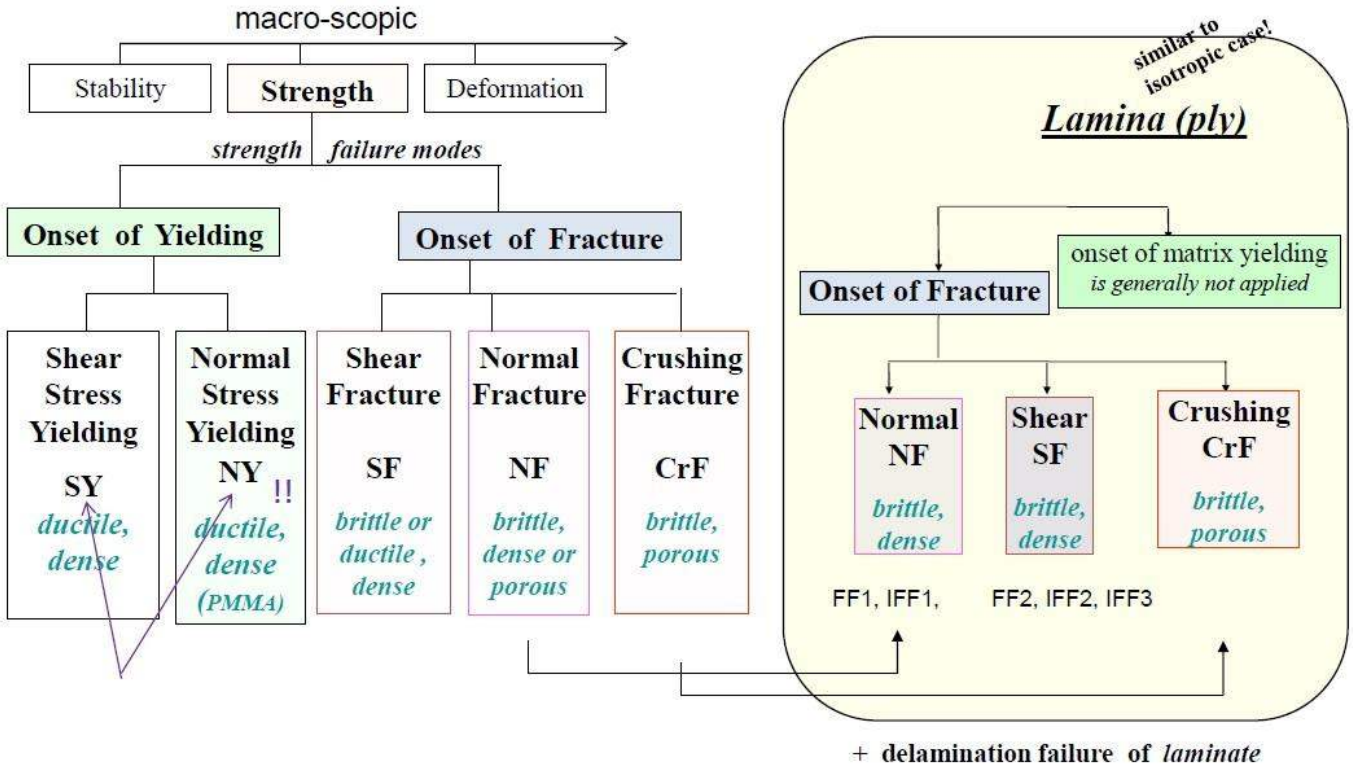

Fig.6-2: Scheme of macro-scopic strength failure types and modes of isotropic materials and transversely-isotropic UD-materials (Cuntze 1998)

LL:

* *Failure behavior of Fiber-Reinforced materials is similar to isotropic ones*
* *Principally, instead of stress-based SFC, strain-based SFC might be applied if the full stress-strain history is accurately considered. However, just limit strain conditions are used in pre-dimensioning (§22), because the certification process is stress-based.*
* *"The strain is not a quantity describing the material behavior".*

Prof. Gottstein, RWTH-Aachen.

6.3 Interaction of Failure Modes

* Global SFCs do not just interact stresses but due to the mathematical approach Failure Modes automatically too.

* Modal SFCs according to the FMC-approach, as still mentioned, require a still mentioned interaction in all the mode transition zones. This is performed by

$$Eff = \sqrt[m]{(Eff^{\text{mode }1})^m + (Eff^{\text{mode }2})^m + ...} = 1 = 100\% \qquad for \quad \text{Onset-of-Failure}$$

and by applying a 'mode interaction exponent' m , being about 2.6 as practiced.

7 Novelties 'Normal Yielding' (NY) and 'Compressive Fracture Toughness'

***Aim**: Proving that a material 'Generic' number of 2 is valid for isotropic materials.*

Regarding 'Generic' number of 2 then there are 2 'empty rooms' in the author-assumed 'Structural Mechanics Building' of Isotropic Materials to be filled by 'Normal Yielding (NY)' and by a counterpart of the tensile fracture toughness $K_{Icr}^{(t)}$ in the compressive domain.

7.1 Crazing-caused Normal Yielding NY of Plexiglass (non-convex failure surface !)

Glassy, amorphous polymers like polystyrene (PS), polycarbonate (PC) and PolyMethylMethAcrylate (PMMA = plexiglass) are often used structural materials. They experience two different yield failure types, namely crazing under tension (*Fig.7-1*)

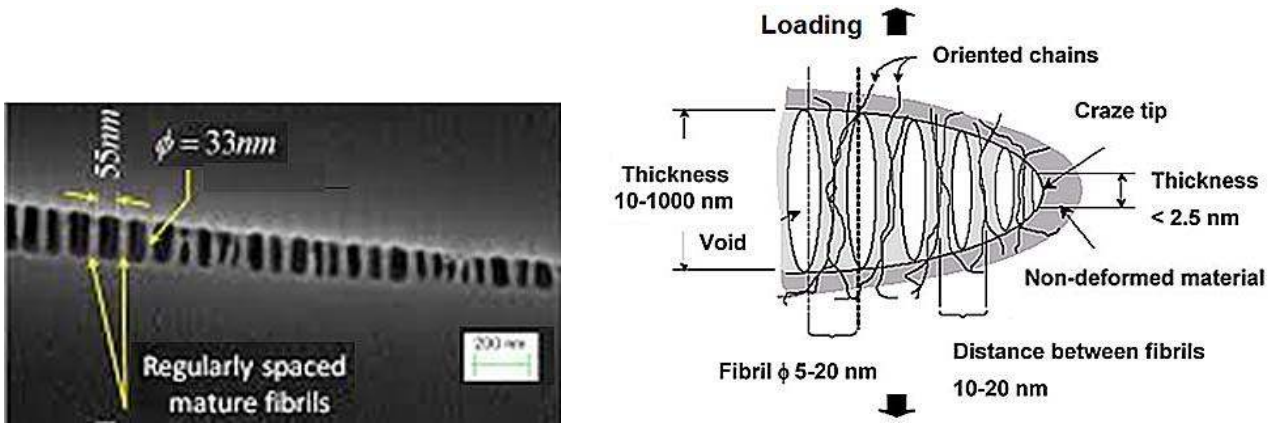

Fig. 7-1: PMMA, SEM image of a craze in Polystyrene Image (created by Y. Arunkumar)

and under compression shear stress yielding which is often termed by the material specialist 'shear-banding'. [*CUN22*, §4]

Crazing can be linked to Normal Yielding (NY) which precedes the crazing-following tensile fracture. Crazing occurs with an increase in volume through the formation of fibrils bridging built micro-cracks

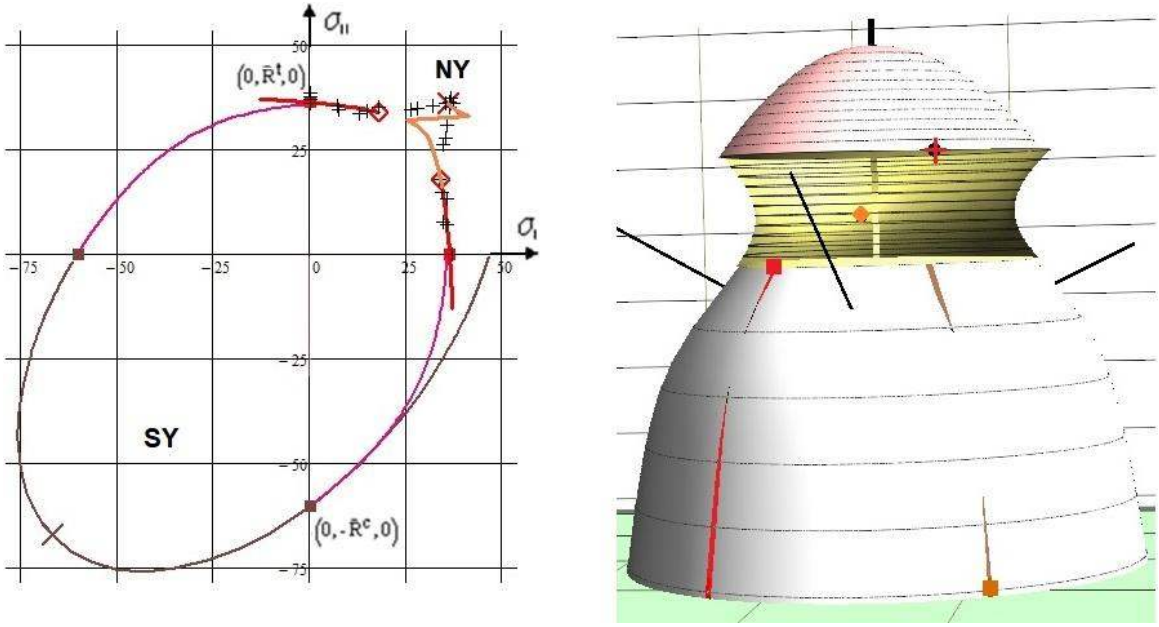

Fig. 7-2, PMMA: (left) Mapping of test data in tension and compression principal stress domain with and without interaction; (right) depiction of the fracture body shape with some representative points. For the validation of the FMC-based SFC for PMMA two data sets were available, one NY-2D-data set from Sternstein-Myers and a SY-3D-data set from Matsushige

[Sternstein S S and Myers F A: *Yielding of glassy polymers in the second quadrant of principal stress space.* J. Macromol. Sci, Phys. B 8 (1973), 539-571. Matsushige K, Radcliffe S V and Baer E: *The mechanical behavior of polystyrene under pressure*. J. of Material Science 10 (1975), 833-845].

and shear banding keeps volume. Therefore, due to the FMC 'rules' the dilatational I_1^2 is to employ in the SFC-approach for tension $I_1 > 0$. Under compression, brittle amorphous polymers classically shear-band (SY) and experience friction. Therefore, I_1 must be employed in the approach for $I_1 < 0$ in order to consider material internal friction. 'Mises' means frictionless yielding and therefore it forms a cylinder.

For obtaining the complete yield failure body (*Fig.7-2*) its parts NY and SY are to interact in the transition zone. Doing this the used Mathcad 15 code had no problems to generate the **3D**-failure body, however the **2D**-cut visualization of the NY failure surface using Mathcad 15 code (*a 35 DIN A4-pages application*) was too challenging for the solver which had to face a concave 2D principal stress plane situation instead of the desired convex one. Often used for the structural TP polymer PMMA that it is pretty brittle with $R^t \equiv R^c / 3$..

LL: *The failure type crazing shows a 'curiosity' under tensile stress states: A non-convex shape exists for Onset-of-Crazing ($\bar{R}_{NY}^{\,t}$). This violates the 'convexity stability postulate' of Drucker, "If the stress-strain curve has a negative slope then the material is not Drucker-stable".*

The inflection point of the hyperboloid results from the derivation dF/dI_1 of the NF criterion,

$$F^{NF} = \frac{\sqrt{4J_2 - I_1^2/3} + I_1}{2 \cdot \bar{R}^t} = 1$$ *neglecting here 120°-symmetry* $\Theta = 1$ *(later chapter).*

7.2 Compression-caused Shear Fracture Toughness $K_{IIcr}^{(c)}$ of Brittle Isotropic materials

Some reasons caused the author to search a compressive fracture toughness: [*CUN22*]

- An early citation of A. Carpinteri [*Car93*], that approximately reads: "*With homogeneous isotropic brittle materials there are 2 real energy release rates* $\mathcal{G}_{Icr}$, $\mathcal{G}_{IIcr}$, *one in tension and one in compression*"
- The number of the (basic) fracture toughness quantities may be *theoretically at least* also 2, namely $K_{Icr}^{\,t} \equiv K_{Ic}$ together with $K_{IIcr}^{\,c}$ (*Fig.7-3*) and
- The novel approach Finite Fracture Mechanics (FFM) that offers a hybrid criterion to more realistically predict the crack initiation in brittle isotropic and UD materials.

A stringent postulate for the author was crack path stability which can be explained "*Only an angle-stable, self-similar crack growth plane-associated critical Stress Intensity Factor (fracture toughness) is a 'basic' property*". This requires as presumption an *ideally* homogeneous isotropic material in front of the crack-tip. Therefore, the investigation is only for an ideal structural mechanics building of importance, because in practice, there are usually no ideal homogeneous conditions at the crack-tip.

Practically, facture mechanics is presently only tensile driven performed using $K_{Ic} = K_{Icr}^{\,t}$ as a clear critical fracture intensity, where the crack plane does not change (the index cr is necessarily to be taken in this document in order to separate tension ^{t} from compression ^{c}). Why shouldn't there not be a quantity $K_{IIcr}^{\,c}$ that fits as an opposite complement to $K_{Icr}^{\,t}$ and where, in an ideal case of no flaws in front of the crack tip, the crack plane grows further along the generated shear fracture angle under a compressive fracture load?

The Fracture Mechanics Mode I delivers a real, 'basic' fracture resistance property generated under a tensile stress. Both the Modes II K_{IIc}, and III K_{IIIc} do not show a stable crack plane situation but are nevertheless essential FM model parameters to capture 'mixed mode loading' for performing a multi-axial assessment of the far-field stress state. $\rightarrow \bar{R}^t$ and $\bar{K}_{I\,cr}^{t}$ correspond! They are 'just' very helpful model parameters driving the crack plane in direction of a finally K_{Ic}-driven failure.

With the Mode-II compressive fracture toughness $K_{IIcr}^{\,c}$ it is like with strength. One says compressive failure, but actually shear (stress) failure is meant, compressive stress is 'only' the descriptive term. Therefore the shear index $_{II}$ is to apply with $K_{IIcr}^{\,c}$.

One has to keep in mind: In mechanical engineering the structural tasks are usually lie in the tension

domain (*index ^{t} is skipped*), whereas oppositely in civil engineering the compression domain is faced (*index ^{c} is skipped*):

*Tension domain: One knows from K_{Icr}^{t} (tension), that – viewing the fracture angle - corresponds to R^{t}.

*Compression domain: Above not generally known second basic SIF K_{IIcr}^{c} seems to exist under ideal conditions. It corresponds to shear fracture SF happening under compressive stress R^{c} and leading to the angle Θ_{fp}^{c}. The crack surfaces are closed for K_{IIcr}^{c}, friction sliding occurs.

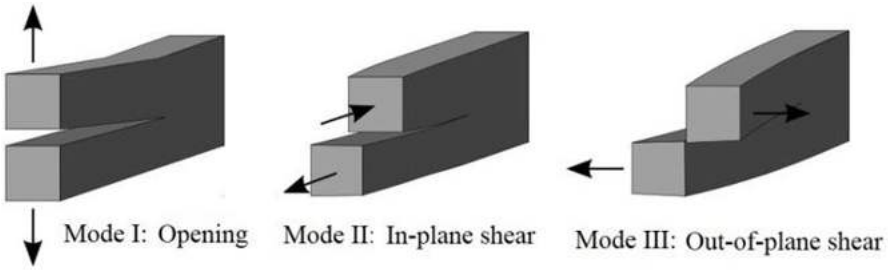

Fig.7-3: Classical Fracture Mechanics modes

Some proof of the author's postulate could be: There exists a minimum value of the compressive loading at a certain fracture angle. This means that the K_{IIcr}^{c} becomes a minimum, too. Liu et al performed in [*Liu14*] tests using a cement mortar material, (*Fig.7-4*).

► From Liu's measured results, by now, it seems to - theoretically at least - that the 'generic' number 2 is met.

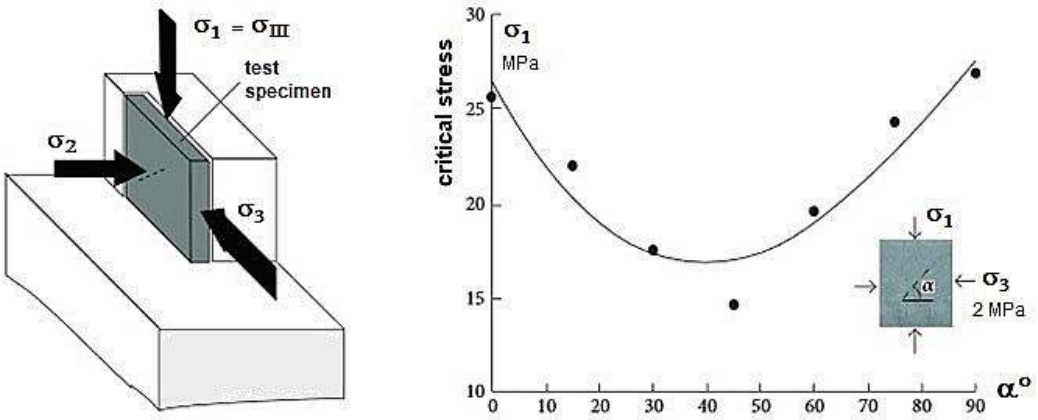

Fig.7-4: Scheme of the test set-up and of the test points obtained for cement mortar [Liu14], σ_1 represents the mathematical stress σ_{III} (largest compressive stress value).

7.3 Fracture Toughness Properties of transversely-isotropic UD lamina materials

For the transversely-isotropic UD lamina materials it seems directly to match:

► 5 fracture toughness properties correspond to 5 strength properties, 'generic' number postulate is fulfilled.

LL:

** Fracture Mechanics seems to follow material symmetry rules and seems to possess a 'generic' number, too.*

** Note on K_{IIcr}^{c} as a design entity: It is of theoretical, but not of practical value due to the usually faced not ideal homogeneous situation of 'isotropic materials' at crack tips.*

** The angle change of cracks under mixed-mode stress is a consequence of the high singular stress field at the crack tip. Mode I drives the growth of the initial crack at the crack tip. The rotation of the propagating crack surface is caused by the non-singular stresses.*

8 Evidencing 120°-symm. Failure Bodies of Brittle, Ductile Isotropic Materials

***Aim**: Proof that all isotropic materials possess 120°- rotationally symmetric failure bodies.*

8.1 General

From experiments is known, that brittle isotropic materials like cast iron and dense concrete possess a so-called 120°-axially symmetric fracture failure body in the compressive domain. The question arises: Should ductile materials in the tensile domain not also possess a 120°-axially symmetric yield loci envelope instead of having just the rotationally symmetric 'Mises cylinder'?

According to the French saying " *Les extrêmes se touchent* " and based on his FMC-thinking the author assumed that there is a large similarity in the description of the behavior of very ductile and very brittle materials. Also with ductile materials a 120°-rotational symmetry should be found. In order to prove a general 120°-rotational symmetry, test results from bi-axially measuring test specimens are necessary, such as from a cruciform or from an internally pressurized cylinder.

Searched is the description of a complete failure body. This requires that the 3D-SFC captures both the positive and the negative I_1-domain. Further, the 120°- rotational symmetry should be mapped by the SFC approach traditionally using the invariant J_3. Thereby, brittle and ductile material behaviors are to discriminate:

Brittle: In order to show the difference of brittle to ductile materials *Fig. 8-1* outlines the brittle material with its features $\bar{R}^{cc}(2D) > \bar{R}^{c}(1D)$ showing an outward dent and $\bar{R}^{tt} < \bar{R}^{t}$ an inward dent (*in [Lem0], however, was published for a brittle concrete* $\bar{R}^{tt} > \bar{R}^{t}$, *which is physically not explainable due to the double mode action and might be the consequence of the difficult measurement faced*).

Ductile: Deformation measurements prove that for the same strain value of the growing yield surface it holds that equi-biaxial stress $\bar{\sigma}^{tt} > \bar{\sigma}^{t}$. This is similar to brittle concrete in the compressive domain where $\bar{R}^{cc} > \bar{R}^{c}$ and demonstrates the validity of the 120°-axial symmetry.

8.2 Brittle Isotropic Materials (Metals, Glass, Ceramics, Concrete, Soil, ..)

2 modes → 2 SFCs, which is in line with the 'generic' number 2 according to the FMC.

Table 8-1: 3D-SFCs of Isotropic Dense brittle Materials

* Normal Fracture NF for $I_1 > 0$ ⇐ SFCs ⇒ Shear Fracture SF for $I_1 < 0$

$$F^{NF} = c_{\Theta}^{NF} \cdot \frac{\sqrt{4J_2 \cdot \Theta^{NF} - I_1^{\,2}/3} + I_1}{2 \cdot \bar{R}^{t}} = 1 \quad \leftrightarrow \quad F^{SF} = c_{1\Theta}^{SF} \cdot \frac{3J_2 \cdot \Theta^{SF}}{\bar{R}^{c2}} + c_{2\Theta}^{SF} \cdot \frac{I_1}{\bar{R}^{c}} = 1$$

after inserting $\sigma = R \cdot Eff$ and dissolving for Eff follows

$$Eff^{NF} = c_{\Theta}^{NF} \cdot \frac{\sqrt{4J_2 \cdot \Theta^{NF} - I_1^{\,2}/3} + I_1}{2 \cdot \bar{R}^{t}} \quad \leftrightarrow \quad Eff^{SF} = \frac{c_{2\Theta}^{SF} \cdot I_1 + \sqrt{(c_{2\Theta}^{SF} \cdot I_1)^2 + 12 \cdot c_{1\Theta}^{SF} \cdot 3J_2 \cdot \Theta^{SF}}}{2 \cdot \bar{R}^{c}}.$$

$$Eff = [(Eff^{NF})^m + (Eff^{SF})^m]^{m^{-1}} \quad \rightarrow \quad f_{RF} = 1/Eff.$$

Note:

The formulation of FNF generates a straight line in the principal stress plane! It is axially hyperbolic (Meridian direction) in the spatial domain, where Haigh-Lode-Westergaard coordinates are used.

In order to illustrate above SFCs with their common interaction zone a pre-view shall be presented of a 3D-concrete Fracture Body:

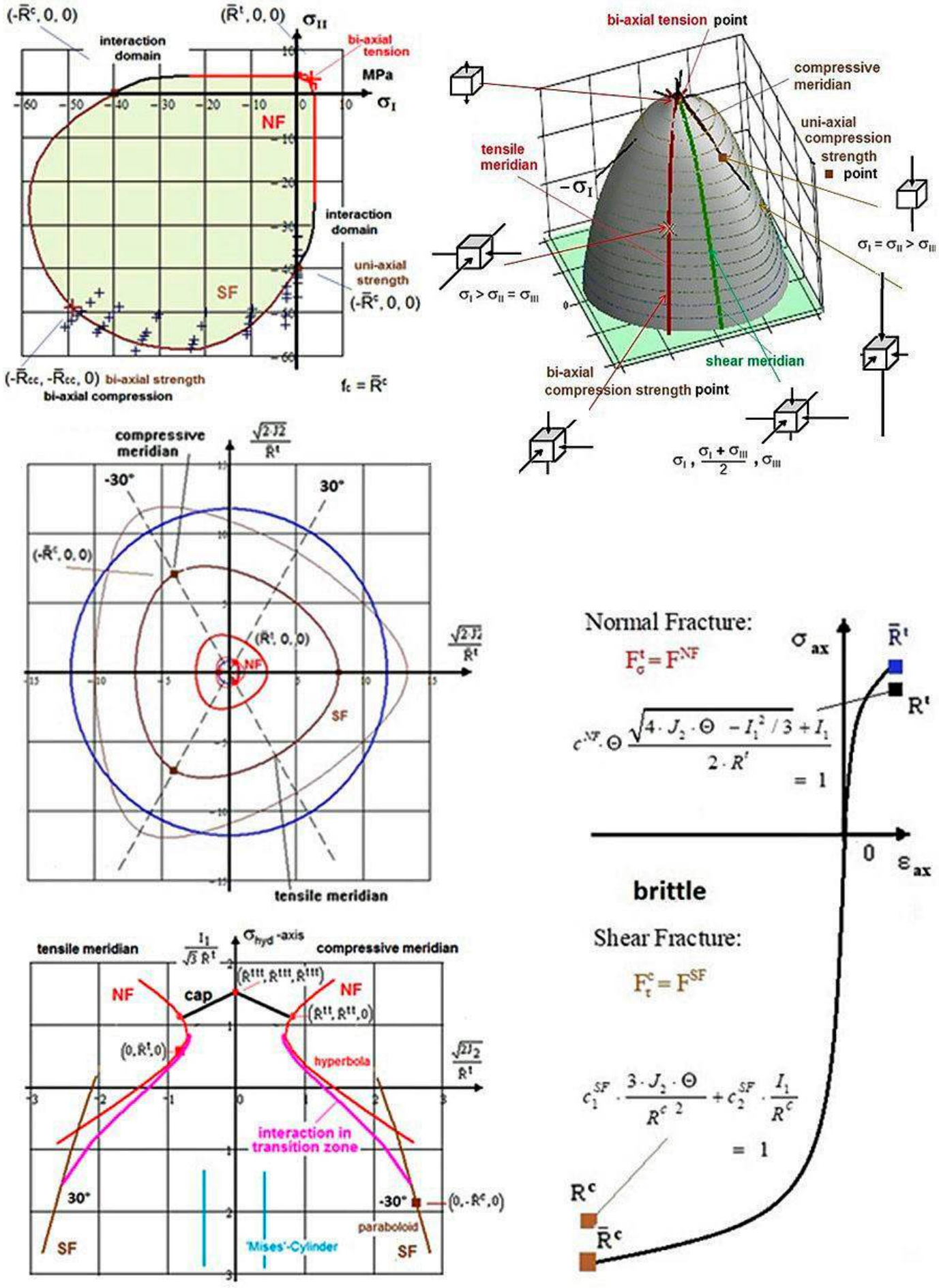

Fig.8-1: Visualization of the behavior of a brittle material (Normal Concrete) considering 1D stress-strain curve with 2D- and 3D-fracture failure curves and fracture body (surface). 120°-rotationally-symmetric

8.3 Ductile isotropic Material's Proof of 120°-rotational axial symmetry in tensile domain

The proof for brittle materials have been given in the tensile domain.

Fig.8-2 (left): a failure body is presented with its meridians as axial lines.

(center): figure fully proves the general isotropic 120°-material rotational symmetry which is supported by the Mises **ellipse** being the *inclined cross-section of the Mises cylinder failure body* is added. In the center figure, Mises is the green curve; red square: the tensile strength point; cross x: the equi-biaxial tensile strength point (trueR^{tt}, trueR^{tt}, 0).

(right): octahedral figure shows the inner green curve with the Mises circle at the '**Onset**-of-yielding' R_{p02} and the outer one at tensile strength R^t-level.

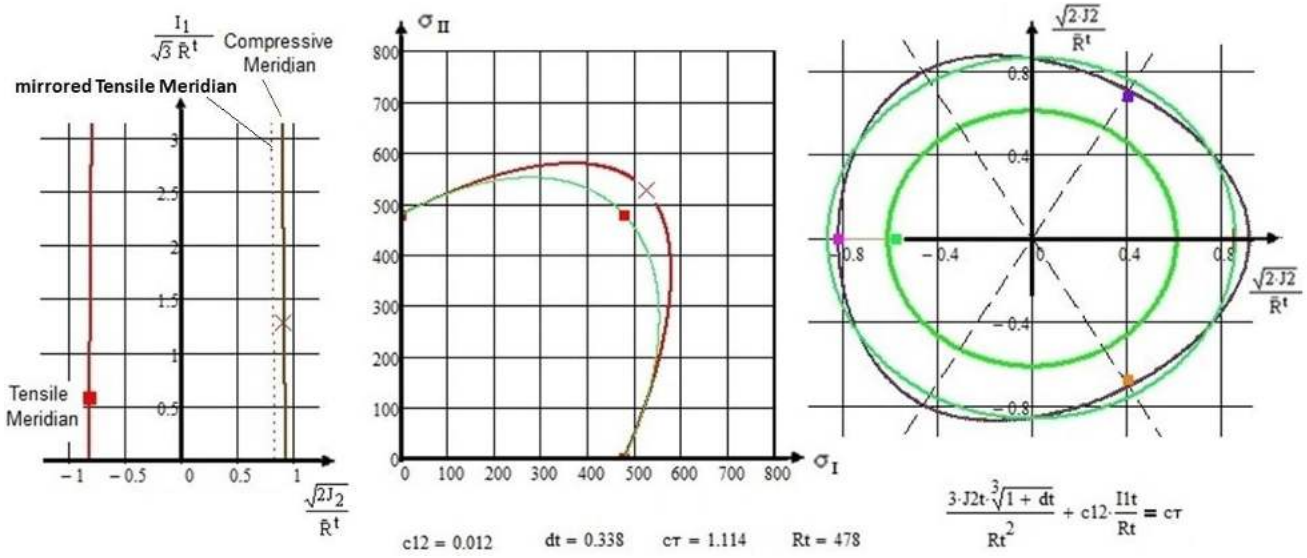

Fig.8-2, isotropic steel AA5182-0: Visualization of the behavior of a ductile material. (left) Yield body in Haigh-Lode-Westergaard coordinates; (center) 120°-symmetry, visualized in the principal stress plane; (right) 120°-symmetry, visualized in the octahedral stress plane.

Test data from T. Kuwabara et al: Journal of Materials Processing Technology 80–81 (1998) 517–523.

The 120°-rotational symmetry can be best displayed in the octahedral stress plane which is a 'horizontal' cross-section of the failure body at a distinct I_1, *Fig.8-2(right)*. The points and curves on the spatial body (*left figure*) are projected onto the octahedral plane (*right figure*). They depend on I_1 and therefore they have different cross-section heights I_1.

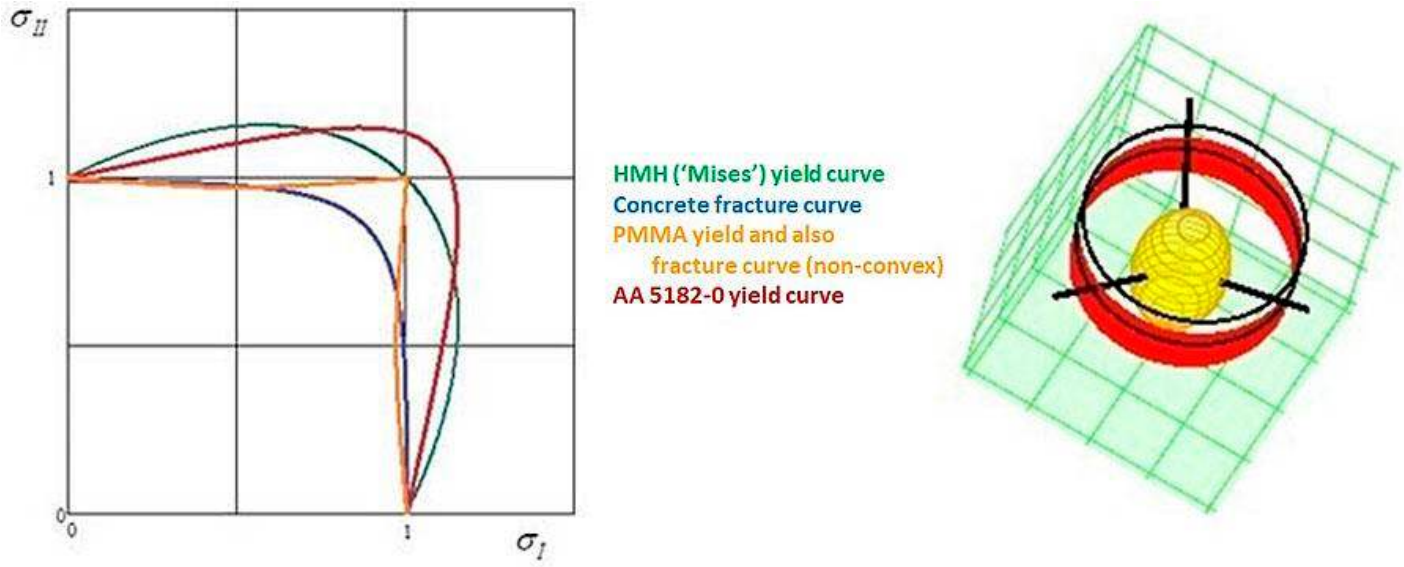

Fig.8-3: (left) Normalized principal stress plane tensile failure curves of a set of fully different isotropic materials. (right) Failure body surface

Viewing *Fig.8-3*, in the case of ductile AA-steel metal it probably may be assumed $\bar{R}^{tt} \cong 1.1 \cdot \bar{R}^{t}$. At least

there seems to be no reduction. However, this is to check by future test results. For an AA-vessel, for the typical stress ratio 2:1, the increase is about 10 percent.

Back to *Fig.8-3* (*Mathcad application*), which shows failure curves of four materials:

Fig.8-3(left) shows extreme curve examples at *true*R^{t} level in the positive principal stress range. The presented curves run through the uniaxial tensile strength points and the equi-biaxial strength R^{tt}. These curves are inclined cross-sections of the failure body. The red curve is occupied by the data of Kuwabara given in the table below the *Fig.8-4, see [Kuw98]*.

Fig.8-3(right), for completion, displays the Beltrami potential surface (egg shaped), the 'Mises' cylinder and the three principal axes.

Fig.8-4 depicts several failure cross-sections of an isotropic ductile steel demonstrating 120°-rotational symmetry in the *tensile* domain like the brittle isotropic material concrete in the *compression* domain.

For the generation of *Fig.8-4* biaxial tensile tests of cold-rolled low-carbon steel sheet were carried out by Kuwabara using flat cruciform specimens with the biaxial loads maintained in fixed proportion. Gotoh's biquadratic yield criterion (not given here) was used to map the test data of the cold-rolled low-carbon steel AA 5182-0 sheets. Contours of plastic work, of the flow potential, were determined in stress space under the shown strain range in the table below.

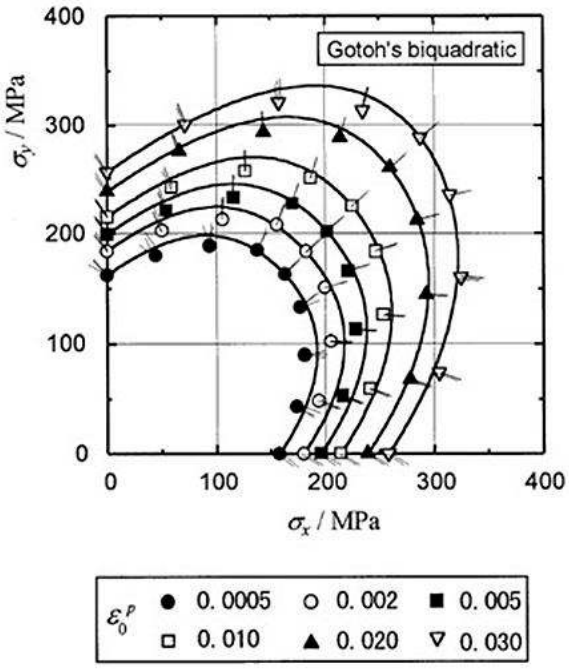

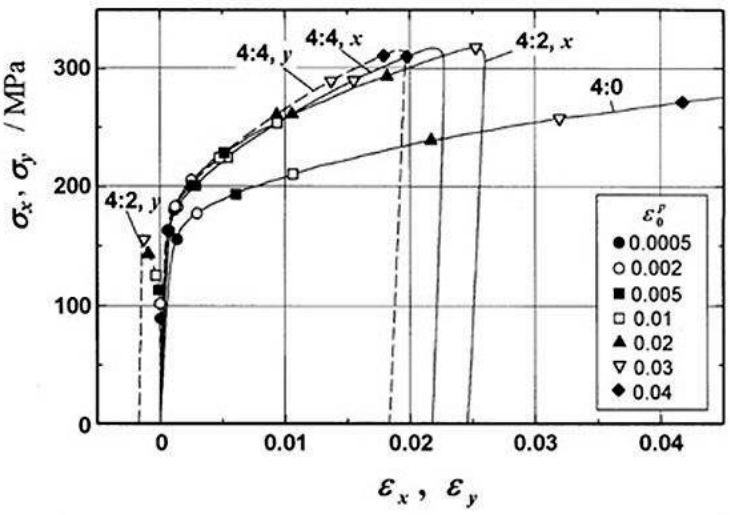

ε_0^p	0.0005	0.002	0.005	0.010	0.020	0.030	0.040
W (MPa)	0.07	0.33	0.89	1.92	4.19	6.68	9.33
σ_0 (MPa)	158	180	196	214	239	258	273
σ_{90} (MPa)	162	184	199	215	238	256	271
σ_{bi} (MPa)	163	184	202	225	260	288	310

Fig.8-4: (left) Test points as function of the experienced plastic straining ε_0^{pl} *; Mathcad15-mapping by using Gotoh's bi-quadratic criterion. (right) True stress–true strain curves for different biaxial loadings= different structural stress ratios. Measured values using* r_0, r_{45}, $r_{90;}$ *t = 1mm, flat cruciform*

The applicability of a *yield* failure condition as a SF failure condition (*Fig.8-4, left*) depends, on how far the final shear fracture failure is still shear stress-governed and not yet fracture mechanics-governed.

In the context to understand stresses and associated strains *Fig.8.5* shall display the strains when an axial stress comes out of the elastic state into the plastic state:

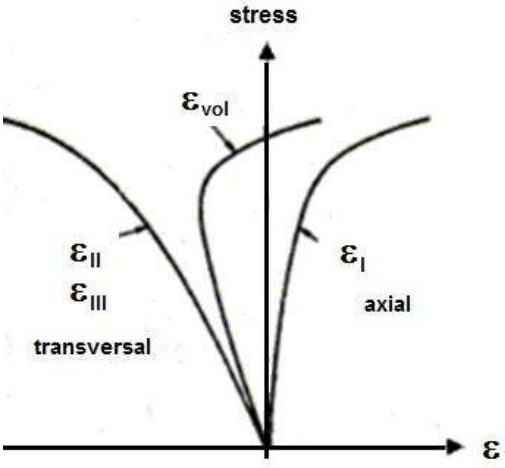

Fig.8-5:
Display of the volume change with increasing axial tensile stress

LL:

** The author was able to map the courses of the four test data sets with his isotropic SFC models.*

** The 120°-rotational symmetry of isotropic materials is principally nothing else than a 'double mode effect.*

** This effect is faced with all isotropic materials independent whether they are ductile or brittle.*

** Elastic deformation of crystalline structures occurs on the atomic scale: The bonds of the atoms in the crystal lattice are stretched. When de-loading, the energy stored within these bonds can be reversed. The material behaves elastic.*

** Plastic deformation or sliding occurs along gliding planes inter-crystalline or intra-crystalline and is permanent (plastic). If no volumetric change is faced the 'Mises' can be applied.*

** Also for ductile materials in the tensile domain, the 120°-rotational symmetry was demonstrated : for the crazing plexi-glass, where the fibrils are linked and for the ductile AA5182-0 metal, where the mechanism is not presently known, by the author at least. An analogous bi-axial deformation restraint??*

* ***For the ductile biaxial tension 120°- proof more test data is needed. The higher equi-biaxial yield failure stress is to check by future test results in order to support a generally valid 120°- rotational symmetry.***

Brittle: bi-axial tension = weakest link failure behavior (inward dent)
*Brittle: bi-axial compression = redundant (*benign*) failure behavior (outward dent)*
Ductile: bi-axial tension = redundant failure behavior (outward dent)
*Ductile: bi-axial compression = redundant yield behavior (*not design relevant, open failure surface*).*

9 Derivation of Constant Fatigue Life curves considering Mean Stress Effect and Residual Strength

***Aim**: Automated derivation of a Constant Life Curve with consideration of the Mean Stress. Going for each failure mode NF, SF via* $\sigma_{eq}(Eff\{\sigma\}) \cong \sigma_{max}$ *to SN-applicability.*

9.1 General

In Design Verification (DV) it is to demonstrate that "No relevant limit failure state is met considering all Dimensioning Load Cases (DLCs)". This involves cyclic DLCs, focusing lifetime with non-cracked and cracked structural parts (*the latter would require Damage Tolerance tools*).

Methods for the prediction of durability, regarding the lifespan of the structural material and thereby of the structural part, involves long time static loading which is linked to 'static fatigue' and in particular to 'cyclic fatigue'. Fatigue failure requires a procedure for the Fatigue Life Estimation necessary to meet above cyclic DV.

Domains of Fatigue Scenarios and Analyses are:

LCF: high stressing and straining

HCF: intermediate stressing 10.000 < n < 2.000.000 cycles (*rotor tubes, bridges, towers, off-shore structures, planes, etc*.)

VHCF: low stress and low strain amplitudes (*see SPP1466 Very High Cycle Fatigue > 10^7 cycles (in centrifuges, wind energy rotor blades, etc*.).

Principally, in order to avoid either to be too conservative or too un-conservative, a separation of the always needed 'analysis of the *average* structural behaviour' in Design Dimensioning (*using average properties and average stress-strain curves*) in order to obtain the best structural information (*= 50% expectation value*) is required. In the mandatory single DV-analysis of the final design, statistically minimum values for strength and minimum, or mean and maximum values for other task-demanded properties are applied as Design Values.

9.2 Fatigue Micro-Damage Drivers of Ductile and Brittle behaving Materials

There are strain-life (*plastic deformation decisive, plastic strain-based* $\varepsilon_{pl}(N)$) and stress-life models (*SN*) used. For ductile materials, strain-life models are applied because a single yield mechanism dominates and the alternating stress amplitude counts. For brittle materials, the elastic strain amplitude becomes dominant and stress-life models are applied. With brittle materials inelastic micro-damage mechanisms drive fatigue failure and several fracture mechanisms may come to act. This asks for a modal approach that captures all failure modes which now become fracture failure modes.

Above two models can be depicted in a Goodman diagram and in a Haigh diagram. The Haigh diagram (σ_a, σ_m) will be applied here because the often used Goodman employs just one quantity σ_a or $\Delta\sigma = 2 \cdot \sigma_a$ or σ_{max}, which is not sufficient concerning the mean stress and probable associate mean stress correction.

A Haigh Diagram represents all available SN curve information by its 'Constant Fatigue Life (CFL) curves, being the focus here and uses the two quantities: σ_a, R .

Basic differences between ductile and brittle materials are the following ones:

- Ductile Material Behavior, isotropic materials: mild steel
  1 *micro-damage* mechanism acts ≡ *"slip band shear yielding"* and drives micro-damage under tensile, compressive, shear and torsional cyclic stresses: *This single mechanism is primarily described by* 1 *SFC, yield failure condition (HMH = 'Mises')!*
- Brittle Material Behavior, isotropic materials: concrete, grey cast iron, etc.
  2 *micro-damage* driving mechanisms act ≡ 2 *fracture failure modes Normal Fracture failure*

(NF) and Shear Fracture failure (SF) under compression described by 2 fracture conditions, the 2 SFCs for NF and SF, where porosity is always to consider

- Brittle Material Behavior, transversely-isotropic UD-materials:
  5 *micro-damage* driving fracture failure mechanisms act ≡ 5 fracture failure modes *described by 5 SFCs or strength fracture failure conditions*.

A very essential topic is the so-called 'Mean stress sensitivity': Within [*Cun23b*] the author attempts to redirect the ***'Thinking, resulting from ductile material behavior using 'Mean stress influence correction factors', which in reality means 'Walking on crutches',*** into a direct ***'Thinking* with *fracture modes facing a realistic brittle material behavior'.*** The not fully ductile isotropic materials show an influence of the mean stress on the fatigue strength depending on the (static) strength ratio R^c/R^t and the material type. Mean stresses in the tensile range, $\sigma_m > 0$ MPa, lead to a lower permanently sustainable amplitude, whereas compressive mean stresses $\sigma_m < 0$ MPa increase the permanently sustainable amplitude or in other words.

LL:

** A tensile mean stress lowers the fatigue strength and a compressive mean stress increases the fatigue strength*

** If it is a pretty ductile material one has one mode 'yielding' and if the material is pretty brittle then many 'fracture modes' are to consider*

** Brittle materials like the transversely-isotropic UD material with its five fracture failure modes possess strong mean stress sensitivity, a brittle steel material just 2 modes*

** Whether a material has an endurance fatigue limit is usually open regarding the lack of VHCF tests. The strength at $2{\cdot}10^6$ cycles might be only termed apparent fatigue strength (*scheinbare Dauerfestigkeit*).*

** Fiber–ruled CarbonFiber Reinforced Polymers (CFRP) can possess a very high fatigue limit*

** Whether the material's micro-damage driver remains the same from LCF until VHCF is questionable and must be verified in each given design case (continuum micro-damage mechanics is asked here for understanding the micro-mechanisms)*

** The 'ductile material behavior thinking' in 'Mean stress influence correction' is to redirect for brittle materials fully into 'Thinking in fracture failure modes'.*

9.3 Haigh diagram with its Mapping Challenge of the decisive Stress Ratio Transition Zone

Exemplarily for a metal as fatigue phases are counted:

Phase I	Phase II	Phase III
micro-cracks initiation at high-stressed flaws	micro-cracks grow to macro-cracks, spans most of the fatigue life	macro-crack growth, sudden fracture

The course of the test data in the transition zone determines the grade of the mean stress sensitivity. In *Fig.9-1,* at first all essential quantities are illustrated. Further, two Constant Fatigue Life (**CFL**)**-curves** of a brittle material are displayed, for the envelopes N = 1 and N = 10^7. The pure mode domains are colored and the so-called transition zone is separated by R_{trans} into two influence parts. The course of the R-value in the Haigh diagram is represented by the bold dark blue lines. The CFL curve N = 1 is curved at top because 2 modes act in the case of brittle materials! This is in contrast to uniaxial static loading, depicted by the straight static envelopes, $N \neq N_f$: One micro-damage cycle results from the sum of 2 micro-damage portions, one comes from uploading and one from unloading! For fully ductile materials practically no transition zone between 2 modes exists, because just one single mode reigns, namely 'shear yielding'.
Therefore, it is no mean stress effect to correct in this case!

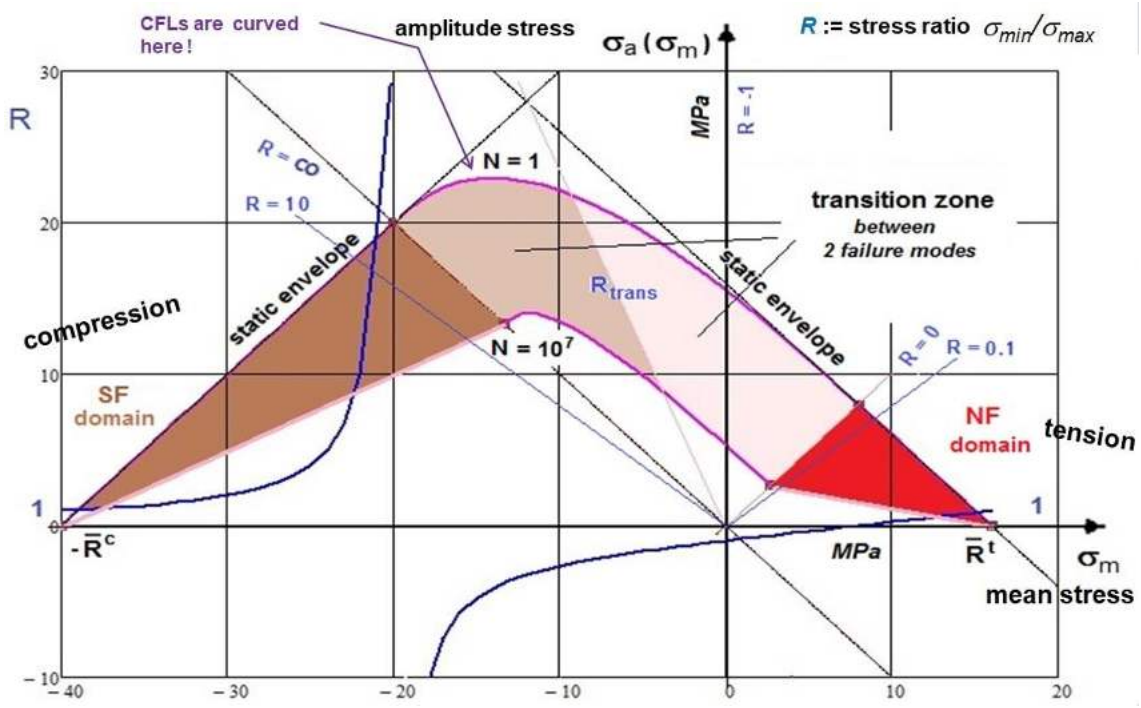

Fig.9-1, Haigh Diagrams: Scheme of pure mode domains, course of R *and transition zone parts .*
(a:= amplitude, m:= mean, N := number of fracture cycles, $\bar{R}$ *:= strength and* R *:=* $\sigma_{min}/\sigma_{max}$

The quality of mapping the course of data in the transition zone is practically checked by "*How good is the more or less steep course along the stress ratio* R_{trans}*-line mapped*?" This is performed by following the physical reality, that the pure SF-domain is fully decoupled from the NF-domain, and by employing oppositely running decay functions f_d, see *Fig. 9-2* exemplarily for a UD material with the interaction equation

$$Eff = [(Eff^{NF})^m + (Eff^{SF})^m]^{m^{-1}} = 100\% \quad \text{or}$$

$$\left(\frac{-(\sigma_{2m}-\sigma_{2a})+|\sigma_{2m}-\sigma_{2a}|)}{2\cdot \bar{R}_{\perp}{}^{c}\cdot f_d}\right)^m + \left(\frac{\sigma_{2m}+\sigma_{2a}+|\sigma_{2m}+\sigma_{2a}|)}{2\cdot \bar{R}_{\perp}{}^{t}\cdot f_d}\right)^m = 1$$

$\rightarrow$ $f_d^{IFF2} = 1/[1+\exp(\frac{c_1+\sigma_m}{c_2})]$ with c_1, c_2 from points $(-\bar{R}_{\perp}^{c}, 0.995)$, (-0.01,+0.01).

and analogously $f_d^{IFF1} = ...$.

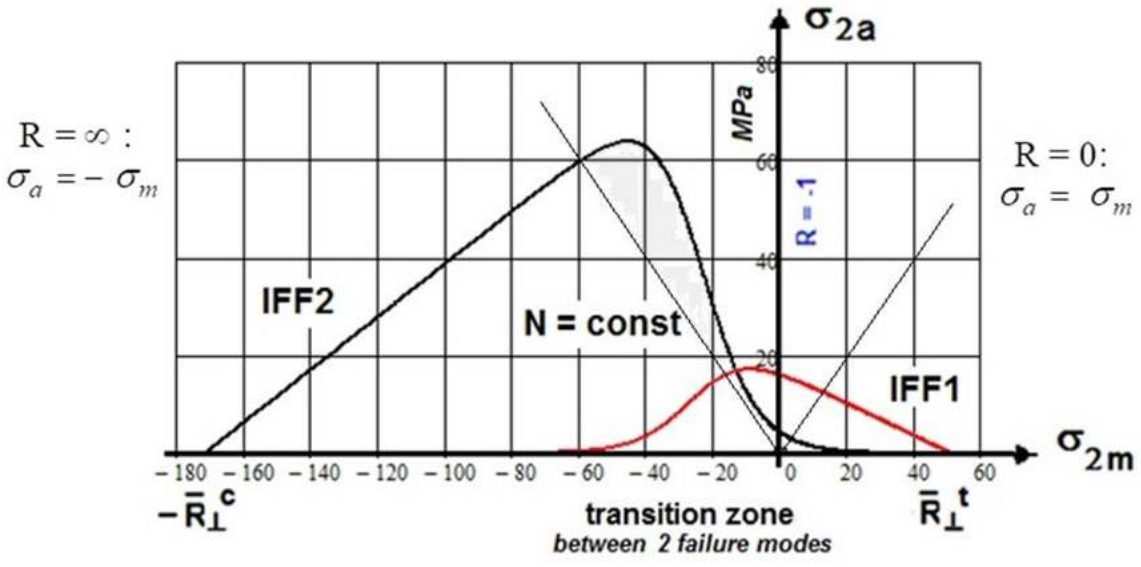

Fig.9-2, example UD material: Course of the decay functions in the transition zone $-\infty < R < 0$

Fig.9-2 illustrates the course of the mode decay functions f_d for the tension and the compression domain. The straight lines in the figure present the extreme SN curve beams, R = ∞ for the SF-domain and R = 0 for the NF-domain. In between, the envisaged slightly colored transition zone ($-\infty < R < 0$) is located. Mean stress sensitivity of brittle materials is demonstrated very impressively if the so-called 'strength ratio' = compressive strength / tensile strength R^c/R^t is high.
The two plots in *Fig.9-3 will* clearly document this.

LL:

** A large strength ratio R^c/R^t stands for a large mean stress sensitivity*

** A steep decay cannot be captured by a 'mean stress correction factor' as can be still performed for not fully ductile materials with the presented tool.*

9.4 Pre-dominantly Brittle Materials: Estimation of the cyclic Micro-damage Portions

A very essential question in the estimation of the lifetime of brittle materials is a means to assess the micro-damage portions occurring under cycling. Here, for brittle behavior the response from practice is: It is permitted to apply validated static SFCs due to the experienced fact:

> *"If the failure mechanism of a mode cyclically remains the same as in the static case, then the fatigue micro-damage-driving failure parameters are the same and the applicability of static SFCs is allowed for quantifying micro-damage portions". This is supported because FMC-based static SFCs apply equivalent stresses of a mode SF or NF. See again Fig.9-2 above,* for more details, see [*Cun23b*].

9.5 Automatic Establishment of Constant Fatigue Life Curves

For a decade the author's intensive concern was to automatically generate Constant Fatigue Life curves on basis of just a few tested Master SN curves coupled to an appropriate physically based model. Such a model the author obtained when M. Kawai gave a presentation during the author's conference on composite fatigue in 2010 at Composites United e.V. Augsburg.
Kawai's so-called '*Modified fatigue strength ratio'* Ψ - model was the fruitful tool found. Kawai's presented procedure was a novelty and is applicable to brittle materials such like UD plies (*depicted later in Fig.10-4*) and isotropic concrete material as well.

Fig.9-3(up) displays the differently-colored failure mode domains FF1-FF2 in a UD-FF Haigh diagram and (*down*) IFF1-IFF2 in a UD IFF Haigh diagram. The available test data set along R_{trans} in the transition zone is represented by the crosses. The model quality in *Fig.9-3* proves the efficiency of the decay functions in the transition zone.

In *Fig.9-4* the course of the cyclic failure test data can be well mapped by the 4-parameter Weibull formula, reading with R = constant : $\sigma_{max}(R, N) = c_1 + (c_2 - c_1) / \exp(\log N / c_3)^{c4}$.

9.6 Lifetime Estimation

The so-called Palmgren-Miner rule is applied for summing up the cyclic micro-damage portions. Statistical analyses in the German aeronautical handbook HSB have shown that the fatigue life estimation using the linear accumulation method of Palmgren-Miner tends to be too optimistic. However a satisfactory reason with correction could not yet found:

- One explanation is the 'Right use of the right SFC: Mises is not anymore fully applicable?'
- A more severe second explanation is the loss of the loading sequence, an effect which is different for ductile and brittle materials. This inaccuracy is practically considered in design by the application of the so-called Relative Miner with defining a $D_{feasible}$ and which must be < 100 %.

In the case of variable amplitude loading several SN curves are needed. An example for the computation of the lifetime estimation is displayed by *Fig.9-5*.

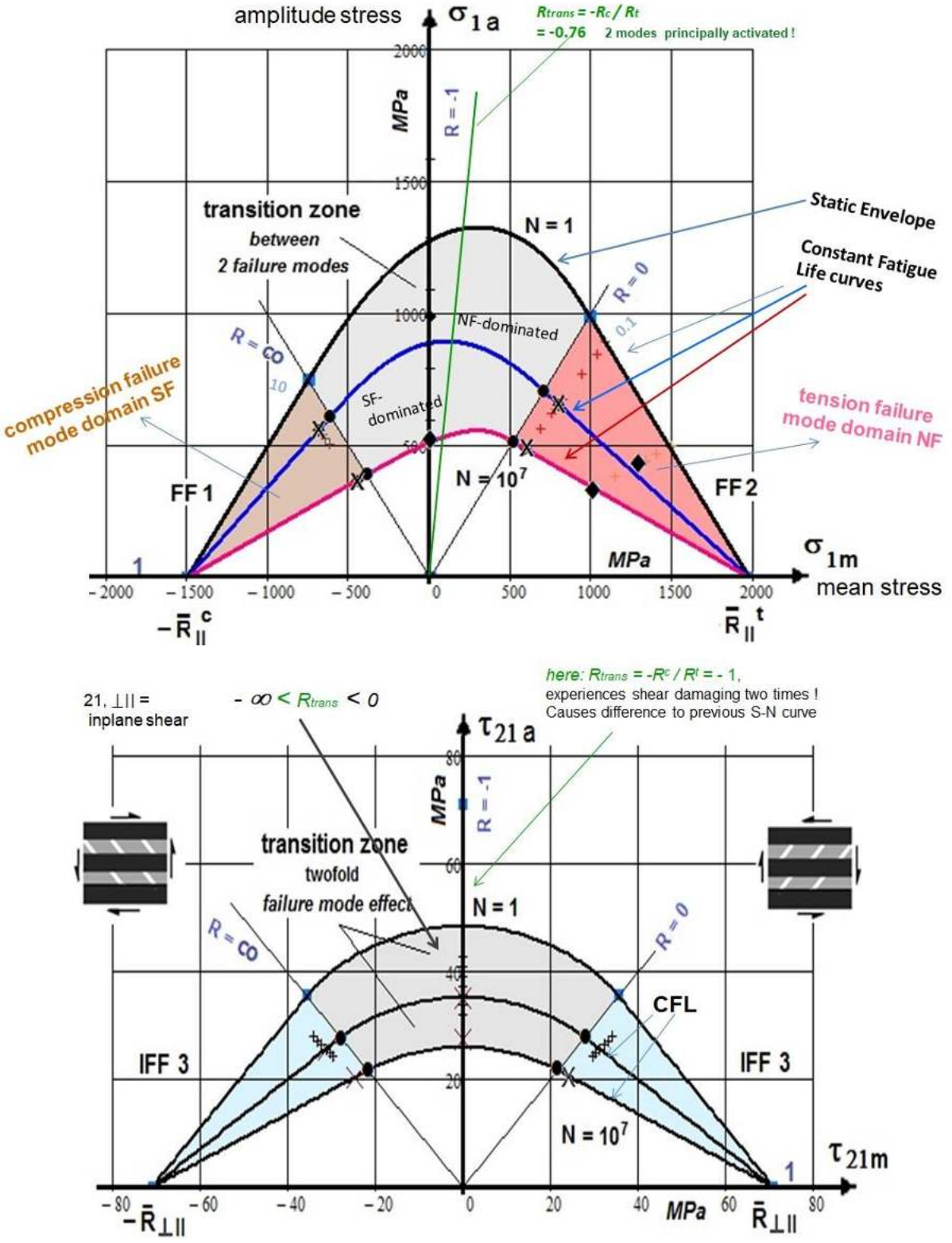

Fig.9-3, UD Haigh diagram:

(up) FF with low strength ratio as with ductile materials. Rigorous Interpretation of the Haigh diagram for the UD-example FF1-FF2 displaying failure mode domains and transition zone, CFRP/EP,
$\bar{R}_{||}^{t} = 1980,\ \bar{R}_{||}^{c} = 1500,\ \bar{R}_{\perp}^{t} = 51,\ \bar{R}_{\perp}^{c} = 172,\ \bar{R}_{\perp||} = 71$ [MPa].

(down) IFF with high strength ratio as with brittle materials Display of a two-fold mode effect (a:= amplitude, m:= mean, N := number of fracture cycles, $\bar{R}$ *:= strength and* R *:=* $\sigma_{min}/\sigma_{max}$*). Test data CF/EP, courtesy Clemens Hahne, AUDI*

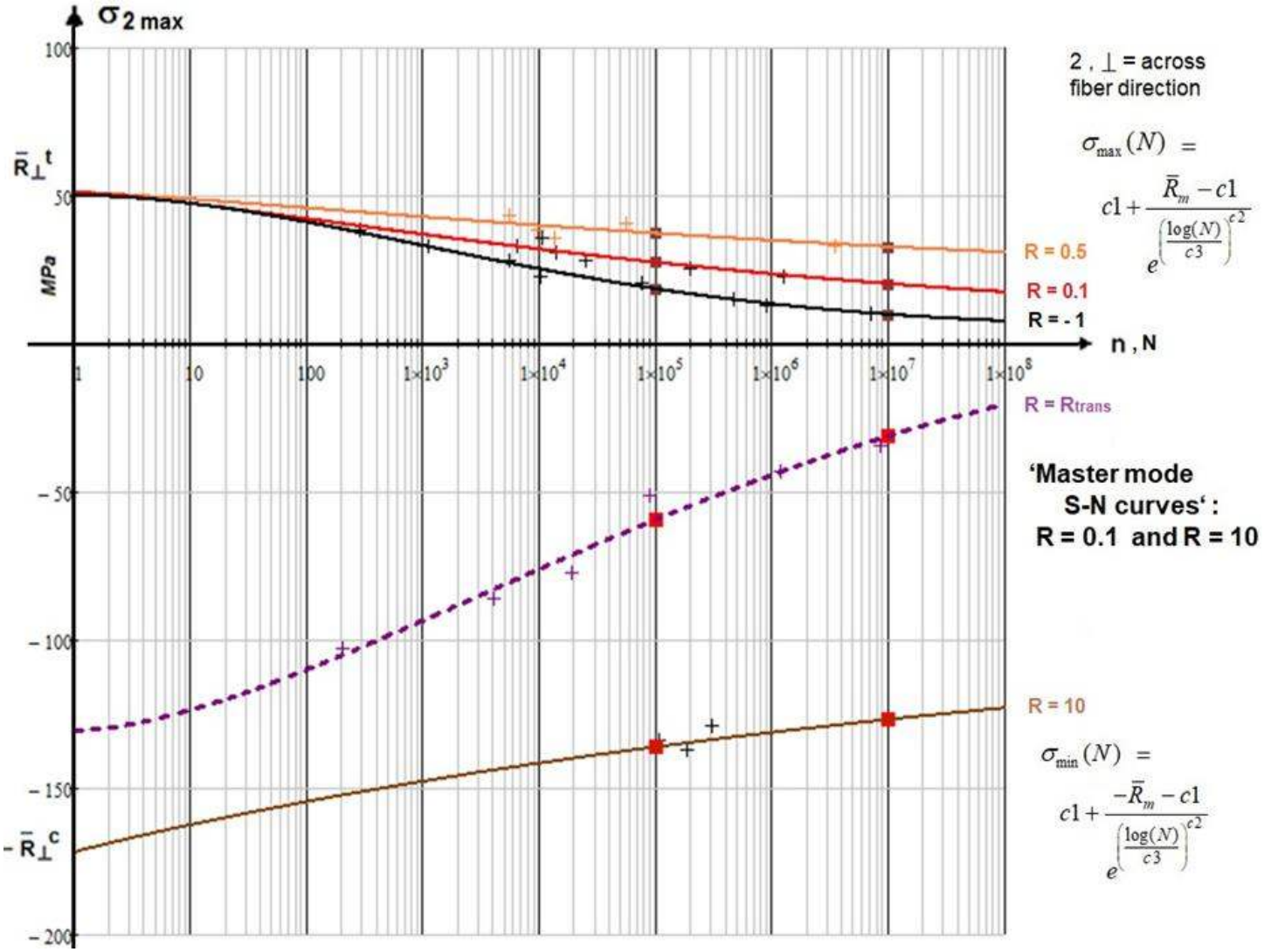

Fig.9-4: SN-curve, lin-log displayed IFF1-IFF2-linked SN curves [test data, courtesy C. Hahne, AUDI]

[Kawai M: A phenomenological model for off-axis fatigue behavior of uni-directional polymer matrix composites under different stress ratios. Composites Part A 35 (2004), 955-963]

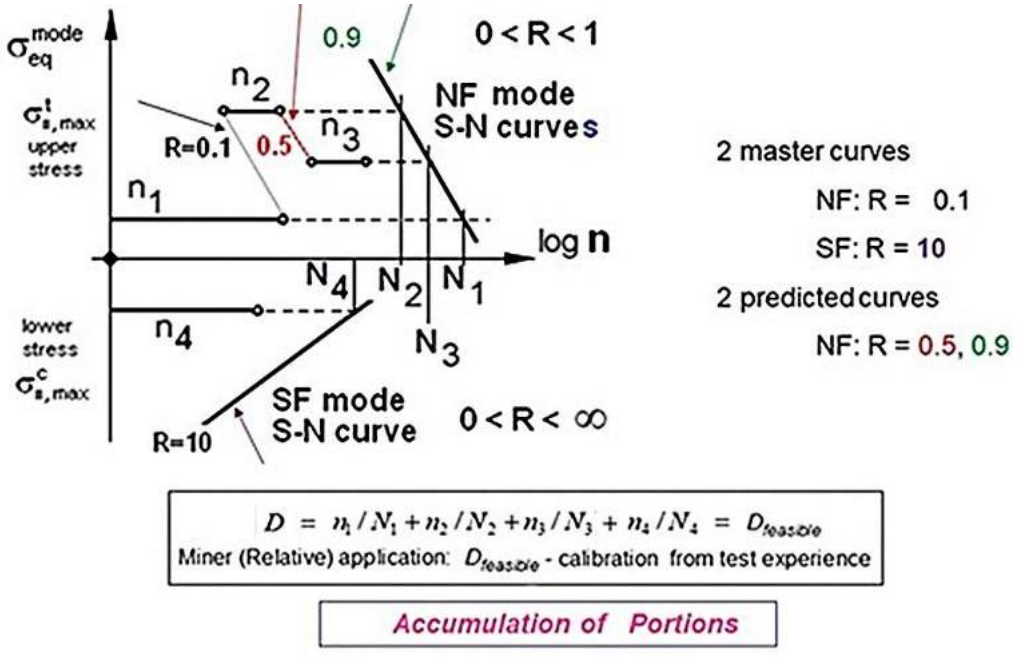

Fig.9-5: Lifetime Prediction (estimation) Method .Summing up of micro-damage portions by application of the Palmgren-Miner rule. Schematic application of a simple example, 4 blocks. $D_{feasible}$ from test experience

Stress states are usually multiaxial. Hence in the case of brittle materials equivalent stresses are to use for the fractures failure modes NF under tension (upper) and SF under compression in order to use the σ_{max} – linked SN curves, for instance in *Fig.9-4* for a UD-material.

For each failure mode is valid: $\sigma_{eq}(Eff\{\sigma\}) \cong \sigma_{max}$.

$$\sigma_{eq} \rightarrow \sigma_{max} \rightarrow N,\ n = \text{known}.$$

9.7 Design Verification of a critically cycled UD lamina within a chosen laminate

To be practical, a work case of fatigue life estimation shall be presented. As the employment of the decay function is too lengthy here just two S – N curves in the tension domain are stressed.

Example UD material, IFF1-IFF2: Test data, courtesy C. Hahne.,

*Given: $\sigma_2 = \sigma_{2a} + \sigma_{2m}$, $\bar{R}_\perp^t = 51$ MPa,

$n_1 = 50{,}000$ cycles, $R = 0.5$, $\sigma_2 = 32$ MPa; $n_2 = 100{,}000$ cycles, $R = 0$, $\sigma_2 = 30$,

$$\sigma_{\max}^{Master} = c1 + (\bar{R}_\perp^t - c1)/\exp\left(\frac{\log(N)}{c3}\right)^{c2} \text{ with } c1 = 7.1,\ c2 = 1.34,\ c3 = 6.05,$$

$$\Psi^t_{Master} = \frac{\sigma_{2a}}{\bar{R}_\perp^t - \sigma_{2m}} = 0.5 \cdot \sigma_{\max}^{Master} \cdot (1-R)/\left[\bar{R}_\perp^t - 0.5 \cdot \sigma_{\max}^{Master}(1+R)\right]$$

and after resolution an equation for the determination of a desired $S-N$ curve, inserting R

$$\sigma_{\max} = 2 \cdot \bar{R}_\perp^t \cdot \Psi^t_{Master}/(\Psi^t_{Master} - R + R \cdot \Psi^t_{Master} + 1),\ 0 < R < 1.$$

*Estimation of fracture cycles N at $D_i = n_i / N_i = 100\%$.

$$\sigma_{R=0.5} = 2 \cdot \bar{R}_\perp^t \cdot \Psi^t_{Master} / (\Psi^t_{Master} - 0.5 + 0.5 \cdot \Psi^t_{Master} + 1) = \sigma_2 \rightarrow N_1 = 4.6 \cdot 10^5,$$

$$\sigma_{R=0} = 2 \cdot \bar{R}_\perp^t \cdot \Psi^t_{Master} / (\Psi^t_{Master} - 0 + 0 \cdot \Psi^t_{Master} + 1) = \sigma_2 \rightarrow N_2 = 1.7 \cdot 10^6.$$

*Summing up the micro-damage portions → total $D_i = \Sigma\, n_i / N_i = 0.17 < 1 = 100\%$.

*From experience with the $S-N$ scatter → RF_{Life} should be >5 (termed 'Relative Miner')

$$RF_{\text{Life}} = 100\% / \text{total } D = 1 / 0.17 = 6 > 5!$$

LL:

* *A 'closed CFL-procedure' - as a coupled method - could be found to generate mandatory test data-based Constant Life Fatigue curves by using a Master SN curve plus the supporting model to determine other required SN-curves employing Kawai's Ψ-model*
* *The challenging decay along* Rtrans = $-R^c / R^t$ *could be modelled (strength R has a bias letter)*
* *Test data along* Rtrans *are more helpful than for* R = -1, *which is standard with ductile behavior*
* *Right use of the right SFC. One cannot blame 'Mises' if yielding is not anymore decisive for the creation of the micro-damage portions*
* *The Palmgren-Miner rule cannot account for loading sequence effects, residual stresses, and for stresses below the fatigue limit (life → ∞ ?)*
* *Ductile material: Degradation-driving is the shear stress yielding independent of tension, compression and torsion*
* *Viewing brittle materials, all the SN curves have their physical origin in the strength points.*

** The mean stress effect increases with decreasing ductility*

► ***Hence, the author would like to repeat: Redirect the* 'Traditional Thinking', *resulting from ductile material behavior with regarding Mean stress correction* into a 'Thinking with fracture modes' *in the case of the usually not fully ductile structural materials.***

9.8 Novel Determination of the Residual Strength R_{res}

Aim: *Derivation of a procedure to determine the also design verification-required residual strength value R*res.

9.8.1 Design Verification in Projects of a not yet cracked Part

Residual strength *Rres* is the fracture stress after fatigue pre-damage and re-loading. Not only in mechanical engineering design but also in civil engineering residual strength values are required such as in soil mechanics or for UD-hangers of a railway bridge at Stuttgart, below a hanger or for tension rods of cranes. The value is of basic interest, because – due to authority demands - Design Ultimate Load is to sustain even after a distinct fatigue life. The residual strength task is one task to demonstrate structural integrity.

Fig.9-6 Stuttgart Stadtbahn bridge.
World's first network arch railway bridge (127 m) that hangs entirely on tension elements made of carbon fiber-reinforced plastic (CFRP). The 72 hangers are produced by Carbo-Link AG

This subject is linked to cyclically micro-damaged structural components (*Phase 2 of fatigue life, strength tools applied*) and macro-damaged ones (*Phase 3 of fatigue life, fracture mechanics problem, damage tolerance mechanics tools applied*), as was displayed for fatigue phase III.
The cyclic loading may range from constant amplitude-loading up to spectrum-loading and has to capture proportional and non-proportional loading scenarios.

This task especially comes up in cases such as: A multiple site damage phenomenon is faced with aerospace components such as fabrication-induced flaw clouds (fatigue strength problem, Ariane 5 Booster wall) or real short-crack 'clouds' from e.g. multiple rivet holes in stringer-stiffened panels of aging aircraft components (fracture mechanics problem). Here, the focus is on the Phase 2 residual strength *Rres*. Mind: residual strength R_{res} should not be confused with *residual stress* σ_{res}).

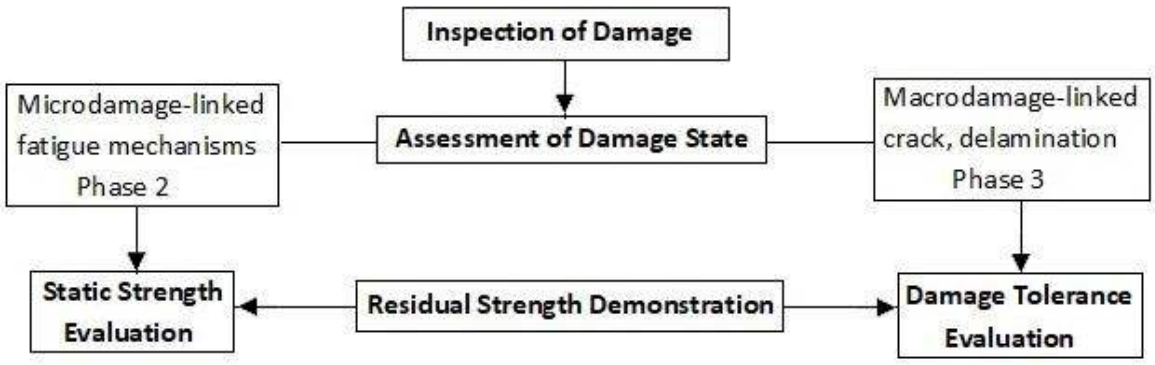

Fig.9-7: Ways of residual strength determination

In some projects a number for the residual strength at a certain operation cycle value is required. This is well known from impact cases of laminated panels. There, a Compression-After-Impact (CAI)

test is to execute after the impact event because the impact may result in a barely visible external damage and it may generate a dramatic reduction of compressive strength due to separation of layers resulting in a large bending stiffness loss. Regarding crack-linked fatigue life Phase 3 residual strength problems the reader is referred to fracture mechanics.

Residual strength tests are long-lasting and expensive. Therefore, procedures are searched that help to reduce the test effort if enough physical knowledge is available.

First step is to map the relevant SN-curve (= Wöhlerkurve) by taking the widely used 4-parameter Weibull function stress ratio $R = \sigma_{min} / \sigma_{max} = \text{constant}: \ \sigma_{max}(R,N) = c1 + (c2 - c1) / \exp(\log N / c3)^{c4}$.

(stress ratio → straight letter R ⇔ strength→ bias letter *R*).

A SN-curve describes the relation between the cyclic loading and the number of cycles to failure *N*. On the horizontal axis in *Fig.9-3* the number of cycles to failure is given on logarithmic scale. On the vertical axis (*either linear or logarithmic*) the stress amplitude $\sigma_{amplitude}$ of the cycle is often given. In the case of brittle materials *sometimes the maximum stress* σ_{max}.. The provided mean SN-curves 'R = constant' base on the fatigue test measurement types 'pearl-chain testing' or 'horizontal load level testing'. Fatigue curves are given for un-notched test specimens (K_t = 1) and for notched ones, the loading can be uniaxial or multi-axial. Considering residual strengths, measurements on the vertical axis at *n* = constant are required.

In design verification very often as fractile (quantile) numbers, representing the failure probability p_f, 5% or 10% are taken in order to capture some uncertainty compared to the average of 50%. For the loading side the design FoS *j*, in construction *γ*, capture the uncertainty of the loading. The residual strength design verification has to meet Design Ultimate Load. Following the Standard HSB the determination of the static residual strength for single load paths must be made with statistically significant A-values; for possible multiple load path structural parts B-values may be used.

Moving to the required statistical properties some notions are to depict. Capturing the uncertainty of the resistance quantities, the following is performed: Denoting P the survival probability and C the confidence level applied, when estimating a basic population value from test samples, partly enriched by some knowledge of the basic population. Regarding C a one-sided tolerance level it reads:

*Static → Statistical reduction of average strength from (P= 50%, C= 50%) to e.g. (B-value: P = 90%, C = **95**%).

*Cyclic→ Statistical reduction of average SN curve from (P=50%, C= 50%) to e.g. (P= 90%, C= **50**%).

All this is executed to keep a generally accepted survival reliability of about $\Re = 1 - p_f > 1 - 10^{-7}$.

9.8.2 Classical way to determine Rres, with rendering

Determination via the interpretation "*The course of the residual strength is the difference of the static strength* and *the maximum strength* $\sigma_{max}(N)$ *of an SN curve* R", see *Fig.9-3*. This leads to the formulation $R_{res} = \sigma_{max}(N) + [R^t - \sigma_{max}(N)] \cdot \rho(n)$ with $\rho(n) = 1 - (n/N)^p \equiv 1 - D^p$,

where the exponent *p* describes the decay of the residual strength capacity and *D* the micro-damage quantity, (see Hahne C: *Zur Festigkeitsbewertung von Strukturbauteilen aus Kohlenstofffaser-Kunststoff-Verbunden unter PKW-Betriebslasten*. Shaker Verlag, Dissertation 2015, TU-Darmstadt).

Fig.9-3 depicts for R = 0.1 the mean (average) 50% SN-curve and the 90% SN-curve. The residual strength curve *Rres* is given for the point (10^5 cycles, σ = 34 MPa). The stress σ belongs to a so-called 'one stage test' or constant amplitude test. Regarding the residual strength value at the 90% SN-curve

the question arises: "*Where does the necessary statistical basis for a reduced SN-curve come from, if not sufficient test series on vertical and horizontal levels were run*"?

Due to missing a full test data set a full test data-based work case cannot be presented. Therefore, the author tried to figure out a procedure which gives an understanding of the subject.

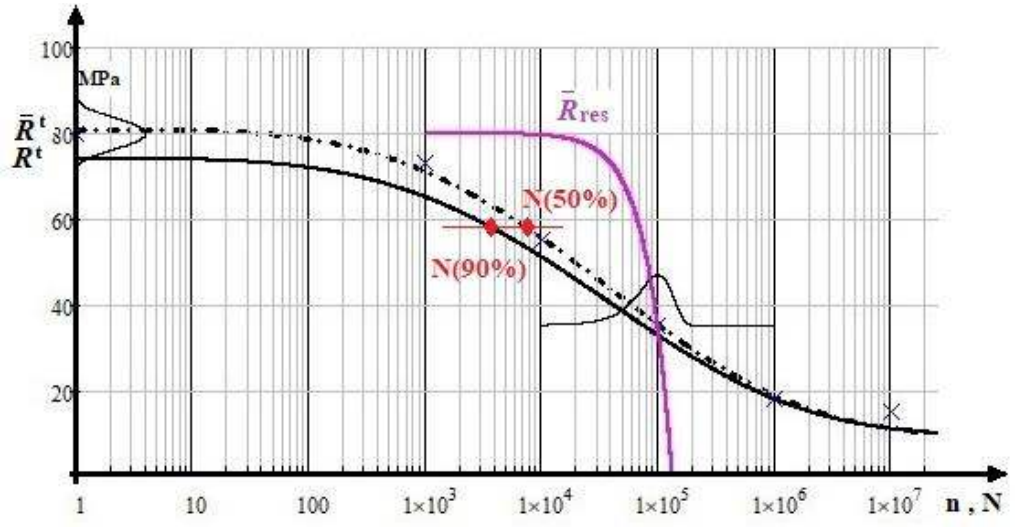

Fig.9-3, Schematic example, uniaxial loading: R= 0.1. $\bar{R}_{res}$ *is mean tensile residual strength*

9.8.3 Probabilistic determination of a 90%- R_{res} *-value using distributions with convolution integral*

A possibility to determine a required 90%-value is given by the application of the so-called convolution integral, using density distributions of R_{res} and of N with just a little hope to find the distribution measured, *Fig.9-3*. The output of the mathematical expression convolution integral represents the probability of failure $p_{f.}$ The numerical analysis is based here on the assumption: 'The density distributions on x- (f_N) and y-axis (f_{Res}) are approximately basic populations and of Normal Distribution-type' f_{ND} (for the density distributions also a logarithmic, a Weibull density function or a truncated function could be employed). The convolution integral, solved by Mathcad 15, reads

$$(1-p_f) = \Re = p_{ü} = \int_{-\infty}^{\infty} \left(\int_{Rres}^{\infty} f_{Res}(R)\cdot dR \cdot f_N(N)\, dN \right) = 90\% \text{ fractile} \quad \text{for ND density distributions}$$

$$\text{with} \quad f_{ND}(x) = \frac{1}{\sigma \cdot \sqrt{2\cdot\pi}} \cdot exp\ \left[-\frac{1}{2} \left(\frac{x-\mu}{\sigma} \right)^2 \right] \quad \text{for abscissa } N \text{ and ordinate } R^t \ .$$

Data base of the numerical probabilistic example (statistical: μ = mean, σ = standard deviation) is:

* Static strength R^t-distribution μ = 80 MPa, σ = 3.2 MPa
* R_{res} -distribution in computation point, y-axis, μ = 43.5 MPa, σ = 2.9 MPa
* Cycle distribution in computation point, x-axis, μ = 3431 cycles, σ = 446 cycles and the

Coordinates of the chosen computation point * (38 MPa, n = 2000 cycles in *Fig.9-4*).

Fig.9-4 depicts the SN-curve, the chosen computation point, static strength distribution (n=1) with an assumed residual strength distribution and cycle distribution, all through the computation point *. It is a semi-logarithmic graph. As it is a brittle example material, the use of σ_{max} (*involves* R^t *as origin*!) as ordinate is of advantage for the 'strength-oriented' design engineer compared to using a stress amplitude σ_a

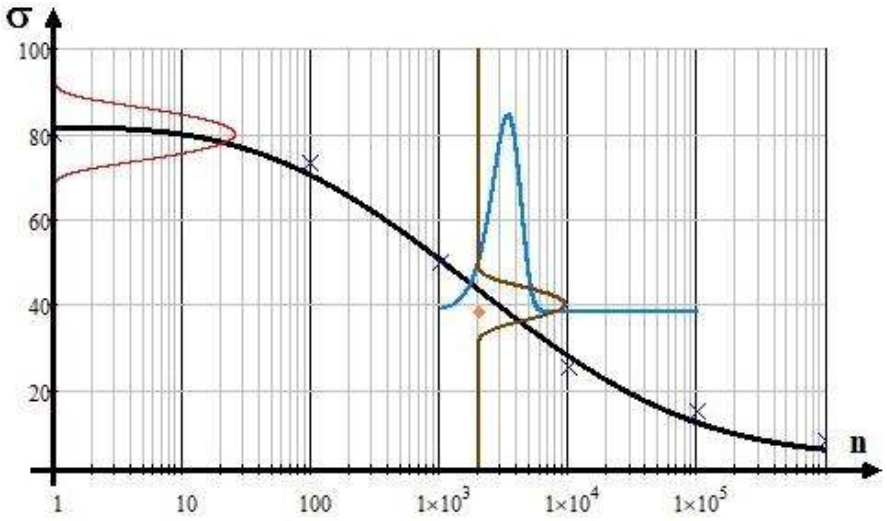

Fig.9-4, Simplified Mathcad calculable example: Assumed distributions of residual strength and cycles linked to R_{res} *(38 MPa, 2000 cycles). SN-curve,* R = 0.1: *c1= 20 MPa, c2= 80 MPa , c3= 3.77, c4= 2.92*

The probabilistic treatment delivers the 'joint' probability hill of both the distribution functions in *Fig.9-5*, (right). The hill's average center coordinates are 43.5 MPa, 3430 cycles. The figure further depicts the density distributions of the residual strength $R_{res}(\sigma)$ and of the fracture cycle N .

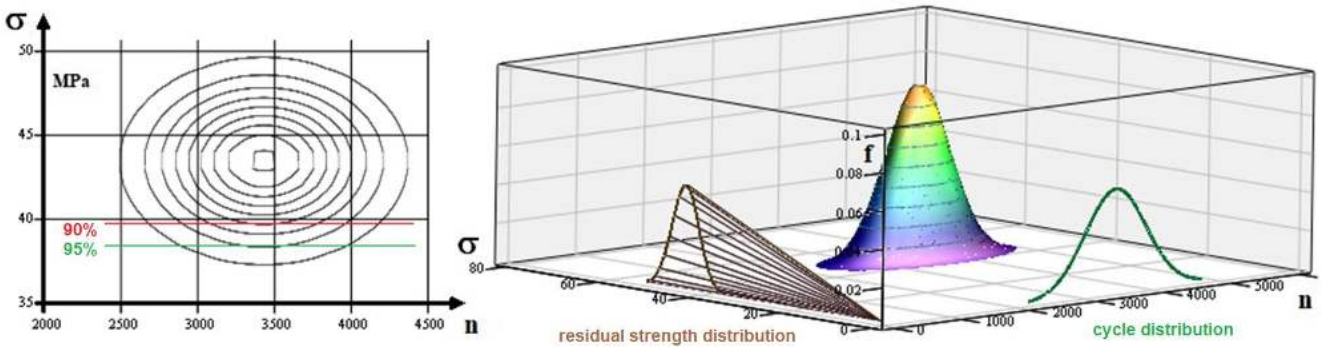

Fig.9-5: (right) Cyclic distributions and assumed residual strength distribution with survival probability hill applying the convolution integral. (left) Projection of lines of equal probability with two chosen residual strength cut-offs , M is the hill designation

In the right part figure, the residual strength distribution is not clearly visible due to the not activated but occurring additional Mathcad-drawn beams, running out from the origin. They are to neglect. The task seems to be an overloading of the Mathcad code which could not anymore handle the numerically effortful task for too large cycle numbers. The left figure shows the projection of the probability hill with lines of equal probability belonging to the chosen computation point *.

(Note, please: The presented application outlines a limit of the Mathcad 15 code application. Mathcad has no computation problem with the computation of the required so-called convolution integral. However, when visualizing the probability hill in Fig.9-5, it was only partly able to manage the 'big data' problem and runs into endless loops. Therefore the author had to sort out a work case with reduced stress and cycle regimes. The original SN data set was for fiber fracture (FF) of CFRP considering the hanger-example. This reduction to a relatively simple numerical example does not matter because the procedure is of interest and will explain the posed task.)

Below, the computation parameter input set is depicted.

Design Safety considering the scatter of the design parameters is tackled as follows:

*The scatter of loading is considered in the residual strength design verification because DUL with its design FoS j_{ult} has to be verified.

*The scatter of the residual strength R_{res} and of the fracture cycle N is captured by a joint probability calculation indicated below. This procedure is effortful, however of high fidelity if test data is available.

Under above assumptions an estimation of a 90%-linked residual (tensile) strength value can be determined according to the formula below representing the probability hill volume truncated by R_{res}

$\mu NR = 3431 \quad \sigma NR = 446 \quad \mu\sigma R = 43.5 \quad \sigma\sigma R = 2.9 \quad n := 2000..6000 \quad \sigma := 0..80$

$x_n := dnorm(n, \mu NR, \sigma NR) \quad y_\sigma := dnorm(\sigma, \mu\sigma R, \sigma\sigma R) \quad F(x,y) := x \cdot y \quad M_{n,\sigma} := F(x_n, y_\sigma) \cdot 750$

$$p\ddot{u} := \int_{\sigma res}^{Rt+\sigma Rt} \int_{2500}^{5500} \frac{1}{\sigma\sigma R \cdot \sqrt{2\pi}} \cdot e^{\left[\frac{-1}{2} \cdot \left(\frac{y-\mu\sigma R}{\sigma\sigma R}\right)^2\right]} \cdot \left[\frac{1}{\sigma NR \cdot \sqrt{2\pi}} \cdot e^{\left[\frac{-1}{2} \cdot \left(\frac{x-\mu NR}{\sigma NR}\right)^2\right]}\right] dx\, dy$$

The computation delivers for the point ($\sigma_{res} \equiv R_{res}$ = 38.0 MPa, 2000 cycles) the value pü = P = 95% = ℜ. Setting the value R_{res} = 39.5 MPa, the demanded survival probability pü = 90% = (1 - p_f) is obtained for a required R_{res} .

LL:

- *The proposed procedure clearly shows how to statistically understand a residual strength value*
- *It could be proven that the proposed model leads to an acceptable value for the residual strength of fatigued, non-cracked structural parts*
- *For a survival probability of pü = 90% could be obtained the value R_{res} = 39.5 MPa.*

9.8.4 Residual Strength R_{res} of a pre-cracked Part

To accurately estimate the residual strength of a pre-cracked structural part or the critical length of an initial macro-crack it is essential to consider the situation questions:

(1) Is the crack-length at the end of static loading critical?

(2) Is the crack-length at the end of cyclic loading critical for further static loading, considering a SN-curve? Here, then the certification of cracked components in aircraft structures requires a damage tolerance assessment.

9.9 Determination of a Load Spectrum-equivalent SN curve

In Standards ‘recommended’ operating load-spectra (collectives) for aircraft, wind energy, automotive etc are given as input for the lifetime estimation. These spectra no longer include a sequence of the loading or its stress history, respectively. If they do model finely mixed processes the prediction quality using the linear Miner micro-damage accumulation formula with $D_{maximum}$ = 1 = 100 % is best. Such operating load spectra are filled differently, whereby the area under a SN curve is marked as 100%. For practical use, the spectrum is sensibly divided into a few individual reasonable blocks, which then means to perform one-level tests with its constant amplitude loading.

The derivation of a spectrum-loading replacing one-level test would be very practical for the design engineer. It would further help to essentially reduce test Cost.

This task is executed on basis of an equivalent micro-damage sum D_{total} of the spectrum and of the one-level test. The same micro-damage has been accumulated in both situations at the end of $\sum n_i = N$.

$$\sigma_{\text{substitute}} \cdot \sum n_i / N = \sigma_{\text{substitute}} \cdot 1 = \sum_{i=1}^{\text{number of classes}} \sigma_i \cdot D_i / D_{\text{total}} \quad \text{in} \quad \underline{\textit{Fig.10-3}}$$

Thus the solution leads to the equivalent substitute stress level $\sigma_{\text{substitute}}$ = 45 MPa of the one-level test.

Herein, the micro-damage portions of the individual classified loading-blocks are weighted with the corresponding stress horizon analogous to $\sigma_i \cdot n_i / N_i$. In other words: The 'i-class micro-damage effective area' $\sigma_i \cdot n_i$ is divided by the associate fracture cycle value N_i in order to get the right proportion of the loading class i. Hence, the residual strength equation becomes

$$R_{\text{res}}^{\text{collective}} = \sigma_{\text{substitute}}(N) + [R^t - \sigma_{\text{substitute}}(N)] \cdot (1 - D^p)$$. (see [*Hah14*]).

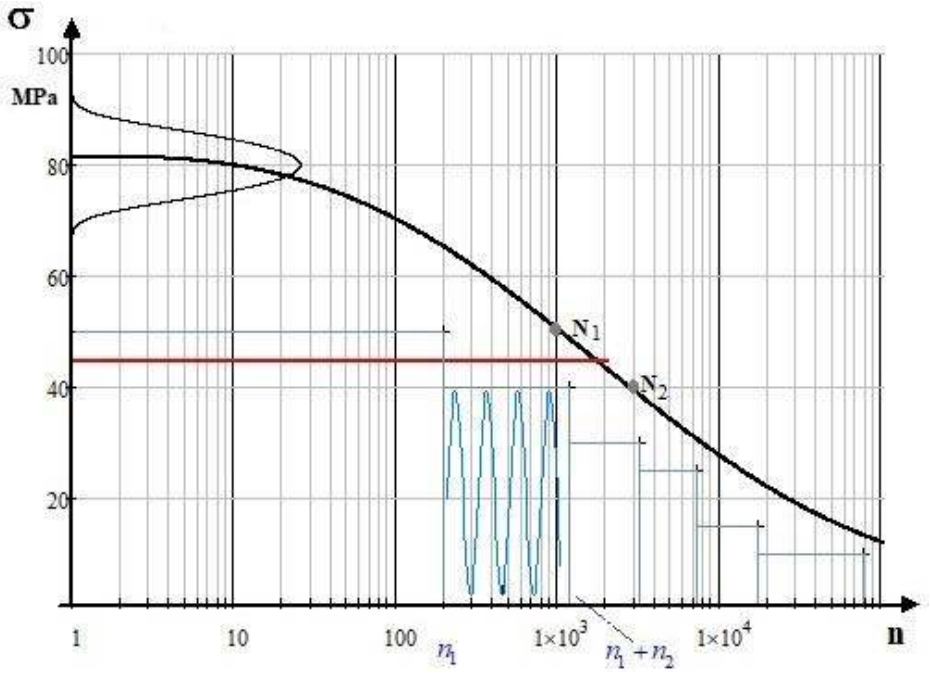

Fig.9-6: Loading blocks, relevant SN-curve R *and equivalent substitute stress level*

For not finely mixed processes the question arises whether the statistical quality is good enough for design verification and to establish a sufficient value for $D_{\text{eff}} < 1$.

10 Nonlinear isotropic Stress-Strain relationships and Models

Aim: *Rendering physical nonlinearity to provide a Basis for the generation of a simple 'Extended Mises' model (*just one measurable parameter on top of the Mises cylinder parameter*) to later replace a fictitious multi-parameter 'Gurson model' by applying Beltrami Theory considering the change of Poisson's Ratio.*

10.1 General on Stress-Strain curves $\sigma(\varepsilon)$, Strengths R and Poisson's Ratio ν

There are two different stress-strain curves existing: the *monotonic* and the *cyclic* stress-strain curve. The first curve is derived by static tests, whereas the second one is generated by fatigue tests. Strain-controlled cyclic hysteresis loops (*Fig.10-1,left down*) are performed on different strain levels with several test specimens. Dependent on hardening and following softening behavior of the actual material these two curves may discriminate significantly.

- Monotonic stress-strain curves have long been used to obtain design parameters for the limitation of stresses in engineering structures subjected to static loading.
- Similarly, cyclic stress-strain curves are useful for assessing the durability of structures subjected to repeated loading.

Further, in the case of monotonic σ-ε-curves there are very different, material-specific stress-strain curves in the elastic-plastic transition domain, see *Fig.10-1, left up* and *right*.

The yield strength is a material property defined as the stress at which a material begins to deform plastically. If it is not well-defined (mind *Lüder*) on the stress-strain curve. So it is difficult to determine a precise onset-of-yield point. Some show an 'Onset-of-yield' at an upper yield stress level $\bar{R}_e^{upper}$ and others at a lower yield strength $\bar{R}_e^{upper}$.

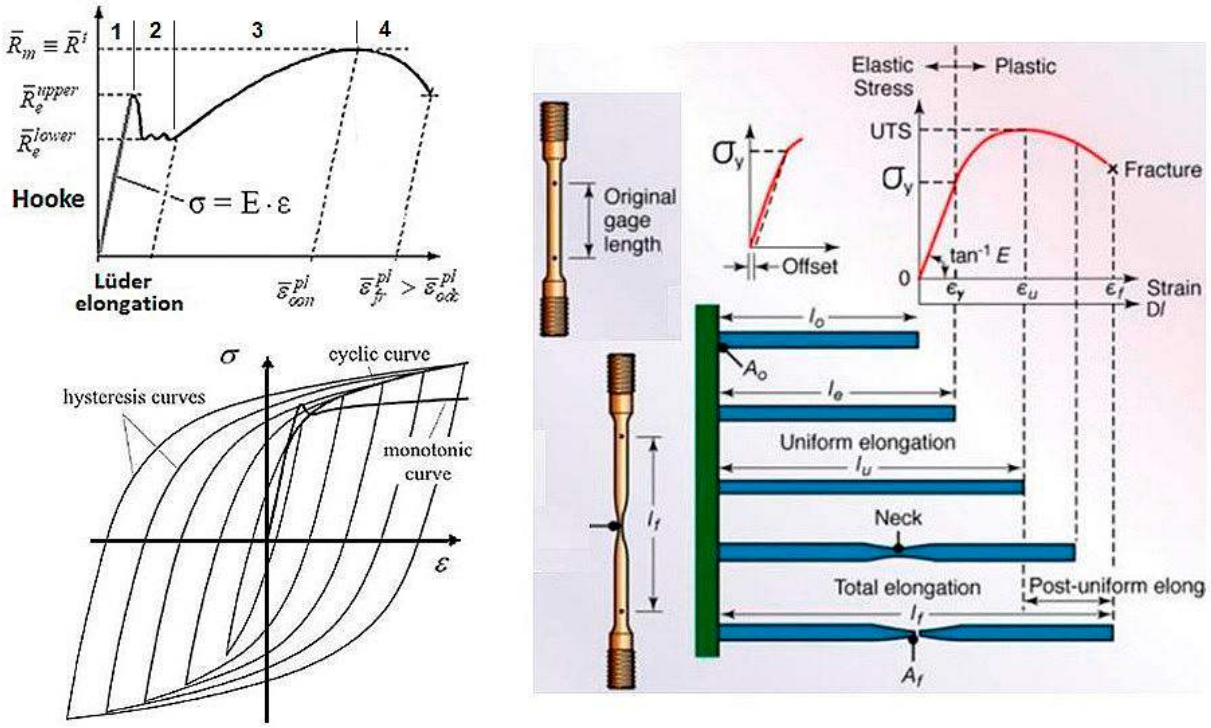

Fig.10-1, engineering quantities. modelling:

(left, up) Discontinuous yielding, mean curve for mild steel showing the yield point phenomenon, termed Lüder's elongation effect. (left, down) Cyclic curves.

(right) Tensile-test specimen with gage length, elongation before and after testing and finally after rupture (from Kalpakjian S and Schmid S: *Evaluation of the Possibility of Estimating Cyclic Stress-strain Para-meters and Curves from Monotonic Properties of Steels*. Manufacturing Engineering & Technology, 2013.

For the 'left up'- metal in the paper below of [Hai Qiu and Tadanobu Inoue: *Evolution of Poisson's Ratio in the Tension Process of Low-Carbon Hot-Rolled Steel with Discontinuous Yielding*. *Metals* ***2023****, 13, 562. https://doi.org/10.3390/met13030562]* four different regimes are distinguished:

Phase 1: Uniform elastic elongation,
Phase 2: Discontinuous yielding,
Phase 3 beyond R_{02} : Uniform elongation in the hardening regime,
Phase 4 beyond $\bar{R}^t$: Macroscopic plastic-strain localization experiencing radial deformation.

Low-alloy iron usually has such an upper yield limit R_e^{upper} (R_{eH}, *Streckgrenze*). If it is stretched during the tensile test, a spontaneous yielding in the crystals-compound takes place under loading. This so-called Lüder's elongation effect of mild metals as a part of plastic stretching disappears until all crystals are finally commonly stretched. Austenitic steels do not have a pronounced yield strength. Usually the lower yield point is taken as the yield strength of the metal.

In general, discriminating the proportional tensile limit R_{prop} and $R_{p0.2}$ ($\equiv R_{0.2}^t$), the offset yield point is taken as the stress at which 0.2% plastic deformation remains (*in English literature $R_{p0.2}$ is termed proof stress).* The mean stress at Onset-of-Yielding, denoted here $\bar{R}_{0.2}$ will be applied for ductile modeling. The stress $\sigma(\varepsilon_{pl})$, considering only the plastic deformation or plastic flow of the material, is termed Flow stress σ_F. By the way, the actual 'Onset-of-yielding at $R_{prop} \equiv \sigma_{prop}$ can be determined by a temperature measurement. If a metallic material is subjected to tensile stress, it first cools down in the area of elastic elongation analogous to an ideal gas, thermo-elastic effect. With onset of plastification heat is released, which leads to an increase in temperature. This temperature is measurable with glued thermocouples. In other words: The proportionality stress σ_{prop} can be allocated to that applied stress level, where the test specimen experiences a temperature increase due to internal dislocations.

Regarding not only metals - for a conflict-free understanding – it will be denoted $R_{p0.2}$ ($\rightarrow R_{0.2}^t$) and $R_{c0.2}$ ($\rightarrow R_{0.2}^c$) in the body text from now on. At the maximum of the curve, characterized by the so-called '*End–of–uniform elongation'* = '*Onset-of-(ductile) necking'* in the ductile material case, the tensile strength R_m ($\rightarrow R^t$) is given. For very ductile materials is valid $R_{0.2}^c \cong R_{0.2}^t$.

10.2 Uniaxial Rod Tensile Test Aspects

Beyond the tensile strength R^t a multiaxial state of stress follows in the tensioned necking ductile behaving rod test specimen. Therefore, the index ax holds up to the '*End–of–uniform elongation'* (Gleichmaßdehnung) at R^t (*index pl for plastic strain, oon for 'Onset-of-(ductile)necking', and odc for 'Onset-of-ductile cracking'* located before *rupture = plastic collapse*). See <u>*Fig.10-2*</u>.

In this respect, any formulations in the necking domain afford equivalent quantities in order to perform an accurate non-linear analysis with a correct input by an average $\sigma(\varepsilon)$-curve, because just the average curve will provide minimum deficiency from the average structural behavior usually focused in an analysis.

Mechanical properties are basically obtained from tensile tests, namely $R_{p0.2}$, R_m, ε_{oon}^{pl}, ε_{fr}^{pl}, E_0, ν_0 applying Standard (ASTM, ISO etc.). Herein ε_{oon}^{pl} is the strain value at the 'End of uniform elongation' (*German: Gleichmaßdehnung, index gl*) of a ductile material and it also represents the 'Onset-of–(diffuse) necking' (index oon). Unfortunately, Onset-of-(diffuse)necking is often termed post-necking. However, post-necking describes the increasing necking elongation regime, namely after hardening.

DIN EN ISO 6892-1: Short bar (rod) tensile test specimens show higher elongations at fracture than long ones. For this reason, an index is given for the plastic or permanent fracture strain, i.e. in Germany, A5 for short and A10 for long test specimens. The index refers to the ratio of original length L_0 and initial diameter d_0 (A5: $L_0 = 5 \bullet d_0$). Hence, the aspect ratio A5 delivers the permanent strain of a rod

test specimen with the aspect ratio 5 at rupture. The actual change in length is measured on the broken test specimen.

The ductile fracture strain is composed of the uniform elongation and the necking elongation part (*Einschnürdehnung*). The uniform elongation is independent of the specimen length. Its end is at 'onset-of-necking' at the load-controlled fracture point. *true* $A_{gl}(\bar{R}_m^t)$, the plastic strain at end of uniform elongation, specifies up to what percentage a material can be formed. As an additional ductility characteristic, the necking value **Z** (*Brucheinschnürung*) is calculated on the basis of the plastic cross-sectional reduction at fracture of the test specimen compared to the initial cross-section and is expressed in %.

Mechanical properties have to be assigned as part of the procurement specification requirements. These values shall adequately represent the effects coming from:

- Form: bar, rod, sheet, plate, laminate stack
- Size, thickness range:
- Manufacturing : metals (extrusion, rolling, forging); fiber reinforced plastics etc. FRP (curing) textiles (weaving, braiding, stitching etc.), fiber crossings
- Direction: metal grain (longitudinal, long. transverse, short transverse), fibers (parallel, transverse, thickness)
- Tempering: heat treatment for metals and fibers parts (*TP matrix*), cold working, (*remaining residual stresses*) *and*
- Test direction.

Susceptibility to environmental effects such as temperature, humidity radiation and cyclic loading has to be taken into account. For a specific project the required data may be tailored to match the particular profile and circumstances of the project in agreement with the customer.

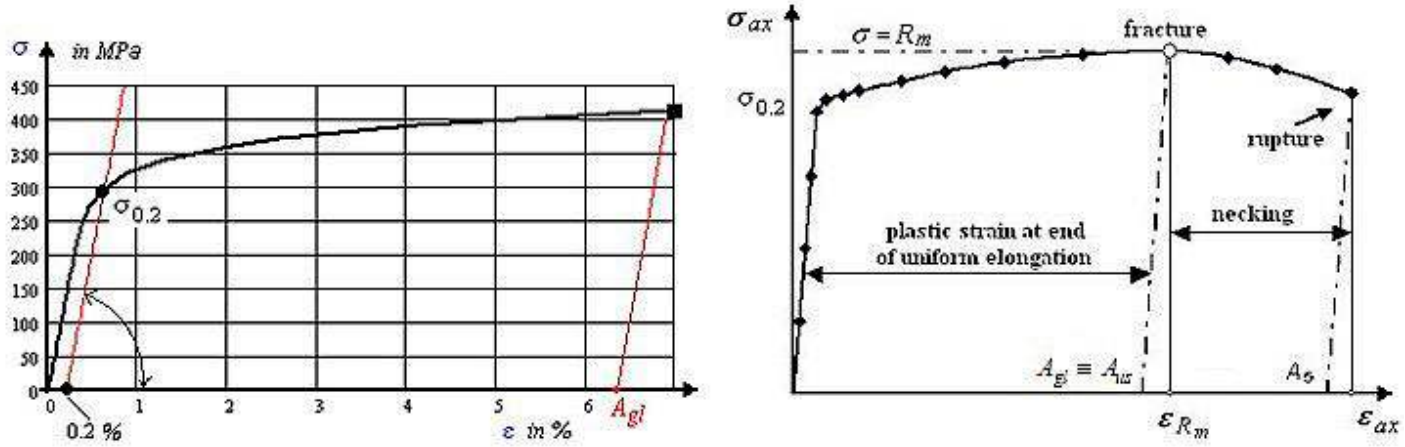

Fig.10-2a: (left) R-O mapping of a single engineering measurement test results. $A_{gl} = min\,\varepsilon_{oon}^{pl}$. (right) *Typical engineering stress-strain curve of a ductile metal material. End of uniform elongation (Gleichmassdehnung)*

Fig.10-2b left shows the scatter and distributions of some strain curves depicting strength and strain quantities. *Fig.0-2b right up* demonstrates that a compression test can, due to barreling, can just give a value for the yield strength $R_{0.2}^c$. This requires the determination of the increased hoop diameter, when aiming at realistic R_{02}- and E-values for tensile and compression. The figure also informs that for a static test specimen of a product the directions are marked by the subscripts L, LT and ST and that these are used for the description of sheet-type test specimens. These specimens are machined in the rolling direction (letter L), transversal direction (T) and thickness direction (S). In the case of thick structural

parts smooth tension bar test specimens are cut out, in the case of thin plates flat test specimens are investigated, which better represent 2D-structural shapes.

This is similarly performed for the radial and axial direction of a cylindrical test specimen.

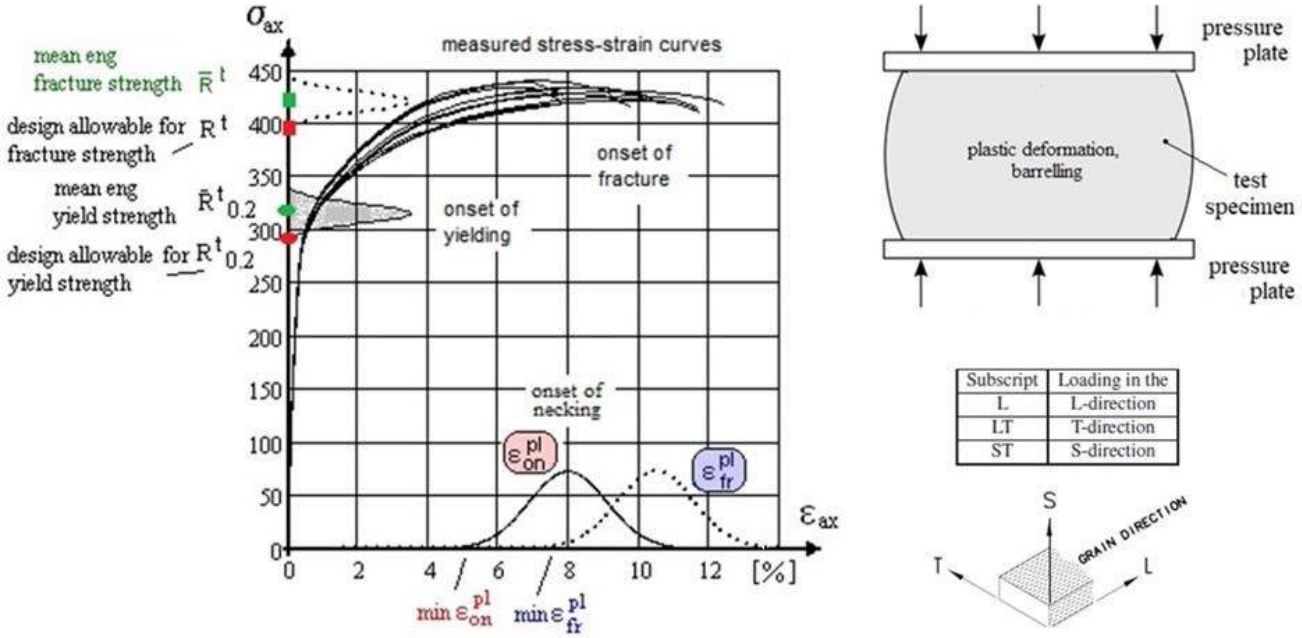

Fig.10-2b: AA2219 engineering quantities and curves, deformation of a compressed ductile test specimen. (right down) Marking of sheet-type test specimens

Eventually *Fig.10-2c* shall show the shape of the tensile rod test specimen and a picture of the finally porous fracture surface of the ductile material used:

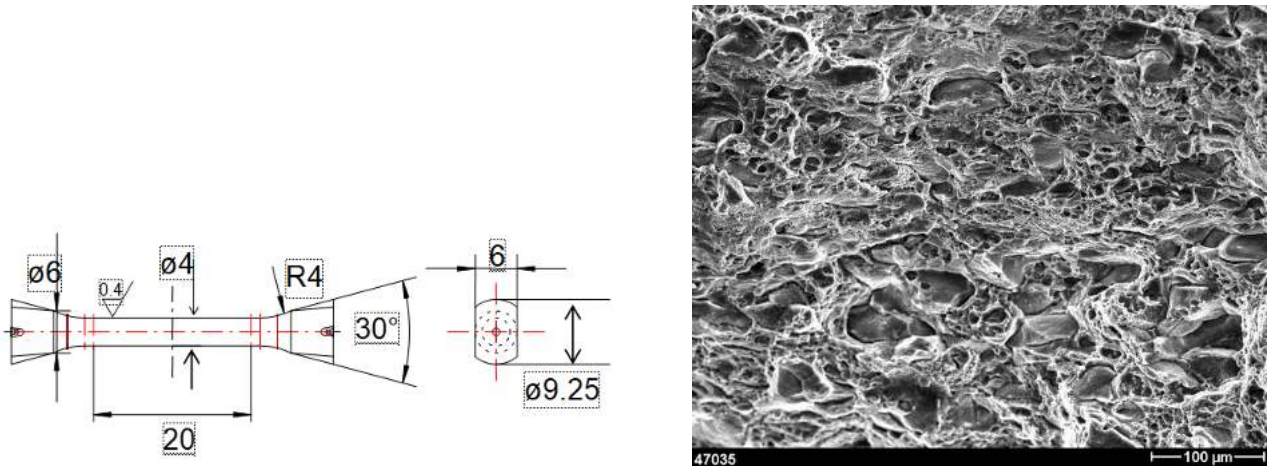

Fig.10-2c: (left) Geometry of the tensile rod; (right) Voids, seen on the fracture surface [IWM Freiburg],

10.3 Derivation of an accurate Average Stress-strain curve, example UD

Essential for an accurate analysis is a stress-strain curve which is derived from a set of test curves, delivering distributions for the *design parameters* $R_{p0.2}, R_m, \varepsilon_{on}^{pl}$ *and* ε_{fr}^{pl}. The use of accurate stress-strain curves of materials builds the basis of structural fidelity.

Below curves in Fig.10-3 exemplarily show a vast scatter. Therefore, a practical method of handling, analyzing and averaging theses curves has to be found for the nonlinear, statistically scattering stress-strain behavior of materials. The measured stress-strain curves are approximated by a mapping function.

That makes it possible to extract, store and update the complete nonlinear behavior of above metals or of composite materials in form of a distinct number of real parameters.

Three different evaluation methods are presented for the statistical analysis of a sample (bunch) of test curves, see [*Cun85*].

10.3.1 Test data recording

The material properties, usually extracted from recorded stress-strain curves are E_0, R and ε_{fr}. However, the amount of information contained in a nonlinear stress-strain curve is much larger. A complete storage of all curves is quite an effort. For numerical analyses, it would therefore be very advantageous to be able to work with only a few parameter values describing a substitute curve. So, for effective storing and processing of a large number of complete curves on a digital computer it is inevitable to substitute the test curves by analytical functions. In addition this leads to a representation, which is very suitable for computational analysis. The industry most often applies the well-known 3-parameter Ramberg-Osgood (R-O) function (*see Mil Hdbk 5, now MMPDS*), still used for aluminum before, that proved to be very suitable for composites (*the envisaged example*), too. This function can be applied as mapping function (*Mind: In material data sheets like in the HSB R-O-parameters for strain-hardening are provided for metal applications*). For shear inter fiber failure IFF3, torsion tests, it reads

$$\varepsilon_{hard} = \sigma / E_0^{\text{mode}} + 0.002\,(\sigma / \bar{R}_{0.2}^{\text{mode}})^n \rightarrow \text{example} \quad \gamma_{21} = \tau_{21} / G_{\|\perp} + 0.002 \cdot (\tau_{21} / \bar{R}_{0.2\,\perp\|})^n ,$$

and one can accept the excellent mapping quality of the R-O-function in the inelastic regime, the hardening curve part. The four values E_0, R, ε_{fr} and n represent in compacted form the complete nonlinear behavior of the test specimen. The curve, or at least a good approximation, can easily be retrieved from them by the R-O formulas. By the way, the values E_0, R, ε_{fr} and R_{02} are also acceptance test values needed for quality assurance.

10.3.2 Statistical evaluation of a bundle of test curves

In *Fig.10-3* nine single stress-strain curves from identical tube torsional experiments made of the same CFRP-material are reproduced. For design analyses this vastly scattering bundle of curves has to be averaged. For the visualization: If we imagine all the curves being written by purling sand onto a surface, the result would be a hill shape, *Fig.10-3 right*. The height of the sand hill at each point is a measure of the probability with which a single curve passes through exactly this place. And the ridge of the resulting hill defines a meaningful average curve $\bar{\varepsilon}\bar{\sigma}$ not to be mixed up with a mapping through the mean points, indicated by $\bar{\varepsilon}(\bar{\sigma})$ and described in Method I.

Method I: As a first naive trial it looks plausible simply to take the arithmetic averages of the curve parameters $\bar{E}_0$, $\bar{R}$, $\bar{\varepsilon}_{fr}$, $\bar{R}_{02}$ or $\bar{n}$, respectively. This method, described by $\bar{\varepsilon}(\bar{\sigma})$, fails due to the strong non-linearity.

Method II: Not detailed here, because to being extremely complicate. *See [Cun85]*.

Method III: To avoid the horrendous calculations necessary, within method II, a third procedure was developed with the following steps:

- harmonic averages for $\bar{E}_0$ from values $E_{0,i}$,
- harmonic averages for $\bar{R}_{02}$ from values $R_{02,i}$,
- arithmetic averages for R_i, $\varepsilon_{fr,i}$ with computing *n* using the averages above.

The harmonic average is a numerical average. It is calculated by dividing the number of observations by the reciprocal of each number in the series. Thus, the harmonic mean is the reciprocal of the arithmetic mean of the

reciprocals. Steps to calculate the arithmetic average: Count the number of values in the set. Add all the values together. Divide the sum by the number of values in the set to obtain the arithmetic average.

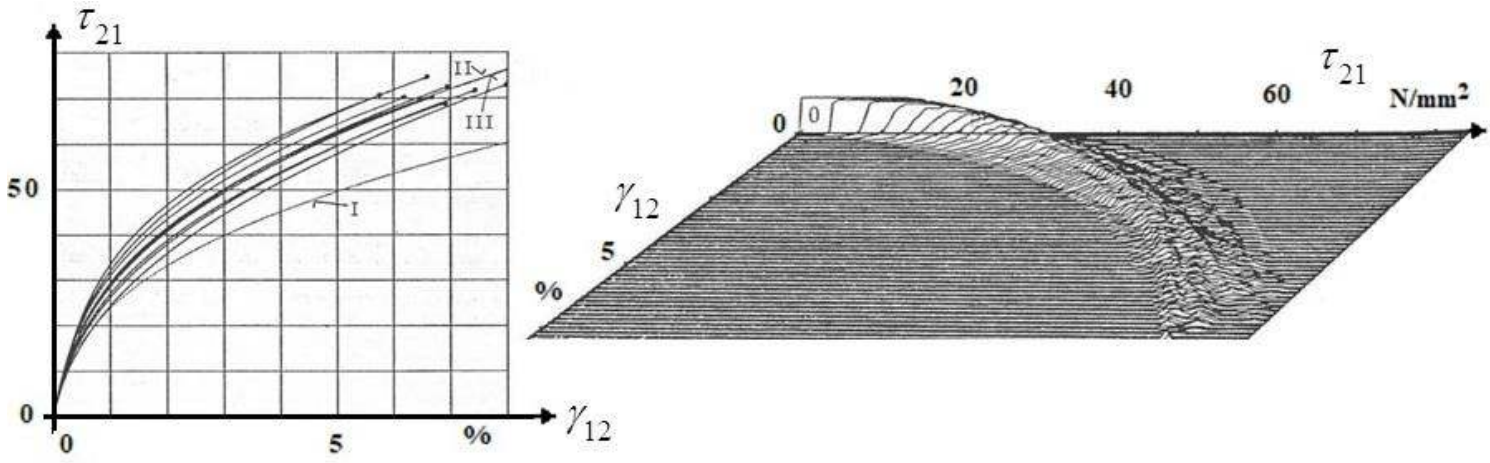

Fig.10-3: (left) R-O- 'reconstructed' curves from a torsion tube test specimen sample test. (right) Probability 'density hill' (fiber T300/ matrix EP)

Fig.10-3 (left) shows the results graphically.

*As can be seen, Method I leads to a curve, which is not acceptable.

*The curve defined by the parameters according to Method II gives accurately what is wanted but this is not engineering-like.

*Method III renders the same, but with less effort and is therefore recommended for usual practice.

LL:

** Before executing any analysis with a distinct code the designer has to check whether the actual stress-strain curve fits to the shape of the implemented curve*

** For the best possible estimation of the component behavior, the average stress-strain curve $\overline{\sigma\varepsilon}$ must be taken*

** The average stress-strain curve $\overline{\sigma\varepsilon}$ does not inescapably run through the means of yield $(\bar{\sigma}-\bar{\varepsilon})_{\text{yield}}$ and of fracture $(\bar{\sigma}-\bar{\varepsilon})_{fr.}$*

$\Rightarrow$ ***Is this realistic mapping really considered in all FEA design codes?***

10.4 Ramberg-Osgood (R-O) Mapping of the average stress-strain curve

The R-O-relationship is an often used mapping function and mathematical representation of the stress-strain curve. It represents (*if applicable to the actual material)* a possibility of well mapping the course of test data. A representation of the stress-strain curve is possible using engineering or true stresses and strains. The R-O-function is a monotonously increasing function and was originally developed for stresses up to the yield strength only. Using it, the elastic strain and additional plastic strain are determined separately. It reads, see *Fig.10-4,*

$$\varepsilon = \frac{\sigma}{E} + 0.002\left(\frac{\sigma}{R_{0.2}}\right)^{n} \qquad \text{with} \quad n = \frac{ln\left(A_{us}/0{,}2\%\right)}{ln\left(R_m / R_{p0.2}\right)} \quad \text{with } A_{us} \equiv A_{gl},$$

where the plastic strain portion follows a power relationship. The stress-strain curve is determined by the mechanical properties E and $R_{0.2}$ and by the material dependent hardening exponent n. Typical R-O curves are based on an average E and an average $\bar{R}_{0.2}$. Values of n are derived from test data. Remind the average stress-strain curve $\overline{\sigma\varepsilon}$ of a bundle.

For tension and compression the same equation is used, with different values of E, $R_{0.2}$ and n for tension and compression. Both, for tension and compression, positive values of ε, σ and E shall be inserted. For compression, the obtained values of ε and σ can be made negative after adaption of the function.

Applying engineering stresses and strains, the R-O-function often yields an adequate approximation of the test data for stresses up to the yield strength. When true stresses and strains are used, the region where a good approximation is obtained can be extended from onset-of-diffuse necking up to the strain where local necking starts and further (see some pages later).

The value of *n* depends on material, condition, product form and loading direction (in L, LT or ST-direction). Usually, only typical values of *E* and *n* are presented in literature and in material data sheets. For the yield strengths and for the ultimate strengths usually only strength design allowables are given (statistically determined minimum values). For A_5 generally only specification values are presented as $_{min}A_5$ values. Consequently, if no test data is available, only these values can be used to obtain an average R-O-function. Typical values of *n* are presented in the MMPDS-2 (*the former Mil-Hdbk 5*) and in the HSB. It should be noted that a value of n is always related to specific values of E and $R_{p0.2}$. For a typical stress-strain curve the value of *n* is different from the value for a minimum curve, see *Fig.16.3-7*. The applied value of *n* must therefore match with the other applicable mechanical properties! Given minimum strength values have to be transformed to average values to achieve a stress-strain average curve. The typical values of *n*, given in MiL-Handbook and HSB, are valid for $\varepsilon \le 1.2 \cdot \left(R_{0.2} / E_0 + 0.002\right)$. Using the R-O stress-strain relationship, the often applied tangent and secant modulus can be expressed as a function of the stress in the hardening domain:

$$E_{sec}^{hard} = \frac{\sigma}{\varepsilon} = \frac{\sigma}{\frac{\sigma}{E_0} + 0.002 \cdot \left(\frac{\sigma}{\bar{R}_{0.2}}\right)^{\bar{n}}} = \frac{E_0}{1 + 0.002 \cdot \frac{E_0}{\bar{R}_{0.2}} \cdot \left(\frac{\sigma}{\bar{R}_{0.2}}\right)^{\bar{n}-1}}, \quad E_{tan}^{hard} = \frac{d\sigma}{d\varepsilon} = \frac{E_0}{1 + 0.002 \cdot \bar{n} \cdot \frac{E_0}{\bar{R}_{0.2}} \cdot \left(\frac{\sigma}{\bar{R}_{0.2}}\right)^{\bar{n}-1}}$$

Also the value of Poisson's ratio *ν*, which increases when stresses become plastic, can be determined as a function of the stress. And vice versa it decreases with increasing porosity i.e. in the case of very ductile metals. This is analogous to brittle porous material, which was still mentioned in the distinct sub-chapter. The change of *ν* with the changing density will be elaborated in a later sub-chapter.

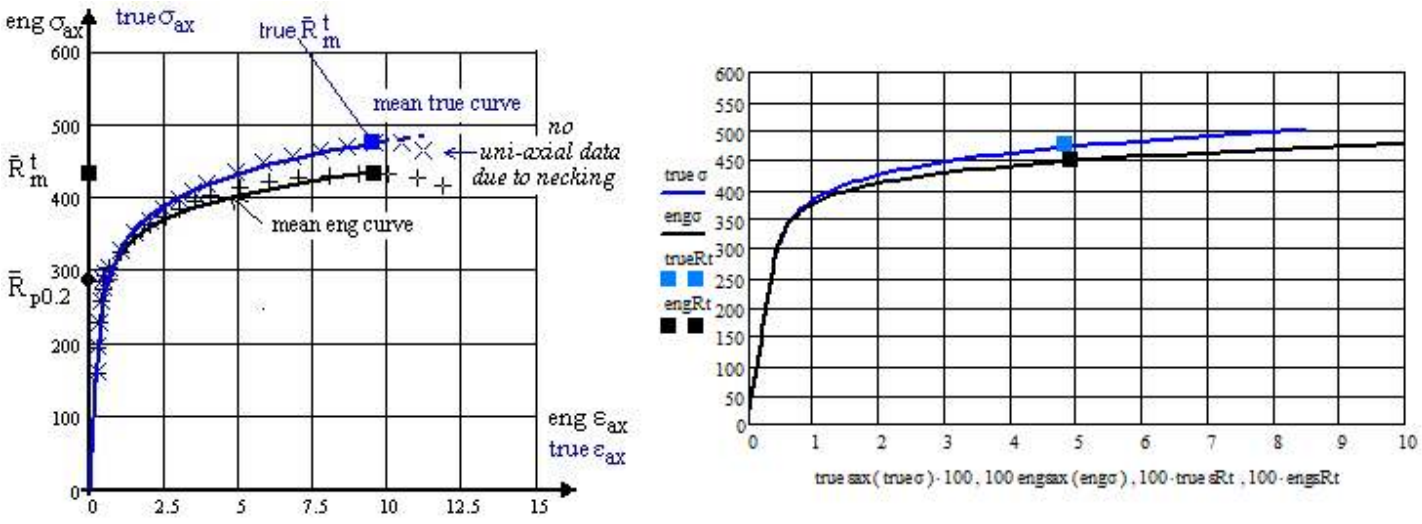

Fig.10-4: (left) Differences in R-O-mapping of engineering and true stress-strain curve, single measurement. (right) Extrapolation of R-O-mapped curve, bar over R indicates a mean value.

'End of uniform elongation' = 'Onset-of-(diffuse) Necking'

Fig.10-4 contains a true and an engineering stress-strain curve. The figure presents a general view and uses classical Ramberg-Osgood mapping. Mapping of the course of stress-strain data in the non-linear domain is well performed by taking the usually applied Ramberg-Osgood equation for the true stress-true strain curve (*maps the true curve better than the engineering curve*)

10.5 Mapping of a measured stress-strain curve by the Ramberg-Osgood Model

In a contract of MAN-NT with the institute IWF at Freiburg all standard model-required properties have been determined. For completion, hopefully in a material-handbook given will be in addition the plastic strain *A*5 and also the final necking value *Z*, being usually a minimum and not an average value. $A_{fr} \equiv A_{rupture}$ comes from measurement of *A*5 (*type:* $L_0 = 5 \bullet d_0$, *original length* L_0 *and initial diameter* d_0) as plastic or permanent change in length, measured on the load-controlled broken test specimen and Z the radial plastic necking *A*-reduction ratio value, in % (*Unfortunately, material mechanics also uses the Area letter A for this strain property).*

Table 10-1 lists analysis-relevant quantities (in MPa and %) to be applied in a Ramberg-Osgood curve modelling.

Table 10-1: AA2219 material properties and Ramberg-Osgood parameters. Isotropic materials, in MPa and %), *d= 4.0 mm . Regarding* $\bar{R}_{odc}$, *see the following Sub-chapter 14-6.*

$\bar{R}_{p0.2}$	$\bar{R}_m$	A_{gl}	true$\bar{R}_m$	trueA_{gl}	$\bar{R}_{odc}$	$A_{fr} = A_{rupt}$	trueA_{fr}	Z	$\bar{n}$	true$\bar{n}$	$R_{p0.2}$	R_m	R_{odc}
352	*453*	*4.9*	*478*	*4.8*	*535*	*7.7*	*7.5*	*20*	*12.7*	*10.6*	*297*	*417*	*492*
MPa	MPa	%	MPa	%	MPa	%	%	%	-	-	MPa	MPa	MPa
average *(mean, typical, characteristic)* values for best mapping											Design Allowables		

$$\text{true}\varepsilon = \frac{\text{true}\sigma}{E_0} + 0.002 \cdot \left(\frac{\text{true}\sigma}{\text{true}\bar{R}_{0.2}} \right)^{\text{true}\bar{n}} = true\varepsilon_{ax}^{el} + true\varepsilon_{ax}^{pl}.$$

10.6 Presentation of Engineering and of True Stress and Strain Quantities

The larger the strains the more the engineering quantities lose their applicability in structural dimensioning. Therefore, logarithmic (*usually termed true*) strains have to be used in an accurate dimensioning process. The derivation of these quantities was collected in *Table 10-1*.

$$\text{eng}\varepsilon = \varepsilon = \varepsilon^{\text{el}} + \varepsilon^{\text{pl}} = \frac{\sigma}{E_0} + 0.002 \cdot \left(\frac{\sigma}{\bar{R}_{0.2}} \right)^{\bar{n}}, \quad \text{true}\varepsilon = \frac{\text{true}\sigma}{E_0} + 0.002 \cdot \left(\frac{\text{true}\sigma}{\text{true}\bar{R}_{0.2}} \right)^{\text{true}\bar{n}}, \quad \bar{n} = \frac{\ln\left(A_{gl} / 0{,}2\% \right)}{\ln\left(\bar{R}^t / \bar{R}_{p0.2} \right)}.$$

In *Fig.10-4* the difference between the mean strength values $\text{eng}\bar{R}^t \rightarrow \text{true}\bar{R}^t$ was shown to be 8% for *AA2219!*

Fig.10-5(left) depicts the linear elastic proportional domain and the hardening domain.

Fig.10-5 (right) presents stress-strain measurement with Ramberg-Osgood mapping. The course of the area reduction would show a slight kink beginning at 'Onset-of-ductile cracking $_{odc}$' (= o*nset-of-localized necking*) according to the deteriorating effect of the void coalescence.

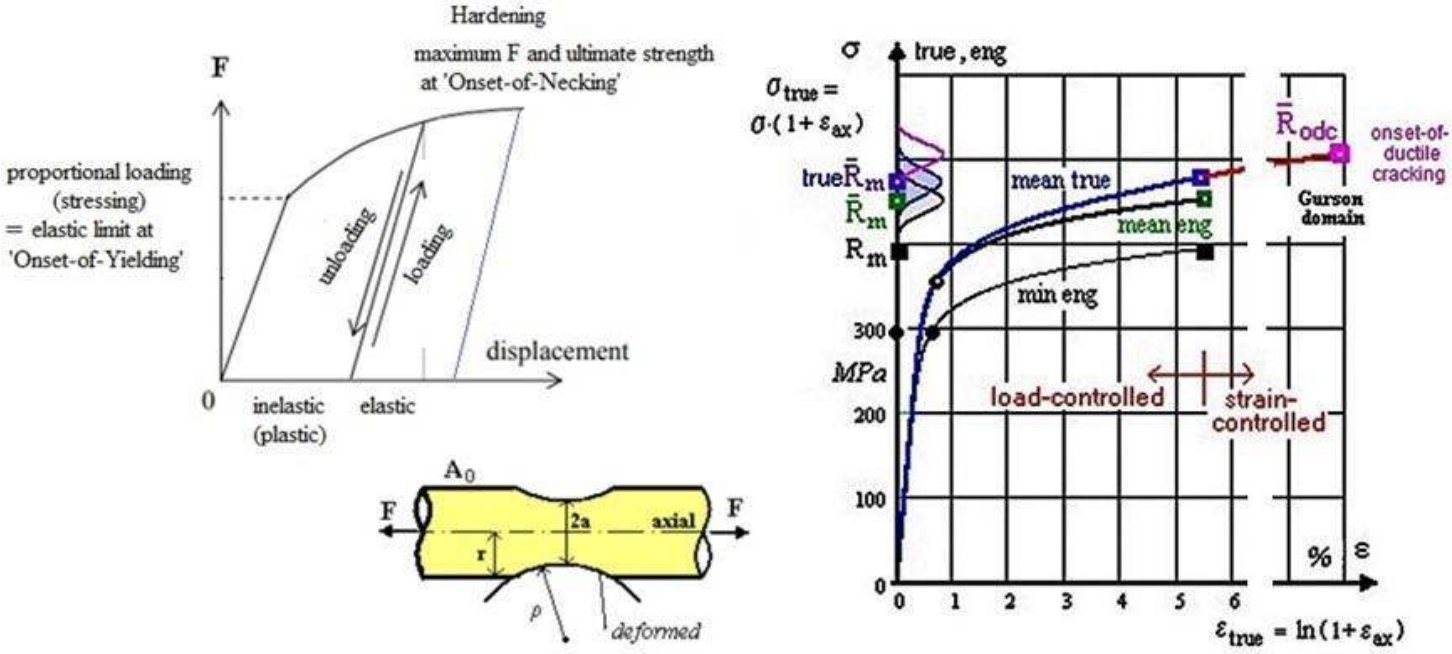

Fig. 10-5, modelling: (left) Display of proportional domain and hardening domain with the tensile rid test specimen. (right) Ramberg-Osgood-mapped true and engineering stress-strain curves of AA2219.

F:= Force F_{ax}, A_0 := original cross-section, A:= actual cross section of the necked rod. $\bar{R}^t = \max F / A_0$, $\varepsilon \le \bar{A}_{gl}$ (*permanent strain linked to load-controlled fracture at* $\bar{R}^t$*). Necking radius is* ρ*, a bar over* $\bar{R}$ *indicates a mean (average) value of a sufficiently large test data set, and no bar over R will generally mean strength and later indicate a 'strength design allowable'.*

Table 10-2 presents the derivation of true stresses and true strains in the 'Mises'-validity domain.

10.7 Variation of Poisson's ratio ν up to Rupture level

Fig.10-6 (left) shows an experiment in the elastic-plastic transition region, carried out by O. Mahrenholtz /H. Ismar.

The test was a flat compression test of a cube: One side constrained, one free, one compressed → Principal stress state ($\sigma_I = \sigma_{action}$, $\sigma_{II} = \sigma_{I\,(re\text{-}action)}$, $\sigma_{III} = 0$) → principal strain → ν .

It turns out that R_{p01} is approximately ν = 0.4. The value at R_{p02} in H-L-W coordinates is 0.82 = $\sqrt{2/3} = \sqrt{2J_2} / R_{02}$ with $J_2 = 2R_{02}/6$ (left, down).

Poisson's ratio, determined by a coupon measurement, reads $\nu = -\varepsilon_{lat}/\varepsilon_{ax}$ or $\nu = -(\Delta d/d)/(\Delta \ell / \ell$. Concerning sheet test specimens the measurement problem increases because localized necking will occur at 'onset-of-ductile cracking and this depends on the thickness of the test specimen.

If analytically necessary the value of Poisson's ratio ν, which increases when stresses narrow the plastic regime, can be determined for stability analyses as a function of the stress. The formula, which uses quantities of the R-O-mapped true stress-true strain curve, is derived in *Table 10-3.*

Table 10-2: Derivation of true stresses and true strains in the 'Mises'-validity domain

True Strains (logarithmic strains):

The application of engineering strain cannot be correct for larger strains, since it is based on the original gage length ℓ_0, whereas the length is continuously growing. Ludwik $[Lud09]$ therefore introduced the true strain $(\text{logarithmic strain})$, the increment of which for a given length is defined as $d(true\varepsilon) = d\ell / \ell$ and the total true strain, integrated from ℓ_0 to current length ℓ, is

$$true\varepsilon_{ax} = \int_{\ell_0}^{\ell} d\ell / \ell = ln(\ell / \ell_0) = ln(1 + eng\varepsilon_{ax}) .$$

Above equation delivers an accurate value up to 'onset-of-necking' or $\bar{R}^t$.

The replacement of the logarithmic function by a Taylor series

$$true\varepsilon_{ax} = eng\varepsilon_{ax} - eng\varepsilon_{ax}^{\ 2} / 2 + eng\varepsilon_{ax}^{\ 3} / 3 - .. +$$

clearly shows that identity is given for small strains, only. Applying the true strain has a physical and a numerical advantage: The incompressibility equation really becomes zero

$$\sum true\varepsilon_i = true\varepsilon_I + true\varepsilon_{II} + true\varepsilon_{III} = 0,$$

whereas in terms of engineering strains the correct equation from solid geometry reads

$$(1 + eng\varepsilon_I) \cdot (1 + eng\varepsilon_{II}) \cdot (1 + eng\varepsilon_{III}) \; - \; 1 \; = 0,$$

which reduces to 0 for negligible strains, only.

Once necking starts most of the deformation occurs in the smallest cross section. The longer the gage length used the smaller the percent elongation will be. Therefore, a better procedure is the measurement of the reduction of the cross-section. → Beyond $\bar{R}^t$, the true σ-ε curve can be more accurately obtained by measuring the radial strain

$$\text{eng}\varepsilon_{radial} = (r - r_0) / r_0 = r / r_0 - 1 \quad \text{and} \quad true\varepsilon_{radial} = -ln(1 + eng\varepsilon_{radial}) = -ln(r / r_0),$$

provided, the tensile test specimen has a circular cross-section, a rod. In this case $\varepsilon_{radial} = \varepsilon_{hoop}$

$$true\varepsilon_{ax} + true\varepsilon_{radial} + true\varepsilon_{hoop} = 0 \quad \text{and it holds} \quad true\varepsilon_{ax} = -2true\varepsilon_{radial} = 2\,ln(r / r_0),$$

which delivers an accurate value above 'onset-of-necking'. The equivalent strain in the center reads

$$true\varepsilon_{eq} = \frac{\sqrt{2}}{3} \cdot \sqrt{(true\ \varepsilon_{ax} - true\ \varepsilon_{hoop})^2 + 0 + (true\ \varepsilon_{hoop} - true\ \varepsilon_{ax})^2}$$

$$= \frac{\sqrt{2}}{3} \cdot \sqrt{2(2 - (-1))^2} \cdot true\varepsilon_{radial} \; = \; \frac{2}{3} \cdot \sqrt{3^2} \cdot true\varepsilon_{radial} = 2\,ln(r / r_0)$$

⇒ Transferring strain data: $true\varepsilon = ln(1 + eng\varepsilon),\ eng\varepsilon = e^{true\ \varepsilon} - 1.$

True Stresses:

Trueσ can be obtained from engσ, if the small changes in volume at the end of the transition domain are neglected. Then, incompressibility $\sum \varepsilon_i^{pl} = 0$ can be assumed and it follows:

$$\text{engσ} = \text{F}/\,\text{A}_0, \;\; \text{trueσ} = \text{F/A} \quad \text{with} \; A \cdot \ell = A_0 \cdot \ell_0 \; , \; \text{F: = load} \; F_{ax}$$

wherein ℓ_0 : = original gage length, and A, ℓ current values of the necking cross-section.

Introducing the equation $\varepsilon_{ax} = (\ell - \ell_0) / \ell_0$ derived above, the true stress is linked by

$$true\sigma_{ax} = F / A = (F / A_0) \cdot (\ell / \ell_0) = eng\sigma \cdot (1 + eng\varepsilon_{ax}) = \sigma_{ax} \cdot (1 + \varepsilon_{ax}) \;\; \text{usually written}$$

⇒ Transferring stress data: $true\sigma = eng\sigma \cdot (1 + eng\varepsilon)$ and $eng\sigma = true\sigma / exp(true\varepsilon)$.

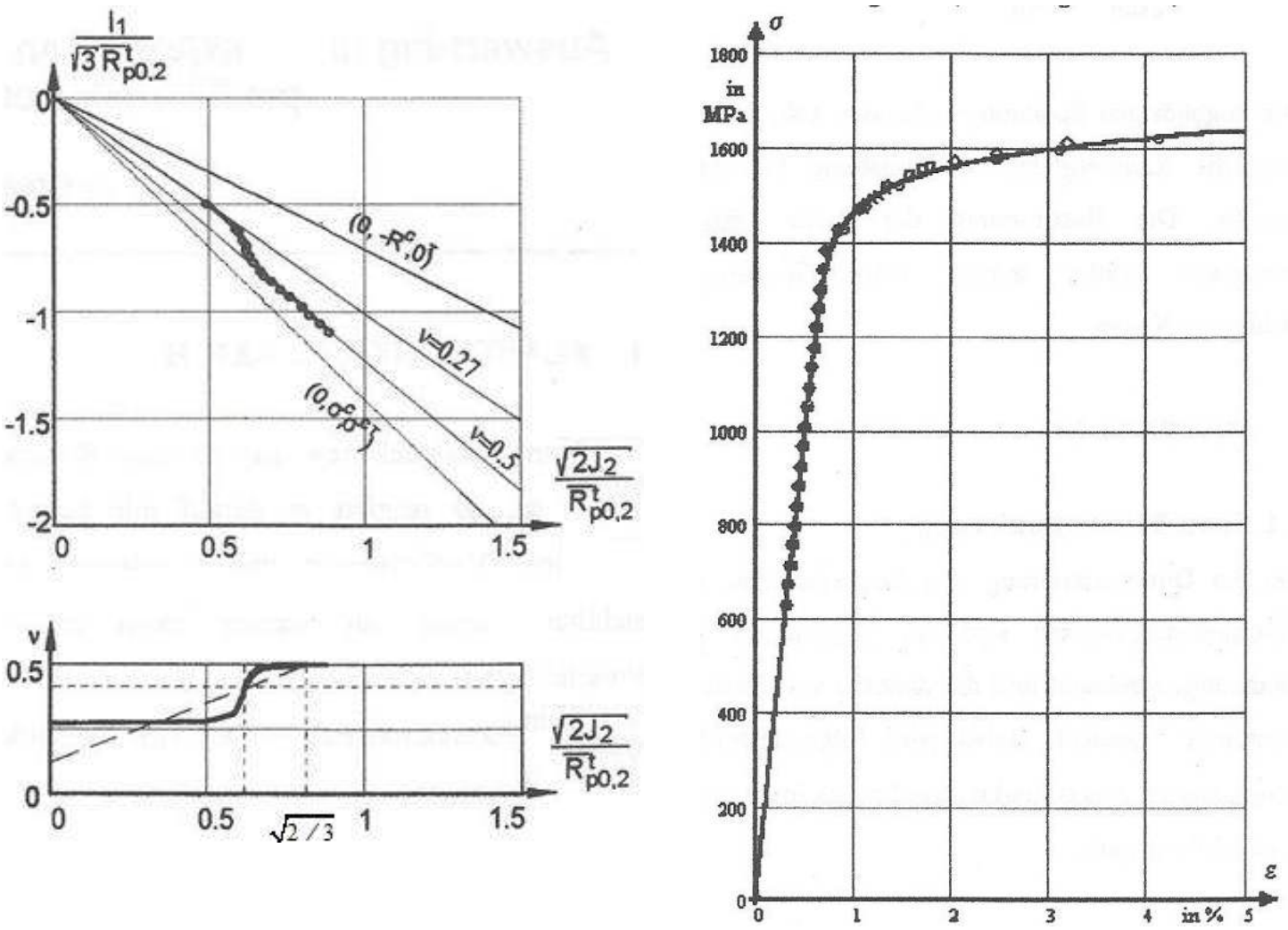

Fig. 10-6: (left) St37 Development of ν in Beltrami's elastic-plastic transition regime, a cube plane compression test. (right) D6AC, Ariane 5 Booster) Stress-strain measurement points with a Ramberg-Osgood engineering stress-strain data mapping curve under axial tension

Table 10-3: Derivation of a formula for Poisson's ratio

$true\varepsilon = true\varepsilon^{el} + true\varepsilon^{pl}$ with $true\varepsilon_{ax} = true\varepsilon^{el}_{ax} + true\varepsilon^{pl}_{ax}$, $true\varepsilon_{lat} = true\varepsilon^{el}_{lat} + true\varepsilon^{pl}_{lat}$, $\nu_0 = \dfrac{-true\varepsilon^{el}_{lat}}{true\varepsilon^{el}_{ax}}$

from incompressibilityin the plastic range (≡ volume conservation law) $\dfrac{V}{V_0} = \dfrac{\ell}{\ell_0} \cdot \dfrac{A}{A_0} = 1$

follows $true\varepsilon^{pl}_{ax} + 2 \cdot true\varepsilon^{pl}_{lat} = 0$ and $true\varepsilon^{el}_{lat} = -\nu_0 \cdot true\varepsilon^{el}_{ax}$, which gives after insertion of above relations

$$true\nu = -\frac{true\varepsilon_{lat}}{true\varepsilon_{ax}} = -\frac{true\varepsilon^{el}_{lat} + true\varepsilon^{pl}_{lat}}{true\varepsilon_{ax}} = -\frac{true\varepsilon^{el}_{lat} - 0.5 \cdot true\varepsilon^{pl}_{ax}}{true\varepsilon_{ax}} = -\frac{true\varepsilon^{el}_{ax}}{true\varepsilon_{ax}} \cdot \left(-\nu_0 - 0.5 \cdot \frac{true\varepsilon^{pl}_{ax}}{true\varepsilon^{el}_{ax}} \right)$$

$$= -\frac{true\varepsilon^{el}_{lat} - 0.5 \cdot true\varepsilon^{pl}_{ax}}{true\varepsilon_{ax}} = -\frac{-\nu_0 \cdot true\varepsilon^{el}_{ax} - 0.5 \cdot true\varepsilon^{pl}_{ax}}{true\varepsilon_{ax}} = -\frac{-\nu_0 \cdot true\varepsilon^{el}_{ax} - 0.5 \cdot (-true\varepsilon^{el}_{ax} + true\varepsilon_{ax})}{true\varepsilon_{ax}}$$

$$= -\frac{-\nu_0 \cdot true\varepsilon^{el}_{ax} - 0.5 \cdot (-true\varepsilon^{el}_{ax} + true\varepsilon_{ax})}{true\varepsilon_{ax}} = 0.5 + \frac{-\nu_0 \cdot true\varepsilon^{el}_{ax} - 0.5 \cdot (-true\varepsilon^{el}_{ax})}{-true\varepsilon_{ax}}$$

$$= 0.5 - \frac{true\varepsilon^{el}_{ax}}{true\varepsilon_{ax}} \cdot (0.5 - \nu_0) \ .$$

In *Fig.10-7* above, the different growth of the engineering and the true stress-strain curve is displayed up to the tensile strength point at the 'End–of–uniform elongation'.

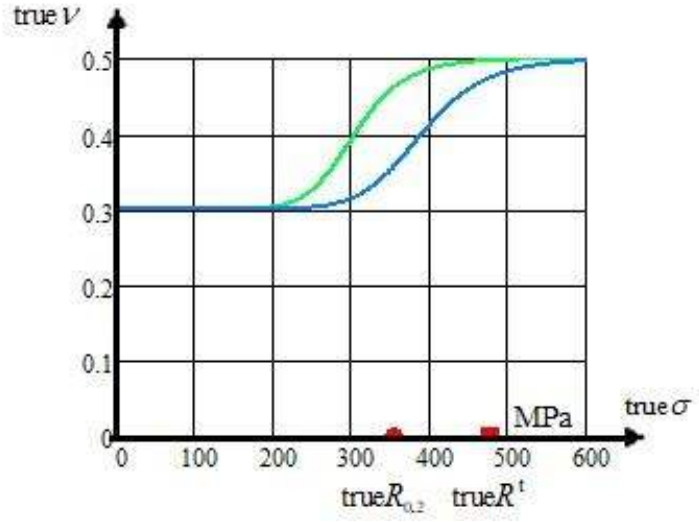

Fig.10-7: Course of Poisson's ratio in the elastic-plastic domain, determined with several formulas

***LL**:*

** The determination of the properties of a solid material requires a force-elongation curve which is then accurately to transfer into a stress-strain curve that is independent from the tested specimen type rod, sheet, coupon, cube.*

** Before any performance of a non-linear analysis is executed it is to check whether true or engineering curve quantities are to provide for numerical input. This then fixes the output*

** Beyond R^t necking occurs generating a hydrostatic stress σ_{hyd} in the tensile rod, which lowers the stress-strain curve in the high plastic regime*

** Poisson's ratio can only approach the limiting points 0.5 > **ν** > -1,* principally. *So-called auxetic materials possess a negative ν. Being strained, the transverse strain in the material will also be positive*

** UD-materials have different ν-values in the directions of anisotropy*

** True strains can be added while engineering strains cannot be added!*

In *Fig.10-8* in test data evaluation, beyond R^t the axial stress has to be replaced by the equivalent stress because necking in the test specimen activates a hydrostatic residual stress state, dependent on the test specimen used.

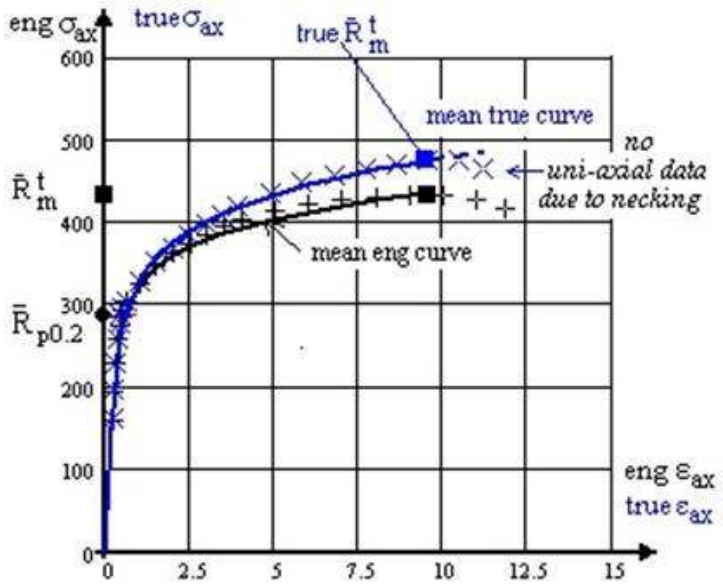

Fig.10-8, Aluminum Alloy AA 2219:

Differences in R-O-mapping of engineering and true stress-strain curve, single measurement.

Bar over R indicates a mean value.

F/A_0 at 'End of uniform elongation' =

'Onset-of-(diffuse) Necking'

In *Fig.10-9* the *full* stress-strain curve is presented and associated significant points including strength design allowables points are depicted. The full curve ends with reaching the 'onset-of-ductile cracking' point at the associated strength R_{odc} before reaching full rupture.

Additionally for 'Onset-of-yielding' a Margin of Safety is rendered in order to visualize the size of the fulfillment of the 'Design Yield' Limit State with respect to the acting stress state.

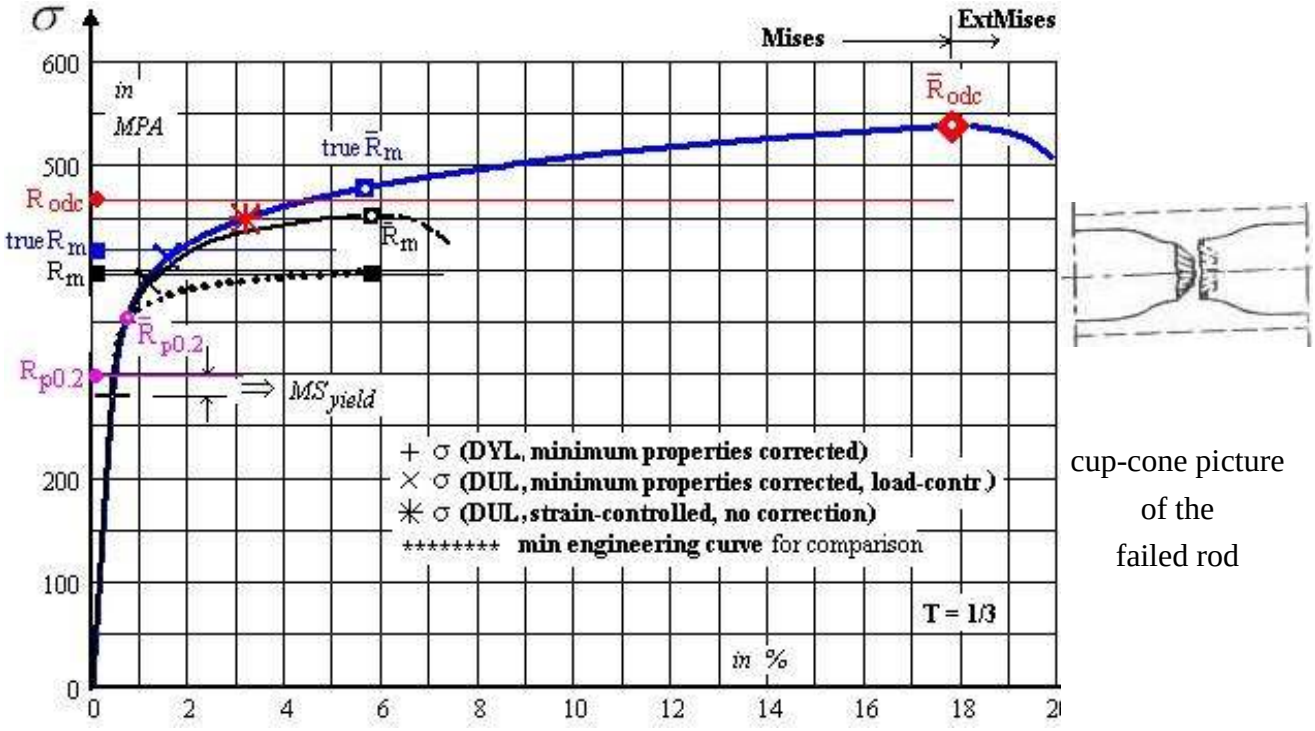

Fig. 10-9: Equivalent true stress-equivalent true strain curve. Proposed local strain-controlled extended stress-strain curve incl. mean fracture points and strength design allowables (no bar over)

LL:

** Opposite to some regulations it is to note "In general, it can be not correct to use a minimum engineering curve in order to obtain the desired realistic structural behavior because structures are usually statically indeterminate".*

** The elliptical shape of the 'Beltrami egg' and its surface potential description will be used in the investigated 'Gurson domain' too, next chapter.*

10.8 Estimation of the 'Onset-of-ductile Cracking' Strength R_{odc}

Beyond 'Onset-of-diffuse necking' the axial strain measurement becomes senseless, only representative is the rod radius-decrease measurement to investigate in this full plastic domain the influence of the hydrostatic stress. From the measured plastic cross-section reduction the plastic portion ε_{odc}^{pl} can be estimated and the 'plastic' curve point $\bar{R}_{odc}$ computed if the only counting associated plastic strain is known, fixed by the diameter reduction.

Because the R/O-model excellently maps the true strength course of test data, its plastic part is employed to estimate a value for the *plastic point* $\bar{R}_{odc}$ ≡'Onset-of-ductile-cracking', which is of interest for plastic structural design. This can be determined by using volume constancy applying the measured reduction of the initial radius $a = d/2$ of the tensile rod. With $Z\,(\bar{R}_{rup})$ taken as $Z\,(\bar{R}_{odc})$ the estimation of $\bar{R}_{odc}$ at $\text{true}\varepsilon_{odc}$ from the Ramberg-Osgood curve is performed as shown in *Table 10-4*.

Ductile collapse or *rupture* $\bar{R}_{rupt}$, respectively, is of theoretical interest, only; practice ends before.

Table 10-4: Derivation of an estimate value for the Strength $\bar{R}_{odc}$

At $\bar{R}^t$ 'Onset-of- (diffuse) necking' $d_{oon} = 3.89$ mm, at 'Onset-of-ductile cracking' $d_{odc} = 3.78$ mm.

$$\varepsilon^{pl} = 0.002\left(\frac{\sigma}{\bar{R}_{0.2}}\right)^n, \quad \varepsilon_{rad}{}^{pl} = \ln(\frac{r}{a}), \quad \frac{\Delta A}{A_0} = \frac{A_0 - A}{A_0} = 1 - \frac{A}{A_0} \rightarrow \frac{A_{rupt}}{A_0} = 1 - Z = \frac{r^2}{a^2}$$

$$\varepsilon_{ax,\,00n}{}^{pl} = -2 \cdot \varepsilon_{rad}{}^{pl} \text{ at } \bar{R}^t \quad \text{and delivers} \quad \text{true}\bar{n} = \frac{\ln\left(\varepsilon_{ax,\,00n}{}^{pl} / 0{,}2\%\right)^n}{\ln\left(\bar{R}^t / \bar{R}_{p0.2}\right)} .$$

With known $\varepsilon_{rad}{}^{pl} = \ln(\frac{r}{a}) = \ln(\sqrt{1-Z}) = \ln(\sqrt{1-0.20}) = -11.2\ \%$ and $\varepsilon_{ax}{}^{pl} = -2 \cdot \varepsilon_{rad}{}^{pl}$

follow for the non-corrected odc-point $\rightarrow true\varepsilon_{ax}^{pl} = 0.002 \cdot \left(\frac{\bar{R}_{odc}}{\bar{R}_{0.2}}\right)^{\text{true}\bar{n}}$

$$\Rightarrow \bar{R}_{odc} \cong \bar{R}_{0.2} \cdot \sqrt[true\bar{n}]{\varepsilon_{ax}{}^{pl}} / 0.002 = 542 \text{ MPa} \quad \text{and}$$

$$\text{true}\varepsilon_{odc} = true\varepsilon_{ax}^{el} + true\varepsilon_{ax}^{pl} = \frac{\bar{R}_{odc}}{E} + 0.002\left(\frac{\bar{R}_{odc}}{\bar{R}_{0.2}}\right)^{\text{true}\bar{n}} .$$

10.9 Beltrami's Potential Surfaces in Elastic-plastic Regime, Idea for the Plastic Porous Regime

From previous investigations the author knows, that any volume change, due to the FMC 'rules', is to describe by the term $I_1{}^2$. If a shape change occurs then the invariant J_2 is required. This is the basis for:

10.9.1 Elastic-plastic transition regime

Beltrami cites: "*The deformation of a material consists of two parts, a shape* and *a volume change*". Based on this, one can formulate for the elastic-plastic transition regime

$$\frac{(2+2\nu)\cdot 3\cdot J_2}{\bar{R}^2} \text{ and } \frac{(1-2\nu)\cdot I_1{}^2}{\bar{R}^2} \rightarrow \frac{3\cdot J_2}{\bar{R}^2} + \kappa \cdot \frac{I_1{}^2}{\bar{R}^2} = c^{\text{Bel}} \text{ with } \kappa = \frac{1-2\nu}{2+2\nu} .$$

Into this formulation a normalizing strength is inserted: $I_1 = \bar{R}$, $J_2 = 2 \cdot \bar{R}^2 / 6 \rightarrow c^{\text{Bel}} = 1 + \kappa$

and for the special yield potential surface (ν=0.5) yields $\frac{3 \cdot J_2}{\bar{R}_{02}{}^2} + 0 \cdot \frac{I_1{}^2}{\bar{R}_{02}{}^2} = 1 + 0$ ('Mises' cylinder).

Beltrami bridges the elastic domain by adding the plastic domain ($3 \cdot J_2$ is Mises part).

His formulation is not a failure function but a descriptive function to predict subsequent Beltrami surfaces $\nu(\bar{R})$, which are surfaces of equal potential. This means: A pair $(\nu, \bar{R})$ must be given for each desired ν-curve of the subsequent potential surfaces are obtained, *see* <u>*Fig.10-8 left.*</u> This part figure shows the change of the potential surface of the growing 'Yield' body with increasing ν in the elastic-plastic transition domain. The two center figures show the cross-section using the principal stresses and below the development of the yield body from the yellow egg ($\nu = \nu_0$) up to full yielding ($\nu = 0.5$).

10.9.2 Plastic porosity affected regime, an anticipation

Porosity causes a volume increase. This works oppositely as in the elastic-plastic transition regime, which can be described by Beltrami, too. Increasing porosity *f* means a decreasing Poisson's ratio *v* and

a more elliptic shape. In the outer figures of *Fig.10-10* both the regimes of the changing Poisson's ratio are displayed. The right part figure, modelled by Beltrami, pre-informs how the surface of the yield body changes its shape with decreasing *v* according to the increasing porosity *f*.

Fig.10-10(right) displays the development of the subsequent failure surfaces whereby an increasing true stress is considered. This is relevant for the critical material location. After achieving the tensile strength a small further radial increase of the surface is obvious together with the initiation of an increasing elliptic failure surface. With increasing degradation the subsequent surfaces become more and more elliptical. This is the opposite process regarding Beltrami in the elastic-plastic transition regime. A growing *f* means higher true stress but less cross-section or load-carrying material in the strain-controlled 'hot spot'.

The Beltrami formulation delivers an *Idea for the ductile porous regime* and is intended to replace the 'Gurson' formulation by Cuntze's so-called 'Extended Mises', reading

$$\frac{3J_2}{\bar{R}^t_{0.2}} + \frac{1-2\nu}{2+2\nu}\cdot\frac{I_1^{\,2}}{\bar{R}^t_{0.2}} = c^{\mathrm{Bel}} \quad \Rightarrow \quad \frac{3J_2}{\bar{R}^t_{0.2}} + c_{12}\cdot\frac{I_1^{\,2}}{\bar{R}^t_{0.2}} = c^{\mathrm{ExtMises}} \quad .$$

Also here, the yield strength can be used for normalization. The parameters c^{Bel}, c^{ExtMises} mark the size parameter of the changing potential surface.

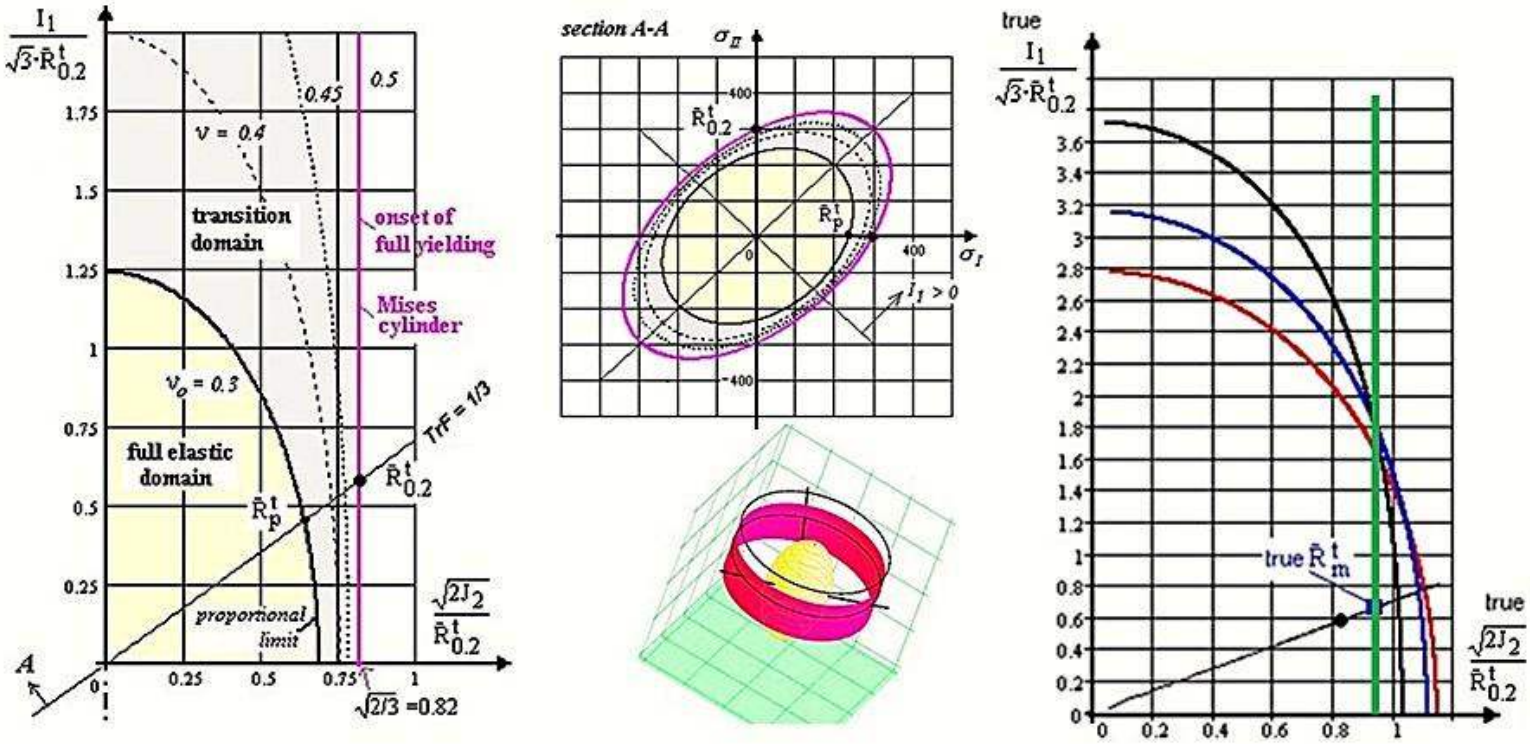

Fig.10-10: (left) Elastic-plastic transition domain, development of the Beltrami surfaces from egg shape (growing yield potential surface with ν_0 = 0.3 for metals (0 for foam = sphere) < ν < 0.5 ('Mises cylinder → J_2 = constant = incompressibility) depicted in Lode-Westergaard coordinates. (center) visualization of the Beltrami potential surfaces. (right) Change of potential surfaces in the porous domain computed with the Extended Mises formulation (see [CUN22, §17]*),* f = 0, 0.1, 0.2, 0.3

In order to understand the chosen Haigh-Lode-Westergaard coordinates *Fig.10-11* is provided. The vector $\{\sigma_{\mathrm{prin}}\} = (\sigma_I, \sigma_{II}, \sigma_{III})^T$ is a vector-addition of the principal stresses. The cone angle between all principal axes and I_1 is 54.75°.

Rendered by the 'Mises cylinder' (c =1) → Poisson's ratio ν drives the elliptic shaping!

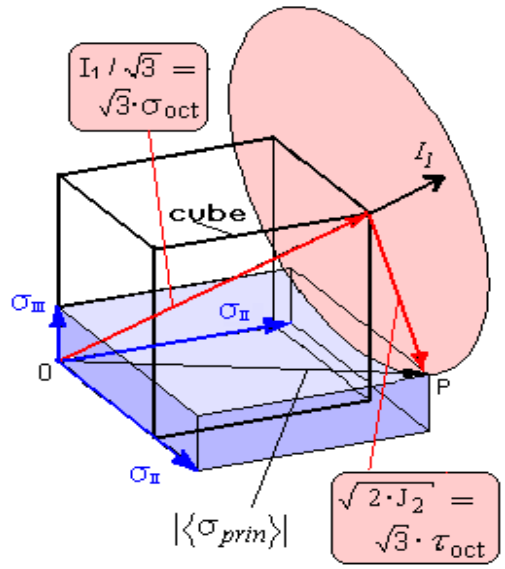

Fig.10-11:
Visualization of the used
Haigh-Lode-Westergaard coordinates
by the principal stresses acting at a material cube.

Octahedral stresses:

$$\sigma_{oct} = I_I / 3 \quad \text{with} \quad I_I = \sigma_I + \sigma_{II} + \sigma_{III}$$

$$\sigma_{eq}^{Mises} = \sqrt{3 \cdot J_2} = f(\tau), \text{ with}$$

$$6 \cdot J_2 = (\sigma_I - \sigma_{II})^2 + (\sigma_{II} - \sigma_{III})^2 + (\sigma_{III} - \sigma_I)^2$$

$$\tau_{oct} = \sqrt{6 J_2}/3 \text{ -}$$

Above coordinates $I_1/(\sqrt{3} \cdot \bar{R}_c)$ and $\sqrt{2 \cdot J_2} / \bar{R}_c$ have the advantage to possess the same scale in the full stress space.

To make more familiar with potential surfaces *Fig.10-11* presents two potential surfaces dedicated to different *Effs*, for the shape fracture *Eff* = 100% and for a loading that generates the shape *Eff* = 50 %.

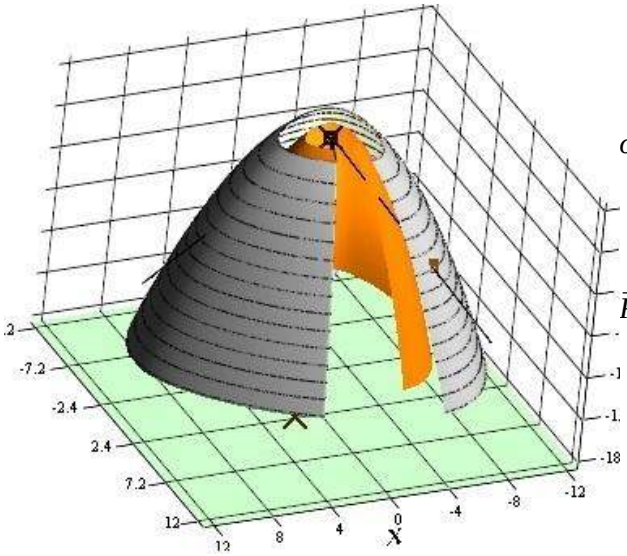

Fig.10-11:
Two potential surfaces. Eff is the measure for the distinct otential surface with Eff=1=100% the fracture surface. The potential surfaces are Eff^{SF}*=50%* *and*
Eff^{SF} *=100%* = *fracture.*
Indicated are the failure stress points
$\bar{R}^t = 4$ MPa, $\bar{R}^{tt} = 3$ MPa, $\bar{R}^c = 40$ MPa, $\bar{R}^{cc} = 49$ MPa
and the principle stress axes.
'Normal Concrete', 3D test data available

$$Eff^{SF} = c^{SF} \cdot \frac{\sqrt{4 J_2 \cdot \Theta^{SF} - I_1^2 / 3} + I_1}{2 \cdot \bar{R}^c}$$

LL:

** The shape of the potential surfaces in the plastic porosity regime changes oppositely to the shape in the elastic-plastic regime. Both the surface shapes one can dedicate to the change of the Poisson ratio v*

** In structural analysis the stresses are most-often determined in the elastic-plastic regime. This is performed very accurately, sometimes over-precise. However in this domain the Poisson's ratio changes significantly, which has a numerical influence and should be considered if over-precise.*

10.10 Post-Necking, a 'measurable parameters-based Extended-Mises' Model replacing 'Gurson'

Aim: *De-complication of highly non-linear plastic analyses by generation of a simplified model to perform Design Verification in a Ductile Metal's high Porous Regime.*

10.10.1 History of the 'Gurson-replacing' Idea

There is stress- and strain-controlled behavior.

Strain-controlled locations in a structure will not break, when the stress level reaches tensile strength R^t. A fuel-outlet hole in the upper tank of the Ariane 5 central stage was such a strain-controlled case at MAN, where the vicinity of the 'overstrained' critical material location takes over the reduced loading capability. No direct fracture is to face.

This task caused MAN-Technologie to perform an analysis together with IWM Freiburg applying a multi-parameter 'Gurson' yield model (such a model is a model of the *Continuum (micro-)Damage Mechanics theory in the ductile materials regime)*. However, its 'fictitious' model parameters cannot be measured directly, but are usually determined by a FE analysis which best models the deformation of the test specimen, a classical simulation process. An example for such a multi-parameter set, determined for the applied aluminum alloy AA2219 and by using the tensile rod test specimen, is given in the table below [*IWM Freiburg*]:

f_0	f_n	f_c	f_F	q_1	q_2	ε_n	s_n
0.00	0.05	0.04	0.15	1.5	1.0	0.20	0.01

.

The applied 'Gurson'-model of the IWM was a refined one, namely the so-called 'GTN-model'. Refinement means that more parameters are to determine than for a simpler 'Gurson' model. Therefore, the optimal model parameter set *of a 'Gurson' model* depends on the FE-mesh fineness and has to be inversely determined by an excellent simulation of the test specimen's behavior, see <u>*Fig.10-12, left*</u> for the tensioned rod.

Using 'Gurson' model results, the responsible design engineer must ask:

What about the scatter of the simulation-won parameters which are to insert in the analysis?

Without knowledge of the scatter there is not a generally accepted design verification possible. Might it be not better to apply a simpler model with minimum parameters at dispense of the little gain of the last load carrying portion after coalescence at 'onset-of-ductile cracking' marked by the corresponding strength value R_{odc}? This is the 'technically relevant point', where the coalescence of voids begins. Only a reduced procedure with directly measurable model parameters has the chance to capture the statistical Design Verification requirements.

In the context above the question comes up:

"*How much Gurson material modelling is necessary to achieve a reliable prediction of the <u>local</u> design-deciding ductile fracture level of the structure?"*

This failure mode 'ductile fracture' is defined here to be met at 'onset-of-ductile cracking' and it shall correspond to Design Ultimate Load. Such an application is a seldom case, where the deformation-controlled strength value $R_{odc} > R^t$ is used to *save the final design*, which is not anymore possible via the load-controlled strength value R^t. A simpler model is required. Two challenging parts tasks are thereby faced:

(1) Creation of a model simpler than a multiple-parameter 'Gurson' model, and

(2) Capture of the porosity *f* in the equivalent σ-ε-curve**,** to be provided, whereby *f* is an additional but measurable model parameter transferring the 'Mises' model to the 'Extended Mises' model. For its derivation, various micromechanical mechanisms during ductile fracture are of interest:

* Void nucleation in the test rod at so-called second phase particles by debonding

* Void growth, controlled by stress Triaxiality Factor *TrF* and growing plastic strain ε_{eq}^{pl}, and

* Coalescence of voids by internal shear stress-driven rod necking with final ductile rupture.

For the evaluation of the usual rod test results, the widely used correction formula of P.W. Bridgman is employed. *Fig.10-12(left)* presents the dependency of the rod's diameter reduction on the load *F* and further shows simulation curve and test curve. The measurement of the diameter reduction is mandatory beyond the 'end of uniform elongation' at the tensile strength point $\bar{R}^t = max\, F / A$, depicting the 'onset-of-diffuse necking $_{oon}$ point and experiencing full plasticity. Beyond $\bar{R}^t$ only true values represent the reality.

In the load-controlled regime axial strain measurements are performed whereas in the transversal, plastic strain-controlled necking regime diameter reduction measurements are to execute. In the *Fig.10-12(right*) attention is drawn to the various stress-strain curves used and to the associated strengths. Displayed are the mean technical and mean true strengths together with the associated Design Allowables.

If metal materials do not fail when the tensile strength is reached, then this is accompanied by the fact (*Fig.10-12, left)* that max*F* does not essentially change over a certain range of the strain because hardening still works until a slight kink will occur due to void coalescence and destruction of piled–up dislocations. Degradation wins over hardening at the 'onset of ductile cracking' strength point R_{odc}. R_{odc} and marks the coalescence-linked kink and is defined here as the critical strength.

Mind: $F(\Delta d)$ is not completely of the same shape like $true\sigma(true\varepsilon)$.

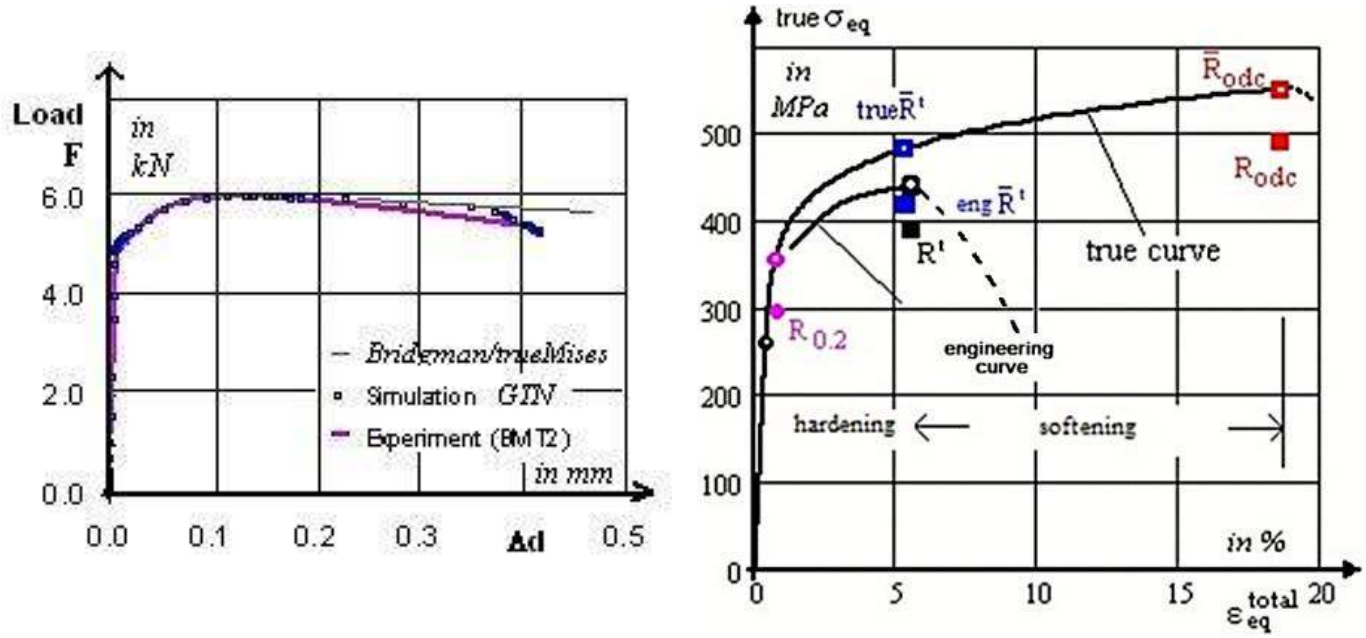

Fig.10-12, material AA2219:

(left) Dependency of diameter reduction Δd on the applied load F. Comparison of global simulation and test results (IWM Freiburg, Dr. Sun). GursonTvergaardNeedleman-model used.

(Gurson A L: *Continuum Theory of Ductile Rupture by Void Nucleation and Growth. Part 1:Yield criteria and flow rules for porous ductile media*. J. Eng. Mater. Techn.99 (1977), 2-15)

(right) Ramberg-Osgood-mapped true and engineering stress-strain curves. (A bar over R indicates a mean value, no bar over R indicates the strength 'design allowable')

Table 10-5 presents the Determination of the model parameters, single mode view, no 120°-rotationally symmetry considered here.

Table 10-5, Isotropic materials: Determination of model parameters, single mode view

* Modelling Functions F describing a subsequent potential surface

elastic-plastic	plastic	plastic porous
Beltrami	Hencky-'Mises'-Huber	'Gurson' type

$$\bar{R}^t_{prop} < \sigma_{\mathrm{Bel}} < \bar{R}^t_{0.2} \quad \leftrightarrow \quad \bar{R}^t_{0.2} < \sigma_{\mathrm{Mis}} < \bar{R}^t_{m} \quad \leftrightarrow \quad \bar{R}^t_{m} < \sigma_{eq} < \bar{R}^t_{\mathrm{odc}}$$

stress - controlled *strain – controlled*

σ : = running variable of the subsequent potential surfaces

$$\bar{R}^{t\ 2}_{prop} / \bar{R}^{t\ 2}_{0.2} < c^{\mathrm{Bel}} < 1 \quad \leftrightarrow \quad 1 < c^{\mathrm{Mis}} < \bar{R}^{t\ 2}_{m} / \bar{R}^{t\ 2}_{0.2}$$

ellipsoid → cylinder → ellipsoid

$$I_1 = (\sigma_I + \sigma_{II} + \sigma_{III}) = \mathrm{f}(\sigma)\ ,\quad 6J_2 = (\sigma_I - \sigma_{II})^2 + (\sigma_{II} - \sigma_{III})^2 + (\sigma_{III} - \sigma_I)^2 = \mathrm{f}(\tau)$$

$$\frac{3J_2}{\bar{R}^{t\ 2}_{0.2}} + \kappa \cdot \frac{I_1^{\ 2}}{\bar{R}^{t\ 2}_{0.2}} = c^{\mathrm{Bel}} \leftrightarrow \quad F^{Mis} = \frac{3J_2}{\bar{R}^{t\ 2}_{0.2}} = c^{\mathrm{Mis}},\ \kappa = \frac{1-2\nu}{2+2\nu}$$

Insertion of a (measurable) normalizing strength, yield strength point with $\nu = 0.5 \rightarrow \kappa = 0$

$$\mathrm{F}^{Bel} = \frac{3\bar{R}^{t\ 2}_{02} / 3}{\bar{R}^{t\ 2}_{02}} + \kappa \cdot \frac{\bar{R}^{t\ 2}_{02}}{\bar{R}^{t\ 2}_{02}} = c^{\mathrm{Bel}} * \rightarrow c^{\mathrm{Bel}} = 1 + \kappa = 1, \text{ and } \kappa \text{ an elliptic shape parameter}$$

* Strength FailureCriteria (SFC), $\bar{R} \rightarrow R$, (with $\Theta = 1$ for full rotational symmetry)

R : = strength design allowable, marking a special potential surface ≡ design limit state

elastic, very brittle	ductile	very ductile

$$Eff = \frac{\sigma_I}{\bar{R}^t_m} = 1\ * \quad \leftrightarrow \quad Eff = \frac{3J_2}{\bar{R}^{t\ 2}_m} = 1 \quad \leftrightarrow \quad Eff = \frac{3J_2}{\bar{R}^{\ 2}_{\mathrm{odc}}} + \mathrm{c}_{12} \cdot \frac{I_1^{\ 2}}{\bar{R}^{\ 2}_{\mathrm{odc}}} - 2\, f_{odc} = 100\%.$$

For similarity reasons: for the 2 modes Normal Fracture NF , Shear Fracture SF (brittle)

and after inserting $\sigma = R \cdot Eff$ and dissolving for Eff follows

$$\mathrm{I}_1 > 0 : F^{NF} = 0.5 \cdot \frac{\sqrt{4J_2 - I_1^{\ 2}/3} + I_1}{2 \cdot \bar{R}^t} = 1 \ ;\ Eff^{NF} = 0.5 \cdot \frac{\sqrt{4J_2 - I_1^{\ 2}/3} + I_1}{2 \cdot \bar{R}^t}$$

$$\mathrm{I}_1 < 0 : F^{SF} = c_1^{SF} \cdot \frac{3J_2}{\bar{R}^{c2}} + c_2^{SF} \cdot \frac{I_1}{\bar{R}^c} = 1; \ Eff^{SF} = \frac{c_2^{SF} \cdot I_1 + \sqrt{(c_2^{SF} \cdot I_1)^2 + 12 \cdot c_1^{SF} \cdot 3J_2}}{2 \cdot \bar{R}^c} = \frac{\sigma^{SF}_{eq}}{\bar{R}^c}$$

$c_1^{SF} = 1 + c_2^{SF}$ with direct consideration of the Poisson ratio $c_2^{SF} = (1 + 3 \cdot \mu) / (1 - 3 \cdot \mu)$

Last unknown to be searched is the elliptic shape linked parameters such as c_1^{SF} by insertation of a bi-axially compressive failure stress or a fracture angle $\mu = \cos(2 \cdot \theta^c_{fp}{}^\circ \cdot \pi / 180)$.

10.10.2 Bridgman-3D Correction of the true σ-ε-Curve employing 'Mises'

Equivalent stress transition: $\mathrm{true}\sigma_{ax} \rightarrow \mathrm{true}\sigma_{eq}$

The validity of the uniaxial stress-strain curve measured in the smooth tensile rod test is terminated at the load-controlled strength point $\mathrm{max}\sigma_{\mathrm{true}} = \bar{R}^t = max\, F / A$, which corresponds to the maximum load F and to the actual minimum cross section of the neck. However, beyond $\bar{R}^t$ ('end-of-uniform-

elongation') at the 'onset-of-diffuse necking $_{odn}$' point the 1D-stress situation in the tensile rod becomes a 3D one and an equivalent stress σ_{eq} has to be considered in order to capture the 3D spatial stress.

Under tensioning, in the plastic regime the lateral contraction of the material at the center of the neck is impeded by neighboring material leading to a 3D-stress state. Hence, a simple extrapolation of the F/A (σ-ε)-curve beyond $\bar{R}^t$ cannot provide a physically accurate curve, because the necking-generated 3D-residual stress state σ_{hyd} is to consider in the evaluation of the tensile rod test results in order to obtain a real σ_{eq}. The three stresses within σ_{eq} reach their maximum values at the center of the rod's cross-section with an approximately equal value $\sigma_{radial} = \sigma_{hoop}$, except close to the surface, as depicted in *Fig.10-13(left)* below. The values of σ_{radial}, σ_{hoop} and of the created necking radius ρ raise with σ_{ax}.

The former F/A-quantified capacity becomes continuously reduced with increasing necking. Hence, the true stress-strain F/A curve is to correct to obtain a realistic equivalent stress. In the center of the rod an increasing stress Triaxiality Factor *TrF* is faced.

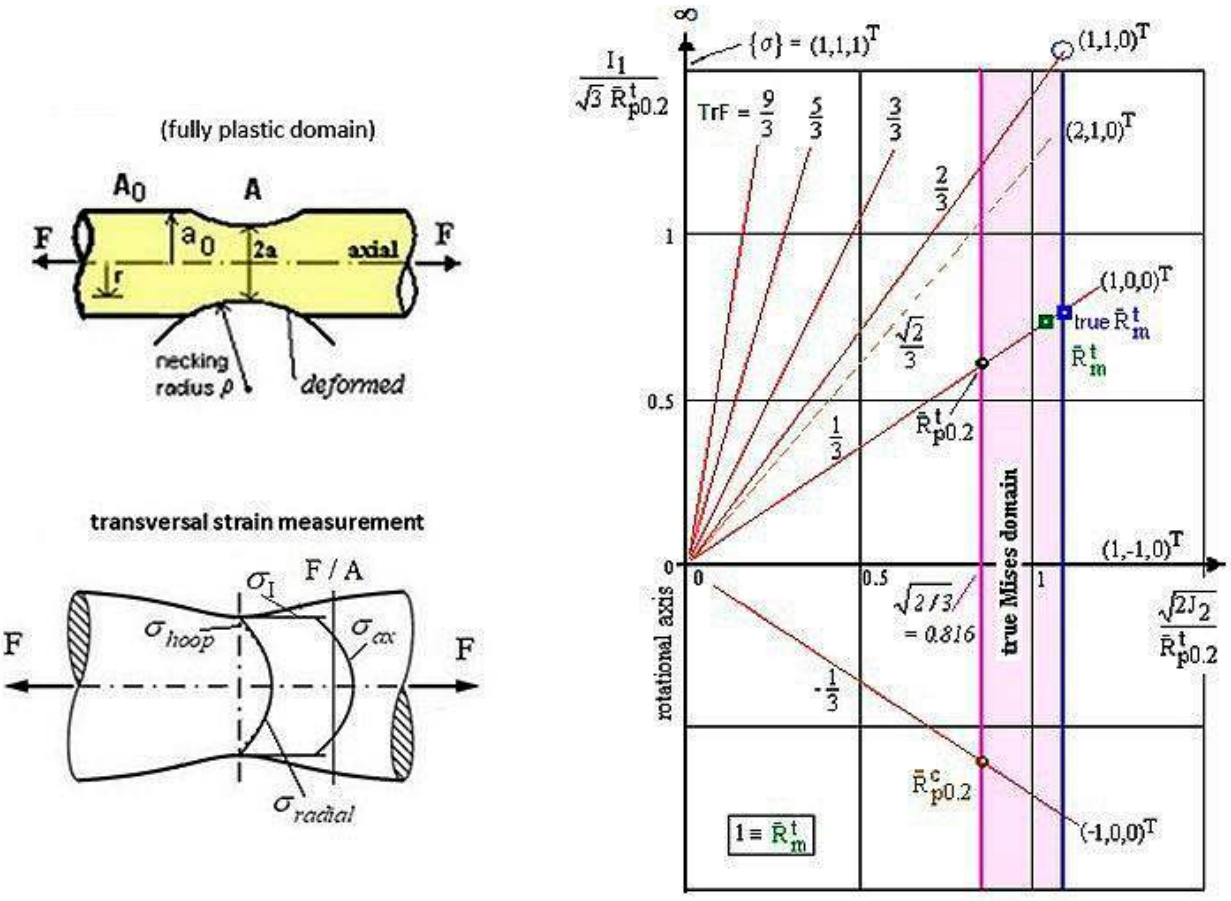

Fig.10-13: (left) Stresses and transversal (radial) strain measurement of the necked round tensile rod. F:=force, A:= minimum actual cross section of the neck. F:=Force F_{ax}, A_0 := original cross-section. $\bar{R}^t = \max F / A_0$, $\varepsilon \le \bar{A}_{gl}$ (permanent strain linked to load-controlled fracture at $\bar{R}^t$). Necking radius is ρ. (right) Schematic visualization of the Triaxiality Factor TrF, responsible for failure in the rod center

$$\{\sigma\} = \{\sigma_I, \sigma_{II}, \sigma_{III}\}^T,\ TrF\{\sigma_I, \sigma_{II} = \sigma_I, 0\}^T = 2/3.$$

Assuming a constant σ over the rod's cross-section, *Fig.10-13(right)* illustrates by a variety of *TrF*-beams that values higher than 2/3 (bi-axial stressing) are practically not possible to test. Assuming constancy is not anymore the case for a plastic rod neck, where the failure decisive location is the center

of the cross-section with also facing there *maxTrF*. Notched test specimens are sometimes applied to capture higher multi-axial stress states with *TrF*-values > 1/3.

Fig.10-14 shows the void volume fraction in the necking region at failure. The highest values are reached in the center of the specimen (Element 20) as expected, *TrF* is highest. From the central region micro-damage spreads out over the whole cross section.

Basic task now will be the necessary transfer from the uniaxial trueσ_{ax}(trueε_{ax}) to the → tri-axial trueσ_{eq} (trueε_{eq}) in the diffuse necking regime. Bridgman provided a correction means how to adjust trueσ_{ax}, but had to make some essential assumptions:

(1) The cross section of the necked region remains angular *(like the 'Mises' cylinder, assuming a rotationally symmetric yield body*).

(2) The inner axial contour of the neck can be approximated by the arc of a circle with the radius ρ.

(3) 'Mises' can be applied (*effect of growing voids is therefore not considered*).

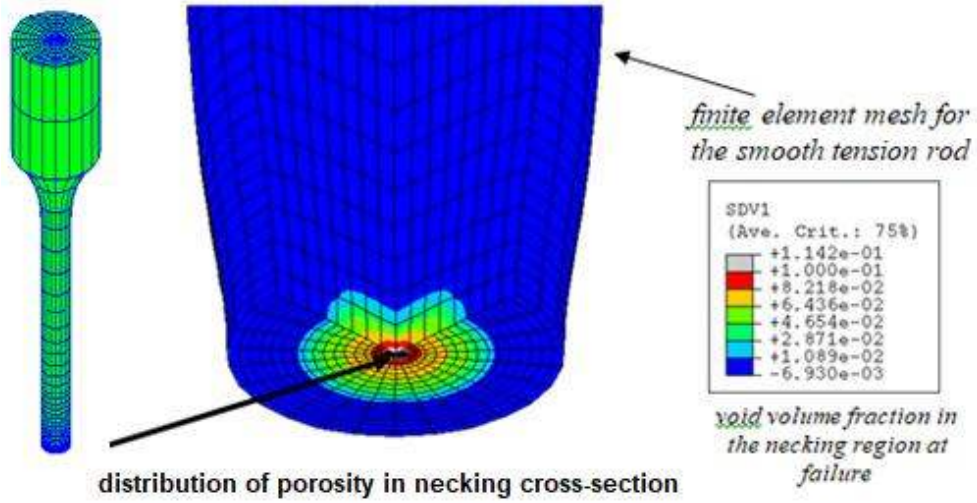

Fig.10-14, material source, AA2219 variant, T2:

Finite element mesh of a tensile rod with porosity distribution in the 'Hot spot' center of the rod. Void volume fraction f in the necking region at failure [Sun97, IWM 7] stresses in MPa, strains in %.

$\rho_{initial} = \infty$, *2 a = 4mm, elasticity properties are E =70000MPa, v = 0.3, t = 6 mm plate. Sample size n = 179, A5 = 7.4 %, Z = 20 %*

Due to the diffuse necking, an axial load increase-caused internal hydrostatic *tensile* stress state σ_{hyd} is generated, representing a deformation-dependent residual stress state. Its radial distribution can be Mises-based estimated - under the axial loading $\{\sigma\} = (\sigma_I, \sigma_{II}, \sigma_{III})^T = (F/A, 0, 0)^T$ - after Bridgman by $\sigma_{hyd}(r) \approx \sigma_I \cdot ln\left(1 + \frac{a^2 - r^2}{2 \cdot a \cdot \rho}\right)$ with $\sigma_I < \frac{F}{A} = \frac{F}{\pi \cdot a^2}$, *Table 10-5 left*

with *F*:= load, *a*:= radius of actual cross section of neck, ρ:= radius of neck curvature and F/A an integral quantity capturing the external loading *F* .

Table 10-5: Bridgman-Derivation of the cross-section quantities of the tensioned rod

$$\frac{F}{A} = 2 \cdot \int_0^a \sigma_{ax}^t \cdot \pi \cdot r \cdot dr \,/\, (\pi \cdot a^2)$$

$$= 2 \cdot \int_0^a (\sigma_I + \sigma_I(r)) \cdot \pi \cdot r \cdot dr \,/\, (\pi \cdot a^2)$$

$$= 2 \cdot \int_0^a (\sigma_I + \sigma_I \cdot \ln(1 + \frac{a^2 - r^2}{2 \cdot a \cdot \rho})) \cdot \frac{\pi \cdot r \cdot dr}{\pi \cdot a^2}$$

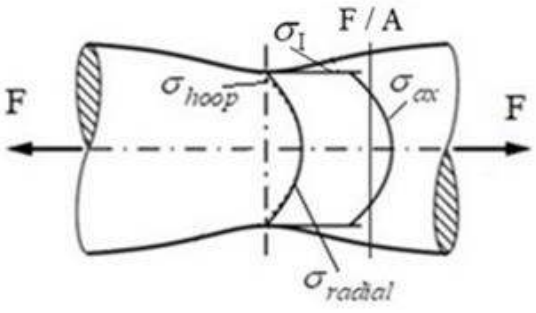

The full set of relevant relations then reads:

$\sigma^{t}_{ax}(r) = \sigma_I + \sigma_{hyd}(r)$ and $\sigma_{radial}(r) \approx \sigma_{hoop}(r) = \sigma_{hyd}(r)$ and as equivalent stress follows

for a single stress $\rightarrow \sigma^{Mises}_{eq} = \sqrt{3 \cdot J_2} = \sqrt{\frac{1}{2}} \cdot \sqrt{\left[(\sigma_I)^2 + (0)^2 + (-\sigma_I)^2 \right]} = \sigma_I$ and also

for a superimposed $\sigma_{hyd} \rightarrow \sigma^{Mises}_{eq} = \sqrt{3 \cdot J_2} = \sqrt{\frac{1}{2}} \cdot \sqrt{\left[(\sigma_I - \sigma_{hyd})^2 + (\sigma_{hyd} - \sigma_{hyd})^2 + (\sigma_{hyd} - \sigma_I)^2 \right]} = \sigma_I$

$I_1 = max\,\sigma^{t}_{ax} + max\,\sigma_{radial} + max\,\sigma_{hoop} = \sqrt{3 \cdot J_2} + 3 \cdot \sigma_{hyd}$, $\sqrt{3 \cdot J_2} = \sigma_I$ ($\leftarrow$ no σ_{hyd} effect).

$TrF(r) = true\sigma_{mean} / true\sigma^{Mises}_{eq} = (I_1/3)/\sqrt{3J_2} = \left[\sqrt{2}/3\right] \cdot (I_1/\sqrt{3})/\sqrt{2J_2} = \frac{1}{3} + \frac{\sigma_{hyd}}{\sigma_I}$.

Decisive for failure in the rod is the still mentioned *TrF*, which increases with the true axial loading. Its maximum is in the center 'hot spot' $r = 0$. In this micro-damage critical cup-cone center the 3D-state of stresses reads

$$max\sigma_{hyd}\ (r=0) = \sigma_I \cdot ln\ (1 + \frac{a}{2 \cdot \rho}),\quad max\sigma^{t}_{ax}(r=0) = \sigma_I + max\sigma_{hyd}$$

with the stress state in the rod's center $\{\sigma\} = (\sigma_I + max\sigma_{hyd}, \max\sigma_{hyd}, \max\sigma_{hyd})^T$.

In the necessary adjusting process of the F/A-curve in the diffuse necking regime the first step is to integrate the axial stress, which varies over the radius. From load balance the following relations are yielded in the following *Table.* Herein, the last unknown is the neck radius ρ. It could be computed during testing by measuring the shape change of the neck via a real-time Digital Image Correlation (DIC) 3D full-field measurement optical technique of the surface strains and an associated surface geometry model.

integrated follows $\frac{F}{A} = \sigma_I \cdot (1 + \frac{2\rho}{a}) \cdot \ln(1 + \frac{a}{2\rho})$ with $\sigma^{Mises}_{eq} = \sqrt{3 \cdot J_2} = \sigma_I$

$\sigma_I = \sqrt{3 \cdot J_2} = \sigma^{MisBri}_{eq} = \frac{F}{A} / (1 + 2 \cdot \rho/a) \cdot \ln(1 + a/2 \cdot \rho)$, valid $> \bar{R}^t$ or $A < Aoon$,

an equation, in which the ratio a/ρ is not known.

If no test result is available, then Lorrek-Hill's approach for rupture is applied at $\bar{R}_{rodc}$:

$$\text{maximum}\ \frac{a}{\rho} = \sqrt{\ln(\frac{A_0}{A_{rupt}}) - \ln(\frac{A_0}{A_{oon}})}\quad ,\ \frac{A_{rupt}}{A_0} = 1 - Z \quad \text{with a}$$

given cross section reduction Z in % at maximum necking at $\bar{R}_{rupt}$

and A_{oon} the cross section at $\bar{R}^t \equiv \bar{R}^t_m$, being 'Onset-of-(diffuse) necking'.

$$\frac{a}{\rho} = c_1 + c_2 + true\varepsilon_{ax} R_{odc}{}^2 + c_3 \cdot true\varepsilon_{ax} R_{odc}{}^3.$$

or presenting a more general insight the corresponding equivalent strains shall be mentioned.

Equivalent strain transition: trueεax → trueεeq

For the Mises equivalent strain is valid in the plastic domain (elastic part is negligible):

$$\varepsilon_{eq}^{Mises} = \frac{\sqrt{2}}{3}\cdot\sqrt{(\varepsilon_I-\varepsilon_{II})^2+(\varepsilon_{II}-\varepsilon_{III})^2+(\varepsilon_{III}-\varepsilon_I)^2} = \frac{\sqrt{2}}{3}\cdot\sqrt{(\varepsilon_I{}^{pl}-\varepsilon_{II}{}^{pl})^2+(\varepsilon_{II}{}^{pl}-\varepsilon_{III}{}^{pl})^2+(\varepsilon_{III}{}^{pl}-\varepsilon_I{}^{pl})^2}$$

considers plastic volume constancy (incompressibility) $\Sigma\varepsilon_i^{pl} = 0$ during plastic deformation it becomes

$$\varepsilon_I{}^{pl}/2 = -\varepsilon_{rad}{}^{pl} = -\varepsilon_{tan}{}^{pl} \text{ and } \varepsilon_{rad}{}^{pl} = ln(r/a) = \varepsilon_{tan}{}^{pl} \Rightarrow \varepsilon_I{}^{pl} = -2\cdot ln(r/a) \text{ and it reads}$$

$$\text{true}\varepsilon_{eq}^{Mises} = \frac{\sqrt{2}}{3}\cdot\sqrt{((\varepsilon_I{}^{pl}+\varepsilon_{rad}{}^{pl})-\varepsilon_{rad}{}^{pl})^2+0+(\varepsilon_{rad}{}^{pl}-(\varepsilon_I{}^{pl}+\varepsilon_{rad}{}^{pl}))^2} = \frac{\sqrt{2}}{3}\cdot\sqrt{2\varepsilon_I{}^{pl2}} = \frac{2}{3}\cdot\varepsilon_I{}^{pl}.$$

LL:

** Bridgman correction = approach, which considers the varying stress over the rod's cross-section regarding that the center is the critical line*

** Lorrek-Hill = approach, which formulates a final value for the change of the curvature radius under loading. The increasing curvature triggers the increasing hydrostatic stress and this is to map*

** Measured ratio F/A = stress capacity smeared over the cross-section = load ability-quantity, which represents an effective (smeared) value, which decays with increasing axial strain*

** $\sigma_I \equiv \sqrt{3J_2}$ = constant basic stress quantity of the Bridgman approach, see Table 15-1*

** The applicability of axial measurement ends with 'End-of-uniform elongation' at $\bar{R}^t$*

** Bridgman model application is limited to about 30% cross-section reduction, due to not considering the coalescence of the voids*

** The Bridgman-correction is applied by using the 'Mises' yield function and not a 'Gurson'-type void growth-capturing (porosity f) yield function. This led the author 20 years ago to propose his so-called 'Extended Mises' yield condition at the end of a joint Research program MAN with IWF-Freiburg.*

** The 'Mises' cylinder is a simplification*

** Increasing porosity also means decreasing Poisson's ratio ν.*

10.10.3 Porosity-improved Bridgman 3D-corrected True σ-ε-Curve employing 'Extended Mises'

Idea:

The replacement of a 'Mises'-based Bridgman correction by a porosity-considering one should lead to a more realistic stress-strain curve and should offer the advantage to escape in the analysis from the high number of non-measurable 'Gurson' model parameters except from *f*.
In order to consider the void growth, the author proposes to replace the Bridgman-corrected Mises-model by the mentioned porosity-capturing ***'Extended Mises**-model*'.

Porosity means volume change due to void coalescence. Such a volume change can be transferred to a decaying Poisson's ratio as it is known from Beltrami. The author experienced, that the usual 'Gurson'-analyses base on a 'Mises'-linked equivalent stress-equivalent strain curve. This should be improved when considering the porosity *f*. The author's hypothesis from 2002 reads:

* Formulation of an egg-shaped yield model, termed Extended Mises, with

* Simplification to 1 measurable 'Gurson' parameter f, only

* Improvement of this simpler model idea by applying a porosity-capturing equivalent $\sigma - \varepsilon$ curve

* Taking a simple 'Gurson' yield model to obtain via a 'comparison of coefficients' a relation to the porosity f in the simple 'Gurson' -model from Gurson-Tvergaard-Needleman, index ^{GTN}

* Probable 120°-material symmetry in the high porosity regime is not documented and therefore not considered. It could be captured by replacing $\frac{3J_2}{\bar{R}^2}$ through $\frac{3J_2}{\bar{R}^2}\cdot\Theta$.

It is known:

*Values for the increasing porosity *f* are strain-controlled detectable.

*The effect of a probably initially not pore-free material is captured in the initial property values.

10.10.4 Measurement of Tensile Rod failure stresses and Estimation of Failure Body Vertex

Even for a porous plastic failure body its vertex should be known from theoretical reasons. A vertex represents the equi-triaxial tensile strength capacity of a load-controlled strength situation, remind *Fig.10-2*. Because the vertex stress state $\{\sigma\} = (\text{true}\bar{R}^{ttt}, \text{true}\bar{R}^{ttt}, \text{true}\bar{R}^{ttt})$ with $TrF = \infty$ practically cannot be measured as best substitute a 3D-stress state - closest possible to the vertex - must be employed. Realistic is a stress state $(\text{true}\sigma_{ax} + \sigma_{hyd}, \sigma_{hyd}, \sigma_{hyd})$ by investigating the center of an un-notched tension rod test specimen, being the 'hot spot' in this test specimen.

In such un-notched rods a neck radius builds up and increases with further increasing axial tensile stress. Due to the diameter reduction a hydrostatic stress state is generated and can be determined from the zero volume strain regime faced in the minimum neck cross-section. Hereby, difference due to rolling of the sheet material and how the test specimen is cut out are neglected and full isotropy assumed.

From the test rig loading comes the subsequently effective stress 'trueσ_{ax}', whereas the remaining neck cross-section experiences in the center the multi-axial stress state $(\text{true}\sigma_{ax} + \sigma_{hyd}, \sigma_{hyd}, \sigma_{hyd})$, is to estimate by the Bridgman model. In order to better understand the stress situation in the rod center the effect of increasing σ_{hyd} is of interest, depicted below. It is to conclude from mechanics, that a hydrostatic stress does not change Mises's representative invariant J_2 for shape deformation of the solid. However, σ_{hyd} affects the tri-axiality value *TrF* which might be interpreted to cause some quasi-embrittlement of the material:

$$I_1 = (\sigma_I + \sigma_{II} + \sigma_{III}) = \text{f}(\sigma)\ ,\quad 6J_2 = (\sigma_I - \sigma_{II})^2 + (\sigma_{II} - \sigma_{III})^2 + (\sigma_{III} - \sigma_I)^2 = \text{f}(\tau)$$

$$(\text{true}\sigma_{ax} + \sigma_{hyd},\ \sigma_{hyd},\ \sigma_{hyd})\ ,\quad \sigma_{ax}^{t}(r) = \sigma_1 + \sigma_{hyd}\ (r)$$

$$\sigma_{eq}^{Mises} = \sqrt{3J_2} = \sqrt{3}\cdot\sqrt{(\sigma_1^{M.} - \sigma_{h.} - \sigma_{h.})^2 + 0 + (\sigma_{h.} - \sigma_1^{M.} - \sigma_{h.})^2} \quad\rightarrow\quad \sigma_{eq}^{Mises} = \sigma_1^{Mises}$$

$$TrF = \sigma_{mean} / \sigma_{eq}^{Mises} = (I_1/3)/\sqrt{3J_2} = \left[\sqrt{2}/3\right]\cdot(I_1/\sqrt{3})/\sqrt{2J_2}$$

$$I_1 = (\text{true}\sigma_{ax} + 3\sigma_{hyd}) = \text{f}(\sigma)\ ,\quad 6J_2 = (\sigma_I - \sigma_{II})^2 + (0)^2 + (\sigma_{III} - \sigma_I)^2 = \text{f}(\tau)$$

uni-axial σ_{ax}, multi-axial $(\sigma_{ax} + \sigma_{hyd}, \sigma_{hyd}, \sigma_{hyd})$ in the rod's minimum neck section $\Rightarrow \sigma_{eq}^{Mises}$.

Again: The use of notched rods is principally also possible but considering that the original notch radius ρ increases. Thereby the critical rod surface stress concentration reduces a little and the originally surface-located critical material location moves to the center. *Fig.10-15(left)* shall display different stress states and the associated points on the respective *TrF*-beams. In the subpicture down left the indicated 2D stress-states and up left further the 3D stress states all collected in the table right down.

Of interest for the designing engineer is that the spatially formulated SFC F^{NF} = 1 dents the failure body at the pressure vesessel situation $\{\sigma\} = (2,1,0) \rightarrow TrF = \sqrt{2}/3$, *Fig.15-2* and *15-9*. Remember: In the 2D principal stress plane F^{NF} is a straight line and in the 3D failure body a hyperbola!

Fig.10-15 shall make the non-linear development of *TrF* more clear and further make familiar with the design failure surfaces in the very ductile regime.

The figure schematically shows that the strain-controlled failure surface is outside and thereby larger than the load-controlled one.

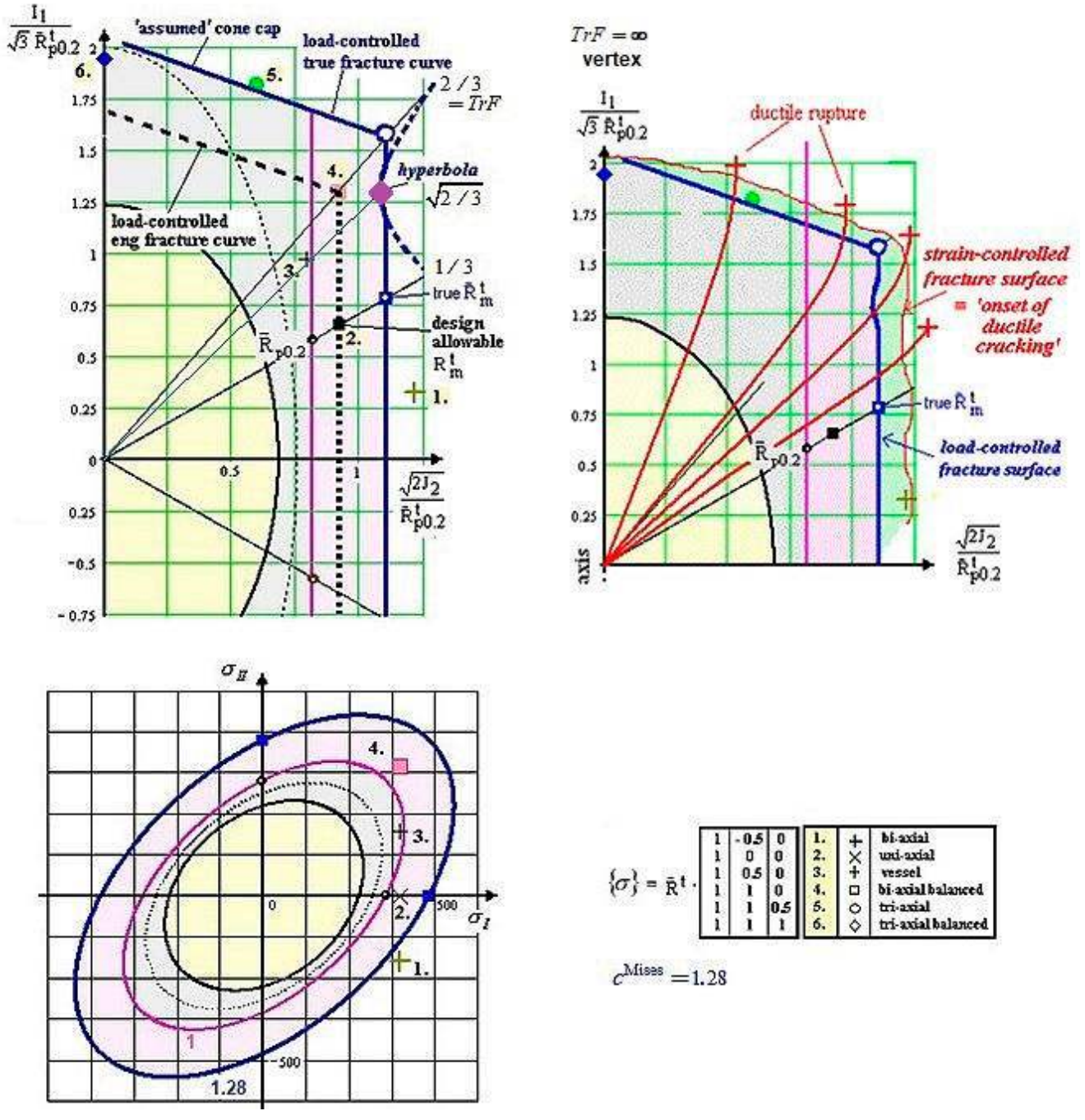

Fig. 10-15: Visualization of the effect of the TrF-beams and the related strengths, illustration of some stress state points and failure zones. 2D-potential surfaces on the inclined cross-section of the rot.-symmetric failure body

Practical engineer's two questions:

How far may the simple one parameter Mises be applied?

Isn't a two parameter Extended Mises sufficient enough to capture the technically interesting domain below R_{odc} ?

10.10.5 Proposal of the Two Parameter 'Extended Mises' Yield function in the Porosity domain

Extended Mises yield potential function

Originally, Gurson proposed for a metal, containing well distributed voids, a yield condition-based solution for a single spherical void. The model was modified later by Tvergaard and Needleman F^{GTN}, including the porosity f and the increasing Flow stress σ_F of the 'matrix' material (smeared): The porous body, called bulk material (= *smeared material*), consists of the matrix material and the voids or pores. The voids are nucleated in tension, only. The dense matrix phase follows the HMH ('Mises') model, and f represents the mean void volume fraction or porosity (*average value of a porous matrix*) as the so-called internal (micro-)damage variable. For $f = 0$, fully dense material, the model reduces to that of von Mises, whereas a ultimate value f_{ult} implies that the material is ultimately voided and that it has lost its stress carrying capacity due to local ductile rupture. Here f_{ult} shall be replaced by the smaller $f_{odc} = f_{crit}$ as practical technical limit. Values for the increasing porosity f are strain-controlled detectable. *Table 10-6* describes the procedure how a relationship between the subsequent 'Gurson' type yield model and the 'Extended Mises' model was developed. A further equation is needed to determine the size parameter, such as with c_{Mises} of the 'Mises cylinder'. The growing potential yield surface comes to its end at rupture fracture.

Void Porosity-linked reduction of Poisson's ratio $0.5 > \nu$

Porosity means volume change due to void coalescence and volume change may be transferred to a decaying Poisson's ratio after Beltrami. From the ExtM-model can be geometrically deduced

$$f^* = f \cdot q_2^2 \quad \text{and} \quad \nu = (4 - f^*) / (8 + 2 \cdot f^*).$$

Fig. 10-16 points out how the Poisson ratio is linked to the true strains (left), schematically to the true equivalent stress (center scheme), and to the porosity f^* right.

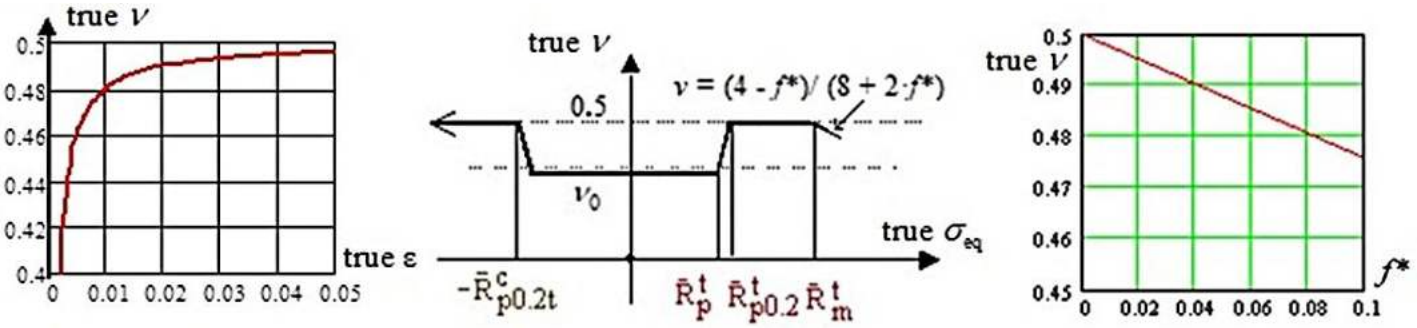

Fig. 10-16: Dependence of ν on the different parameters, the various regimes

Here, $f_{ult}\ (\bar{R}_{odc}) < f_{rup}$ is employed as that critical porosity which was dedicated by the author to 'Onset of ductile cracking', in order to 'remain on the safe side'. The evolution function of f is assumed to follow an exponential course with practically $f = 0$ at the tensile strength point up to the defined ultimate value f_{ult} located at $\bar{R}_{odc}$.

10.10.6 Visualization of a specific 'Gurson'-model versus the 'Extended Mises'-model

Failure conditions enable the designer to assess multi-axial states of stress $\{\sigma\}$ by an equivalent stress σ_{eq} and to map multi-axial stress-strain behavior $\sigma_{eq}(\varepsilon_{eq})$ via a measured, smeared stress F/A.

For $f = 0$, fully dense material, the model reduces to that of HMH, whereas a maximum value f_{ult} implies that the material is ultimately voided that it loses its stress carrying capacity due to local ductile rupture.

Table 10-6: 'Comparison of Coefficients' of the models 'Gurson' ↔ 'Extended Mises' with σ_F as increasing true Flow stress as running stress variable

$F^{GTN} = \frac{3J_2}{\sigma_F^2} + 2\cdot f\cdot q_1 \cdot cosh\left(\frac{I_1\cdot q_2}{2\cdot\sigma_F}\right) + q_3\cdot f^2 = 1$ ductile micro-damage failure function,

simplified to $\frac{3J_2}{\sigma_F^2} + 2\cdot f\cdot cosh\left(\frac{I_1\cdot q_2}{2\cdot\sigma_F}\right) + f^2 = 1$; for idea demonstration: $q_3 = q_3 = 1$, $q_3\cdot f^2 <<$

If the cosh-function is replaced by the first two terms of the associated Taylor row [*Cun*98,*Cun*01]

$cosh\, x = \pm\,(1 + x^2/2 + ...) \rightarrow \cosh(I_1\cdot q_2/2\cdot\sigma_F) = \pm\,(1 + (I_1^2\cdot q_2^2/8\cdot\sigma_F^2) + ..)$.

The negative sign is to chose because porosity reduces strength capacity

$$\frac{3J_2}{\sigma_F^2} - 2\cdot f\cdot\left(1+\frac{I_1^2\cdot q_2^2}{8\cdot\sigma_F^2}\right) + f^2 = 1 \quad \Rightarrow \quad \frac{3J_2}{\sigma_F^2} - 1\cdot f\cdot\left(\frac{I_1^2\cdot q_2^2}{4\cdot\sigma_F^2}\right) - 2f - f^2 = 1.$$

With $f^2 << f$ can be derived $\frac{3J_2}{\sigma_F^2} - f\cdot\frac{q_2^2}{4}\cdot\frac{I_1^2}{\sigma_F^2} - 2f = \frac{3J_2}{\sigma_F^2} - f^*\cdot\frac{I_1^2}{\sigma_F^2} - 2f = 1$.

Applying Beltrami gives a relationship between porosity and Poisson's Ratio

$$\kappa = \frac{1-2\nu}{2+2\nu} \equiv f\cdot\frac{q_2^2}{4} = f^* \text{ (elliptic shape parameter)} \rightarrow \nu = (4 - f^*)/(8 + 2f^*)$$

taking i. e. q_2=1.5 as guess for the plastic damage flow function.

$\Rightarrow$ Failure state is , normalized again with the yield strength, if $\sigma = \bar{R}_{odc}$ is inserted.

'Gurson' comparison: $F = \frac{3J_2}{\bar{R}_{0.2}^2} - f_{ult}^*\cdot\frac{I_1^2}{\bar{R}_{0.2}^2} - 2\cdot f_{ult} = 1$,

F = 100% = potential surface, which may be a fracture surface or a growing yield surface.

From 'Comparison of Coefficients' finally is obtained using $f_{ult}(\bar{R}_{odc})$

ExtendedMises: $F = \frac{3J_2}{\bar{R}_{0.2}^2} + c_{12}\cdot\frac{I_1^2}{\bar{R}_{0.2}^2} = c^{ExtMis}$ (potential surface, growing with load)

follows $c_{12} = f_{ult}^*$, $c^{ExtMis} = 1 + 2\cdot f_{ult}$ $\Rightarrow$ $\sigma_{eq}^{ExtMises} = \sqrt{\frac{3J_2 - f^*\cdot I_1^2}{1+2f}}$.

The conventional visualization – as a parameter investigation - of the Gurson model is presented in *Fig.10-17 (left)* with *f* being the porosity parameter of the curves and q2 a Gurson parameter from the comparison. A growing *f* means higher true stress but less cross-section or load-carrying material in the strain-controlled 'hot spot'. This is displayed in the figure by the change of the cylinder shape versus an egg shape.

Another visualization, usually practiced in structural mechanics, is given by using the Lode-Haigh-Westergaard parameters. This leads to a change in the shape, *Fig.10-17 (center)*. For *f* = 0 the Mises cylinder is obtained.

Fig.10-17 (right) depicts the various strength values such as $true\bar{R}^t, \bar{R}_{odc}$ as increasing true strength points to be inserted into the Extended Mises function size parameter, finally visualized as flow potential surfaces for four strength-linked porosity levels.

The parameter comparison with 'Gurson' let to take a reduced value q_2 = 1.13, however, due to missing test data the author sticks to 1.5. In this context, the respective Extended Mises parameter c_{12} can be

determined, decoupled from the 'Gurson' Comparison of Coefficients, if having a reliable test data set available

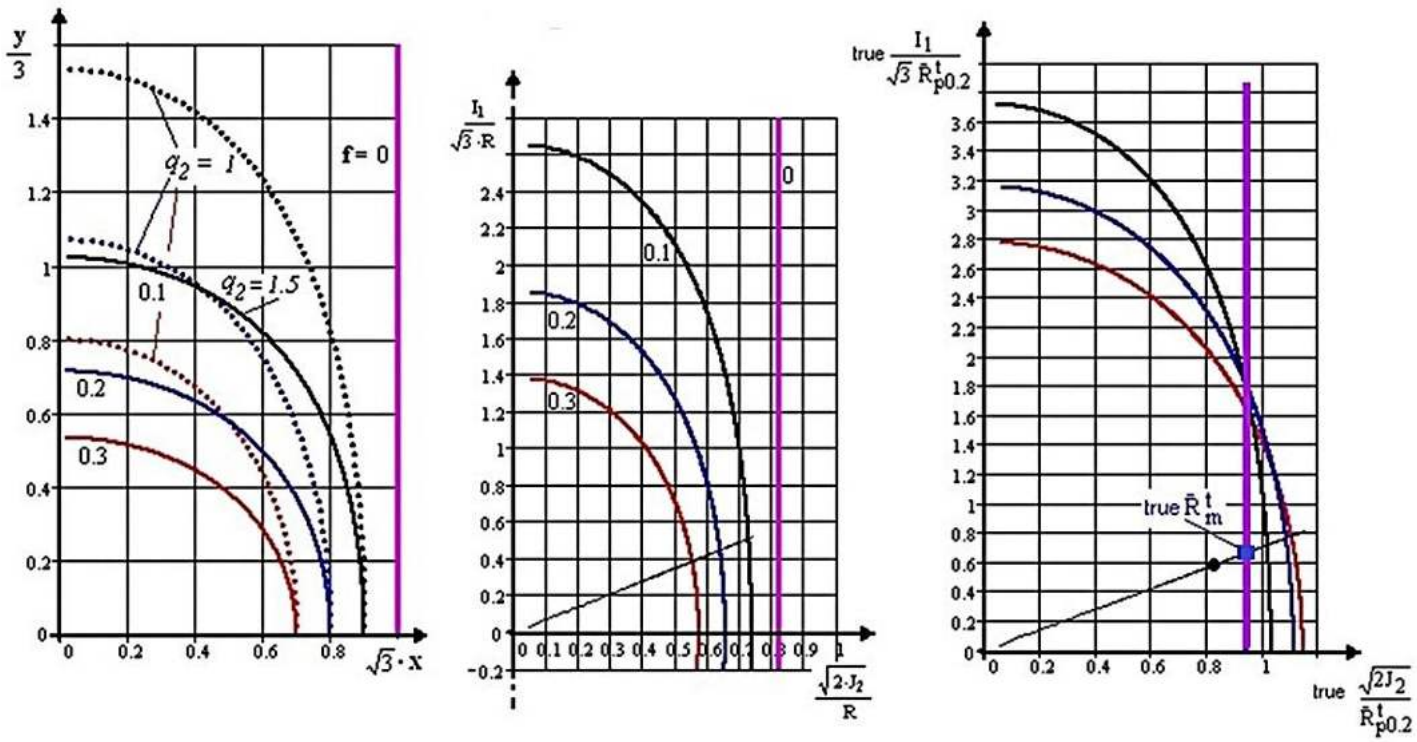

Fig. 10-17: Schematic comparison of the Gurson model (dots) and Extended Mises model Potential surfaces. (left) Display of curve parameter porosity f influence, using the 'Gurson' coordinates $x = (\sqrt{J_2}/\sigma_F)$, $y = (I_1/\sigma_F)$, $\sigma_F = \bar{R}^t_{p0.2}$;

(center) Display of the Gurson yield model in Lode-Haigh-Westergaard parameters $\bar{R}^t_{p0.2}$ *= normalisation strength)*

(right) Potential surfaces of the ExtMises-model with four increasing true (graphs made about 2001) AA2219, (q2=1.5, $q2_{ExrM}$ *=1.13) , points* $true\bar{R}^t$ and $\bar{R}_{odc}$ *(1.5, apart fromliitle hidden)*

Table 10-7: Replacement of the Mises-based Bridgman curve $\sigma_{eq}(\varepsilon_{eq})$ *by an ExtMises one*

In center $\sigma^t_{ax}(r) = \sigma_I + \sigma_{hyd}(r)$ and from Bridgman $\sigma_{hyd} \approx \sigma_I \cdot \boldsymbol{ln}\left(1+\frac{a^2-r^2}{2\cdot a\rho}\right)$

$\sigma^{MisBri}_{eq} = \sqrt{3\cdot J_2} = \sigma_I = \frac{F}{A} / (1+2\cdot\rho/a)\cdot\ln(1+0.5\cdot a/\rho)$, valid > $\bar{R}^t$ < ?,

$I_1 = \sigma_I + 3\sigma_{hyd} = \sigma_I \cdot \left(1+3\cdot \boldsymbol{ln}\left(1+0.5\cdot a/\rho\right)\right)$ for the critical central 'rod fiber' at r = 0

considering Bridgman (above) and the notch-curvature change by Lorrek-Hill's approach,

giving a maximum value for the unknown $\rightarrow$ $\max\frac{a}{\rho} = \sqrt{\ln\left(\frac{1}{1-Z}\right) - \ln\left(\frac{A_0}{A_{oon}}\right)}$,

inserting $\sqrt{3\cdot J_2} = \sigma_I$ and $\frac{F}{A} = true\sigma_{ax}$ the equivalent stress reads:

$$\sigma^{ExtMises}_{eq} = \sqrt{\frac{3J_2 - f^*\cdot {I_1}^2}{1+2f}} = \sigma_I \cdot \sqrt{\frac{1-f^*\cdot\left(1+3\cdot\boldsymbol{ln}\left(1+0.5\cdot a/\rho\right)\right)^2}{1+2f}}$$

valid $\bar{R}^t < \bar{R}_{odc}$, (shape parameter) $f\cdot\frac{q_2^2}{4} \equiv f^*$, set $q_2 \cong 1.5 \rightarrow 1.13$.

Porosity parameter f and curvature parameter a/ρ increase from about 0 to the maximum at $\bar{R}_{odc}$.

The author's full idea consisted of the two parts: Above ExtMises model plus porosity-improved Bridgman evaluation, which was depicted in *Table 15-3*. The table displays all relations in order to establish the 'searched' equivalent stress $\sigma_{eq}^{ExtMises}$.

Reminder: To capture '120°-rotational symmetry' would require to replace J_2 by $J_2 \cdot \Theta$.

10.10.7 Visualization of the Bridgman–corrected true curve with consideration of porosity

In order to obtain a realistic equivalent stress curve it is physically mandatory to consider the increase of porosity f and the increase of the notch curvature by applying a / ρ. The mapping of the changing notch curvature and the changing porosity is shown below:

* Mapping of the changing notch curvature: Determination procedure

$$\frac{a}{\rho} = \sqrt{\ln\left(\frac{A_0}{A_{rupt}}\right) - \ln\left(\frac{A_0}{A_{oon}}\right)} = 1.096 \quad \text{from} \quad \frac{A_{rupt}}{A_0} = 1 - Z = 1 - 0.20 = 0.80,$$

$$\frac{A_0}{A_{rupt}} = \frac{1}{0.80} = 1.25, \quad \frac{A_0}{A_{oon}} = \left(\frac{4.0}{3.89}\right)^2 = 1.057 \rightarrow \max\frac{a}{\rho} = 0.409 \text{ at } R_{rup}.$$

Applying Lorrek-Hill's value Bridgman's approach delivers $\max\left(1+\frac{2\rho}{a}\right)\cdot\ln\left(1+\frac{a}{2\rho}\right) = 1.096.$

Then, for the previously proposed formulation the curve parameters can be computed:

stressing $\frac{a}{\rho} = a\rho = c_1 + c_2 + \text{true}\varepsilon_{ax}R_{odc}{}^2 + c_3 \cdot \text{true}\varepsilon_{ax}R_{odc}{}^3$.

Vorgabe $a\rho = 1.096$ $\text{true}\varepsilon axR02 = 0.0071$ $\text{true}\varepsilon axRt = 0.055$ $\text{true}\varepsilon axRodc = 0.231$

$c1 := 1$ $c2 := 100$ $c3 := 1$

$1 = c1 + c2 \cdot \text{true}\varepsilon axR02^2 + c3 \cdot \text{true}\varepsilon axR02^3$

$1.00005 = c1 + c2 \cdot \text{true}\varepsilon axRt^2 + c3 \cdot \text{true}\varepsilon axRt^3$

$a\rho = c1 + c2 \cdot \text{true}\varepsilon axRodc^2 + c3 \cdot \text{true}\varepsilon axRodc^3$

$A\rho := \text{Suchen}(c1, c2, c3)$

$$A\rho = \begin{pmatrix} 1 \\ -0.548 \\ 10.148 \end{pmatrix}$$

$c1 := A\rho_0$ $c1 = 1$ $c2 := A\rho_1$ $c2 = -0.5476$ $c3 := A\rho_2$ $c3 = 10.1478$

$A\rho_j := c1 + c2 \cdot \left(\text{true}\varepsilon ax_j\right)^2 + c3 \cdot \left(\text{true}\varepsilon ax_j\right)^3$

* Mapping of the changing porosity *f*: Data set used and determination by Mathcad

The set points of the curve are the porosity values at the tensile strength point R^t and at R_{odc}.

Vorgabe $e1 := 0$ $e2 := 1$

$$0.0002 = \left(e1 \cdot \exp\left(\frac{\text{true}\varepsilon axRt}{\text{true}\varepsilon axRodc} - 1\right)\right)^{e2} \qquad fodc = (e1 \cdot \exp(1-1))^{e2}$$

$Af := \text{Suchen}(e1, e2)$

$$Af = \begin{pmatrix} 0.6292 \\ 6.9469 \end{pmatrix}$$

$e1 := Af_0$ $e1 = 0.6292$ $e2 := Af_1$ $e2 = 6.947$

$$fexp_j := \left(e1 \cdot \exp\left(\frac{\text{true}\varepsilon ax_j}{\text{true}\varepsilon axRodc} - 1\right)\right)^{e2}$$

Fig.10-18 displays the author's design verification idea of about 2001.

The influence of f practically starts at R_{odc}.

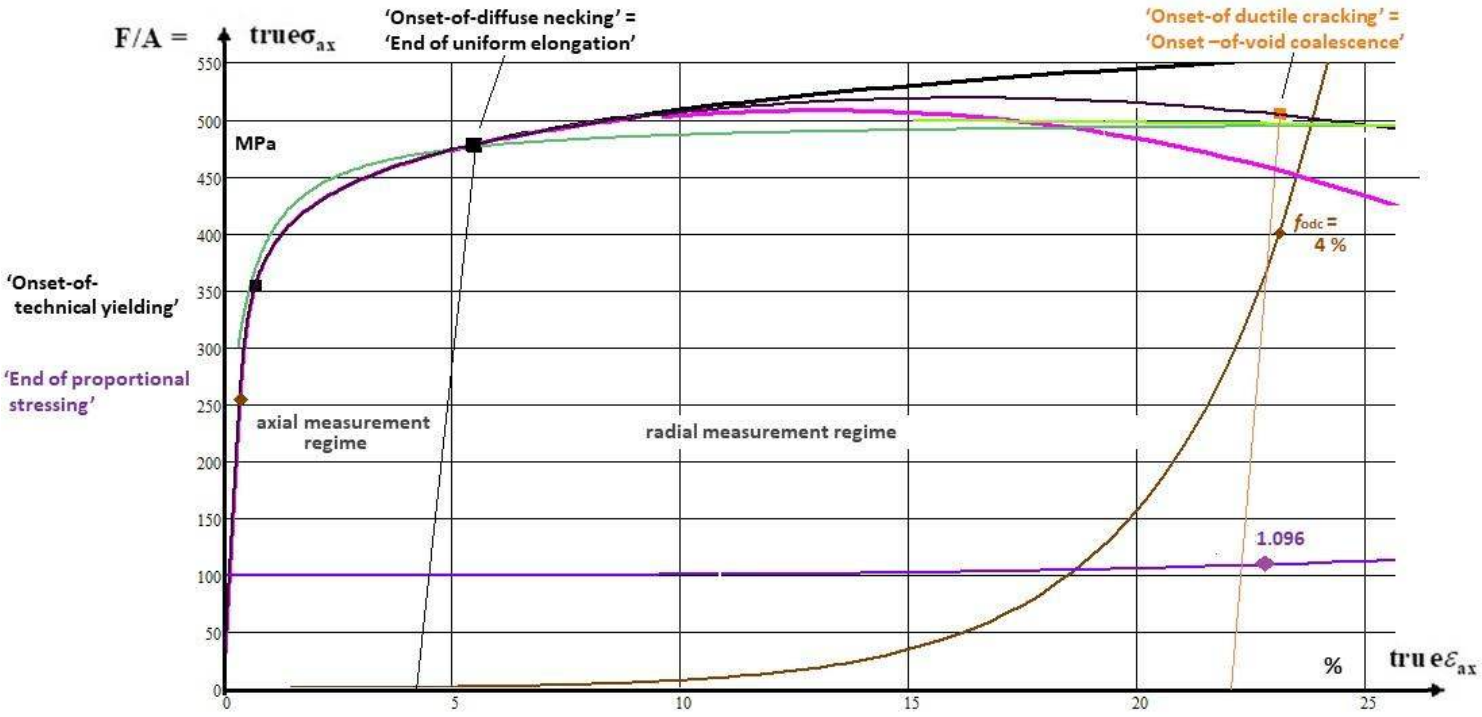

Fig. 10-18, AA2219, base material T2, 6 mm thick: Visualization of the equivalent stress curve $\sigma_{eq}^{ExtMises}$ *; Ramberg-Osgood-mapped measured cross-section smeared axial stress F/A; Increase of plastic porosity f with* f_{odc} *= 4% at* R_{odc} *; Increase of the notch curvature* a / ρ *with* $a / \rho = 0.409$ at R_{ult} (replacing the higher R_{odc}); *Increase of ν in the elastic-plastic transition domain approaching 0.5 and barely visible the decrease in the porous domain of a small porosity-linked decease*

10.11 Specific Potential Surfaces representing Strength Failure Criteria

Brittle 'porous' materials may still fracture in the elastic-plastic transition domain. For this fact, Ismar and Mahrenholtz [*Ism82*] developed a Beltrami-based SFC model describing the failure behavior of a material between the proportional limit and the 'onset of yielding'. In *Table10-8* the SFC-formulations in all regimes shall be comparatively displayed. This includes potential surface descriptions and associate strength failure criteria SFCs.

Note on Non-linear stress–strain analysis:

Usually Co-axiality, Prandtl-Reuss equations and an Associated Flow Rule is employed in order to predict strain rate $\dot{\varepsilon}_{ij}$ and the Lagrange multiplication (*proportionality*) factor $\dot{\lambda}$.

Table 10-8, Isotropic materials: Determination of model parameters, single mode view.

* Modelling Functions F describing a subsequent potential surface

elastic-plastic	plastic	plastic porous
Beltrami	Hencky-'Mises'-Huber	'Gurson' type

$$\bar{R}^t_{prop} < \sigma_{\text{Bel}} < \bar{R}^t_{0.2} \quad \leftrightarrow \quad \bar{R}^t_{0.2} < \sigma_{\text{Mis}} < \bar{R}^t_{m} \quad \leftrightarrow \quad \bar{R}^t_{m} < \sigma_{eq} < \bar{R}^t_{\text{odc}}$$

stress - controlled *strain – controlled*

σ : = running variable of the subsequent potential surfaces

$$\bar{R}^{t\,2}_{prop} / \bar{R}^{t\,2}_{0.2} < c^{\text{Bel}} < 1 \quad \leftrightarrow \quad 1 < c^{\text{Mis}} < \bar{R}^{t\,2}_{m} / \bar{R}^{t\,2}_{0.2}$$

ellipsoid → cylinder → ellipsoid

$$I_1 = (\sigma_I + \sigma_{II} + \sigma_{III}) = \text{f}(\sigma), \quad 6J_2 = (\sigma_I - \sigma_{II})^2 + (\sigma_{II} - \sigma_{III})^2 + (\sigma_{III} - \sigma_I)^2 = \text{f}(\tau)$$

$$\frac{3J_2}{\bar{R}^{t\,2}_{0.2}} + \kappa \cdot \frac{I_1^{\,2}}{\bar{R}^{t\,2}_{0.2}} = c^{\text{Bel}} \quad \leftrightarrow \quad F^{Mis} = \frac{3J_2}{\bar{R}^{t\,2}_{0.2}} = c^{\text{Mis}}, \; \kappa = \frac{1-2\nu}{2+2\nu}$$

Insertion of a (measurable) normalizing strength, yield strength point with $\nu = 0.5 \rightarrow \kappa = 0$

$$\text{F}^{Bel} = \frac{3\bar{R}^{t\,2}_{02} / 3}{\bar{R}^{t\,2}_{02}} + \kappa \cdot \frac{\bar{R}^{t\,2}_{02}}{\bar{R}^{t\,2}_{02}} = c^{\text{Bel}} * \rightarrow c^{\text{Bel}} = 1 + \kappa = 1, \text{ and } \kappa \text{ an elliptic shape parameter}$$

* Strength FailureCriteria (SFC), $\bar{R} \rightarrow R$, (with $\Theta = 1$ for full rotational symmetry)

R : = strength design allowable, marking a special potential surface ≡ design limit state

elastic, very brittle	ductile	very ductile

$$Eff = \frac{\sigma_1}{\bar{R}^t_{\text{m}}} = 1 * \quad \leftrightarrow \quad Eff = \frac{3J_2}{\bar{R}^{t\,2}_{m}} = 1 \quad \leftrightarrow \quad Eff = \frac{3J_2}{\bar{R}^{\,2}_{\text{odc}}} + c_{12} \cdot \frac{I_1^{\,2}}{\bar{R}^{\,2}_{\text{odc}}} - 2\, f_{odc} = 100\%.$$

For similarity reasons: for the 2 modes Normal Fracture NF , Shear Fracture SF (brittle)

and after inserting $\sigma = R \cdot Eff$ and dissolving for Eff follows

$$\text{I}_1 > 0 : F^{NF} = 0.5 \cdot \frac{\sqrt{4J_2 - I_1^{\,2} / 3} + I_1}{2 \cdot \bar{R}^t} = 1 \; ; \; Eff^{NF} = 0.5 \cdot \frac{\sqrt{4J_2 - I_1^{\,2} / 3} + I_1}{2 \cdot \bar{R}^t}$$

$$\text{I}_1 < 0 : F^{SF} = c_1^{SF} \cdot \frac{3J_2}{\bar{R}^{c\,2}} + c_2^{SF} \cdot \frac{I_1}{\bar{R}^c} = 1; \; Eff^{SF} = \frac{c_2^{SF} \cdot I_1 + \sqrt{(c_2^{SF} \cdot I_1)^2 + 12 \cdot c_1^{SF} \cdot 3J_2}}{2 \cdot \bar{R}^c} = \frac{\sigma^{SF}_{eq}}{\bar{R}^c}$$

$c_1^{SF} = 1 + c_2^{SF}$ with direct consideration of the Poisson ratio $c_2^{SF} = (1 + 3 \cdot \mu) / (1 - 3 \cdot \mu)$

Last unknown to be searched is the elliptic shape linked parameters such as c_1^{SF} by insertation of a bi-axially compressive failure stress or a fracture angle $\mu = \cos(2 \cdot \theta^c_{fp}\,° \cdot \pi / 180)$.

LL:

- ✓ *Whereas with the elasticity formulation of Beltrami the Poisson ratio v is growing this is opposite with the formulation of a porosity-linked plastic model due to the increasing porosity*
- ✓ *The hypotheses of Beltrami, Mises and Gurson describe an increase or decrease of surfaces of constant potential. The shape of the surface theoretically begins with $\nu = 0$ (sphere, found with foams) growing up from $0 < \nu$ to $\nu = 0.5$ via the growing Mises cylinder keeping $\nu = 0.5$ and ending with an ellipsoid, which shrinks into a spherical direction represented by $0.5 > v$.*
- ✓ *For two domain limits a clear value for the varying Poisson ratio is given:*

proportional limit $\sigma \le \bar{R}^t_{prop} \Rightarrow \nu = \nu_0$ *and yield limit* $\sigma = \bar{R}^t_{p0.2} \Rightarrow \nu = 0.5$

- ✓ *Designing requires to use limit state formulations, termed failure criteria (SFCs). These are fracture failure criteria for brittle materials namely for 'Onset-of-fracture' and yield failure criteria for ductile materials. In practice, for ductile materials these failures are 'Onset-of-yielding' and - for the author - 'Onset-of-void coagulation = Onset of ductile Cracking ' in the case where strain-softening applies*
- ✓ *A Strength Failure Criterion represents a defined Design Limit State and is therefore a special critical Potential Surface F.*
- ✓ *For engineering reasons* $true\bar{R}^t \Rightarrow \bar{R}_{odc}$ *will represent the load carrying capacity to be considered.*
- ✓ *With the novel porosity-capturing σ-ε curve, being a ductile porosity-improved Bridgman correction, a simplified plastic analysis procedure could be achieved.*

*The **novel Extended Mises model** just requires*
the determination of one more parameter
- apart from the Mises cylinder parameter c -
namely the porosity value f.

⇒ *All model **parameters are measurable quantities.***

Research proposal experience in the context above:

(MAN-driven idea for a DFG project (2006) to create a simple verification procedure for critical boreholes of the Ariane 5 upper stage tanks concerning generally the design of rocket tanks, submitted by my Prof-friends Volker Ulbrich (GAMM secretary) and Werner Hufenbach (ILK Dresden). This proposal was rejected by three DFG reviewers without addressing the idea or providing a clear explanation. This behavior was so shameful for us that I resigned from my own DFG reviewer position. Rejection cause?: Gurson parameter tests are costly and finance people!

11 Engineering Note on Continuum (micro-) Damage Mechanics (CDM)

***Aim**: Primarily checking CDM application whether it is mature for a reliable Design Verification.*

CDM is applied for ductile and brittle materials. The loading may be static and cyclic, with the latter requiring fatigue investigation. Regarding stress-strain curves, CDM principally captures the load-controlled hardening part and the deformation-controlled softening part. Softening part examples are the still mentioned embedded UD layer (*Fig.11-1*) and the ductile metal tensile rod described in the last Chapter by a porosity–capturing 'Gurson' model. Results of isotropic analyses, employing the softening curve branch, can be used to better design notches, openings in pressure vessels (fuel tank task in Ariane 5 upper stage) etc.

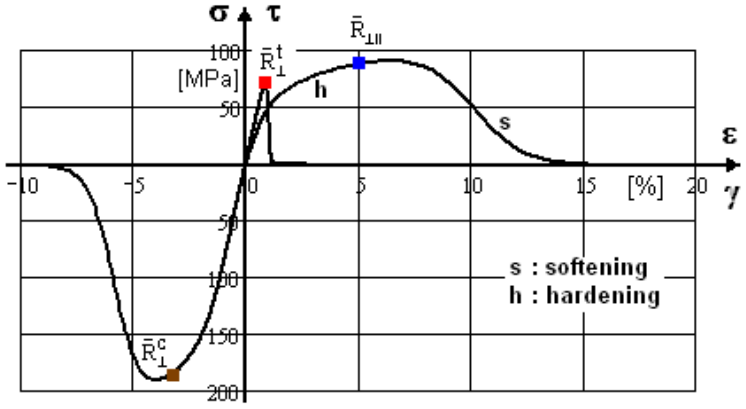

Fig.11-1, example UD ply: Full stress-strain curve with load-controlled hardening and deformation-controlled softening of the layer (ply) embedded in a laminate

CDM is pretty linked to multi-scale modelling, which will be looked at in the following Section, §12.

All materials are generally composites.

Applying CDM one goes down to the constituents of a composite to metallic grains or to fiber and matrix for instance. Moving down on the scales it is helpful to use the physical formulations gained on the macro-scale such as Mises yielding with ductile metals in the tension and compression loading domain and Mohr-coulomb friction behavior of brittle materials in the compression domain.
Shear stress loading is composed of a tensile stress with an associated compressive stress. This principally activates two failure modes, which leads to normal fracture in the case of brittle materials. These physical effects stay valid at the lower scale and are to consider *adjusted*.

***LL**:*

It is always to check, whether a Mises yield criterion can be applied to quantify static *micro-damage portions D or a fracture criterion in the case of very brittle behavior, i.e. Grey cast iron and Fiber Reinforced Plastics (FRP), when the matrix experiences yielding.*

11.1 Static Behavior

11.1.1 Micro-damage formulations

CDM is basically used to capture the evolution of the micro-damage state from micro-damage $D = 0$ up to 'Onset-of-Failure' at *maxD*, which is for brittle materials at the end of hardening or at achieving the tensile strength *R*.

In CDM, the formulation of the describing constitutive equation is based on one of the following two approaches (h*ere the stress-strain curve is meant*):

(1) The strain equivalence principle approach or on

(2) The stress equivalence principle approach.

From engineering side, the latter is preferred because 3D stress states and residual stresses have to be considered in design dimensioning.
The constitutive relationships are formulated in the effective undamaged configuration

$$\sigma_{eff} = \sigma / (1 - D)$$

with a stress-strain relation linked by the stiffness elasticity matrix [C], which reduces due to growing micro-damage. *Fig.11-2* exemplarily depicts the relationship for a 2D-loaded transversely-isotropic UD material. By inversion of the effective compliance matrix S_{eff} the decaying stiffness matrix C_{eff} is obtained

$$\{\sigma\} = [C] \cdot \{\varepsilon\} \rightarrow \{\varepsilon\} = [S] \cdot \{\sigma\}$$ as preferred practical test-data evaluation formulation

$$S_{\text{eff}} = \begin{bmatrix} \frac{1}{E_1 \cdot (1 - D_{11})} & \frac{-\nu_{21}}{E_1} & 0 \\ \frac{-\nu_{12}}{E_2} & \frac{1}{E_2 \cdot (1 - D_{22})} & 0 \\ (\text{symm}) & 0 & \frac{1}{G_{12} \cdot (1 - D_{66})} \end{bmatrix} \quad \text{with} \quad D = \begin{bmatrix} D_{11} & D_{21} & 0 \\ D_{21} & D_{22} & 0 \\ (\text{symm}) & 0 & D_{66} \end{bmatrix}$$

usually not considering the off-diagonal D_{21}.

Fig.11-2, 2D-example UD material: Compliance matrix [S] and micro-damage matrix [D].

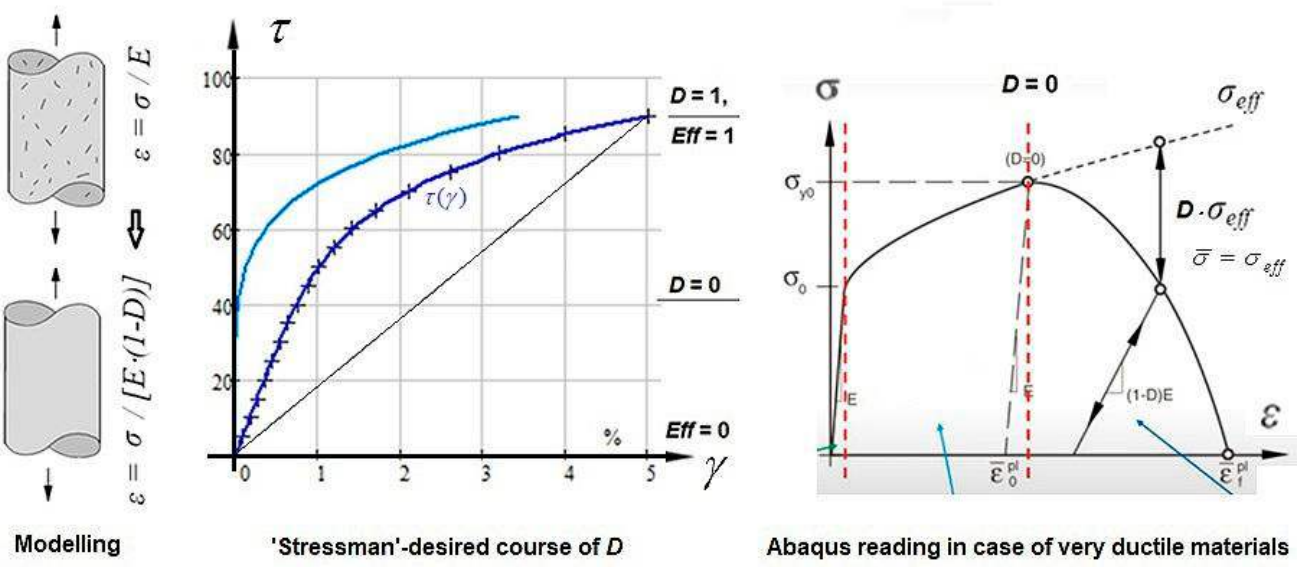

Fig.11-3: The various 'Onset- of- Failure' envelopes: (left) Smearing of the micro-damaged material, (center) shear of a slightly brittle material, (right) Ductile material picture from Ansys FEA code

The D_{ij} represent the accumulation of the micro-damage process portions and are theoretically terminated by max$D$ at the tensile strength point in the case of brittle materials and at the rupture point for very ductile isotropic materials. These portions may occur during a monotonically increasing static loading. For brittle materials micro-damage starts at the 'elastic end' being a level where *Eff* has still reached a value, see *Fig.11-3*. Unfortunately, max$D$ in static CDM cannot become 100% due to its usual modelling basis! The center figure outlines how a stress-man views the 'onset of micro-damage' of a slightly brittle material. In the elastic domain < $R_{prop} \equiv R_{e(lastic)}$ there is no D-contribution. The blue 'flow curve' then will contribute.

The right figure (from Abaqus) surprisingly outlines that the micro-damage there first begins with void nucleation and coagulation which raises the Question:

Does really not any micro-damage happens below R^t ??

Micro-Damage-free (*in German schädigungsfrei, nicht schadensfrei*) and crack (= macro-damage, *in German Schaden*)-free does not mean free of flaws.

***LL**:*

** CDM is generally always good for understanding static & cyclic material behavior*

** Confusing is faced regarding 'onset of counting micro-damage' portions in the static case: domains $< R^t >$.*

11.1.2 Material behavior-caused Slip and Failure angles preview of Isotropic and UD materials

The number of slip systems in ductile metals is usually high, and those that are active possess an orientation near to the planes with maximum shear stress.

Under uniaxial loading the planes of micro-cracks are always inclined approximately θ_{fp} = 45° to the direction of the applied tensile stress, see (*Fig.11-4*).

In single crystals, the lattice structure is spatially oriented in such a way that a sliding plane is obtained at an angle of 45°. In poly-crystalline metals with randomly distributed lattice sub-structures this will change a little.

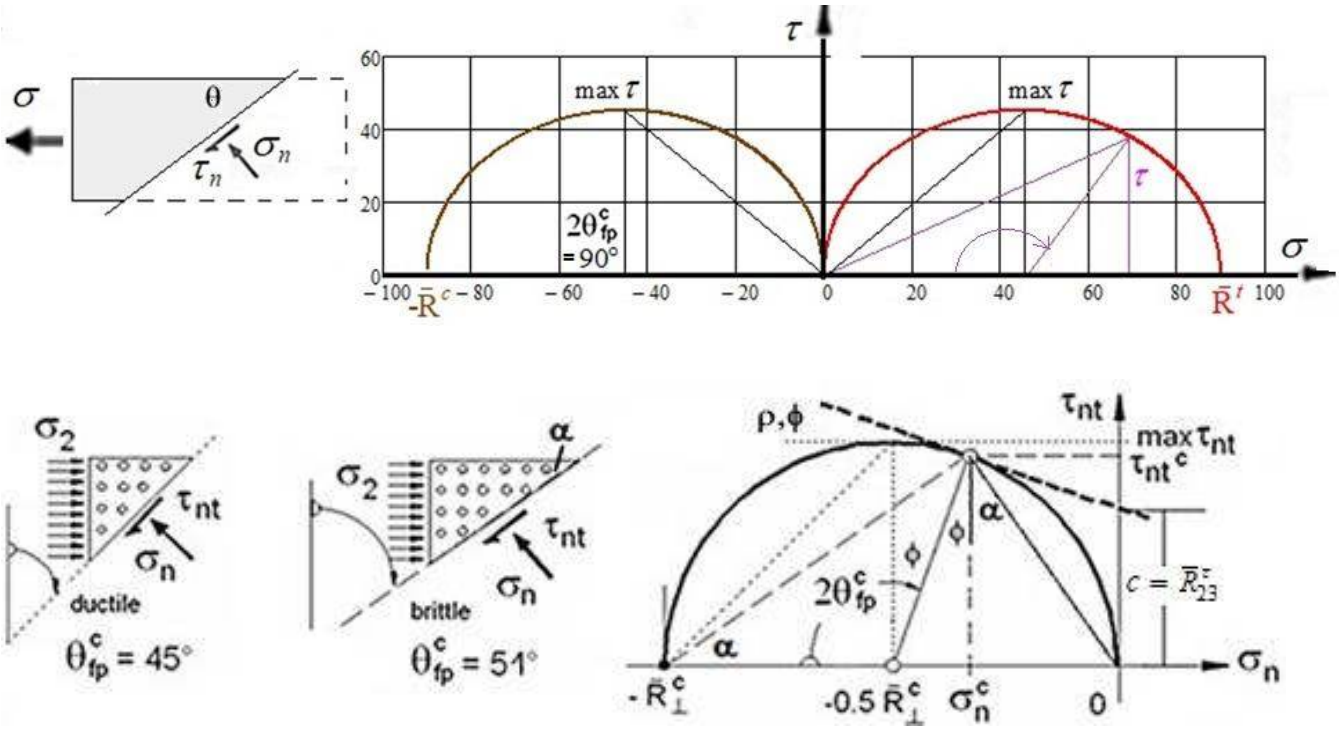

Fig. 11-4, Mohr stresses and failure angles:
(up) ductile metal material:
(below) Mohr stress circle for a compressive and a tensile uniaxial external stress of a semi-brittle material
$\tau_n = \sigma \cdot \cos(\alpha) \cdot \sin(\alpha)$ with α the angle to σ direction, $2 \cdot \max \tau = \sigma$ for $\alpha = 45°$

Known from brittle material behavior under compression is: *The failure angle depends on the friction value μ*. After the formula, derived in [§22.8, *Cun23c*], the computation of the failure angle with the Mohr-Coulomb model delivers exemplarily for a material friction value μ = 0 (*fully ductile)* the expected value of 45° and for a friction value μ = 0.2 the angle 51°, see *Fig.11-5*. The author presents in this figure for a UD-ply that the angle changes from θ_{fp} = 51° at the lateral compression strength point $\bar{R}_\perp^c$ up to 90° at the lateral tensile strength point $\bar{R}_\perp^t$. As so-called Mohr-Coulomb curves the simple linear 'Mohr curve' and a more realistic curved Mohr-Coulomb friction curve.

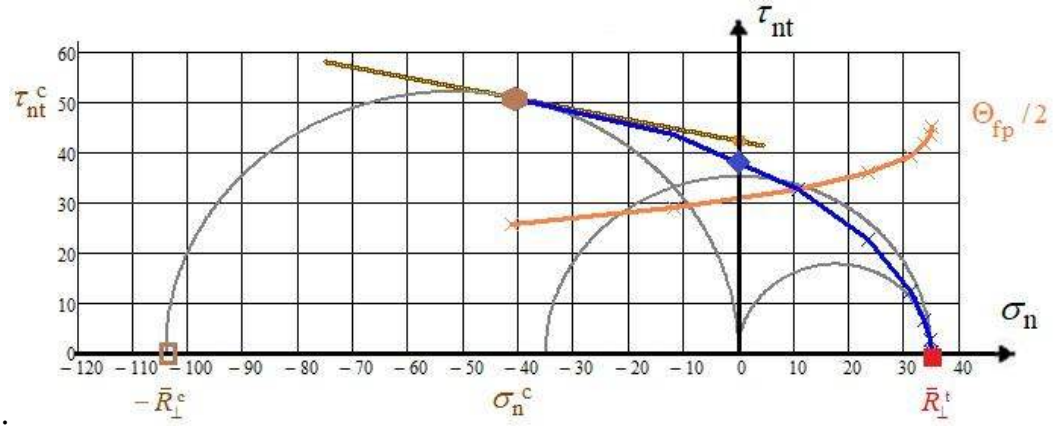

Fig.11-5, brittle UD-material: Display of the UD failure curve in Mohr stresses, indicating a fracture angle increase $\Theta_{fp}/2$ when approaching $\bar{R}_{\perp}^{t}$. Shear fracture plane angle in the touch point 51°, defined by $(\sigma_n^c, \tau_{nt}^c)$ under $\{\sigma\} = (R^c, 0, 0)^T$

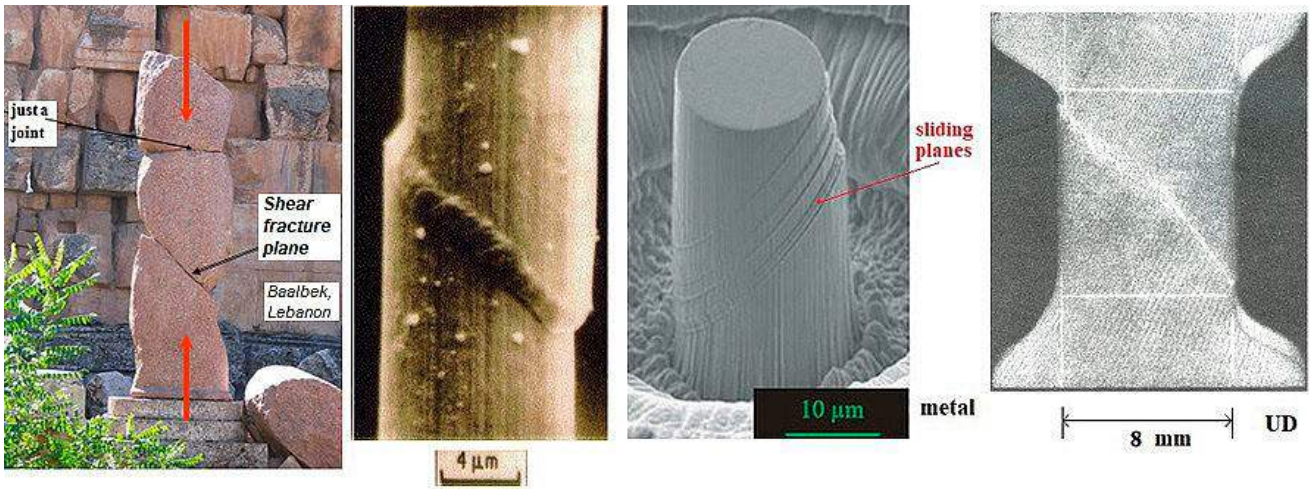

Fig.11-10, Friction driven shear fracture planes at extreme length scales.anes : Facture angles of the brittle materials Rock material, Carbon fiber [K. Schulte, TU Hamburg-Harburg], Ductile metal compression cut from a single crystal (deformed pillar after compression testing. Monnet, G. & Pouchon, M. A. (2013), Determination of the so-called critical resolved shear stress and the friction stress in austenitic stainless steels by compression of pillars extracted from single grains', Mater. Letters 98, 128-130) and laterally compressed UD-CFRP

11.2 Cyclic Behavior of Ductile Metals applying Micro-scale Material Modelling

Once micro-cracks have nucleated due to strain accumulation from cyclic slipping, they grow in the early stage typically in the order of the material's grain size (*text from M. Mlikota - S. Schmauder*). In the course of further cyclic loading, micro-cracks, formed along these slip bands, will grow and link together. In metals and alloys they grow predominantly along the crystallographic planes because they are highly affected by microstructural barriers such as grain boundaries or other micro-structural features. The coalescence of trans-granular micro-cracks, namely, if two micro-cracks meet each other at the same grain boundary, is performed in the numerical simulation of the crack initiation after Tanaka-Mura. It occurs if the average stress in between their tips surpasses the elastic limit *Re* of the material's new micro-crack, created on this grain boundary line, uniting the two trans-granular micro-cracks into a single one (*example pure iron Re = 260 MPa).*

Already nucleated crack segments tend to extend along the whole grain, causing local stress relaxation as well as concentrations at their tips and by that amplifying the likelihood for new crack formation in the vicinity. In the course, micro-cracks form along the slip bands, grow and join.

The change of the crack plane from the crystallographic plane to a non-crystallographic plane perpendicular to the external stress axis is called the transition from Stage I (*crystallographic growth*) to

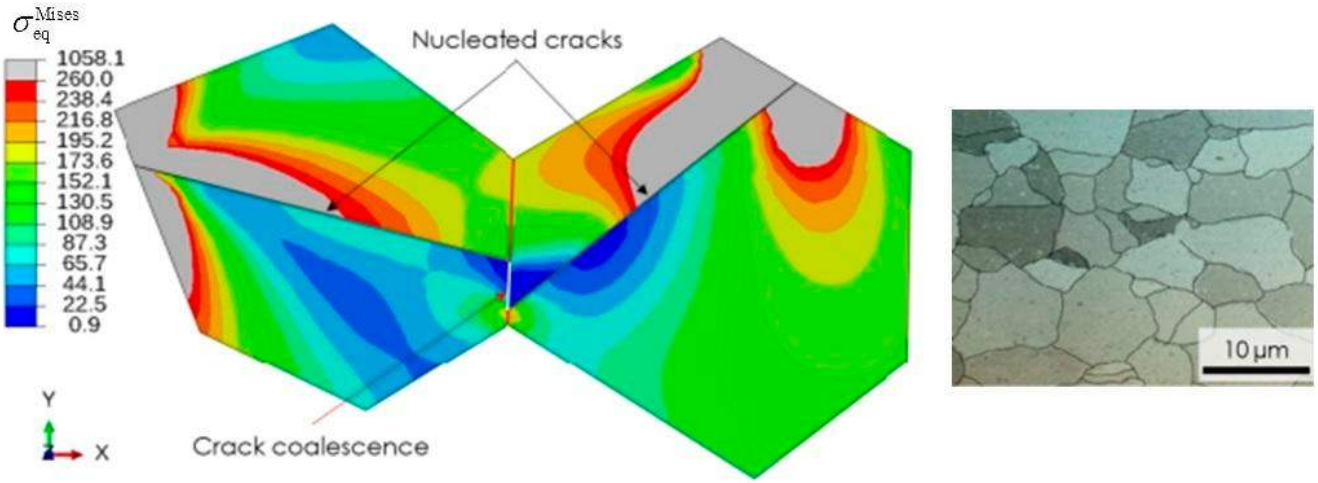

Fig.11-6: Simulation of AA micro-crack coalescence (Lorenzino, P., Navarro, A. & Krupp, U. (2013), 'Naked eye observations of microstructurally short fatigue cracks', Int. J. of Fatigue 56(0), 8-16.

Stage II (*non-crystallographic growth*) or transition from the micro-crack initiation to a micro-crack growth stage resulting in a short crack, as was depicted in *Fig.11-6* above.

However, the dominant short crack does not always continue propagating. Namely, in the case of a lower stress level, the short crack may stop growing. Such a situation is typically known as run-out, which indicates that at very low stress levels an infinite life may be obtained. Run-out below the endurance limit means crack-retardation, *Fig.11-7*. In the long-crack regime the fatigue crack growth rate da/dn can be characterized by the stress intensity factor range ΔK as a dominant driving parameter.

The CDM-driven Region I in the figure below is here of interest, but should be illustrated as part of the full crack failure picture: A typical fatigue crack growth rate curve da/dn (ΔK) for the long crack is illustrated in *Fig.11-7*, too. If in a double logarithmic scale the long crack propagation rate follows a

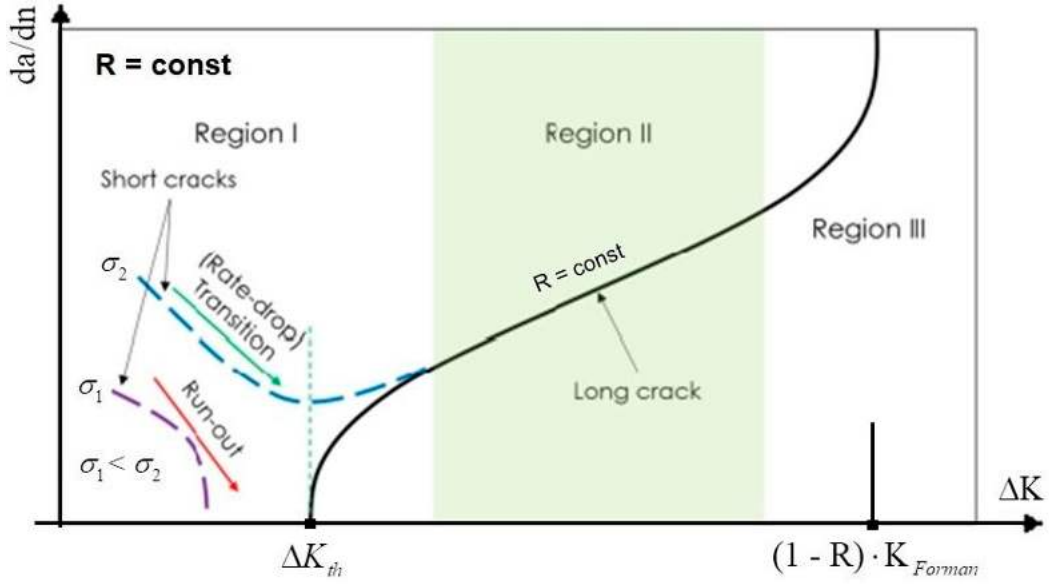

Fig.11-7: Fatigue growth rates of micro-cracks (short) and long cracks in dependence of Δ stress intensity factor. Schematic representation of the loading level- dependent transition from region I into region II.

n = number of cycles, a is crack size

straight line in Region II, in sufficient distance from the threshold ΔK_{th}, then the long crack growth rate domain can be well described for most engineering alloys by the so-called simple Paris law and the improved Forman:

$$\text{Paris:} \quad da/dn = C_{Paris} \cdot \Delta K^{n_{Paris}} \quad , \quad \text{Forman:} \quad da/dn = \frac{C_{Forman} \cdot \Delta K^{n_{Forman}}}{(1\text{-R}) \cdot \text{K}_{Forman} - \Delta K} \quad [HSB\ 63205\text{-}01]$$

In the figure and in the formulas above *da/dn* is the crack growth increment per cycle, and $\Delta K = maxK - minK$ is the range of the stress intensity factor, parameter *C* (*intercept with the y-axis*) and n_{Forman} (*slope*) are material curve parameters that are deduced by fitting the course of experimental data. K_{Ic} is the so-called fracture toughness.

***LL**:*

** There seems to be some hope, that in future for metals a basis will provided, that the estimation of an endurance limit will be possible.*

** A grain is usually polycrystalline with crystal planes in various spatial orientations. Hence, a metallic 'composite' material can be only termed homogeneous and isotropic if these orientations are randomly distributed in order to become quasi-homogeneous.*

By the way, this is the same for an isotropic short fiber-reinforced polymeric material, otherwise the so-called orientation tensor has to take care of the non-isotropy.

11.3 Application of Continuum (micro)-Damage Mechanics (CDM) in Static Strength

11.3.1 Note on Stressing effort Eff versus micro-damage development D

For the designer of interest is how the material's stiffness decreases with increasing stress effort or load, respectively. Design allowable *R* and average strength $\bar{R}$ lead to different stress efforts in *design verification* and in modelling the material micro-damage (*50% value = highest expectance probability*), see *Fig.11-8.* The enlarging effect of the design FoS *j* on the value of *Eff*, when reaching failure, is

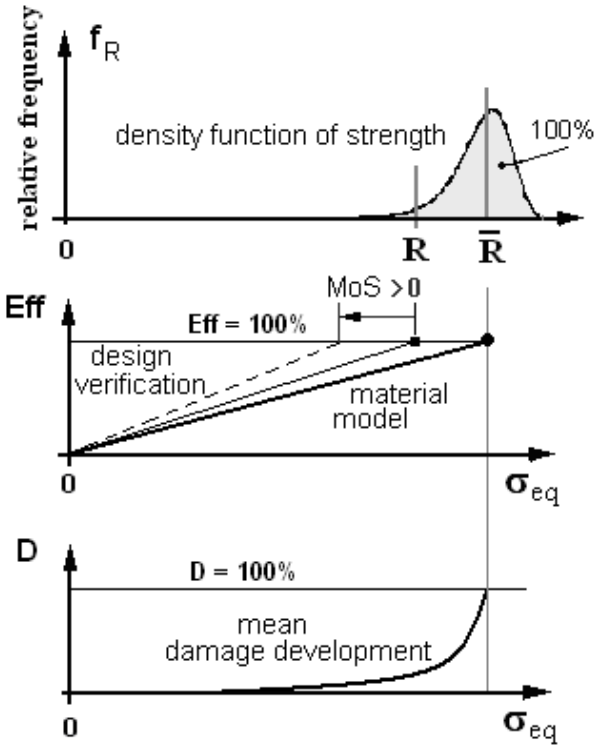

Fig.11-8:

Visualization of the development of stress effort, strength value, equivalent strength, and

Micro-damage understanding of a 'stress man'.

MoS = RF - 1

considered in the design verification curve (*dashed line*) depicted below. The more reserve is, indicated by a positive Margin of Safety *MoS*, the lower *Eff* is. This has an effect on the actual strain in the non-linear analysis case. It becomes smaller and the strain is less plastic, which is of interest for the validity limit of an elastic analysis and the micro-damage amount.

In the case of 3D modal SFCs (for comparison) the common micro-damage-caused degradation is considered by an interaction equation that reflects the micro-damage influence of all acting stress states and associated modes. The single mode efforts are interact via the experience-based interaction exponent m being about m = 2.6.

11.3.2 Stress Man's Assessment of CDM applications

During the author's engineering life CDM was often propagated to make in future a Design Verification possible. In literature, i.e. [*Jai20*], Continuum (micro-)Damage Mechanics (CDM) models are also used to determine a *RF*. However, this intention faces some obstacles.

Analogous to the standard Design Verification (DV) procedure then for CDM application statistically-based micro-damage model parameters would be required and a total maximum value *D* is to define according to $D < D_{admissible} < 100\%$ at failure and this must be statistically based. Defining such a *D*–value is a challenge for the application of (micro-)Damage Models in the Design Verification for serial production certification. This challenge would be novel and higher than providing the classical strength design allowables *R*, necessary for computing *Eff* or *RF*.

Further, in known standard procedures

Eff runs in the range **$0 < Eff < 100\%$,** whereas

***D* begins at a distinct *Eff*-value but should principally also end at 100% !!??**

Here, very essential questions come up:

"*How does the designer assess a stress level that is below the 'onset-of-micro-damage?"*

"*How are to consider low stresses in Low Cycle Fatigue*?"

The provision of a CDM-failure body would be mandatory for obtaining DV. Hence, up to now CDM seems not to meet the authority-demanded DV-requirements regarding the statistically reduced design strength *R* and regarding the relationship $\sigma \sim R \cdot Eff$, which is valid in the linear elastic and in the non-linear regime.

***LL**:*

** Stiffness decay CDM model parameters are difficult to apply*

** The 'stress-man' will not understand that at maximum load, which is at the tensile strength point, the sum of micro-damage does not approach 100%.*

** The author could not sort out a consistent procedure that might be used in design verification. A clear derivation of the maximum micro-damage values seems to be missing.*

** Viewing $Eff(\{\sigma\})$: How is the multiaxial stress state –linked interaction of the damage portions in CDM solved?*

** Stiffness decay CDM model parameters are difficult to apply*

** Looking at 'well analyzing', which requires well-mapping of the stress-strain behavior in the hardening domain, one should always remember the scatter of the measured curves.*

Engineer's question: *"Is it possible in future to really provide the engineer the necessary design verification data when using **static** micro-damage quantities D_i ?"*

There are two crack-free tasks generally to manage

$$\text{If static failure} \rightarrow \max\sigma = \bar{R}_{static} \text{ at } Eff = 1 \quad \text{and} \quad \text{if cyclic failure } \max\sigma = \bar{R}_{cyclic}, \text{ at } D = 1.$$

The second task shall be shortly described.

11.4 Macroscopic SN-curve with Relation Material Stressing Effort *Eff* ↔ Micro-damage *D*

11.4.1 General application

There are practically two possibilities to present SN curves, see §9:

(1) Ductile: Applying the stress amplitude σ_a(R,*N*), also termed alternating stress

(2) Brittle: Applying the upper stress σ_{max}(R,*N*)

Maximum stress is physically simpler to understand by the 'stress-man' than an amplitude, according to delivering a smooth transfer from the static to the cyclic behavior, *Fig.11-9*. Namely, a decaying SN curve is interpretable like a decaying 'static' strength after a micro-damage process with *n* cycles. for brittle materials the strength value $\bar{R}^t = \sigma_{max}$ (n = N = 1) is preferably used as origin in the tension domain and anchor point of the SN curve and in the compression domain $-\bar{R}^c = \sigma_{min}$ (n = N = 1).

The course of the cyclic failure test data, termed SN-curve, again mapped by the 4-parameter Weibull formula, is $\text{R = constant}: \quad \sigma_{max}(R, N) = c_1 + (c_2 - c_1) / \exp(\log N / c_3)^{c4}$.

As the average SN-curve is not *allowed* in fatigue life Design Verification, a statistically reduced curve is to determine as design curve. This design curve defines a full D_{design} = 100% -SN-curve from the tensile strength as original point and ends in the running-out defining an endurance limit stress. Run-out below the endurance limit means crack-retardation.

11.4.2 Transfer from classical Fatigue Damage to the (micro-)Damage Mechanics view

*The accumulated **cyclic** micro-damage sum D(N) = 100% replaces the static maximum Eff !*

Fatigue, classical :

Fig.12-10 visualizes the classic transfer from the static load-driven increase of the material stressing effort (n = N = 1) *Eff* = 100% (expectance value 50%) at the strength point to the accumulated cycle-driven cyclic micro-damage sum $D_{mapping}$ = 100% (expectance value 50%) of the decreasing SN curve.

As can be recognized at the left edge: The evolution of *Eff* is not linked to the accumulation of the micro-damage.

For brittle materials *Eff* (Werkstoffanstrengung) seems to be able to quantify the portions (n/N) summing up the full activated $D = \Sigma D_i < D_{feasible}$.

$$D = n_1/N_1 + n_2/N_2 + n_3/N_3 + n_4/N_4 = D_{feasible}$$

Miner (Relative) application: $D_{feasible}$ - calibration from test experience

(micro-)Damage Mechanics: Definition of the D_i

How does Continuum Damage Mechanics formulate and take over the quantification of its D_i portions?

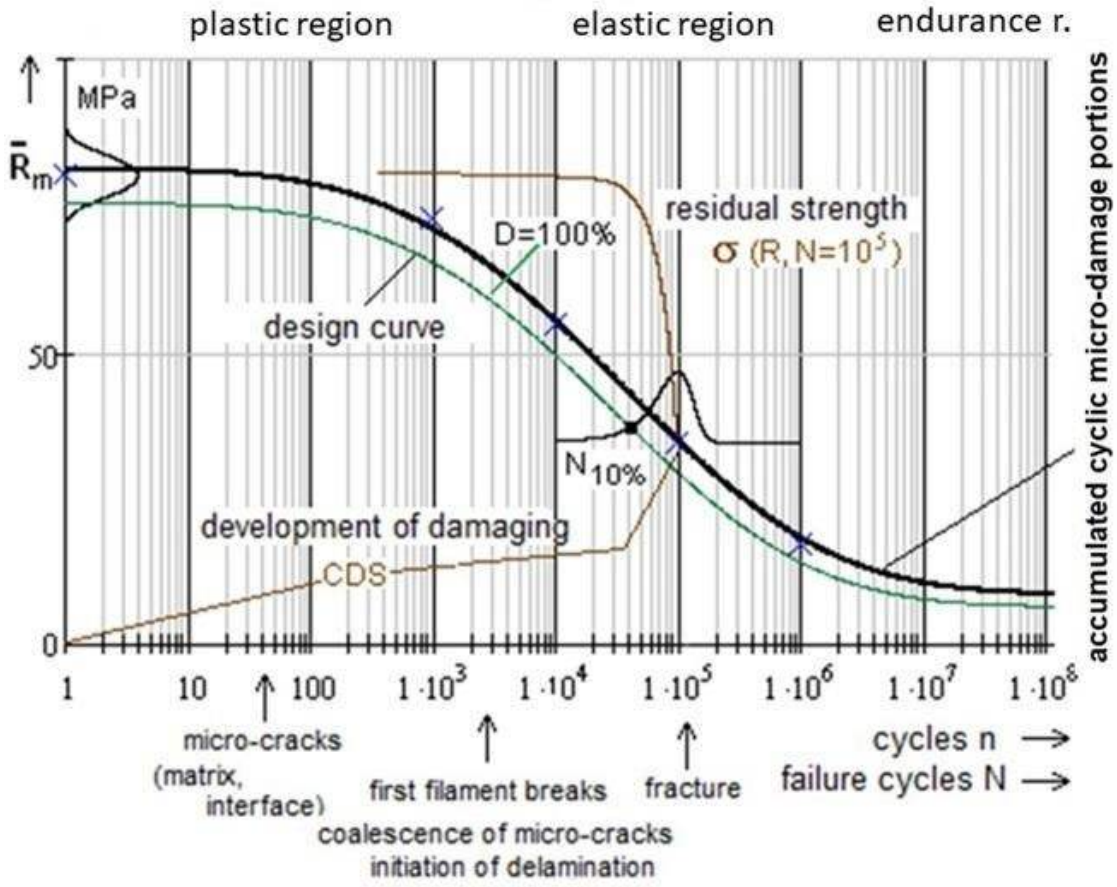

Fig.11-9, Design Verification: Fatigue average curve and ***design curve*** **R = 0.1.** *D = D_{design} for a survival probability P with a confidence level C. CDS is 'characteristic damage state' of a lamina*

[Hiatt, J. (2016), 'What is a SN-Curve?', Technical report, Siemens PLM Community). N = $N_{initial}$ + $N_{crackgrowth}$.

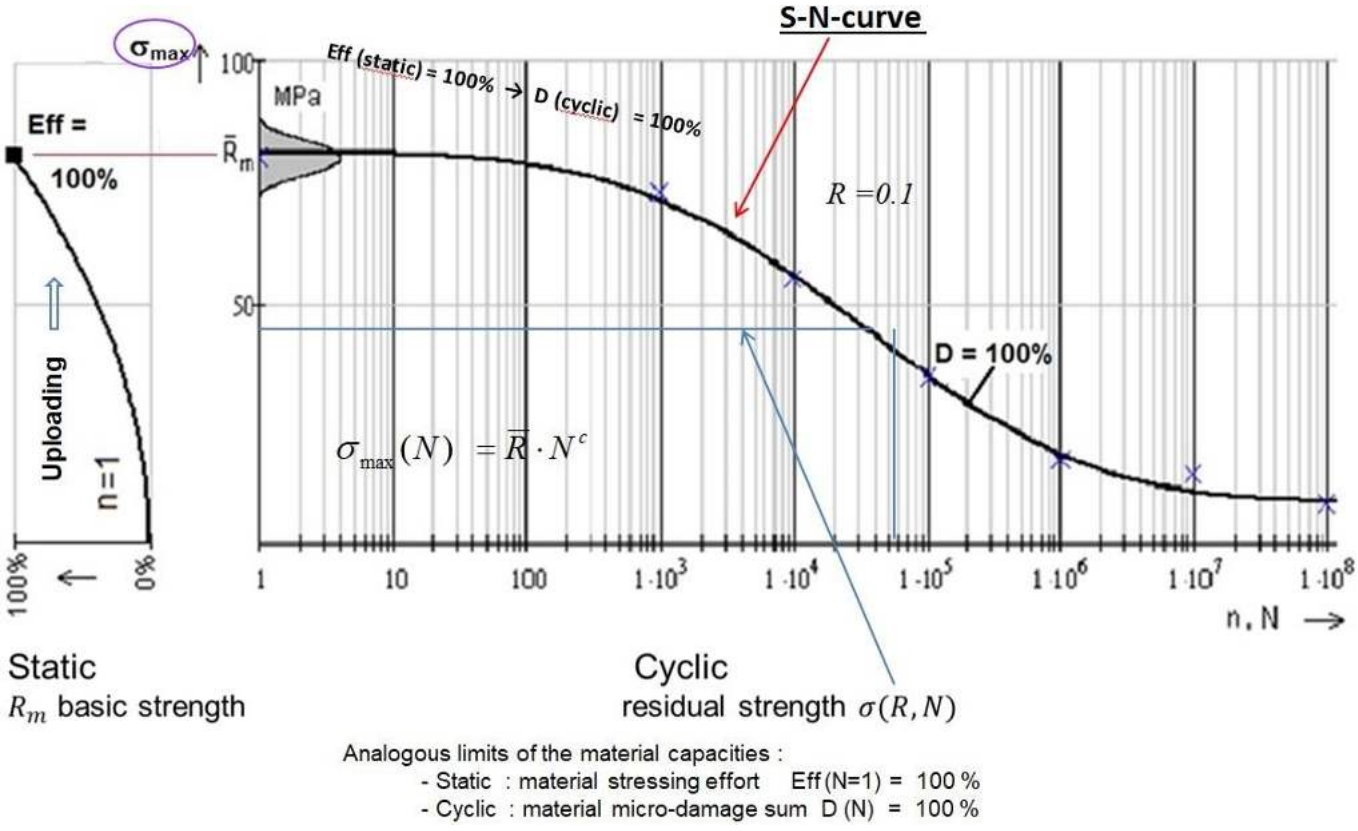

Fig.11-10, Mapping: Eff versus D. Mapping deals with averages ≡ 50% expectance value

11.5 Multiscale Modelling approach of Infinite Life and Endurance limit of Metals

Infinite life or, in other words, the endurance limit is an ever-lasting topic of highest interest in structural design and concerns all materials. Nowadays, valuable investigations on the micro-mechanics level seem to bring a significant progress for isotropic metals by using Continuum Damage Mechanics (CDM).

Mlikota and Schmauder found that the so-called 'Critical Resolved Shear Stress' CRSS is the relevant fatigue-responsible quantity, (*Fig.11-11*), regarding the behavior of ductile metals in the micro-scale regime. Multi-scale Material modelling (MMM), based on enough computer power will probably allow in future 'Computational material mechanics' from < micro-scale models (*Molecular Dynamics-treated and test results-supported from statically and cyclically loaded 10 µm thick pillars for instance*) via micro-scale to bridge with the necessary properties (*hopefully statistically based)* to the classical macro-scale models in structural design. Multiscale materials modelling could grow and become a significant tool for understanding complex material micro-damage processes for many homogeneous isotropic materials, a benefit for macroscale investigations.

The conclusions of Mlikota are:

- The CRSS is the resistance for the dislocations to move through the crystal. It is governed by the present strengthening mechanisms in the crystal. The CRSS is - according to critical stress strength - a micro-shear strength.
- The fatigue crack growth modeling procedure in the High Cycle Fatigue regime should include the following steps: Micro-crack nucleation within a grain → Coalescence of already existing flaws and/or arrest at grain boundaries → Short crack or Stage I growth → Transition from Stage I to Long crack or Stage II growth
- The discovered relation between endurance limit and the CRSS allows the virtual selection of those types of materials, which are more fatigue resistant! The physically-based MMM approach represents a breakthrough in the field of fatigue research
- The higher the CRSS magnitude of the metal of interest, the higher the loading stress level σ will be necessary to accomplish the transition from infinite to finite life
- The multiscale fatigue simulation approach is capable of properly taking into account the mean stress $\sigma_m = max\,\sigma \cdot (1+R)/2$ with the stress ratio R = minσ/maxσ and capturing the stress concentration factor K_t, which are influencing factors when designing structural components.
- Experimental tests demonstrate, that there is a drop in resistance to fatigue fracture with the increase of the grain size.

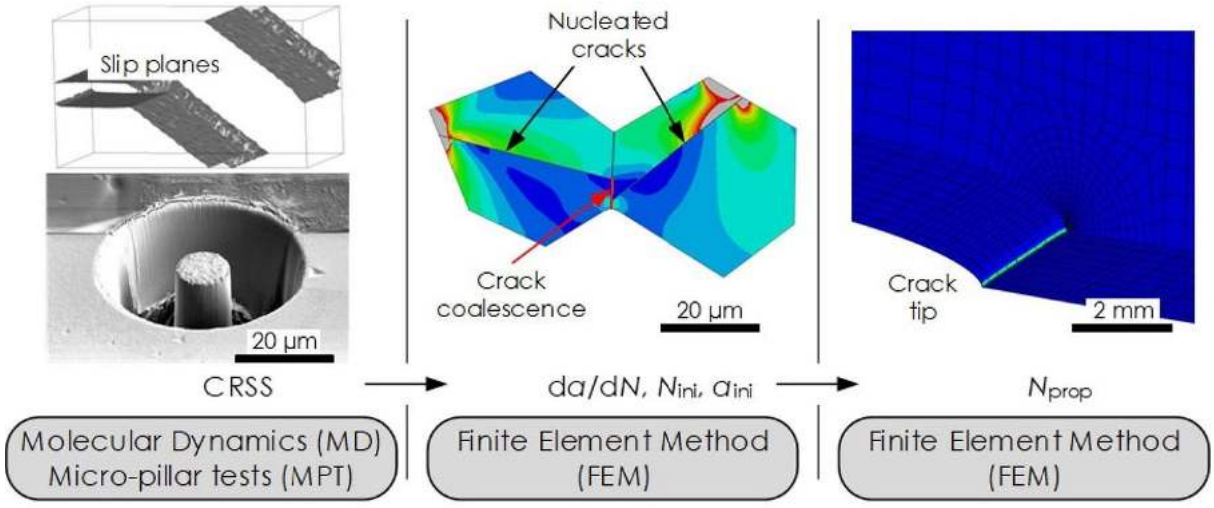

Fig.11-12: Full modelling approach. CRSS critical resolved shear stress, da/dn crack growth rate, N_{in} number of stress cycles until short-crack initiation, a_{ini} initiation short-crack length, N_{pro} number of stress cycles until short-crack propagation.

[Mlikota M. & Schmauder S. (2018), 'On the critical resolved shear stress and its importance in the fatigue performance of steels and other metals with different crystallographic structures', Metals 8(11), 883]

LL:

* *There is a hope for some ductile materials in future to estimate the endurance limits of various metallic materials in the Ultra HCF regime just by knowing their CRSS values !*

  Available CDM models seem to be neither to be clear-defined nor classified to be used for Design Verification (DV). A DV-procedure is to generate

* *A grain is usually polycrystalline with crystal planes in various spatial orientations. Hence, a metallic material can be only termed homogeneous and isotropic if these orientations are randomly distributed in order to become quasi-homogeneous. (*By the way, this is the same for an isotropic short fiber-reinforced polymeric material. Otherwise, the so-called orientation tensor has to take care of the non-isotropy*).*

* *For the isotropic analysis the Mises SFC was employed in order to localize the peaks of shear banding (yielding) of the investigated steel material*

$$\sigma_{eq}^{Mises} = \sqrt{3 \cdot J_2} \quad \text{with} \quad 6J_2 = (\sigma_I - \sigma_{II})^2 + (\sigma_{II} - \sigma_{III})^2 + (\sigma_{III} - \sigma_I)^2 = \; f(\tau), \; \tau_{oct} = \sqrt{J_2 / 3}$$

* *Clearly to be defined is the quantification of the D-portions for ductile and brittle behavior with a maximum value of total D = 100%:*

  - static case: the achieved micro-damage value at a distinct (equivalent) stress level

  - cyclic case: cycle-associated micro-damage portion with its derivation formula.

.

12 Note on Multi-scale Structural with Material Modelling and Analysis

Aim: *Making aware of limits when applying validated macro-scale formulations regarding lower scales.*

12.1 Structural Modelling and Analyses over the Scales

Structural modelling with associate analyses is performed at many scales, see *Fig.12-1*, from the macro-scale up to the Burj Khalifa building size.

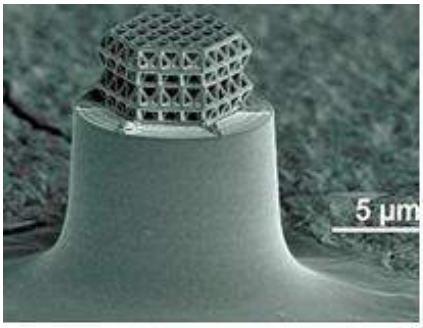

Fig.12-1: *Size variety of structures.*

(left) Truss structure, created by J. Bauer and O. Kraft with laser lithography.

Glass-like carbon nano-framework R^c = 3000 MPa. Advanced Materials, Progress Report, 'Nanolattices: An Emerging Class of Mechanical Metamaterials'. JensBauer, Lucas R. Meza, Tobias A. Schaedler, Ruth Schwaiger, Xiaoyu Zheng, Lorenzo Valdevit. 2017,Wiley Online Library

Structural Modelling, Substructuring

Fig.12-2 presents the so-called sub-structuring (*affecting shares between the participating Ariane partners)* an example for violating mechanics: MAN was not permitted to include the neighboring structural part despite of the fact that it was also a MAN contract part. We could not implement the FE model of this neighboring part in order to optimally represent the real boundary stiffness conditions in the model of the 'studied structural part' but had to implement the given boundary conditions of the contract. This caused a wrong behavior of the 'studied structure' and was a real mess regarding the evaluation of the test results and comparison with analysis results.

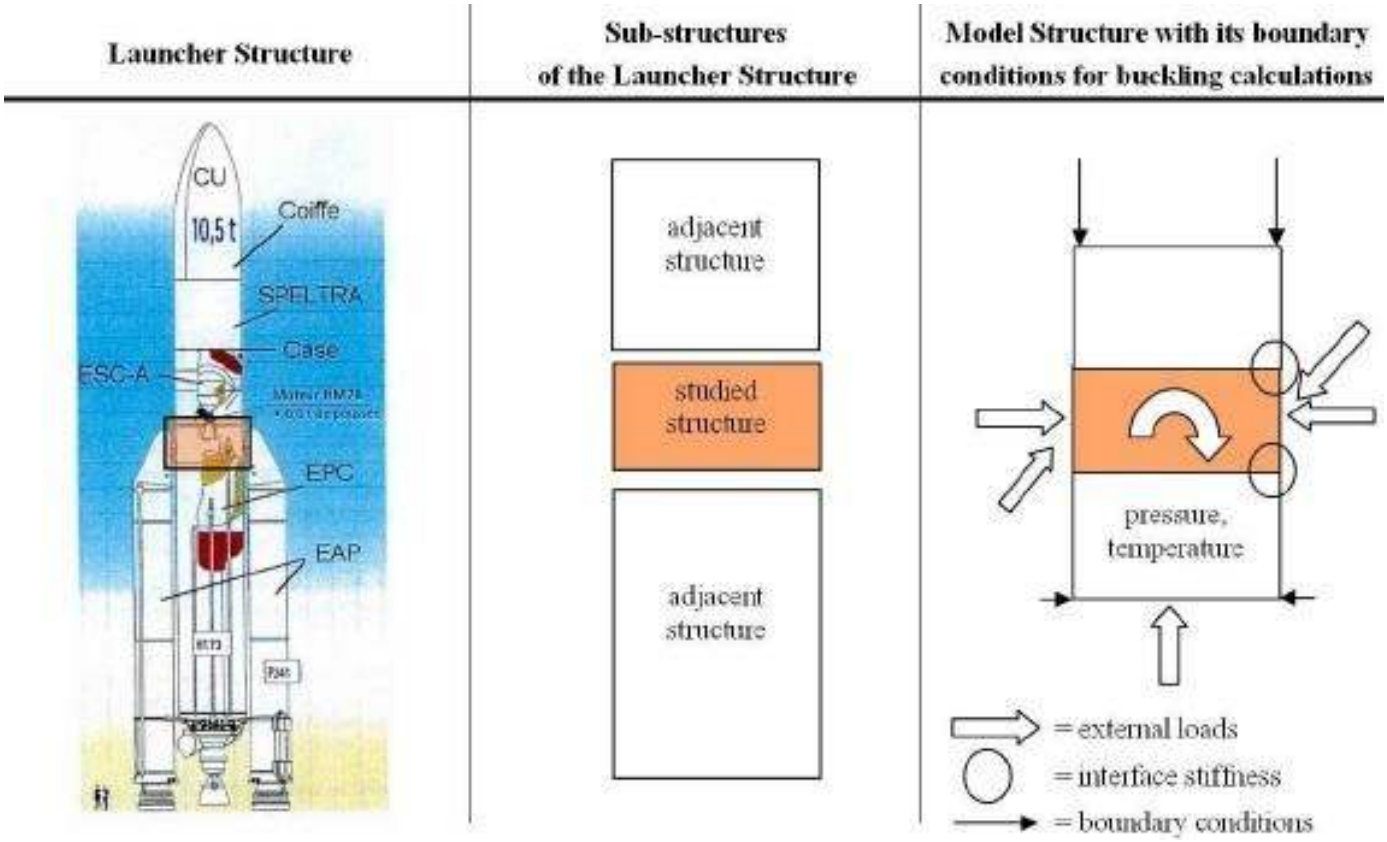

Fig.12-2: Sub-structuring of the Ariane 5 launcher, Front Skirt

All this requires to investigate the applicability of the usual macro-scale formulations especially concerning static strength, fatigue and fracture mechanics. For the assessment of a stress state, when viewing Design Verification (DV), it is to know the 'Onset-of-micro-damage' and the later following 'Onset-of-micro-cracking'.

Multi-scale modelling is executed for static and cyclic problems. In the cyclic case, there are three key 'points' that separate the regions in *Fig.12-2*:

- Ultimate strength $R_m^{\ t}$: Stress level required to fail with one cycle, n = 1
- Onset of Yield, R_e: Stress value at onset of plastic behavior with being $R_e < R_{0.2}$
- Endurance limit $S_{e(ndurance)}$: Stress corresponding to the horizontal asymptote of the SN-curve.

LL:

** It is always necessary to check whether the material at the lower level behaves in such a way that physically-based macro-mechanical formulations can be used*

** The material data input should satisfy physical model demands, which includes measurable parameters*

** DV demands for a statistically reduced SN-curve.*

Thereby, the challenging task is the input of the right material properties:

Which values are to insert when analyzing at the lower scale?

What about the stress-strain curve, and which for instance for the anisotropic UD material remains always bound to the macro-scale?

12.2 'Meso'–Material Modelling of the Example UD material

Fig.12-5 exemplarily gives a look at the present multi-scale modelling performed with Fiber-Reinforced-Polymers (FRP). Two scales are linked together, the micro-scale with the macro-scale by a meso-model. What is meso? Meso is no scale, per definitionem!

* Micro-scale > μ *m*, macro-scale > *mm*.

* The author experienced (1999) in a BMFT R&D discussion round on three MaTech Competence centers of institutes working from the polymer-scale to the structural macro-scale - after one day - that the term meso-scale is used in polymer mechanics by the research colleagues at the nano-level. This level is one thousand times smaller than the solid mechanics people apply meso.

* A further classification is available for porous materials, according to pore size: 'microporous' pores < 2 nm, 'mesoporous' pores between 2 nm and 50 nm, 'macro-porous' pores > 50 nm. [*International Union of Pure and Applied Chemistry*].

LL: arduous experience from WG discussions

The term meso is a task-linked chosen size level.

Apply the term meso-model, not meso-scale, and define it. In structural engineering meso is used at about 0.1 mm.

12.3 Material Mixture Rules: Example Micro-mechanical Formulas of UD laminas (ply)

***Aim**: Guideline how to use micro-mechanical models and properties with giving some warning.*

Mixture rules are employed in many technical disciplines (polymer and mineral composites like concrete). Exemplarily, here at the so-called micro-mechanical formulas of UD-materials will be looked at, only.

Creep investigations and pressure-related effects on the matrix and in consequence on the UD material of composite materials i.e. usually require a micro-mechanical input.

Examples of the author, a centrifuge and a WWFE Test Case: The non-creeping constituent fiber is to separate from the creeping/relaxing constituent matrix. In order to capture these features the use of 'micro-mechanical mixture rules' in structural engineering is common practice. It requires properties of the constituents and the so-called mixture rule, how these constituent properties are linked, to be able to predict properties of the envisaged ('smeared') material on the macro-scale.
Not all micro-mechanical properties applied can be measured. A solution will be obtained by setting up mixture rules and calibrate them via macro-mechanical test results on the lamina macro-level. This makes an inverse parameter-identification necessary.

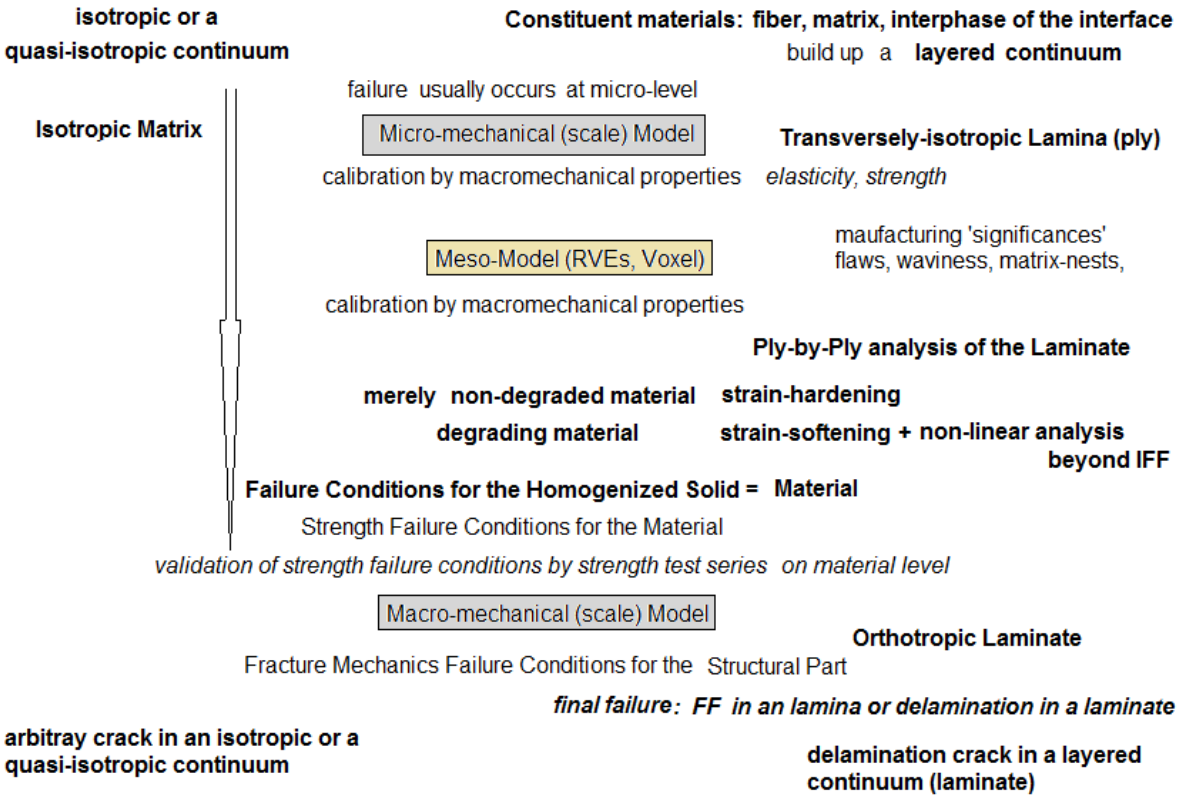

Fig.12-5:Multi-scale modelling, example FRP, brittle. 2 scales. RVE: Representative Volume Element, Voxel: volumetric pixel

Hence, the application of a micro-mechanical formula underlies the constraint that the given micro-mechanical properties can be only used together with the formulas they are based on. Otherwise the results might be pretty wrong. For example within the WWFE, Test Case 1, the organizer QinetiQ just provided micro-mechanical material properties but not the associated micro-mechanical formula. Therefore, the author had to apply micro-mechanical UD formulas from [VDI 2014, sheet 3] and found a discrepancy of a factor 2 for the data to be predicted! This is not acceptable for the WWFE-task model validation.

For imposing pressure-related effects on the matrix and in consequence on the UD material 5 micromechanical formulas had to be applied in the WWFE together with the associated evaluated experimental data.

The following equations of H. Schuermann were employed, and may be used for the regime $0.3 \leq V_f \leq 0.65$:

$$E_{||} = E_{||f} \cdot V_f + E_m \cdot (1 - V_f) \cong E_f \cdot V_f,\ E_{\perp} = \frac{E_m}{1 - \nu_m^2} \cdot \frac{1 + 0.85 \cdot V_f^2}{(1 - V_f)^{1.25} + V_f \cdot E_m / (E_{\perp f} \cdot (1 - \nu_m^2))},$$

$$G_{\perp||} = \frac{G_m \cdot (1 + 0.4 \cdot V_f^{0.5})}{(1 - V_f)^{1.5} + V_f \cdot G_m / G_{\perp||f}},\ \nu_{\perp||} = \nu_{\perp||f} \cdot V_f + \nu_m \cdot (1 - V_f),\ G_m = E_m / (2 + 2 \cdot \nu_m)$$

with the result, that a not acceptable factor of 2 was faced.

LL:

Micro-mechanical properties can be used only together with the formulas they have been generated with ! ⇐ Significant Warning due to painful time-wasting experience in the WWFEs !!

**Macroscopic modelling requires that averaging is applicable.*

13 Some Notes on Structural and Material Testing with Evaluation of Results

***Aim**: Forwarding Lessons Learned from own structural Ariane tests and own material tests together with those from the WorldWideFailureExercise (WWFE).*

13.1 General

In structural design one basically faces 3 types of testing**:**

- Structural Testing (destructive, non-destructive)
- Materials Testing (destructive, non-destructive) and
- Non-Destructive Testing of structure and material (NDT, NDI, NDE).
  Other tasks here are: Failure detection, localization, size + shape, Failure assessment (risk-based).

All structural tests to be performed aim to uncover a deficiency: Workmanship, design mistake, oversight of a failure mode, tightness, shock resistance etc.

Fig.13-1 presents the test strategy of the MIL handbook 17, a forerunner guideline for the development of composite structures which are more challenging than developing isotropic structures.

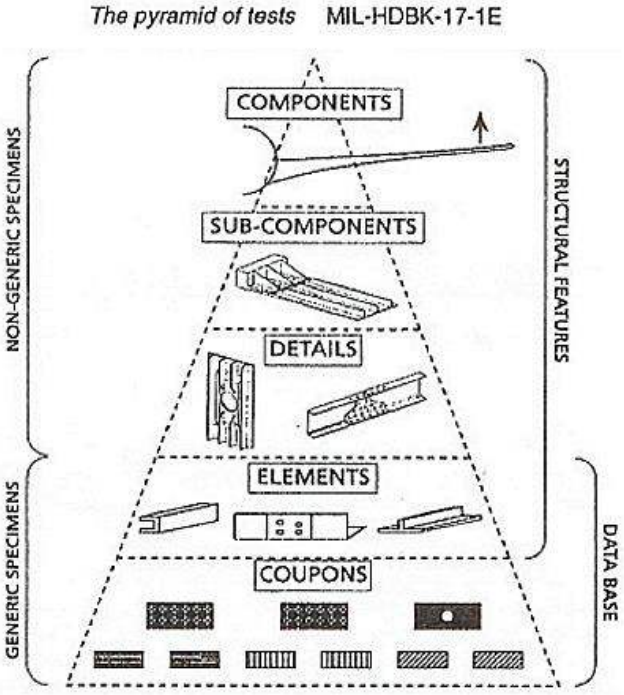

Fig13-1: Test strategy of MIL-HDBK 17 (original edition about 1970). MIL-HDBK-17/1F (VOL. 1 OF 5), DEPARTMENT OF DEFENSE HANDBOOK: COMPOSITE MATERIALS HANDBOOK - POLYMER MATRIX COMPOSITES GUIDELINES FOR CHARACTERIZATION

At first, a Test Agreement is to provide. It consists of test rig, test specification, test specimen and test data evaluation method and the Test Procedure.

Therefore, one can only speak about 'exact' test results in the frame of the obtained test quality.

In this Chapter some personal experience is presented, beginning with structural testing.

13.2 Structural Testing, primarily based on the Ariane launcher development

In the case of a large structure the full structure had to be sectioned in the past, considering project partners and computer power, into sub-structures and all the analyses are carried out at the level of these sub-structures. In addition, various contractors dimensioned specific sections of the launcher and provide finite element sub-structures for the complete mathematical model. This model is dedicated to dynamic analysis. As a result of the sectioning, the first buckling mode can appear on an adjacent

structure and not on the envisaged one due to unrealistic boundary conditions in stiffness. Fig.13-2 (left) visualizes to some extent the so-called sub-structuring (*affecting shares between the participating Ariane partners)*, project architect-given. It can be a striking example for violating mechanics. In the final test the fictitious given boundary stiffness conditions could not be in line with the launcher reality. Once, in order to meet the given requirements the test article had been allegedly strengthened, which was senseless, because the launcher force distribution had been changed by this!

Fig.13-2: (left) Structuring of the Ariane 5 launcher; (right) assembly of Ariane 517, Front Skirt test

Another not desired result of sub-structuring a large structure is: The first buckling mode can appear on an adjacent structure and not on the studied one. In this case the designer can locally modify the structural stiffness of the adjacent parts in order to make the buckling mode appear first in the studied structure. In any case, the load path should not be changed by these modifications. This kind of process is based on much engineering experience. To improve the precision of the results in the critical areas where buckling is supposed to appear, some detailed models can be directly introduced into the global model.

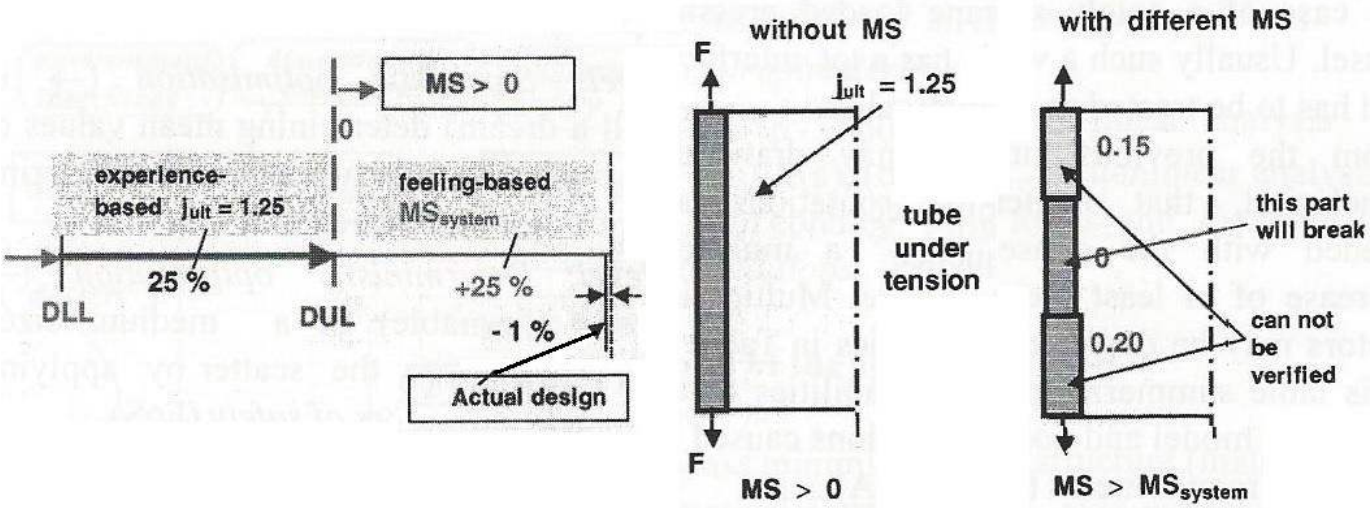

Fig.13-3: Non-testability effect, when using different System Margins [Cun00], MS = MoS

For the linear buckling analysis, the nominal thickness should be used to ensure the correct elastic behavior of the structure. For a nonlinear collapse analysis, the minimal thickness is used to take thickness variations and imperfections into account.

In some spacecraft projects on top of the FoS so-called system-margins ($MoSsys \neq MoS = RF - 1$) are required to be met in the structural tests. *Fig.13-3* depicts one example in which on a distinct structural component composed of several sub-structures, according to a part-associated uncertainty 'feeling', an additional margin of MoS_{sys} = 25% was put on top. Unfortunately, even for adjacent sub-structures the required values had been different. This action leads to a disaster in test design verification.

13.3 Some practical Hints for Applications on *Design Process and Modelling*

Structure design is a balance between mass and safety (*structural reliability*) with an essential goal to be as light as possible (*required not in aerospace only*). The designer must develop a structure which has to meet stiffness, loads, environments, mass requirements, time and costs. Thus, Dimensioning is a complex process: It shall combine the different external and internal loadings acting on the structure of the sources: static, dynamic (impact), cyclic, thermal, environmental, residual stresses. Special concern is on the effect of local loadings due to attachments, joints and so on. This is particularly true in buckling design, when different kinds of loadings act on the same structure and it is to correctly combine mechanical, thermal and local loading. Once the first design is obtained, the resistance against local and global buckling of the structure can be assessed according to the procedures presented above.

Always a series of calculation with different sets of loadings is to perform in order to:

- understand the behavior of the structure with respect to buckling,
- define a reference configuration with a set of imperfections.

13.3.1 Stability Loading processing

The loading to which each structure is submitted can be classified in two categories:

- the destabilizing loads, which create a stress field decreasing the apparent stiffness of the structure leading to its buckling. For instance, for a launcher tank, destabilizing loads are external pressure or compression loads.
- the stabilizing loads, which in the case of the buckling create a field of constraints increasing the apparent stiffness of the structure. In the case of a cylindrical shell, they can be the internal pressure or the tension loads.

A loading combination which does not take into account the distinction between these two types of loads leads to apply the same FoS to both loading types *destabilizing* and *stabilizing* and therefore leads to increase these loads simultaneously until the structure breaks down. This way to consider the loads is correct if it is assumed that the stabilizing loads are statistically dependent on the destabilizing loads, which is a priori not always the case. In this last case, the method is optimistic with regard to the critical buckling load and overestimates it. If the two types of loads are statistically independent, the approach to be followed is to apply the FoS to the destabilizing loads and to increase them until collapse whereas stabilizing loads are maintained at their specified level (*design limit loads DLL*).

Exemplarily for a shell it is to be accounted for: (1) Geometric specifics of the structural elements tubes, frames, stiffeners, (2) Geometrical deviations (i.e. w*eld joints*), (3) Ovalization effects. Radial buckling and axial buckling may occur.

The measurement of the test article is always accompanied by analyzing the test article by an analytical model. On this basis the evaluation of the test results may cause a re-analysis to better simulate the test results and to finally improve the Design Verification.

13.3.2 Validation of the analytical model

Essential step of the qualification process is the correlation of the numerical models, see *Fig.13-4*, a task where the time devoted to it is often underestimated. The part of the logic discussed is the one surrounded by the blue oval in the figure.

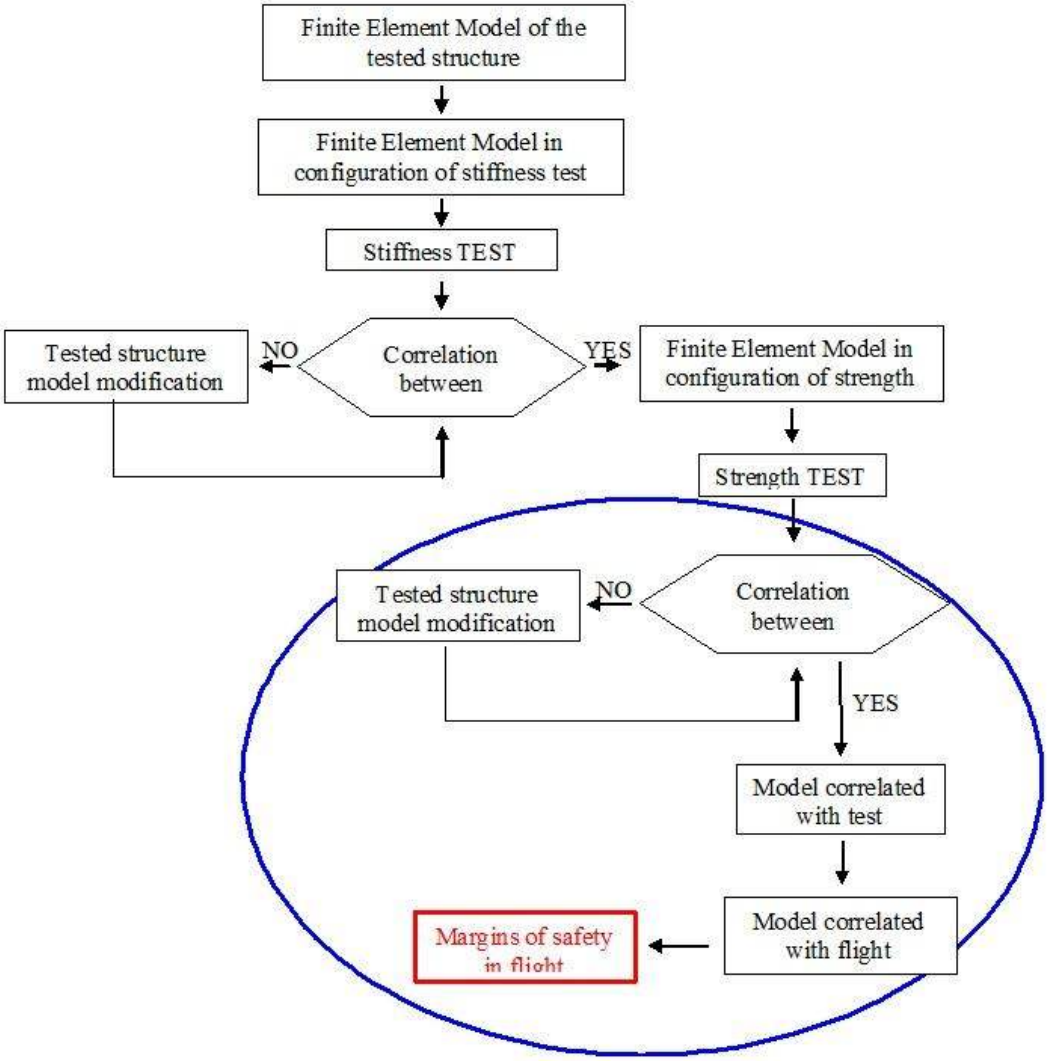

Fig.13-4: Logic of model correlation

The correlation task consists in, first comparing the test predictions to the measured data and checking the mismatches, and second, if the mismatches are considered as not acceptable, to adapt the model according to several means. Among others, the main ones are:

- refining meshes - globally or locally, by using volume finite elements
- being fully representative of the fine geometry (all discontinuities like stiffeners, connections, holes…).

Criteria of acceptation of a 'good enough coherency' between predictions and test results are commonly agreed by the design responsible and the customer. One example of the Ariane community asked for less than 15% of mismatch on displacements and 20% on stresses.

Once the correlation is considered as acceptable (*correlation by comparison with the test or by cross-checking*), the numerical model is considered to be validated. However, it is not to forget that the full reality of loadings and boundary conditions cannot be implemented because of the complexity to perform tests on large structures and its components and because of the consequent cost and time which is usually not affordable.

13.3.3 Stability Proof testing considering analysis and test

In aircraft even for 'simple' stability-endangered structural elements seldom a test series is available to compute statistically-based stability design allowables. Aircraft certification standards usually do not require statistics to be performed on stability tests. For example, in EASA CS 25.307 (Certification Specifications for Large Aeroplanes) is cited: "When static or dynamic tests are used to show compliance with the requirements of CS 25 for flight structures, appropriate material correction factors must be applied to the test results, unless the structure or part thereof, being tested has features such that a number of elements contribute to the total strength of the structure and the failure of one element results in the redistribution of the load through alternate load paths." Thus, for all multiple load path structures a statistics-aimed testing is not required by CS 25.

In spacecraft, an improvement of the predictions of the traditional stability analysis result is aimed at by applying a statistically based estimation procedure for the failure load. This requires knowledge about the design variables such as geometrical tolerances, imperfections and scatter of properties. This knowledge is the input of - for instance a Monte-Carlo method - which predicts sensitivities and delivers a statistically based failure load, an improved value compared to the traditional analysis one.

13.3.4 Test Data Evaluation of a Qualification Pressure Tank (deterministic and probabilistic)

As a structural test evaluation example shall be given a 'qualification pressure tank'. It will be evaluated deterministically and probabilistically in order to get a measure for the evaluation possibilities:

1 Task Internal pressure vessel of a motor housing; Qualification test series (old examples)

- Design requirements:
  Action *S*: MaximumExpectedOperatingPressure MEOP ≡ DesignLimitLoad DLL, DUL = $j_{ult} \cdot$ DLL

  Given : μ_S = 17.0 MPa (N/mm^2), σ_S = 1.70 N/mm^2

  Resistance *R*:

  Given : μ_R = 17.0 N/mm^2, σ_R = 1.70 N/mm^2
- Safety Concept:

  UT = UpperTolerance limit = $\mu_S + 2.3 \cdot \sigma_S$ and LT = LowerTolerance limit = $\mu_R - 2.3\ \sigma_R$

  Deterministic: j_{ult} = 1.5, proof test j_{proof} = 1.3 , extra a $MoS_{nominal}$ = 0.2

  Probabilistic: Reliability value = survival probability $\Re$ = 0.99999 or failure probability p_f = 1 - $\Re$
- Requirements for achievement of test design verification by meeting the limits
  Deterministic : $MoS_{nom} > 0.2$, Probabilistic: $\Re > 0.99999$.

2 Test Data

The qualification tests lead to the following results for mean, standard deviation and density distribution: μ_R = 33.7 N/mm^2, σ_R = 3.3 N/mm^2, Normal Distribution.

3 Statistical Evaluation of the Test Results

The test verification was carried out for above main design parameter, the internal pressure p_{int}. The distribution of its action $f_S(x)$ is the density distribution of the maximum motor pressures measured in operation and the distribution of the resistance, the load capacity $f_R(x)$, is the density distribution of all burst pressures measured in the qualification series. The probabilistic calculation can be carried out in this simple case with the help of the Gaussian integrals employing the Hasofer-Lind Z-transformation (see p. 57):

$\mu_Z = \mu_R - \mu_S$ = 16.7 N/mm^2, $\sigma_Z = (\sigma_R^2 + \sigma_S^2)^{0.5}$ = 3.48 N/mm^2,

$\beta = \mu_Z / \sigma_Z = 4.8.$ → from a statistical handbook $\Phi(\beta) = 0.99999922 = \Re = 1 - p_f > 0.99999$

or $p_f = 7.8 \cdot 10^{-7} < 1 \cdot 10^{-5}$.

Margins for nominal safety are obtained from

$UT_S = 17.0 + 2.3 \cdot 1.70 = 20.9$ N/mm^2, $LT_R = 33.7 - 2.3 \cdot 3.03 = 26.7$ N/mm^2

$\boldsymbol{MoS}_{nominal} = LT_R / UT_S - 1 = 0.27 > 0.2$ (O.K.) and for thinking as comparison number $\boldsymbol{MoS}_{central} = \mu_R / \mu_S - 1 = 0.98$, fixing, that the ratio of the mean values of the two distribution is a non-safe number!

LL

** Test article analysis is mandatory to interpret the test results and simulation-based improve the design. Only well-understood experiments can verify the design assumptions made!*

** Splitting of a large structure (Ariane experience) is dangerous: The first buckling mode can appear on an adjacent structure and not on the studied one*

** Mandatory for a realistic qualification of a sub-structure is a realistic set of cross-section loadings and pressure loading with an accurate structural designing of the interface stiffness of the adjacent structural parts. If the interface is too stiff in the test assembly this will attract loading and lead to a non- realistic failure site (experience from Ariane 5 tests). The total system determines the behavior*

** Not all critical locations of a structural component can be tested, because an 'over-testing' of some parts may happen to be. 'Verification By-Analysis-Only' is to be considered if the structure is too big or if the test model shall e.g. be applied later as flight model*

** Put strain gauges there where a clear stress situation is in order to avoid useless discussions about the interpretation. Check locally by strain measurements and then rely globally on FEA-test result comparison. Specific design requirements drive the testing*

** Requiring different so-called system margins MoS_{sys}* (suffered nonsense in a Ariane Technical Specification) *for the various structural parts, then not all critical locations can be tested without overloading other integrated parts. Components of such a structural assembly cannot be verified by a qualification test, because system margins cannot be used locally like a 'fitting factor'. They should have been considered directly in the Ariane 5 as a usual design FoS, applying $j_{sys} = (MoS_{sys} + 1) \cdot j$. Otherwise, the design process is obscured and is prevented from applying the most economic measure in order to take risk out of the structure*

** Requirement to put a design FoS j on a design temperature violates physics and structure behavior*

** So-called test correction factors are applied to adjust the design verifications by accurately evaluated structural test results linked to the test article analysis results.*

⇒ *Bad personal experience from Ariane 5 offer and later from project tests:*

**The given Sub-structuring becomes risky, if the boundary stiffness between the structural parts is not provided by the structural architect.*

**Worse, because during the project later MAN could not use the boundary stiffness of the neighboring part which MAN was also responsible for. This led to senseless test measures.*

13.4 Pre-Assessment of UD-Material Testing Data Input primarily based on WWFE-I and -II

The author succeeded with test-validation of 3D-strength criteria models for isotropic concrete, transversely-isotropic UD-material, orthotropic ceramic (fabrics) with visualization of the derived 3D failure surfaces if reliable test data sets were given. A lot of test data sets were only in the *the World*-WWFE-I, *concerning2D-mapping*, and WWFE–II, *concerning 3D-mapping of UD materials.*

The author's I and II contributions had to be based on an intensive assessment of the provided test results. In this sub-chapter the Lessons Learned during the examination of several WWFE-Test Cases (TC) shall be collected.

Validation of the lamina-material SFCs models can be only achieved by 2D- together with 3D-lamina test results. Since SFC-model validation is focused just lamina-TCs are now investigated in detail. The user is basically interested to well map his course of failure test data by a UD-SFC and not on the laminate.
The laminate test cases serve for the *verification* of the laminate design. There the full WWFE failure theory is required. This makes a comparison between the contributions very challenging because different FE codes were applied by the contributing competing institutes. These better tools further had to be equally compared to the simpler tools of the retired author. He could just use his handmade non-linear CLT-code, non-linearly upgraded by experience and using his sensibleness for the problem and the delivered input.

***LL**, more general ones*

** Never trust input data including your own data.*

** Measurement data is the result of a Test Agreement (norm or standard), that serves the desire to make a comparability of different test procedure results possible. Hence, there are no exact property values. Material properties are the result of the material model applied inclusively mapping process.*

** Stresses, strength, strains and elasticity properties cannot be directly measured*

** Check of assumptions is necessary before designing for the example WWFE on UD-material. Pore-free material, specimen surfaces polished, well-sealed, fiber volume is constant, tube specimens show no warping and do not bulge, perfect bonding, no layer waviness, edge effects do not exist*

** Sometimes one must live with a substitute test situation in order to get some approximate properties (Example: UD-Tension/Compression-Torsion test device → Arcan test device)*

** Before thinking about test data evaluation the associated underlying micro-damage processes must be sorted out in order to get a better understanding of failure especially macro-failure*

** Test specimens shall be manufactured like the structure ('as-built')*

** Comparisons between theoretical predictions and test data help to identify the major discrepancies, limitations, and areas which require further theoretical and experimental work. There is always a lot to be done and following Moslik Saadi: "All is difficult prior to becoming simple"! This begins with the provision of appropriate test specimens for the various material families being extreme ductile or brittle and ends with appropriate test procedures and an appropriate test data evaluation*

** Considering FE-results: We must more and more 3D-design! However the situation of properties, especially for composites is: „Expensive reliable 3D-property data test sets are seldom sufficiently available for the designing engineer".*

Of high interest for future scientists and engineers might be the following assessment results of the provided properties during the author's many WWFE-designated years. They are results which stem from a very careful and effortful test data evaluation lasting about *one man year*. Otherwise, a successful WWFE-contribution could not have been made possible.
Making aware of input shortcomings, here now will be presented a survey on some essential lamina test data input shortcomings regarding the WWFE Test Case-examples *(a deeper elaboration follows in §19*) and how to tackle some of them as far as possible:

* WWFE-I, TC1: the provided strengths have been changed from Part A to B and two test points are doubtful regarding own test results (*Reason became known for me: non-accurate raw test data evaluation of the test engineer at DLR Stuttgart. Organizers did not question the test data but required mapping of the false ones*!).

* WWFE-I TC2: the author informed the organizers that apples and oranges have been put here together in a diagram. One cannot fill into the same diagram 90°-wound tube test specimen data together with 0°-wound tube data. The 0°-stresses have to be transformed in the 2D-plane due to the fact that shearing under torsion loading turns the fiber direction (§19 and *Fig 13-3*) and the lamina coordinate system CoS is not anymore

identical with the structure coordinate system of the tube. In order to also use these test data the author exemplarily transformed two fracture test points by the occurring twisting angle γ using a non-linear CLT-analysis. Then he could achieve a good mapping showing, that the two transformed fracture points accurately lie in the lamina CoS on the 90°-tube curve.

* WWFE-II, TC3: the same mistake happened again! However, here the much more complicated 3D-stress situation was to face, so that the 3D-transformation of the 0°-data set could be finally simply performed.

* WWFE-II, TC2 an average stress-strain curve should have been provided because otherwise no realistic treatment is possible. Therefore the Part A results could be only inaccurate. From the Part B information the author could derive an average curve and then all 3 TC test data courses could be mapped and the mutual check points in the fully connected TC2-TC3-TC4 matched. Incomprehensively, there was no response of the organizers to the author's idea, which made 3 TCs to successful test cases (more WWFE etc test evaluations are found in [*Cun13*], on laminas and laminates)

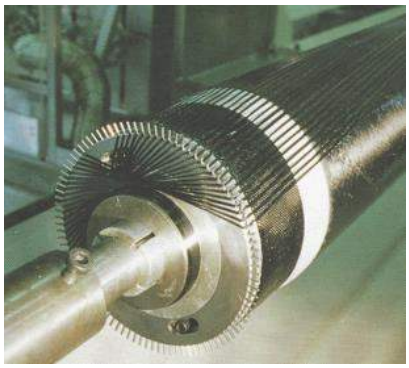

MAN thread winding machine
(pin winding)
with CNC control and
heatable multi-thread guide.
*Thread placement from ≅ **0°** to **90°** possible.*
See the magenta curve outside located 0°-test points in Fig. 13-3.

Fig.13-3: Variable angle winding machine

"Theory is the Quintessence of all Practical Experience" *(A. Föppl) .*
Theory creates a model of the reality, one experiment shows one realization of the reality.

Finally, *Fig. 13-4* presents details of the high-qualified tension-compression-torsion test rig.

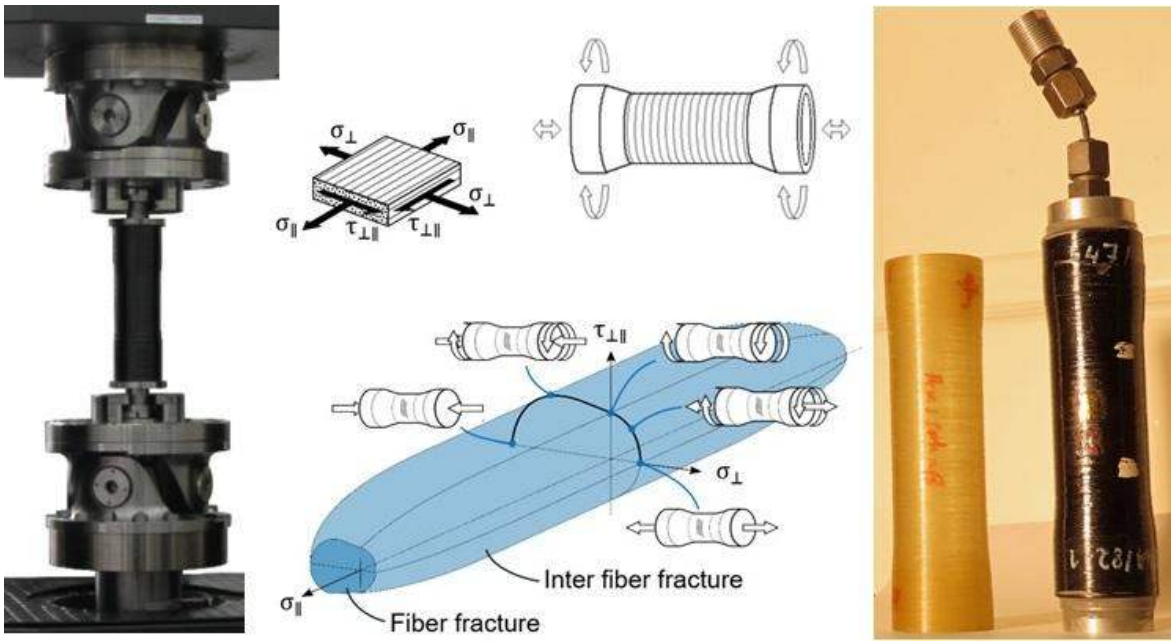

Fig.13-4: The tension-compression-torsion test:
Test set-up of Leibniz-Institut für Verbundwerkstoffe GmbH Kaiserslautern and (right)
GFRP and CFRP (internal pressure loadable) test specimens of MAN Technologie

14 Replacing fictitious Model Parameters by Measurable Friction Values

Aim: *Enable engineers to use measurable friction values instead of fictitious friction parameters.*

14.1 Brittle Isotropic Materials

14.1.1 Visualization of the Friction Value μ by the linear Mohr-Coulomb relation

In the next *Tables 14-1, -2* all those relations are presented which are necessary for the not simple transformation task in order to find a relationship between the fictitious friction model parameter in the SFC and a measurable friction value.

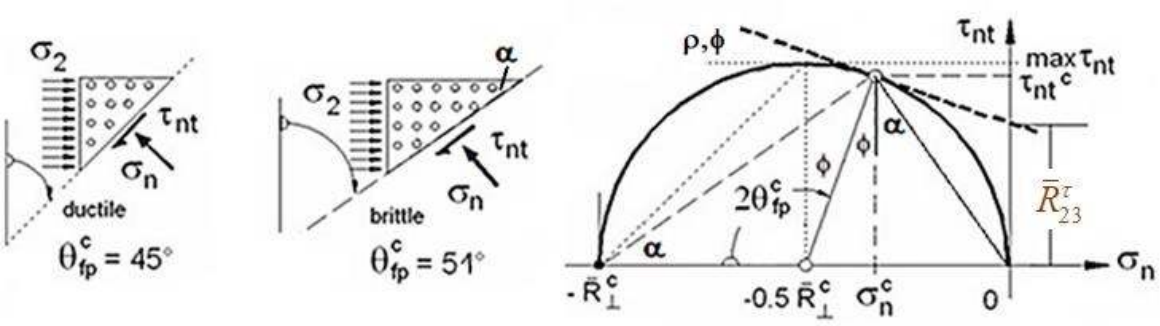

Fig.14-1 Fracture angle visualization, shear stressing situation for isotropic and UD:

Shear fracture plane angle in the touch point and 'linear' Mohr-Coulomb friction curve.

The touch point is defined by $(\sigma_n^c, \tau_{nt}^c)$ *and linked to* $\bar{R}_\perp{}^c$. $90° = 2\cdot\theta_{fp}{}^\circ - \phi^\circ$

In order to be able to derive the friction value μ, the slope of the linear Mohr envelope at the compressive strength associated point, termed touch point, must be provided. $\Theta_{fp}{}^c$ denotes the fracture angle in the touch point which is linked to the compressive strength, indexed ^{c}. Viewing *Fig.14-1* the relation exists $(\rho \equiv \phi)$: $\mu = -\tan\rho \cong -C^c = -\cos(2\cdot\Theta_{fp}^c{}^\circ \cdot \pi/180°)$, see *Table 14-2.*

Table 14-1: Derivation of relations $\mu(\Theta_{fp}{}^c)$ *applying the Linear Mohr-Coulomb approach*

$$F_{Mohr}^{SF} = \frac{\tau_{nt}}{\bar{R}^\tau - \mu\cdot\sigma_n} = 1 \qquad \text{- compressive SFC, angle } \Theta_{fp}{}^c \text{ unknown}$$

$$\frac{dF_{Mohr}^{SF}}{d\sigma_n} = \frac{\mu\cdot\tau_{nt}}{(\bar{R}^\tau - \mu\cdot\sigma_n)^2} \quad \text{and} \quad \frac{dF_{Mohr}^{SF}}{d\tau_{nt}} = \frac{1}{\bar{R}^\tau - \mu\cdot\sigma_n}$$

$$\rightarrow \frac{d\tau_{nt}}{d\sigma_n} = \frac{-\mu\cdot\tau_{nt}}{(\bar{R}^\tau - \mu\cdot\sigma_n)^2} / \left(\frac{1}{\bar{R}^\tau - \mu\cdot\sigma_n}\right) = \frac{-\mu\cdot\tau_{nt}}{(\bar{R}^\tau - \mu\cdot\sigma_n)^1} = \frac{-\mu\cdot(\bar{R}^\tau - \mu\cdot\sigma_n)}{(\bar{R}^\tau - \mu\cdot\sigma_n)}$$

$= -\mu$ (negative sign due to implicite differentiation).

$$F_{Mohr}^{NF} = \sigma_n / \bar{R}^t = 1 \qquad \text{- tensile SFC,} \qquad \text{angle } \Theta_{fp}{}^t = 90° \text{ known.}$$

$F^\tau = \tau_n/(R^\tau - \mu\cdot\sigma_n) = 1$, shear stress hypothesis $\Leftrightarrow$ $F^\sigma = \sigma_n / R^\sigma = 1$, normal stress hypothesis.

14.1.2 Derivation of the relationship Friction Parameter with Friction Value μ

The derivation of the Mohr stresses-transformed FMC-based strength failure conditions is depicted in *Table 14-2.* As a numerical example a material has been chosen with the friction quantities

$$\text{fracture angle } \Theta_{fp}^c{}^\circ = 50° \rightarrow C^c = C^c = \cos\left(\frac{2\cdot\Theta_{fp}{}^\circ}{180°}\cdot\pi\right) = -0.174, \quad \mu = 0.176.$$

C is termed 'fracture angle measure'. Link to friction angle: $\mu = -\tan\rho = -\tan\phi$.

Table 14-2: Derivation of the Mohr stresses-transformed FMC-based strength failure conditions

$$F^{SF} = c_{1\Theta}{}^{SF} \cdot \frac{3J_2 \cdot \Theta^{SF}}{\bar{R}^{c2}} + c_2{}^{SF} \cdot \frac{I_1}{\bar{R}^c} = 1 \quad \text{or} \quad Eff^{SF} = \frac{c_{2\Theta}^{SF} \cdot I_1 + \sqrt{(c_{2\Theta}^{SF} \cdot I_1)^2 + 12 \cdot c_{1\Theta}^{SF} \cdot 3J_2 \cdot \Theta^{SF}}}{2 \cdot \bar{R}^c}$$

Inserting compressive strength $\bar{R}^c$ delivers $1 + c_{2\Theta}{}^{SF} = c_{1\Theta}{}^{SF} \cdot \Theta^{SF}$ with the non-circularity function $\Theta^{SF} = \sqrt[3]{1 + d^{SF} \cdot \sin(3\vartheta)} = \sqrt[3]{1 + d^{SF} \cdot 1.5 \cdot \sqrt{3} \cdot J_3 \cdot J_2^{-1.5}}$

which reads $\Theta = 1$ if $\bar{R}^{cc} = \bar{R}^c \Leftrightarrow$ rotationally-symmetric

$$\frac{c_{1\Theta}{}^{SF}}{2\bar{R}^{c2}} \cdot [(\sigma_n - \sigma_t)^2 + (\sigma_t - \sigma_\lambda)^2 + (\sigma_\lambda - \sigma_n)^2 + 6 \cdot (\tau_{nt}{}^2 + \tau_{n1}{}^2 + \tau_{t1}{}^2)] + c_{2\Theta}{}^{SF} \cdot \frac{\sigma_n + \sigma_\lambda + \sigma_t}{\bar{R}^c} = 1$$

Derivation of the slope equation in Mohr stresses, $\sigma_\lambda,\ \tau_{t\lambda},\ \tau_{n\lambda} = 0$

$$\frac{dF^{SF}}{d\sigma_n} = \frac{c_{1\Theta}{}^{SF}}{2\bar{R}^{c2}} \cdot [4\sigma_n - 2\sigma_t - 2\sigma_\lambda] + \frac{c_{2\Theta}{}^{SF}}{\bar{R}^c}; \qquad \frac{dF^{SF}}{d\tau_{nt}} = 12\frac{c_{1\Theta}{}^{SF} \cdot \tau_{nt}}{2 \cdot \bar{R}^{c2}}$$

$$\frac{d\tau_{nt}}{d\sigma_n} = -\frac{dF}{d\sigma_n} / \frac{dF}{d\tau_{nt}} \ (\text{implicit diff.}) = -\ [\frac{c_{1\Theta}{}^{SF}}{\bar{R}^{c2}} \cdot [2\sigma_n - \sigma_t - \sigma_\lambda] + \frac{c_{2\Theta}{}^{SF}}{\bar{R}^c}] \ / \ [6\frac{c_{1\Theta}{}^{SF} \cdot \tau_{nt}}{\bar{R}^{c2}}]$$

Transformed structural stresses and addition theorems used: $\sigma\lambda = 0$ set

$$S^2 + C^2 = 1,\ C = c^2 - s^2 = 2c^2 - 1,\ S = 2sc,\ c^2 = (C+1) \cdot 0.5,\ s^2 = (1-C) \cdot 0.5$$

$$\sigma_n - \sigma_t = C \cdot (\sigma_{II} - \sigma_{III}),\ \tau_{nt} = -s \cdot c \cdot (\sigma_{II} - \sigma_{III}) = -0.5 \cdot S \cdot (\sigma_{II} - \sigma_{III})$$

Transformation relations for equalizing the angle in the touch point , $\sigma_{II} - \sigma_{III} = \eta$

$$\frac{d\tau_{nt}}{d\sigma_n} = -\ [\frac{c_{2\Theta}{}^{SF} \cdot \eta + c_{1\Theta}{}^{SF} \cdot (2 \cdot c^2 - s^2) \cdot \eta}{6 \cdot c_{1\Theta}{}^{SF} \cdot (-s \cdot c \cdot \eta)}] = -\ [\frac{c_{2\Theta}{}^{SF} - c_{1\Theta}{}^{SF}(2\frac{C+1}{2} - \frac{1-C}{2})}{6 \cdot c_{1\Theta}{}^{SF} \cdot (-0.5 \cdot S)}].$$

Equal slope of curves in touch point: η is multi-axial and cut out

$$\frac{d\tau_{nt}}{d\sigma_n} = \frac{C}{S} = -\ [\frac{c_{2\Theta}{}^{SF} - c_{1\Theta}{}^{SF}(C + 1 - \frac{1-C}{2})}{6 \cdot c_{1\Theta}{}^{SF} \cdot (-0.5 \cdot S)}] \quad \text{with} \quad C \Rightarrow C^c = \frac{c_{2\Theta}{}^{SF} - c_{1\Theta}{}^{SF}}{-3 \cdot c_{1\Theta}{}^{SF}}$$

Determination of $c_{2\Theta}{}^{SF}$ after inserting $1 + c_{2\Theta}{}^{SF} = c_{1\Theta}{}^{SF}$ for neutral meridian $\Theta^{SF} = 1$:

$$C^c = \frac{c_{2\Theta}{}^{SF} - (1 + c_{2\Theta}{}^{SF})}{-3 \cdot (1 + c_{2\Theta}{}^{SF})} = \frac{-1}{-3 \cdot (1 + c_{2\Theta}{}^{SF})} \quad \Rightarrow \quad c_{2\Theta}{}^{SF} = \frac{-3 \cdot C^c + 1}{3 \cdot C^c + 1}$$

Mohr, linear fracture condition: $\tau_{nt} = \mathrm{R}^\tau - \mu \cdot \sigma_n$ *or* $F = \frac{\tau_{nt}}{\mathrm{R}^\tau - \mu \cdot \sigma_n} = 1$

$$\frac{d\tau_{nt}}{d\sigma_n} = -\frac{dF}{d\sigma_n} / \frac{dF}{d\tau_{nt}} = -\frac{\tau_{nt} \cdot \mu}{(\mathrm{R}^\tau - \mu \cdot \sigma_n)^2} / \frac{1}{\mathrm{R}^\tau - \mu \cdot \sigma_n} = -\frac{\tau_{nt} \cdot \mu}{(\mathrm{R}^\tau - \mu \cdot \sigma_n)} = -\mu \equiv \frac{C^c}{S^c}$$

Now, it is possible to sort out the relations between all friction-linked parameters

$$\mu = -\tan\rho = \frac{d\tau_{nt}}{d\sigma_n} = \frac{-C^c}{S^c}, \text{ small friction angles} \cong -C^c, \quad \tan\phi \equiv \tan\rho$$

$$c_{2\Theta}{}^{SF} = \frac{3\mu + 1}{-3\mu + 1} \quad \text{and} \quad \text{if an angle is measured, then } C^c = \cos(\frac{2 \cdot \Theta_{fp}{}^\circ}{180^\circ} \cdot \pi).$$

From *Fig.*14-1 relationships can be derived and from them follows for $\Theta_{fp}^c{}^\circ = 50^\circ$

brittle $\Theta_{fp}^c{}^\circ = 50^\circ \rightarrow C^c = -0.174,\ c_{2\Theta}{}^{SF} = c_2{}^{SF} = 3.7\ ,\ \mu = 0.18,$

F^{SF}bound $\Theta_{fp}^c{}^\circ = 45^\circ \rightarrow C^c = 0;\ \mu = 0,\ \rho = -\mathrm{atan}(\mu) = 0.$

► For <u>isotropic</u> materials the result reads: $c_{2\Theta}{}^{SF} = \frac{3\mu + 1}{-3\mu + 1} \rightarrow 1 + c_{2\Theta}{}^{SF} = c_{1\Theta}{}^{SF}$.

14.2 Transversely-isotropic UD Materials

14.2.1 Derivation of the relationship Friction Parameter $a_{\perp\perp}$ with Friction Value $\mu_{\perp\perp}$ (θ_{fp}^{c})

The measurement of a realistic fracture angle θ_{fp}^{c} is practically not possible [*VDI97*], just the determination of the friction curve parameter $a_{\perp\perp}(\mu_{\perp\perp})$ by mapping the course of test data points which is a practical approach. Then, from the mapped test curve the relation of the curve parameter $a_{\perp\perp}$ to the friction value $\mu_{\perp\perp}$ and to the fracture angle $\theta_{fp}°$ can be derived according to the formulas in *Table 14-3*. This is to perform in the compressive strength point $\bar{R}_{\perp}^{c}$, as before.

Basic assumption is the *brittle-fracture hypothesis* which goes back to O. Mohr's "*The strength of a material is determined by the Mohr stresses on the fracture plane".* This means for the Linear Mohr-Coulomb (M-C) formulation $\tau_{nt} = \bar{R}_{23}^{\tau} - \mu_{\perp\perp} \cdot \sigma_n$ including the friction value $\mu_{\perp\perp}$, being an intrinsic property of the UD material.

If IFF occurs in a parallel-to-fiber plane of the UD lamina, the components of the failure stress vector are the normal Mohr stress σ_n and the two Mohr shear stresses σ_{nt} and σ_{n1}. The shear stress σ_{tl} and the normal stress σ_t will have no influence and this was proven in the derivation in *Table 14-3*. Further, the Mohr stress σ_{n1} belongs to IFF3 and is not of interest, here.

The transformation of the IFF2 SFC in lamina stresses into Mohr stresses-based formulation works via addition theorems as for the isotropic material.

During the elaboration of the transformation procedure in *Table 14-2* there were a lot of Lessons to Learn**:**

LL:

- *The Linear Mohr-Coulomb model can be employed to obtain a sufficiently good relationship for the determination of the friction value μ in the compressive strength point $\sigma_2 = -\bar{R}_{\perp}^{c}$.*
- *Establishing the relationship $a_{\perp\perp}(\mu_{\perp\perp})$ it is assumed that the tangent of the FMC-curve has the same value as that of the straight Linear Mohr envelope curve $\tau_{nt}(\sigma_n)$ in the touch point of Mohr's circle, see Fig.14-1*
- *σ_1 is not relevant, shear stress τ_{23} can be assumed zero because it would anyway vanish after a principal stress transformation. No reduction of generality is caused*
- *The stress σ_t has no influence! It is not representative such as Mohr supposes. Failure responsible are τ_{nt} and $\sigma_{n\,,}$ only. But mind in the differentiation process: the Mohr stress σ_t cannot be simply set zero at the beginning of the derivations, it must be considered due to its relation to $\sigma_{n\,,}$!!*
- *Above derivation demonstrates that, if really desired, the fracture plane angle θ_{fp}^{c} of an UD-material could be also determined from an invariant-based SFC and not only from Mohr-based formulations*
- *Viewing Fig.14-1, it is obvious that the cohesive strength $\bar{R}_{23}^{\tau}$ (Civil engineers take the letter c) belongs to the transition zone of the normal fracture mode domain IFF1 and therefore not alone to the shear fracture mode domain IFF2. Hence, one cannot simply extrapolate from the compressive strength point. See further § 22 on the cohesive strength.*

14.2.2 Derivation of a relationship Friction Parameter $a_{\perp\parallel}$ with Friction Value $\mu_{\perp\parallel}$

The same procedure is analogously to perform for the mode IFF3, see *Table 14-4*.

Table 14-3: Determination of the friction curve parameter $a_{\perp\perp}(\mu_{\perp\perp})$

IFF2: $F_{\perp}^{\tau} = [a_{\perp\perp}\cdot(\sigma_2+\sigma_3) + b_{\perp\perp}\cdot\sqrt{(\sigma_2-\sigma_3)^2+4\tau_{23}^2}\,] / \bar{R}_{\perp}^{c} = 1$, in Mohr stresses, after inserting $\bar{R}_{\perp}^{c}$

$= [a_{\perp\perp}\cdot(\sigma_n+\sigma_t) + b_{\perp\perp}\cdot\sqrt{(\sigma_n-\sigma_t)^2+4\tau_{nt}^2}\,] / \bar{R}_{\perp}^{c} = 1$ and $a_{\perp\perp} = b_{\perp\perp} - 1$ is friction parameter

$$\frac{dF}{d\sigma_n}\cdot\bar{R}_{\perp}^{c} = a_{\perp\perp} + b_{\perp\perp}\cdot(\sigma_n-\sigma_t)/\sqrt{(\sigma_n-\sigma_t)^2+4\tau_{nt}^2},\quad \frac{dF}{d\tau_{nt}}\cdot\bar{R}_{\perp}^{c} = 4\cdot b_{\perp\perp}\cdot\tau_{nt}/\sqrt{(\sigma_n-\sigma_t)^2+4\tau_{nt}^2}$$

$$\frac{d\tau_{nt}}{d\sigma_n} = -\frac{dF}{d\sigma_n}/\frac{dF}{d\tau_{nt}} = -[\frac{b_{\perp\perp}\cdot(\sigma_n-\sigma_t) + (b_{\perp\perp}-1)\cdot\sqrt{(\sigma_n-\sigma_t)^2+4\tau_{nt}^2}}{4\cdot b_{\perp\perp}\cdot\tau_{nt}}],$$ minus due to implicit derivation

Use of addition theorems ($\sigma_\lambda = 0$), gives the relationships $c = \cos(\theta_{fp}{}^{\circ}\cdot\pi/180°)$

$$\sigma_n-\sigma_t = c^2\cdot(\sigma_2-\sigma_3) - s^2\cdot(\sigma_2-\sigma_3) = C\cdot(\sigma_2-\sigma_3),\quad S = \sqrt{1-C^2},\ C = \cos(2\cdot\theta_{fp}{}^{\circ}\cdot\pi/180°)$$

$$\sigma_t = \sigma_n - C\cdot(\sigma_2-\sigma_3),\ C = c^2-s^2 = 2c^2-1 = 1-2s^2,\quad \sigma_n+\sigma_t = \sigma_2+\sigma_3 \quad \text{and}$$

$\tau_{nt} = -0.5\cdot S\cdot(\sigma_2-\sigma_3) = -0.5\cdot\sqrt{1-C^2}\cdot(\sigma_2-\sigma_3),\ \sigma_n = (C+1)\cdot0.5\cdot\sigma_2 + (1-C)\cdot0.5\cdot\sigma_3.$

Stress σ_t has no influence, as Mohr assumed! Failure responsible due to Mohr are just τ_{nt} with σ_n !

$$\frac{d\tau_{nt}}{d\sigma_n} = -\,\mu_{\perp\perp} = \frac{C}{S} = -[\frac{b_{\perp\perp}\cdot(\sigma_n-\sigma_t) + (b_{\perp\perp}-1)\cdot\sqrt{(\sigma_n-\sigma_t)^2+4\tau_{nt}^2}}{4\cdot b_{\perp\perp}\cdot\tau_{nt}}] =$$

$$= -[\frac{b_{\perp\perp}\cdot(C\cdot\sigma_2) + (b_{\perp\perp}-1)\cdot\sqrt{(C\cdot\sigma_2)^2+4\cdot(-0.5\cdot S\cdot\sigma_2)^2}}{4\cdot b_{\perp\perp}\cdot(-0.5\cdot S\cdot\sigma_2)}]$$

$$C = -[\frac{b_{\perp\perp}\cdot(C\cdot\sigma_2) + (b_{\perp\perp}-1)\cdot\sqrt{(C\cdot\sigma_2)^2+4\cdot(-0.5\cdot\sigma_2)^2\cdot(1-C^2)}}{4\cdot b_{\perp\perp}\cdot(-0.5\cdot\sigma_2)}]\ ;\ C\to C_{fp}{}^{c}$$ inserting strength $\bar{R}_{\perp}{}^{c}$

$$\to C_{fp}{}^{c} = -[\frac{b_{\perp\perp}\cdot C_{fp}{}^{c}\cdot(-\bar{R}_{\perp}{}^{c}) + (b_{\perp\perp}-1)\cdot\sqrt{C_{fp}{}^{c2}\cdot(-\bar{R}_{\perp}{}^{c})^2+4\cdot(-0.5\cdot(-\bar{R}_{\perp}{}^{c}))^2\cdot(1-C_{fp}{}^{c2})}}{4\cdot b_{\perp\perp}\cdot(-0.5\cdot(-\bar{R}_{\perp}{}^{c}))}]$$

Resolving : $b_{\perp\perp} = \frac{1}{C_{fp}{}^{c}+1} \cong \frac{1}{1-\mu_{\perp\perp}}$, $a_{\perp\perp} \cong \frac{\mu_{\perp\perp}}{1-\mu_{\perp\perp}}$, $\mu_{\perp\perp} = -\frac{C}{S} = -\frac{C_{fp}{}^{c}}{S_{fp}{}^{c}} \cong -C_{fp}{}^{c}$ (being a small value).

Assuming $\theta_{fp}^{c}{}^{\circ} = 51°$: *Example* $C_{fp}^{c} = \cos(\frac{2\cdot\theta_{fp}^{c}{}^{\circ}}{180°}\cdot\pi) = -0.21$, $\mu_{\perp\perp} = 0.21 \cong -C_{fp}^{c}$, $a_{\perp\perp} = 0.26$.

Table 14-4: Relationships for the determination of friction curve parameter $a_{\perp\parallel}(\mu_{\perp\parallel})$

$$F_{\perp\parallel} = \frac{I_3^2}{\bar{R}_{\perp\parallel}{}^{4}} + b_{\perp\parallel}\cdot\frac{I_2\cdot I_3 - I_5}{\bar{R}_{\perp\parallel}{}^{3}} = 1 \quad \text{with} \quad I_{23-5} = 2\cdot\sigma_2\cdot\tau_{21}^2 + 2\cdot\sigma_3\cdot\tau_{31}^2 + 4\cdot\tau_{23}\tau_{31}\tau_{21} \text{ from}$$

$$I_2 = \sigma_2+\sigma_3\ ,\ I_3 = \tau_{21}^2+\tau_{31}^2,\ I_5 = (\sigma_2-\sigma_3)\cdot(\tau_{31}^2-\tau_{21}^2) - 4\cdot\tau_{23}\cdot\tau_{31}\cdot\tau_{21}.$$

The transfer to a Mohr-shaped SFC is directly possible, because the fracture plane is already known (parallel to the fibre direction), via $(\tau_{n1},\ \sigma_n) \equiv (\tau_{21},\ \sigma_2)$, $|\tau_{21}| = \bar{R}_{\perp\parallel} - \mu_{\perp\parallel}\cdot\sigma_2$

* FMC: $\frac{\tau_{21}^4}{\bar{R}_{\perp\parallel}{}^{4}} + a_{\perp\parallel}\cdot\frac{2\cdot\sigma_2\cdot\tau_{21}^2}{\bar{R}_{\perp\parallel}{}^{3}} = \frac{\tau_{nt}^2}{\bar{R}_{\perp\parallel}{}^{4}} + a_{\perp\parallel}\cdot\frac{2\cdot\sigma_n\cdot\tau_{nt}^2}{\bar{R}_{\perp\parallel}{}^{3}} = 1 \to \sigma_n = \frac{\bar{R}_{\perp\parallel}{}^{3}\cdot(\tau_{21}^4/\bar{R}_{\perp\parallel}{}^{4}-1)}{2\cdot\tau_{nt}^2\cdot a_{\perp\parallel}}$

$\frac{d\tau_{n1}}{d\sigma_n} \to$ simpler to perform is $\frac{d\sigma_n}{d\tau_{n1}} = \frac{2\cdot\tau_{21}}{\bar{R}_{\perp\parallel}\cdot a_{\perp\parallel}} - \frac{\bar{R}_{\perp\parallel}{}^{3}\cdot(\tau_{21}^4/\bar{R}_{\perp\parallel}{}^{4}-1)}{\tau_{21}^3\cdot a_{\perp\parallel}}$

* Simple linear Mohr: $\tau_{n1} = \bar{R}_{\perp\parallel} - \mu_{\perp\parallel}\cdot\sigma_n \to \sigma_n = \frac{\bar{R}_{\perp\parallel}-\tau_{21}}{\mu_{\perp\parallel}}$ and $\frac{d\sigma_n}{d\tau_{nt}} = \frac{-1}{\mu_{\perp\parallel}}$.

In the strength point $\tau_{n1} = \bar{R}_{\perp\parallel}$ an equal slope exists, then equating delivers

$$\frac{2\cdot\tau_{21}}{\bar{R}_{\perp\parallel}\cdot b_{\perp\parallel}} - \frac{\bar{R}_{\perp\parallel}{}^{3}\cdot(\tau_{21}^4/\bar{R}_{\perp\parallel}{}^{4}-1)}{\tau_{21}^3\cdot a_{\perp\parallel}} = \frac{-1}{\mu_{\perp\parallel}} \to a_{\perp\parallel} = \frac{\mu_{\perp\parallel}\cdot(\bar{R}_{\perp\parallel}{}^{4}+\tau_{21}^4)}{\tau_{21}^3\cdot a_{\perp\parallel}} \Rightarrow a_{\perp\parallel} = 2\cdot\mu_{\perp\parallel},$$

being a good guess for $\mu_{\perp\parallel}$ and sufficient for application.

► For UD materials the result reads: $b_{\perp\perp} = \frac{1}{C_{fp}^{\ c} + 1} \cong \frac{1}{1-\mu_{\perp\perp}}$ and $a_{\perp\perp} \cong \frac{\mu_{\perp\perp}}{1-\mu_{\perp\perp}}$, $a_{\perp\parallel} = 2 \cdot \mu_{\perp\parallel}$.

14.3 Evaluation of UD Friction Values $\mu_{\perp\perp}, \mu_{\perp\parallel}$ from test results

The experimental determination of curve parameters *a(μ)* and thereby also of μ can be performed differently:

1. One strength value with one multi-axial failure stress point on the respective pure mode curves, usually applying a linear Mohr friction envelope (*sufficient, see Figs.14-2 and -3 below, it requires some fitting to optimally map the course*)
2. A more sophisticated fitting optimization process of the test data course (*minimum error square*) in the 'pure' friction failure mode domain
3. By the so-called Tension/Compression-Torsion test machine delivering the test points in *Fig.14-2 left*.
4. If a Tension/Compression-Torsion test machine is not available, then, one point on the pure mode IFF2-curve plus one in the transition zone IFF2-IFF1, can become an approximation basis, see *Fig.14-3 right.* So, if the test machine allows a $\mu_{\perp\perp}$-test in the transition zone of the modes, then, the estimation from strength point $(\sigma_3^{c\,fr}, \sigma_2^{t\,fr})$ demands for a really qualified stress interaction-mapping SFC because for the evaluation the interaction equation has to be employed, shown by the MathCad procedure reading

Mathcad implicite calculation: *Vorgabe* $\mu_{\perp\perp} := 0.1$ (estimation)

$$\left(\left[(\sigma_2+\sigma_3) + \sqrt{(\sigma_2-\sigma_3)^2+0}\,\right] / 2\bar{R}_{\perp}^{t}\right)^m + \left(\left[\left(\frac{\mu_{\perp\perp}}{1-\mu_{\perp\perp}}\right)\cdot(\sigma_2+\sigma_3) + \frac{1}{1-\mu_{\perp\perp}}\sqrt{(\sigma_2-\sigma_3)^2+4\tau_{23}^{\ 2}}\,\right] / \bar{R}_{\perp}^{c}\right)^m = 1 = Eff = 100\%\ .$$

Search *Suchen* ($\mu_{\perp\perp}$)

5. For $\mu_{\perp\perp}$, in addition: Principally the derivation from fracture angle measurements θ_{fp}^{c}° is possible, see experience in the associate figure in [*VDI 97, p.138*], where we faced a pretty high scatter.

The formulas for the friction values read:

- Linear Mohr envelope: $\mu_{\perp\parallel} \cong (\tau_{21}^{\ fr} - \bar{R}_{\perp\parallel}) / \sigma_2^{\ fr}$ from tension-compression/torsion test machine with tube test specimens, evaluating at least two curve points or if sufficient tests from curve fitting .
- From bi-axial compression test in order to compute the friction value from evaluating $\mu_{\perp\perp} = (\bar{R}_{\perp}^{c} + \sigma_3^{fr}) / \sigma_2^{fr}$. However, the danger to buckle is to face.

LL:

**A relationship of the measurable friction value and the fictitious friction parameter could be derived*

**The application of a tension-compression-torsion test machine is recommended.*

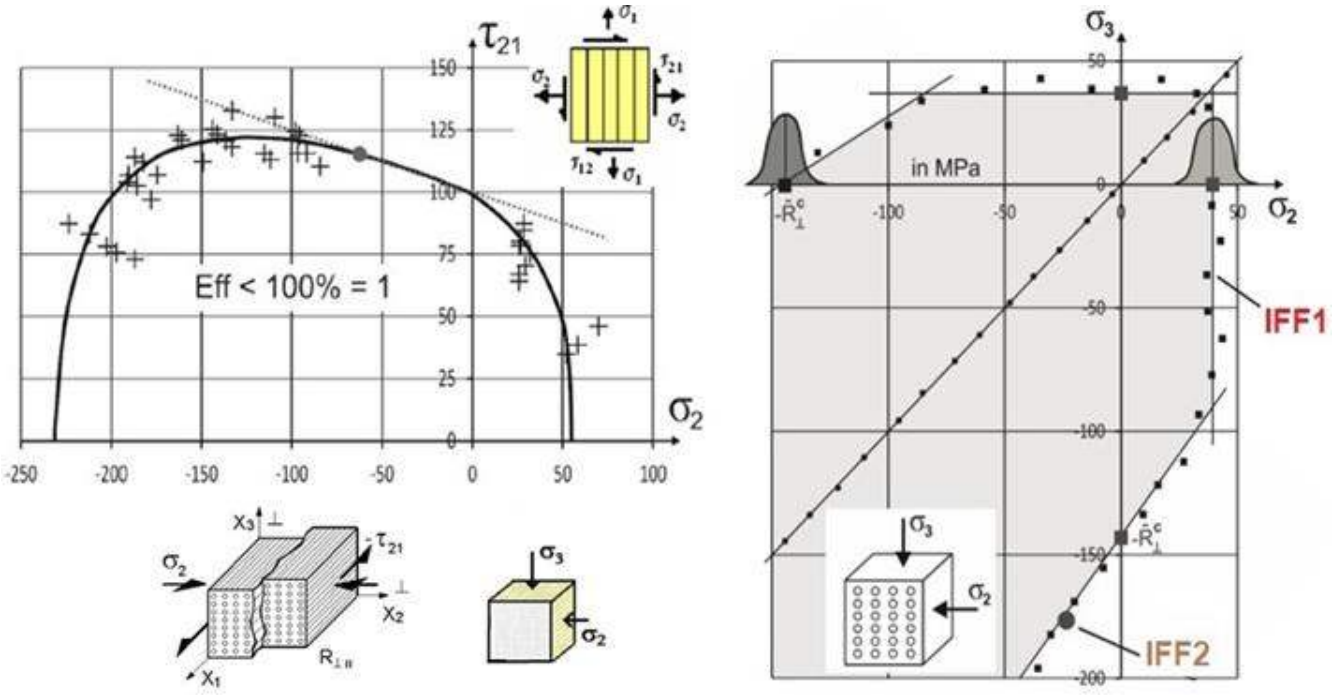

Fig.14-2: Determination of the friction values $\mu_{\perp\perp}$, $\mu_{\perp\parallel}$ (own results)

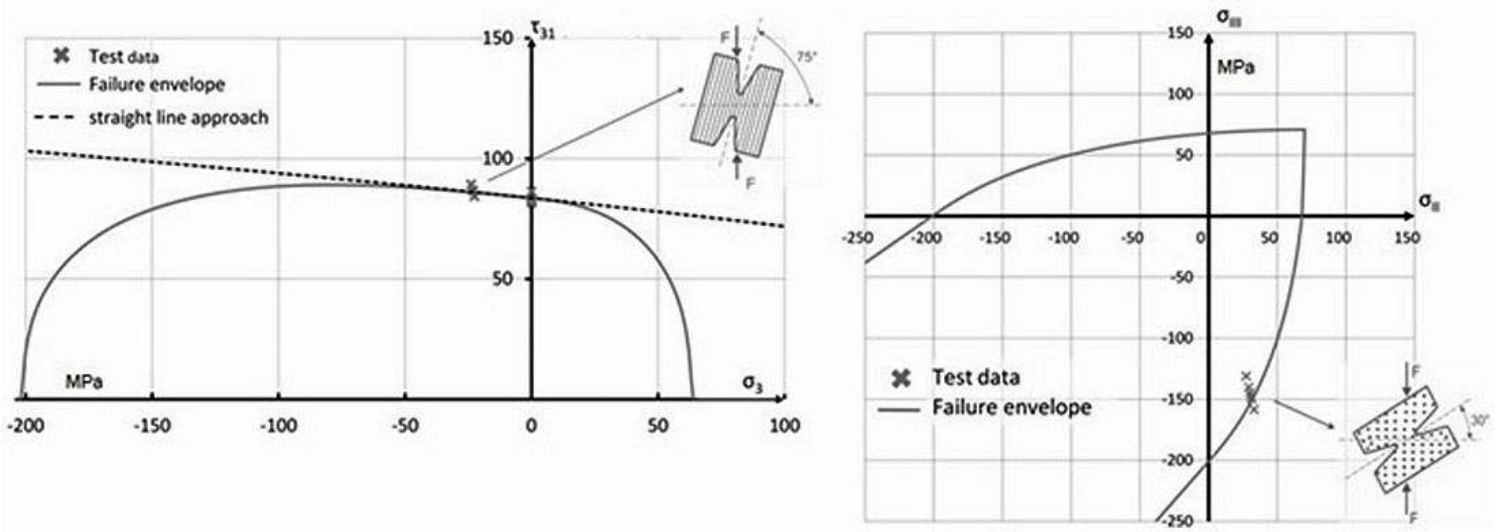

Fig.14-3: ARCAN tests performed on distinct stress paths. UD prepreg [*Pet15*]

15 Ductile Isotropic Materials' Strength Failure Criteria

Aim: *Making 'optically' familiar with multiaxial yield and fracture failure stress states of isotropic materials.*

Tradionally applied yield predicting SFCs are related to the Hencky-Mises-Huber (HMH) hypothesis ('*Mises', in short*. Termed a so-called *'single' property SFC)* or to the 'corner-suffering' SFC Tresca. Both describe pressure-insensitivity under compression. In the past Tresca was preferred from numerical hand calculation reasons. Now, its corners make numerical problems in 3D-FE-analysis and it is no need any more for applying '*corner Tresca*' instead of '*smooth Mises'*.

Cuntze's SFCs for homogeneous isotropic and transversely isotropic materials have no corners.
And, the inherent '120°-rotational symmetry' of isotropic materials (*see a distinct section before*) is considered.

15.1 Onset-of-yielding: 'Mises' (Hencky-Mises-Huber) or Tresca Yield Hypothesis

There are the two well-known SFCs for Yielding, Mises and Tresca. Tresca was preferred in the very past due to its less computational effort however is for the present digital analyses of dis-advantage. The HMH-SFC shall be only cited: $Eff = c_{Mis} \cdot \frac{\sqrt{3 \cdot J_2}}{\bar{R}_{p02}} = \frac{\sigma_{eq}}{\bar{R}_{p02}}$, c represents the Mises cylinder diameter.

This SFC delivers an ellipse as the cylinder's cross-section, whereas Tresca leads to a hexagon, see *Fig.15-1*.

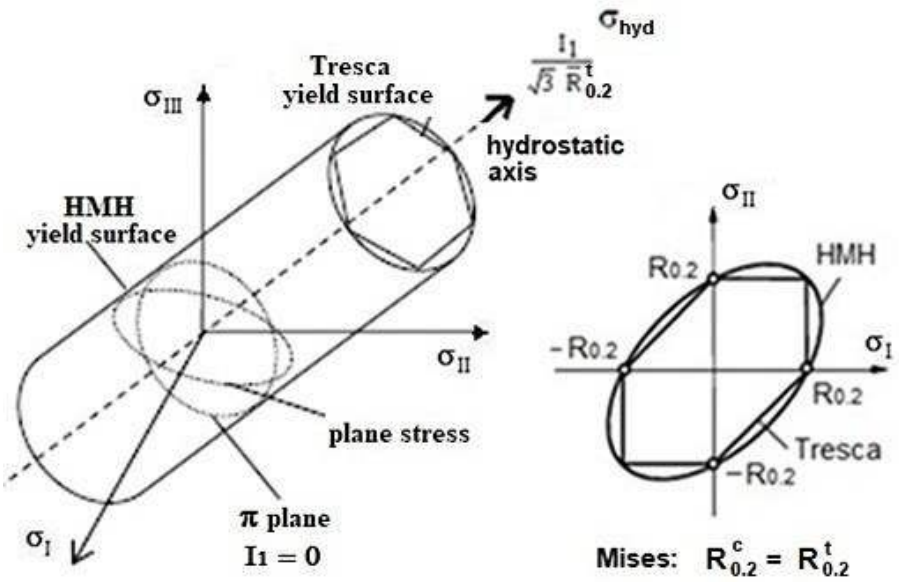

Fig.15-1: 'Mises' versus Tresca

Despite of the fact that both the hypotheses are yield hypotheses, i.e. Tresca was often mistakenly used as strength fracture failure condition seduced by its failure surface shape in tension in the principal stress plane: the line is straight like the NF-curve, with biaxial tensile fiber stress = tensile strength (*see figure above right).*

15.2 Failure Determination using Mises with Tresca and regarding Prior Test data

The following belongs to a tough longtime Ariane Design discussion ending unfortunately with a compromise to use Misca (not given here) as a non-physically-based mathematical mixture of 'Mises' and Tresca.

For the design of pressure vessels (*here, i.e. Ariane 5 Booster steel tank*) with their typical stress state of 2:1 the design is penalized by 15% less if one uses Tresca and not Mises. This effect, sometimes

termed ‘flattening effect’ (*Fig.15-2*) means that the Mises ellipse becomes a dent-deformation, which would mark a strong design drawback, if the 15% were fully to respect.

This flattening of the Mises ellipse occurs in the tensile quadrant and depends on specimen quality, grain size, grade of ductility and testing and the specific stress state as will be shown. Not to be forced to fully Mises-lose above 15% , using Tresca, the author investigated at that time available literature and own experiments with the result that theory, test results, fracture morphology and non-linear analyses outline the following:

* Test results show differences to Mises between 0 and about 7 % in the positive stress domain as the domain of highest principal stresses. Test results confirm that ’Onset-of-Fracture’ begins at the outer surface of the traditional tube test specimen loaded by internal pressure.
* The Mises ellipse outlines for a stress state (2:1) the highest principal tube stress. Before plastic collapse this principle hoop stress wanders under increasing loading from the inner to the outer surface. This complies with the fact that bad polished tubes generate a distance to Mises.

For information: The high vessel stress state associated principal stress is the addition of the two structural stresses and reads

$$\frac{\sigma_x}{\sigma_y}=\frac{2}{1}:\ \sigma_I=\frac{\sigma_x+\sigma_y}{2}\pm\sqrt{\left(\frac{\sigma_x-\sigma_y}{2}\right)^2+{\tau_{xy}}^2}\ \rightarrow\ \sigma_I=\sigma\left[\frac{2+1}{2}+\sqrt{\left(\frac{2-1}{2}\right)^2+0}\right]=2\sigma\,.$$

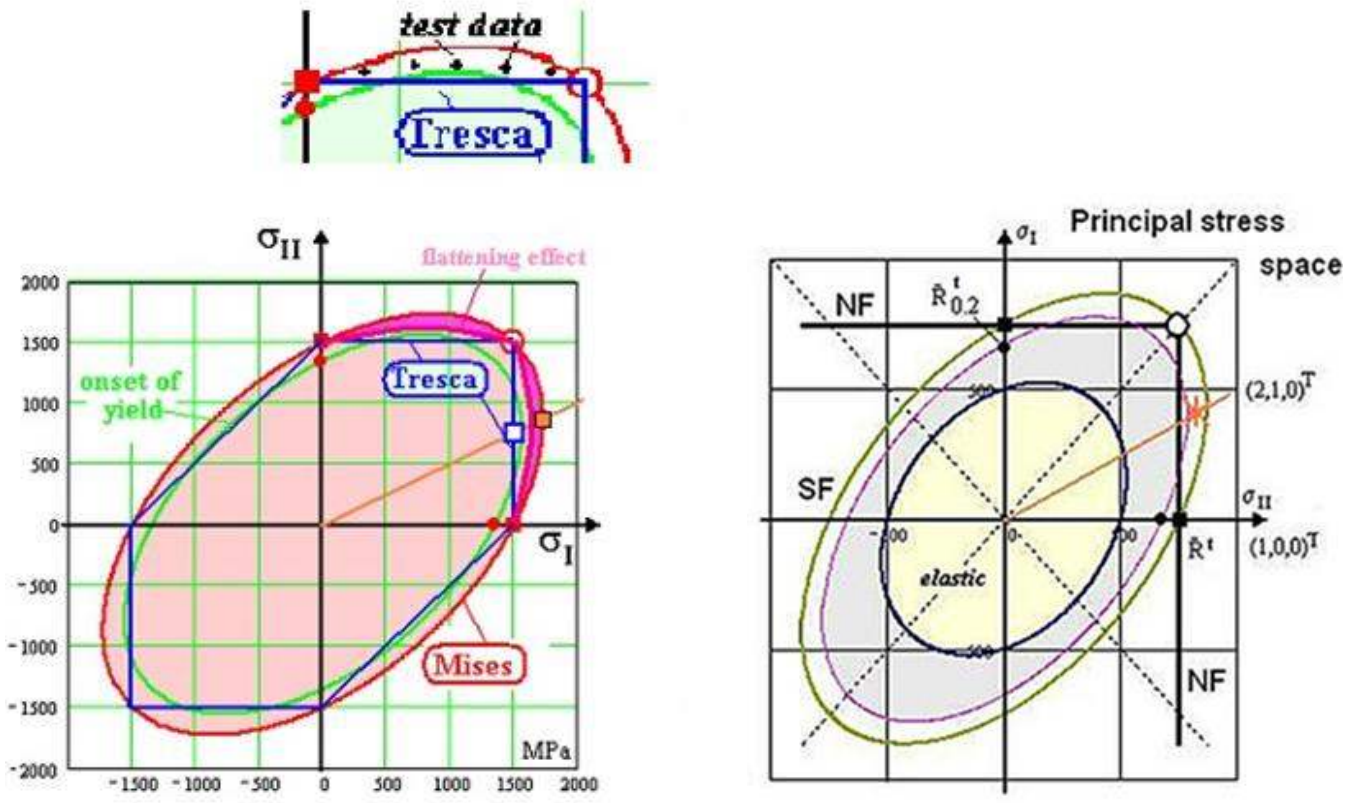

Fig. 15-2: Mises, Tresca and flattening of AA2219 regarding the ratio 2/1.
Tresca corners in the figure are smooth in reality.

Some further thoughts about the flattening effect: From mini-vessel tests on the Ariane Booster D6AC steel we could learn [*Tay90*]:

> Possible flattening of the Mises fracture ellipse may be not caused by a ductile *strength failure mode* but by a principal stress-driven *fracture mechanics failure mode. For a* ‘vessel stress ratio’ (2:1) or the stress vector $(2, 1, 0)^T$ the principal stress value is the largest and the

so-called flattening effect may play a role considering the following considering that a higher triaxiality usually causes a higher failure risk, it is understandable that *TrF* (= Tr) = 1/3 for the uniaxial stress state 1:0 is less critical than *TrF* = √2 / 3 for the vessel stress state 2:1. The minor straining at the outer wall surface changes with increasing ductile behavior up to the level at the inner surface. This means, that the always existing flaws at the outer surface may grow (*2D stress state*) and drive ductile rupture. On the inner surface, the internal normal compressive stress from pressure (*3D stress state)* reduces *Eff* and thereby the rupture danger.

Dawicke and Pollock cite in NASA CR 4782: "*The von Mises yield criterion was shown to accurately describe the (ductile) behavior of 2219-T87 aluminum alloy*". All this speaks for the application of Mises as the more correct condition for shear stress-driven failures.

Therefore, Mises is recommended as basic yield condition and as yield potential.

Result at that time:

► A practical approach is to reduce the Mises ultimate stress by just a Mises-loss of 7% in the case of load-controlled 'hot spots' on structural surfaces of good quality. Damage tolerance always must check the final design.

15.3 Failure Determination using novel 120°-rotational symmetry documenting test data (see §8)

Novel test data were given Chapter 8 in order to proof the 120°- axial symmetry of isotropic failure bodies or envelopes, respectively, see *Fig.8-3* partly again, now as *Fig.15-2*.

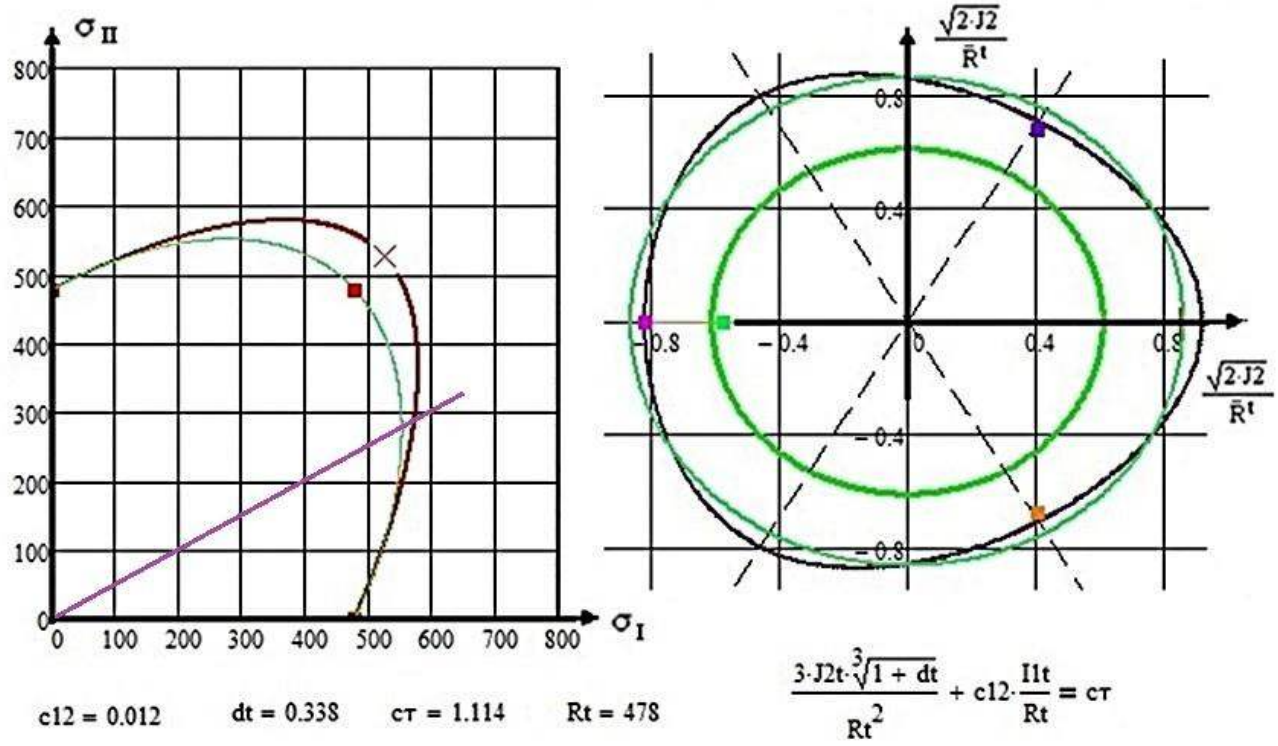

Fig.15-3, isotropic steel AA5182-0: Visualization of the behavior of a ductile material. 120°-symmetry, visualized in the principal stress plane; (right) 120°-symmetry, visualized in the octahedral stress plane

The center figure fully proves the general isotropic 120°-material rotational symmetry, supported by the incorporated Mises **ellipse** being the *inclined cross-section of the Mises cylinder failure body*.
The right octahedral figure shows the Mises curves: inner green curve at '**Onset**-of-yielding' and the outer one at tensile strength R^t. Biaxial ductile load-governed tensile failure stress (R^{tt}, R^{tt}, 0) corresponds to uniaxial strength R^t

Conclusion after novel test data knowledge:

In the case of ductile metals it can be assumed $R^{tt} \cong 1.1 \cdot R^{t}$, cross X. This effect reduces for the vessel stress ratio 2:1 but is still larger than Mises gives, namely > 15%.

► ***This asks for further research on the 120°-rotationally symmetry of ductile materials.***

A non-linear analysis is required which looks at both test tube surfaces, considers the pressure at the inner surface, reflects the change of the stress state over the wall thickness with the load increase and regards fracture mechanics relevant flaws at the outer surface (Fig.15-4 right) together with the tri-axialty effect from TrF.

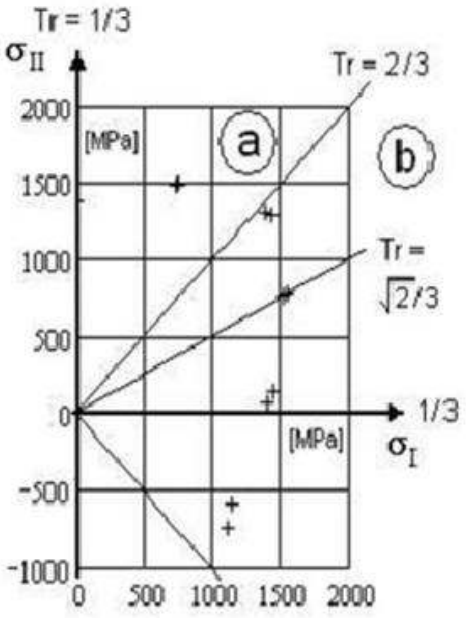

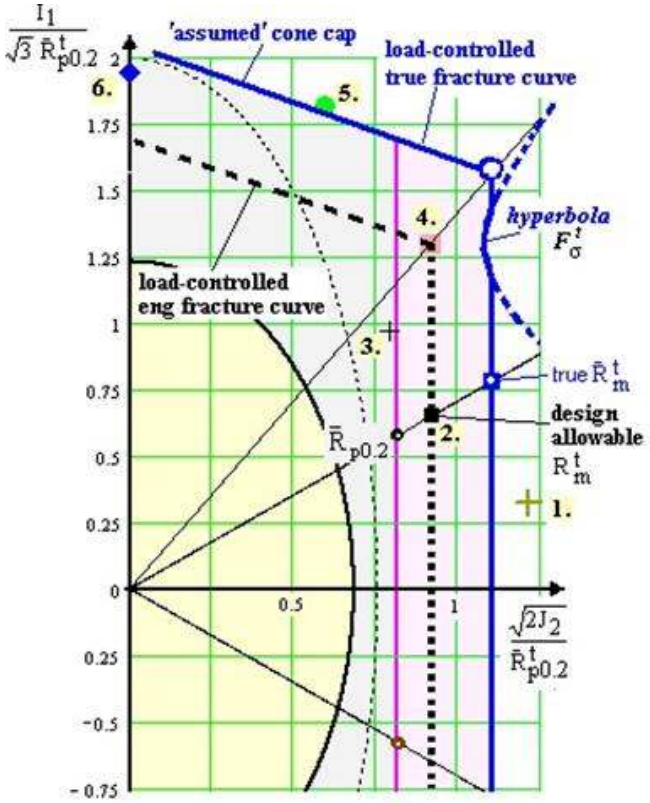

,

Fig. 15-4: (left) TrF lines. (right) Meridian cross-section of the failure body
2D- and 3D-Visualisation: (left) Ttriaxialities. (right) $-\infty < I_1 < maxI_1$, , dashed hyperbola shows load-controlled, damage tolerance based fracture . $\sigma_{eqM} := \sqrt{3 \cdot J2}$

Stress state	$\sigma_{hyd} = I_1 / 3$	σ_{eq}^{Mises}	TrF
(1,0,0)	1/3	1	1D: 1/3=0.33
(1,1,0)	2/3	1	2D: 2/3= 0.67
(2,1,0)	1	1.73	2D: **0.58**

LL:

** The theory of plasticity requires a:*

(1) Yield SFC (for indicating onset of yielding + consideration of multiaxial stressing), and

(2) Strain hardening rule for the progression of plastic deformation (isotropic or kinematic strain hardening + Ramberg-Osgood or a power-law); and

(3)Flow rule which relates the plastic increments (not the elastic ones) to the stresses.

** Just as long as the failure mechanism does not change a yield criterion might be used as fracture criterion, too.*

** TrF increases with 3D tensile stress state.*

15.4 SFC-Application to Semi-brittle isotropic Matrix WWFE-II Data, for Hydrogen Tanks

***Aim**: A further isotropic test data set of a matrix material, facing modelling problems due to unclear input. Thereby, knowledge shall be provided which will deliver physical understanding of the behavior in the present development of Composite Hydrogen Tanks*

***WWFE-II*, TC1 :** $\sigma_{x,fr}(\sigma_y = \sigma_z)$, epoxy matrix MY750 (*Fig.15-5*)

TC1-Problem: How does tri-axial compression influence the failure behaviour if two components of the stress vector are equal?

Necessary Part A test performance information: *"Test data from a sealed cylindrical bar epoxy specimen in a container filled with a highly pressurized fluid. The axial loading is carried out by a pull rod. The necessary two seals cause friction which is considered in the provided fracture stress data. The axial failure stress is computed from the measured load divided by the original cross-section".* Barrelling was not monitored! Not all physically needed properties, such as the low material friction could be provided by the organizers.

It is well known from the cited literature and at QinetiQ that hydrostatic pressure stress states higher than 200 MPa = 2000 bar change the second glass temperature point of the matrix with the described stiffness worsening effect on the matrix.

In the context above this information:

- Part A, additional:
  Reported: All test specimens under compression failed by yielding. → Conclusion for me: Matrix failure is yielding. This practically means no friction. Hence a very low friction value μ was assumed by me according to "matrix failure is yielding". Unfortunately, yielding was an organizer's lack of information to us regarding the later Part B information.
  Further, a discrepancy was found: Beyond the kinking point lower slope (*the author gave the effect the name 2nd Tg-effect)* is obtained decreasing Young's modulus E in [*Bir38*], *Fig.15.5.* I*n several other papers, see Part A, [Cun13])* the related shear modulus G_m is decreasing. Of course, there is no strong relationship between E and G any-more $E \neq G \cdot (2 + 2 \cdot \nu)$, but, also Birch's formulas do not confirm such a different behaviour.

- Part B: For this, now as semi-brittle to be treated, epoxy matrix material was no friction value μ given.
  Matrix failure is fracture (*now significant friction has to be considered*). This caused the author to change to friction modelling because the altered material behavior in B is very different to A and this has a strong influence. From the newly provided data set a friction value could be estimated. Note that $\mu = 0$ means 'Mises yield cylinder' and full yielding $R_{p0.2} \equiv R^t_{0.2} = R^c_{0.2}$.

Part A Treatment:

According to available knowledge, the thermoset Ep-matrix material had to be assumed in Part A to possess the 2nd Tg-effect. Therefore, the 2nd Tg-affected WWFE-II TCs 6 and 7 have been programmed to consider this effect. However, the course of the provided test data does not exhibit the 2nd Tg-effect, demonstrated by a slope beyond the epoxide-typical σ_{hyd} = -200 MPa kinking point (hydrostatic pressure of 3 *equal* compressive stresses). This of course also meets the 2nd Tg-matrix modelling under a general 3D compression loading with *different* stresses in the three coordinate directions. Information for modelling the change of stiffness and 'strength' was not directly given, and in literature the data vary. Therefore a correction factor f_{2ndTg} had to be assumed for stiffness and for 'strength' as well. For stiffness and for 'strength' of the distinct TC the same value was taken, namely an assumed 10% decay of the slope between -200 MPa and (pretty arbitrarily) -600 MPa.

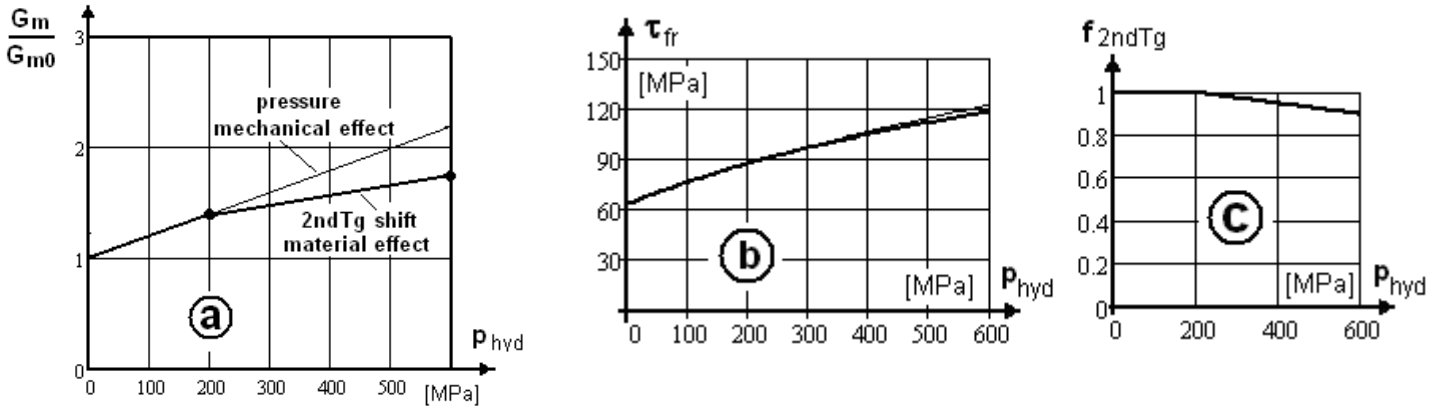

Fig. 15.5: Modelling the 2ndTg-effect

Part B Treatment:

- The 2nd Tg-effect is inherent in the epoxide matrix of TC1 but was not outlined by the provided Part B TC test data! Hence, this Mathcad-code implemented effect could never be considered in the Part B computations. → 2nd Tg-effect had to be taken from the matrix model in the relevant ultra-high compression domain
- As the providers have changed the information on the EP-matrix behaviour from yielding to fracture, for the friction model parameter *b(μ)* a friction value *μ* had to be assumed for Part B. → Re-work of the matrix model regarding now significant friction.

The provided Part B-data set formed a straight line and thereby does not show any 2nd Tg-effect, *Fig.15-5a*. On the contrary, beyond the indicated kink level at about -200 MPa the *Fig.15-5c* shows a slight widening of the failure surface instead of a shrinking.

Viewing *Fig.15-6* it looks as if the effect needs not to be addressed for this matrix material. Nevertheless, for a visualisation of the tendency of the *2nd Tg* shift effect a 10% slope decay was originally assumed and displayed in the figure.

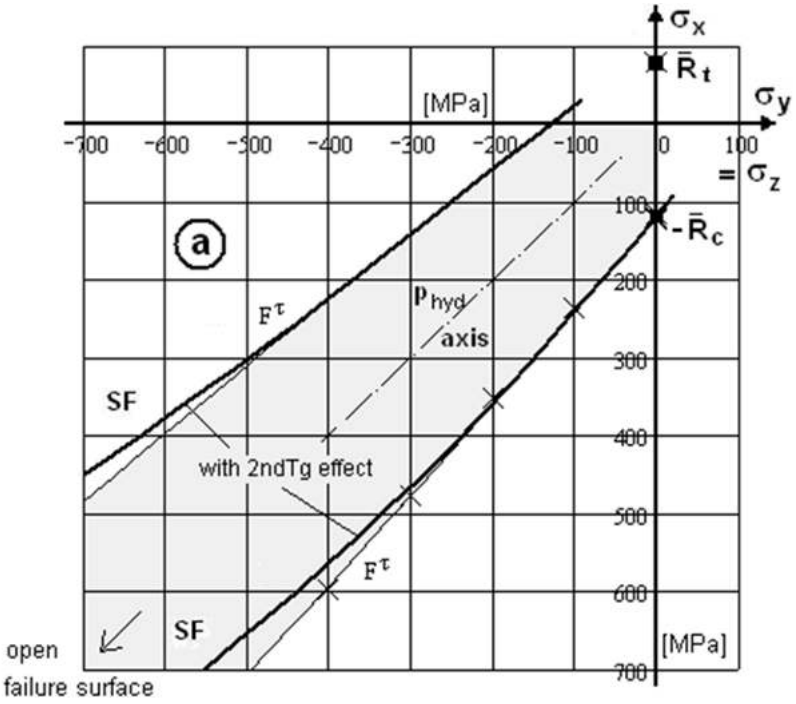

Fig. 15-6: Provided WWFE, TC1 test data visualization.

$$F^{SF} = c_1^{SF} \cdot \frac{3J_2}{\bar{R}^{c2}} + c_2^{SF} \cdot \frac{I_1}{\bar{R}^{c}} = 1 \quad \text{with} \quad c_2^{SF} = 0.18, \quad 2 \cdot c_1^{SF} = 1 + c_2^{SF}. \; \bar{R}^{c} = 120 \text{ MPa}, \; \bar{R}^{t} = 80 \text{ MPa}, \; m = 2.7$$

Fig.15-7, left, presents the test results in the traditional 'space' coordinates

Fig.15-7, right, visulizes the complicate curve mapping in the tension domain (not of interest for high pressure vessels) including the closing cap.

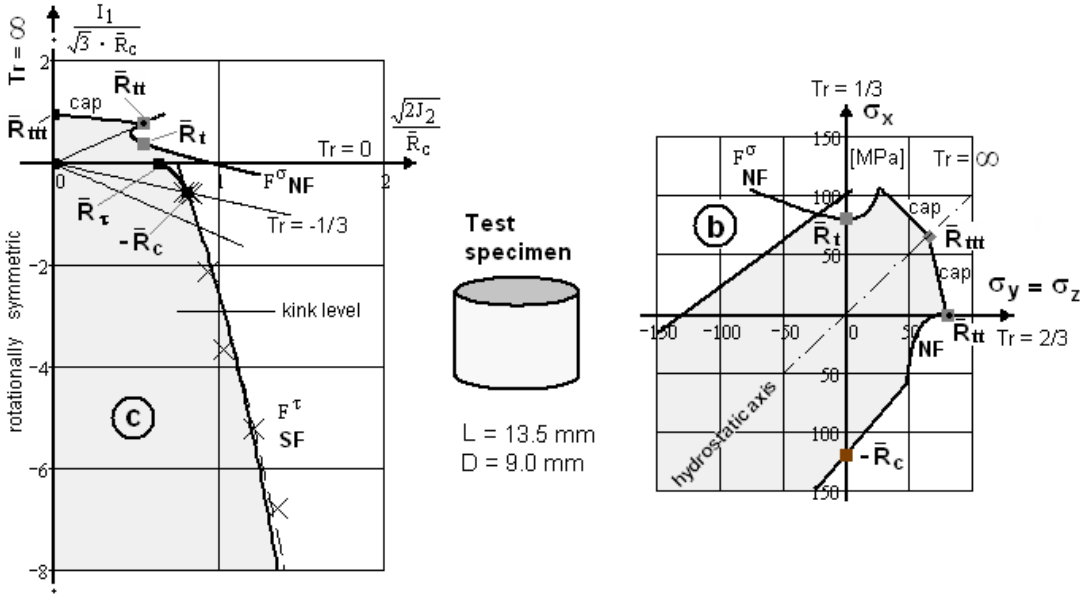

Fig. 15-7: WWFE, TC1modelling. 'Space' coordinates $I_1 / (\sqrt{3}\cdot\bar{R}^c)$ and $\sqrt{2\cdot J_2} / \bar{R}^c$

***LL and conclusion**:*

* *High triaxial compressive stress states affect the failure behavior and may result in a sudden brittle fracture failure. An equi-triaxial stress state of a dense Matrix leads to an open failure surface and in the case of a porous matrix to a closed failure surface.*
* *The effect is significant for WWFE-II, TC6 and TC7. Unfortunately, it was also never discussed that the provided thermoset matrix data did not demonstrate the physically inherent 2nd Tg-effect beyond 200 MPa of an epoxy matrix material, although this was well-known by the organizer QinetiQ.This matrix weakening effect was known but unfortunately could not be considered in the respective TC computations.*
* *Whether the effect is significant for the increasingly used thermoplastic matrices (resin systems) for high pressure tanks is to check*

As former member of the Ultra High Pressure Vessel Standard of ESA-ESTEC the study of the then edited booklet is recommended for a safe development of the present composite and metal Hydrogen Tanks.

16 Brittle Isotropic Materials' Strength Fracture Failure Criteria

Aim: *Provision of SFCs for Grey Cast Iron, Glass C90, Concrete, Foam with visualizations.*

16.1 3D-SFC Fracture Failure Formulations with Interaction Formula

16.1.1 Used Stresses and Invariants

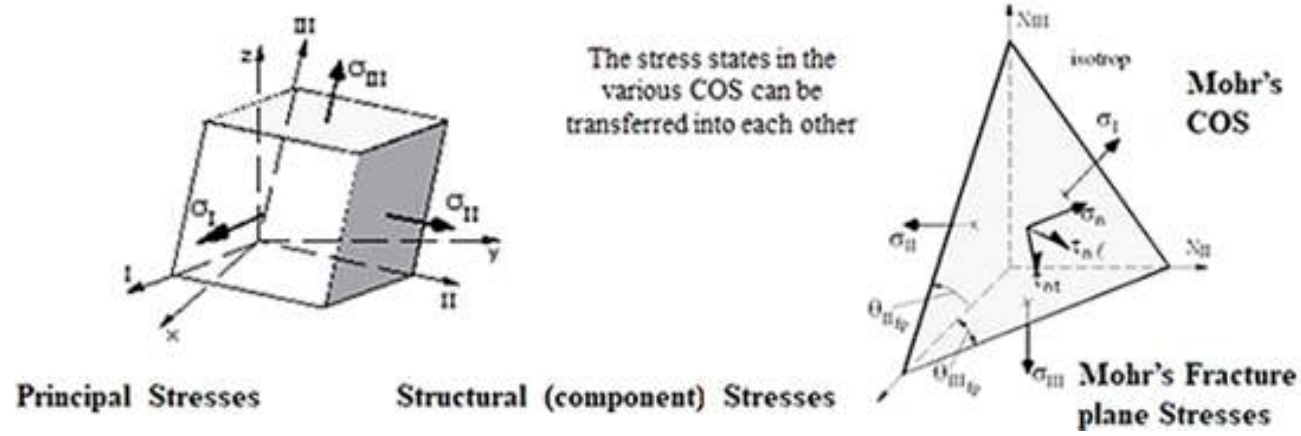

$$\{\sigma_{\text{principal}}\} = (\sigma_I, \sigma_{II}, \sigma_{III})^T, \quad \{\sigma_{\text{struct}}\} = (\sigma_x, \sigma_y, \sigma_z, \tau_{yz}, \tau_{xz}, \tau_{xy})^T, \quad \{\sigma_{\text{Mohr}}\} = (\sigma_\lambda, \sigma_n, \sigma_t, \tau_{nt}, \tau_{\lambda t}, \tau_{n\lambda})^T$$

16.1.2 Strength Failure Criteria (SFC), Eff-linked

Interaction requires to go from *F* to *Eff (F)*. Linked due to the 'proportional stressing concept' this

results in for instance $c_2^{SF} \cdot \frac{I_1 / Eff}{\bar{R}^c} + c_1^{SF} \cdot \frac{3 \cdot J_2 / Eff^2}{\bar{R}^{c2}} = 1.$

In <u>*Fig.16-1*</u> the 'basic' formulations are displayed, and finally, how the two shear mode parameters depend on another after having inserted R^c into F^τ :.

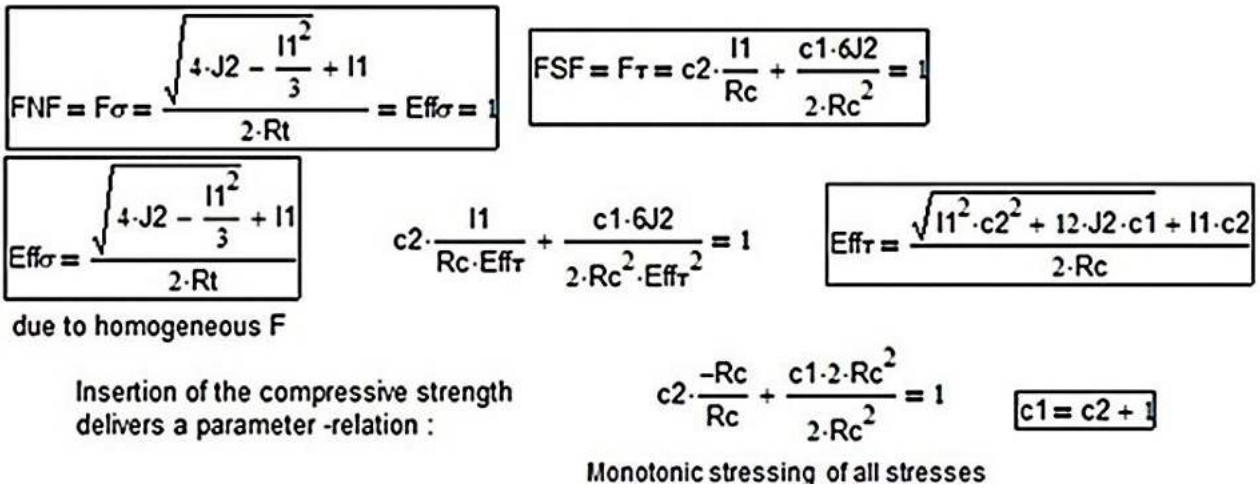

Fig.16-1: Repeated procedure how to determine the model parameters of the two Effs to compute the associated Fracture Body

<u>*Table 16-1*</u> summarizes the Eff^{mode} -formulations for the usually as rotationally-symmetric *assumed* fracture failure body, and further the realistic isotropic 120°-rotational symmetry relations.

Table 16-1: 3D-SFCs of Isotropic Dense Materials with model parameter determination

(1) Fracture failure body is rotationally symmetric (like the Mises yield body)

* Normal Fracture NF, $I_1 > 0$ ↔ * Shear Fracture SF, $I_1 < 0$

$$F^{NF} = F^{\sigma} = \frac{\sqrt{4J_2 - I_1^2/3} + I_1}{2 \cdot \bar{R}^t} \qquad F^{SF} = F^{\tau} = c_2^{SF} \cdot \frac{I_1}{\bar{R}^c} + c_1^{SF} \cdot \frac{3 \cdot J_2}{\bar{R}^{c2}}$$

with σ and τ as failure driving stresses. Resistances $\bar{R}$ are average values (We model !).

Strength Failure Criterion (SFC), mode interaction exponent m, friction μ

$$Eff^{NF} = \frac{\sqrt{4J_2 - I_1^2/3} + I_1}{2 \cdot R^t} = \frac{\sigma_{eq}^{NF}}{\bar{R}^t} \leftrightarrow Eff^{SF} = \frac{c_2^{SF} \cdot I_1 + \sqrt{(c_2^{SF} \cdot I_1)^2 + 12 \cdot c_1^{SF} \cdot 3J_2}}{2 \cdot R^c} = \frac{\sigma_{eq}^{SF}}{\bar{R}^c}.$$

with $c_1^{SF} = 1 + c_2^{SF}$, $c_2^{SF} = (1 + 3 \cdot \mu)/(1 - 3 \cdot \mu)$ from $\mu = -\cos(2 \cdot \theta_{fp}^c \circ \cdot \pi / 180)$

or from fitting of the test data course.

(2) Fracture failure body is 120°- rotationally symmetric = Reality !

In a chapter before we had to learn: Each isotropic material is "120° – rot. symmetric",

which leads to the little more complicate *Effs* below

$$Eff_{\Theta}^{NF} = c^{NF} \cdot \frac{\sqrt{4J_2 \cdot \Theta^{NF} - I_1^2/3} + I_1}{2 \cdot R^t} \leftrightarrow Eff_{\Theta}^{SF} = \frac{c_2^{SF} \cdot I_1 + \sqrt{(c_2^{SF} \cdot I_1)^2 \cdot \Theta^{SF} + 12 \cdot c_{1\Theta}^{SF} \cdot 3J_2}}{2 \cdot R^c}$$

$c_{1\Theta}^{SF} \cdot \Theta^{SF} = 1 + c_2^{SF}$, and above friction parameter c_2^{SF} (later denoted c_2)

Modelling of the cap is performed by the function $y_{cap} = \frac{I_1}{\sqrt{3} \cdot \bar{R}^t} = s^{cap} \cdot (\frac{\sqrt{2J_2 \cdot \Theta^{NF}}}{\bar{R}^t})^2 + \frac{max\, I_1}{\sqrt{3} \cdot \bar{R}^t}$.

For $R^c >> R^t$ can be set : $\Theta^{NF} \to \Theta^{TM} = \sqrt[3]{1 + d^{NF} \cdot (+1)}$, $c^{NF} = \Theta^{NF} = 1$.

Θ as non-circularity function with d as non-circularity parameter , (d^{SF} later d^{τ})

$\Theta^{SF} = \sqrt[3]{1 + d^{SF} \cdot sin(3\vartheta)} = \sqrt[3]{1 + d^{SF} \cdot 1.5 \cdot \sqrt{3} \cdot J_3 \cdot J_2^{-1.5}}$, compr. angle -30° $\to \Theta^{SF} = \sqrt[3]{1 + d^{SF} \cdot (-1)}$.

Significant Testing information:

3D-tests are performed by adding an axial load, generating a stress σ_{ax}, upon a hydrostatic loading $p_{hyd.}$ The associated 3D-concrete test data sets have been forwarded by Dr.-Ing. Silke Scheerer and Dr.-Ing. Kerstin Speck (*IfM, TU-Dresden, Prof. Dr. M. Curbach).* From their provided raw data sets as sub-sets the meridian data sets, the constant Lode angles for the envisaged meridians had to be extracted by the author. The usual tests are run along the tensile meridian (TM) and the compressive meridian (CM). This situation causes to apply the realistic isotropic 120°-rotationally-symmetric model in order to account for the Lode angle ϑ.

Determination of the model parameters in the mode domain of F^{τ} : The measurement of Θ_{fp} –based on the usually small-scale test level - is practically not possible. The determination of the curve parameters ci by mapping the course of test data points is the better and practical procedure. Then, the relationship of the curve parameter c2 to the friction value μ and to the fracture angle Θ_{fp} can be derived. These relations are obtained in the touch point, still pointed out in *Fig.14-1*.

16.2 Isotropic Materials, some Brittle Fracture Envelopes and Fracture Bodies

From mechanics is known that the fracture body possesses a circle-shape for $I_1 = 0$ and from testing is known, that the body becomes more and more circular with increasing negative I_1. At least for the Ultra-High-Performance-Concrete (UHPC) this must be considered when mapping, because the SFC F^{τ} cannot capture this effect alone. See

In the next box are collected all relationships and further the determination of the two additional parameters ατ, βτ, which ensure that the two fracture failure envelope (body surface) parts have a common smooth transition curve.

Table 16-2: 3D-SFCs of Isotropic Dense Materials, considering UHPC specifics

Maximum Θτcc in the bi-axial reference point (-Rcc, -Rcc.0) on the TM

$$\Theta_{\tau CM} = \sqrt[3]{1 - d_{\tau ex}} \qquad \Theta_{\tau TM} = \sqrt[3]{1 + d_{\tau ex}} \qquad x = \frac{\sqrt{2J2}}{Rc} \qquad I1 = \sqrt{3}\cdot Rc\cdot y$$

Model : $d_{\tau ex}(y) = \alpha\cdot\beta\cdot(-y)^{\beta-1}\cdot\exp\left[-\alpha\cdot(-y)^{\beta}\right]\cdot d_{\tau cc}$ Two unknowns require two equations

* Differentiation, in order to obtain a formula for the horizontal tangent in (-Rcc, -Rcc.0)

$$\frac{d}{dy}\left[\alpha\cdot\beta\cdot(-y)^{\beta-1}\cdot\exp\left[-\alpha\cdot(-y)^{\beta}\right]\cdot d_{\tau cc}\right] \rightarrow \beta^2\cdot\alpha^2\cdot d_{\tau cc}\cdot(-y)^{2\cdot\beta-2}\cdot e^{-\alpha\cdot(-y)^{\beta}} - \beta\cdot\alpha\cdot d_{\tau cc}\cdot(-y)^{\beta-2}\cdot e^{-\alpha\cdot(-y)^{\beta}}\cdot(\beta-1)$$

$$\left[\alpha\cdot\beta\cdot\left(-\frac{I1cc}{\sqrt{3}\cdot Rt}\right)^{\beta-1}\cdot\frac{\beta-1}{\frac{I1cc}{\sqrt{3}\cdot Rt}}\cdot e^{(-\alpha)\cdot\left(-\frac{I1cc}{\sqrt{3}\cdot Rt}\right)^{\beta}} - \alpha^2\cdot\beta^2\cdot\left(-\frac{I1cc}{\sqrt{3}\cdot Rt}\right)^{\beta-1}\cdot\frac{\left(-\frac{I1cc}{\sqrt{3}\cdot Rt}\right)^{\beta}}{\frac{I1cc}{\sqrt{3}\cdot Rt}}\cdot e^{(-\alpha)\cdot\left(-\frac{I1cc}{\sqrt{3}\cdot Rt}\right)^{\beta}}\right]\cdot d_{\tau cc} = 0$$

$d_{\tau cc}$ vanishes

Dissolved for $\alpha_T = \alpha$ (NF, ασ not of interest here) delivers an equation for the first curve parameter

$$\alpha_T = \frac{\beta_T - 1}{\beta_T\cdot\left(\frac{-1}{3}\cdot I1cc\cdot\frac{3^{0.5}}{Rz}\right)^{\beta_T}}$$

* Second curve parameter is determined by assuming that the non-circularity reduction is 50% at 2 x I1cc

Vorgabe $\beta_T := 1.5$ Material data insertion now !

$$0.5 = \frac{\frac{\beta_T - 1}{\beta_T\cdot\left(\frac{-1}{3}\cdot I1cc\cdot\frac{3^{0.5}}{Rt}\right)^{\beta_T}}\cdot\beta_T\cdot\left(-\frac{I1cc\cdot 2}{\sqrt{3}\cdot Rt}\right)^{\beta_T-1}\cdot\exp\left[-\frac{\beta_T - 1}{\beta_T\cdot\left(\frac{-1}{3}\cdot I1cc\cdot\frac{3^{0.5}}{Rt}\right)^{\beta_T}}\cdot\left(-\frac{I1cc\cdot 2}{\sqrt{3}\cdot Rt}\right)^{\beta_T}\right]\cdot 1}{\frac{\beta_T - 1}{\beta_T\cdot\left(\frac{-1}{3}\cdot I1cc\cdot\frac{3^{0.5}}{Rt}\right)^{\beta_T}}\cdot\beta_T\cdot\left(-\frac{I1cc}{\sqrt{3}\cdot Rt}\right)^{\beta_T-1}\cdot\exp\left[-\frac{\beta_T - 1}{\beta_T\cdot\left(\frac{-1}{3}\cdot I1cc\cdot\frac{3^{0.5}}{Rt}\right)^{\beta_T}}\cdot\left(-\frac{I1cc}{\sqrt{3}\cdot Rt}\right)^{\beta_T}\right]\cdot 1}$$

$A_T := Suchen(\beta_T)$ $\beta_T := A_T$ $\boxed{\beta_T = \blacksquare}$ $\boxed{\alpha_T =}$

$$\Theta_T(y) = \sqrt[3]{1 + d_T(y)\cdot\sin(3\theta)} \quad \text{with} \quad d_T(y) = \alpha_T\cdot\beta_T\cdot(-y)^{\beta_T-1}\cdot\exp\left[-\alpha_T\cdot(-y)^{\beta_T}\right]\cdot d_T$$

$$\Theta_{Tcc} = \sqrt[3]{1 + \alpha_T\cdot\beta_T\cdot(-ycc)^{\beta_T-1}\cdot\exp\left[-\alpha_T\cdot(-ycc)^{\beta_T}\right]\cdot d_T\cdot(1)} \qquad \Theta_{Tc} = \sqrt[3]{1 + \alpha_T\cdot\beta_T\cdot(-yc)^{\beta_T-1}\cdot\exp\left[-\alpha_T\cdot(-yc)^{\beta_T}\right]\cdot d_T\cdot(-1)}$$

$$\Theta_{TTM_j} = \sqrt[3]{1 + \alpha_T\cdot\beta_T\cdot\left(-y_j\right)^{\beta_T-1}\cdot\exp\left[-\alpha_T\cdot\left(-y_j\right)^{\beta_T}\right]\cdot d_T} \qquad \Theta_{TCM_j} = \sqrt[3]{1 + \alpha_T\cdot\beta_T\cdot\left(-y_j\right)^{\beta_T-1}\cdot\exp\left[-\alpha_T\cdot\left(-y_j\right)^{\beta_T}\right]\cdot d_T\cdot(-1)}$$

Some 2D-test data are provided in literature: for Grey Cast Iron and Glass C 90, the latter used as window pane of the ISS. For completion the author's accompanying evaluations shall be presented at the end of chapter 16. (The generation of the following §16-figures has been performed about 2015).

16.2.1 Mapping (Visualization) of Normal Concrete 3D compression test data

In *Fig.16-2 left*, the course of test data is mapped. As coordinates, as usually again the Lode-Haigh-Westergaard coordinates are used which equally count in all directions of the 3D stress space (*for understanding see Fig.16-9*). The tensile strength is used for normalization in the case of brittle materials.

The right part figure displays the fracture failure body, on which the 3 main meridians are depicted. For the tensile meridian a Lode angle ϑ = +30° is valid and for the compressive meridian ϑ = -30°. The shear meridian was chosen by the author as neutral meridian with the Lode angle ϑ = 0. For each mode, the SFC model parameters must be determined in each associated 'pure'failure mode domain. In this context physics of slightly porous isotropic materials is to remember: **bi-axial tension = weakest link failure behavior ($R^{tt}<R^t$, which partly seems to be not accepted in civil engineering) and * bi-axial compression = redundant (benign) failure behavior ($R^{cc}>R^c$).*

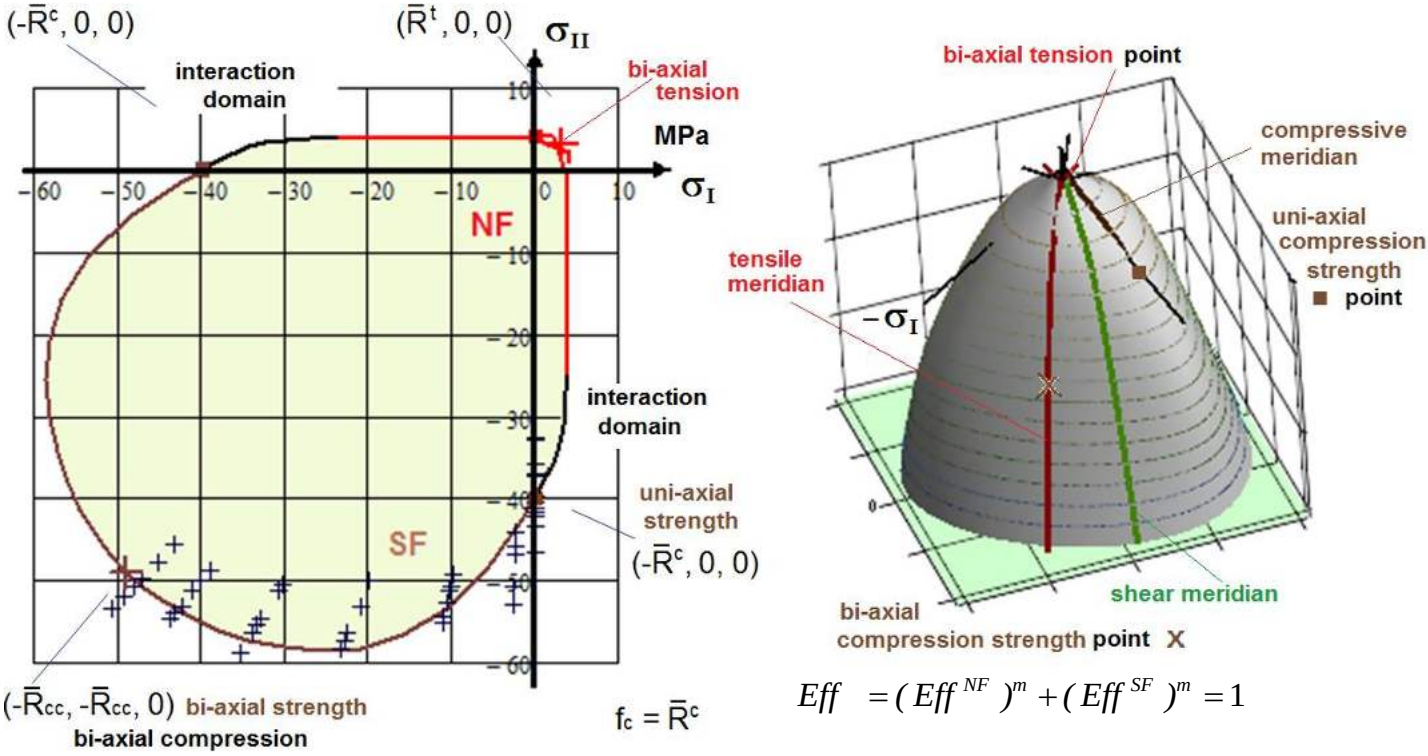

Fig.16-2, Normal Concrete: mapping of 2D-test data in the Principal Stress Plane as the bias cross-section of the fracture body. R= strength, t=tensile, c=compressive; bar over means average (mean) value. μ ≅ 0.2. (test data, courtesy: IfM Dresden)

Fig.16-3 through *16-5* present a hoop cross–section (*octahedral stress plane or so-called π-plane*), two axial cross-sections, the meridians of the failure body, and two views of the failure body.

The interaction to be performed has to capture both the modes. Hence for a common display, a normalization strength is to employ, generally the tensile strength.

Table 16-3, Normal Concrete: Data set input

$$F^{NF} = F^{\sigma} = c^{NF} \cdot \frac{\sqrt{4J_2 - I_1^2/3} + I_1}{2 \cdot \bar{R}^t} \;,\; F^{SF} = F^{\tau} = c_{1\Theta}^{SF} \cdot \frac{6J_2 \cdot \Theta^{SF}}{2 \cdot \bar{R}^{c2}} + c_2(\mu) \cdot \frac{I_1}{\bar{R}^c} = 1$$

Normalizing here with $\bar{R}^t$ and $\bar{R}^c$. Tension dent too small to be practically of interest $\rightarrow c^{NF} = 1$.

2 remaining unknowns require 2 fix stress fracture points on the surface of the fracture body:

$$\{\sigma_{fr}\}: \left(-\bar{R}^c, 0, 0\right)^T, \left(-\bar{R}^{cc}, -\bar{R}^{cc} 0, 0\right)^T, \quad m = 2.9,$$

with the values in MPa = N/mm^2: $\bar{R}^t = 4$, $\bar{R}^c = 40$, $\bar{R}^{cc} = 49$, $\Theta_{f\,p}{}^{c} = 50° \rightarrow \mu = 0.2$,

$c_{1\Theta}^{SF} \cdot \Theta^{CM} = 1 + c_2$ with $c_2 = 4.3$ as friction parameter, $\vartheta = -30°$ for CM, +30° for TM

$c_{1\Theta}^{SF} = 6.8$, $d^{SF} = 0.51$, $\Theta^{SF} = \sqrt[3]{1 + d^{SF} \cdot \sin(3\vartheta)} \rightarrow \Theta^{TM} = 1.15$, $\Theta^{CM} = 0.79 \equiv \Theta^{\tau}$.

For the determination of the closing cap and the open bottom of the fracture body:

$\bar{R}^{ttt} = 3.6 \rightarrow$ closing cap point $\max I_1 = 3 \cdot \bar{R}^{ttt}$, $\bar{R}^{ccc} = 1000$ MPa (set for computation).

With Awaji-Sato the non measurable $\bar{R}^{ttt}$ is estimated: $\bar{R}^{ttt} = \bar{R}^t / 3^{1/M}$, $M = \ln(2) / \ln(\bar{R}^t / \bar{R}^{tt})$.

$\bar{R}^{tt} = 0.9 \cdot \bar{R}^t$ (assumed), $s^{cap} = -0.57$. Further $\alpha_\tau = 0.0037$, $\beta_\tau = 1.92$.

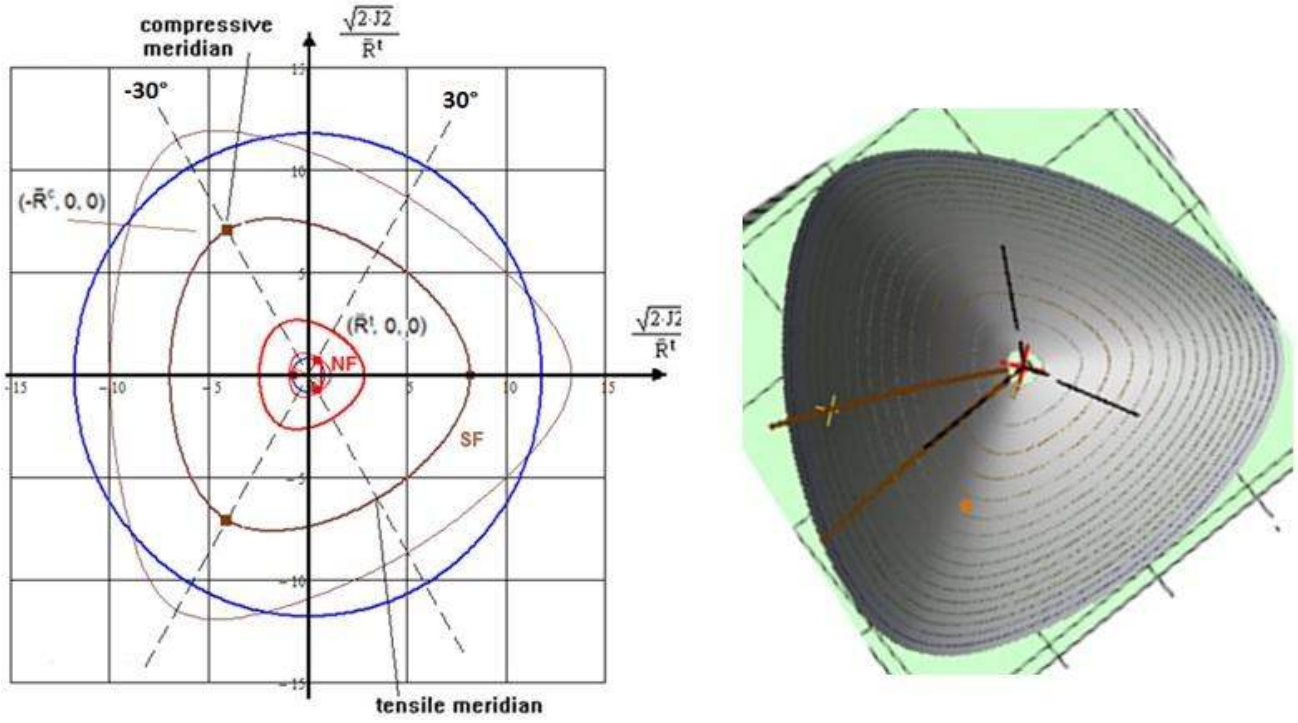

*Fig.16-3, Normal Concrete: Top view: Octahedral stress plane (π-plane) exhibiting the constant Eff- lines on the body (the **blue** line refers to $I_1 = 0$, neutral shear meridian). Right: X R^{cc}, ● R^c.*

In *Fig.16-4* the modeling of cap, NF domain (marginal) and of the SF fracture domain is depicted. Modelling of a cap is shown in the sub-chapter foam.

Fig.16-5 shows the three basic meridians and two strength points, compressive strength (dot) and bi-axial compressive strength (cross). The Neutral Meridian represents the shear meridian.

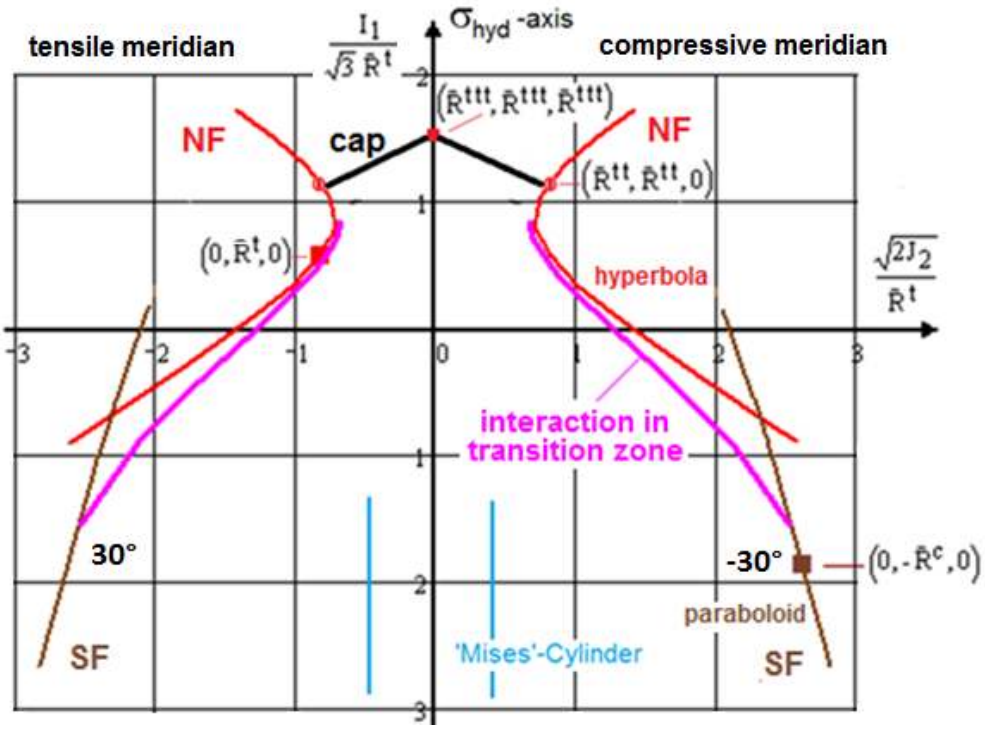

*Fig. 16-4, axial cut: Visualization of the courses of the 2 mode mapping functions for NF and SF along the meridian cross sections of the fracture body (180° cut of the 120°-body) and after **interaction***

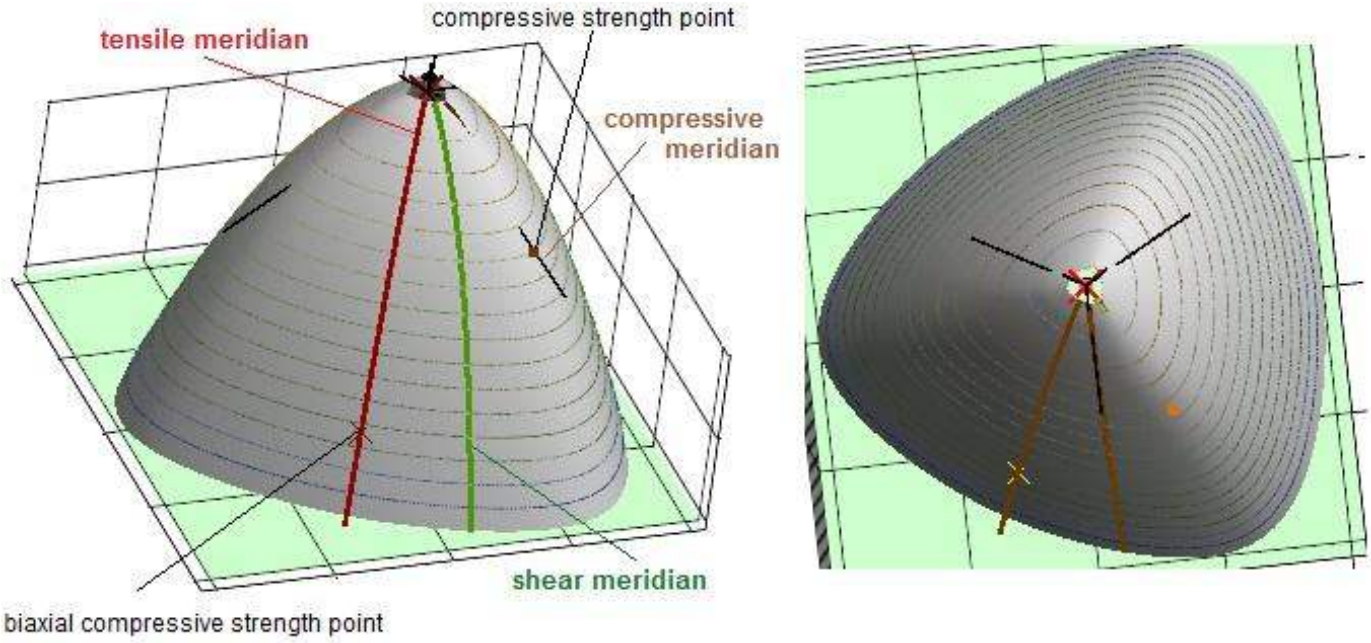

Fig.16-5: Two views of the 120°-rotationally-symmetric fracture body (hoop cross-section) of Normal Concrete with the basic three meridians and the strength points [Cun17]

Fig.16-6 informs about the test data scatter of the 3D fracture states experienced under hydrostatic pressure when running test on the tensile meridian and on the compressive meridian (-30°, CM), selection of test data performed.

In *Fig.16-6* the two meridian failure curves CM, TM are depicted and two test points are inserted indicating where the determination of the Mohr quantities τ_n , σ_n , θ_{fp} has been performed. As coordinates, the Haigh-Lode-Westergaard coordinates are used which equally count in all directions of the space. For information the included Drucker-Prager failure envelope shows the applicability.

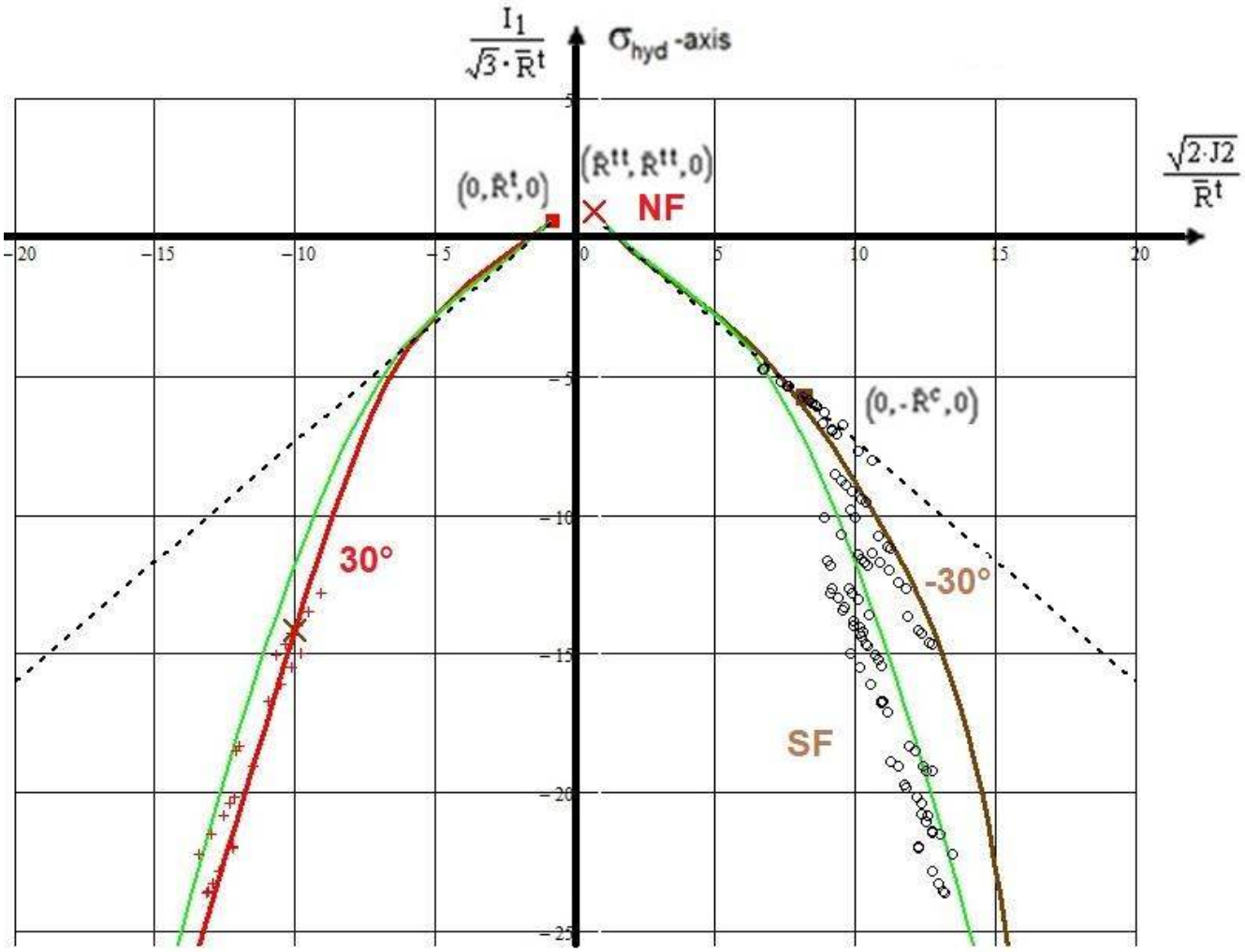

Fig.16-6: (left) Tensile meridian curve (TM) with sorted-out test points and associated test data (x, ϑ =30°), (right) compressive meridian (ϑ =-30°) curve (CM) and the other test data on the respective hoop ring o (these circles o are located at different meridian angles ϑ), courtesy IfM Dresden. Drucker-Prager black, dashed.

Extrapolated guess of the CM-curve on basis of mapped TM test data and vice versa. How??

Just replace the Lode angle part for 30°, sin (3ϑ) = 1, by that for -30°, sin (3ϑ) = -1.

The *Fig.16-6b-* depicted basic three meridians are:

Tensile Meridian TM (ϑ = +30°) inside, favorite test meridian
Neutral Meridian NM (0°) and
Compressive Meridian CM (ϑ = -30°), outside.

As still mentioned, $F = 1$ or $Eff = 100\%$ mathematically defines the surface of the fracture failure body. Such a body is rendered here using the Haigh-Lode-Westergaard coordinates with $I_1 / \sqrt{3}$ as y-coordinate and $\sqrt{2 \cdot J_2}$ as x-coordinate.

Fig.16-7 depicts the stress states belonging to the Tensile Meridian and to a Compressive Meridian. These are those axial cross–sections of the failure body (right) along most of the compression tests are run. Test points lie on the respective meridian, determined by ϑ, which means 'On different distances' from the axis for a specific $x = I_1 / \sqrt{3 \cdot \bar{R}^t}$ value. For Normal Concrete, the figure significantly supports the existence of the 120°-rotational symmetry of brittle isotropic materials.

Introduced are curves of the rotationally-symmetric Drucker-Prager SFC outlining that this SFC cannot predict accurate results when approaching the equi-biaxial failure stress point $(-\bar{R}^{cc}, -\bar{R}^{cc}, 0)$. See § 16.6.

16.2.2 Mapping of UltraHighPerformanceConcrete (UHPC) 3D compression test data

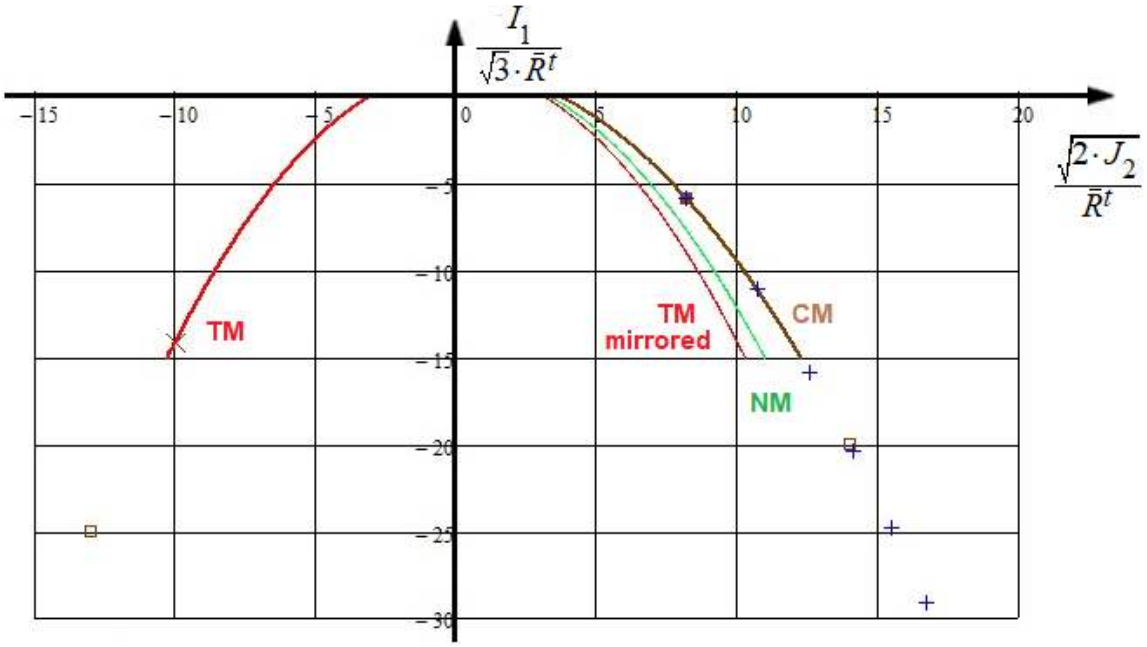

Fig.16-6b: Display of all basic meridians of Normal Concrete. The + are the points where the evaluation of τ_{nt}, σ_n, θ_{fp} was performed. $p = p_{hyd}$. TM Tensile Meridian, CM Compressive Meridian, NM Normal Meridian.
(Mathcad unfortunately did not draw below y = -15, an often faced Mathcad problem)

Fig.16-7, left depicts the separated and later intensively investigated TM and CM test data points.

Fig.16-7, right presents all 3D test points located at different Lode angles. View *Fig.16-6* again.

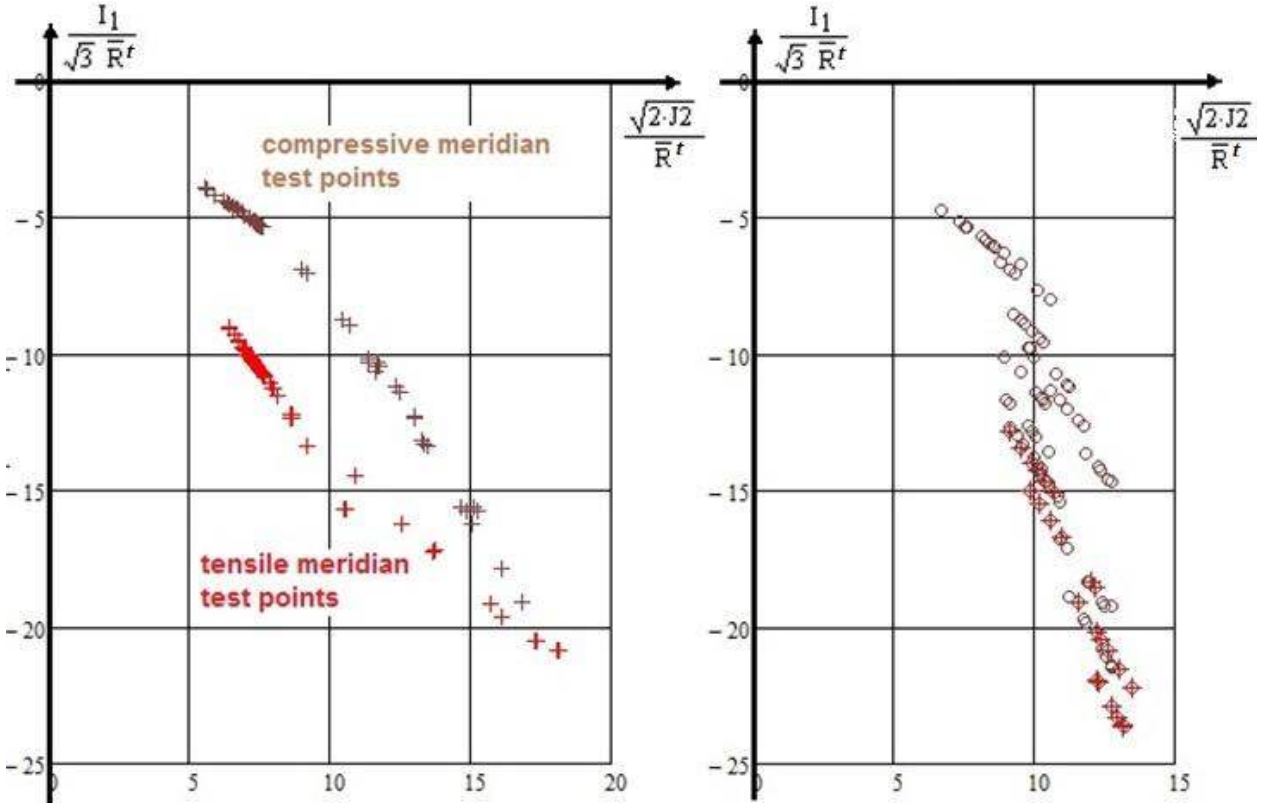

Fig.16-7 UltraHighPerformanceConcrete (UHPC): Compressive and tensile meridian points
UHPC, separated test points: (left) tensile meridian + (ϑ = +30°) and compressive meridian + (ϑ = -30°) ;
(right) all 3D test points are marked by **o** *(hoop ring, (ϑ ≠ ,+, - 30°)), visualizing to be located at different meridians*

Fig.16-8 outlines modelling ideas for UHPC._As could be still recognized for Normal Concrete, the failure body possesses inward dents for $I_1 > 0$ and outward dents for $I_1 < 0$ in contrast to porous

concrete stone, where it is also inward, see <u>*Fig.16-9.*</u> Due to *Fig, 16-7*, the dents become smaller with increasing negative I_1. This is to consider by the envisaged correction function.

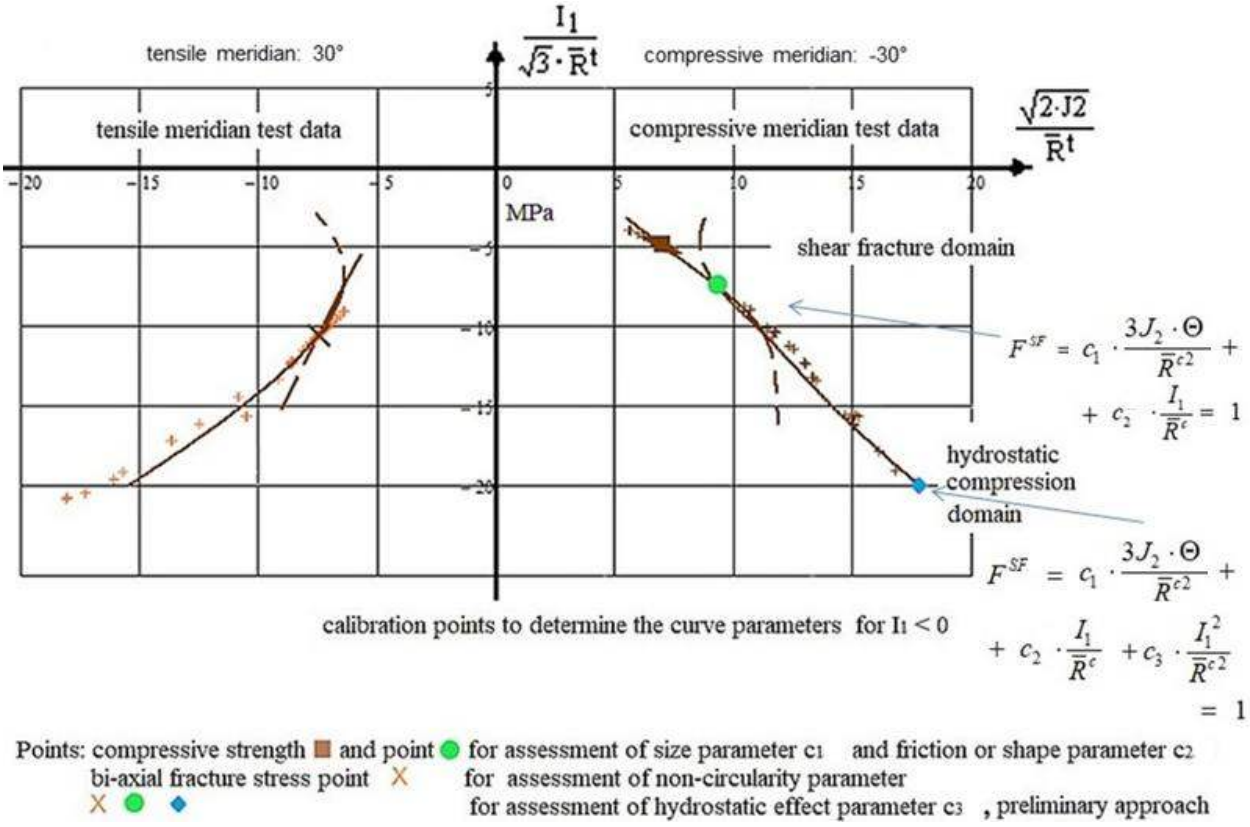

Fig.16-8 Ultra-High-Performance-Concrete (UHPC): [Test data: Dr. Speck, IfM, TU-Dresden]. From this general data set as sub-sets the meridian data sets (constant Lode angles) have been extracted by the author

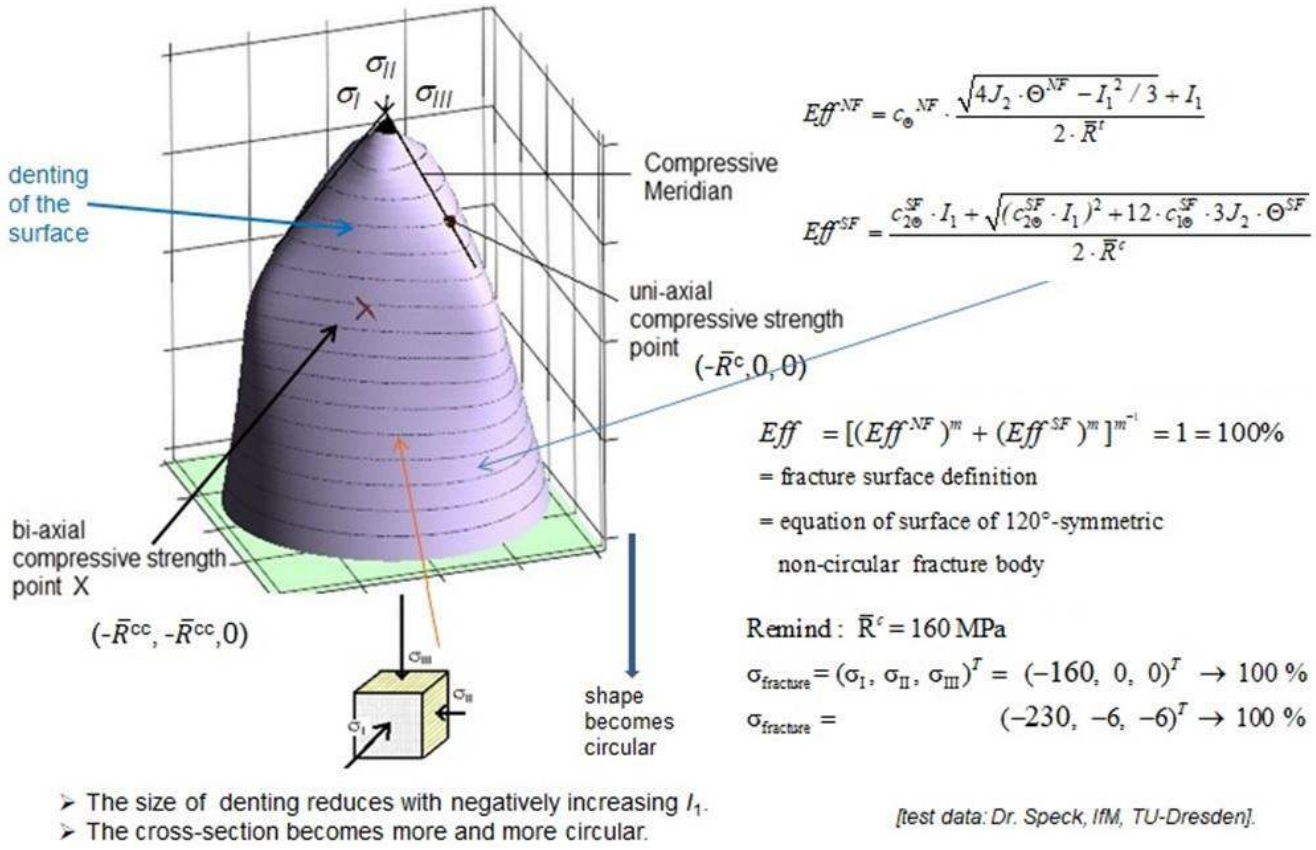

Fig.16-9, UHPC: Fracture body showing decay of denting with a negative I_1. R = f

<u>*Fig.16-10*</u> shows a graph the bi-axial compressive strength over the uniaxial compressive strength. It turns out that with increasing uniaxial strength the bi-axial strength approximates the uniaxial strength.

The author tries to explain this: The effect of redundancy under hydrostatic loading can be interpreted as an out-smoothing of stress concentrations. In the case of Normal Concrete this effect becomes more chances according to being more roughly grained than UHPC. This explains why the bi-axial strength capacity increase of a roughly grained Normal Concrete is higher than for UHPC.

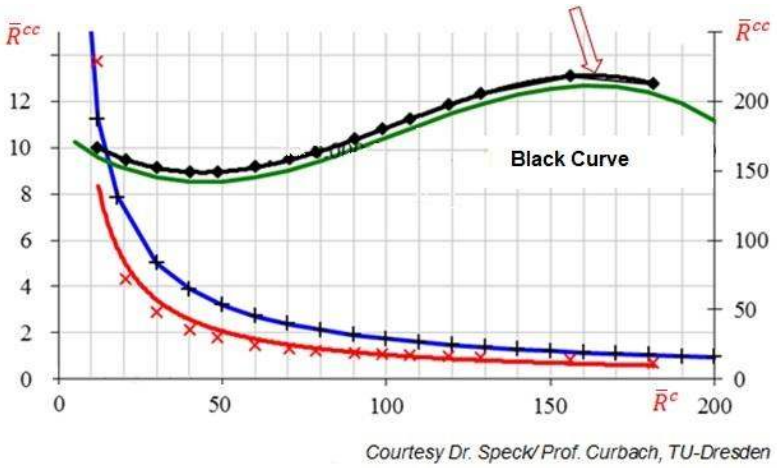

Fig.16-10: compressive strength capacity ratio of concrete $\bar{R}^{cc} / \bar{R}^{c}$ (Normal Concrete) > $\bar{R}^{cc} / \bar{R}^{c}$ (UHPC)

In *Fig.16-11* are depicted the 2 mode domains and its transition zone obtained with the interaction formula. This task concentrated about performing an interaction in the principal plane $I_1 > -2R^{cc}$.

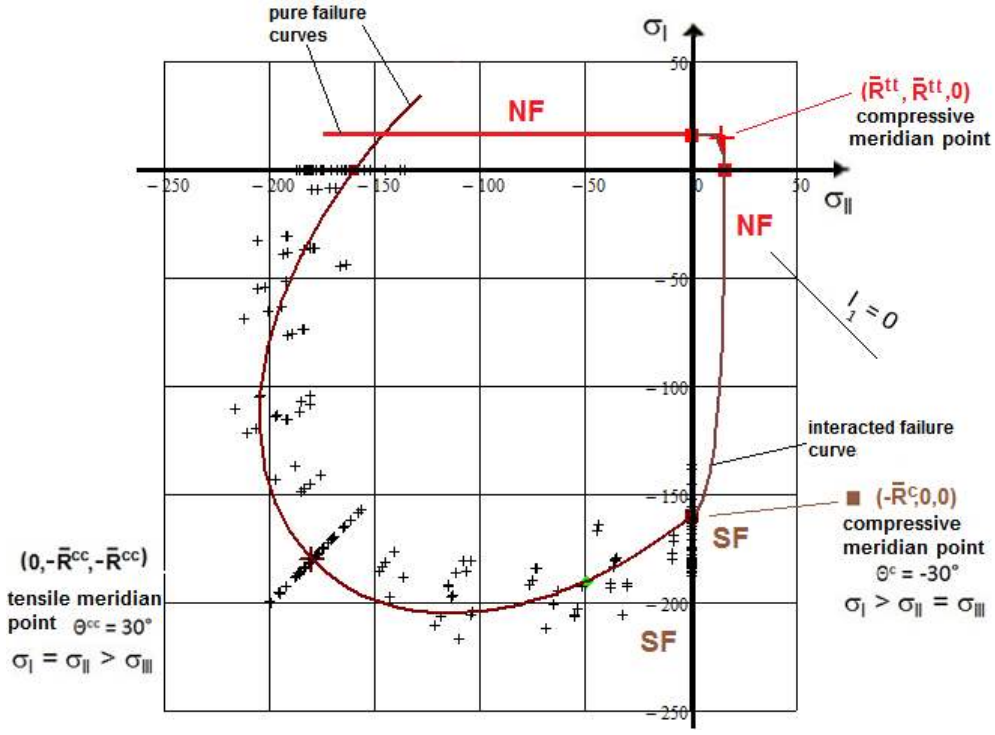

Fig.16-11, UHPC: Principal stress plane with measured test data and evaluated strength points

16.2.3 Mapping of Grey-cast Iron Test Data

Fig.16-12 presents an old evaluation (about 1995) of a data set for Grey-cast iron.

The SFCs are compiled in *Table 16-4*.

Of interest is the meridional cross section, which depicts a curvature change in the tensile domain, before the intended cut-off. Drucker 'Stability postulate' problem, like for PMMA in §9.

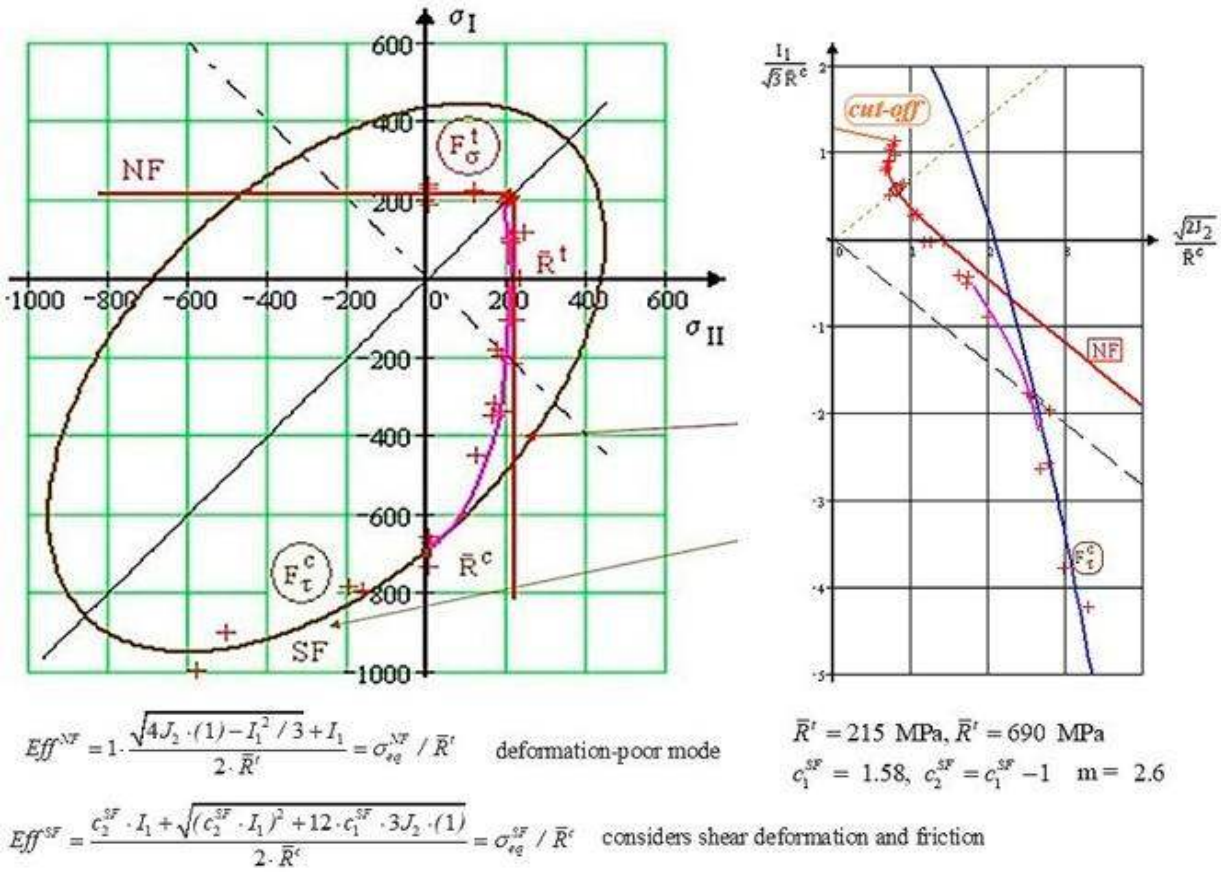

Fig.16-12: 2D-application to Grey-cast Iron [Coffin]. Principal stress plane and meridional cross section

Fig.16-13 presents a 2D-SFC-visualization in the principal stress plane and a 3D-Visualization in the meridional cross-section.

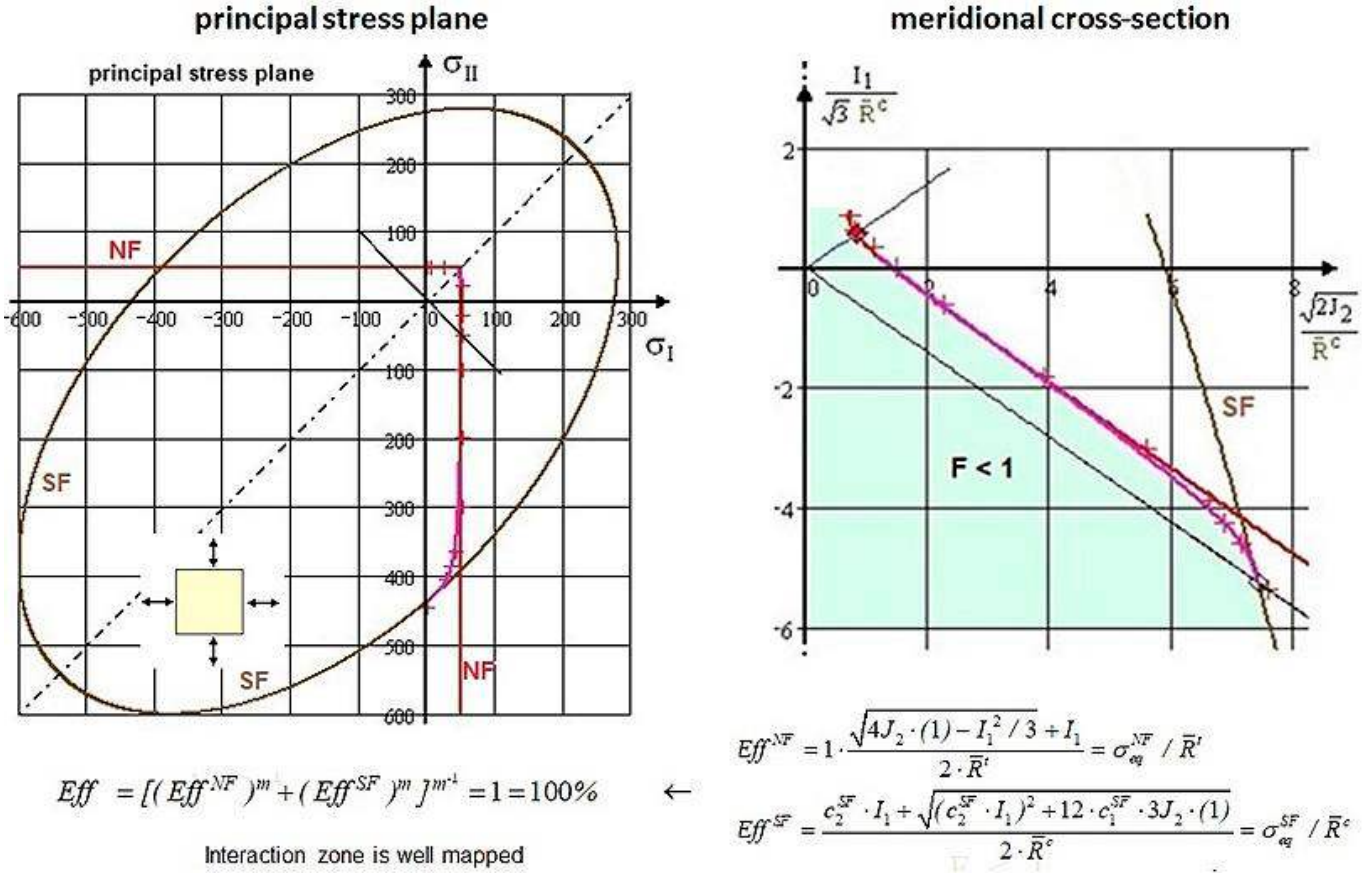

Fig.16-13, Glass C 90: [Kow83], 2D and 3D-visualizations

16.2.4 Mapping of Glass C 90 Test Data (window pane of ISS)

A glass fiber SiO_2 (E, S, R, AR) is made by blending raw materials, melting them at 1720°C in a three-stage furnace, extruding the molten glass through a bushing in the bottom of the fore-hearth (Vorherd), cooling the filaments with water (*to prevent the crystallization to quartz and obtain an amorphous, randomly ordered atomic structure we know as glass*) and then applying a chemical sizing. The filaments then are gathered to rovings and wound on spools.
Commercial glass fiber can be made from silica alone, other ingredients are added to reduce the working temperature and impart other properties that are useful in specific applications such as making alkali-resistant (by ZrO_2) for use in fiber-reinforced concrete, [*Source OCV*].

Table 16-4:

*3D-isotropic SFCs of dense Isotropic Materials for **NF** and **SF**, 120°-rotational symmetry*

2 modes → 2 SFCs, which is in line with the 'generic' number according to the FMC.

Normal Fracture NF for $I_1 > 0$ ↔ Shear Fracture SF for $I_1 < 0$

$$F_\sigma^t = F^{NF} = c^{NF} \cdot \Theta^{NF} \cdot \frac{\sqrt{4J_2 \cdot \Theta^{NF} - I_1^2/3} + I_1}{2 \cdot \bar{R}^t} = 1 \quad \leftrightarrow \quad F_\tau^c = F^{SF} = c_{1\Theta}^{SF} \cdot \frac{6J_2 \cdot \Theta^{SF}}{2\bar{R}^{c2}} + c_{2\Theta}^{SF} \cdot \frac{I_1}{\bar{R}^c} = 1$$

$$Eff^{NF} = c^{NF} \cdot \frac{\sqrt{4J_2 \cdot \Theta^{NF} - I_1^2/3} + I_1}{2 \cdot \bar{R}^t} = \frac{\sigma_{eq}^{NF}}{\bar{R}^t} \leftrightarrow Eff^{SF} = \frac{c_{2\Theta}^{SF} \cdot I_1 + \sqrt{(c_{2\Theta}^{SF} \cdot I_1)^2 + c_{1\Theta}^{SF} \cdot 12J_2 \cdot \Theta^{SF}}}{2 \cdot \bar{R}^c} = \frac{\sigma_{eq}^{SF}}{\bar{R}^c}.$$

If a failure body is rotationally symmetric, then $\Theta = 1$ like for the neutral or shear meridian.

A two-fold acting mode makes the rotationally symmetric fracture body 120°-symmetric and is modelled by $\Theta(J_3)$ using the invariant J_3 and Θ as non-circularity function with d as non-circularity parameter

$$\Theta^{NF} = \sqrt[3]{1 + d^{NF} \cdot \sin(3\vartheta)} = \sqrt[3]{1 + d^{NF} \cdot 1.5 \cdot \sqrt{3} \cdot J_3 \cdot J_2^{-1.5}}, \quad \Theta^{SF} = \sqrt[3]{1 + d^{SF} \cdot 1.5 \cdot \sqrt{3} \cdot J_3 \cdot J_2^{-1.5}}$$

Lode angle ϑ, here set as $\sin(3 \cdot \vartheta)$ with 'neutral' shear meridian angle set $\vartheta = 0°$;

Tensile Meridian angle 30° $\rightarrow \Theta^{NF} = \sqrt[3]{1 + d^{SF} \cdot (+1)}$; Compr. Merid. angle -30° $\rightarrow \Theta^{SF} = \sqrt[3]{1 + d^{SF} \cdot (-1)}$.

Equation of the fracture failure body: $Eff = [(Eff^{NF})^m + (Eff^{SF})^m]^{m^{-1}} = 1 = 100\%$ total effort

$$Eff = \sqrt[m]{\left(c^{NF} \cdot \frac{\sqrt{4J_2 \cdot \Theta^{NF} - I_1^2/3} + I_1}{2 \cdot \bar{R}^t}\right)^m + \left(\frac{c_{2\Theta}^{SF} \cdot I_1 + \sqrt{(c_{2\Theta}^{SF} \cdot I_1)^2 + c_{1\Theta}^{SF} \cdot 12J_2 \cdot \Theta^{SF}}}{2 \cdot \bar{R}^c}\right)^m} = 1.$$

Curve parameter relationships obtained by inserting the compressive strength point (0, $-\bar{R}^c$, 0):

* Rotationally symmetric: $c_1^{SF} = 1 + c_2^{SF}$, $d^{SF} = 0$, friction parameters are equal $c_2^{SF} \equiv c_{2\Theta}^{SF}$

$c_2^{SF} = c_{2\Theta}^{SF} \approx (1 + 3 \cdot \mu)/(1 - 3 \cdot \mu)$ from $\mu = \cos(2 \cdot \theta_{fp}^c \circ \cdot \pi / 180)$ and for 50° $\rightarrow \mu = 0.174$.

* 120°-rotationally symmetric: $c_{1\Theta}^{SF} = 1 + c_2^{SF} \cdot \sqrt[3]{1 + d^{SF} \cdot (-1)}$ with

c^{NF}, Θ^{NF} from the two points $(\bar{R}^t, 0, 0)$ and $(\bar{R}^{tt}, \bar{R}^{tt}, 0)$ or by a minimum error fit, if data,

c^{SF}, Θ^{SF} from the two points $(-\bar{R}^c, 0, 0)$ and $(-\bar{R}^{cc}, -\bar{R}^{cc}, 0)$ or by minimum error fit.

A paraboloid serves as closing cap $\frac{I_1}{\sqrt{3} \cdot \bar{R}^t} = s^{cap} \cdot \left(\frac{\sqrt{2J_2 \cdot \Theta^{NF}}}{\bar{R}^t}\right)^2 + \frac{\max I_1}{\sqrt{3} \cdot \bar{R}^t}$.

$$I_1 = (\sigma_I + \sigma_{II} + \sigma_{III}) = f(\sigma), \quad 6J_2 = (\sigma_I - \sigma_{II})^2 + (\sigma_{II} - \sigma_{III})^2 + (\sigma_{III} - \sigma_I)^2 = f(\tau)$$

$$27J_3 = (2\sigma_I - \sigma_{II} - \sigma_{III}) \cdot (2\sigma_{II} - \sigma_I - \sigma_{III}) \cdot (2\sigma_{III} - \sigma_I - \sigma_{II}).$$

Mechanical strength behavior shows up: Different structural materials

- can possess similar material behavior
- can belong to the same class of material symmetry.

Welcomed Consequence is: The same strength failure function SFC can be used for different materials. Exemplarily, the Foam SFC is applicable to Concrete Stone, thus offering the advantage:
→ For a concrete stone material more information is available for pre-dimensioning and modelling in the case of a newly applied material from available foam experiments as a still being tested similarly behaving material.

LL:

** 120°-rotational symmetry is inherent for isotropic materials*

** R^c lies on the CM, R^t on the TM and R^τ in the transition zone between the two modes F^σ and F^τ. This indicates, that an estimation of R^τ, obtained by just an extrapolation from R^c, will be questionable*

** The failure body possesses inward dents for $I_1 > 0$ and outward dents for $I_1 < 0$ in contrast to porous concrete stone, where it is also inward. These dents become smaller with increasing $|I_1|$.*

** There is a pretty large scatter of the compressive strength data in the 2D-figure*

** Mapping of the course of test data with the SFCs worked very well*

** Fracture body shows a decay of denting with increasing negative I_1*

** The higher the strength ratio $SR = R^c/R^t$ becomes, the more the Cohesive Strength value narrows R^t !*

** The strong influence of IFF1 is fully demonstrated.*

An extrapolation from the compression strength - just applying F^τ - cannot be accurate !

** A smaller μ value is more conservative.*

16.2.5 Mapping of Porous Foam Rohacell 71 IG Test Data

Usually, for structural parts of high stiffness, honeycombs are used. With the new Rohacell Hero (Evonik) a PMI (Poly-Methacryl-Imide) structural foam of an increased tensile fracture strain is available which may replace the expensive honeycombs. In order to apply this material in structural parts Structural Integrity must be proven. This requires reliable multi-axial strength test data as well as reliable Strength Failure Conditions SFCs (criteria) for an optimal Design Development process. Given is 'only' a 2D-Test Data Set and therefore just a realistic mapping in the Principal Stress Plane is possible. To apply is the 2D subversion of the 3D SFC.

$$\bar{R}^t = 1.8;\ \bar{R}^{tt} = 1.25;\ \bar{R}^{ttt} = 1.01;\ \bar{R}^c = 1.65;\ \bar{R}^{cc} = 1.4;\ \bar{R}^{ccc} = 1.53,\ \max I_1 = 3.03;$$
$$\min I_1 = -4.58,\ d^{NF} = -0.71;\ d^{CrF} = 0.21;\ c^{CrF} = 1.03, s^{cap} = -0.27;\ s^{bot} = 0.87,$$
$$\vartheta^{NF} = -0.57;\ \vartheta^{CrF} = 0.52;\ \Theta^{NF} = 1.2;\ \Theta^{CrF} = 1.07, m = 2.5.$$

(*thanks to Dr. Vladimir Kolupaev for the test data set*)

→ From this follows: Validation of the 3D SFC is 'just' 2D-based.

Table 16-5 collects all information necessary to dimension a porous isotropic material like a foam or a concrete stone. These materials experience *120°-rotational symmetry.*

The SFC-model for porous Foam Rohacell including the cap model from Concrete Stone material is applicable, too. Due to the closed body on top a bottom shape is now to model.

Table 16-5: 3D-SFCs of Isotropic Porous Materials with model parameter determination

Normal Fracture NF for $I_1 > 0$ $\Leftarrow$ SFCs $\Rightarrow$ Crushing Fracture CrF for $I_1 < 0$

$$F^{NF} = c^{NF} \cdot \Theta^{NF} \cdot \frac{\sqrt{4J_2 \cdot \Theta^{NF} - I_1^2/3} + I_1}{2 \cdot \bar{R}^t} = 1 \leftrightarrow F^{CrF} = c^{CrF} \cdot \Theta^{CrF} \cdot \frac{\sqrt{4J_2 \cdot \Theta^{CrF} - I_1^2/3} + I_1}{2 \cdot \bar{R}^c} 1$$

$$Eff^{NF} = c^{NF} \cdot \frac{\sqrt{4J_2 \cdot \Theta^{NF} - I_1^2/3} + I_1}{2 \cdot \bar{R}^t} = \frac{\sigma_{eq}^{NF}}{\bar{R}^t} \leftrightarrow Eff^{CrF} = c^{CrF} \cdot \frac{\sqrt{4J_2 \cdot \Theta^{CrF} - I_1^2/3} + I_1}{2 \cdot \bar{R}^c} = \frac{\sigma_{eq}^{CrF}}{\bar{R}^c},$$

with $I_1 = (\sigma_I + \sigma_{II} + \sigma_{III}) = f(\sigma)$, $6J_2 = (\sigma_I - \sigma_{II})^2 + (\sigma_{II} - \sigma_{III})^2 + (\sigma_{III} - \sigma_I)^2 = f(\tau)$,

$$27J_3 = (2\sigma_I - \sigma_{II} - \sigma_{III}) \cdot (2\sigma_{II} - \sigma_I - \sigma_{III}) \cdot (2\sigma_{III} - \sigma_I - \sigma_{II}).$$

If a failure body is rotationally symmetric, then $\Theta = 1$ like for the neutral or shear meridian, respectively .

A 2-fold acting mode makes the rotationally symmetric fracture body 120°-symmetric and is modelled by using the invariant J_3 and Θ as non-circularity function with d as non-circularity parameter

$$\Theta^{NF} = \sqrt[3]{1 + d^{NF} \cdot \sin(3\vartheta)} = \sqrt[3]{1 + d^{NF} \cdot 1.5 \cdot \sqrt{3} \cdot J_3 \cdot J_2^{-1.5}} \quad \leftrightarrow \quad \Theta^{CrF} = \sqrt[3]{1 + d^{CrF} \cdot 1.5 \cdot \sqrt{3} \cdot J_3 \cdot J_2^{-1.5}}$$

Lode angle ϑ, here set as $\sin(3 \cdot \vartheta)$ with 'neutral' (shear meridian) angle $\vartheta = 0°$ ($\rightarrow \Theta = 1$);

tensile meridian angle 30° $\rightarrow \Theta^{NF} = \sqrt[3]{1 + d^{NF} \cdot (+1)}$; compr. mer. angle -30° $\rightarrow \Theta^{CrF} = \sqrt[3]{1 + d^{CrF} \cdot (-1)}$.

Mode interaction $\rightarrow$ Equation of the fracture body: $Eff = [(Eff^{NF})^m + (Eff^{SF})^m]^{m^{-1}} = 1 = 100\%$

$$Eff = \sqrt[m]{(c^{NF} \cdot \frac{\sqrt{4J_2 \cdot \Theta^{NF} - I_1^2/3} + I_1}{2 \cdot \bar{R}^t})^m + (c^{CrF} \cdot \frac{\sqrt{4J_2 \cdot \Theta^{CrF} - I_1^2/3} + I_1}{2 \cdot \bar{R}^c})^m} = 1.$$

Curve parameter relationships obtained by inserting the compressive strength point (0, -$\bar{R}^c$, 0):

* Rotationally symmetric $\Theta = 1$: $d^{SF} = 0$, $c_{1\Theta}^{SF} = 1 + c_2^{SF}$

* 120°-rotat. symmetric $\Theta \neq 1$: $c_{1\Theta}^{SF} = 1 + c_2^{SF} \cdot \sqrt[3]{1 + d^{SF} \cdot (-1)}$, with

c^{NF}, Θ^{NF} from the two points $(\bar{R}^t, 0, 0)$ and $(\bar{R}^{tt}, \bar{R}^{tt}, 0)$ or by minimum error fit, if data available,

c^{CrF}, Θ^{CrF} from the two points $(-\bar{R}^c, 0, 0)$ and (-$\bar{R}^{cc}$,-$\bar{R}^{cc}$, 0) or by minimum error fit.

The failure surface is closed at both the ends: A paraboloid serves as closing cap and bottom

$$\frac{I_1}{\sqrt{3} \cdot \bar{R}^t} = s^{cap} \cdot (\frac{\sqrt{2J_2 \cdot \Theta^{NF}}}{\bar{R}^t})^2 + \frac{\max I_1}{\sqrt{3} \cdot \bar{R}^t} \quad , \quad \frac{I_1}{\sqrt{3} \cdot \bar{R}^t} = s^{bot} \cdot (\frac{\sqrt{2J_2 \cdot \Theta^{CrF}}}{\bar{R}^t})^2 + \frac{\min I_1}{\sqrt{3} \cdot \bar{R}^t}$$

Slope parameters s are determined connecting the respective hydrostatic strength point with the associated point on the tensile and compressive meridian, $\max I_1$ must be assessed whereas $\min I_1$ can be measured. $\bar{R}^t$ is normalization strength.

The *Figs. 16-14* and *16-15* show the application of the respective SFC for the given Rohacell.

The test points in *Fig.16-14* and *-16* are located at a distinct Lode angle of its associated ring o, 120°-symmetry.

Cap and bottom are closed by a conical shape, a shape being on the conservative side, + means bi-axial.

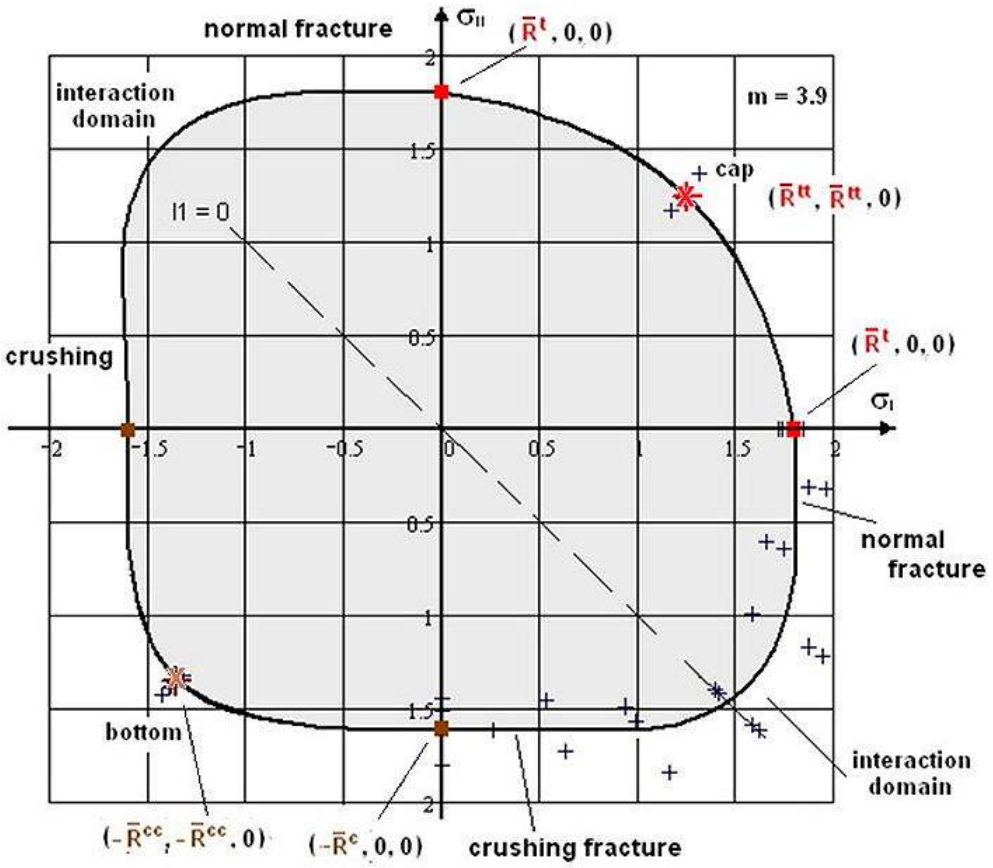

Fig.16-14, Foam Rohacell 71 IG: Mapping of 2D-test data in the Principal Stress Plane. MathCad plot [test data: courtesy V. Kolupaev, LBF Darmstadt]

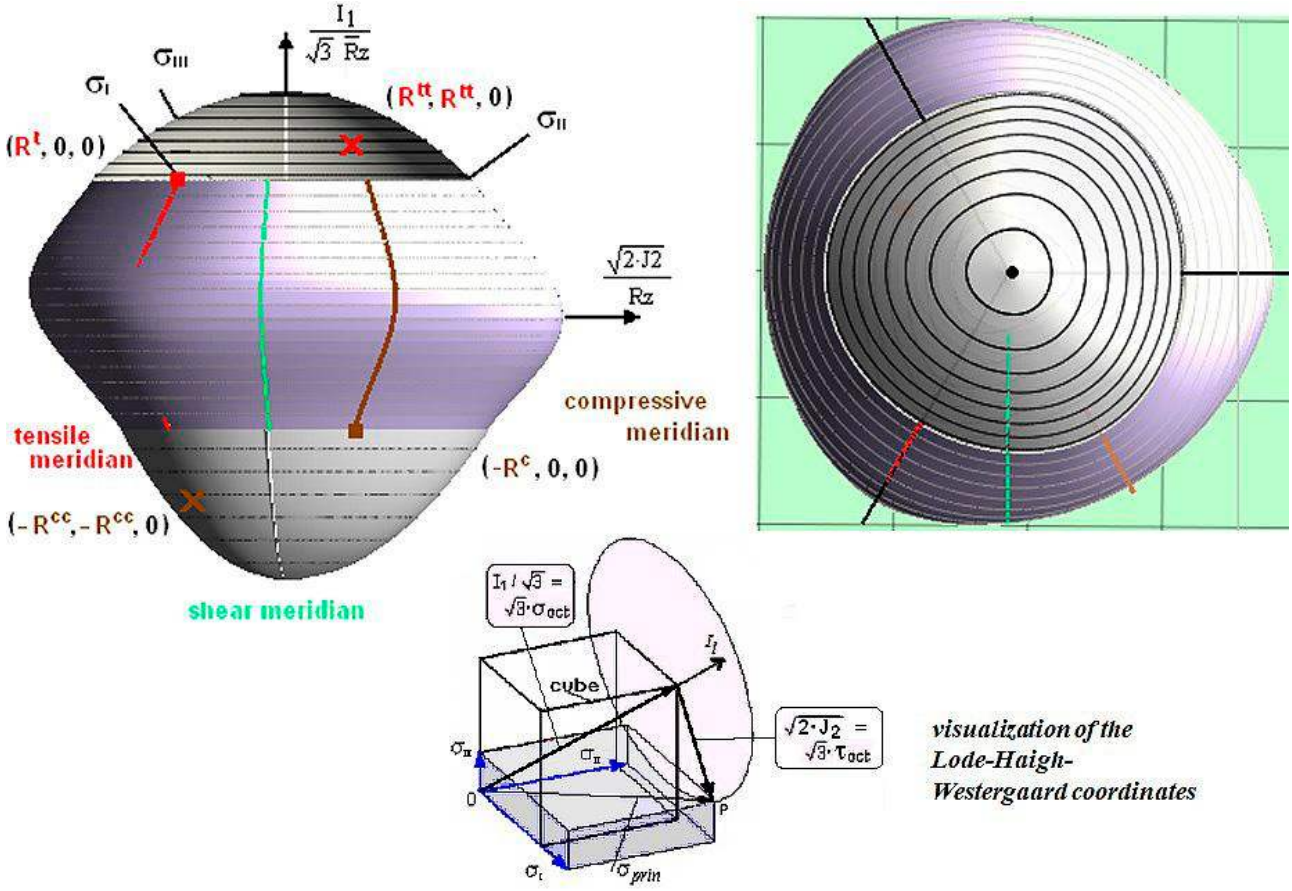

Fig.16-15, Rohacell 71 IG: Fracture body with its different meridians (left) and view from top (right).

Table 16-6: Derivation of model parameters (θcr should read here ϑ_{cr})

$Rc = 1.36 \quad Rcc = 1.35 \quad maxI1 = 3.03 \quad \frac{I1c}{\sqrt{3}\cdot Rt} = -0.57 \quad \frac{I1cc}{\sqrt{3}\cdot Rt} = -0.962 \quad \theta crc := -0.52 \quad \theta crcc := 0.52 \quad \theta\sigma ccc := 0$

$Rt = 1.62 \quad Rtt = 1.25 \quad minI1 = -3.67 \quad \frac{I1t}{\sqrt{3}\cdot Rt} = 0.642 \quad \frac{I1tt}{\sqrt{3}\cdot Rt} = 0.891 \quad \theta\sigma t := 0.52 \quad \theta\sigma tt := -0.52 \quad \theta\sigma ttt := 0$

$x = \frac{\sqrt{2J2}}{Rt}$

$$ycap = \frac{maxI1}{\sqrt{3}\cdot Rt} + scap\cdot\left(\frac{\sqrt{2J2}}{Rt}\cdot\sqrt[3]{1 + d\sigma\cdot\sin(3\theta\sigma)}\right)^2$$

$y = \frac{I1}{\sqrt{3}\cdot Rt}$

Vorgabe $scap := 1 \quad d\sigma := -0.4$

Cap: maxI1 > I1t

$$\frac{I1t}{\sqrt{3}\cdot Rt} = \frac{maxI1}{\sqrt{3}\cdot Rt} + scap\cdot\left(\frac{\sqrt{2J2t}}{Rt}\cdot\sqrt[3]{1 + d\sigma\cdot\sin(3\theta\sigma t)}\right)^2 \qquad \frac{I1tt}{\sqrt{3}\cdot Rt} = \frac{maxI1}{\sqrt{3}\cdot Rt} + scap\cdot\left(\frac{\sqrt{2J2tt}}{Rt}\cdot\sqrt[3]{1 + d\sigma\cdot\sin(3\theta\sigma tt)}\right)^2$$

$Acap := Suchen(scap, d\sigma) \quad Acap = \begin{pmatrix} -0.506 \\ 0.168 \end{pmatrix} \quad scap := Acap_0 \quad d\sigma := Acap_1$

$scap = -0.51 \quad d\sigma = 0.17$

$$F\sigma = c1\Theta\sigma\cdot\frac{\sqrt{4\cdot J2\cdot\Theta\sigma - \frac{1}{3}\cdot I1^2} + I1}{2Rt} = 1$$

Vorgabe $c1\Theta\sigma := 0.5$

NF: I1t > I1

$$c1\Theta\sigma\cdot\frac{\sqrt{4\cdot J2t\cdot\sqrt[3]{1 + d\sigma\cdot\sin(3\theta\sigma t)} - \frac{1}{3}\cdot I1t^2} + I1t}{2\cdot Rz} = 1$$

$A\sigma := Suchen(c1\Theta\sigma) \quad A\sigma = 0.885 \quad c1\Theta\sigma := A\sigma \quad c1\Theta\sigma = 0.88$

$$ybot = \frac{minI1}{\sqrt{3}\cdot Rt} + sbot\cdot\left(x\cdot\sqrt[3]{1 + dcr\cdot\sin(3\theta cr)}\right)^2$$

Vorgabe $sbot := 1 \quad dcr := -1$

SF: 0 > I1c

$$\frac{I1c}{\sqrt{3}\cdot Rt} = \frac{minI1}{\sqrt{3}\cdot Rt} + sbot\cdot\left(\frac{\sqrt{2J2c}}{Rt}\cdot\sqrt[3]{1 + dcr\cdot\sin(3\theta crc)}\right)^2 \qquad \frac{I1cc}{\sqrt{3}\cdot Rt} = \frac{minI1}{\sqrt{3}\cdot Rt} + sbot\cdot\left(\frac{\sqrt{2J2cc}}{Rz}\cdot\sqrt[3]{1 + dcr\cdot\sin(3\theta crcc)}\right)^2$$

$Abot := Suchen(sbot, dcr) \quad Abot = \begin{pmatrix} 0.977 \\ -0.558 \end{pmatrix} \quad sbot := Abot_0 \quad dcr := Abot_1$

$sbot = 0.98 \quad dcr = -0.56$

$$Fcr = c1\Theta cr\cdot\frac{\sqrt{4\cdot J2\cdot\Theta cr - \frac{1}{3}\cdot I1^2} - I1}{2Rc} = 1$$

Vorgabe $c1\Theta cr := 1$

$$c1\Theta cr\cdot\frac{\sqrt{4\cdot J2c\cdot\sqrt[3]{1 + dcr\cdot\sin(3\theta crc)} - \frac{1}{3}\cdot I1c^2} - I1c}{2\cdot Rc} = 1$$

Bottom: I1c > minI1

$Acr := Suchen(c1\Theta cr) \quad Acr = 0.809 \quad c1\Theta c := Acr \quad c1\Theta c = 0.81$

Since there are 3D test data and three-axis tensile fracture data practically impossible to measure, the cap value can only be estimated probabilistically. According to Awaji-Sato [*Awa73*], a Weibull-based estimation of the 3-axis breaking stress value R^{ttt} results from measured values for R^{t} and R^{tt}. This type of estimation is also applied for the bottom. *For* R^{ccc}, a surcharge of 10% is applied because of the supporting pressure effect.

Viewing the various figures of interest might be the Estimation of hydrostatic points, *Table 16-7*, and the determination of the turning point of F_σ , *Table 16-8*.

Table 16-7: Estimation of hydrostatic points

$Rt = 1.8 \quad Rtt = 1.25 \quad Rc = 1.6 \quad Rcc = 1.35$

$Mt := \frac{\ln(2)}{\ln\left(\frac{Rt}{Rtt}\right)} \quad Rttt := \frac{Rt}{\frac{1}{3}Mt} \quad Mc := \frac{\ln(2)}{\ln\left(\frac{Rc}{Rcc}\right)} \quad Rccc0 := \frac{Rc}{\frac{1}{3}Mc} \quad Rccc = Rccc0 \cdot 1.1$

$maxI1 := 3 \cdot Rttt \quad maxI1 = 3.03 \quad \frac{maxI1}{\sqrt{3} \cdot Rt} = 0.97 \quad minI1 := -3 \cdot Rccc0 \quad minI1 = -3.67 \quad \frac{minI1}{\sqrt{3} \cdot Rt} = -1.18$

Table 16-8: Determination of the turning point of F_σ

$$F\sigma = \frac{\sqrt{4 \cdot J2 - \frac{1}{3} \cdot I1^2} + I1}{2Rt} = 1$$

Turning point of Fσ (index w)

$$J2 = \frac{1}{3} \cdot I1^2 - I1 \cdot Rt + Rt^2 \quad \text{derivation} \quad \frac{d}{dI1}\left(\frac{1}{3} \cdot I1^2 - I1 \cdot Rt + Rt^2\right) \quad \frac{2}{3} \cdot I1W - Rt = 0 \quad I1W := 1.5 \cdot Rt$$

$$J2W = \frac{1}{3} \cdot (1.5Rt)^2 - 1.5Rt \cdot Rt + Rt^2 \quad J2W := .25 \cdot Rt^2 \quad minJ2 := 0.25 \cdot Rt^2$$

$$x1W := \frac{\sqrt{2J2W}}{Rt} \quad x1W = 0.707 \quad x2W := \frac{I1W}{\sqrt{3} \cdot Rt} \quad x2W = 0.866$$

The following figure in *Table 16-9* proves that in the performed modelling no gap exists between Cap- and *F*σ-domain at the axial coordinate x including the tensile strength point and between *F*τ-domain and Bottom at the compressive point including coordinate x.

Table 16-9: Proof, no gap exists between the differently modelled fracture body domains

$$\Theta\sigma_m = \sqrt[3]{1 + d\sigma \cdot \sin(3\delta_m)}$$

$$ycap = \frac{maxI1}{\sqrt{3} \cdot Rz} + scap \cdot \left(xcap \cdot \sqrt[3]{1 + d\sigma \cdot \sin(3\delta_m)}\right)^2$$

$$x\sigma F_m = \frac{\sqrt{2\frac{I1t^2 \cdot c1\Theta\sigma^2 - 3 \cdot c1\Theta\sigma \cdot I1t \cdot Rt + 3 \cdot Rt^2}{3 \cdot \Theta\sigma_m \cdot c1\Theta\sigma^2}}}{Rt}$$

$$xcrF_m = \frac{\sqrt{2\frac{I1c^2 \cdot c1\Theta cr^2 + 3 \cdot c1\Theta cr \cdot I1c \cdot Rc + 3 \cdot Rc^2}{3\,\Theta cr_m \cdot c1\Theta cr^2}}}{Rt}$$

$$\Theta cr_m = \sqrt[3]{1 + dcr \cdot \sin(3\delta_m)}$$

$$ybot = \frac{minI1}{\sqrt{3} \cdot Rt} + sbot \cdot \left(xbot \cdot \sqrt[3]{1 + dcr \cdot \sin(3\delta_m)}\right)^2$$

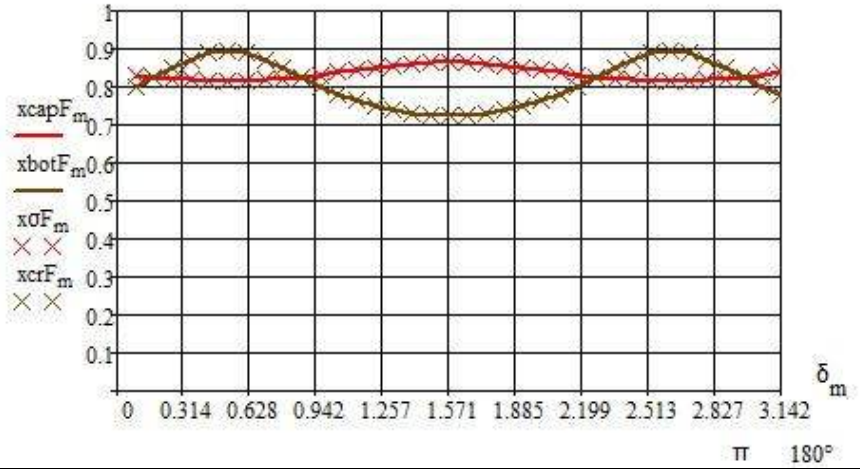

Cap and Bottom equations have to be resolved for x_{cap} and x_{bot}.

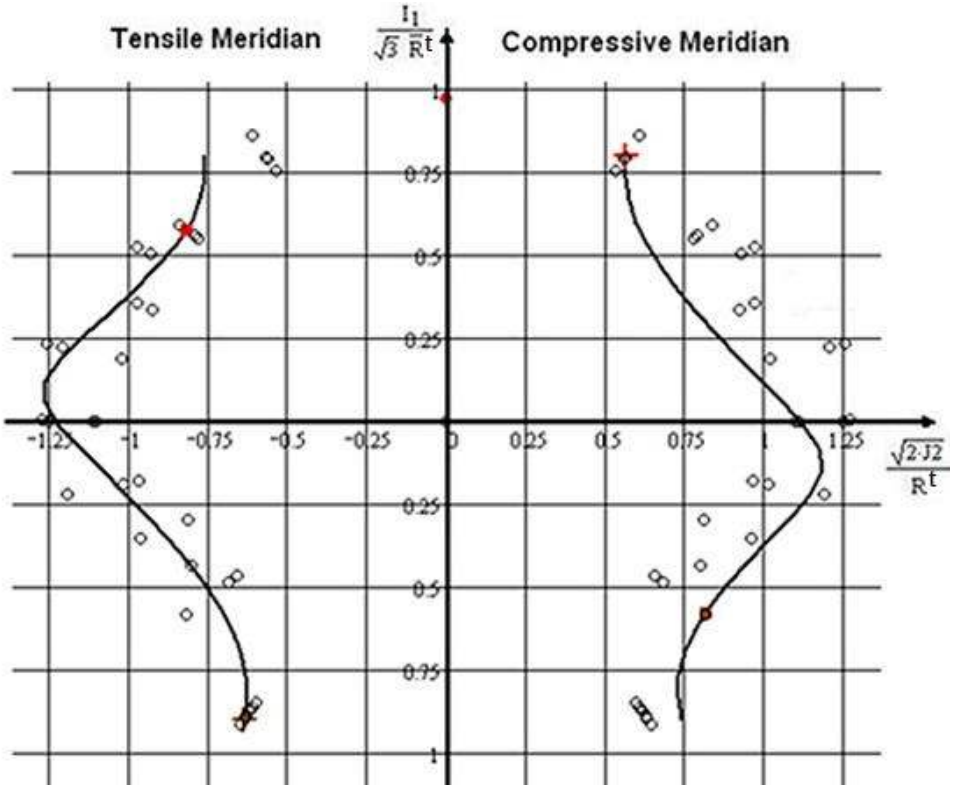

Fig16-16, Rohacell 71 IG: Meridional cross-section of the fracture body.

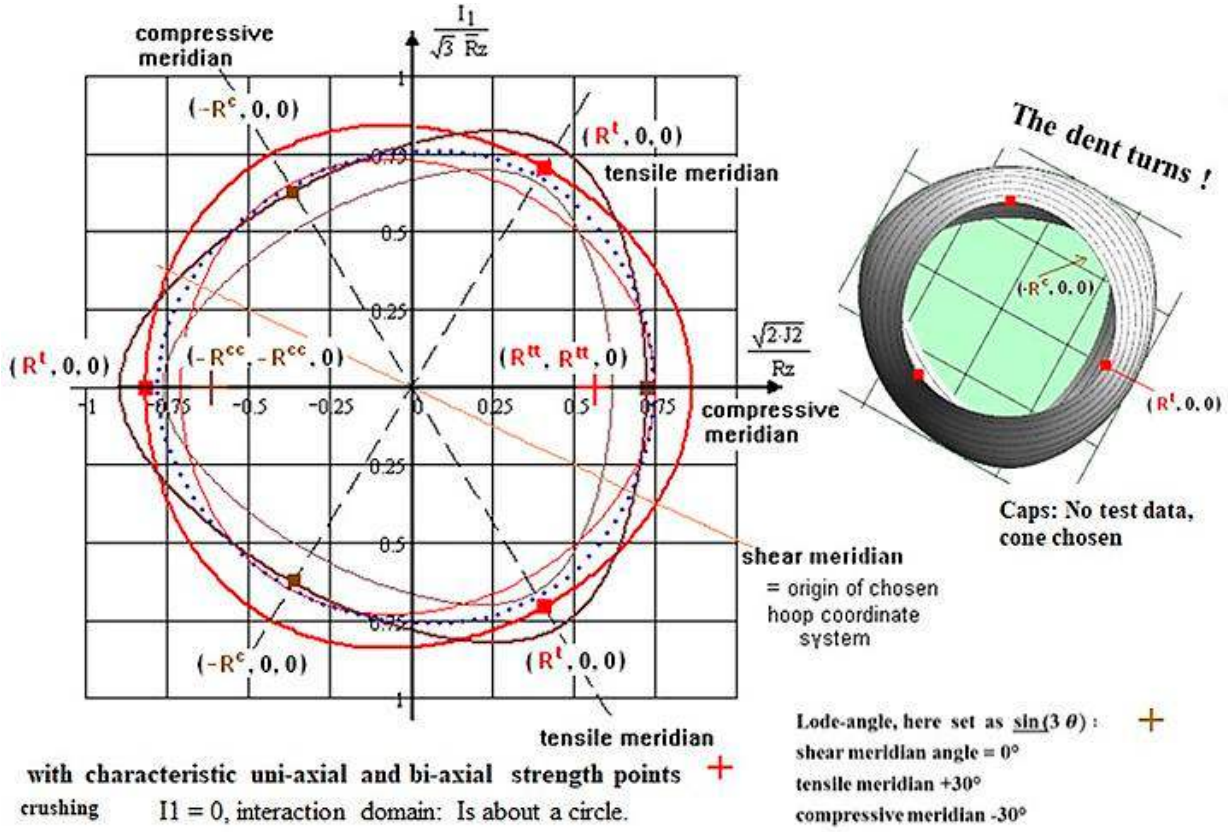

Fig.16-17: Rohacell 71 IG 2D Test Data and Mapping in the Orthogonal Stress Plane (brittle, porous)

Caps were taken away to better visualize that the dent in Fig.15-17turns for this material along the hydrostatic axis.

16.3 Mapping 3D Test Results of UHPC and Rocks obtained on the Meridians TM and CM

Aim: *Good tuning in 2D-plane and 3D-space of meridian test data.*

General: Meridians are axial cross-sections of the fracture body

Sufficient strength of tunnels and dam slopes are vital Design Verification requirements in geo-engineering. In order to achieve this, the course of the measured fracture data on Tensile Meridian (TM) and Compressive Meridian (CM) is to map. TM and CM are the standard test meridians.

For this design task several SFC approaches are applied:

"Classical, linear Mohr-Coulomb shear curve"

Shear stresses below the curve mean 'No fracture' or 'Stress states' below the τ^n- curve in *Fig.16-18* are not dangerous. In civil engineering this well-known simple SFC reads:

$$\tau^n(\sigma_I, \sigma_{III}) = \sigma \cdot tan\phi \; + \; c \, .$$

→ values for cohesive shear strength $R^\tau \equiv$ c and friction angle $\phi(\mu)$ are required.

(The derivation of a value for R^τ will be the objective of § 25).

Above approach is an extrapolation from the compressive strength point, see *Fig.16-18* .

"Linear Mohr-Coulomb criterion in geo-mechanics"

In order to achieve Design Verification in several numerical Rock mechanics Codes the use of the widely applied 'Mohr-Coulomb (M-C) Criterion' is recommended in order to map the course on that meridian where the tests have been run, on TM or CM. The criterion below says that a stress below the M-C curve is conservative.

$\sigma_1 = \sigma_3 \cdot tan^2(\Phi) + 2 \cdot c \cdot tan(\Phi)$, applying $\Phi = \pi / 4 + \phi / 2$

where c = cohesive shear strength $\equiv R^\tau$, ϕ = internal friction angle, and

σ_1 = most negative principal stress $\rightarrow \sigma_{III}$, σ_3 = most positive principal stress $\rightarrow \sigma_I$,

which are transferred due to the mathematical principal stress convention $\sigma_I > \sigma_{II} > \sigma_{III}$.

The final formulation reads: $\sigma_{III} = \sigma_I \cdot tan^2(\Phi) + 2 \cdot c \cdot tan(\Phi)$.

However, in application a difficult to be answered question arises: Which parameters are to insert? This concerns the fracture angle ϕ and the cohesive strength R^τ .

→ values for cohesive shear strength c and friction angle are required.

The procedure is also performed as an extrapolation from the compressive strength point.

In *Fig.16-18* the associated input quantities are depicted.

"Cuntze's FMC-based curve, SFCs regarding the common acting of SF and NF"

The FMC model, spanning up the full isotropic fracture body, is shown in *Table 16-10*.

As still described before, the first part of the SFC in *Table 16-10* represents the shape change, the second the friction effect, the third the volume change and Θ^τ the 120°-symmetry of isotropic materials. Mapping the test data in the very high negative compression domain of UHPC could require a fifth part, which may be dedicated to a further effect: discontinuous densification including at first a failure body hoop reduction and later widening.

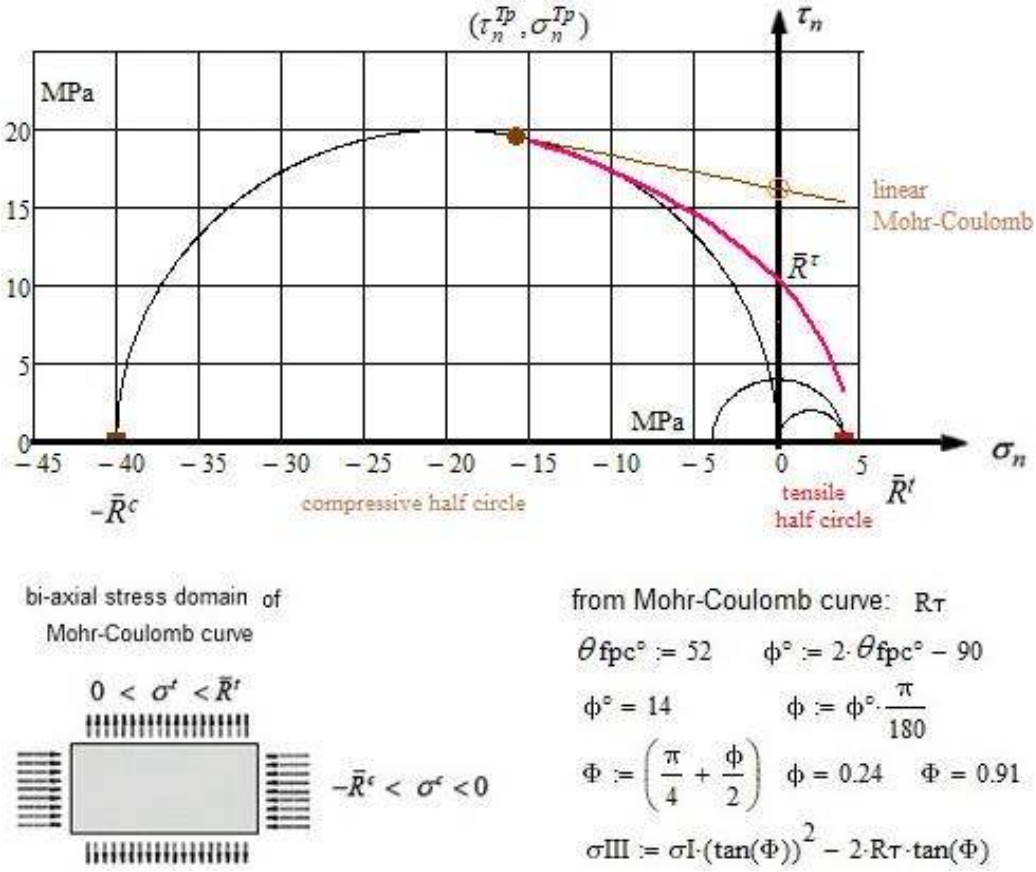

Fig.16-18, example Normal Concrete, 51°: Basics

The SFC contains five un-known parameters. For their determination, mathematically at minimum, five reliable test points on the surface of the fracture body are to provide by tests along the TM and CM. Better fitting procedures could be applied, of course.

Good Mapping requires to capture physics and to apply SFCs being as simple as possible. Cuntze's approach includes a multifold mapping task, which can be a compromise, only:

(1) Mapping the 2D test data in the principal stress plane, considering here the friction effect.

(2) Mapping the 3D test data along tensile test meridian (TM) and compressive test meridian (CM) along these two axial (180°-opposite) cross-sections of the fracture body with $(\sigma_I, \sigma_{II} = \sigma_{III}) \rightarrow \sigma_I(2\sigma_{III})$ and CM $(\sigma_I = \sigma_{II}, \sigma_{III}) \rightarrow 2\sigma_I(\sigma_{III})$.

All subfigures, principal stress plane and meridian cross-sections must be able to be derived from the well mapped fracture body and this with sufficient precision.

→ cohesive shear strength $c = R^\tau$ and friction angle ϕ are not required.

Points on the fracture body surface are used to fix the model parameters.

Reminder:

All isotropic materials possess a more or less significant 120°-rotational symmetry of the fracture body, most often depicted in Haigh-Lode-Westergaard coordinates, viewing *Fig.16-19*. Thereby, the well-known invariant J_3 is an excellent function to map this type of rotational symmetry (caused by $R^{cc} \neq R^c$ and $R^{tt} < R^t$) and to determine the Lode angle ϑ. Well-known is that the tests are run on the CM and on the TM, meaning that data sets are given for CM with $\vartheta = -30°$ and for TM with $\vartheta = 30°$.

For the chosen Model in *Table 16-10* the tricky procedure how to obtain the required model parameters c_i is principally shown for Normal Concrete in *Table 16-11* by three steps. For the cohesive strength, required by the extrapolation approaches, numerical values are determined in the third step.

Different models deliver different values for R^{τ}, improved models deliver a lower value, because these consider both damaging modes, SF and NF.

Table 16- 10, example Normal Concrete: Procedure to obtain the model parameters.

1 *Relationship of friction parameter and value considering the simple Two Parameter Model*

$F^{\tau} = c_2 \cdot \frac{I_1}{\bar{R}^c} + c_{1\Theta} \cdot \frac{6 \cdot J_2 \cdot \Theta^{SF}}{2 \cdot \bar{R}^{c2}} = 1$ ← insertion of the compression point $c_2 \cdot \frac{-\bar{R}^c}{\bar{R}^c} + c_{1\Theta} \cdot \frac{6 \cdot \bar{R}^{c2} / 3 \cdot \Theta^{SF}}{2 \cdot \bar{R}^{c2}} = 1$

($c_{2\Theta} = c_2$, because the friction parameter does not depend on 120°-rotational symmetry)

$\Rightarrow c_{1\Theta} = \frac{1 + c_2}{\Theta^{CM}}$ with non-circularity function $\Theta^{CM} = \sqrt[3]{1 - d_{\tau}}$ (if rotationally-symmetric, $d^{\tau} = 0$, $\Theta^{SF} = 1$),

Estimation of c_2, by a guess of the friction value μ, from $c_2 = (1 + 3 \cdot \mu) / (1 - 3 \cdot \mu)$.

With a guess $\theta_{fp}^{c\,\circ} = 51°$ ≡ friction value $\mu = 0.208$ and $C^c = \cos(2 \cdot \theta_{fp}\,° \cdot \frac{\pi}{180°}) = -\mu$ follows

$c_2 = (3 \cdot C^c - 1) / (3 \cdot C^c + 1) = (1 + 3 \cdot \mu) / (1 - 3 \cdot \mu) = 4.32.$

2 *Combined Determination of non-circularity parameter d^{τ} and $c_{1\Theta}$* (Mathcad Coding)

If no test value is available, this would require an estimate for $\bar{R}^{cc} > \bar{R}^c$ (lies on the TM).

$I1c := -Rc$ $\quad J2c := \frac{Rc^2}{3}$ $\quad I1cc := -2 \cdot Rcc$ $\quad J2cc := \frac{Rcc^2}{3}$

Vorgabe $\quad c1\Theta := 2$ $\quad d\tau := 0.6$ $\quad c2 = 4.32$

$$\frac{\sqrt{I1c^2 \cdot c2^2 + 12 \cdot J2c \cdot c1\Theta \cdot \sqrt[3]{1 - 1 \cdot d\tau}} + I1c \cdot c2}{2 \cdot Rc} = 1$$ strength point on CM

$$\frac{\sqrt{I1cc^2 \cdot c2^2 + 12 \cdot J2cc \cdot c1\Theta \cdot \sqrt[3]{1 + 1 \cdot d\tau}} + I1cc \cdot c2}{2 \cdot Rc} = 1$$ bi-axial compressive failure stress point on TM

$A\tau := Suchen(c1\Theta, d\tau)$ $\quad A\tau = \begin{pmatrix} 6.727 \\ 0.507 \end{pmatrix}$ $\quad c1\Theta := A\tau_0$ $\quad c1\Theta = 6.7$ $\quad d\tau := A\tau_1$ $\quad d\tau = 0.51$

3 *Estimation of the Touch point and Cohesive Strength* for application of the Mohr-Coulomb Criterion

From §22:

Touch point: $\tau_n^{Tp} = 19.6$ MPa, $\sigma_n^{Tp} = -15.8$ MPa.

Cohesive strength: $\bar{R}^{\tau} = \sqrt{\frac{-\bar{R}^{c2} + c_2 \cdot \bar{R}^c \cdot \sigma_{t0} + c_1 \cdot \sigma_{t0}^2}{3 \cdot c_1}}$ with $\sigma_{t0} = -C^c \cdot (-\bar{R}^c) = 12.9$ MPa

16.4 Mapping of 3D Ultra-High-Performance-Concrete UHPC (relatively dense) Test Data

UHPC principally behaves similarly to Normal Concrete unless the normalized hydrostatic compression does not become larger than $I_1 / R^t \cdot \sqrt{3} \approx -10$ (> -300 MPa). Then however, in contrast to Normal Concrete with usually relatively low hydrostatic pressure loadings the UHPC experiences a hydrostatically activated effect, 'densification with volume shrinkage'. Therefore, the volume change must be considered by I_1^2. This explains why for the less 'dense' Normal Concrete R^{cc}/R^c is higher than

with UHPC according to the possible higher densification. Combined with this a 'healing' of the flaw effects is principally faced.

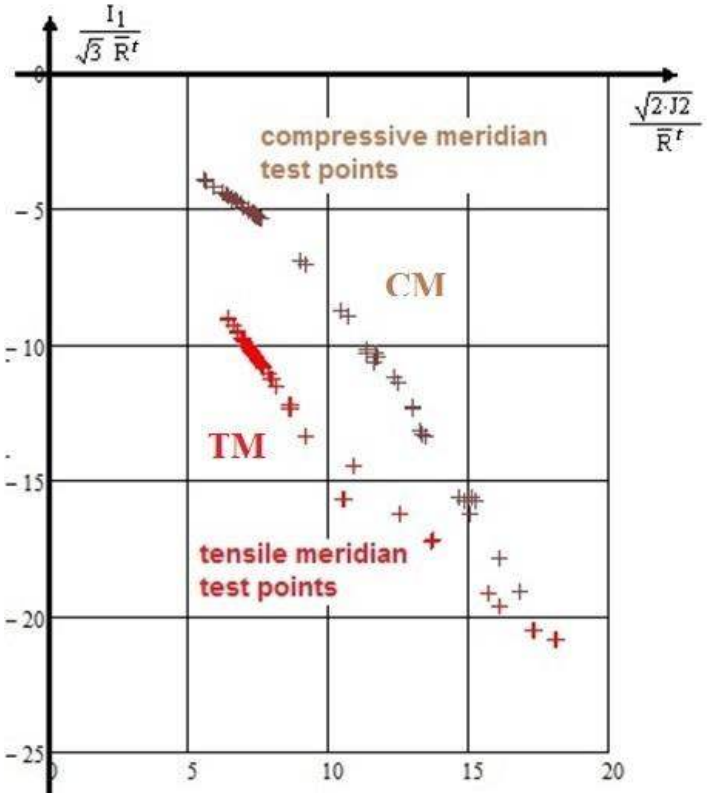

Fig.16-19, example UHPC: Compressive + and tensile meridian +test points.

Intentionally depicted on the positive abscissa to outlne the difference stemming from the brittle isotropic material's inherent 120°-rotational symmetry of the fracture failure body

. *Table 16-11: UHPC-SFC model*

shape change friction volume change

$$I_1 < 0: \; F^{SF} = F^{\tau} = c_1^{SF} \cdot \frac{6J_2 \cdot \Theta^{SF}}{2 \cdot \bar{R}^{c2}} + c_2^{SF}(\mu) \cdot \frac{I_1}{\bar{R}^c} + c_3 \cdot \left(\frac{I_1}{\bar{R}^c}\right)^2 + c_4 \cdot \left(\frac{I_1}{\bar{R}^c}\right)^3 = 1$$

'Mises Cylinder' formula

Above SFC is here normalized by the compressive strength $\bar{R}^c$. J_2 is the 'Mises' invariant.

$$I_1 = (\sigma_I + \sigma_{II} + \sigma_{III}) = f(\sigma), \quad 6J_2 = (\sigma_I - \sigma_{II})^2 + (\sigma_{II} - \sigma_{III})^2 + (\sigma_{III} - \sigma_I)^2 = f(\tau)$$

$$27J_3 = (2\sigma_I - \sigma_{II} - \sigma_{III}) \cdot (2\sigma_{II} - \sigma_I - \sigma_{III}) \cdot (2\sigma_{III} - \sigma_I - \sigma_{II}),$$

$$3 \cdot \sigma_{oct} = \sigma_I + \sigma_{II} + \sigma_{III} \; ; \quad 9 \cdot \tau_{oct}^2 = 6J_2 = 4 \cdot (\tau_{III}^2 + \tau_I^2 + \tau_{II}^2), \; \tau_{II} = max\,\tau(mathem.)$$

$\sigma_I, \sigma_{II}, \sigma_{III}$ are principal stresses, $\sigma_I > \sigma_{II} > \sigma_{III}$ are mathematical stresses (> more positive)

with $I_1 = (\sigma_I + \sigma_{II} + \sigma_{III})$, $6 \cdot J_2 = (\sigma_I - \sigma_{II})^2 + (\sigma_{II} - \sigma_{III})^2 + (\sigma_{III} - \sigma_I)^2$

Consideration: 120°-rotational symmetry of isotropic materials: $d^{SF} \equiv d_{\tau}$ *later*

$$\Theta^{SF}(J_3, J_2) = \sqrt[3]{1 + d^{SF} \cdot sin(3\vartheta)} = \sqrt[3]{1 + d^{SF} \cdot 1.5 \cdot \sqrt{3} \cdot J_3 \cdot J_2^{-1.5}}$$

with the non-circularity function Θ^{SF} including d^{SF} as non-circularity parameter.

Compr. Meridian: $\Theta^{SF} = \sqrt[3]{1 - d^{SF}}$, Tensile Meridian: $\Theta^{SF} = \sqrt[3]{1 + d^{SF}}$, Neutral Meridian: $\Theta^{SF} = 1$.

The fracture body of a theoretically dense concrete matrix possesses in the high hydrostatic compressive domain ($I_1 < 0$) an open fracture surface due to the densification. Practically however, the fracture body does only exist once according to the final spatial micro-crack state and cannot be loaded a second time after de-loading.

Further, the bi-axial compressive strength R^{cc} ($\equiv f^{cc}$, internationally used letter in construction, stems from the German term Festigkeit) may be not only linked to SF but also to NF due to the Poisson's ratio activated tensile strain in the axial direction despite $\sigma_{ax} = 0$.

An SFC-model validation requires reliable test results. These have been provided as original data sets by the IMb Dresden (*many thanks to Prof. Curbach and his co-workers*). Hence, the author had to search out of the huge test data package which test points belong to TM and which to CM. Therefore, the full bunch of obtained 3D test data had to be processed. Such a separation bases on the use of the Lode angle (meridian angle) ϑ values: Which test point belongs more to the tensile meridian sin(3ϑ) = 1 or to the compressive meridian sin(3ϑ) = -1, see *Table 16-12* and *Fig.16-20*. For the shear meridian (neutral meridian NM) angle is valid sin(3ϑ) = ϑ = 0.

The data set for the F^{τ}-SFC reads (in MPa):

$$F^{\tau} = c_1 \cdot \frac{6J_2 \cdot \Theta^{SF}}{2 \cdot \bar{R}^{c2}} + c_2(\mu) \cdot \frac{I_1}{\bar{R}^c} + c_3 \cdot \left(\frac{I_1}{\bar{R}^c}\right)^2 + c_4 \cdot \left(\frac{I_1}{\bar{R}^c}\right)^3 = 1 \quad \text{with}$$

5 unknowns, which at least require 5 fix stress state failure points on the failure surface

$\{\sigma\} = (,\ ,\ ,)^T : (-\bar{R}^c,0,0),\ (-\bar{R}^{cc},-\bar{R}^{cc}0,0),\ (\sigma_I^{frict},\sigma_I^{frict},0),\ (\bar{R}^c,0,0),\ (\bar{R}^c,0,0).$

The values in MPa = N/mm^2 are: $\bar{R}^c = 175$, $\bar{R}^{cc} = 183$, $\sigma_{II}^{frict} = -195$, $\sigma_{II}^{frict} = -50$ (*Fig*.26 - 5),

Points: $\sigma_I^{TM} = -40$, $\sigma_{II}^{TM} = \sigma_{III}^{TM}$, $\sigma_{III}^{TM} = -375$; $\sigma_I^{CM} = -61$, $\sigma_{II}^{CM} = \sigma_I^{CM}$, $\sigma_{III}^{CM} = -420$.

As proven mode interaction coefficient is taken again m = 2.7.

Table 16-12 makes aware of 3D-stress state effects by presenting the essential numbers of some measured failure stress states. The table indicates the Lode angle ϑ°, too. On basis of redundancy effects it may be concluded that with increasing hydrostatic pressure both the meridians run into a common scatter band, ending with a circle shape of the hoop. Then, the effect of flaws generating micro-damaging in this heterogeneous material reduces. Thereby, the fracture failure body becomes more and more cylindrical.

Fig. 16-20 links multi-axial stress states to the Lode angles ϑ = -30° (CM) and +30° (TM). Only stress states on the two meridians can be really depicted in the cross-sections. All other test points lie on the fixed hoop radius on a Lode angle different to ϑ = +30° and -30°. These points are marked by o.

Fig.16-21 displays the mapping quality in the principal stress plane. For comparison the elliptical curve, as the bias cross-section of a cylinder is included. The figure indicates that there is no Mises cylinder given, 120°- rotational symmetry acts.

Fig.16-22 (left) displays the mapping of the TM and the CM data course on the cross section of the fracture body in the traditional Haigh-Lode-Westergaard coordinates.

Fig.16-22 (right) depicts the mapping of the TM data set in a diagram using the 'rock mechanics coordinates' (σ_I, σ_{III}) for TM and $(2\sigma_I, \sigma_{III})$ for CM. How the effortful programming has been performed is compiled in *Table 16-13*. Unfortunately Mathcad did not compute the CM curve. The 'Mohr-Coulomb (M-C) Criterion', using the calculated UHPC-parameters, produces a straight line.

The author could not find any explanation for this unacceptable mapping.

According to the 180°-material relationship the TM curve could be 'mirrored' from the CM curve by switching from ϑ^{CM} to ϑ^{TM}.

Table 16-12: Characteristic material data from evaluated UHPC fracture tests.

$E = 20000$ *MPa*, $\nu = 0.2$, $\tau_{max} = \sigma_I - \sigma_{III}$

$\bar{R}^t = 16$ MPa, $\bar{R}^c = 160$ MPa, $\bar{R}^{tt} = 14$ MPa (assumed), $\bar{R}^{cc} = 175$ MPa

	Stress state *in MPa*	$I_1/\sqrt{3}$ $/\bar{R}^t$	$\sqrt{2 \cdot J2}$ $/\bar{R}^t$	τ_{max} *in MPa*	$(\sigma_{hyd}; \sigma_{ax})$ *in MPa*	$\vartheta°$	$\varepsilon_{ax\,el}$ *in* 10^{-3}	*remarks*
R^{tt}	(14, 14, 0)	1	0.7	-	-	-30	0.6	*two-fold NF*
R^c	(0 , 0, -160)	-5.8	8.2	80	(-0; -160)	-30	-8	Eff_{SF}
	(-6, -6,-230)	-8.7	11.4	111	(-6; -224)	-30	-11	
Compressive	(-16,-16,-272)	-11.0	13.1	128	(-16; -256)	-30	-13	
	(-35,-35,-350)	-15.2	16.1	157	(-35; -315)	-30	-17	
comput.	(-83,-83, -490)	-23.7	20.8	204	(-83; -407)	-30	-23	
	(-23,-23,-305)	-12.6	14.4	141	(-23; -282)	-30	-15	
R^{cc}	(0,-175,-175)	-12.6	8.9	88	(0;-)	+30	3.5	*two-fold SF*
	(-2,-210,-210)	-15.2	10.6	104	(-2; -)	+30	4.1	
Tensile	(-24,-310,-310)	-23.2	14.6	143	(-24; -)	+30	5.0	
R^t	(-54,-388,-388)	-30	17	167	(-54; -)	+30	5.1	
	(16, 0, 0)	0.6	0.8	-	-	+30	0.8	Eff_{NF}
shear	(9, -9, 0)	0	0.8	9	-	0	0.5	$Eff_{NF} > Eff_{SF}$
change	(0,-52,-193)	-8.8	8.8	97	-	-15	-9.1	

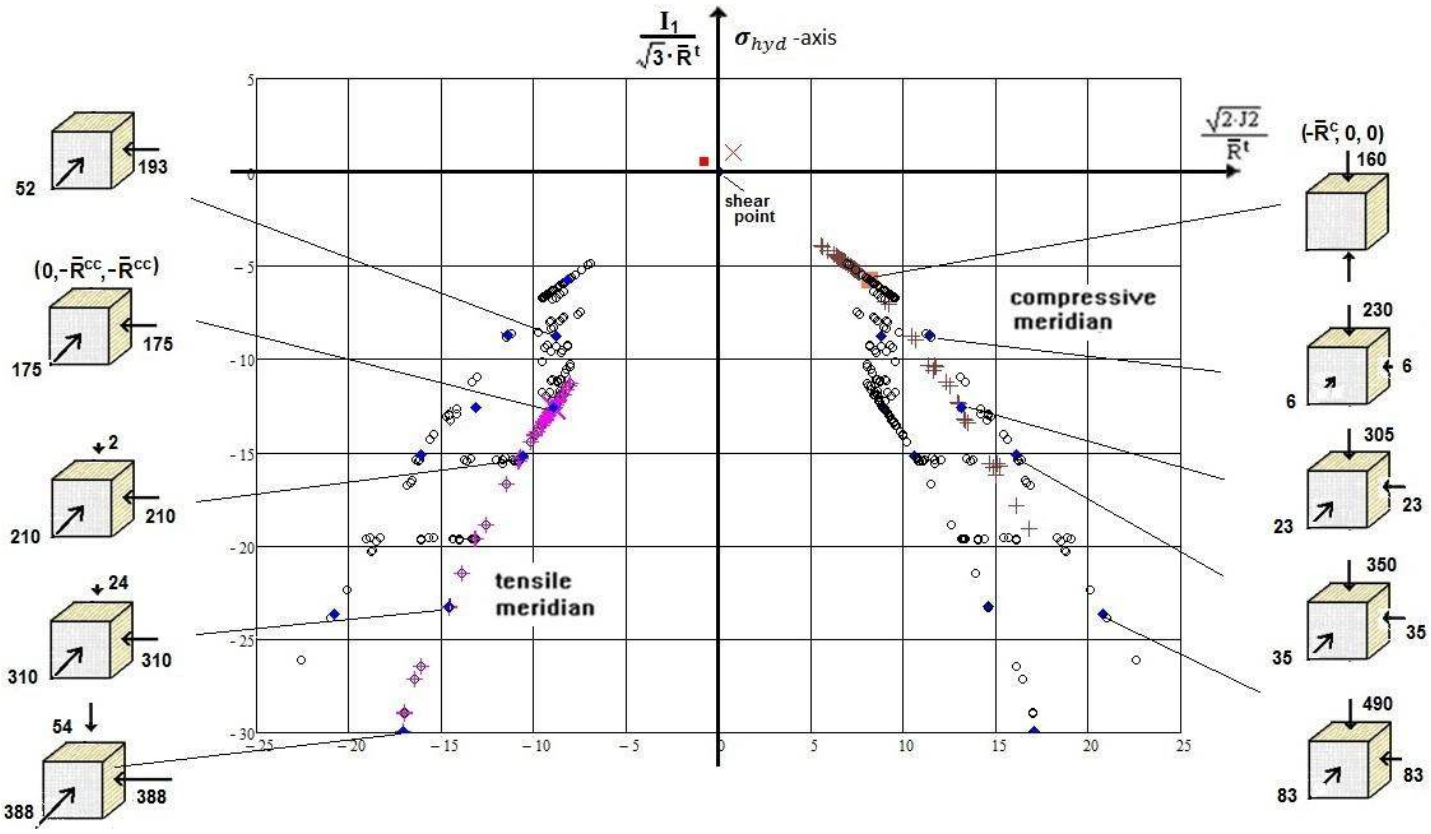

Fig.16-20, UHPC: Compressive and tensile meridian of the fracture body with associated stress states. (left) mirrored TM test points + with CM ones +; (right) all 3D test points are marked by **o** *(hoop ring), visualizing to be located at different meridians ϑ.*

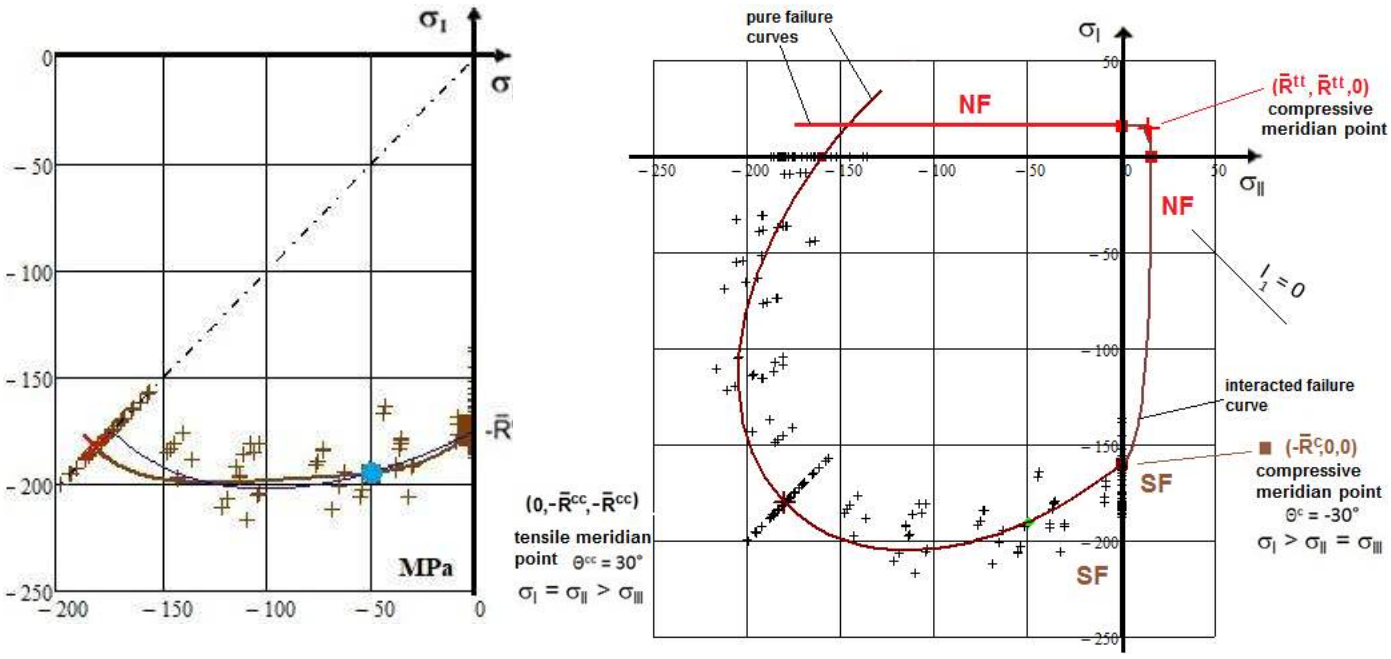

Fig.16-21, UHPC:

(left) Mapping the course of 2D test data in the principal stress plane. The blue fix point serves for friction quantification, mapping course of test data in the SF-domain only (normalization by R^c) *considering the alternating Lode angle* ϑ

(right) Principal stress plane view, mapping interaction NF with SF in their transition zone (normalized by R^t).

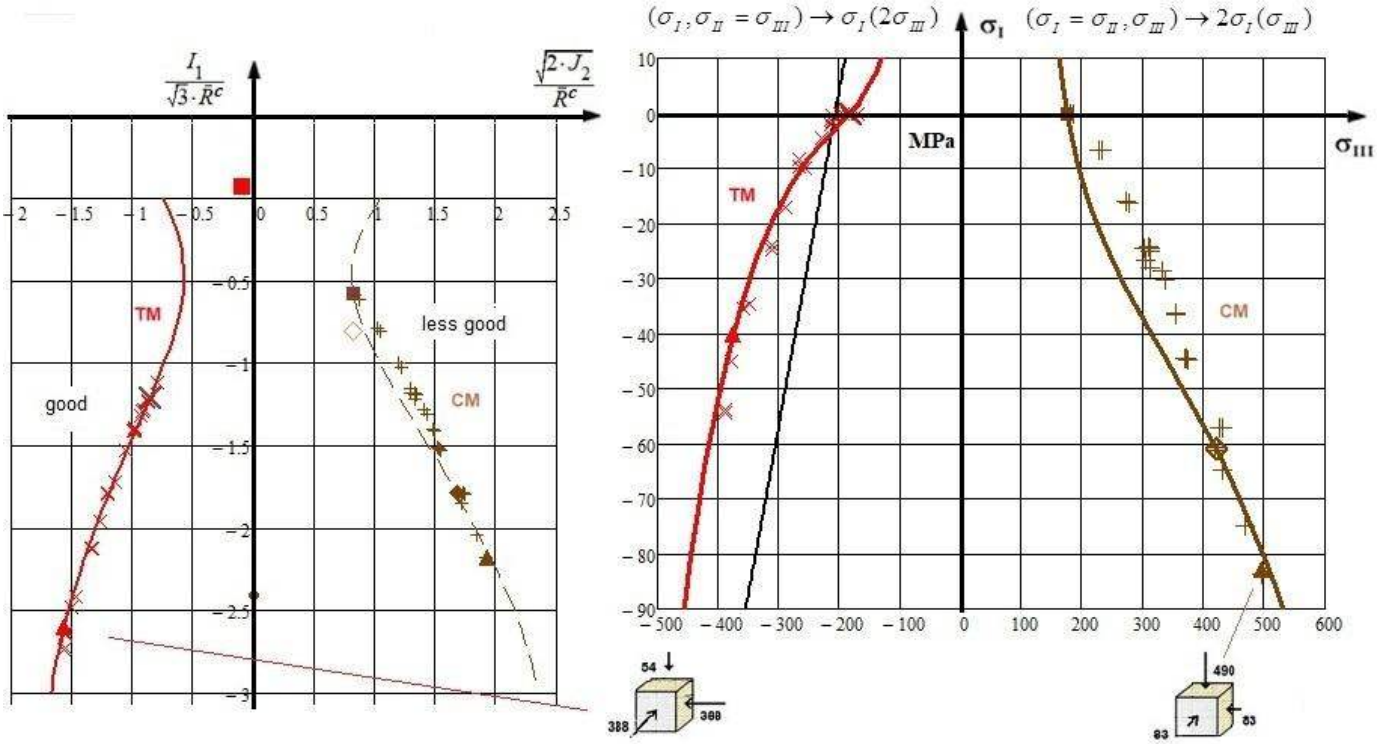

Fig. 16-22, UHPC: (left) mapping display of the two test data sets in Haigh-Lode-Westergaard coordinates. (right) Display using confining stress coordinates.

Eventually, *Table 16-13* presents the determination of the 5 UHPC model parameters. Note, please: In order to meet the objective 'Optimum 2D-3D-mapping' the parameter c2 is also determined in the complete parameter computation process of *Table 16-13* and not computed due to *Table 16-11*.

Table 16-13, UHPC: Determination of the SFC model parameters

$$F\tau = \frac{c1 \cdot 6J2 \cdot \Theta\tau}{2Rc^2} + c2 \cdot \frac{I1}{Rc} + c3 \cdot \left(\frac{I1}{Rc}\right)^2 + c4 \cdot \left(\frac{I1}{Rc}\right)^3 = 1$$

$$I1 = \sigma I + \sigma II + \sigma III \qquad J2 = \frac{(\sigma I - \sigma II)^2 + (\sigma II - \sigma III)^2 + (\sigma III - \sigma I)^2}{6}$$

$$J3 = \frac{(2 \cdot \sigma I - \sigma II - \sigma III) \cdot (2 \cdot \sigma II - \sigma I - \sigma III) \cdot (2\sigma III - \sigma I - \sigma II)}{27}$$

$$\Theta\tau = \sqrt[3]{1 + d\tau \cdot 1.5 \cdot 3^{0.5} \cdot J3 \cdot J2^{-1.5}} = \sqrt[3]{1 + d\tau \cdot \sin(3\theta)}$$

$$\Theta\tau TM = \sqrt[3]{1 + d\tau \cdot \sin(3\theta t)} = \sqrt[3]{1 + d\tau} \qquad \Theta\tau CM = \sqrt[3]{1 + d\tau \cdot \sin(3\theta c)} = \sqrt[3]{1 - d\tau}$$

$$\theta = \frac{1}{3} \cdot \operatorname{asin}\left[1.5 \cdot 3^{0.5} \cdot \frac{(2 \cdot \sigma I - \sigma II) \cdot (2 \cdot \sigma II - \sigma I) \cdot (-\sigma II - \sigma I)}{27} \cdot \left(\frac{2 \cdot \sigma I^2 - 2 \cdot \sigma I \cdot \sigma II + 2 \cdot \sigma II^2}{6}\right)^{-1.5}\right]$$

Vorgabe $c1 := 2$

$$c1 \cdot \frac{3 \cdot J2c \cdot \sqrt[3]{1 - 1 \cdot d\tau}}{Rc^2} + c2 \cdot \frac{I1c}{Rc} + c3 \cdot \left(\frac{I1c}{Rc}\right)^2 + c4 \cdot \left(\frac{I1c}{Rc}\right)^3 = 1$$

$$c1 \cdot \frac{3 \cdot J2cc \cdot \sqrt[3]{1 + 1 \cdot d\tau}}{Rc^2} + c2 \cdot \frac{I1cc}{Rc} + c3 \cdot \left(\frac{I1cc}{Rc}\right)^2 + c4 \cdot \left(\frac{I1cc}{Rc}\right)^3 = 1$$

$$c1 \cdot \frac{3 \cdot J2f \cdot \sqrt[3]{1 + 1 \cdot d\tau \cdot \sin(3\theta f)}}{Rc^2} + c2 \cdot \frac{I1f}{Rc} + c3 \cdot \left(\frac{I1f}{Rc}\right)^2 + c4 \cdot \left(\frac{I1f}{Rc}\right)^3 = 1$$

$$c1 \cdot 3 \cdot \frac{J2vc1}{Rc^2} \cdot \sqrt[3]{1 - 1 \cdot d\tau} + c2 \cdot \frac{I1vc1}{Rc} + c3 \cdot \left(\frac{I1vc1}{Rc}\right)^2 + c4 \cdot \left(\frac{I1vc1}{Rc}\right)^3 = 1$$

$$c1 \cdot 3 \cdot \frac{J2v}{Rc^2} \cdot \sqrt[3]{1 + 1 \cdot d\tau} + c2 \cdot \frac{I1v}{Rc} + c3 \cdot \left(\frac{I1v}{Rc}\right)^2 + c4 \cdot \left(\frac{I1v}{Rc}\right)^3 = 1$$

$A\tau := \text{Suchen}(c1, d\tau, c2, c3, c4)$

***LL**:*

** Reliable mapping requires an approach which shall be physically-based and 'practical'. Such an approach should equally well map (1) the course of test data fixing the 3D fracture body, (2) the course of test data in the Principal Stress plane (bias 2D cross-section of the 3D fracture body), and (3) of the test data course along the two 3D-test meridians TM and CM. ⇒ In this context: Engineering mapping has basically to capture physics, must be simple and understandable and shall use measurable parameters. Therefore, concerning all part figures 2D and 3D, these show that SFC-models applied for mapping can be good compromises, only. All theoretical approaches have their applicability limits and the very difficult 3D-testing as well*

** Fracture initiation in solid mechanics is given, if the multi-stress state vector touches the surface of the fracture body which represents the surface of all failure 1D-, 2D- and 3D-failure stress vectors. The fracture body surface is defined by a material stressing effort Eff = 100% = 1.*

** A display using a confining stress (TM: $\sigma_{II}= \sigma_{III}$, CM: $\sigma_{I}= \sigma_{II}$) as coordinate leads to another mapping figure than the Haigh-Lode-Westergaard coordinates give.*

** Using just TM or just CM test data cannot result in a reliable physical fracture body.*

** Of course, general 3D-failure stress states may not lie on TM (30°) or CM (-30°) but on another Lode angle around the hoop.*

** The fracture planes of TM and CM are different.*

** Both, the different course of the test data points compared to the also incorporated ellipse in the principal stress plane and the difference of the TM and the CM-curve document the inherent 120°-rotational symmetry of isotropic materials. (360°/3= 120° is given, because all 3 principal stresses are of equal mechanical importance, see Fig.10-11, again.*

** The fracture body of a dense isotropic material has an open bottom fracture surface!*

Table 16-14 follows with the derivation of the mapping curves in confining stress coordinates from the model parameters for the full UHPV fracture body.

16.5 Mapping specific Sandstone Test Data

As for concrete the properties for Underground Rock Failure Stress Analysis are also provided by tests on the tensile and the compressive meridian.

Tensile domain:

Also in rock materials in the vicinity of excavations and boreholes tensile stresses will occur. Further, an undesirable brittle sudden failure is to prevent when a bore-hole is drilled. Therefore, a tensile strength proof requires a tensile strength $\bar{R}^t$ for the distinct rock material.

An estimation for the tensile strength value delivers the Brazilian splitting test (*indirect* tensile strength test) because a classical tensile test specimen is merely to obtain. A solid cylinder or disk (short cylinder) test specimens is used for the initially crack-free (intact) material, see *Fig.16-23.* The evaluation is performed via the formula $f_{sp} = \bar{R}^t = 2 \cdot q \,/(\pi \cdot d \cdot \ell)$, from [*The constructor.org*].

Note: This 'indirect' measurement caused researchers to predict a value by using a Mohr-Coulomb-based SFC but the determined value must be wrong. In this context the author fully supports Mingqing You [*You15*] that a tensile strength R^t is a separate parameter and cannot be estimated by models working in the tensile-compressive transition zone. A real value for $\bar{R}^t$ is only to obtain by a uniaxial tensile stress test $\{\sigma\} = (\sigma^t_{ax} = F^t/A,\ 0,\ 0)^T$

Compressive domain:

Usual test series for concrete material (*see the concrete applications before)* are most often performed along CM and not so often along TM. For the general demonstration of the strength capacity, however, the full fracture failure body is required because all mixed 3D-compressive stress states are principally possible and their failure stress vectors determine the surface of the fracture body.

In rock mechanics the stress situation seems to be normally just linked to stress states along the compressive meridian. This explains why no bi-axial strength $\bar{R}^{cc}$ is provided in rock literature an entity that enables to describe the 120°-symmetry. Mapping just the course of test data along a meridian simplifies the task: Just the functional description of the test meridian remains of interest.

A stress state in a material, formulated in Mohr's *mathematical* stresses, reads

$\{\sigma\} = (\sigma_I,\ \sigma_{II},\ \sigma_{III})^T$ with σ_I becoming the smallest failure stress (most positive)

$\sigma_I > \sigma_{II} > \sigma_{III}$ mathematically and σ_{III} the largest compressive failure stress (most negative).

Table 16-14: Relationships to derive mapping with the confining stress coordinates

TM **Transfer to confing stress coordinates** **CM**

$\sigma II = \sigma III$ $\quad J2 = \frac{(\sigma I - \sigma II)^2 + (\sigma II - \sigma III)^2 + (\sigma III - \sigma I)^2}{6}$ $\quad \sigma II = \sigma I$

$(\sigma It - \sigma IIt)^2 + (0)^2 + (\sigma IIIt - \sigma It)^2$ same function $0^2 + (\sigma IIc - \sigma IIIc)^2 + (\sigma IIIc - \sigma Ic)^2$

$J2 := \frac{\left[(\sigma I - \sigma III)^2 + (\sigma III - \sigma I)^2\right]}{6}$ for TM and CM equal !

$J2 = \frac{Rc^2 \cdot x^2}{2}$

$x^2 = \frac{\left[(\sigma I - \sigma III)^2 + (\sigma III - \sigma I)^2\right]}{3 \cdot Rc^2}$

$I1t = \sqrt{3} \cdot Rc \cdot yt$

$I1 = \sigma I + \sigma II + \sigma III \quad yt = \frac{I1t}{\sqrt{3} \cdot Rc} = \frac{\sigma It + 2\sigma IIIt}{\sqrt{3} \cdot Rc} \quad \sigma IIIt = \frac{\sqrt{3} \cdot Rc \cdot yt}{2} - \frac{\sigma It}{2} \quad yc = \frac{\sigma Ic + 2\sigma IIIc}{\sqrt{3} \cdot Rc}$

$$xTM = \sqrt{\frac{\left[\left[\sigma It - \left(\frac{\sqrt{3} \cdot Rc \cdot y}{2} - \frac{\sigma It}{2}\right)\right]^2 + \left(\frac{\sqrt{3} \cdot Rc \cdot y}{2} - \frac{\sigma It}{2} - \sigma It\right)^2\right]}{3 \cdot Rc^2}} = \sqrt{\frac{\frac{1}{2} \cdot \left(3 \cdot \sigma It - \sqrt{3} \cdot Rc \cdot y\right)^2}{3 \cdot Rc^2}}$$

$$xCM = \sqrt{\frac{\left[\left[\sigma Ic - \left(\sqrt{3} \cdot Rc \cdot y - 2 \cdot \sigma Ic\right)\right]^2 + \left(\sqrt{3} \cdot Rc \cdot y - 2 \cdot \sigma Ic - \frac{\sigma Ic}{2} - \sigma Ic\right)^2\right]}{3 \cdot Rc^2}} = \sqrt{\frac{2 \cdot \left(3 \cdot \sigma Ic - \sqrt{3} \cdot Rc \cdot y\right)^2}{3 \cdot Rc^2}}$$

Values for x are given by inserting the y-coordinate into the SFC

$j := 0, 1 .. 40 \qquad y_j := \frac{-j}{10} - 1$ y runs negative

$$xTM_j = \sqrt{\left[-\frac{2 \cdot \left[c2 \cdot Rc^2 \cdot I1_j - Rc^3 + c3 \cdot Rc \cdot \left(I1_j\right)^2 + c4 \cdot \left(I1_j\right)^3\right]}{3 \cdot Rc^3 \cdot c1 \cdot \Theta\tau TM}\right]} \qquad xCM_j = \sqrt{\left[-\frac{2 \cdot \left[c2 \cdot Rc^2 \cdot I1_j - Rc^3 + c3 \cdot Rc \cdot \left(I1_j\right)^2 + c4 \cdot \left(I1_j\right)^3\right]}{3 \cdot Rc^3 \cdot c1 \cdot \Theta\tau CM}\right]}$$

Finally the y-value is inserted into the confing stress version of x xTM, xCM are known

Vorgabe $\sigma It := -100$

$$xTM = \sqrt{\frac{\left[\left[\sigma It - \left(\frac{\sqrt{3} \cdot Rc \cdot y}{2} - \frac{\sigma It}{2}\right)\right]^2 + \left(\frac{\sqrt{3} \cdot Rc \cdot y}{2} - \frac{\sigma It}{2} - \sigma It\right)^2\right]}{3 \cdot Rc^2}}$$

$V(xTM, y) := Suchen(\sigma It) \qquad \sigma It_j := V\left(xTM_j, y_j\right) \qquad \sigma IIIt_j := \frac{\sqrt{3} \cdot Rc \cdot y_j}{2} - \frac{\sigma It_j}{2}$

Mathcad did not compute σIc_j however the formula can be simplified and σI extracted

$$\sigma It_j := \frac{\sqrt{6} \cdot Rc \cdot xTM_j}{3} + \frac{\sqrt{3} \cdot Rc \cdot y_j}{3} \qquad \sigma Ic_j := \frac{\sqrt{3} \cdot Rc \cdot y_j}{3} + \frac{\sqrt{2} \cdot \sqrt{3} \cdot Rc \cdot xCM_j}{6}$$

$$\sigma IIIt_j := \frac{\sqrt{3} \cdot Rc \cdot y_j}{2} - \frac{\sigma It_j}{2} \qquad \sigma IIIc_j := \sqrt{3} \cdot Rc \cdot y_j - 2 \cdot \sigma Ic_j$$

Tensile stresses must be signed positive in this context, otherwise confusion becomes extreme!

For the tensile meridian follows $\{\sigma\} = (\sigma_I, \sigma_{II}, \sigma_{III} = \sigma_{II})^T$ with $\sigma_I = \sigma_{ax}^t - p_{hyd}$

and the compressive meridian $\{\sigma\} = (\sigma_I = \sigma_{II}, \sigma_{II}, \sigma_{III})^T$ with $\sigma_{III} = \sigma_{ax}^c - p_{hyd}$.

TM captures $\bar{R}^{cc}$ (and $\bar{R}^{t}$, in the domain of the Normal Fracture mode) and CM captures $\bar{R}^{c}$ (and principally also $\bar{R}^{tt}$ in the domain of the Normal Fracture mode).

In rock mechanics, being one part of civil engineering, hydrostatic pressure is used, when testing concrete and UD material, but is to replace by the term Confining Pressure CP. This makes to introduce some definitions of rock mechanics terms: In construction, tensile stress is usually still negative, but not always. It begins to change, This makes literature interpretations difficult!

- Multi-axial rock compressive strength capacity [*You15*]
  (the stress-sketch in Figure 1 of [Lan19] must be corrected. It does not fit to the provided failure stress states. In Fig.26-7 this is corrected)

  $\sigma_{III} \equiv \sigma_S \equiv \sigma_1$ termed here min or principal stress

- 1D uniaxial strengths: UTS = $\bar{R}^{t}$, UCS = $\bar{R}^{c}$
  Unfortunately the author found different meanings: In engineering design dimensioning UTS means Ultimate Tensile Strength and not Uniaxial Tensile Strength and UCS ultimate compressive strength *(still also applied in 'geo engineer'! Why is it not generally used in rock mechanics?)* and not for instance Unconfirmed Compressive Strength [*Wikipedia*]. UCS stands for the maximum axial compressive stress that a specimen can bear under zero Confining Pressure (*compressive stress*), which means it is nothing else than the usual simple standardized technical compression strength $\bar{R}^{c}$ in engineering.

- ✓ Confining pressure CP: maximum level of hydrostatic compression applied in a tri-axial compression test of a concrete, a rock material or a neat resin test specimen defined by

  $\{\sigma\}$ = (σ_{ax}^{t} - CP , -CP, -CP) or with σ_{ax}^{c} (tensile meridian)

  $\{\sigma\}$ = (σ_{ax}^{c} - CP , -CP, -CP) (*induced by test rig brushes in case of concrete*)

- ✓ Confining litho-static pressure: CP = p_{hyd} + overlying weight.

The author would like to conclude: *Using usual mathematical stresses it reads*

- Sealed, polished dog-bone test specimens deliver the failure stress points
  ($-\bar{R}^{ccc}$,$-\bar{R}^{ccc}$,$-\bar{R}^{ccc}$) no pore pressure, ($-\bar{R}^{c}$, 0, 0) , ($\bar{R}^{t}$, 0, 0) and
  further multi-axial compressive failure stresses on the compressive meridian.

- A bi-axial compressive failure stress ($-\bar{R}^{cc}$,-, 0) is obtainable by the dog-bone test specimen for $\sigma_1 = 0$ or $\sigma_{ax}^{t} = -CP$. However, the author did not find one single bi-axial strength value $\bar{R}^{cc}$ in the papers he examined!
  However, the UHPC fracture stress data set, thankfully left by IFM Dresden, brought a statistically good base which should have a similar tendency as rock material

- A bi-axial tensile failure stress ($\bar{R}^{tt}$, $\bar{R}^{tt}$, 0) can be obtained by cube test specimens prepared by a good gluing in order to load the needed bi-axial tensile stresses.

Test procedure: The confining pressure CP is achieved and then kept constant during the test. The axial stress σ_1 is increased at a certain rate until the test specimen fails at $\max\sigma_1$. It is to consider whether the porosity of the rock or the soil material and the moisture saturation plays a role.

Fig.16-23 presents fracture pictures of the investigated Berea sandstone. Essential is that the fracture angle increases with CP.

Similarly to other brittle materials the task always is the full (onset-of-fracture) body surface capturing NF and SF and not by SF just $I_1 < 0$ and thereby not regarding the intrinsic 120°-rotational symmetry. The TM and CM test data points are two oppositely located cross-sections of the body. The classical

type of visualization is to use the Haigh-Lode-Westergaard coordinates count equally in all directions. Visualization by using a confining stress cannot lead to the same mapping curve (see *Fig. 16.24*).

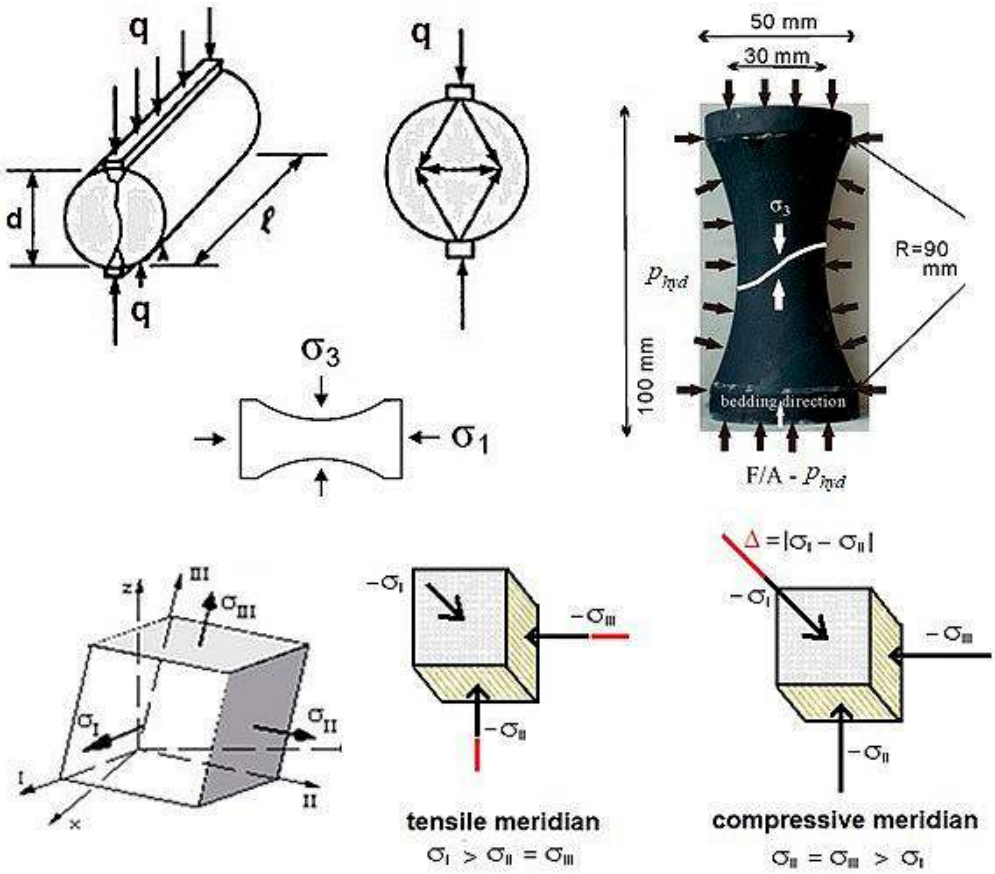

Fig. 16-23: Brazilian cylinder or disk (short length) for an indirect estimation of $\bar{R}^t$ and dog-bone (sealed, highest preparation effort, grinding from solid block with axial bedding layers) test specimen for direct measurement of tri-axial fracture stress states along compressive meridian including the tension-compression domain. (Δ depicts the differential stress entity causing shear stress with shear deformation)

LL:

The interpretation of the concrete-diagrams above leads to the following results for rock materials:

- *Using just TM or just CM test data incorporates a bottleneck concerning the achievement of a reliable physical fracture body SFC model*
- *The use of the geo-Mohr-Coulomb Criterion leads to a straight mapping of the course of test data along the tensile meridian. The model of the author captures the curved course*
- *Engineers in other disciplines become pretty stressed because we civil engineers unfortunately use construction design tools which still call tensile stresses negative stresses. This completely disturbs the logic of the well-known 'civil engineer' A. Mohr in context with his use of mathematical stresses!*

Fig.16-24, Sandstone: Fracture pictures of Berea sandstone from [Lan19].

Failure: Associated personal Experience

A dangerous cohesive shear strength with an associated critical sliding angle lead to a huge land slide at the West-East Main road of Bhutan. Large rocks are still falling.

16.6 Do we accurately apply accurate isotropic SFCs? Example Normal Concrete test data

Aim: Comparison of Drucker-Prager SFC and Cuntze SFC. *See further § 17.4, please*.

*16.6.1 **Comparison with Drucker-Prager's global SFC** a rotationally-symmetric conical fracture body*

This SFC is often used in civil engineering. It was originally introduced to deal with the 'plastic' better the **in-elastic** deformation of soils. Its many variants have been applied to brittle construction materials like rock, concrete, polymers, foams, and other pressure-dependent material behavior (*this practically just means:* I_1 is to use). See further *Fig.16-6*.

$$\sqrt{J_2} = c_1 + I_1 \cdot c_2 \ , \ \ c_1 = (2 \cdot R^c \cdot R^t \ / \sqrt{3} \cdot (R^c + R^t), c_2 = (R^t - R^c) / \sqrt{3} \cdot (R^c + R^t)$$

Drucker-Prager *Eff* study. Effect of uniaxial and multi-axial stress states on the Reserve Factor *RF*:

Example Normal Concrete: $\{\bar{R}\} = (\bar{R}^t = 4, \bar{R}^c = 40)^T$ MPa , $\mu = 0.2$. $\bar{R}^{cc} = 49$ MPa, $\bar{R}^{tt} = 2$ MPa

$$(\sigma_I, \sigma_{II}, \sigma_{III})^T = (\bar{R}^t, 0, 0)^T \quad \Rightarrow \quad Eff = 1.0, \quad RF = 1/Eff = 1, \quad F = Eff.$$
$$(\sigma_I, \sigma_{II}, \sigma_{III})^T = (2, 2, 0)^T \quad \Rightarrow \quad Eff = 0.725, \quad RF = 1/Eff = 1.4,$$
$$(\sigma_I, \sigma_{II}, \sigma_{III})^T = (0, 0, -\bar{R}^{cc})^T \quad \Rightarrow \quad Eff = 1.0, \quad RF = 1/Eff = 1,$$
$$(\sigma_I, \sigma_{II}, \sigma_{III})^T = (0, -\bar{R}^{cc}, -\bar{R}^{cc})^T \quad \Rightarrow \quad Eff = -4.3, \quad RF = 1/Eff = -0.23 \ .$$

Loading could be further monotonically increased by the factor RF = f_{RF} to reach fracture.

For civil engineers, basically just the SF domain is of interest.

The applicability range of the Drucker-Prager SFC is clearly outlined in the table above and in *Fig.16-25.* In the biaxial compression domain no reliable Reserve Factor can be computed.

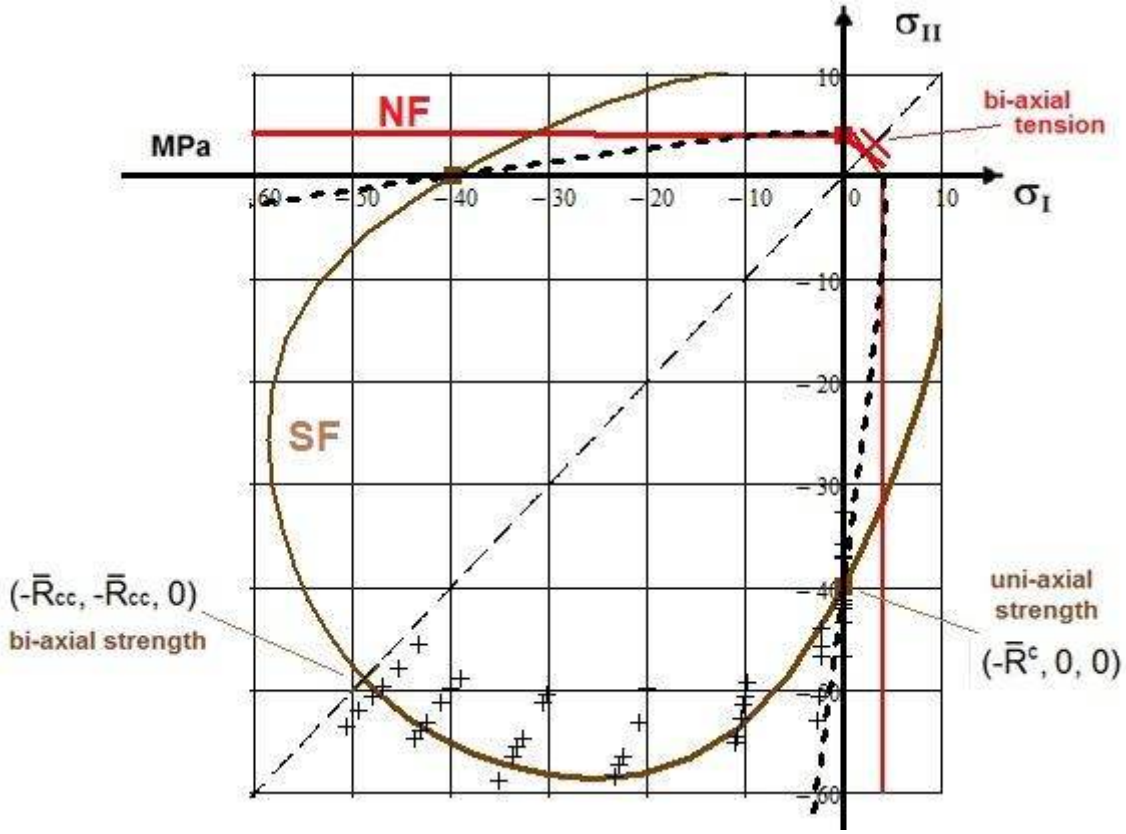

Fig.16-25, 2D-plane: Comparison of the global Drucker –Prager SFC and Cuntzes modes NF and SF intentionally depicted as pure modes (interacted curves, see16-2)

*16.6.2 **Cuntze's modal SFCs,** rotationally-symmetric body version*

For comparison reasons this simpler version is taken in *Table 16-15*, the computational basis for the values in the table below.

Effect of uniaxial and multi-axial stress states on the Reserve Factor *RF*:

$(\sigma_I, \sigma_{II}, \sigma_{III})^T = (\bar{R}^t, 0, 0)^T \quad \Rightarrow \quad Eff^{NF} = 1.0, \quad RF = 1/Eff = 1$

$(\sigma_I, \sigma_{II}, \sigma_{III})^T = (2, 2, 0)^T \quad \Rightarrow \quad Eff^{NF} = 1.0, \quad RF = 1/Eff = 1$

$(\sigma_I, \sigma_{II}, \sigma_{III})^T = (0, 0, -\bar{R}^c)^T \quad \Rightarrow \quad Eff^{SF} = 1.0, \quad RF = 1/Eff = 1$

$(\sigma_I, \sigma_{II}, \sigma_{III})^T = (0, -\bar{R}^{cc}, -\bar{R}^{cc})^T \quad \Rightarrow \quad Eff^{SF} = 1, \quad RF = 1/Eff = 1$

$(\sigma_I, \sigma_{II}, \sigma_{III})^T = (0, -15, -40)^T \quad \Rightarrow \quad Eff^{SF} = 0.72, RF = 1/Eff = 1.39$ benign effect

$(\sigma_I, \sigma_{II}, \sigma_{III})^T = (2, -15, -40)^T \quad \Rightarrow \quad Eff^{SF} = 0.89, RF = 1/Eff = 1.13$ benign effect .

The effects of multiaxial stress states is clearly outlined by the numbers.

Loading could be further monotonically increased by the factor RF = f_{RF} to reach fracture.

Table 16-15: Cuntze's modal SFC-based Eff study

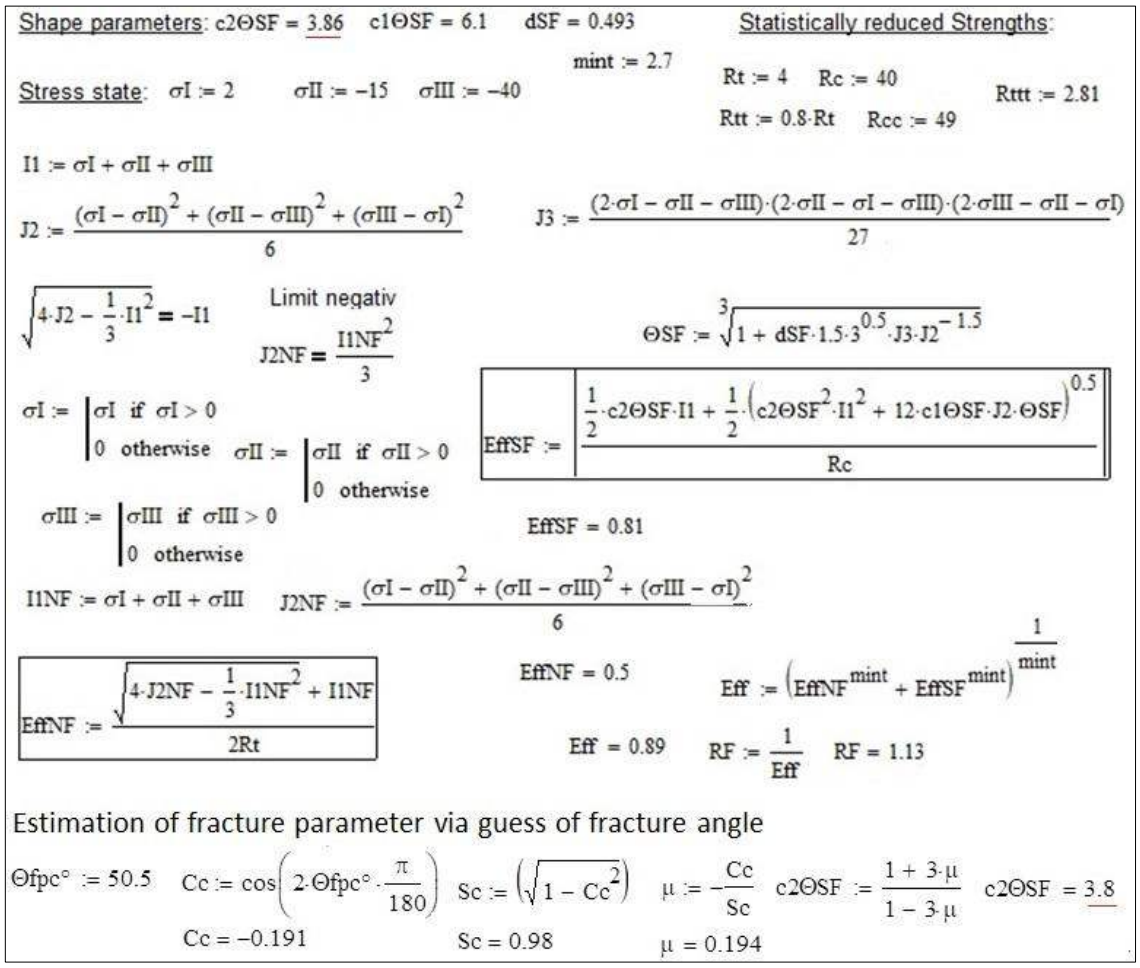

***LL**: Comparing the modal FMC-based results with the global Drucker-Prager results it is to conclude:*

(1) The Reserve Factor values are different.

(2) An automatic application of the Drucker-Prager's model without any queries is not possible and can be not recommended. Just the uniaxial strength points are captured, the equi-biaxial compressive strength not.

(3) Does this not require further investigation?

And this also because 120°-symmetry was not taken care of.

(4) Thereby on top the elaboration of § 17.4 should be included.

17 ‘Brittle’ Transversely-isotropic UD Materials

***Aim**: Provision of a physically based set of UD Strength Failure Criteria considering material symmetry.*

17.1 Proposal of a 2D Yield Condition SY

Aim: The yield failure curve is of importance e.g. for indicating micro-damage begin and for creeping in case of not well-designed laminates.

Generally, so-called ‘fiber-dominated’ laminates are optimal in terms of fiber utilization. However, this is not always the case for all load scenarios and then matrix yielding has some importance. Thereby, the thermoplastic resin systems are more ductile then the cross-linked thermo-set epoxy systems.

According to the FMC for the transversally-isotropic material, similarly to isotropic materials, just terms describing the shape change of the UD material cube can contribute to a failure function. Based on this, for the failure mechanism yielding, the proposed approach yields the ***yield condition***

$$F_y = \frac{\sigma_2}{(\bar{R}_{\perp\|p0.2})^2} + \frac{\tau_{21}{}^2}{(\bar{R}^c_{\perp p0.2})^2} = c_y{}^2$$

with the body diameter size parameter c_y and the two yield strengths $\bar{R}_{\perp\|p0.2}, \bar{R}^c_{\perp p0.2}$, at a permanent plastic strain of 0.2% dedicated to the two non-linear stress-strain curves $\tau_{21}(\gamma_{21})$ and $\sigma^c_2(\varepsilon_2)$. Its regime is growing from the yield initiation value 1 due to $1 \le a_y \le$ *IFF value*.

Above SFC involves two yield strength values what seems to be in contradiction to the FMC. But, these values are highly correlated due to the matrix material the yield strength value of which is the governing quantity. *Fig.17-1* visualizes how the ($\tau_{21}(\sigma_2)$ initiation yield or onset of yielding curve lies within the IFF envelope. This so-called single (global) *yield* surface is confined by the five partial fracture surfaces formulated below.

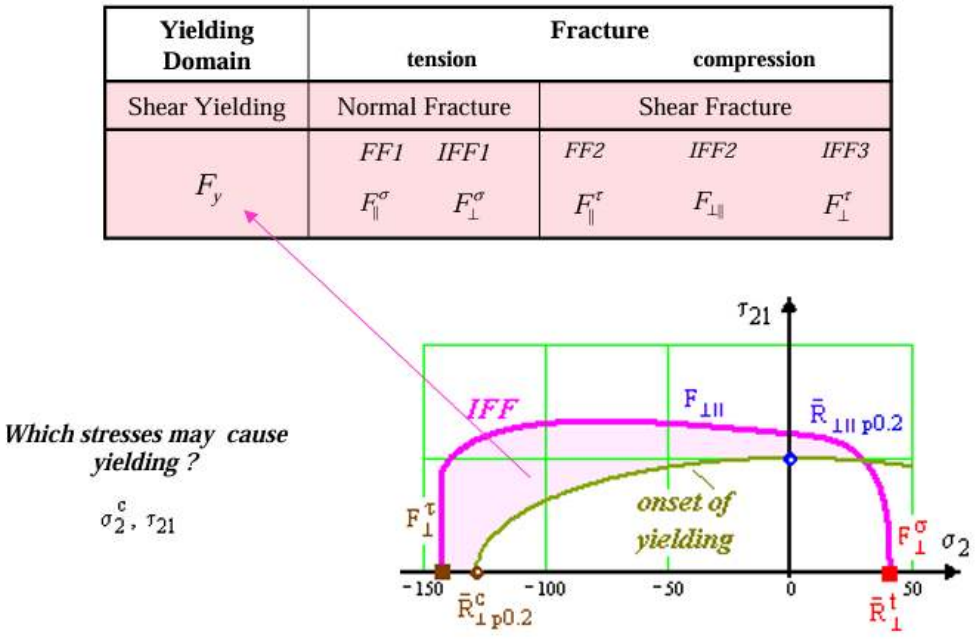

Fig.17-1, UD: Yield SFC area

17.2 3D-SFCs of Dense UD Materials

$I_1 = \sigma_1,\ I_2 = \sigma_2 + \sigma_3,\ I_3 = \tau_{31}{}^2 + \tau_{21}{}^2,\ I_4 = (\sigma_2 - \sigma_3)^2 + 4\cdot\tau_{23}{}^2,\ I_5 = (\sigma_2 - \sigma_3)\cdot(\tau_{31}{}^2 - \tau_{21}{}^2) - 4\cdot\tau_{23}\cdot\tau_{31}\cdot\tau_{21}.$

5 modes → 5 SFCs, which is in line with the ‘generic’ number assumed as one of the FMC-basics. IFF1 generates a straight line in the stress plane!

The following set of failure functions F is to apply on lamina level:

$$FF1:\ F_{\|}^{\sigma} = \frac{I_1}{\bar{R}_{\|}^{t}},\ FF2:\ F_{\|}^{\tau} = \frac{-I_1}{\bar{R}_{\|}^{c}},\ IFF1:\ F_{\perp}^{\sigma} = \frac{I_2 + \sqrt{I_4}}{2\bar{R}_{\perp}^{t}},$$

$$IFF2:\ F_{\perp}^{\tau} = (b_{\perp}^{\tau} - 1)\frac{I_2}{\bar{R}_{\perp}^{c}} + \frac{b_{\perp}^{\tau}\sqrt{I_4}}{\bar{R}_{\perp}^{c}},\ IFF3:\ F_{\perp\|} = \frac{I_3^{3/2}}{\bar{R}_{\perp\|}^{\ 3}} + b_{\perp\|}\frac{I_2 \cdot I_3 - I_5}{\bar{R}_{\perp\|}^{\ 3}},\ (I_2 \cdot I_3 - I_5 = I_{23-5})$$

After inserting the stress-invariant relations the full UD material SFC set reads, *Table 17-1*:

Table 17-1, dense UD materials: mathematically homogeneous, linear 3D SFC formulations for FF1, FF2, and for IFF1, IFF2, IFF3

FF1: $Eff^{\|\sigma} = \overset{\square}{\sigma}_1 / \bar{R}_{\|}^{t} = \sigma_{eq}^{\|\sigma} / \bar{R}_{\|}^{t}$ with $\overset{\square}{\sigma}_1 \cong \varepsilon_1^{t} \cdot E_{\|}$ (matrix neglected)

FF2: $Eff^{\|\tau} = -\overset{\square}{\sigma}_1 / \bar{R}_{\|}^{c} = +\sigma_{eq}^{\|\tau} / \bar{R}_{\|}^{c}$ with $\overset{\square}{\sigma}_1 \cong \varepsilon_1^{c} \cdot E_{\|}$

IFF1: $Eff^{\perp\sigma} = [(\sigma_2 + \sigma_3) + \sqrt{\sigma_2^{\ 2} - 2\sigma_2 \cdot \sigma_3 + \sigma_3^{\ 2} + 4\tau_{23}^{\ 2}}] / 2\bar{R}_{\perp}^{t} = \sigma_{eq}^{\perp\sigma} / \bar{R}_{\perp}^{t}$

IFF2: $Eff^{\perp\tau} = [a_{\perp\perp} \cdot (\sigma_2 + \sigma_3) + b_{\perp\perp}\sqrt{\sigma_2^{\ 2} - 2\sigma_2\sigma_3 + \sigma_3^{\ 2} + 4\tau_{23}^{\ 2}}] / \bar{R}_{\perp}^{c} = \sigma_{eq}^{\perp\tau} / \bar{R}_{\perp}^{c}$

IFF3: $Eff^{\perp\|} = \{[b_{\perp\|} \cdot I_{23-5} + (\sqrt{b_{\perp\|}^{\ 2} \cdot I_{23-5}^{\ 2} + 4 \cdot \bar{R}_{\perp\|}^{\ 2} \cdot (\tau_{31}^2 + \tau_{21}^2)^2}]/(2 \cdot \bar{R}_{\perp\|}^{\ 3})\}^{0.5} = \sigma_{eq}^{\perp\square} / \bar{R}_{\perp\square}$

$\left\{\sigma_{eq}^{\text{mode}}\right\} = \left(\sigma_{eq}^{\|\sigma},\ \sigma_{eq}^{\|\tau},\ \sigma_{eq}^{\perp\sigma},\ \sigma_{eq}^{\perp\tau},\ \sigma_{eq}^{\|\perp}\right)^T,\quad I_{23-5} = 2\sigma_2 \cdot \tau_{21}^2 + 2\sigma_3 \cdot \tau_{31}^2 + 4\tau_{23}\tau_{31}\tau_{21}$

Inserting the compressive strength point $(0, -\bar{R}_{\perp}^{c}) \rightarrow a_{\perp\perp} \cong \mu_{\perp\perp} / (1 - \mu_{\perp\perp})$, $b_{\perp\perp} = a_{\perp\perp} + 1$

from a measured fracture angle $\rightarrow \mu_{\perp\perp} = \cos(2 \cdot \theta_{fp}^{c}\,° \cdot \pi / 180)$, for $50° \rightarrow \mu = 0.174$.

$b_{\perp\|} = 2 \cdot \mu_{\perp\|}$. Typical friction value ranges: $0 < \mu_{\perp\|} < 0.25,\ 0 < \mu_{\perp\perp} < 0.2$.

Interaction Equation:

$$Eff^{m} = [(\sigma_{eq}^{\|\sigma} / \bar{R}_{\|}^{t})^m + (\sigma_{eq}^{\|\tau} / \bar{R}_{\|}^{c})^m + (\sigma_{eq}^{\perp\sigma} / \bar{R}_{\perp}^{t})^m + (\sigma_{eq}^{\perp\tau} / \bar{R}_{\perp}^{c})^m + (\sigma_{eq}^{\perp\|} / \bar{R}_{\perp\|})^m]$$

or $Eff = \sqrt[m]{(Eff^{\text{mode 1}})^m + (Eff^{\text{mode 2}})^m + \ldots} = 1 = 100\%$ *for* Onset-of-Failure .

In the equations above, $\bar{R}$ denotes an average = typical strength value that should be used for the stress-strain curves in stress and deformation analysis. In the design verification the statistically reduced strength values are applied. The superscripts ^{t}, ^{c} stand for tensile, compressive. The superscripts $^{\sigma}$ and $^{\tau}$ mark the type of fracture failure whether it is caused by a tensile stress (Normal Fracture, NF, 'cleavage') or a shear stress (Shear Fracture, SF), e.g. due to a compressive normal stress $\sigma_{\|}^{c}$ or a transverse normal stress $\sigma_{\perp}^{c}$. Failure activated in two directions is considered by adding a multi-fold failure term, proposed in [*Awa78*] for isotropic materials. It can be applied to brittle UD material in the transversal (quasi-isotropic) plane as well.

For the 2D-case, a simplified friction modelling is possible for IFF3 and used in the 2D-interaction equation below.

After application of the interaction *Fig.17-2* shows the main cross-section of the failure body.

Fig.17-3 depicts two main cross-sections of the failure body in *Fig.17-4*. The right figure outlines the strength distributions. The corner depicts the double failure mode $\sigma_2 = \sigma_3$, whereby the straight lines become inward-curved according to the hgher failure danger because flaws are twofold 'activated'.

$$Eff^{m} = [(Eff^{||\sigma})^{m} + (Eff^{||\tau})^{m} + (Eff^{\perp\sigma})^{m} + (Eff^{\perp\tau})^{m} + (Eff^{\perp||})^{m}]$$

with the mode portions inserted, 2D,

$$Eff = [(\frac{(\sigma_1 + |\sigma_1|)}{2 \cdot \bar{R}_{||}^{t}})^{m} + (\frac{(-\sigma_1 + |\sigma_1|)}{2 \cdot \bar{R}_{||}^{c}})^{m} + (\frac{\sigma_2 + |\sigma_2|}{2 \cdot \bar{R}_{\perp}^{t}})^{m} + (\frac{-\sigma_2 + |\sigma_2|}{2 \cdot \bar{R}_{\perp}^{c}})^{m} + (\frac{|\tau_{21}|}{\bar{R}_{\perp||} + 0.5 \cdot \mu_{\perp||} \cdot (-\sigma_2 + |\sigma_2|)})^{m}]^{1/m}.$$

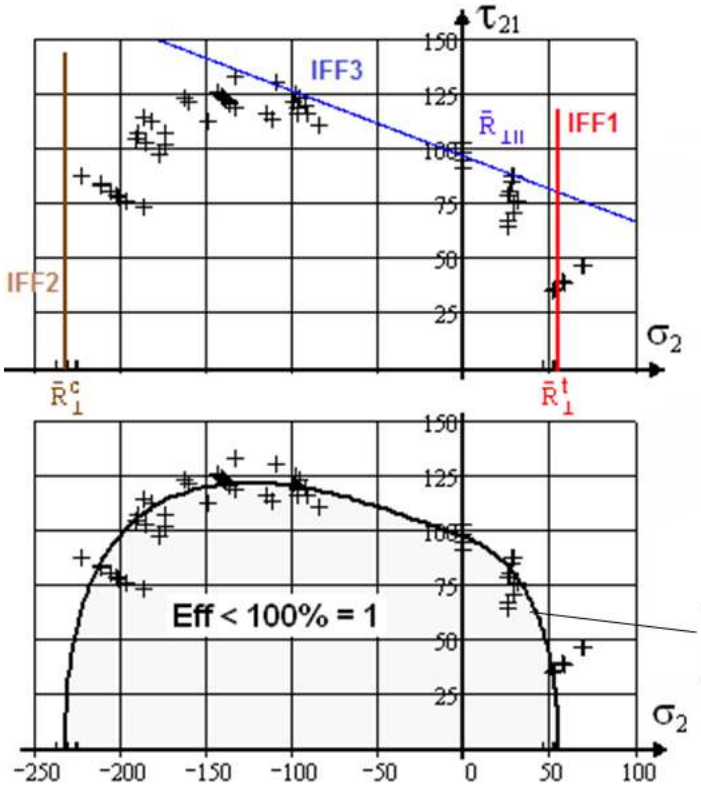

Mapping of course of IFF test data in a pure mode domain by the associated *Mode Failure Condition*.

3 IFF pure modes =* straight *lines !.

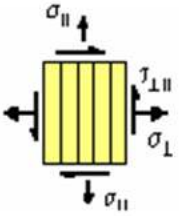

IFF 1 : $\frac{\sigma_2}{\bar{R}_{\perp}^{t}} = 1$

IFF 2 : $\frac{-\sigma_2}{\bar{R}_{\perp}^{c}} = 1$

IFF 3 ***(2D simplified)*** : $\frac{|\tau_{21}|}{\bar{R}_{\perp||} - \mu_{\perp||} \cdot \sigma_2} = 1$

$\tau_{21}(\sigma_2)$, $\breve{\sigma}_1 = 0$

Mapping of course of test data by *Interaction Model*

$$(Eff^{\perp\sigma})^{m} + (Eff^{\perp\tau})^{m} + (Eff^{\perp||})^{m} = 1$$

$$m = 2.5, \ \mu_{\perp||} = 0.3$$

Fig.17-2: Visualisation of the interaction with a UD-material

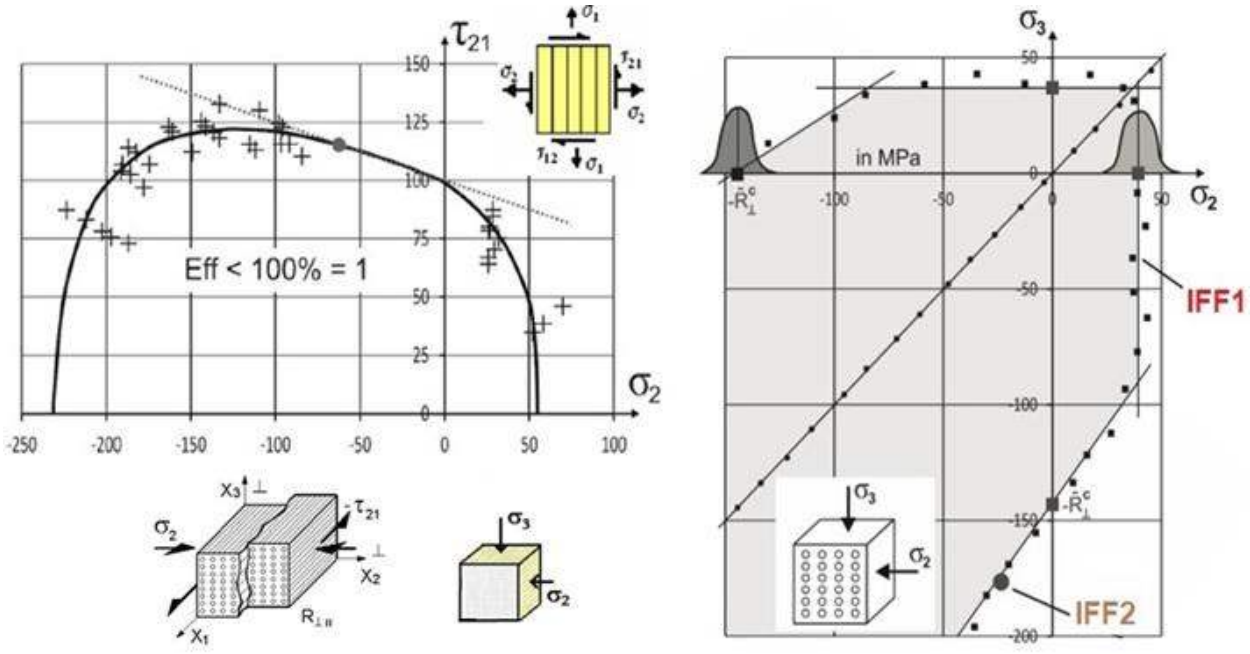

Fig.17-3: Two main cross-sections of the following failure body

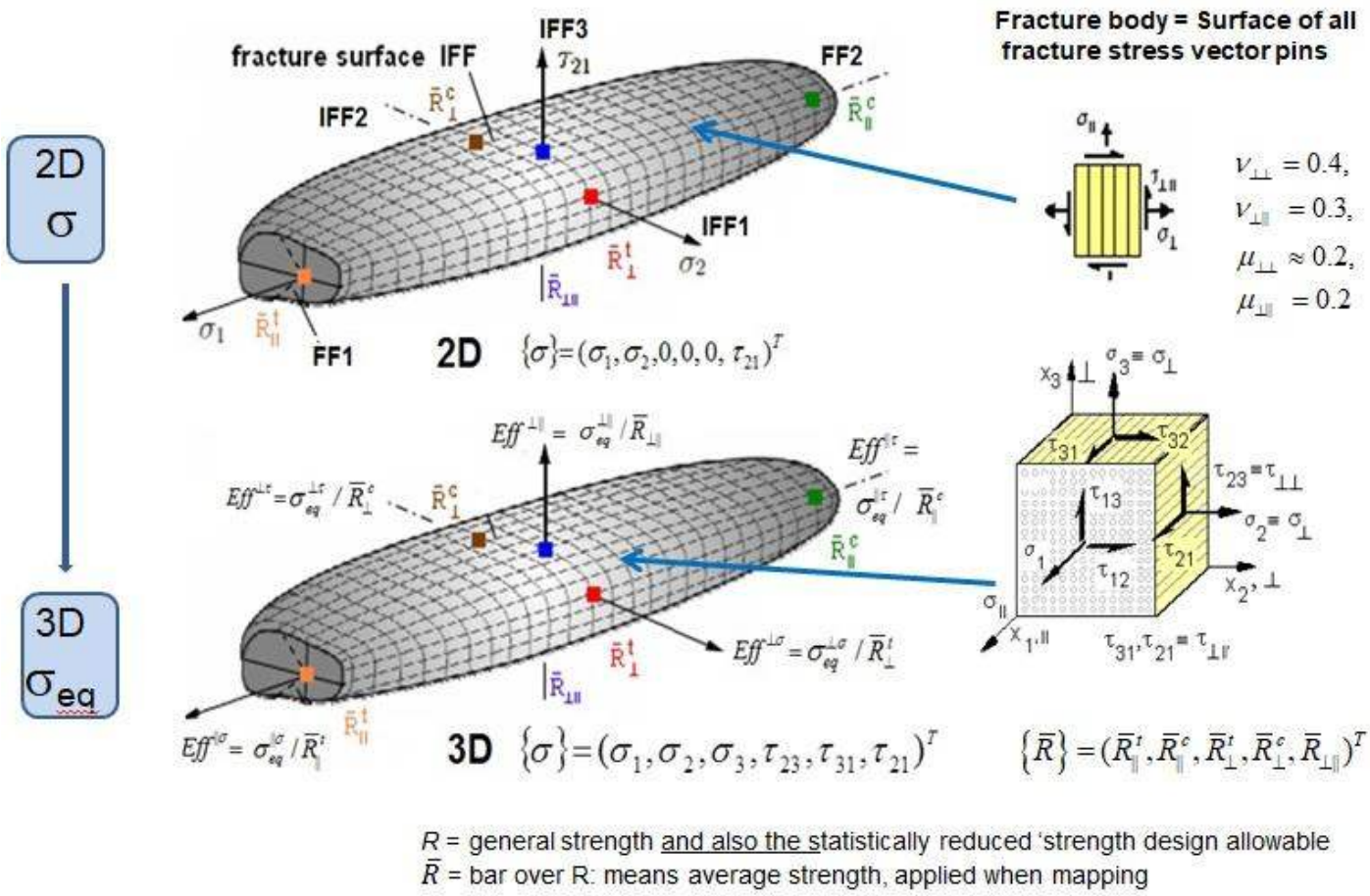

Fig.17-4: From the 2D failure body to the 3D failure body by replacing stresses by equivalent stresses

The upper figure displays the UD failure body as the visualization of the associated SFC set. The lower figure documents that if moving from the ply *stresses* to the mode-linked *equivalent ply stresses* one keeps the same UD failure body, usable now as 3D failure body!

LL: *Only some years ago the author found:*

If one replaces the stresses by the associate equivalent mode stresses then the 2D-failure body becomes a general 3D-failure body.

17.3 3D-SFCs of Porous UD Materials

Porosity practically meets just IFF2. The *Table 17-2* below shows the different formulation:

Table 17-2, porous UD materials: IFF2

* IFF2 Failure Function for the dense UD material (for comparison)

$$F^{SF} = [a_{\perp\perp}\cdot I_2 + b_{\perp\perp}\cdot\sqrt{I_4}\,] \,/\, \bar{R}_{\perp}^{c} = 1 \quad \text{with} \quad a_{\perp\perp} = b_{\perp\perp} - 1 \quad \text{after inserting} \quad \bar{R}_{\perp}^{c}$$

$$= [a_{\perp\perp}\cdot(\sigma_2+\sigma_3) + b_{\perp\perp}\cdot\sqrt{(\sigma_2-\sigma_3)^2+4\tau_{23}^{\,2}}\,] \,/\, \bar{R}_{\perp}^{c} = 1$$

$$= [a_{\perp\perp}\cdot(\sigma_2^{\,pr}+\sigma_3^{\,pr}) + b_{\perp\perp}\cdot\sqrt{(\sigma_2^{\,pr}-\sigma_3^{\,pr})^2+0^2}\,] \,/\, \bar{R}_{\perp}^{c} = 1 \leftarrow \text{2 structural stresses}$$

* IFF2 Failure Function for the porous UD material (index por, *author's simple approach*)

$$F^{SF}_{porosity} = \sqrt{a_{\perp\perp por}^{\,2}\cdot I_2^{\,2} + b_{\perp\perp por}^{\,2}\cdot I_4} - a_{\perp\perp por}\cdot I_2\,] \,/\, 2\bar{R}_{\perp}^{c} = 1\,.$$

The two curve parameters are determined - as before performed - from insertion of the compressive strength point and from the bi-axial fracture stress point.

Mind: In contrast to an isotropic dense material the fracture body of a extremely high hydrostatically compressed dense UD-material has a closed bottom fracture surface, because the filaments may break under the tensile stress caused by biaxial compression due to the Poisson effect, when $\varepsilon^{t}_{axial} = \varepsilon^{fr}_{||}$.

17.4 'Proportional Stressing' versus 'Design Driving Stress' concept and "Failure Index

It is mandatory that the chosen *F*- or *Eff*-formulation does become zero with a vanishing failure driving stress, see the Mohr model for in-plane shear below. This is not given viewing the simple linear, mathematically homogeneous (*functional parts of F possess the same power*) Mohr-Coulomb SFC and the definition $\boldsymbol{Eff = \sigma / R}$. Therefore the following was considered:

$$\tau_{21} = \bar{R}_{\perp||} - \mu_{\perp||} \cdot \sigma_2 \;\Rightarrow\; F = \frac{\tau_{21} + \mu_{\perp||} \cdot \sigma_2}{\bar{R}_{\perp||}} = 1:$$

Proportional Stressing concept: $\dfrac{\tau_{21}}{Eff} = \bar{R}_{\perp||} - \mu_{\perp||} \cdot \dfrac{\sigma_2}{Eff} \;\Rightarrow\; Eff = \left(\tau_{21} + \mu_{\perp||} \cdot \sigma_2\right) / \bar{R}_{\perp||}.$

Design-driving Stress concept: $\dfrac{\tau_{21}}{Eff} = \bar{R}_{\perp||} - \mu_{\perp||} \cdot \sigma_2 \;\Rightarrow\; Eff = \tau_{21} / (\bar{R}_{\perp||} - \mu_{\perp||} \cdot \sigma_2).$

Failure Index (FI): (*dangerous, especially if different power*) $FI = |F| = \left(\tau_{21} + \mu_{\perp||} \cdot \sigma_2\right) / \bar{R}_{\perp||}.$

Dividing just the basic failure driving shear stress fulfills the demand and enables an automatic realistic computation.

The two friction-linked equations below do not cause such a problem:

IFF2: $Eff^{\perp\tau} = [a_{\perp\perp} \cdot (\sigma_2 + \sigma_3) + b_{\perp\perp} \sqrt{\sigma_2^{\,2} - 2\sigma_2\sigma_3 + \sigma_3^{\,2} + 4\tau_{23}^{\,2}}] \;/\; \bar{R}^{c}_{\perp} = \sigma^{\perp\tau}_{eq} / \bar{R}^{c}_{\perp}$

IFF3: $Eff^{\perp||} = \{[b_{\perp||} \cdot I_{23-5} + (\sqrt{b_{\perp||}^{\,2} \cdot I_{23-5}^{\,2} + 4 \cdot \bar{R}_{\perp||}^{\,2} \cdot (\tau_{31}^2 + \tau_{21}^2)^2}] / (2 \cdot \bar{R}_{\perp||}^{\,3})\}^{0.5} = \sigma^{\perp||}_{eq} / \bar{R}_{\perp||}$.

LL:

- *If the design-driving stress is zero, then Eff must be zero.* ***At least the two concepts invite for discussion.***
- *In the case of a linear, mathematically homogeneous equation* $Eff \equiv F$ *or it does not correspond to Eff , if the functional parts of F possess different power.*
- *Mathematically homogeneous and non-homogeneous SFCs outline the difference of Failure Index |F| and material stressing effort Eff .*
- *Of course, there are Validity Limits of UD SFC applications: "Models cannot map all test (average) data course domains equally well, because they are basic physics-modelling models."*
- *Cuntze's 3D-failure criteria set for transversely-isotropic laminas is as well invariant-based (transfer between coordinate systems is automatically given) like 'Mises' as physically-based*

17.5 Comparison of 2D-UD-Strength Failure criteria: Which one should I take?

***Aim**: Assisting the user, not to follow FE Manual recommendations reading "*Take the worst result of all*".*

In the future, we will be forced to compute 3D-based reserve factors in static component Design Verification. The 2D-based Classical Laminate Theory for unidirectional fiber-reinforced matrices is not sufficient for this. For these reasons, the author has tried to compare those SFCs that were 'contributing' to the World Wide Failure Exercises (WWFE) for UD materials, namely Tsai-Wu, Hashin, Puck and Cuntze. The comparison carried out (*generally too little test data is available*) looks at the necessary input, shows the received failure envelopes for three 2D stress combinations and tries to evaluate the results, so that FE Manual recommendations "*Take the worst result of all*" is not to be followed anymore!

Regarding the chapters before, the SFCs of Hashin and Tsai-Wu will be presented, only, and some missing things of Puck's SFC.

17.5.1 SFC Hashin, 4 failure modes

* Hypothesis 2, valid for Cuntze's FMC-based SFC-formulations:

"*For UD-material the SFCs should be invariant under any rotation around the fiber direction.*"

Hashin with the Hypothesis 2 also proposed an invariant-based global quadratic approach with two different stress invariants:

$$I_1=\sigma_1,\ I_2=\sigma_2+\sigma_3,\ I_3=\tau_{31}{}^2+\tau_{21}{}^2,\ I_4=\tau_{23}{}^2-\sigma_2\cdot\sigma_3,\ I_5=4\tau_{23}\tau_{31}\tau_{21}-\sigma_2\cdot\tau_{31}{}^2-\sigma_3\cdot\tau_{21}{}^2).$$

Table 17-3 compiles the four SFCs of Zvi Hashin.

Table 17-3: Four SFCs, for FF1, FF2, IFF1 and IFF2

$\{\sigma\}=(\sigma_1,\sigma_2,\sigma_3,\tau_{23},\tau_{31},\tau_{21})^{\mathrm{T}}$, $\{\bar{R}\}=(\bar{R}_{\parallel}^{t},\bar{R}_{\parallel}^{c},\bar{R}_{\perp}^{t},\bar{R}_{\perp}^{c},\bar{R}_{\perp\parallel};\ \bar{R}_{23})^{\mathrm{T}}$; 6 strengths, principally Interaction of the 4 modes necessary.

Hypothesis 1: $F\left(\{\sigma^A\},\{\bar{R}^A\},\theta_{\mathrm{fp}}\right)=1$, Puck's way

Hypothesis 2: $F\left(\{\sigma\},\{\bar{R}\}\right)=1$, Cuntze's way, *below*

FF1, $\sigma_1>0$: $\left(\frac{\sigma_1}{\bar{R}_{\mathrm{II}}^{t}}\right)^2+\frac{\tau_{31}^2+\tau_{21}^2}{\bar{R}_{\perp\parallel}{}^2}$; FF2, $\sigma_1<0$: $\left(\frac{-\sigma_1}{\bar{R}_{\mathrm{II}}^{c}}\right)^2=1,$

IFF1, $\sigma_2+\sigma_3>0$: $\frac{(\sigma_2+\sigma_3)^2}{\bar{R}_{\perp}^{t}}+\frac{\left(\tau_{23}{}^2-\sigma_2\cdot\sigma_3\right)}{\bar{R}_{23}{}^2}+\frac{\left(\tau_{31}^2+\tau_{21}^2\right)}{\bar{R}_{\perp\parallel}{}^2}=1,$

IFF2, $\sigma_2+\sigma_3<0$: $\left(\frac{\bar{R}_{\perp}^{c\,2}}{4\cdot\bar{R}_{23}{}^2}-1\right)\cdot\frac{(\sigma_2+\sigma_3)}{\bar{R}_{\perp}^{c}}+\frac{(\sigma_2+\sigma_3)^2}{4\cdot\bar{R}_{23}{}^2}+\frac{\left(\tau_{23}{}^2-\sigma_2\cdot\sigma_3\right)}{\bar{R}_{23}{}^2}+\frac{\left(\tau_{31}^2+\tau_{21}^2\right)}{\bar{R}_{\perp\parallel}{}^2}=1,$

Interlaminar failure: $\sigma_3>0$: $\left(\frac{\sigma_3}{R_3^t}\right)^2=1;$ $\sigma_3<0$: $\left(\frac{-\sigma_3}{R_3^c}\right)^2=1\,.$

* Hypothesis 1, valid for Puck's Action Plane IFF formulation:

"In the event that a failure plane under a distinct fracture angle can be identified, the failure is produced by the normal and shear stresses on that plane".

Hashin proposed this modified Mohr-Coulomb IFF approach but did not pursue this idea due to numerical difficulties (*A. Puck succeeded on this way*).

Info-Question:

What about the determination of $\bar{R}_{23} \neq \bar{R}_{23}^{\tau}$? *Did Hashin present a procedure*?

17.5.2 SFC Tsai-Wu, global SFC

A general anisotropic tensor polynomial expression of Zakharov and Goldenblat-Kopnov with the parameters F_i, F_{ij} as strength model parameters was the basis of the Tsai-Wu SFC $\sum_{i=1}^{6}(F_i \cdot \sigma_i)+\sum_{j=1}^{6}\sum_{i=1}^{6}(F_{ij} \cdot \sigma_i \cdot \sigma_j)=1$. From this tensor formulation, Tsai-Wu used the linear and quadratic terms, see *Table 17-4*:

Table 17-4: 3D SFCs of Tsai-Wu

$\{\sigma\} = (\sigma_1, \sigma_2, \sigma_3, \tau_{23}, \tau_{31}, \tau_{21})^T$, $\{\bar{R}\} = (\bar{R}_{\parallel}^t, \bar{R}_{\parallel}^c, \bar{R}_{\perp}^t, \bar{R}_{\perp}^c, \bar{R}_{\perp\parallel}; \bar{R}_{23})^T$, 6 strengths

$F(\{\sigma\},\{\bar{R}\}) = 1$. *The* int*eraction is global SFC – inert*

$F_i \cdot \sigma_i + F_{ij} \cdot \sigma_i \cdot \sigma_j = 1$ with (i,j = 1,2..6) or executed

$$F_{11} \cdot \sigma_1^2 + F_1 \cdot \sigma_1 + 2F_{12} \cdot \sigma_1 \cdot \sigma_2 + 2F_{13} \cdot \sigma_1 \cdot \sigma_3 + F_{22} \cdot \sigma_2^2 + F_2 \cdot \sigma_2 +$$
$$+ 2F_{23} \cdot \sigma_2 \cdot \sigma_3 + F_{33} \cdot \sigma_3^2 + F_{33} \cdot \sigma_3^2 + F_3 \cdot \sigma_3 + F_{44} \cdot \tau_{23}^2 + F_{55} \cdot \tau_{13}^2 + F_{66} \cdot \tau_{12}^2 = 1$$

with the strength model parameters

$F_1 = 1/\bar{R}_{\parallel}^t - 1/\bar{R}_{\parallel}^c$, $F_{11} = 1/(\bar{R}_{\parallel}^t \cdot \bar{R}_{\parallel}^c)$, $F_2 = 1/\bar{R}_{\perp}^t - 1/\bar{R}_{\perp}^c$, $F_{22} = 1/(\bar{R}_{\perp} \cdot \bar{R}_{\perp}^c) = F_{33}$,

$F_{13} = F_{12}$, $F_{55} = F_{66} = 1/\bar{R}_{\perp\parallel}^2$, $2F_{23} = 2F_{22} - 1/\bar{R}_{23}^2$, $F_{44} = 2 \cdot (F_{22} + F_{23})$

and - *in order to avoid an open failure surface* - the so-called interaction term

$F_{12} = \bar{F}_{12} \cdot \sqrt{F_{11} \cdot F_{22}}$ with $-1 \le \bar{F}_{12} \le 1$; usually applied $F_{12} = -0.5$.

Question, again:

What about the determination of $\bar{R}_{23}$ and the value for F_{12} ?

17.5.3 SFC Puck, failure mode-based, IFF conditions interacted by Master Fracture Body approach

Some history:

**As early as 1969 A. Puck recognized to separate FF from IFF (not Hashin as is sometimes said). Since the mid-eighties Puck from Uni Kassel, Cuntze from MAN and colleagues of the DLR-Braunschweig looked together for an improved IFF-SFC.*

** H. Schuermann, Uni Darmstadt, found the article [Has80] with the Hashin Hypothesis 1 which Puck could successfully execute. Cuntze recommended to use the matrix formulation to mathematically simpler convince the reader, which was more successful than his excellently written model description.*

** Beside several dissertation works, Puck's IFF model was further developed in a founded research project 1994. Results were published in VDI Progress Reports Series 5 Vol.506, VDI-Verlag, Düsseldorf, 1997, [VDI97]. The investigations for this book gave valuable results for Puck's book, 1996.*

** Due to the still highly established Puck IFF model Cuntze invited Puck to put his SFC into the [VDI 2014] German Guideline, Sheet 3, Development of Fibre-Reinforced Plastic Components, Analysis.*

Puck's so-called Action Plane IFF Conditions (1991) base on Mohr-Coulomb and Hashin.

In his interaction approach for the 3 IFF modes Puck interacted the 3 Mohr stresses σ_n , τ_{nt} , τ_{n1} on the IFF fracture plane, see *Fig.17-5*. He uses parabolic or elliptic polynomials to formulate a so-called master fracture body in the (σ_n , τ_{nt} , τ_{n1}) space. Thereby he assumes that a compressive σ_n cannot cause fracture on its action plane and that the stress σ_1 does not have any influence on the angle of the IFF fracture plane. The stresses on the fracture plane are decisive for fracture: A tensile stress σ_n supports the fracture, while in contrast a compressive stress makes the material 'stronger'. In other words: A compressive σ_n impedes IFF which is caused by the action plane shear stresses τ_{nt} and $\tau_{n1,}$ or – in other words - cannot cause fracture on its action plane. Fracture-responsible are only those stresses which act on a common action plane.

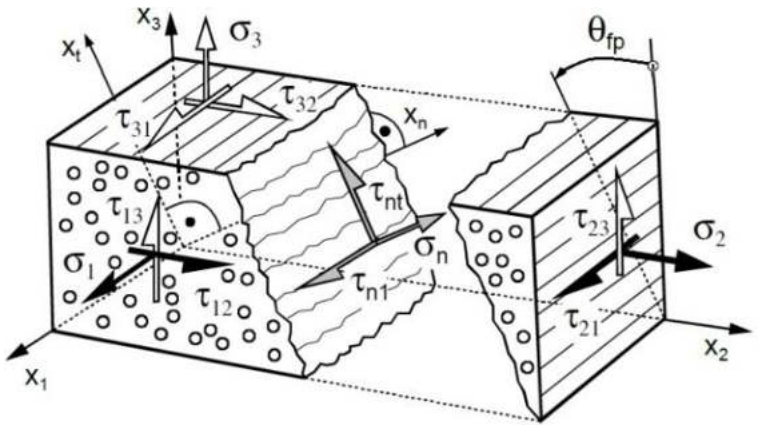

Fig.17-5, UD-composite element: Lamina and action plane stresses at an inclined failure angle θ_{fp} (from [Lut05, SAMPE])

Fig.17-6 presents Puck's 3 IFF modes: mode A (= IFF1), mode B (≡ IFF3), mode C (≡ IFF2. The modes A and B lead to transversal fracture planes with $\theta_{fp} = 0$, whereas in mode C inclined planes occur $0° < \theta_{fp} < 55°$ (for CFRP). The determination of the unknown IFF action plane angle θ_{fp} is

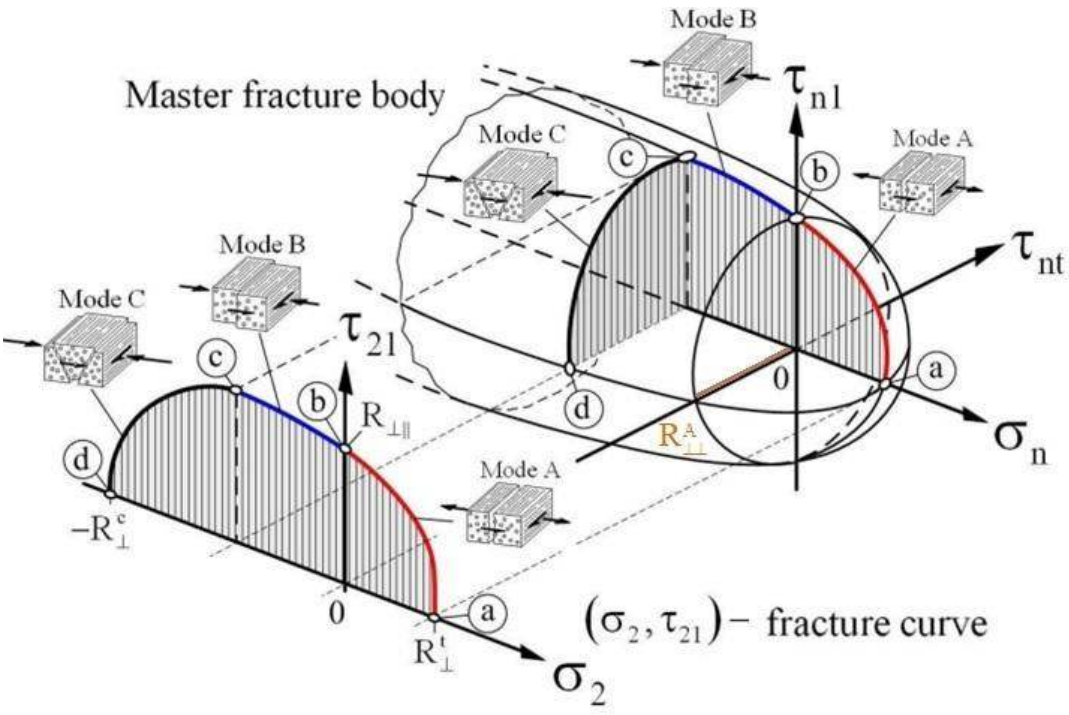

Fig.17-6: Master fracture body with Puck's IFF modes and action plane stresses (σn, τnt, τn1). *(left) Lamina stresses and main IFF cross section of the fracture body in lamina stresses* (σ_2, τ_{21}) *[courtesy H. Schürmann]*

performed by a search process in the domain -90° < θ_{fp} < + 90°. For the in-plane stress state $\tau_{21}(\sigma_2)$ which is dominant in many structural components, Puck found an analytic solution for the angle of the fracture plane [*Puc02*]:

$$\cos\theta_{fp} = \sqrt{\frac{1}{2+2\cdot p^{c}_{\perp\perp}}\cdot\left[\left(\frac{\bar{R}^{A}_{23}}{\bar{R}_{\perp\parallel}}\right)^{2}\cdot\left(\frac{\tau_{21}}{\sigma_2}\right)^{2}+1\right]}\,.$$

In *Table 17-5* Puck's Action Plane Mohr-Coulomb-linked (global) IFF SFCs discriminate 3 IFF domains and are completed by the simple maximum stress modes FF1 and FF2. Two IFF fracture plane resistances (superscript ^{A}) directly are technical strengths.

Table 17-5: SFCs for FF1, FF2, IFF1, IFF2 and IFF3

$\{\sigma\} = (\sigma_1,\sigma_2,\sigma_3,\tau_{23},\tau_{31},\tau_{21})^{T}$, $\{\bar{R}\} = (\bar{R}^{t}_{\parallel},\bar{R}^{c}_{\parallel},\bar{R}^{t}_{\perp},\bar{R}^{c}_{\perp},\bar{R}_{\perp\parallel};\ \bar{R}^{A}_{23})^{T}$, 6 strengths, principally

In Mohr's action plane stresses the IFF-SFC reads $F\left(\sigma_n,\tau_n,\bar{R}_{\sigma},\bar{R}_{\tau},\theta_{fp}\right)=1$,

$F\left(\{\sigma^{A}\},\{\bar{R}^{A}\},\theta_{fp}\right)=1$ with $\{\bar{R}\} = (\bar{R}^{t}_{\parallel},\bar{R}^{c}_{\parallel},\bar{R}^{A}_{\perp}=\bar{R}^{t}_{\perp},\bar{R}^{A}_{23},\bar{R}^{A}_{\perp\parallel}=\bar{R}_{\perp\parallel})^{T}$; *Puck* : $\bar{R}^{A}_{23}\neq\bar{R}_{23}$!

FF1, $\sigma_1>0$: $\left(\frac{\sigma_1}{\bar{R}^{t}_{II}}\right)^{2}$; FF2, $\sigma_1<0$: $\left(\frac{-\sigma_1}{\bar{R}^{c}_{\parallel}}\right)^{2}=1$, (maximum stress criteria)

and due to the IFF hypotheses, two different eqations are provided [*Puc* 96, *p.*118]

IFF: $\sigma_n>0$: $\varepsilon=\left(\frac{\tau_{nt}}{\bar{R}^{A}_{23}}\right)^{2}+\left(\frac{\tau_{n\ell}}{\bar{R}^{A}_{\perp\parallel}}\right)^{2}+\left(\frac{\sigma_n}{\bar{R}^{A}_{\perp}}\right)^{2}=1$, $\tau_n=\sqrt{\tau_{nt}^{2}+\tau_{n1}^{2}}$

IFF: $\sigma_n<0$: $\varepsilon=\left(\frac{\tau_{nt}}{\bar{R}^{A}_{23}-p_{\perp\perp}{}^{c}\cdot\sigma_n}\right)^{2}+\left(\frac{\tau_{n\ell}}{\bar{R}^{A}_{\perp\parallel}-p_{\perp\parallel}{}^{c}\cdot\sigma_n}\right)^{2}=1$, [*Puc*96, *p.*143]

$\Rightarrow$ from originally assumed 6 material strengths down to 5 action plane resistancies which capture all 3 sub-modes IFF1, IFF2 and IFF3.

The following transfer relationship is to apply above ($_{fp}$ = failure plane)

$$\begin{Bmatrix}\sigma_n(\theta_{fp})\\ \tau_n(\theta_{fp})\\ \tau_{n\ell}(\theta_{fp})\end{Bmatrix}=\begin{bmatrix}c^2 & s^2 & 2sc & 0 & 0\\ -sc & sc & c^2-s^2 & 0 & 0\\ 0 & 0 & 0 & s & c\end{bmatrix}\cdot\begin{Bmatrix}\sigma_2\\ \sigma_3\\ \tau_{23}\\ \tau_{31}\\ \tau_{21}\end{Bmatrix},\quad c=\cos\theta_{fp}\ \text{ and }\ s=\sin\theta_{fp}\ .$$

R^{A}_{23} is a model parameter and is found in the horizontal cross-section of Puck's Master failure body, depicted in *Fig.17-7*. It is an IFF-Mohr model-linked quantity and consequently a given model strength parameter and not a technical strength.

Puck's $\bar{R}^{A}_{23}$ is defined by Puck's Mohr-Model using two strengths $\bar{R}^{A}_{\perp\parallel}\equiv\bar{R}_{\perp\parallel}$, $\bar{R}^{A}_{\perp}\equiv\bar{R}^{c}_{\perp}$ and the so-called inclination parameter $p_{\perp\parallel}{}^{c}$. It finally did vanish therefore as a measurable technical strength.

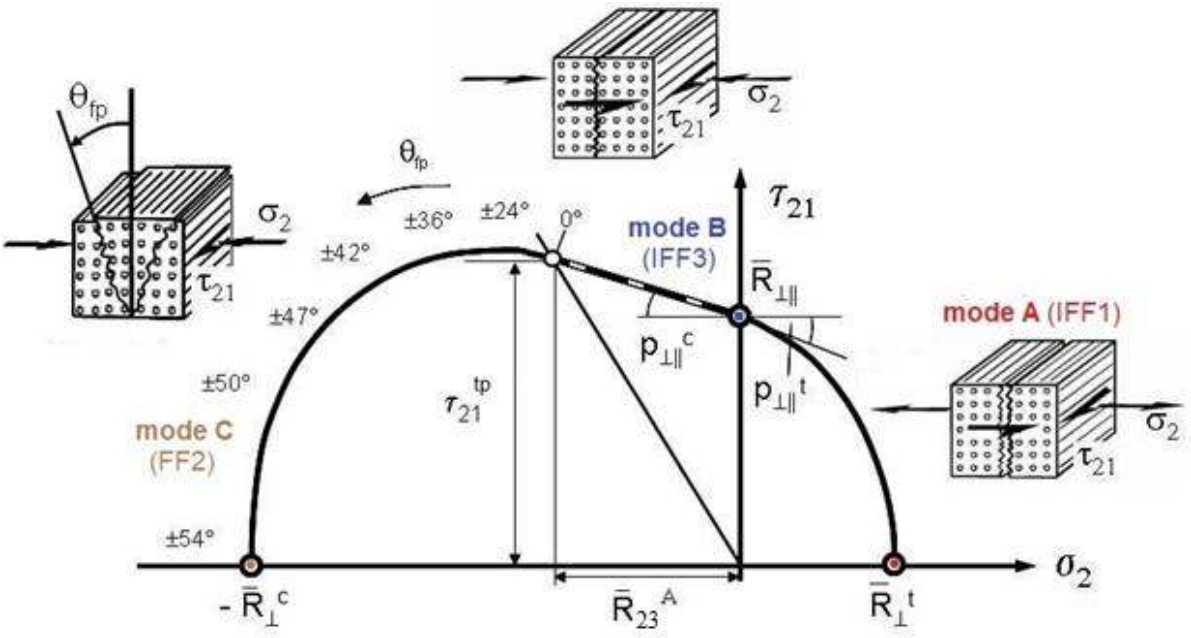

Fig. 17-7: Fracture modes of the (σ_2,τ_{21})-failure envelope; index tp marks the touchpoint between mode B and C, [Lut13, Puc96]

Table 17-6: 2D-IFF [VDI2014]

Mode A (= IFF1) : $$\varepsilon = \frac{1}{\bar{R}_{\perp\parallel}} \cdot \sqrt{\left(\frac{\bar{R}_{\perp\parallel}}{\bar{R}^t_{\perp}} - p^t_{\perp\parallel}\right)^2 \cdot \sigma_2^{\,2} + \tau_{21}^2} + p^t_{\perp\parallel} \cdot \sigma_2;$$

Mode B (≅ IFF3) : $$\varepsilon = \frac{1}{\bar{R}_{\perp\parallel}} \cdot \sqrt{p^{c\,2}_{\perp\parallel} \cdot \sigma_2^{\,2} + \tau_{21}^2} + p^c_{\perp\parallel} \cdot \sigma_2;$$

Mode C (≅ IFF2) : $$\varepsilon = \frac{\tau_{21}^2}{4 \cdot \left(\bar{R}_{\perp\parallel} + p^c_{\perp\parallel} \cdot \bar{R}^A_{23}\right)^2} \cdot \frac{\bar{R}^c_{\perp}}{-\sigma_2} + \frac{-\sigma_2}{\bar{R}^c_{\perp}}$$

ε is also termed f_E [*Lut*05, *VDI* 2014]

$$\tau^{tp}_{21} = \bar{R}_{\perp\mathrm{II}} \cdot \sqrt{1 + 2 \cdot p^c_{23}}, \quad \sigma^{tp}_2 = -\bar{R}^A_{23}, \quad \bar{R}^A_{23} = \left[\bar{R}_{\perp\mathrm{II}} \cdot \sqrt{1 + 2 \cdot p^c_{\perp\mathrm{II}} \cdot \bar{R}^c_{\perp} / \bar{R}_{\perp\mathrm{II}}} - 1\right] / 2 \cdot p^c_{\perp\parallel},$$

* The action plane resistance $\bar{R}^A_{23}$ depends on the chosen fracture body model such as the parabolic Mohr envelope and not just the linear Mohr approach.

* Assumption on coupling the inclination parameters: $p^c_{23} = p^c_{\perp\parallel} \cdot \bar{R}^A_{23} / \bar{R}_{\perp\parallel}$.

Practically, 5 independent failure activing stresses are left, which would support Cuntze's material symmetry-based 'generic' number of 5 he elaborated for UD materials.

Of course, an interaction of IFF with the two FF modes is also with Puck mandatory, in order to capture the combined (joint) failure danger. This procedure is documented in detail in the VDI 2014, sheet 3. One reason to do that is that experiments demonstrate micro-damage activation at the ends of broken filaments. Puck terms this 'weakening of the matrix' and uses a so-called weakening factor.

Applying Cuntze's interaction equation *Eff* = 1, then the FF-IFF interaction is automatically performed.

17.5.4 Comparison of the mapped four different SFC Failure Envelopes

In order to be able to generate above different envelopes the author had to harmonize terminology and to make them to apply his interaction formula for the modal SFC ones. This limited the amount of further numerical comparisons, $\tau_{21}(\sigma_1)$ could be investigated.

In consequence of the rare test data sets and of the effortful '*terminology harmonization process'* just **2D**-models of Tsai-Wu, Hashin, Puck and Cuntze could be numerically investigated. A comparison is only possible if the interaction can be equally performed for each model and the same interaction.

This could be realized for the 4 models by a transfer to the single 2D-*Eff*-formulation, example Tsai-Wu:

$$\frac{\sigma_1^{\,2}/Eff^2}{\bar{R}_{\parallel}^{\,t}\cdot\bar{R}_{\parallel}^{\,c}}+\frac{\sigma_1}{Eff}\cdot\left(\frac{1}{\bar{R}_{\parallel}^{\,t}}-\frac{1}{\bar{R}_{\parallel}^{\,c}}\right)+\frac{2F_{12}\cdot\sigma_1\cdot\sigma_2/Eff^2}{\sqrt{\bar{R}_{\parallel}^{\,t}\cdot\bar{R}_{\parallel}^{\,c}\cdot\bar{R}_{\perp}^{\,t}\cdot\bar{R}_{\perp}^{\,c}}}+\frac{\sigma_2^{\,2}/Eff^2}{\bar{R}_{\perp}^{\,t}\cdot\bar{R}_{\perp}^{\,c}}+\frac{\sigma_2}{Eff}\cdot\left(\frac{1}{\bar{R}_{\perp}^{\,t}}-\frac{1}{\bar{R}_{\perp}^{\,c}}\right)+\frac{\tau_{12}^2/Eff^2}{\bar{R}_{\perp\parallel}}=1$$

The investigation focuses mapping of the curves of test data by SFCs. In these formulations each single strength is an average strength consequently indicated by a bar over. The following figures present the failure envelopes of investigated three plane stress combinations.

Fig.17-8 visualizes, how the four models map the most interesting cross-section of the UD fracture body, namely $\tau_{21}(\sigma_2)$.

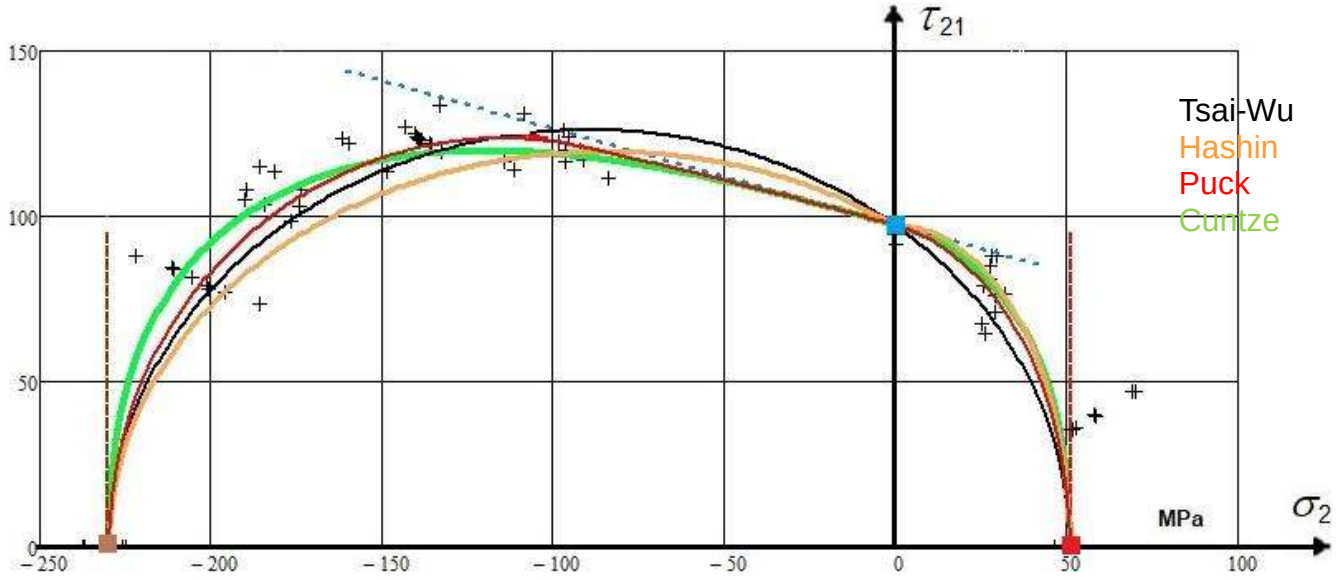

Fig. 17-8, $\tau_{21}(\sigma_2)$: CFRP test results (MAN Technologie research project with A. Puck, IKV Aachen et al.)

$$\{\bar{R}\}=(1280,\ 800,\ 51,\ 230,\ 97)^T\,\text{MPa},\ \mu_{\perp\parallel}=0.3\ [\textit{VDI 97}]$$

Fig.17-9 depicts the failure envelope $\sigma_2(\sigma_1)$, being the WWFE Test Case 3. In this test case below, just the 4 strength values were provided together with the not $R_{\perp}^{c}$ -matching test data of a Russian test data provider showing a test discrepancy (*he passed away, no request possible*) in the fourth quadrant of *Fig.17-9*. However, the tendency of the two different (*assumed*) test sets can be carefully used for validation.

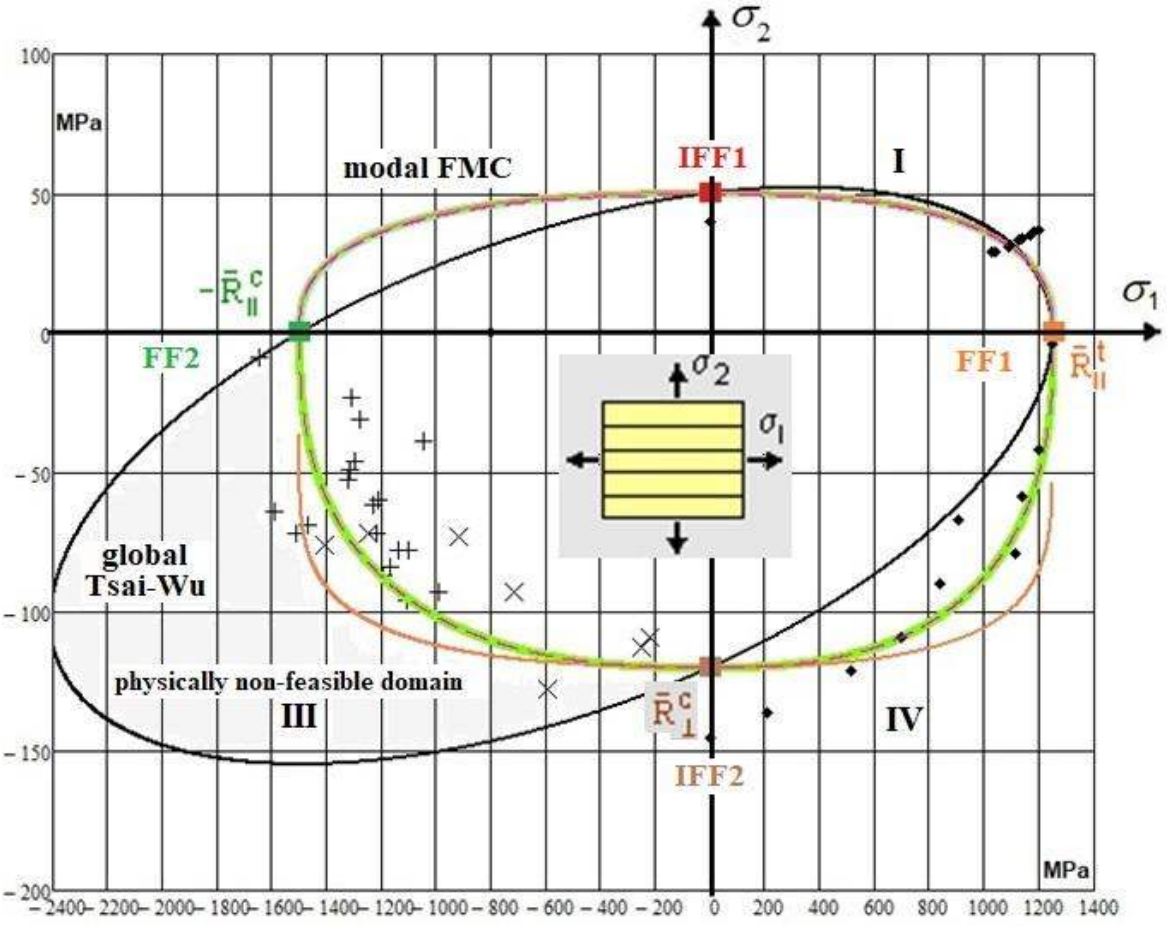

Fig.17-9, $\sigma_2(\sigma_1)$, WWFE-I, TC3: Hoop wound tube lamina. E-glass/MY750 Ep. $\{\bar{R}\} = (1280,\ 800,\ 51,\ 230,\ 97)^T$

The global Tsai-Wu SFC lies fully outside, which would be of high effect for stability analysis. The test data set in the quadrant III was provided by Martin Knops, IKV Aachen, [*Kno03*].

Above mapping tells, that modal modelling is the better choice.

From *Fig.17-10* can be concluded that the envelopes of Puck and Cuntze lie upon another. Modal Hashin and Global Tsai-Wu are lying inside.

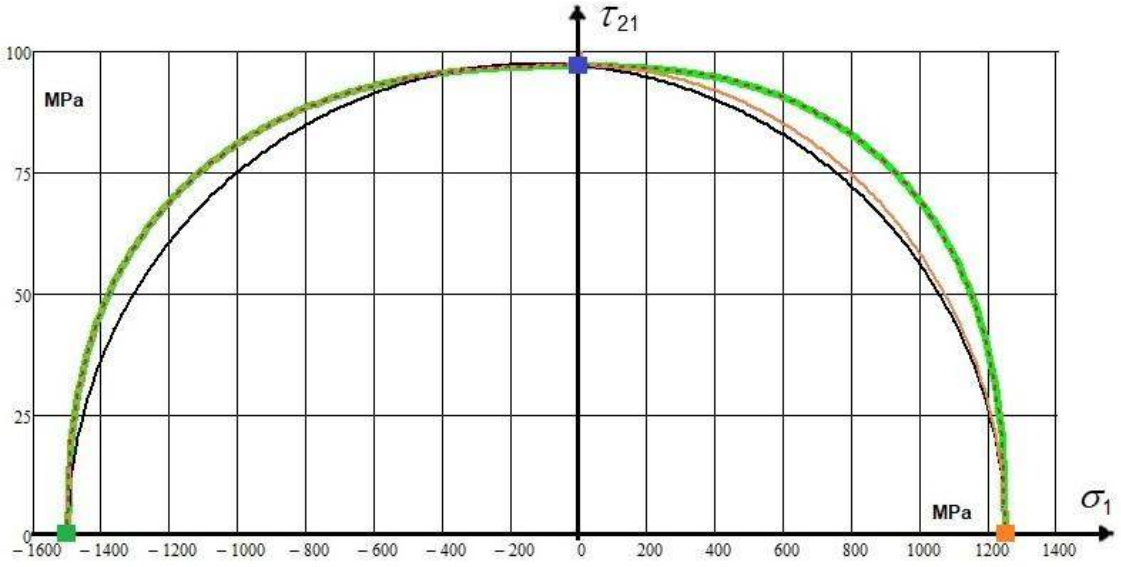

Fig.17-10, $\tau_{21}(\sigma_1)$: $\{\bar{R}\} = (1280,\ 800,\ 51,\ 230,\ 97)^T$

17.6 Computation of a SFC-linked Reserve Factor

Principally, in order to avoid either to be too conservative or too un-conservative, a separation is required of the always needed 'Analysis of the average structural behavior' in Design Dimensioning (*using average properties and average stress-strain curves*) in order to obtain optimum structural information (= 50% expectation value) from the mandatory single Design Verification analysis of the final design, where statistically minimum values for strength and minimum, mean or maximum values for the task-demanded other properties are applied as Design Values. There it is to demonstrate that '*A relevant Limit State is not met yet'*.

Fig.13-5 presented a numerical example how exemplarily a UD reserve factor *RF* is to compute. A very simple example of the Design Verification of a critical UD lamina in a distinct wall design was depicted as *RF*-calculation procedure. The certification–relevant load-defined Reserve Factor *RF* corresponds in the linear case to the material reserve factor f_{RF}. Its value in §13.5 was $RF = 1.25 > 1$ → Laminate wall design is verified!

The multiple Lessons Learned and conclusions are incorporated in the following list:

LL

- ✓ *Considering FE-results and necessary properties: We must more and more 3D-design! However properties, especially for composites is 3D-property data test sets, are seldom sufficiently available*
- ✓ *So-called global SFCs couple physically different failure modes whereas the modal SFCs describe each single failure mode and therefore will better map the course of test data*
- ✓ *First-Ply-Failure (FPF) envelopes are searched by these SFCs, which means determination of 'Onset-of-damage' and includes both Inter Fiber Failure (IFF) and Fiber Failure (FF). Last Ply Failure (LPF) usually requires a non-linear analysis, which can be used to save a design*
- ✓ *Material symmetry seems to require for UD materials a 'generic' number of 5, valid for strengths and elasticity properties and the distinct SFCs.*
- ✓ *In this context: The Standard 3D SFCs of Tsai-Wu and Hashin employ the so-called cohesive (shear) strength* R_{23} *and regard it as a technical strength and not as a general strength quantity. The mystery behind the various interpretations is tried to be unlocked by the author. Because most of the published applications are 2D-ones the employed SFCs do not require* R_{23} *and its determination by tests needed not to be presented*
- ✓ *Often, SFCs employ just strengths and no friction value. This is physically not accurate and the undesired consequence in Design Verification is: RF may be not on the safe side*
- ✓ *SFCs are 'just' necessary but not sufficient for the prediction of strength failure. Basically, due to internal flaws, also an energy criterion is to apply. The novel approach 'Finite Fracture Mechanics (FFM)' offers a hybrid criterion to more realistically predict the stress-based crack initiation in brittle isotropic and UD materials, too.*
- ✓ *The physically clear-based quantity Eff gives an impressive interpretation of the failure envelope or what 100% strength capacity in 3D stress states physically really means.*
- ✓ ***From the nevertheless well performed WWFEs the author had to learn that provided test results can be far away from the reality like an inaccurate theoretical model.*** *Theory creates a model of the reality and one experiment shows 'just' one realization of the reality. Test article analysis is mandatory to interpret the test results and for a simulation-based improvement of the design. Only well-understood experiments can verify the design assumptions made!*
- ✓ *Assuming 6 strengths seems to violate material symmetry. Cuntze's SFC set just employs 5 measurable strengths and 2 friction parameters.*

17.7 On Modelling General Laminates

Modelling of laminates may be lamina-based (*basic layers are UD layers*), sub-laminate-based (*semi-finished non-crimp orthotropic fabrics*) or even laminate-based. Thereby, modelling complexity grows

from UD, via non-crimp fabrics (NCF) through plain weave and finally to the spatial 3D-textile materials. Model parameters are just the measurable technical strengths R and the friction values μ, and on top the Weibull statistics-based interaction exponent m. The value of μ comes from mapping the compression stress-shear stress domain and of m by mapping the transition zone between the modes. A good guess is $m = 2.6$ for all mode transition domains and all material families. Model parameters are just the measurable technical strengths R and the friction values μ, and on top the Weibull statistics-based interaction exponent m. The value of μ comes from mapping the compression stress-shear stress domain and of m by mapping the transition zone between the modes. A good guess is $m = 2.6$ for all mode transition domains and all material families.

Mind:

Full exploitation of the Carbon Fiber (CF) is only to achieve by pre-tensioning.

This will compression-loading linked help to better exploit the usual low tensile strength of i.e. the matrices concrete and plastic. Pre-tensioning of concrete plates is still series production!

18 Brittle Orthotropic Materials

***Aim**: Providing a basic SFC set in order to have a mapping basis for further test results and validation.*

Ceramic Strength Failure Criteria for Monolithic (isotropic), Transversely-isotropic UD and Fabric Materials, for more details, see [*Cun24b]**. Of interest here shall be the *Model Validation and Design Verification of orthotropic Ceramic Structural Components.*

18.1 Fabric Properties Specifics

To quantify the always present differences between R_W^t and R_F^t or R_W^c and R_F^c, test specimens in both the directions W and F are equally (*i.e. plain weave*) to produce and statistically to test (50% each), so that the necessary information in both the fiber directions is obtained. Under shear τ_{WF}, the shear stress-shear strain curve continues to rise after initial fracture, because the so-called scissor effect causes a rearrangement in the direction of fibers, which means the originally 90°-angle of the fabric becomes smaller, see later this effect in *Fig.18-2*.

Fig.18-1 visualizes different fabrics. The upper part figure depicts the modelling of differently woven fabrics, the center shows three basic fabrics, and the bottom part figure fabric 'pocket' effects. The pockets with their porosity impact the progressive micro-damage under orthogonal uni-axial tensile stress states. Under compression, the above still mentioned micro-instability is faced. Differently woven means different fracture failure due to the ceramic pockets.

Pocket-driven supported micro-fracture failure is sometimes desired if some quasi-ductility is to provide.

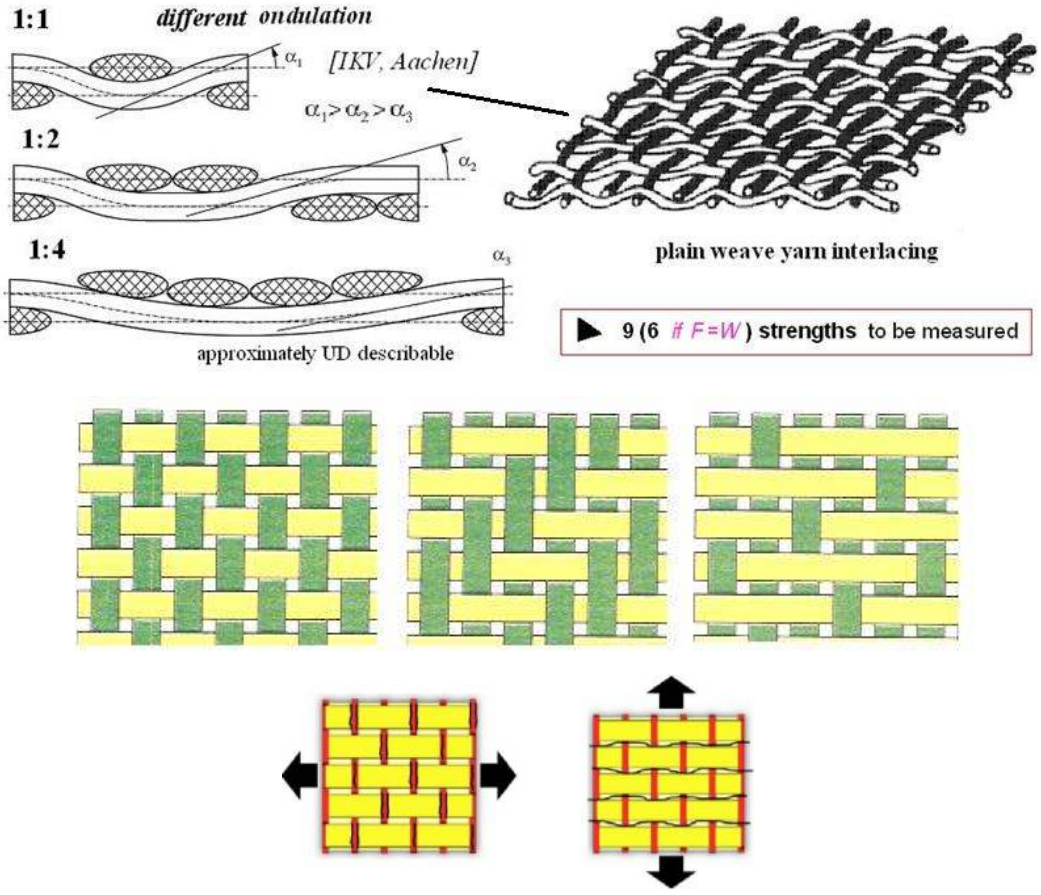

Fig.18-1: (up) Differently woven fabrics [IKV Aachen].
(center) Plain weave (Leinwandbindung) → Twill weave (Köperbindung) 2/2 → Atlas or Satin weave1/4 [Wikipedia 2023];
(down) Different fracture failure due to ceramic pockets impacting progressive failure

18.2 3D-SFCs of Orthotropic Fabrics

9 modes → 9 SFCs. This is in line with Cuntze's 'generic' number 9 according to the FMC.

In this 'generic' context, my thanks to Roman (Prof. Dr R. Keppeler, UniBW; formerly Siemens AG), (see [*Cun*24*b*]) .

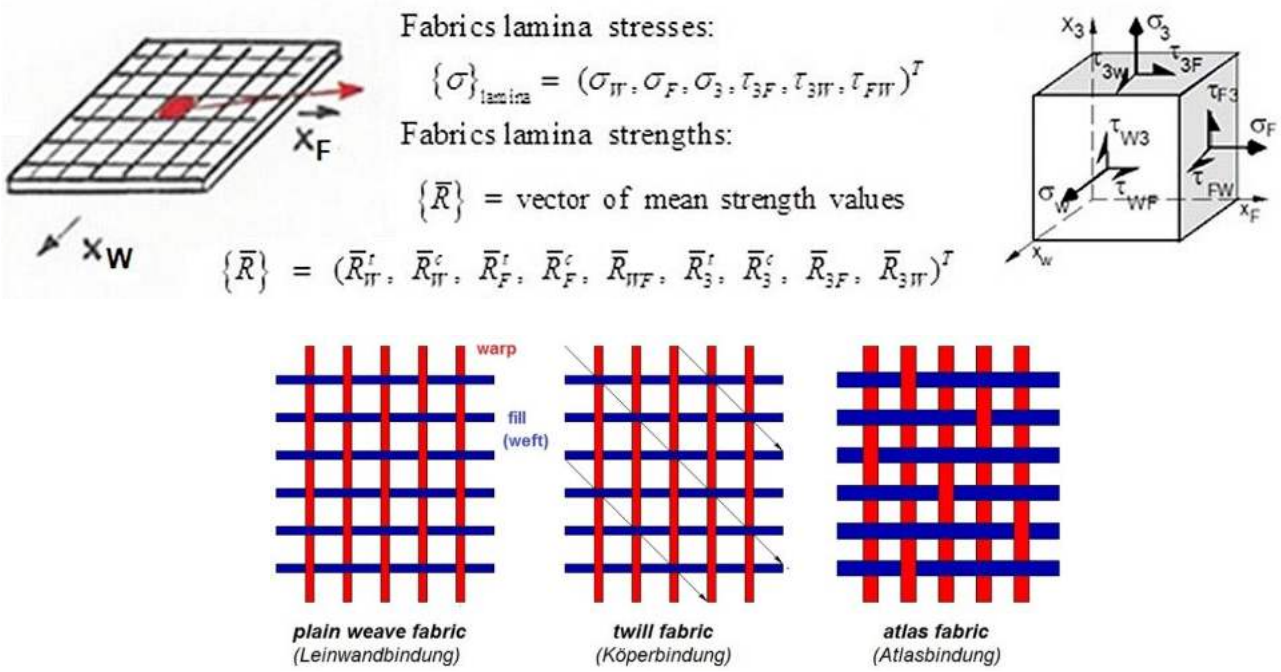

Fig.18-2: Visualization of stresses, strengths and structural fabric elements

The following table includes the FMC-based SFCs for **porous orthotropic** (rhombic-anisotropic) **materials** composed for instance of 2D-woven fabrics**.** Three essential 2D-woven fabrics (Atlas or Satin) are depicted

Table 18-1: Orthotropic SFCs

$$Eff = \left(\frac{\sigma_W + |\sigma_W|}{2\cdot\bar{R}^t_W}\right)^m + \left(-\frac{\sigma_W + |\sigma_W|}{2\cdot\bar{R}^c_W}\right)^m + \left(\frac{\sigma_F + |\sigma_F|}{2\cdot\bar{R}^t_F}\right)^m + \left(\frac{-\sigma_F + |\sigma_F|}{2\cdot\bar{R}^c_F}\right)^m + \left(\frac{|\tau_{WF}|}{\bar{R}_{WF} - \mu_{WF}\cdot(\sigma_W + \sigma_F)}\right)^m$$

$$+\left(\frac{\sigma_3 + |\sigma_3|}{2\cdot\bar{R}^t_3}\right)^m + \left(\frac{-\sigma_3 + |\sigma_3|}{2\cdot\bar{R}^c_3}\right)^m + \left(\frac{|\tau_{3W}|}{\bar{R}_{3W} - \mu_{3W}\sigma^c_3}\right)^m + \left(\frac{|\tau_{3F}|}{\bar{R}_{3F} - \mu_{3F}\sigma^c_3}\right)^m = 1 = 100\% \,.$$

For a cross-ply fabric with Warp = Fill → $\bar{R}^t_W = \bar{R}^t_F$, $\bar{R}^c_W = \bar{R}^c_F$, the inter-laminar *Eff*s, suffix $_3$, vanish and just the in-plane (intra-laminar) *Eff*s remain.

The range of parameters is for the interaction-exponent 2.5 < m < 2.9, and since the strong porosity-dependency is very different → recommendation: $\mu_{WF} < 0.2$, $\mu_3 < 0.2$.

If σ_F is also active, this double mode contributes via $\left(\frac{|\tau_{WF}|}{\bar{R}_{WF} - \mu_{WF}\cdot(\sigma^c_W + \sigma^c_F)}\right)^m$.

18.3 2D-Mapping of shear stress-normal stress τ_{WF} (σ_W) with Test Data Evaluation

The test specimens are cut out of a laminate plate at an angle to the specified 0°- direction angle of the fabric test specimen $\left[\begin{smallmatrix}0\\90\end{smallmatrix}\right]_S$, [*courtesy Siemens AG*]. For in-plane stressing of this off-axis test specimen, the following SFC set remains:

2D: $\left(\frac{\sigma_W+|\sigma_W|}{2\cdot\bar{R}_W^t}\right)^m+\left(-\frac{\sigma_W+|\sigma_W|}{2\cdot\bar{R}_W^c}\right)^m+\left(\frac{\sigma_F+|\sigma_F|}{2\cdot\bar{R}_F^t}\right)^m+\left(\frac{-\sigma_F+|\sigma_F|}{2\cdot\bar{R}_F^c}\right)^m+\left(\frac{|\tau_{WF}|}{\bar{R}_{WF}-\mu_{WF}\cdot(\sigma_W+\sigma_F)}\right)^m=1.$

For the uniaxial stress states $\sigma_W{}^c$ (*Warp stability danger faced, same is valid for the Fill direction*) and $\sigma_W{}^t$ fiber failure modes are identified in the case of plain weave fabrics. Under τ_{WF}, accompanied by scissoring, micro-mechanical matrix failure may be faced in off-axis testing. This is of marginal importance for $\tau_{WF}(\sigma_W{}^c)$ but essential for $\tau_{WF}(\sigma_W{}^t)$. Namely, at small tensile warp stresses fracture danger for the matrix (suffix *m*) due to σ_m^t under shear stresses τ_{WF} is given through the matrix tensile fracture-causing tensile component of the shear stress, $\tau_{WF}\equiv(\sigma_m^c,\sigma_m^t)$. This lasts until fiber tensile failure stress $\sigma_W{}^t\equiv\sigma_{||}{}^t$ dominates the failure state. Matrix tensile fracture leads to an inward dent as logical consequence, see *Fig.18-2*. However why is there a dent, represented by the two marked test points? The inward dent or pop-in is just the consequence of the off-axis angle test specimen, which activates matrix failure in this not adequate $\tau_{WF}(\sigma_W{}^t)$-test. In the so-called off-axis coupons, a tensile stress-controlled matrix break is generated from about 15°. The fibers are no longer continuous over the test length, which means that the matrix is practically the highest stressed constituent. To capture this effect would require a matrix constituent strength criterion. A smeared composite criterion cannot

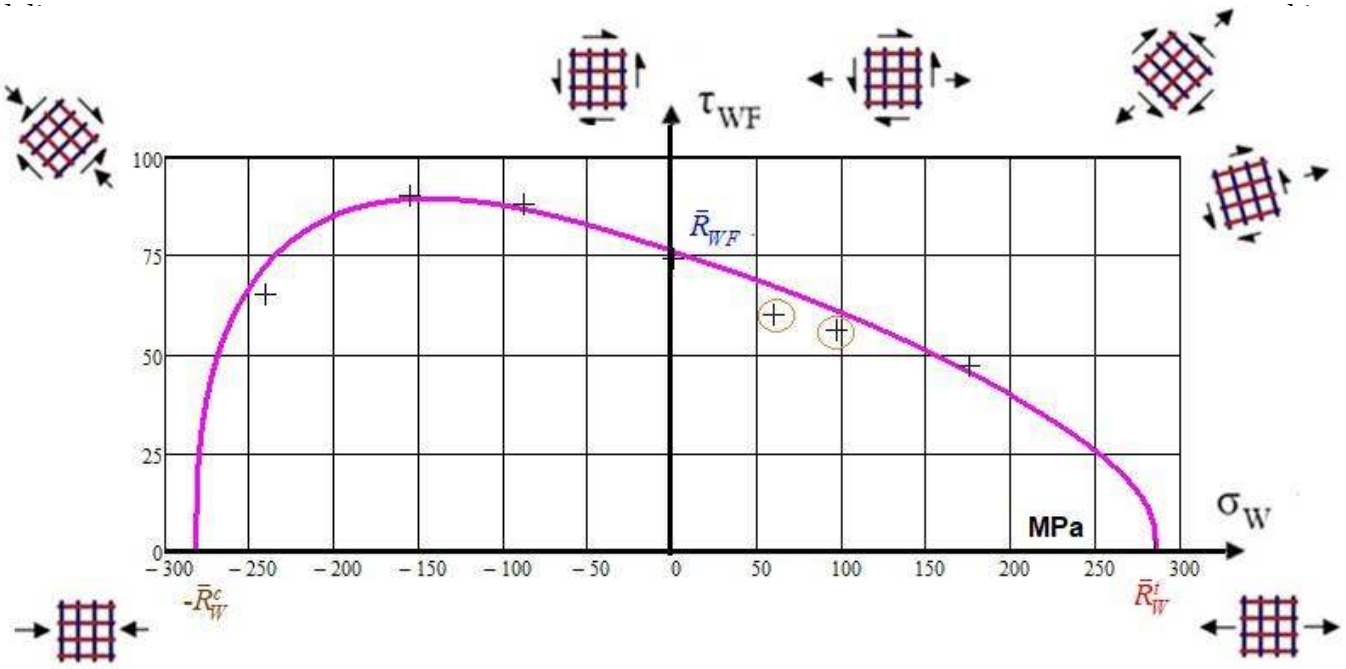

Fig. 18-2, plain weave fabric laminate: Off-axis coupon tests

, $\left[\begin{smallmatrix}0\\90\end{smallmatrix}\right]_S$ *Failure envelope* $\tau_{WF}(\sigma_W)$. *(data set Siemens AG). m =* ***2.6****. RT=23°C.*

From mapping derived strength values.

$R_W{}^t$ *= 286 MPa,* $R_W{}^c$ *= 282 MPa. Josipecu shear test:* R_{WF} *= 76 MPa,* μ_{WF} *= 0.14*

If a mapping of the dent would be really desired: A numerical solution to map the dent would be to move from the shear mode at α = 15° to a matrix tensile mode and about 50° from the matrix tensile mode back to the warp tensile mode. This requires the formulation of a matrix failure mode. Built on practical experience a decay function is to employ. This decay function for each interacting mode is physically accurately terminated in each opposite 'pure' domain τ_{WF} and $\sigma_W{}^t$.

Lessons Learned from ceramic testing:

* The transfer of test results from the test specimen to the real part requires deep insight! One must know the characteristics of the test specimen before transferring properties to the structural part
*Application limit of the usually and here applied series spring model is given if abrupt changes of a mode are faced. An inward dent cannot be mapped since this violates the basis of the series failure model
* Each test method has its application limit. Not plausible test points have to be checked by physical interpretation
*The dent is an off-axis coupon-caused result and does not reflect a real $\tau_{WF}(\sigma_W{}^t)$-failure curve
* The hinge or increase of the shear failure curve in the negative σ_2-domain – indicated by an increasing shear stress – is not caused by an increase of the (*uni-axial*) shear 'strength'. *Eff* remains constant, Mohr-Coulomb improves the bi-axial 'strength capacity'
* Uncover the reasons of large scatter
* In the case of very large scatter, a mapping of the course of test data points with a SCF model makes no much sense and might partly also not be possible. Also a strength design value *R* cannot be determined or would mathematically result in a reduced strength value of practically zero
*A validated SFC model cannot model physically false test points, however, it can help to sort out bad measurements or physically doubtful ones
* Loading can be practically only applied to a straight edge
* From bad experience interpreting CMC-test results: A figure capture must indicate whether it is a UD ply or a fabric ply or something else??

Well-<u>understood</u> experiments have to verify the design assumptions made!

In this context, Avula stated in 1987 "Experimental observations and measurements are generally accepted to constitute the backbone of physical sciences and engineering because of the physical insight they offer to the scientist for formulating the theory.
Concepts, which are developed from observation, are used as guides for the design of new experiments, which in turn are used for validation of the theory.
Thus, experiments and theory have a hand-in-hand relationship".

Above text directly leads over to the author's elaboration on the provided WWFE test results in the next chapter!

►My present feeling considering 3D-applications, especially of UD-materials:

(below left)
Much is reached with plenty of effort!
After so much effort, the pain will be soon over? The top seems to be reached?

(above right)

No, the view of the SFC-climber widens: Validation by SFC applications at first will require many numerically challenging long-lasting difficult visualizations → These required most of the worktime and persistence in the performance of the numerical analyses with graphical visualization.

Only when you get 'higher' the real ‘3D-peaks’ do appear.
Hence, despite all these elaborations more effort will be required for the 3D-SFC Validation.

And this much more for composites:

3D-applications are much more challenging, especially because data is missing.

►*It seems to be easier to launch a new ARIANE rocket type*
than a new idea on strength criteria *[the author, 1996]*

19 World-Wide Failure Exercise Contribution with Evaluation of Test data

***Aim**: Highlight the importance of checking the quality of provided test data.*

19.1 General

This is a good place to make the reader aware of the meritorious World-Wide-Failure-Exercises on endless-fiber-reinforced transversely-isotropic UD-material. "*Many thanks to the QinetiQ-team, UK, the organizers Mike Hinton, Sam Kaddour and Peter Soden for setting up and survive such a long lasting effortful world-wide exercise and later Shuguang Li.". I enjoyed the honor to support Sam a little with WWFE-II .*

The author did not participate in WWFE-III on Continuum Micro-damage Theories. Where are the practical results of this WWFE presented?

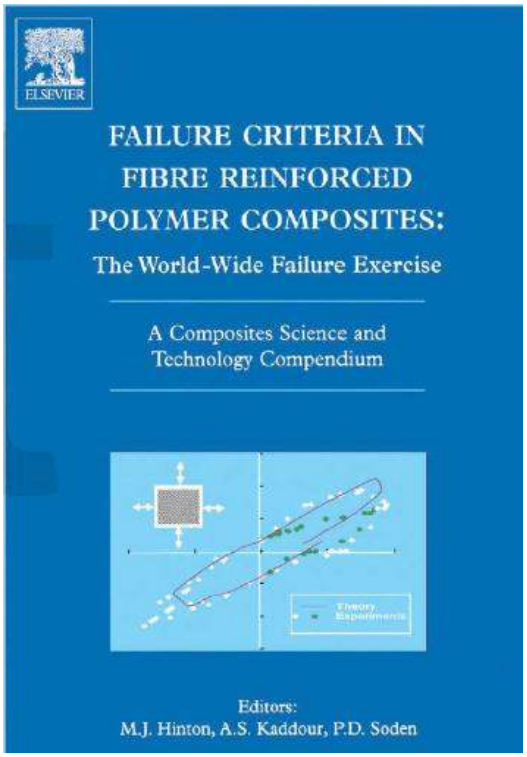

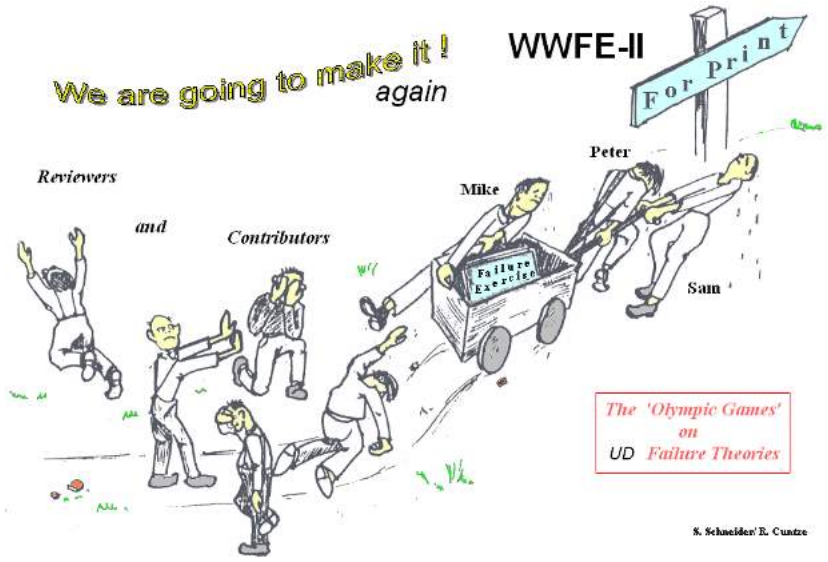

Organizer: QinetiQ , UK, since 1991

[Hinton, Kaddour, Soden, Smith, Shuguang Li]

Aim: For UD materials, only!

'Testing Predictive Failure Theories for Fiber–Reinforced Polymer Composites to the full !'

Method of the World-Wide-Failure-Exercises-I (2D test data, start 1994**) and -II (**3D, start 2005**)**

Part A : *Blind Predictions on basic strength data, only*

Part B: *Comparison Theory-Test with hopefully reliable* <u>*Uniaxial*</u> *'Failure Stress Test Data' (the technical* <u>*basic strengths)*</u> and *Multi-axial 'Failure Stress Test Data' from* <u>plain</u> test specimens (not notched) as well.

We contributors know that the organizers could only provide the contributors with test data sets which were available. The quality of them was not known enough well. Hence, the following information shall be given before mapping the courses of some UD lamina Test Cases (TC):

- Part A: Prediction was to made without provision of all needed properties. With strength values alone – in general - a SFC cannot be validated. For compression, however, a friction information should have been given.
- Part B: Test data sets partly not applicable. Comments on the respective input are given in each Test Case TC.
- Validation of lamina SFCs models can be only achieved by lamina 2D- and 3D- test results. 3D-laminate results serve for verification of the laminate design.

- QinetiQ's meaning of the term 'Failure Theory' in the WWFEs: Failure concludes 3 elements: Failure criterion, numerical procedure (such as FE codes) and non-linear analysis tools. However, the user looks just for a reliable macro-mechanical failure criterion that hopefully captures the micro-scopic failures by the proposed equations.

WWFE-I : 14 Test Cases, 2D stress state
TC1-TC3: UD lamina, failure stress envelopes
TC4-TC14: UD lamina-composed laminates (Quasi-isotropic, angle-ply, cross-ply) failure stress envelopes and loading-caused stress-strain curves.

WWFE-II: 12 Test Cases, 3D stress state
TC1: Isotropic Epoxy matrix
TC2,3,4-TC7: UD lamina
TC8-TC12: UD lamina-composed laminates.

Presumptions:

- As temperature drop the difference stress free temperature 120° minus room temperature 23° as effective temperature difference is applied in order to consider the effect of the curing stresses as residual stresses of the 1st kind.
- Moisture may be assumed here to have a balancing effect of 30°C. Chemical shrinking and thermal curing stresses do not affect the shear stresses.
- Micromechanical curing stresses considering residual stresses of the 2nd kind at filament/matrix level could not be assessed and considered. They are assumed here to be respected in the values for the UD-strengths.
- The given stress-strain curves of the UD-lamina are interpreted to be mean curves, the type one needs for test data mapping, however, this was not always the case (WWFE TC2,TC3, TC4) and had to be corrected by the author to obtain mapping success.
- A so-called edge effect (3D state of stress) is not considered, because the laminates are assumed to be part of a 'closed' composite structure.
- Model modification from Part A to Part B principally not permitted.
- Significant in the Test Cases was failure *due to* FF, IFF, leakage, deformation limit, delamination size limit. Strength was the envisaged main failure.
- Mohr-Coulomb-required friction values had not been provided for Part A and could be estimated by simulating the Part B results. Just strengths were the basis for the Part A prediction.

Basically, the step from insufficient Part A information to an improved Part B information level made small modifications of the theoretical model necessary. These modifications were mandatory, primarily, because test data sets were modified by the organizer and because additional Part B information was given. Even in Part A provided strengths were changed! Therefore, it makes not much sense to compare the contributors' blind predictions' if data provision in Part A does not contain all material parameters, i.e. the two material internal friction values, which are physically necessary: *Brittle behaving materials follow Mohr-Coulomb and therefore exhibit friction*. It further makes no sense to provide sample data generated by different test specimens, i.e. torsion tests of a hoop wound 90°-tube together with a 0°-tube, as the latter twists and the stress state must be transformed by the twisting angle in order to obtain the lamina stress state which then can be judged by the SFCs, see [*Cun04, Cun13*].

Validation of the lamina-material SFCs models can be only achieved by 2D- together with 3D-lamina test results. ***Since SFC-model validation is focused just lamina-TCs are now investigated in detail***.
The normal user is just interested to well map his course of failure test data by a UD-SFC and not on laminate analysis tools.

The laminate test cases serve for the verification of the laminate design. There the full WWFE failure theory is required. This makes a comparison between the contributions very challenging because

different FE codes were applied by the contributing competing institutes. These better tools further had to be equally compared to the retired author's tools. He could just use his handmade non-linear CLT-code upgraded by experience and using his sensibleness for the problem and the delivered input.

The author's WWFE-I and -II contributions had to be based on an intensive assessment of provided test results.

In this section details on some mapped UD lamina TCs are given and associate information when and why a modification in Part B had to be made. For the laminate TCs, which do not directly serve for SFC validation it is referred to WWFE-I: [*Cun04b*] and WWFE-II: [*Cun 13a, Cun14a*].

19.2 Mapping of some UD-material World-Wide-Failure-Exercises-I and -II Test Cases (TC)

19.2.1 Failure Stress state $\tau_{21}(\sigma_2)$

WWFE-I, TC1, UD lamina, GFRP, E-glass/LY556 Ep [*Test data DLR Stuttgart*]?

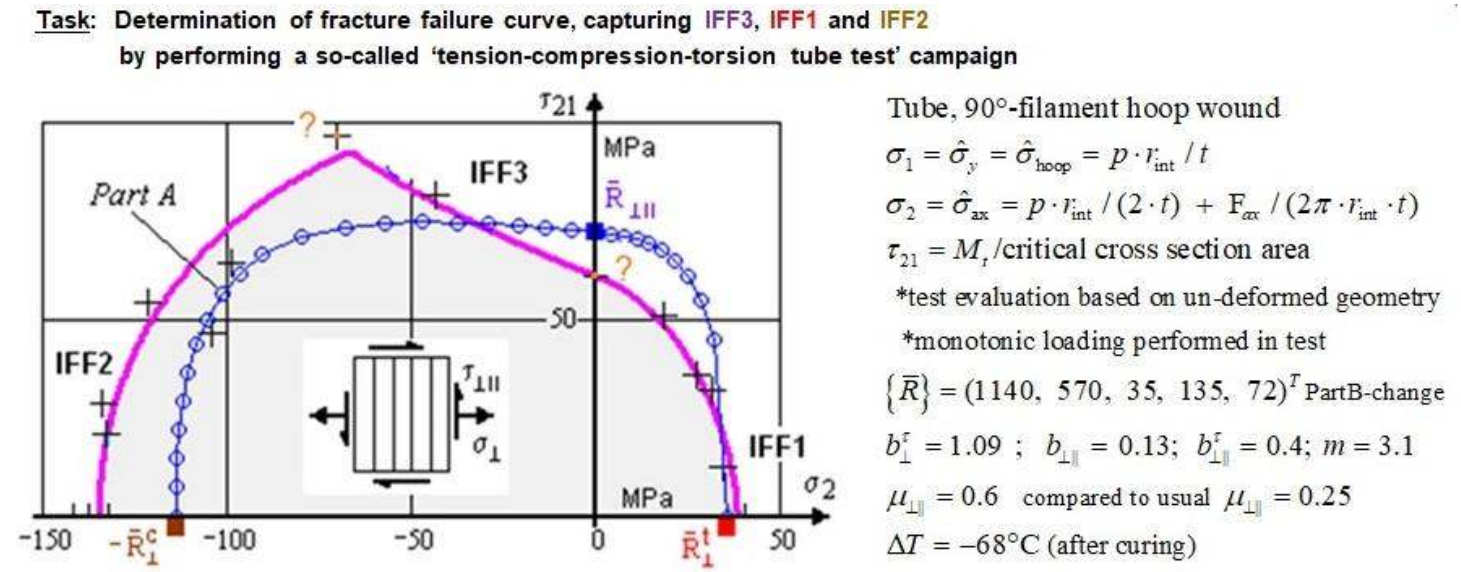

Part A, prediction: Data of elasticity properties, UD strengths $\bar{R}$ provided, only. No friction value μ for IFF3 slope provided! Lowest value for μ in Part A assumed (safe side)

Part B: the 3 strength points were altered! Two doubtful (?) failure stress points were provided. Nevertheless, QinetiQ asked to map the course of PartB-test data (magenta curve) despite of the fact that a Poissons ratio $\mu_{\parallel\parallel}$ had to be taken which is much too large, compared to values of own and other test campaigns !

- Before test data evaluation: Check whether a thin tube test specimen (r / t > 10), otherwise ‚thick' formula is tu use.
- No reasonable PartA-mapping possible with the provided PartA-information, see blue curve!
- After later discussion with the former test engineer at DLR: "The upper test point must be false"!
  ▶ TC1 test data set (Part B) is not acceptable for a model validation!

Fig.19-1: WWFE-I, TC1

WWFE-I, TC1:

Part A: Provision of strength data, no friction value μ given.

Part B: Strength points altered! 2 doubtful single failure stress points (marked by a ?). A much too high friction had to be considered to map this case, unrealistic, as own and other measurements prove [*Cun14*]. On top it is 'Not on the safe side'.

For this TC the author knew about the test inaccuracy of above two false test points from my colleague Rodolfo Aoki at DLR, Stuttgart. Reason is known: non-accurate raw test data evaluation of the test engineer colleague at DLR Stuttgart.

Despite my warning the organizers did not question the test data!
However, **I was forced to map above false course of test data with an unrealistic friction value, otherwise I would have been thrown out of the exercise!**

For comparison, have a look at our test points in *Fig.19-2*, please.

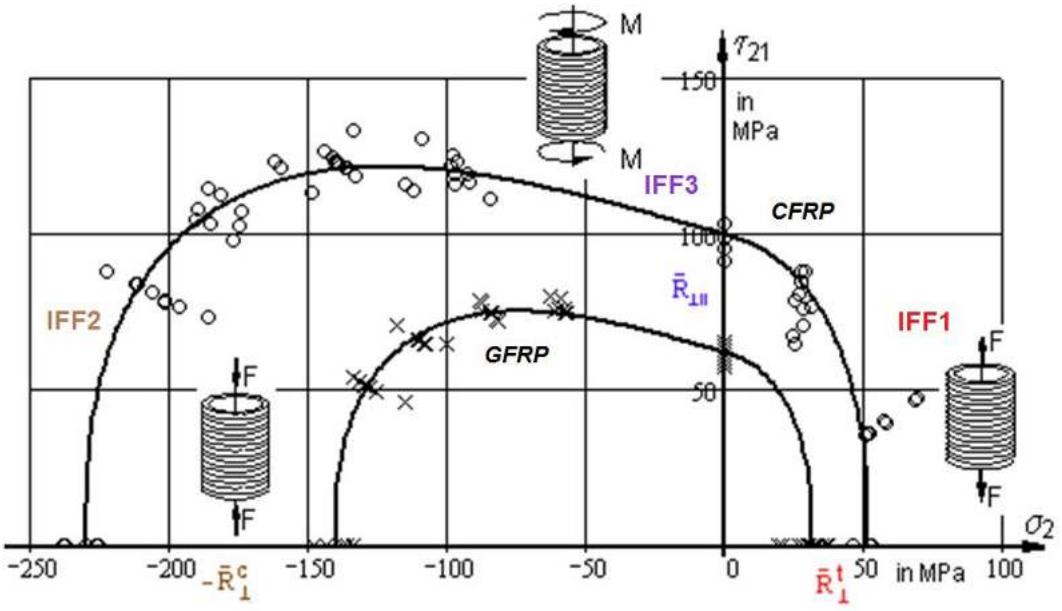

Fig.19-2, own IFF test results: 2 GFRP with 1 CFRP test series

19.2.2 Failure Stress state $\tau_{21}(\sigma_1)$

WWFE-I, TC2, UD lamina, CFRP, T300/BSL914C Ep, $\tau_{21}^{fr}(\sigma_1)$

Basic cross-section of the fracture failure body:

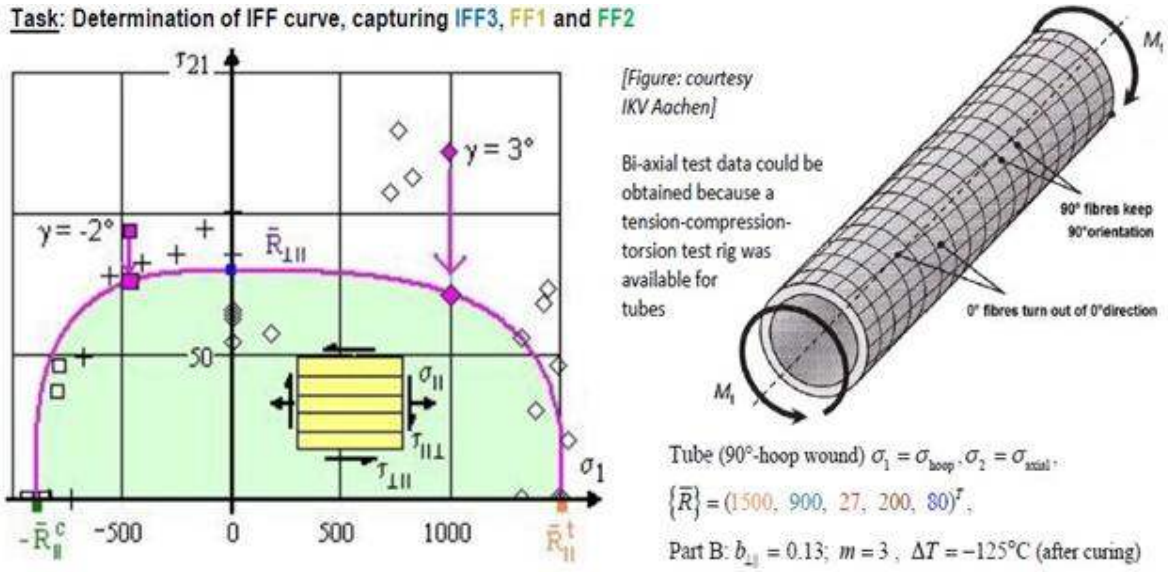

Part A, prediction: Strength data only provided, no friction value (slope) μ.

Part B, comparison: Strength data sets were provided, partly from 0°-test specimens (axial fiber direction) and partly from the traditional 90°- tube test specimen! After transformation, the two chosen ■◆, by executing a *non-linearly CLT*-computed shear strain analysis, these two 0°-points exemplarily could be shifted onto the magenta envelope. The shear strength point (blue) had to be adjusted according to new B information.

Fig.19-3: Example WWFE-I TC2 and WWFE-II TC3. CFRP, T300/BSL914C Ep

WWFE-I TC2:

The author informed the organizers that apples and oranges have been put here together in above diagram. One cannot fill into the same diagram 90°-wound tube test specimen data together with 0°-wound tube data. The 0°-stresses (see also *Fig.13-3*) have to be transformed in the 2D-plane due to the fact that shearing under torsion loading turns the fiber direction and the lamina coordinate system CoS

is not anymore identical with the structure coordinate system of the tube. In order to also use these test data the author exemplarily transformed magenta-colored two fracture test points by the occurring twisting angle γ using a non-linear CLT-analysis. Then he could achieve a good mapping showing, that the two transformed fracture points accurately lie in the lamina CoS on the 90°-tube curve.

19.2.3 Failure Stress state $\sigma_2(\sigma_1)$

WWFE-I, TC3, UD lamina, GFRP, E-glass/MY750EP $\sigma_2(\breve{\sigma}_1 \equiv \sigma_1)$

Task: Mapping in all four quadrants without obtaining sufficient test results fracture modes: (FF1, FF2, IFF1, IFF2, −)

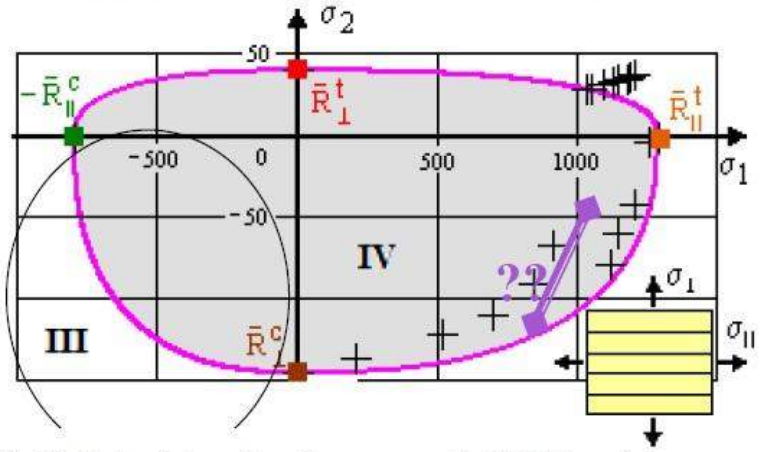

Tube (90°-hoop filament wound)

$\sigma_1 = \sigma_{hoop}$, $\sigma_2 = \sigma_{axial}$

$\{\bar{R}\} = (1280,\ 800,\ 40,\ 145,\ 73)^T$

(Part A, old IFF3 formula:

$b_{\perp\|} = 0.13,\ b^r_{\perp\|} = 0.4,\ b^r_{\perp} = 1.5,\ m = 3)$,

Part B: $b_{\perp\|} = 0.13, b^r_{\perp} \rightarrow b_{\perp\perp} = 1.5;$

$m = 3$

Part A: Data of strength points were provided $\{\bar{R}\}$. Remaining necessary frictions μ were assumed by the author.

Part B: For the quadrants II and III no multi-axial data sets were provided. Test data in quadrant IV show discrepancy ! Real winding angle was ±85° instead of 90° (effect on strength and stiffness was not regarded w.r.t. other missing information and to scatter). *IKV , Aachen with Puck, filled the gap in the Tsai-Wu non-feasible domain, of quadrant IV.*

- *In quadrant IV it seems that two different 'test procedures' have been used obvious in the domain of 1000 MPa.*
- *In quadrant I the test data set could be better mapped by a higher m-value, however this was not done due to the inside oriented scattering data in quadrant IV and that m = 3 well matched the IKV-data set in quadrant III (next slide).*

► *The provided TC3 test data set cannot really serve for a SFC material model validation.*
Questions arise w.r.t. quadrant IV: (1) Are different tests used? (2) Was the test data evaluation, regarding the specimen type, performed considering widening of the tube?

Fig.19-3: Example from [Cun04]

Mapping in the 'Tsai-Wu non-feasible domain' (quadrant III):

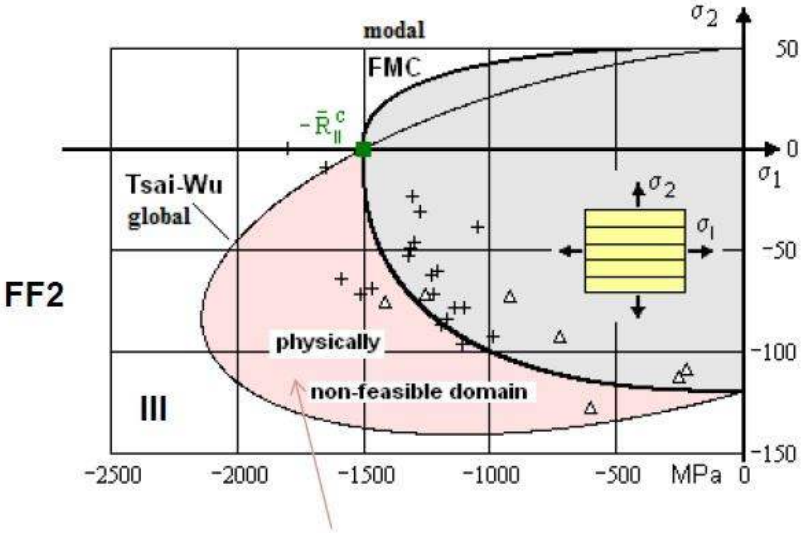

[Data, quadrant III: courtesy, Knops, IKV Aachen, 2003]

The modal FMC maps correctly, the **global** *Tsai-Wu formulation predicts a non-feasible domain !*

► *TC3 test data set does serve for validation of the SFC model in quadrant III after obtaining the IKV test results.*

Fig.19-4, WWFE-I: Test Data from Dr. Martin Knops, formerly IKV Aachen (thanks to Martin)

* WWFE-I TC3: The test data were obtained from tests on ±85° tubes. The effect of the actual winding angle of 85° instead of 90° was not considered due to the fact it will not help to overcome the test data discrepancies. This effect will slightly reduce the strength values. Another missing feature in the test data is the amount of scatter of each strength value.

*WWFE-I, TC13: Data provision of accurate data, further example: could be first mapped after having full test information obtained for Part B. The right failure strain was not given for Part A prediction, a discrepancy was found, too.

19.2.4 WWFE-II, UD lamina

In the WWFEs addressed are brittle behaving UD materials. These are materials with inherent friction - due to Mohr-Coulomb. Therefore global and modal SFCs cannot be based on uni-axial strength data only. The conditions must consider a friction parameter to accurately map the material behaviour. If the organizer cannot provide a friction parameter, then a good Part A prediction is not possible, in general. One has to estimate a value. To do this, required is the knowledge of a fracture angle or of multi-axial compression test data, see [*Cun13, Pet14*].

Of high interest for future scientists and engineers might be my assessment results of the provided properties during the author's many WWFE-designated years. These are results which stem from a very careful and effortful test data evaluation lasting about *one 'man year'* in my vacant time. Otherwise, my successful WWFE-contribution could not have been made possible! Thereby, some essential WWFE TestCase-examples for lamina-input shortcomings were found:

* WWFE-II, TC3: the same mistake happened again as with WWFE-I, TC2! However, here the much more complicated 3D-stress situation was to face, so that the 3D-transformation of the 0°-data set could be performed.

* WWFE-II, TC2 an average stress-strain curve should have been provided because otherwise no realistic treatment is possible. Therefore the Part A results could be only inaccurate. From the Part B information the author could derive an average curve and then all 3 TC test data courses could be mapped and the mutual check points in the fully connected TC2-TC3-TC4 matched. Incomprehensively, there was no response of the organizers to the author's idea, which thereby necessarily made 3 related TCs to common successful test cases.

For the complete Lamina and Laminate-TCs it is referred to the author's contribution in [*Cun13a*] and to [*Cun14a*].

19.3 Gaps and Shortfalls in the experimental data sets of the WWFE-II TCs

19.3.1 '2ndTg-effect' in the various ultrahigh-compressed TCs

In several WWFE-II Test Cases - for the used matrix materials in the CFRPs - the physically existing stiffness and strength lowering '2^{nd}-Tg effect' is active. In TC1 (isotropic matrix test specimen), however, this is unfortunately not demonstrated by the QinetiQ-well-known kink of the provided course of test data beyond a hydrostatic compression of -200 MPa. Question: Why is this true physical effect not shown and never discussed somewhere throughout the WWFE-II? The '2ndTg-effect' would have been of highest impact for TC6 and TC7. (By the way, why should the 2^{nd}Tg- effect be my novel idea as a reviewer said. I just gave this effect a name.) This effect is standard knowledge when performing tests under high hydrostatic pressures, executed for instance by Parry, DeTeresa etc., and QinetiQ, too! The author integrated the impact of this effect into his MATHCAD program. This took much time. Unfortunately in Part B, the author could not perform a calculation to show this kink because the matrix

data in TC1 did not show the effect and because the change of the failure curve of the two branches in TC 6 and 7 beyond -200 MPa is opposite, [*Cun13a*] and to [*Cun14a*].

The test cases II-TC10 and TC11 (thick-walled tube, milled from a laminated rectangular thick plate) did not show a uniform (smooth, homogeneous) stress state with a small stress gradient in the failure critical location. This multi-site failure situation increases the joint failure probability of the full test specimen, that turns to be a very complicated 'failure system'. More material volume is stressed in the vicinity of the fracture stress state which results – following Weibull - in a lower fracture failure stress and thereby in a higher failure risk. The specimen encounters multi-site damaging and failure within each lamina and multi-fold failure modes in all laminas. The pre-requisites are violated in II- TC10 and TC11.

The needed fidelity for 2D- and 3D-laminate design will be obtained after provision of the missing test data sets. Therefore, Professor Hashin's remark at a conference at Brussels (1998) "*I must say to you that I personally do not know how to predict the failure of a laminate and furthermore, that I do not believe that anybody else does*" will remain a bad message for the designing engineer from industry. We have made good progress! However, some final missing test data must be delivered by reliable tests and data evaluation.

So-called physically-based modal criteria (failure mode- based such as with Puck and Cuntze) need friction values. Standard Gobal criteria do more data fitting and do not need a friction value because they mathematically combine different failure modes, with friction and without friction. A prediction, in general, is physically not possible and not correct on basis of strength values alone. Otherwise the Mohr-Coulomb theory would not exist. In order to capture friction the global criteria need more test data points in the shear failure prone compression domain, than the modal criteria require. With modal criteria a friction value is estimated and these need just a few points within each pure failure mode domain.

19.3.2 Some Conclusions from the necessary effortful evaluation of the WWFEs

We must try our best with the test data sets we have! In WWFE-II again the provided test data packs were seen to give evidence. No discussion where this is not and where it might be not the case! So, the author draws the following conclusions from the two WWFEs:

- The existing, but missing 2nd-Tg-effect of matrices (WWFE-II TC1 beyond -200MPa) was never questioned!?.
- An invitation, to speak about the many obviously false test data, found no response at QinetiQ. Consequence: Users nowadays apply the false test data for model validation! This is a pity. One cannot validate a hopefully good failure criterion using false test data, however one can check the course of test data with an associated validated failure criterion
- The single isotropic test case was not sufficient to obtain enough knowledge for the matrix and the necessary micro-mechanical analysis. Here, QinetiQ provided just micromechanical material properties but forgot to provide with the associated micromechanical relationship. This is mandatory and therefore the author found a discrepancy of factor 2 for the data to be predicted! The description of the matrix Test Case did not fully inform whether one should use 'Mises' for a ductile matrix or 'Mohr-Coulomb' for a brittle matrix. Finally, *friction of a brittle matrix under compression and shear seemed to be assumed in WWFE-II.*
- QinetiQ demand: Does it make sense to require from a physically different failure criterion for transversely-isotropic material that it should capture the isotropic matrix failure behavior, too?
- Buckling failure seemed to have occurred in one multi-axial failure stress domain. However specimen cannot be described by a strength failure (material) condition but by a structural (stability) condition. No mapping in this domain possible

- The author still informed in WWFE-I that in TC 1 apples and oranges (90° with 0° test specimen results) have been put together. One cannot depict in the same diagram 90°-wound tube test specimen data together with 0- wound tube data. However in WWFE-II TC 2 the same mistake happened again
- Stress- or strain-based failure criteria? Stresses are used in Fracture Mechanics and allow to 'add' residual stresses in solid strength mechanics. Strains are used in forming materials like ductile metals
- Delamination is a failure in the 'structure' laminate or at its edges termed edge effect. Between the layers of a laminate it can be predicted by the application of the 3D failure criteria (here intentionally termed SFCs). At the laminate edges it is - due to the stress singularity – a task of fracture mechanics tools using cohesive zone models.
- A physically-based model cannot map a course of false test data! However, fitting procedures used in simulation can fit nearly 'every' course of test data. It just depends on the number of free parameters. So, even good mapping of a course of test data does not guarantee 'validation of a theory'.
- To apply a SFC means to address material failure. If material failure behavior is terminated and its presumption violated, then the application of a structural failure condition is required, for instance in TC12 a (micro)-mechanical structural failure condition
- Material symmetry requires the use of separate SFCs for isotropic (matrix, TC1) and transversely-isotropic UD materials! Each UD criterion must fulfil the material symmetry requirements for a transversely-isotropic UD material. This seems to be not the case for some contributing criteria
- Preliminary design: Modal SFCs require a minimum test data points in each pure mode domain. The interaction exponent *m* can be estimated on the safe side. Global SFCs need sufficient test data in the pure and in the interaction domains to perform fitting
- The nominal higher load carrying capacity or – more accurate – the higher multi-axial resistance, obtained under p_{hyd}, is the result of the favourably p_{hyd}-affected, *lowered* equivalent stress σ_{eq}. It does not rise from an *increased* uni-axial technical strength $\bar{R}$ and therefore cannot be called 'Increased strength' as often done
- Test results of a test series vary around the average value. In consequence, the course of test data points varies around an average curve, e.g. TC3, τ_{21}(phyd). A theory shall well capture the material behaviour in the technical application domain. For instance, the II-TC9 Cuntze model is valid for fracture strains smaller than 0.5%. This is still larger than usual design limit strain of 0.3%
- Most engineers assume that FF in at least one lamina of a laminate means final failure of the laminate. Therefore, the bi-axial (non-)failure envelopes for final failure of laminates predicted by the various authors do not differ that much, as long as the laminates are 'well-designed and have three or more fiber directions. The multi-axial 'strength', better resistance, of these laminates is 'fiber dominated'. Further, the predicted stress-strain curves of such laminates look very similar because the fibers, being much stiffer than the matrix carry almost the full loading. Different degradation procedures after the onset of inter-fiber failure (IFF) do therefore not influence the predicted strains very much. This is especially true for CFRP laminates.

19.3.3 Some final remarks with Lessons Learned

- *Experimental results can be far away from the reality like a bad theoretical model. Theory creates a model of the reality, 'only' and one experiment is 'just' one realization of the reality*
- *One third of the provided TC test data was at least questionable till ' not applicable' for a reliable model validation !*
- *There was a qualitative assessment of the organizers view of the respective theories but not on the*

respective data sets. My hints on non-qualified WWFE tests data sets got no response

- *Having personally spent - as a single, non-funded author - about 2 man years of my 'vacant' time in 17 years of contribution and further processing of WWFE topics:* ***If we simply accept physically not plausible test data then we do undermine the excellent WWFE efforts. Did we really exploit costly 3D test data sets for the sake of the designing engineers? Why did we not discuss obviously not reliably looking test curves? Probably the only reason is, as experienced with II-TC5, that just the hydrostatic stress was not correctly considered. For TC5, the original input test data set was re-evaluated. Might the evaluation of the basic test data of TC6 and TC7 be not also partly wrong?***
- *One should always fully indicate the test information (test specimen, test rig, etc.). The author for instance had thought about another test rig (ARCAN scissor test) in Part II A for TC10 and TC11 which led to another failure curve because another layer became failure-critical in Part A than in Part B (deTeresa torque test).*
- *For in-elastic analysis non-linear stress-strain curves are needed with a yield surface. The growing yield surface is confined by the fracture failure surface*
- *Principally, just the lamina test cases II-TC2 through TC7 are directly applicable for validating the UD-FMC-based strength failure conditions. The laminate test cases II-TC8 through TC12 can 'only' serve as benchmarks for verification of the full failure theory, where the SFCs are just one part of. In each TC the investigation of the influence of wall-thickness on hoop stress is mandatory.*
- *Providing micro-mechanical properties (necessary to capture the '2ndTg-effect') is obsolete without providing the associated micromechanical formulas where these properties were determined with. It is a closed system! The organizers did not pick up this point, from my response. That made the author much fitting work because he had to use own micro-mechanical formulas. Adjusting them, of course, was no full success.*
- *A physically based modal strength condition just maps one single failure mode*
- *Full validation of a theory is possible with reliable test data, only*
- *The normal user is just interested to well map his course of failure test data by a SFC.*

19.3.4 Open or closed failure surface? A recurring question in WWFE-II

The ends of a failure surface (body) are always the result of the acting multi-axial stress state. In the tensile cap domain this always leads to a closed surface wherever for the multi-axially compressed bottom this may happen or not happen. Modal strength criteria do just capture one failure mode and in the closing usually the same failure mode acts two-fold or three-fold. This has to be considered! Otherwise it is a *global test data fit* and not a *physical mapping*. If the material has no pores (dense), which is the assumption in the WWFEs for UD-material then it is differently treated to the porous material where the ends are always closed. Therefore, any judgement whether the surface is open or closed cannot be performed if the specimen consistency is not clearly given.

Closed and open failure envelopes:

TC1: closed;
TC2, TC3: closed, by material failure 'kinking' FF2 leading to structural (instability) failure;
TC4: not applicable;
TC5: closed;
TC6, TC7: theoretically open;
TC8, TC10, TC11: closed;
TC12: not applicable.

In contrast to a dense isotropic material a dense UD material might fracture under a very high hydrostatic compression stress ($\sigma = -p_{hyd}$), according to the Poisson effect which makes the filament strain (TC5) to reach the fracture strain $e_{||}^{c} = p_{hyd} \cdot (1 - 2 \cdot \nu_{\perp||}) / E_{||}$ under the pre-requisite $2 \cdot \nu_{\perp||} < 1$. The failure surface is therefore closed.

19.4 WWFE-II, ranking and the citation" *Cuntze's SFC-set needs 75 parameters*" [*Kad13*]

*"For his set of 5 modal UD failure criteria Cuntze needs **75 parameters".*** This fully mixes up apples and oranges". (I can never believe that you Sam formulated this! Unfortunately you are the main author).

The reality is: *Necessary are just **7 measurable model parameters** (5 strengths + 2 friction values) and **1** chosen **interaction exponent m**, a value derived from more than 25 years of mapping experience with isotropic, transversely-isotropic and orthotropic materials. A small value of m = 2.5 is on the safe side, because it smoothens the transition zone between two modes harsher, which means a more inside rounding.*

One might value this as a 'Damage to reputation' because respected colleagues like Christensen have taken the value 75 for contra-argumentation of my SFC set.

In this context it is to note:

*Counting parameters of the SFCs is a comparison of apples and oranges. If an author employs more theoretical subjects than another contributor, then, one counts more parameters.

Of practical relevance is:

Which SFC is the most reliable one and has a minimum number of parameters, and, can all the model parameters be measured or estimated like m and μ?

*Failure envelopes are not just an empirical fit through uniaxial tensile and compressive strength points as it was still assumed in the WWFE-I and –II, further! Friction is acting. For all those contributors which did not perform all required tasks a smaller number of parameters has been counted, of-course.

*Ranking the contributing SFCs on basis of insufficient test data input is not helpful, like for the WWFE-II-Part A contributions. One can just compare Part B-mappings of the reliable Test Cases and further recognize each contributor's enhancements to improve mechanical understanding which shall support further scientific progress. And, adding Part A predictions to Part B results on the same graph makes no sense if a change occurred to B. And further not, if necessary parameters such as the friction parameters have not been provided in A

* **Viewing the final papers of the WWFE-organizers**

"*A comparison of the predictive capabilities of current failure theories for composite (UD-composed) laminates, judged against experimental evidence*" and "*Maturity of 3D failure criteria for fiber-reinforced composites, comparison between theories and experiments*", **there is not any doubt to find concerning the quality of the only available, provided test data** despite of warnings from me and other contributors. (Nevertheless again: Many thanks to QinetiQ)

* It was very astonishing for me that the WWFE organizer QinetiQ thought that the isotropic matrix Test Case 'WWFE-II, TC1' could be treated by a transversely-isotropic UD-SFC.

* Organizers did not question the test data but required mapping of false ones.

……..

WWFE-I:

The private contributors Cuntze and Puck collected the most points and ranked top. The SFC models of Puck and Cuntze are most probably those SFC models, which are best validated by 2D and the few 3D UD experiments.

WWFE-II:

No clear assessment of the contributing SFCs. See above comments.

19.5 WWFE-provided Mechanical Properties of the UD laminas

Fibre type	IM7	T300	A-S	S2-glass	E-Glass
Matrix	8551-7	PR-319	Epoxy1	Epoxy2	MY750
Fibre volume fraction V_f (%)	60	60	60	60	60
Longitudinal modulus E_1 (GPa)	*165**	*129*	*140**	*52*	*45.6*
Transverse modulus E_2 (GPa)	*8.4*	*5.6+*	*10*	*19*	*16.2*
Through-thickness modulus E_3 (GPa)	8.4	5.6+	10	19	16.2
In-plane shear modulus G_{12} (GPa)	*5.6**	*1.33+*	*6**	*6.7**	*5.83**
Transverse shear modulus G_{13} (GPa)	5.6*	1.33+	6*	6.7*	5.83*
Through-thickness shear modulus G_{23} (GPa)	2.8	1.86	3.35	6.7	5.7
Major Poisson's ratio υ_{12}	*0.34*	*0.32*	*0.3*	*0.3*	*0.28*
Major transverse Poisson's ratio υ_{13}	0.34	0.32	0.3	0.3	0.28
Through-thickness Poisson's ratio υ_{23}	*0.5*	*0.5*	*0.49*	*0.42*	*0.4*
Longitudinal tensile strength X_T (MPa)	*2560*	*1378*	*1990*	*1700*	*1280*
Longitudinal compressive strength X_C (MPa)	*1590*	*950*	*1500*	*1150*	*800*
Transverse tensile strength Y_T (MPa)	*73*	*40*	*38*	*63*	*40*
Transverse compressive strength Y_C (MPa)	*185***	*125***	*150***	*180***	*145***
Through-thickness tensile strength Z_T (MPa)	63	40	38	50	40
Through-thickness compressive strength Z_C (MPa)	185**	125**	150**	180**	145**
In-plane shear strength S_{12} (MPa)	*90***	*97***	*70***	*72***	*73***
Transverse shear strength S_{13} (MPa)	90**	97**	70**	72**	73**
Through-thickness shear strength S_{23} (MPa)	57	45	50	40	50
Longitudinal tensile failure strain ε_{1T} (%)	*1.55*	*1.07*	*1.42*	*3.27*	*2.81*
Longitudinal compressive failure strain ε_{1C} (%)	*1.1*	*0.74*	*1.2*	*2.21*	*1.75*
Transverse tensile failure strain ε_{2T} (%)	*0.87*	*0.43*	*0.38*	*0.33*	*0.246*
Transverse compressive failure strain ε_{2C} (%)	*3.2*	*2.8*	*1.6*	*1.5*	*1.2*
Transverse tensile failure strain ε_{3T} (%)	0.76	0.43	0.38	0.263	0.25
Through-thickness compressive failure strain ε_{3C} (%)	3.2	2.8	1.6	1.5	1.2
In-plane shear failure strain γ_{12u} (%)	*5*	*8.6*	*3.5*	*4*	*4*
Transverse shear failure strain γ_{13u} (%)	5	8.6	3.5	4	4
Through-thickness shear failure strain γ_{23u} (%)	2.1	1.5	1.5	0.59	0.88
Longitudinal thermal coefficient α_1 (10^{-6}/°C)	-1	-1	-1	8.6	8.6
Transverse thermal coefficient α_2 (10^{-6}/°C)	18	26	26	26.4	26.4
Through-thickness thermal coefficient α_3 (10^{-6}/°C)	18	26	26	26.4	26.4
Energy release rates G_{Ic}, G_{IIc} ($J/m^2 = 1N/m$) mixed (fracture mechanics) mode to be assumed	200				240, 1500
Stress free temperature (°C)	177	120	120	120	120
Test Case	TC10,11,12	TC2,3,4	TC7	TC6	TC1,5,8,9

* Initial modulus.

** Nonlinear behaviour and stress strain curves and data points are provided

\+ These values are considered to be low, compared with typical data for the same material published somewhere else or quoted by the manufacturers. QinetiQ has not attempted to change them in order to facilitate a comparison with test data in Part B.

20 Laminate 2D-Design with Tsai's 'Omni Failure Envelopes'

Aim: *Replacing the ply-by-ply proof of multiple-ply laminates by a much simpler method*

Steve Tsai's idea was to by-pass the effortful ply-by-ply analysis of multiple-ply laminates by using a so-called 'Omni-(principal FPF strain) failure envelope'. This envelope surrounds an intact Non-FirstPlyFailure (FPF) area whereby FPF includes Fiber Failure FF and Inter-Fiber-Failure (IFF).
Such an 'Omni failure envelope' is to determine for each composite material, applying a FPF-Strength Failure Criterion (SFC), and will capture all possible laminate stacks. Naturally, the used SFC significantly determines the shape of the envelope, see *Fig.20-1*.

Dimensioning is performed by showing that the design loading-caused principal strains are lying within the Non-FPF area. This idea can serve as a very practical Pre-design tool!

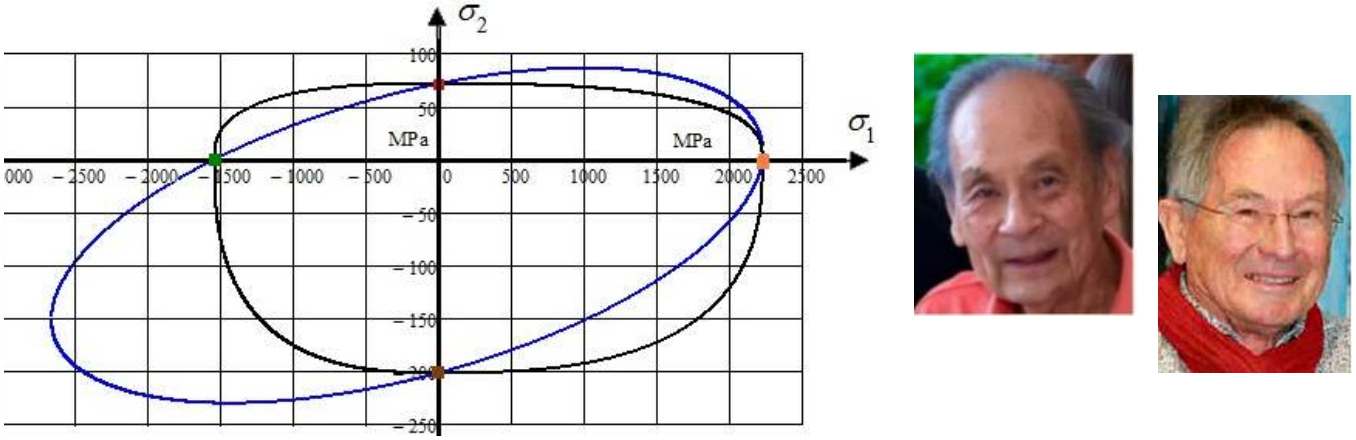

Fig.20-1: Cross-section $\sigma_2(\sigma_1)$ of the failure body, Tsai-Wu versus Cuntze. (Steve and me)

20.1 Tsai's indirect Determination of the 2D 'Omni principal FPF strain failure envelope'

Fig.20-2 displays different 'butterflies' (*name, how the author Cuntze termed the bundle of **i** FPF-curves)*, derived using the SFCs of Tsai-Wu and Cuntze). These numerical results of the FPF-linked principal strain curves clearly depict the significant effect of the chosen SFC, see above figure.
The different lateral properties determine the shape (wing edge) of the obtained symmetric 'butterfly wing' with its single, grey-marked principal strain curves, provided by E. Kappel.

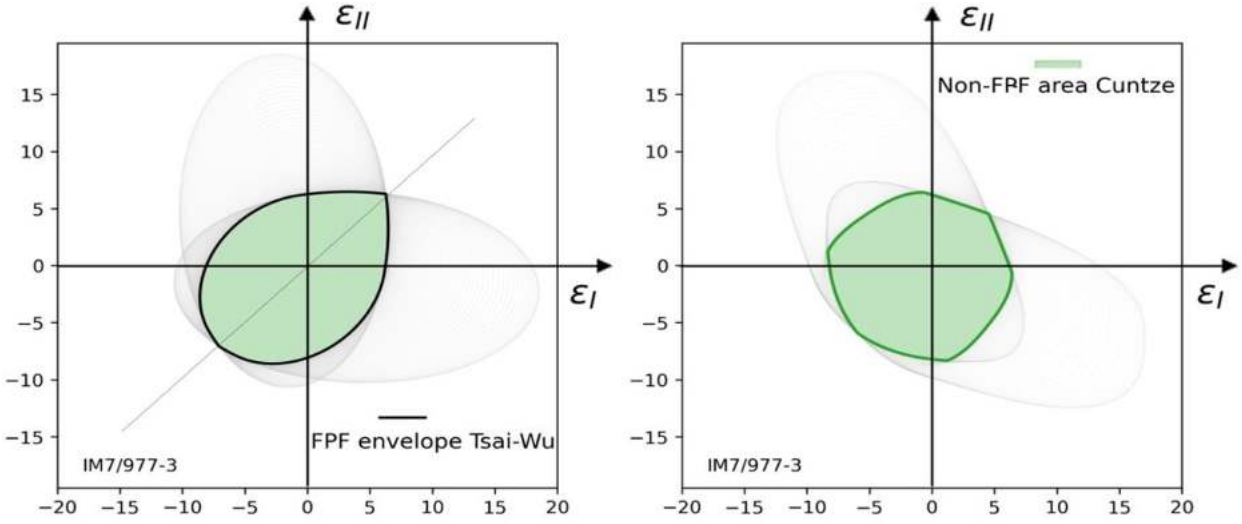

Fig.20-2, bundle of all FPF envelopes = 'butterflies veins': All ply FPF-envelopes enclosing a non-FPF failure area; 0°< α < 90° (91 ply angles). Principal strain in ‰, suffix FPF is skipped. CFRP IM7/977-3.

In all pictures: (left) Tsai-Wu with $\mu_{\perp\parallel} = 0$, $F_{12} = -0.5$ *and (right) Cuntze with* $\mu_{\perp\parallel} = 0.2$, $m = 2.7$

Barely visible are the ‘butterfly veins’ in *Fig.20.2* (outside), the internal Non-FPF area is green shadowed.

20.2 Cuntze’s Determination of the 2D ‘Omni Envelope’

The derivation of such an ‘Omni failure envelope’ is pretty effortful and no direct formulation could be found in the past. Recently, this bottleneck could be by-passed by an idea of the author, who examined various horizontal cross–sections τ_{21} = constant of the UD-FPF fracture body in *Fig.20-3* below. He found that τ_{21}=0 delivers the smallest Non-FPF area.

► Pre-Dimensioning can now be performed by showing that the design loading-caused principal strains are located within the Non-FPF area, a simpler pre-design of arbitrary laminates is possible.

.

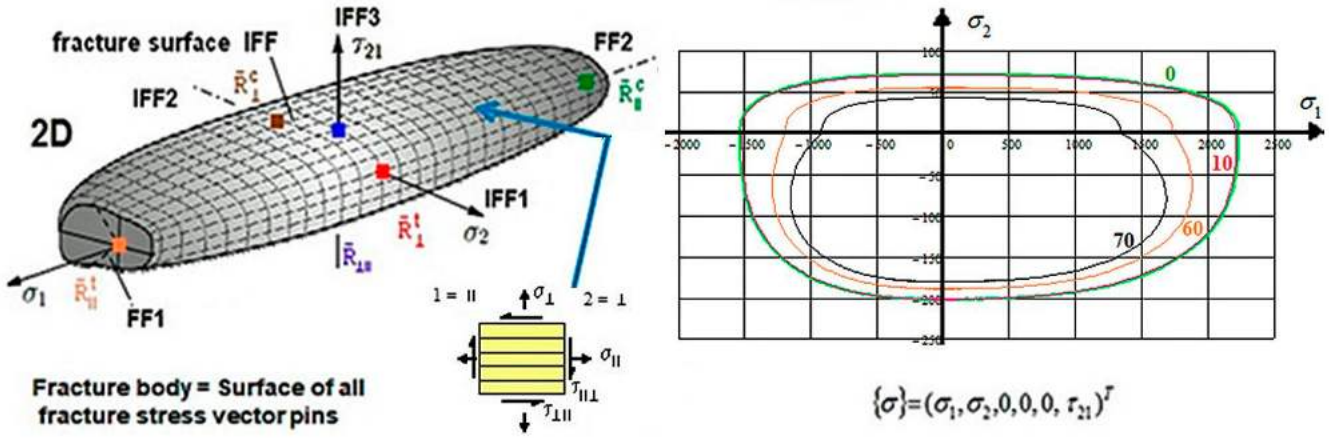

Fig.20-3: (left) 3D UD Failure body. (right) FPF-envelopes for 3 planes τ_{21}= const. CFRP IM7/977-3

Fig.20-4 (left) presents the resulting Omni principal strain FPF curves $\varepsilon_{II}(\varepsilon_I)$ with a not unambiguously solution $\varepsilon_{II}(\varepsilon_I)$ for parameter levels τ_{21} = const. → The failure curve $\sigma_2(\sigma_1, \tau_{21}=0)$ describes the ‘Omni envelope’.

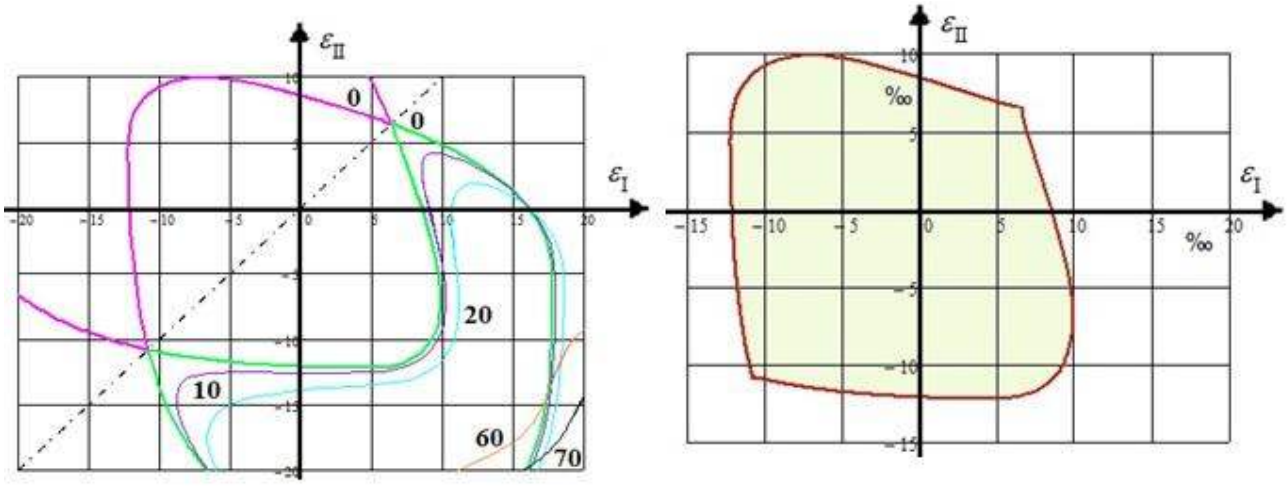

*Fig.20-4: Mirrored envelope of the N**on-FPF area** (Cuntze procedure), CFRP IM7/977-3*

Originally, the ‘second’ solution-linked additional outer curve parts were excluded in the graph and the right figure eventually shows the ‘cleaned-up’ envelope, representing the limit *Eff* = 100%, enveloping the Non-FPF area. The cleaned-up graph is identical to the Non-FPF area obtained by the standard Tsai ‘butterfly’-determination procedure. Domains of the envelope could be dedicated to the locally faced failure mode types FF and IFF.

In a novel investigation, detailed in *Table 20-1*, Cuntze could give a complete look of the different envelopes in *Fig.20-4* (*left*). For optical comparison reasons E. Kappel 'traditionally' provided the 'butterfly wing' procedure plots for *Fig.20-4* (*right*) and *Fig.20-5*.

Table 20-1: Procedures, how to obtain the material reserve factor f_{RF}

SFC Cuntze: Failure Function $F\left(\{\sigma\},\{\bar{R}\},\mu \text{ directly}\right)=1$

$$Eff_{FPF}=[(Eff^{||\sigma})^m+(Eff^{||\tau})^m+(Eff^{\perp\sigma})^m+(Eff^{\perp||})^m+(0)^m]^{m^{-1}}=1,\ m=2.7$$

Input

$$\{\sigma\}=(\sigma_1,\sigma_2,\sigma_3,\tau_{23},\tau_{31},\tau_{21})^T\rightarrow(\sigma_1=900\ ,\sigma_2=20\ ,0,\ 0\ ,0\ ,\tau_{21}=25)^{\mathrm{T}}\text{MPa},$$

$$\{\bar{R}\}=(\bar{R}_{||}^t,\bar{R}_{||}^c,\bar{R}_{\perp}^t,\bar{R}_{\perp}^c,\bar{R}_{\perp||})^{\mathrm{T}}\rightarrow(2230,537,71,202,78)^{\mathrm{T}}\ \text{MPa},\ \mu_{\perp||}=0.2.$$

$\{\sigma\}$-loading-caused ply strains and loading-reperesenting principal strains

$$\varepsilon_1=s_{11}\cdot\sigma_1+s_{21}\cdot\sigma_2,\ \varepsilon_2=s_{21}\cdot\sigma_1+s_{22}\cdot\sigma_2,\ \gamma_{21}=s_{66}\cdot\tau_{21}$$

$$\varepsilon_I=0.5\cdot\left[(\varepsilon_1+\varepsilon_2)+\sqrt{(\varepsilon_1-\varepsilon_2)^2+\gamma_{21}^2}\right],\ \varepsilon_I=0.5\cdot\left[(\varepsilon_1+\varepsilon_2)-\sqrt{(\varepsilon_1-\varepsilon_2)^2+\gamma_{21}^2}\right]$$

$$\varepsilon_I=0.0083\equiv\text{UD}\varepsilon\text{I},\ \varepsilon_{II}=f_\varepsilon\cdot\varepsilon_I=0.0009,\ f_\varepsilon=\varepsilon_{II}/\varepsilon_I=-0.109.$$

*Stress Procedure Cuntze: Lamina task, solved by ply-by-ply failure analysis

$$Eff^m=[(Eff^{||\sigma})^m+(Eff^{||\tau})^m+(Eff^{\perp\sigma})^m+(Eff^{\perp\tau})^m+(Eff^{\perp||})^m]\ \text{with the mode portions inserted,}$$

$$Eff=\left[\left(\frac{(\sigma_1+|\sigma_1|)}{2\cdot\bar{R}_{||}^t}\right)^m+\left(\frac{(-\sigma_1+|\sigma_1|)}{2\cdot\bar{R}_{||}^c}\right)^m+\left(\frac{\sigma_2+|\sigma_2|}{2\cdot\bar{R}_{\perp}^t}\right)^m+\left(\frac{-\sigma_2+|\sigma_2|}{2\cdot\bar{R}_{\perp}^c}\right)^m+\left(\frac{|\tau_{21}|}{\bar{R}_{\perp||}+0.5\cdot\mu_{\perp||}\cdot(-\sigma_2+|\sigma_2|)}\right)^m\right]^{1/m}$$

$$\rightarrow\ Eff=0.513\ \Rightarrow\text{material reserve factor}\ \ f_{\mathrm{RF}}=1/Eff=1.95.$$

*Principal Strain Procedure Cuntze: classical laminate task, solved by a laminate failure analysis; $\tau_{12}=0$

Due to $\varepsilon_1=\varepsilon_I$, $\varepsilon_2=\varepsilon_{II}$ for the 2 failure determining stresses follows, $\gamma_{21}=0$

$\sigma_1=(s_{21}\cdot\varepsilon_2-s_{22}\cdot\varepsilon_1)/(s_{21}^2-s_{11}\cdot s_{22})$ and $\sigma_2=(\varepsilon_2-s_{21}\cdot\sigma_1)/s_{22}$ which is to insert into the FPF-criterion-based 'Omni principal strain failure envelope' formula

$$\left(\frac{(\sigma_1+|\sigma_1|)}{2\bar{R}_{||}^t}\right)^{\mathrm{m}}+\left(\frac{(-\sigma_1+|\sigma_1|)}{2\bar{R}_{||}^c}\right)^{\mathrm{m}}+\left(\frac{\sigma_2+|\sigma_2|}{2\bar{R}_{\perp}^t}\right)^{\mathrm{m}}+\left(\frac{-\sigma_2+|\sigma_2|}{2\bar{R}_{\perp}^c}\right)^{\mathrm{m}}+(0)^m=1=100\%\ .$$

With the chosen SFC the $\rightarrow$ Non-FPF area $\varepsilon(\sigma_{FPF})$ is to derive .

On the strain beam $f_\varepsilon=\dfrac{\varepsilon_{II}}{\varepsilon_I}=\dfrac{\varepsilon_{II,\mathrm{FPF}}}{\varepsilon_{I,\mathrm{FPF}}}$ it will be finally obtained

$$f_{\mathrm{RF}}=\sqrt{\left(\varepsilon_{I,\mathrm{FPF}}^2+\varepsilon_{II,\mathrm{FPF}}^2\right)}/\sqrt{\left(\varepsilon_I^2+\varepsilon_{II}^2\right)}=\varepsilon_{I,\mathrm{FPF}}/\varepsilon_I=1.06\ .$$

20.3 Pre-design Example using the 'Omni Non-FPF area' and Determination of Reserve Factors

Of highest interest is the reserve factor which must be smaller for a simplified design method than obtained by the classical 'Ply-by-ply procedure', thus remaining on the Safe Side. Laminate Design Verification is traditionally performed by above 'ply-by-ply' analysis, assessing the obtained ply (lamina) stresses $\{\sigma\}$ in the critical location of the most critical plies. Now, a simpler more global assessment is possible (*Table 20-2*) by using the in-plane principal strains of the laminate, strains which represent the loading.

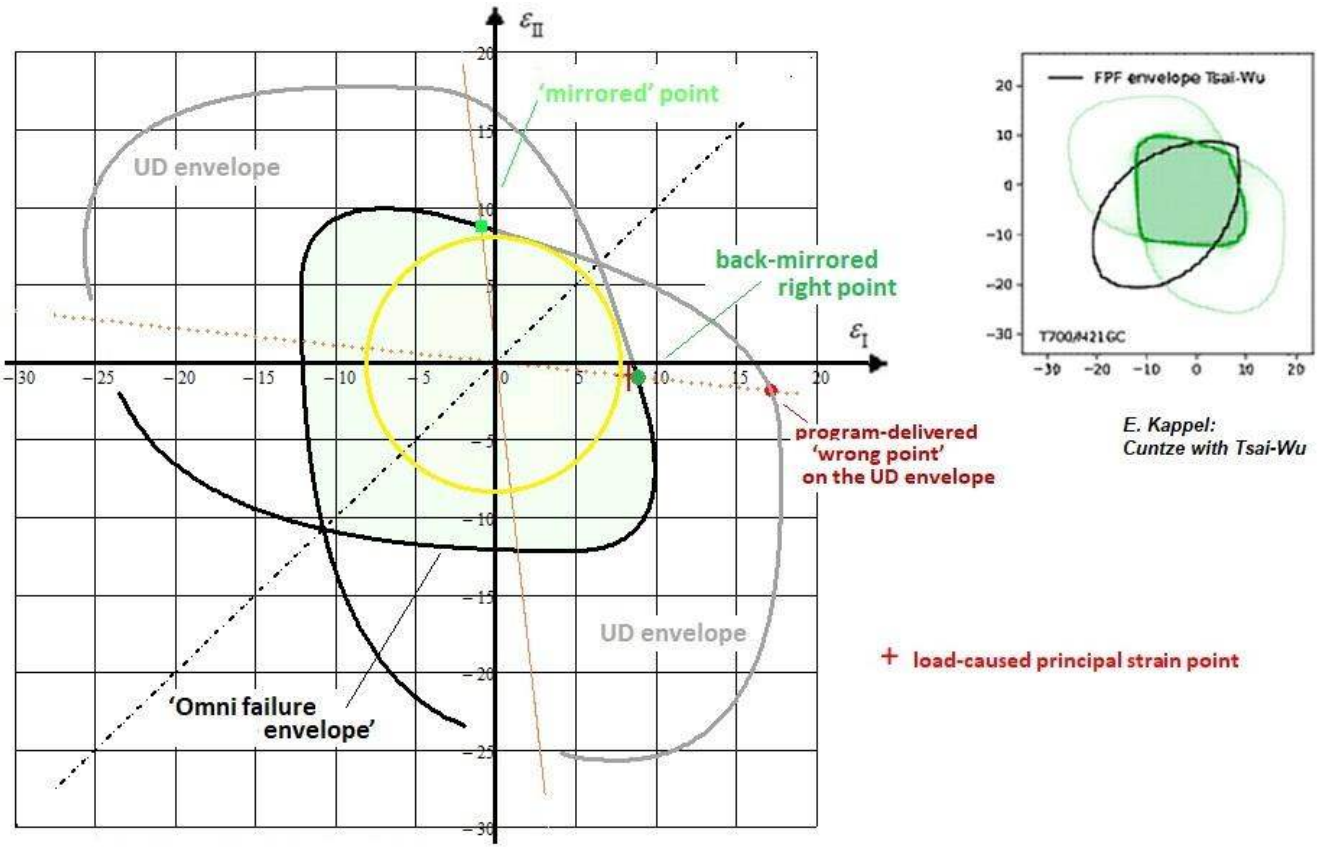

Fig.20-5: (left) Various envelopes of the Non-FPF area (Cuntze procedure following Principal Strain Procedure Cuntze in Table 21-1). (right up) 'Butterfly' and Non-FPF area applying the SFCs of Tsai-Wu and Cuntze

*Table 20-**2:** Procedure of checking a probably critical design stress state*

A Non-FPF area within an 'Omni failure envelope' is given for the chosen laminate material
➢ FEA delivers the maximum state of the 3 strains of the laminate stack
➢ Transformation into the 2 principal strains as coordinates of the Non-FPF area
➢ Check, whether the strain point lies $(\varepsilon_I, \varepsilon_{II})$ within the envelope or Non-FPF area
➢ Determine material reserve factor f_{RF} = vector length ratio of *failure strain/design strain.*

Such principal strains are a standard output of modern FE software. They are mathematical and not material symmetry-linked quantities.

Remember, please, that the execution of the Design Check runs under the Presumption:

"*Linear Analysis, 'proportional stressing concept', $\sigma \sim \varepsilon$ is permitted*".

Cuntze's direct determination of the 'Omni failure envelope' enables to determine the reserve factor straightforward instead of using the *Non-FPF* internal circle - yellow in *Fig.20-5* and green in *Fig.1* of the presentation - how it was usually performed up to now, see [*Cun24a, c*].

However, there was a solver computational problem:

Mathcad unfortunately delivers a principal failure strain value ε_{FPF} outside of the Non-FPF area as result of its solution process. The other solution seems to be received, if a shear strength is involved. This wrong point value can be localized on the UD 'butterfly wing' edge in *Fig 20-4* and this enabled to successfully use the symmetry of the envelope as it is executed in *Fig-20-5*.

Now, Design Verification can be performed as described below:

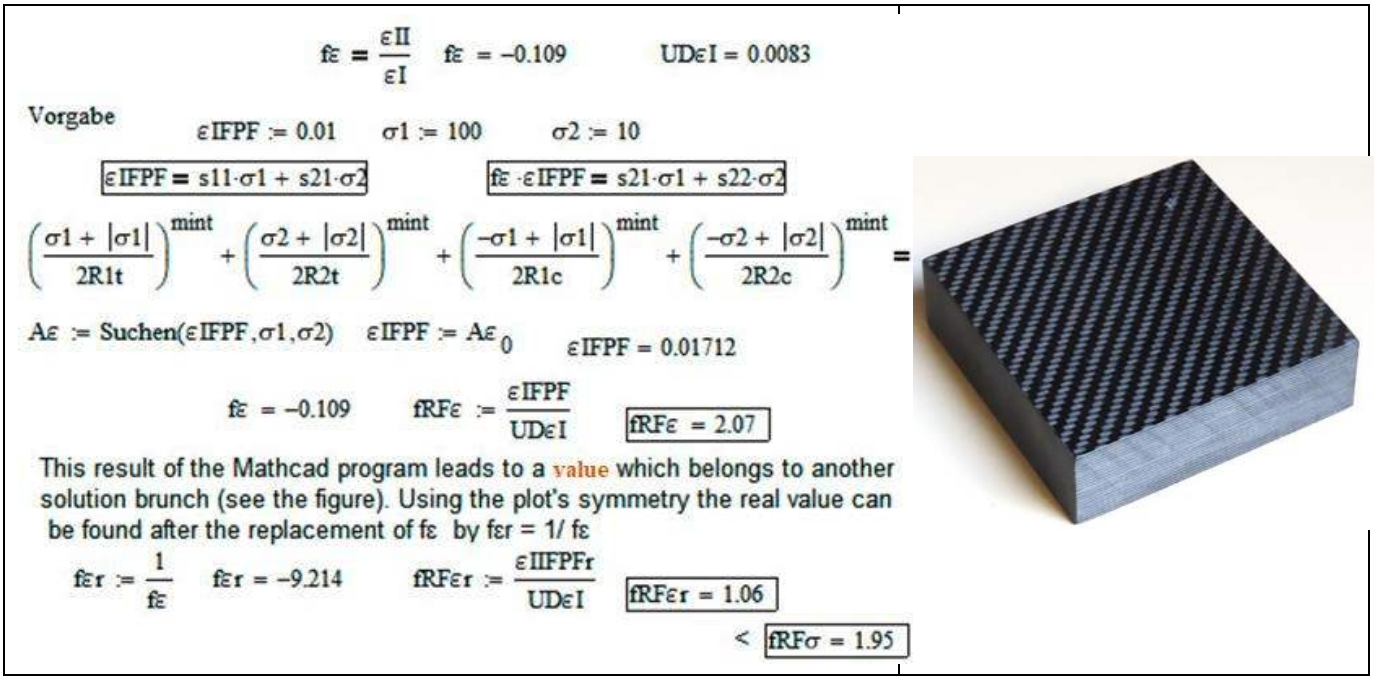

Fig.20-6 Successful implicit computation of f_{RF} *after utilizing the plot's symmetry (code Mathcad 15),* $\varepsilon_I \equiv UD\varepsilon_I$.

Note, once again please:

Tsai's 'Omni principal strain envelope' principally surrounds a Non-FPF or even a Non-LPF area.

*FPF is required if the design requirement asks to fulfill a First-Ply-Failure in the critical locations of the plies of the laminate.

*LPF, if to apply, is required to fulfill a Last-Ply-Failure limit. However, this usually involves a non-linear analysis up to the ultimate failure load of the structural part.

In order to cope with the reserve factor definition these shall be sketched again below:

$$\text{About 'linear' FPF, then a stress-defined } f_{\mathrm{RF}} = \frac{\text{Strength Design Allowable } R}{\text{Stress at } j \cdot \text{Design Limit Load}} > 1$$

LL:

* The method is more or less a linear method.
* The investigation of various cross–sections τ_{21}=constant, proved, that τ_{21}=0 delivers the smallest Non-FPF area, thus making a simpler pre-design of arbitrary laminates possible
* Basic result: The principal strain approach delivers the required smaller reserve factor compared to the conventional ply-by-ply stress-based procedure. → The approach is 'on the safe side' **!**

For completion:

for above not unusual thick multi-ply laminate an associated Abstract for the annual "Munich Symposium on Lightweight Design 2025" is displayed below.

Engineering Strength Assessment of UD-multiply-composed Elastic Laminates

Ralf Cuntze, Prof. Dr.-Ing. habil., supported by Erik Kappel, Dr.-Ing.***
** Retired from industry, MAN-Technologie, Augsburg, Germany*, Ralf_Cuntze@t-online.de
*** Institute for Lightweight Systems (SY), German Aerospace Center (DLR), Braunschweig*

In practical multiply-laminate development there are to capture so-called 'Quad-stacked' laminates of the (0 / 45/90/-45)-family and Tsai's novel 'Double-Double-stacked' laminates of the $\{\varphi/-\psi/-\varphi/\psi\}$-family (*NCF, stitched layers product).* Due to the fact, that these laminates are just in-plane loaded it is very helpful for a structural engineer to have 2D Design Sheets, at least for checking Finite-Element-Analysis results of arbitrarily-stacked multi-ply laminates. Since strength failure envelopes significantly depend on the applied Strength Failure Criterion (SFC) exemplarily two SFCs, those of Tsai-Wu and Cuntze are examined, which requires a challenging transformation of the Tsai-Wu SFC into the more often used notation of the *VDI 2014 guideline*.

An idea of Stephen Tsai is followed on 'Designing Laminates to First-Ply Failure (*FPF*)', which includes Fiber Failure (FF) and Inter-Fiber-Failure (IFF) and thereby marks the 'Onset-of-fracture'. When realizing this, failure stress-based 'Omni-(principal strain) failure envelopes' (*term from S.Tsai*) are to derive. These envelopes surround the intact 'Non-FPF area'. The process requires that combinations of each ply orientation angle with principal strain ratio (here 361, chosen 1°-increment) are to evaluate. Thereby the smallest reserve factor determines the FPF limit and thereby generates one point on the bias-symmetric envelope. Each computation represents a faint 'vein' in *Fig.1,* ($‰$). The principal strain approach delivers the required smaller *laminate* reserve factor compared to the conventional ply-by-ply stress-based procedure with its minimum *ply* reserve factor. The approach is 'on the safe side' if $f_{RF}^{lam} < \min f_{RF}^{ply}$!

The determined Non-FPF areas are further reduced to an internal circle in order to find a FPF-limit-defining envelope-function for the computation of the laminate reserve factor. The circle's radius depends on the principal strain magnitude $r = min\sqrt{\varepsilon_I^2 + \varepsilon_{II}^2}$. Cuntze sorted out a function for the envelope, because he found that $(\sigma_{\parallel} = \sigma_1, \sigma_{\perp} = \sigma_2, \tau_{\perp\parallel} = \tau_{21} = 0)$ defines it. This means that the full area can be exploited for f_{RF}^{lam}, not just the internal circle area, *Fig.2*.

A thereon based design sheet would enable to reduce the effort for Design Dimensioning.

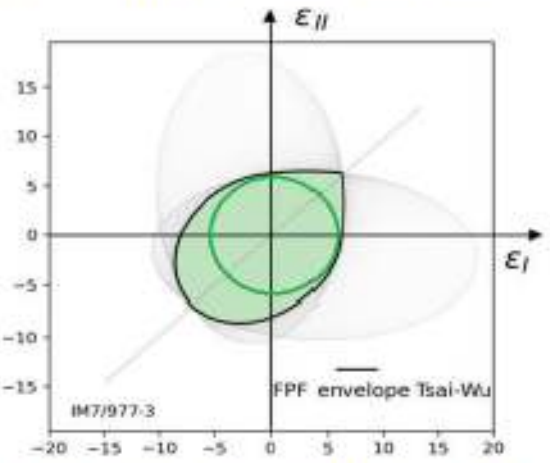

Fig.1:Faint 'Veins' of all computations for IM7/977-3 forming the merely visible veins of a butterfly's wing

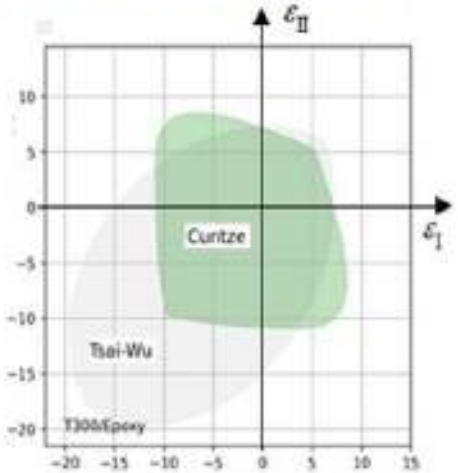

Fig.2: SFC-dependent Non-FPF areas for T300/Cytec (Tsai-Wu bottleneck in negative domain)

21 Investigation on Criticality of Carbon Fiber Micro-Fragments and Dusts

Matter of my heart: Supporting the application of sustainable carbon concrete *with no-risk PAN-CFs in the production of structural parts in construction.* CFR-Plastic/CFR-Concrete?

21.1 General

Carbon Fibers (CFs) usually are produced using the precursors PolyAcryloNitrile (PAN) and Pitch.

Problem and question: Machined Pitch CFs generated many toxic split-up fiber fragments. What about the PAN-based CFs? They can be classified into the types: intermediate-modulus (IM), high-modulus (HM) and ultrahigh-modulus (UHM), whereby UHM-CFs seem to show some and the lower modulus Standard PAN no hazard. These facts ask for an investigation of the UHM-CF with the objective to finally sort out that the use of the less '*risky*' Standard PAN CF causes no threat.

Inhaled particles with its size, geometric shape and contaminants adhering to the surface are relevant for a health effect. Of course, targeted workplace prescriptions always have to counteract the occurrence of excessive stress on the lungs from inhaling too large amounts. Respirable bio-persistant particles accumulate in the alveoli of the lungs. These so-called 'WHO fibers' pierce the macrophages in the lungs and can migrate into the abdomen and pleural tissues and cause cancer.

This Chapter is an Excerpt from the private elaboration [*Cun23d*]* *Gedanken eines faseranwendungserfahrenen Ingenieurs zum Umgang mit Faser-Mikrobruchstücken und Feinstäuben bei Herstellung und Recycling faserverstärkter Bauteile*], 80 pages

CF application in Construction

As structural engineer, who has founded and led two working groups in the carbon concrete sector for 10 years: "*It is my deep wish to use more fatigue-resistant [VDI2014] PAN-CF in the construction industry in order to increase the life of bridges and to save concrete, a composite material, which has a negative CO_2 footprint due to the necessary clinker (cement constituent) production*."

Fig.21-1 displays a CFRP application 'Fiber grid (*mat*)' as a slack reinforcement (*no pretension*) of a bridge:

Fig.21-1: Bridge Wurschen, 2022: (left) Superstructure made exclusively of carbon concrete, shell construction. (right) Textile FRP mats in the super-structure) (Foto: Stefan Gröschel, IMB,TU Dresden)

21.2 Carbon Fiber Production

CF-properties strongly depend on the production process and above precursors which need different conditions but the essential processes are similar. A CF requires a heating and stretching treatment to get the high strength products. A thermoset treatment is first applied in the temperature range from 200 to 400 °C in air under stretching to get the stabilized fiber, followed by a carbonization process in the temperature range from 800 to 1500 °C in oxygen-free condition to remove impurities and to improve

the crystallinity of carbon. To further improve the performance of CFs, a graphitization process is required to graphitize carbonized fibers with temperature up to 3000 °C. During these processes, stretching is required to get preferred orientated carbon crystals, because the crystal alignment makes the fiber incredibly strong and stiff. The graphitization process leads to differences between PAN and Pitch and within the PAN-CFs.

The very expensive Pitch CF is mainly used in spacecraft and antennas. The market is dominated by the PAN-CF. With regard to possible toxic fragments, PAN-CF (Ø 7 µm, usually) is therefore of interest, especially the 'highly' graphitized UHM-PANCF such as Torayca's M60J, which comes next to the Pitch-CF considering the tensile modulus (stiffness). CF tensile modulus and fracture toughness naturally depend on the fabrication regarding precursor, on carbonization and graphitization. Furthermore, Pitch-CFs are more layer-like in their crystal structure in contrast to the more granular PAN-CF. This probably further explains the higher tensile modulus compared to the PAN-CF. Knowing the different crystal structure is therefore important for explaining the splintering process, originator of possible toxic fragments.

21.3 WHO-‘Fiber’ hazard criticality

WHO criterion for respirable fibers: ‘WHO-Fiber‘

≡ tiny fragment of a filament with a diameter Ø of less than 3 µm, a length L of greater than 5 µm and a length-to-diameter ratio of L/Ø > 3:1.

About using the name WHO fiber*:*

(1) Does not address a long CF, which of course never meets the WHO criterion.

(2) Asbestos fiber, for example, is just a fiber-like looking particle, a fluff, which may break into above tiny WHO-size fragments).

Too many dust-related particles, smaller than the WHO 'fiber' size, can also cause a hazard. A so-called Particulate Matter of the µm-size PM2.5 can penetrate into the alveoli and ultrafine particles with a diameter of less than 0.1 µm (*Corona virus size level*) can even penetrate into the lung tissue.
Aerosol particles from the environment have diameters ranging from about 1 nanometer (nm) to several 100 micrometers (µm). Larger particles quickly sink to the ground, particles smaller than 10 µm can remain in the air for days.

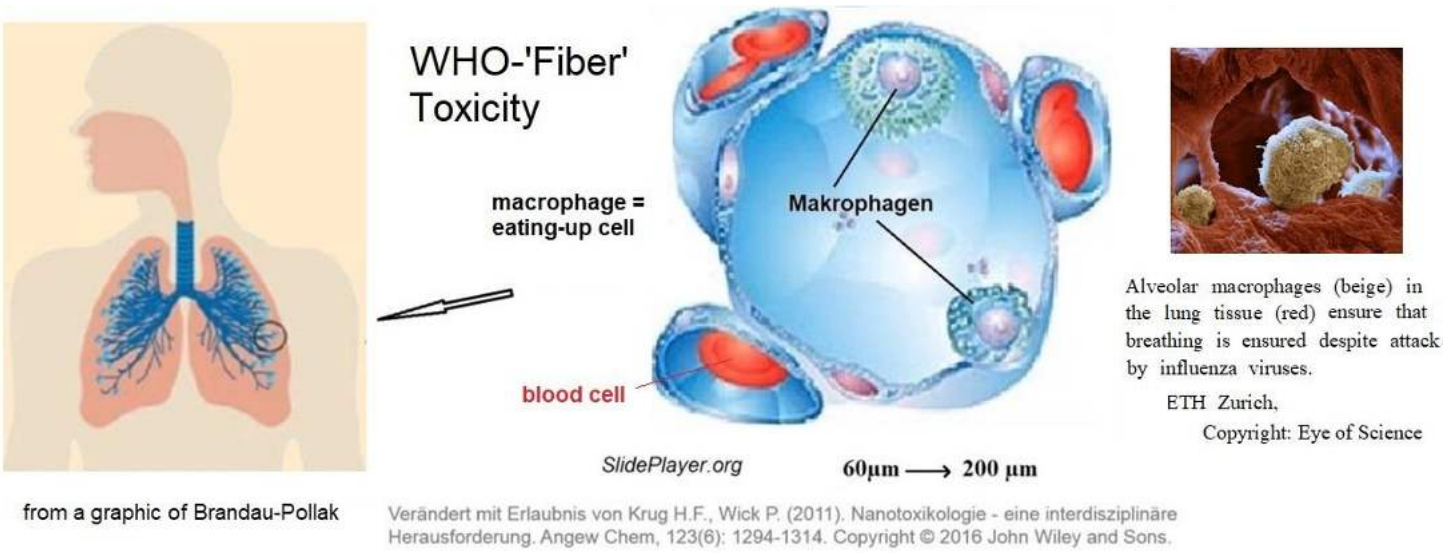

Fig.21-2: Effect of WHO-‘Fibers'

The figure above summarizes the topics faced when considering the criticality.

Essential for the risk assessment is that the macrophage lifespan of a few weeks is a decisive factor for the success of disposal or 'cleaning'. ‘WHO-fiber’-pierced macrophages usually die.

Looking generally at criticality a distinction must be made between long fibers, micro-fragments of fibers such as the ‘WHO-fiber' size, as well as the micro-fragments of composite constituents, i.e. fiber-reinforced polymers FRP or fiber-reinforced concrete FRC. In addition to the fiber, the matrix with the interphase material in the fiber-matrix interface must be considered, too.

Criticality-relevant variables are geometry and bio-resistance:

Geometry: Critical are the already defined ‘WHO-'fiber', as well as dusts and fiber fragments with Ø < 3µm, which penetrate directly into the alveoli and the lung tissue. Since the WHO-‘fiber’ size is smaller than the diameter of common CFs, the fiber fragment must experience a reduction of the diameter. This can happen by splintering or by burning. CF is not toxic per se!

Bio-persistance: High bio-persistance causes high toxicity, a low bio-solubility in living organisms already speaks as an indication of possible carcinogenicity. Fragments with short residence times that are quickly dissolved or removed are less risky.

Only if a sufficiently high amount of CF-WHO-'fibers' is produced and inhaled there is a potential for danger, whereby the following applies:

Risk = hazard potential (severity) • probability of occurrence.
Hazard potential = exposure to CF-WHO (size) particles combined with toxicity.

The duration of the exposure in terms of quantity and the possible frequency of occurrence of the event per unit of time are therefore decisive.

Generation and Counting of WHO ’fibers’

A quantity for the risk assessment delivers the counting of the fragments which are generated in machining processes.

Question: *Which machining processes seems to be the worst for the generation of WHO-‘fiber' shaped CF particles, faced in production and recycling*?

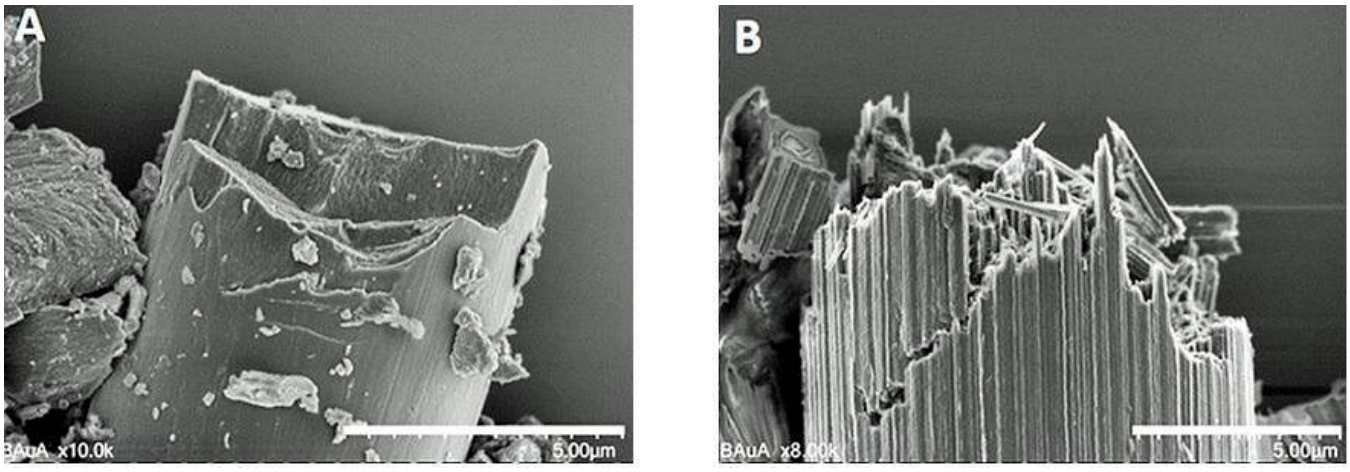

Fig. 21-3: (left) PAN-based, (right) Pitch-based. (Courtesy BAuA, Berlin)

Some answer is given in the BMBF research project *CarboBreak* (*headed by BAuA: the Federal Institute for Occupational Safety and Health conducts research for a safe, healthy and humane working environment*): Investigation of the release behaviour of respirable fragments made of pure fibers and fiber composites consisting of CF, sizing material, matrix etc. under mechanical stress. Basically there, rovings were subjected to an extreme mechanical stress in a so-called ball vibrating mill (*an assumed 'worst case' machining process*), the resulting CF fragments were evaluated with regard to their morphology and then the WHO 'fibers' counted, namely the ‘WHO-Fiber’ quantity / unit volume. The CF portion is considered to be the critical part of the full composite.

One significant finding was the assumed different splintering process between PAN in *Fig.21-3, left* and Pitch CF (*right*).

21.4 Fact & Idea to sort out Application-carefree Fibers

(1) Pitch fibers are obviously more dangerous because they do extremely splinter. Since the UHM-CF comes closest to the pitch fiber in terms of stiffness of all PAN-CFs, the PAN-UHM represents the more critical PAN CF in terms of risk of splintering.
(2) A CF-parameter is being sought that could be a parameter for explaining the fiber splintering hazard and finding a characteristic.

The sought-after, splinter hazard-descriptive parameter could be the fracture toughness. This property is likely to show some difference in relatively similarly stiff (Young's modulus) brittle materials. *The author lectured fracture mechanics, which he also had to apply at MAN*.

His test proposal was a micro-fracture mechanics investigation of a laser-notched single fiber to determine the different brittleness based on the fracture toughness values of K_{Ic} to be measured. In fracture mechanics, fracture toughness describes the resistance of a material to unstable crack progression An ultra-high graphitized UHM PAN CF such as Torayca's M60J is to be basically investigated, because it is to place narrowest to the behavior of the critical Pitch-Fiber.

Asssumption: *Different fracture toughness values indicate different risk of splintering*.

*The proposed test specimens, together with the difficult notching of a single CF by a laser beam, have already been realized in Kaiserslautern by the institutes IVW with PZKL!

*The search for a fracture mechanics model that allows us to estimate the fracture toughness of a CF is essential for the qualitative differentiation of the envisaged fibers. A formula will provide a not realistic ‘exact’, but a quantified relationship which is fully sufficient.

The searched characteristic for the tensioned notched test specimen is the so-called critical stress intensity factor (SIF) K_{Icr} (= fracture toughness), at which unstable crack progression begins. Its formula reads $K_{Icr} = \sigma_{fracture} \cdot \sqrt{\pi \cdot a_{cr}} \cdot Y$, with the so-called geometry factor Y taking the fact into account that the SIF value is theoretically independent of the dimensions of the test specimen only for infinitely large plates. Therefore, the corresponding function Y must be sought for the intended test specimen 'Notched Single Fiber'. This was made possible by the author-available Manual "*NASGRO Reference Manual Version 9.01 Final; December 2018. Fracture Mechanics and Fatigue Crack Growth Analysis Software*".

The application of the full model requires several assumptions:

- CF is a very brittle material
- The crack instability, expressed by the formula, can be applied at the µm-level (micromechanics) for these brittle materials!
- The cross-section, cut by the laser beam, is just a circle section but can be transferred to the elliptical shape of a typical crack

- The 'model for a full cylinder' given as SC07 in the NASGRO document is applicable. Experience has shown that the impact is small, the model can be used also in the µm range
- The crack depth a is given by the laser notch depth.
- Diameter D = Ø = 0.007 mm, UHM 60J.
- The applied stress $\sigma_{fracture}$ at the fiber ends = breaking tensile force F / area A
- The cross-section cut by the laser beam can be transferred to the elliptical shape of a typical SC07 crack. The difference in surface area is neglected because it is the same for all tested fibers. In the SC07 associated Table C15: For R/t = 0, i.e. a solid cylinder with R = 0 (*t = wall thickness = R),* approximately to be expected a/t = 0.3, gives c/t = 0.35 and thus Y = 1.6.

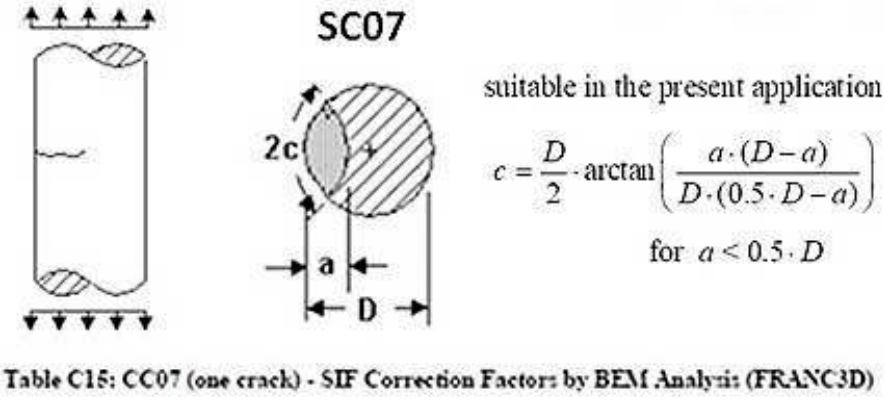

Table C15: CC07 (one crack) - SIF Correction Factors by BEM Analysis (FRANC3D)

Fig. 21-4: Thumbnail crack in a solid cylinder. Surface crack case SC07
*Manual NASGRO Reference Manual Version 9.01 Final; December 2018***.**
Fracture Mechanics and Fatigue Crack Growth Analysis Software

LL:
*** The test idea could be fully realized, which is a seldom experienced luck when testing a novel thing!*
Unfortunately there is no deeper research ongoing, which would give the basis for the realization of the author's desire to open a non-dangerous standard CF-market in construction by providing an answer to the big resentment (sensitivities), published in media, concerning new carbon fiber-reinforced products.

The author's big **wish** when performing this private work,
driven as a GROWIAN wind turbine co-responsible (built *1980, Ø 103m*) and due to his carbon-reinforced concrete works in the last decade,
in view of future fear-spreading media about a wind turbine fractures with blades made of standard CFs, i.e. never UHM-CFs: was the

Submission of an 'official recommendation' by the BAuA, together with Composites United (CU), including adapted recycling safety requirements on working with CFRP in general and specially on PAN-CF carbon reinforced concrete.

22 Derivation of Mohr-Coulomb Curve and Cohesive Shear Strength Values

22.1 Improved Mohr-Coulomb Curve and Cohesive shear Strength R^{τ} of Isotropic materials

Aim: *Enabling a correct understanding of the often used cohesive strength value* $\bar{R}^{\tau}$ *, however not clearly explained how to test, as a bi-axial fracture quantity.*

22.1.1 General

As the author had to design with all three basic material families isotropic, transversely-isotropic and orthotropic for him a conflict comes up, if the used index-letters are not material-dedicated, not self-explaining and not generally used in mechanics. This caused him as civil engineer to publish a Glossar.

In order to not disturb the co-working engineering family in construction the practiced fiber-reinforced polymer matrix-linked terminology (*world-wide applying the suffixes* $_{1,\,2}$) should be also used with fiber-reinforced mineral matrix-linked Carbon Concrete (*another field of the author*). Further, the following analogous and more general letters will be intentionally proposed to use: $c \rightarrow R^{\tau}$, $\sigma_1 \rightarrow \sigma_{II}$.

As some researchers in construction still began, when investigating Mohr-Coulomb friction, according to general mechanics they attribute old tradition positive marked compressive stresses now an accurate negative sign. The author is forced to follow them. Hence, the positive direction is to display rightward, *Fig. 22-1 (left)*. (Historically, civil engineers basically were more faced by compression and mechanical engineers by tension. This explains the different sign choice).

Fig.23-1 outlines at the left the Mohr entities and right the transformation matrix for transforming principal structural stresses into Mohr stresses.

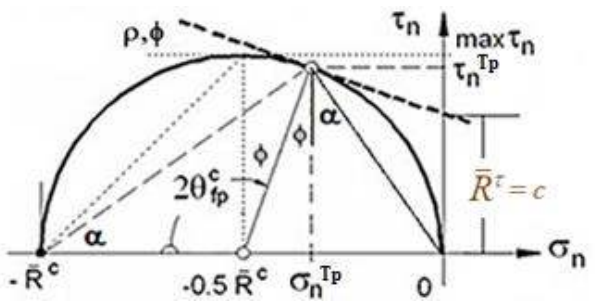

$$\begin{Bmatrix}\sigma_{\lambda}\\ \sigma_{n}\\ \sigma_{t}\\ \tau_{n}\\ \tau_{t\lambda}\\ \tau_{t\lambda}\end{Bmatrix} = \begin{bmatrix}1 & 0 & 0 & 0 & 0 & 0\\ 0 & c^2 & s^2 & 2sc & 0 & 0\\ 0 & s^2 & c^2 & -2sc & 0 & 0\\ 0 & -sc & sc & (c^2-s^2) & 0 & 0\\ 0 & 0 & 0 & 0 & c & -s\\ 0 & 0 & 0 & 0 & s & c\end{bmatrix} = \begin{Bmatrix}\sigma_{I}\\ \sigma_{II}\\ \sigma_{III}\\ 0\\ 0\\ 0\end{Bmatrix}$$

With $\eta = \sigma_{II} - \sigma_{III}$ and σ_{λ}, $\tau_{t\lambda}$, $\tau_{n\lambda} = 0$, the used addition theorems read: $\tau_{nt} \equiv \tau_n$

$$\sigma_n - \sigma_t = c^2 \cdot \eta - s^2 \cdot \eta = C \cdot \eta \;,\quad S = \sqrt{1-C^2},\quad C = c^2 - s^2 = 2c^2 - 1 = 1 - 2s^2,$$

$$\sigma_n + \sigma_t = \sigma_{II} + \sigma_{III} = I_1,\quad \sigma_t = \sigma_n - C \cdot (\sigma_{II} - \sigma_{III}),\quad \eta = \sigma_{II} - \sigma_{III},$$

$$\tau_n = -s \cdot c \cdot \sigma_{II} + s \cdot c \cdot \sigma_{III} = -0.5 \cdot \sqrt{1-C^2} \cdot (\sigma_{II} - \sigma_{III}) \quad \text{with} \quad c = \cos\theta,\quad s = \sin\theta,$$

$$\sigma_n = c^2 \cdot \sigma_{II} + s^2 \cdot \sigma_{III} = \frac{(C+1)\cdot\sigma_{II} + (1-C)\cdot\sigma_{III}}{2}. \qquad 2 \cdot \theta_{fp}\,^{\circ} = 90^{\circ} + \phi^{\circ}.$$

Fig. 22-1: Transformation of Principal Structural Stresses into Mohr Stresses and helpful Addition Theorems outlining the fracture plane angle measure C(θ_{fp}). (bar over due to model mapping)

22.1.2 Assumption of Otto Mohr

History of the Mohr-Coulomb (M-C) curve = 'Mohr Envelope':

* *Otto Mohr did not commit himself to the intersection of the envelope with the* σ_n*-axis. A. Leon was probably the first to use an envelope, taking a parabolic one.*

* Linear Mohr –Coulomb proposed by Coulomb and later put into form by Mohr

Mohr's basic assumption was: *"The strength of a material is determined by the (Mohr) stresses on the fracture plane".* This means for the linear Mohr-Coulomb (M-C) formulation $\tau_n = \bar{R}^\tau - \mu \cdot \sigma_n$.

Herein, the value μ is the intrinsic friction value of the material and $\bar{R}^\tau$ the so-called cohesion strength. The other two shear stresses $\tau_{t\lambda}$, $\tau_{n\lambda}$ in *Fig.22-1* are zero. The normal stress σ_t must be accounted for in the transformation process but will finally have no influence, which has to be proven when following Mohr and this must be proven. According to Mohr, the stresses σ_n and τ_n are the only fracture-responsible stresses, the normal stress σ_λ can be set zero.

A stress analysis with Mohr stresses is principally simpler than with structural stresses, however the fracture plane angle θ_{fp} must be known and this makes it difficult. Let's begin classically:

Linear M-C approach delivering a relationship C(μ) to friction value μ and Touch point coordinates

$F_{\text{linM-C}} = \dfrac{\tau_n}{R^\tau - \mu \cdot \sigma_n} = 1.$ Implicit differentiation (minus sign) of the SFC $F_{\text{linM-C}}$

$$\frac{d\left(\dfrac{\tau_n}{R^\tau - \mu \cdot \sigma_n}\right)}{d\sigma_n} = \frac{\mu \cdot \tau_n}{\left(R^\tau - \mu \cdot \sigma_n\right)^2} \quad \text{and} \quad \frac{d\left(\dfrac{\tau_n}{R^\tau - \mu \cdot \sigma_n}\right)}{d\tau_n} = \frac{1}{R^\tau - \mu \cdot \sigma_n}$$

finally gives a friction relation $\dfrac{d\tau_n}{d\sigma_n} = -\dfrac{dF\tau / d\sigma_n}{dF\tau / d\tau_n} = -\dfrac{\dfrac{\mu \cdot \tau_n}{\left(R^\tau - \mu \cdot \sigma_n\right)^2}}{\dfrac{1}{R^\tau - \mu \cdot \sigma_n}} = \dfrac{-\mu \cdot \tau_n}{R^\tau - \mu \cdot \sigma_n} = -\mu$.

The Touch point coordinates from a given fracture angle θ^c_{fp} or the related friction value μ: bar skipped

$(\tau_n^{Tp}, \sigma_n^{Tp}) \rightarrow (\tau_n = R^\tau, \sigma_n = 0)$ applying $c = \cos\theta^c_{fp}$, $s = \sin\theta^c_{fp}$,

$\sigma_n^{Tp} = c^2 \cdot \left(-R^c\right)$, $\tau_n^{Tp} = -s \cdot c \cdot \left(-R^c\right)$ leading to $\tau_n = \tau_n^{Tp} + \mu \cdot \sigma_n^{Tp}$.

22.1.3 Note on the Mohr-Coulomb (M-C) criterion (also see § 26.1)

In a paper, recently published in *Scientific Reports (2024) nature portfolio [Stress-dependent Mohr–Coulomb shear strength parameters for intact rock* [*Li24*], a critical assessment of the M-C criterion is performed. This report shall be not scientifically reworked here. However, my summarizing private elaboration at hand shall give some discussion points. It just tries to inform about my procedure to derive an accurate Mohr-Coulomb Envelope including Cohesive Strength.

Basis of my procedure is the knowledge, that the M-C Envelope, practically spanning from the Touch point $(\tau_n^{Tp}, \sigma_n^{Tp}) \rightarrow (\tau_n = R^\tau, \sigma_n = 0)$, is affected (*Fig.25-1*) by the shear failure mode together with the tensile failure mode and thus belonging to a transition zone, as a mode interaction domain.

22.1.4 3D-SFCs regarding material-inherent 120°-rotational symmetry of isotropic fracture bodies

When using for the determination of the cohesive strength - for an extrapolation from the compressive strength point - just the SFC $F^{SF} \rightarrow F^\tau$, then the isotropic material-inherent 120°-rotational symmetry of the fracture body is to consider, as shown below, where both the SFCs $F^{NF} \rightarrow F^\sigma$ and F^τ are displayed in the next box together with the required invariants and non-circularity parameter $\Theta^{SF} \equiv \Theta^\tau$.

The cohesive strength point lies in the interaction zone of the mode regimes, see *Fig.22-2*. Therefore, a generation of a realistic, decaying Mohr-Coulomb curve $\tau_n(\sigma_n)$ requires the determination of the slope *along* the realistic curved M-C curve up to $\sigma_n = 0$ at least, not a constant value $C = C^c$ in the

compressive strength-linked Touch *point* only, being sufficient for the determination of the friction value μ. This means, instead of the single F^{SF}-formulation the SF-NF-interaction managing *Eff*-formulation is to apply when moving from the structural stress formulation to a Mohr stress-based one.

To search is an equation for the unknown fracture angle measure $C(\theta_{fp})$, linked to the growing fracture angle θ_{fp}. This is performed by equating the slopes in the so-called Touch point:

$$F^{\sigma} = \frac{\sqrt{4J_2 - I_1^{\,2}/3} + I_1}{2 \cdot \bar{R}^t} \quad (\Theta^{NF}=1) \quad \text{and} \quad F^{\tau} = c_2^{SF} \cdot \frac{I_1}{\bar{R}^c} + c_1^{SF} \cdot \frac{6 \cdot J_2}{2 \cdot \bar{R}^{c2}} \cdot \Theta^{SF}$$

$$I_1 = (\sigma_I + \sigma_{II} + \sigma_{III}), \text{ considering Mohr-Coulomb skip } \sigma_I$$

$$6J_2 = (\sigma_I - \sigma_{II})^2 + (\sigma_{II} - \sigma_{III})^2 + (\sigma_{III} - \sigma_I)^2$$

$$\rightarrow 6J_2 = \sigma_{II}^{\,2} + (\sigma_{II} - \sigma_{III})^2 + \sigma_{III}^{\,2}),$$

$$27J_3 = (2\sigma_I - \sigma_{II} - \sigma_{III}) \cdot (2\sigma_{II} - \sigma_I - \sigma_{III}) \cdot (2\sigma_{III} - \sigma_I - \sigma_{II})$$

$$\rightarrow 27J_3 = (-\sigma_{II} - \sigma_{III}) \cdot (2\sigma_{II} - \sigma_{III}) \cdot (2\sigma_{III} - \sigma_{II})$$

$$I_1 = (\sigma_n + \sigma_t + \sigma_\lambda), \quad \text{considering Mohr-Coulomb skip } \sigma_\lambda, \tau_{n\lambda}, \tau_{t\lambda}$$

$$I_2 = \sigma_n \cdot \sigma_t + \sigma_t \cdot \sigma_\lambda + \sigma_n \cdot \sigma_\lambda - \tau_{nt}^{\,2} - \tau_{n\lambda}^{\,2} - \tau_{t\lambda}^{\,2} \quad \rightarrow \quad \sigma_n \cdot \sigma_t - \tau_n^{\,2}$$

$$I_3 = \sigma_n \cdot \sigma_t \cdot \sigma_\lambda - \sigma_n \cdot \tau_{t\lambda}^{\,2} - \sigma_t \cdot \tau_{n\lambda}^{\,2} - \sigma_\lambda \cdot \tau_{nt}^{\,2} + 2 \cdot \tau_{nt} \cdot \tau_{n\lambda} \cdot \tau_{t\lambda} \quad \rightarrow \quad 0$$

$$6J_2 = (\sigma_n - \sigma_t)^2 + (\sigma_t - \sigma_\lambda)^2 + (\sigma_\lambda - \sigma_n)^2 + 6 \cdot (\tau_{nt}^{\,2} + \tau_{n\lambda}^{\,2} + \tau_{t\lambda}^{\,2})$$

$$\rightarrow 6J_2 = (\sigma_n - \sigma_t)^2 + \sigma_t^{\,2} + \sigma_n^{\,2} + 6 \cdot \tau_{nt}^{\,2}$$

$$27J_3 = 2 \cdot I_1^{\,3} - 9 \cdot I_1 \cdot I_2 + 27 \cdot I_3$$

$$\rightarrow 27J_3 = 2(\sigma_n + \sigma_t)^3 - 9 \cdot (\sigma_n + \sigma_t) \cdot (\sigma_n \cdot \sigma_t - \tau_n^{\,2})$$

$$\Theta^{\tau} = \sqrt[3]{1 + d^{SF} \cdot \sin(3\vartheta)} = \sqrt[3]{1 + d^{SF} \cdot 1.5 \cdot \sqrt{3} \cdot J_3 \cdot J_2^{-1.5}}, \quad \sigma_t = \sigma_n - C \cdot (\sigma_{II} - \sigma_{III}).$$

A first slope equation $d\tau_n / d\sigma_n$ is given by the transformation of structural stresses into Mohr stresses. The fracture angle differentiation of the Mohr stresses in the Touch point delivers:

$$\tau_n = -s \cdot c \cdot \sigma_{II} + s \cdot c \cdot \sigma_{III}, \quad \sigma_n = c^2 \cdot \sigma_{II} + s^2 \cdot \sigma_{III} \quad \text{with} \quad c = \cos\theta, \quad s = \sin\theta,$$

$$\frac{d\left(-s \cdot c \cdot \sigma_{II} + s \cdot c \cdot \sigma_{III}\right)}{d\theta} = (-c^2 + s^2) \cdot \sigma_{II} - (-c^2 + s^2) \cdot \sigma_{III} \quad \text{and}$$

$$\frac{d(c^2 \cdot \sigma_{II} + s^2 \cdot \sigma_{III})}{d\theta} = -2sc \cdot (\sigma_{II} - \sigma_{III})$$

$$\frac{d\tau_n}{d\sigma_n} = \frac{(-c^2 + s^2) \cdot \sigma_{II} - (-c^2 + s^2) \cdot \sigma_{III}}{-2sc \cdot (\sigma_{II} - \sigma_{III})} = \frac{c^2 - s^2}{2sc} = \frac{C}{S} \quad \Rightarrow \quad \frac{d\tau_n}{d\sigma_n} = \frac{C}{\sqrt{1 - C^2}},$$

$$\text{and} \quad \operatorname{cotan}(2\theta_{fp}) = \frac{\cos(2 \cdot \theta_{fp})}{\sin(2 \cdot \theta_{fp})} = \frac{C}{S}, \; C^c = \cos(2 \cdot \theta_{fp}{}^\circ \cdot \frac{\pi}{180^\circ}) \; ; \; \tan(\rho) = -\operatorname{cotan}(2 \cdot \theta_{fp}{}^\circ \cdot \frac{\pi}{180^\circ}).$$

Secondly, one has to find a further tangent equation by the differentiation of F^{τ} or physically accurate F^{τ} with F^{σ}. *Table 22-1* depicts both the SFCs.

On the classical way 'Extrapolation from the compression strength point', represented by the touchpoint in the Mohr diagram, *Fig 22-1*, just the SFC F^{τ} is required. *Table 22-2* will later show the full procedure $C(\theta_{fp})$ of the different ways of an extrapolation. It displays the 2nd quadrant of the bi-axial failure

curve in structural stresses. This fully represents the Mohr-Coulomb curve domain. The joint mode situation of the Mohr-Coulomb curve - capturing the transition zone between the pure mode domains NF and SF - requires the application of the interaction equation $Eff^{m} = (Eff^{NF})^{m} + (Eff^{SF})^{m} = 1$ (material stressing effort 100%) and it spans over the ordinate regime $0 < \sigma_{III} < \bar{R}^{t}$, the *transition zone* of the modes, and covers Lode angles $-30° < \vartheta < +30°$.

If the full M-C curve and the associated fracture angle are of interest up to $\sigma_{III} = R^{t}$, then both the modes are to employ with their *Effs*.

Table 22-1: Formulation of Mohr stress-based Effs.

$$F^{NF} = F^{\sigma} = Eff^{NF} = c^{NF} \cdot \frac{\sqrt{4J_2 \cdot \Theta^{NF} - I_1^{\,2}/3} + I_1}{2 \cdot \bar{R}^{t}}, \quad \text{for Normal Concrete can be set } c^{NF}, \Theta^{NF} = 1,$$

$$Eff^{NF} = 1 \cdot \frac{\sqrt{4 \cdot [(\sigma_n - \sigma_t)^2 + \sigma_t^{\,2} + (-\sigma_n)^2 + 6 \cdot \tau_n^{\,2}] \cdot 1/6 - (\sigma_n + \sigma_t)/3} + (\sigma_n + \sigma_t)}{2 \cdot \bar{R}^{t}}.$$

Using the concept of 'proportional loading':

$$F^{SF} = F^{\tau} = c_2^{SF} \cdot \frac{I_1}{\bar{R}^{c}} + c_1^{SF} \cdot \frac{6 \cdot J_2}{2 \cdot \bar{R}^{c2}} \cdot \Theta^{SF} \quad \Rightarrow \quad c_2^{SF} \cdot \frac{I_1 / Eff}{\bar{R}^{c}} + c_1^{SF} \cdot \frac{6 \cdot J_2 / Eff^{\,2}}{2 \cdot \bar{R}^{c2}} \cdot \Theta^{SF}$$

$$Eff^{SF} = \frac{\sqrt{(c_2^{SF} \cdot I_1)^2 + 12 \cdot c_{1\Theta}^{SF} \cdot J_2 \cdot \Theta^{SF}}}{2 \cdot \bar{R}^{c}} + \frac{c_2 \cdot I_1}{2 \cdot \bar{R}^{c}} \quad \text{with} \quad \Theta^{SF} \to \Theta^{CM} = \sqrt[3]{1 + d^{SF} \cdot (-1)},$$

$$Eff^{SF} = \frac{\sqrt{c_2^{SF\,2} \cdot (\sigma_n + \sigma_t)^2 + c_{1\Theta}^{SF} \cdot \Theta^{SF} \cdot 2 \cdot [(\sigma_n - \sigma_t)^2 + \sigma_t^{\,2} + (-\sigma_n)^2 + 6 \cdot \tau_n^{\,2}]}}{2\bar{R}^{c}} + c_2 \cdot \frac{\sigma_n + \sigma_t}{2\bar{R}^{c}}.$$

with $c_{1\Theta}^{SF} \cdot \Theta^{CM} = 1 + c_2$, $\Theta^{CM} = \Theta^{SF} = \sqrt[3]{1 + d^{SF} \cdot \sin(3\vartheta)} = \sqrt[3]{1 - d^{SF}}$ and

Θ non-circularity function, d non-circularity parameter, ϑ Lode angle.

22.1.5 *Improved Mapping of Failure Stress data to obtain a more realistic* $\theta_{fp}°(\vartheta)$

As still experienced with the UD-materials in a chapter before, also here it is to face that a SFC is 'just' a practical approach and therefore cannot sufficiently well map all domain parts in detail. Therefore, when searching a local fracture angle $\Theta_{fp}°$ in the transition zone a correction is to be material-dependently applied to numerically determine a better value for $\Theta_{fp}°$, if really desired.

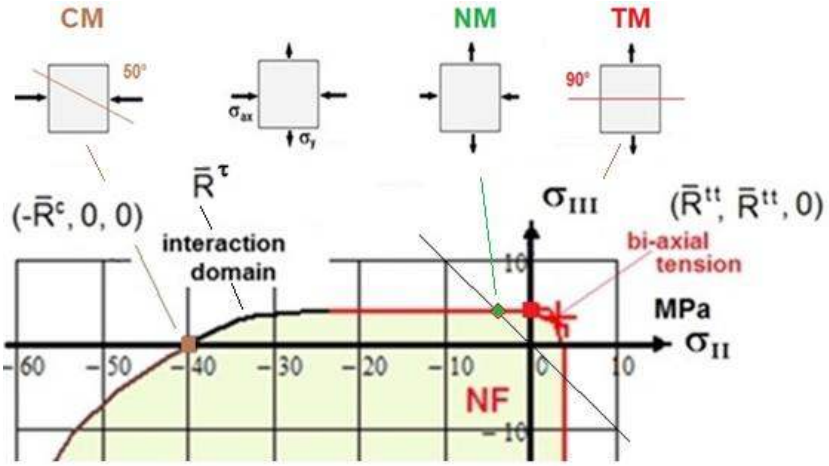

Fig.22-2: Second quadrant and associated stress states, transition zone between the 2 mode domains SF, NF. Tensile Meridian (TM), Compressive Meridian (CM)

According to the fact that the compression strength point is located on the compressive meridian and the tensile strength point on the tensile meridian the different Lode angle ϑ is to consider in order to

achieve a locally necessary more accurate SFC-model. This requires to consider inherent '*120°-rotationally-symmetry'*.

The pure shear point in *Fig.22-2* is a point on the Neutral Meridian ($\delta = 0$, $\Theta = 1$, $I_1 = 0$) and also a characteristic point of the transition zone between the tensile domain and the compressive domain is when the first invariant becomes zero (*see the bias grey line in Fig.25-2*), meaning pure shear:

$$I_1 = \sigma_I + \sigma_{II} + \sigma_{III} = 0 \quad \rightarrow \quad \sigma_{II}{}^{c} = -\sigma_{III}{}^{t} \; .$$

A physical demands is given with θ_{fp} °= 90° at $\sigma_{III} = R^t$ (is σ_{III} coordinate) and $Eff^{\tau} = 0$ for $\sigma_{II} = 0$.

The shear material stressing effort Eff^{τ} must physically become zero at the tensile strength point $(0, R^t)$.

Fig.22-3 outlines the local shortcoming of the FMC-based choice of the SF-formula at $\sigma_n = 0$.

As simple correcting function f_σ , being just a crutch of-course,

$$f\sigma = 1 - \left(\frac{\sigma nTp + Rt - \sigma n0}{|\sigma nTp|} \right)^6 = 1 - \left[\frac{\sigma nTp + Rt - \frac{(Cc + 1)\cdot \sigma II + (1 - Cc)\cdot Rt}{2}}{|\sigma nTp|} \right]^6$$

was taken. This correction function is decisive in the low negative σ_{II} and σ_n-domain. The magenta **curve** in *Fig.22-3* outlines the desired result.

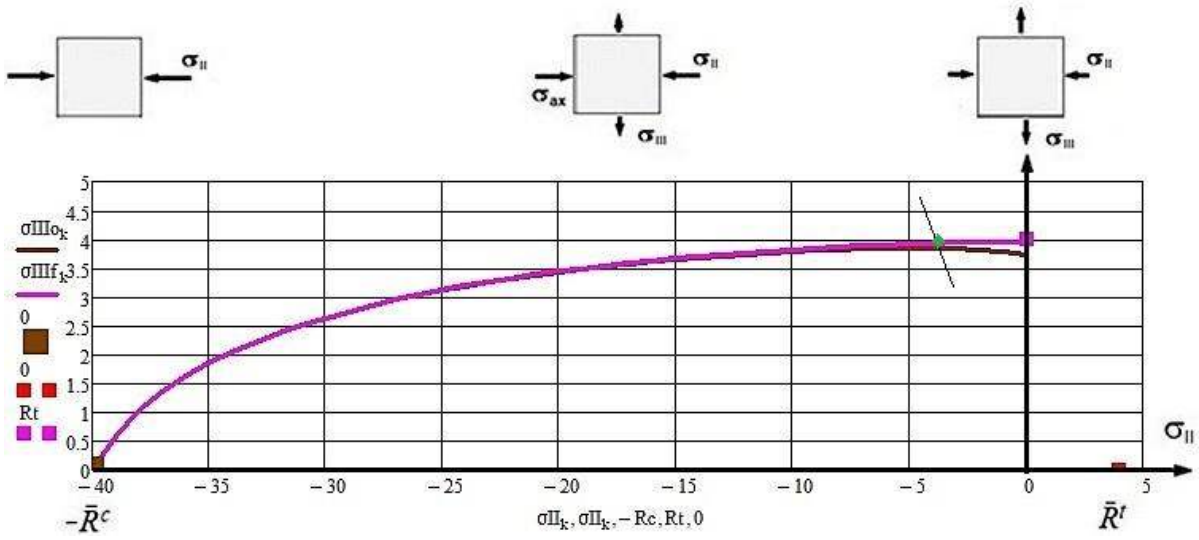

Fig.22-3, Θ-considered: Visualization of the course of the original and the corrected $\sigma_{III}(\sigma_{II})$.

Note, please: In any case, the given SFC F^{τ} calculates a conservative Reserve Factor, based on both the modes. The SFC is on the safe side and Design-Verification as well.

The next sub-chapters will outline:

- extrapolation approaches
- a trial on the physically accurate, much more complicated two modes approach and finally
- a guess of the cohesive strength R^{τ}.

At first the simplest way: There are three ways gone, each one an approximation.

22.2 R^c-extrapolation-based estimation of cohesive strength R^τ, M-C curve $\tau_n(\sigma_n)$ and angle $\theta_{fp}°$

1 Linear Mohr-Coulomb, C = C^c constant, $\theta_{fp}°$ =constant, classical path

$$F_{\text{linM-C}} = \frac{\tau_n}{R^\tau - \mu\cdot\sigma_n} = 1 \;\Rightarrow\; (\text{M-C curve})\;\; \tau_n = \tau_n^{Tp} - \mu\cdot\sigma_n \quad \text{and} \quad R^\tau = \tau_n^{Tp} + \mu\cdot\sigma_n^{Tp}$$

This basic approach delivers the highest cohesion strength value and a straight M-C line.

2 Use of Shear Mode F^τ *only*, $\theta_{fp}°$ grows with C, $c_{1\Theta}^{SF} \rightarrow\; c_1 = c_2 + 1,\;\; C^c = \cos(2\cdot\theta_{fp}^c°\cdot\frac{\pi}{180°})$

Two variants are possible to obtain an alternating fracture angle measure $C(\theta_{fp}°)$ and thereby R^τ.

If just performing an extrapolation from compression strength point no interaction of modes is needed: The simpler F^τ can be used instead of *Eff*$^\tau$. *Table 22-2* summarizes the relations for the derivation of

Table 22-2: Estimation of R^τ, $\tau_n(\sigma_n)$ and fracture plane angle $\theta_{fp}°$ considering the F^τ only

$$F^\tau = c_2\cdot\frac{I_1}{\bar{R}^c} + c_1\cdot\frac{6\cdot J_2}{2\cdot\bar{R}^{c2}}\cdot c_2\cdot\frac{\sigma_n+\sigma_t}{\bar{R}^c} + c_1\cdot\frac{(\sigma_n-\sigma_t)^2+\sigma_t^{\,2}+\sigma_n^{\,2}+6\cdot\tau_n^{\,2}}{2\cdot\bar{R}^{c2}} = 1$$

inserted $I_1 = \sigma_n + \sigma_t$, $6J_2 = (\sigma_n-\sigma_t)^2 + \sigma_t^{\,2} + \sigma_n^{\,2} + 6\cdot\tau_n^{\,2}$ and resolved for

$$\tau_n = \sqrt{-\frac{c_2\cdot Rc\cdot(\sigma_n+\sigma_t) - Rc^2 + c_1\cdot(\sigma_n^{\,2} - \sigma_n\cdot\sigma_t + \sigma_t^{\,2})}{3\cdot c_1}},$$

$$\frac{C}{\sqrt{1-C^2}} = \frac{d\tau_n}{d\sigma_n} \quad \text{with} \quad \tau_n(\sigma_n) \quad \text{and/or} \quad \frac{C}{\sqrt{1-C^2}} = \frac{d\tau_n}{d\sigma_n} = -\frac{dF\tau/d\sigma_n}{dF\tau/d\tau_n}$$

The latter will be taken: $\Theta^\tau = 1$

$$\frac{C}{\sqrt{1-C^2}} = \frac{-c_2\cdot\bar{R}^c + c_1\cdot(\sigma_t - 2\sigma_n)}{6\cdot\tau_n\cdot c_1} = \frac{-c_2\cdot\bar{R}^c + c_1\cdot(\sigma_t - 2\sigma_n)}{6\cdot\tau_n\cdot c_1}$$

$$\sigma_n = (C+1)\cdot 0.5\cdot\sigma_{II} + (1-C)\cdot 0.5\cdot\sigma_{III},\;\; \tau_n = -0.5\cdot\sqrt{1-C^2}\cdot(\sigma_{II}-\sigma_{III}),$$

$$(\sigma_t - 2\sigma_n) = -0.5\cdot[(\sigma_{II}+\sigma_{III}) + 3\cdot C\cdot(\sigma_{II}-\sigma_{III})].$$

Guess $\bar{R}^\tau = \sqrt{\frac{-\bar{R}^{c2} + c_2\cdot\bar{R}^c\cdot\sigma_{t0} + c_1\cdot\sigma_{t0}^{\,2}}{3\cdot c_1}}$ with $\sigma_{t0} = -C^c\cdot(-\bar{R}^c)$.

$\tau_{nt}(\sigma_n)$ and $\theta_{fp}°$ from σ_{II} (σ_{III}). It is to consider the change of the fracture plane angle $\theta_{fp}°$ with the Lode angle ϑ from $\theta_{fp}°$ at ϑ = -30° on up to a value < 90° (maximum at $\sigma_{III} = R^t$), which the model permits. The table shows the M-C formula $\tau_n(\sigma_n)$, the C-equation and the transformation of the Mohr stresses into principal structural stresses for determining C.

*This approach delivers an intermediate and lower value for the cohesive strength and the M-C curve.

3 Improved Estimation with F^τ and correction function f_σ

In the M-C-calculations the mode-linked Θ^τ and correction function f_σ ('crutch') principally should have been differentiated within the SFC F^τ. However, this makes no sense if F^τ is employed only.

Therefore, in order to take their influence into account at all, the respective quantity is treated as being fixed, being a constant. Hence, this variant just applies the correction $\tau_n \cdot f_\sigma$.

*This approach delivers the lowest value for the cohesive strength but more accurate $\bar{R}^\tau > \bar{R}^t$.

22.3 Accurate Mode-interactive determination of R^τ, M-C curve, fracture angle $\theta_{fp}° > \theta_{fpc}°$

A physically accurate determination of above quantities may be possible by applying the jointly acting SFCs, F_τ with F_σ. *Table 22-3* collects all relevant relationships. It displays the final differentiation-equations and solution procedure. Naturally this huge 'improved' solution procedure is very challenging for a mathematical code concerning the necessary symbolic differentiation.

Table 22-3: Determination of R^τ, $\tau_n(\sigma_n)$, considering modes, Θ^τ, fracture angle measure $C(\theta_{fp})$

* Task: Known $\sigma_{II}, \sigma_{III}$; $\bar{R}^t$, $\bar{R}^c$; searched σ_n, τ_n, $\theta_{fp}°(C)$, $C = \cos(2 \cdot \theta_{fp}° \cdot \pi / 180°))$

* Interaction equation, 2 modes are activated: $(Eff^\sigma)^m + (Eff^\tau)^m = 100\%$

$$Eff^\sigma = \frac{\sqrt{4 \cdot [(\sigma_n - \sigma_t)^2 + \sigma_t^2 + \sigma_n^2 + 6 \cdot \tau_n^2] / 6 - (\sigma_n + \sigma_t)^2 / 3} + (\sigma_n + \sigma_t)}{2 \cdot \bar{R}^t},$$

$$Eff^\tau = \frac{c_2 \cdot (\sigma_n + \sigma_t)}{2 \cdot \bar{R}^c} + \frac{\sqrt{(c_2 \cdot (\sigma_n + \sigma_t))^2 + 2 \cdot c_{1\Theta} \cdot \Theta^\tau [(\sigma_n - \sigma_t)^2 + \sigma_t^2 + \sigma_n^2 + 6 \cdot \tau_n^2]}}{2 \cdot \bar{R}^c}$$

* Solution of the task means: Equalizing the 2 slopes at each stress state $\sigma_{II}(\sigma_{III})$

- Slope 1: Differentiation of the structural stresses-linked Mohr stresses delivered before

$$\frac{d\tau_{nt}}{d\sigma_n} = \frac{(s^2 - c^2) \cdot \eta}{-2 \cdot s \cdot c \cdot \eta} = \frac{C}{S} = \frac{C}{\sqrt{1 - C^2}},$$ valid uni-axially and bi-axially, $\eta = \sigma_{II} - \sigma_{III}$

- Slope 2: Differentiation of the interaction equation, abbreviation $\eta_m = 2\sigma_n - C \cdot \eta$

$$Eff^\sigma = \left\{\sqrt{4 \cdot [(C \cdot \eta)^2 + (\sigma_n - C \cdot \eta)^2 + \sigma_n^2 + 6 \cdot \tau_n^2] / 6 - \eta_m^2 / 3} + \eta_m\right\} / 2 \cdot \bar{R}^t, \quad \Theta^{NF} = 1$$

$$Eff^\tau = \left\{c_{1\Theta} \cdot \eta_m + \sqrt{(c_2^2 \cdot \eta_m^2 + 2 \cdot c_{1\Theta} \cdot \Theta^\tau \cdot [(C \cdot \eta)^2 + (\sigma_n - C \cdot \eta)^2 + \sigma_n^2 + 6 \cdot \tau_n^2]}\right\} / 2 \cdot \bar{R}^c$$

$$\Theta^\tau(\vartheta) = \sqrt[3]{1 + d^\tau \cdot \sin(3\vartheta)} = \sqrt[3]{1 + d^\tau \cdot 1.5 \cdot \sqrt{3} \cdot J_3 \cdot J_2^{-1.5}}$$

$$Eff^m = (Eff^\sigma)^m + (Eff^\tau)^m \quad \text{with} \quad dEff / d\sigma_n \quad \text{and} \quad dEff / d\tau_n.$$

Equating the 2 equations, considering the implicit differentiation by a negative sign,

with $\frac{C}{\sqrt{1 - C^2}} = -\frac{dEff / d\sigma_n}{dEff / d\tau_{nt}}$, a huge formula for determining C is obtained.

This formula is to be re-transformed from Mohr stresses into structural stresses

$$\sigma_n = (C + 1) \cdot 0.5 \cdot \sigma_{II} + (1 - C) \cdot 0.5 \cdot \sigma_{III}, \quad \tau_n = -0.5 \cdot \sqrt{1 - C^2} \cdot (\sigma_{II} - \sigma_{III}).$$

The altering C depends on the bi-axial fracture stress states $\sigma_{III}^{fr}(\sigma_{II})$, achieved, when inserting σ_{II} into the failure criterion $Eff = 1$ along the span between Mohr's Touch point and Cohesive Strength point, providing. the fracture angle measure $C(\theta_{fp}°)$ and $R^\tau(C)$

$$C = C(\sigma_{II}, \sigma_{III}^{fr}) = \cos(2 \cdot \theta_{fp}), \quad \theta_{fp} = 0.5 \cdot \arccos C, \quad \theta_{fp}° = \theta_{fp} \cdot 180° / \pi.$$

22.4 Application to Normal Concrete - computation data input

* Basic Data set

$\theta_{fp}^{c\,\circ} = 51°$ or friction value $\mu = 0.208.$, $C^c = \cos(2 \cdot \theta_{fp}\,° \cdot \frac{\pi}{180°}) = -\mu$

$c_2 = (3 \cdot C^c - 1)/(3 \cdot C^c + 1) = (1 + 3 \cdot \mu)/(1 - 3 \cdot \mu) = 4.32.$

Inserting the compressive strength point into $F^\tau = c_2 \cdot \frac{I_1}{\bar{R}^c} + c_{1\Theta} \cdot \frac{6 \cdot J_2}{2 \cdot \bar{R}^{c2}} \cdot \Theta^\tau = 1$

gives $c_2 \cdot \frac{-\bar{R}^c}{\bar{R}^c} + c_{1\Theta} \cdot \frac{2 \cdot \bar{R}^{c2}}{2 \cdot \bar{R}^{c2}} \cdot \Theta^\tau \rightarrow c_{1\Theta} = \frac{c_2 + 1}{\Theta^\tau}$ (c_2 is not dependent on C).

* Determination of the missing parameters $c_{1\Theta}$, d^τ

In order to capture the 120°-symmetry requirement a 2-parameter approach is to employ. Its two missing model parameters are calculated in *Table.22-4*.

Table 22-4: Determination of SF-model parameters $c_{1\Theta}$, d_τ

$I1c := -Rc$ $J2c := \frac{Rc^2}{3}$ $I1cc := -2 \cdot Rcc$ $J2cc := \frac{Rcc^2}{3}$

Vorgabe $c1\Theta := 2$ $d\tau := 0.6$ $c2 = 4.32$

$\frac{\sqrt{I1c^2 \cdot c2^2 + 12 \cdot J2c \cdot c1\Theta \cdot \sqrt[3]{1 - 1 \cdot d\tau}} + I1c \cdot c2}{2 \cdot Rc} = 1$ strength point on CM

$\frac{\sqrt{I1cc^2 \cdot c2^2 + 12 \cdot J2cc \cdot c1\Theta \cdot \sqrt[3]{1 + 1 \cdot d\tau}} + I1cc \cdot c2}{2 \cdot Rc} = 1$ bi-axial compressive failure stress point on TM

$A\tau := Suchen(c1\Theta, d\tau)$ $A\tau = \begin{pmatrix} 6.727 \\ 0.507 \end{pmatrix}$ $c1\Theta := A\tau_0$ $c1\Theta = 6.7$ $d\tau := A\tau_1$ $d\tau = 0.51$

$\Theta^\tau = 1 : c_{1\Theta} \rightarrow c_1 = c_2 + 1 = 5.32$ and $\Theta^\tau \neq 1 : c_{1\Theta} = \frac{c_2 + 1}{0.79} = 6.73$

$\Theta^t = \sqrt[3]{1 + d_\tau}$ (tensile meridian TM) $= 1.15$, $\vartheta = +30°$;

$\Theta^c = \sqrt[3]{1 - d_\tau}$ (compressive meridian CM) $= 0.79$, $\vartheta = -30°$.

Touch point: $\tau_n^{Tp} = 19.6$ MPa, $\sigma_n^{Tp} = -15.8$ MPa.

Final task is equalizing the two slope angles along the full domain, generated by the joint action of the two modes and considering the correction function $f\sigma$. Focused are the uni-axial classical procedure and a realistic 'bi-directional mode' procedure.

22.5 Results: Extrapolation Solution Path Variants $\Theta_{fp}°(F^\tau)$

Fig.22-4a,b display several M-C failure curves and the course of the altering fracture plane angle $\Theta_{fp}°(F^\tau)$. The angle changes from 51° up to 90°. Figure (*a*) presents the entities in Mohr stresses and (b) in structural stresses. This involves the classical Linear Mohr-Coulomb fracture curve an F^τ-based M-C curve $\tau_{nt}(\sigma_n)$ and an assumed, $f\sigma$-corrected one. The 3 Mohr half-circles are incorporated. *Fig.22-4a* presents model-dependent cohesive strength values R^τ, the interaction-based $\tau_n(\sigma_n)$-curve, topped by the

course of the increasing fracture angle, factored by 2. And, a joint display of the (fσ-corrected) failure curve in principal stresses

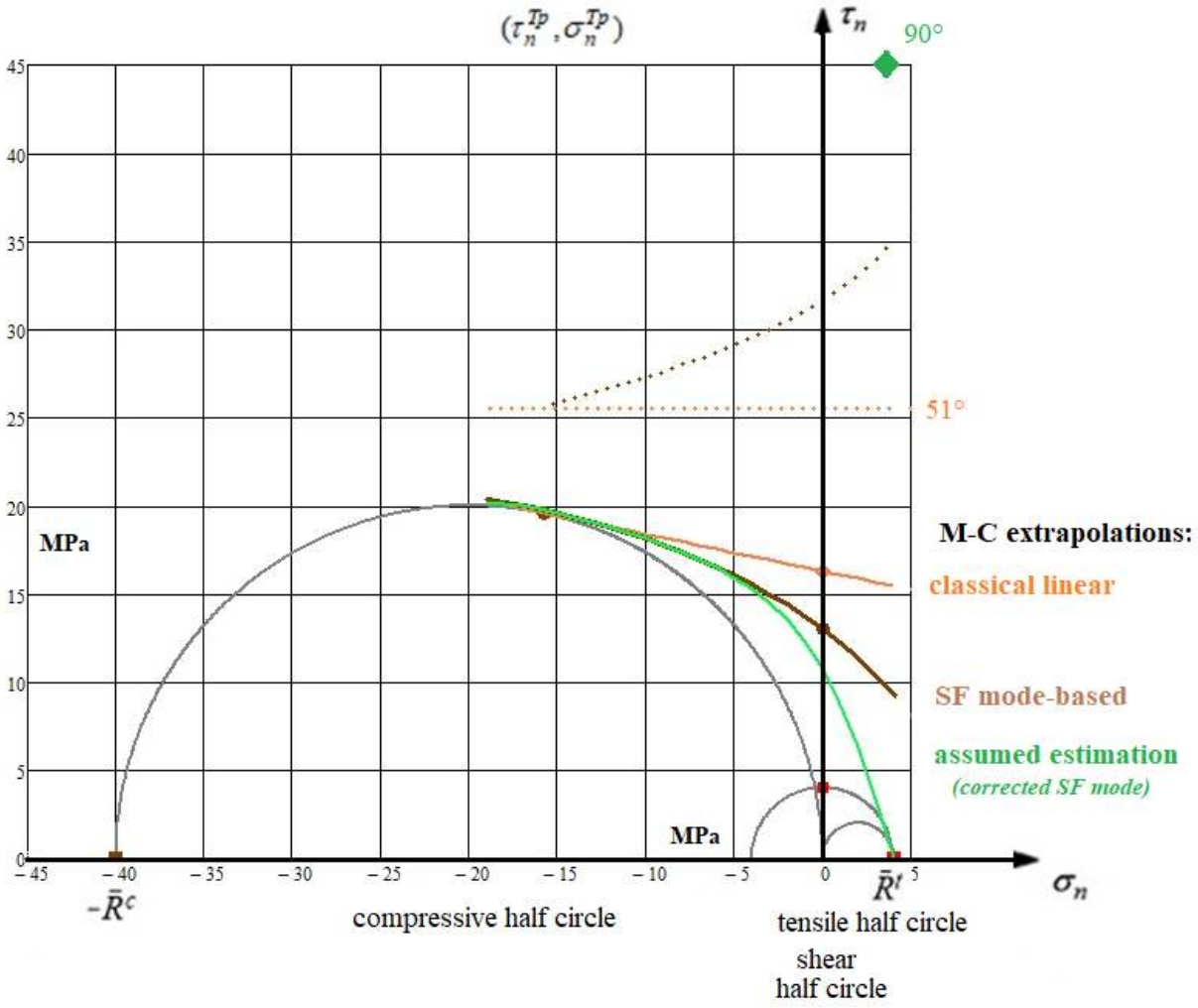

Fig.22-4a, Normal Concrete: $\bar{R}^{\tau}$, $\tau_n(\sigma_n)$ *.Mohr-Coulomb extrapolations with fracture angle increase* θ_{fp}°,

Fig.22-4b presents the interaction-based, fσ-corrected $\tau_n(\sigma_n)$-curve, topped by the course of the increasing fracture angle, factored by 10.

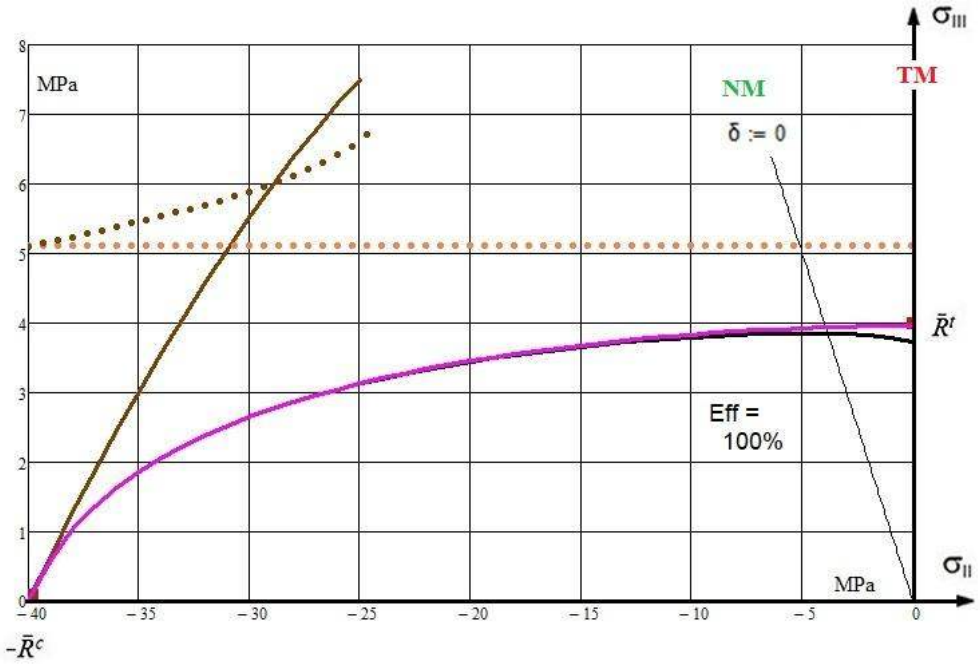

Fig.22-4b, Normal Concrete: $\bar{R}^{\tau}$, $\sigma_{III}(\sigma_{II})$. *120°-rotational-symmetric model.*

Above figure leads to the result

"With decreasing σ_{II} an extrapolation of $\theta_{fp}°(F^{\tau})$ soon comes to its end. An estimation of values in the low σ_{II}-abscissa domain is not possible. Both the modes have to be applied".

In this context, *Fig.22-5* presents the span of the M-C curve on the 120°-rotationally-symmetric isotropic fracture body, outlining that it belongs to two modes the Shear Fracture mode (SF) F^{τ} and Normal Fracture mode (NF) F^{σ}. The envisaged accurate way consists of the following two paths.

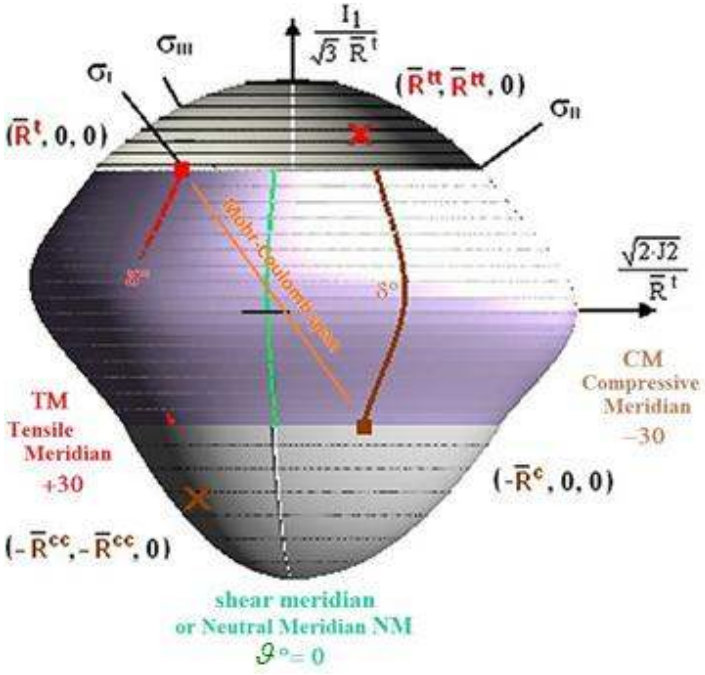

Fig.22-5, Normal Concrete: Visualization of all M-C-linked quantities

First Lessons Learned from Fig.22-4a and viewing Fig.22-5:

**Classically, employing Fτ only, the increasing angle θ_{fp} is linked to the slope of the plane M-C-curve.*

**Realistically, employing Fτ with Fσ, the increasing angle θ_{fp} is linked to the slope of the spatial fracture body surface. This makes the task still much more difficult.*

22.6 Results: Accurate Mode interaction Solution Path $\Theta_{fp}°$(Fτ, Fσ)

Values for $\Theta_{fp}°(F^{\tau})$ are fictitious information values if just F^{τ} is applied. An improvement will be now executed beginning with a mathematically, mechanically simple version, however by considering Θ^{τ} and f_{σ} as constants in the differentiation process.

The final formulation for *fracture plane angle measure C* can be found after using the abbreviations in *Table 22-5* in the necessary re-transformation process of the Mohr stresses back to structural stresses. This is supported by using addition theorems and by inserting the well-known structural stress invariants I_1, J_2, J_3. *Table22-6* for the simpler UD material depicts the full process.

Applying 'Mathcad 15 Symbolic Differentiation' on the interaction equation *Eff* = 1 results for $d(Eff)/d\sigma_n$ (*numerator of the formula for C*) and for $d(Eff)/d\tau_n$ (de-numerator) are obtained in Mohr stresses. Then, in order to achieve a practical equation for the final computation of *C*, an effortful manual evaluation by the determined re-transformation formulas above had to be performed.

However, this improved solution path, requiring the consideration of the 120°- rotational symmetry by capturing Θ^{τ} for the determination of cohesive strength R^{τ} and for the changing fracture angle θ_{fp} could not be gone to its end: The solver Mathcad found no solution. So the author had to 'suffer' that an elaborate, physically more accurate mathematical solution is not possible, see [*CUN25*].

Table 22-5: Re-transformation of stresses

Re-transformation

$2\sigma n = (C+1)\cdot\sigma II + (1-C)\cdot\sigma III$ $\quad \sigma t = \sigma n - C\cdot(\sigma II - \sigma III)$ $\quad 2\sigma n - \sigma t = 0.5\cdot(\sigma II + \sigma III) + 1.5\cdot C\cdot(\sigma II - \sigma III)$

$\sigma n = \frac{1}{2}\cdot[(C+1)\cdot\sigma II + (1-C)\cdot\sigma III]$ $\quad \sigma t = \frac{1}{2}\cdot[\sigma II\cdot(1-C) + \sigma III\cdot(1+C)]$ $\quad \tau n = -0.5\cdot\sqrt{1-C^2}\cdot(\sigma II - \sigma III)$

$a1 = \sigma II + \sigma III$

$a2 = \left[\frac{2\cdot\sigma t}{3} - 2\cdot\sigma n + \frac{4\cdot\sigma t}{3} = \frac{1}{3}\cdot(2\cdot\sigma t - 6\cdot\sigma n + 4\cdot\sigma t) = \frac{1}{3}\cdot(2\cdot\sigma t - 6\cdot\sigma n + 4\cdot\sigma t) = \frac{6}{3}\cdot(\sigma t - \sigma n) = -2C\cdot(\sigma II - \sigma III)\right]$

$a2 = -2C\cdot(\sigma II - \sigma III)$

$a3 = \left[\frac{2\cdot\sigma n^2}{3} - \frac{(\sigma t + \sigma n)^2}{3} + 4\cdot\tau n^2 + \frac{2\cdot\sigma t^2}{3} + \frac{2\cdot(\sigma n - \sigma t)^2}{3} = \frac{1}{3}\cdot\left[2\cdot\sigma n^2 - (\sigma t + \sigma n)^2 + 12\cdot\tau n^2 + 2\cdot\sigma t^2 + 2\cdot(\sigma n - \sigma t)^2\right]\right]$

$a3 = \frac{1}{3}\cdot\left[2\cdot\sigma n^2 - (\sigma t + \sigma n)^2 + 12\cdot\tau n^2 + 2\cdot\sigma t^2 + 2\cdot(\sigma n - \sigma t)^2\right] = \frac{1}{3}\cdot 3\cdot C^2\cdot(\sigma II - \sigma III)^2$

$a3 = C^2\cdot(\sigma II - \sigma III)^2$

$a4 = 12\cdot\tau n^2 + 2\cdot\sigma t^2 + 2\cdot\sigma n^2 + 2\cdot(\sigma n - \sigma t)^2 = 12\cdot\left[-0.5\cdot\sqrt{1-C^2}\cdot(\sigma II - \sigma III)\right]^2 + \left(3\cdot C^2\cdot\sigma II^2 - 6\cdot C^2\cdot\sigma II\cdot\sigma III + 3\cdot C^2\cdot\sigma III^2 + \sigma II^2 + 2\cdot\sigma II\cdot\sigma III + \sigma III^2\right)$

$= 12\cdot\left[-0.5\cdot\sqrt{1-C^2}\cdot(\sigma II - \sigma III)\right]^2 + \left(3\cdot C^2\cdot\sigma II^2 - 6\cdot C^2\cdot\sigma II\cdot\sigma III + 3\cdot C^2\cdot\sigma III^2 + \sigma II^2 + 2\cdot\sigma II\cdot\sigma III + \sigma III^2\right)$

$a4 = 12\cdot\left[-0.5\cdot\sqrt{1-C^2}\cdot(\sigma II - \sigma III)\right]^2 + \left[3\cdot C^2\cdot(\sigma II - \sigma III)^2 + a1^2\right]$

$a4 = 4\cdot\left(\sigma II^2 - \sigma II\cdot\sigma III + \sigma III^2\right)$

$a5 = \left[8\cdot\sigma n - 4\cdot\sigma t = 4\cdot(2\sigma n - \sigma t) = 4\cdot[0.5\cdot(\sigma II + \sigma III) + 1.5\cdot C\cdot(\sigma II - \sigma III)]\right]$

$a5 = 4\cdot[0.5\cdot(\sigma II + \sigma III) + 1.5\cdot C\cdot(\sigma II - \sigma III)]$

There was some hope, that a better physical consideration of Θ^{τ} and f_{σ} , namely as variables in the differentiation process might lead to a solution.

Physically and mathematically improved Θ^{τ} and fσ , now also differentiated

Applying Mathcad Symbolic Differentiation on $d(Eff)/d\sigma_n$, the numerator in Mohr stresses, leads to the extremely long equation in *Table 22-6*. And, for the more complicated differentiation $d(Eff)/d\tau_n$, the de-numerator, no applicable result was presented, only the citation "*The returned result is too large to* display". Trying to be physically and mathematically fully accurate this citation from Mathcad was a frustrating result.

Due to his mountain experiences the author never gave up,

but here the author gives in to the practically unsolvable problem.

22.7 Results: Guessing a Cohesive Strength value R^{τ} considering $f\sigma$

After the failure to follow the above accurate path, the task remains to offer a practical estimate. Formulas, see *Table 22-6*. This approach consists of the following steps: $Eff^m = (Eff^{NF})^m + (Eff^{SF})^m = 1$

- Guess of a value for R^{τ} , assumed 10 MPa
- Guess of a value for θ_{fp}°, using the knowledge that it must lie much below the 90° but significantly higher than θ_{fpc}°= 51° → assuming here: 71° = (51° + 90°) / 2 $\quad \rightarrow CF\tau(\sigma_n = 0)$
- Insertion into the relationships for the structural stresses and thereby into the lengthy interaction equation
- Checking, whether the material stressing effort meets *Eff* =100% =1, considering *fσ*-correction
- The implicit Mathcad solution process proves by the 1.03 that R^{τ} = 10 MPa was a good guess ! .

Table 22-6: Guessing a Cohesive Strength R^{τ}

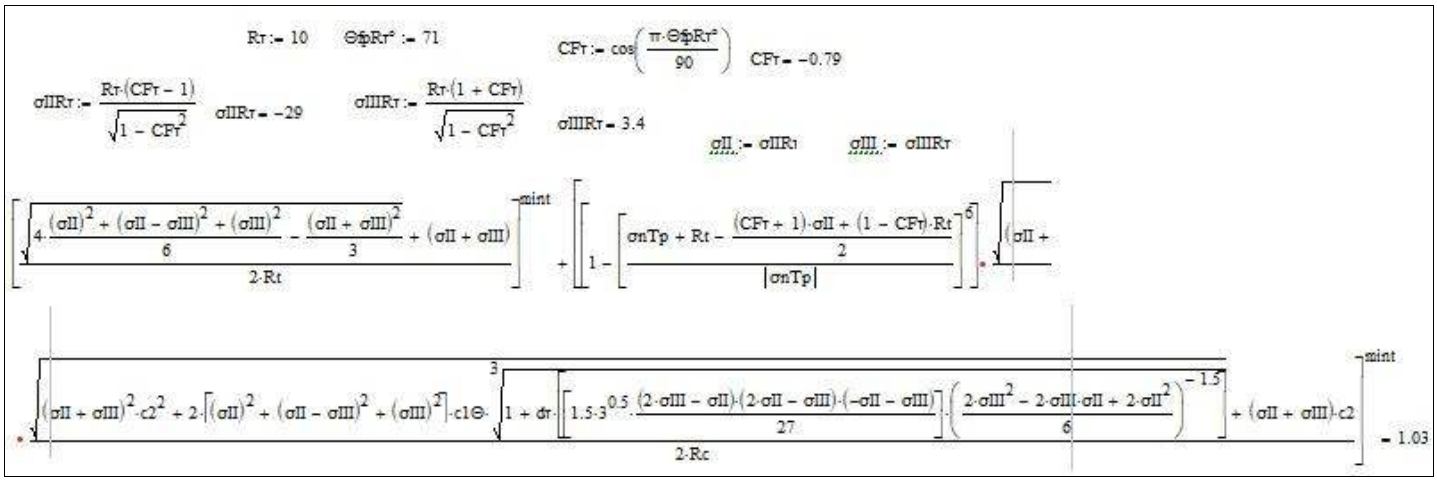

Limits of R^{τ}, *learned from Fig.22-4a*

$$\tau_n^{Tp} + \mu \cdot \sigma_n^{Tp} \text{ (classical M-C)} > R^{\tau} = \tau_{nt}(\sigma_n = 0) > R^{t} \quad \text{with} \quad \theta_{fp}^{c}\,° = 51°$$

$$\sigma_n^{Tp} = c^2 \cdot \left(-R^c\right),\ \tau_n^{Tp} = -s \cdot c \cdot \left(-R^c\right) \text{ and } c = \cos\theta_{fp}^{c} = \cos\left(\theta_{fp}^{c}\,° \cdot \frac{\pi}{180°}\right),\ s = \sqrt{1-c^2}$$

$$\text{assuming fracture angle } \theta_{fp}^{c} \text{ or friction value } \mu = -\cos(2 \cdot \theta_{fp}^{c}\,° \cdot \pi / 180°).$$

LL *from interpretation of the results including the Summary Table 25-6:*

- ✓ *The modes F^{τ}, F^{σ} and the interaction equation Eff - representing the surface of the fracture body in structural stresses - can be transferred into Mohr stresses and 'Addition Theorems-based' re-transformed in order to make a solution possible*
- ✓ *With the extrapolation approaches it was not possible to determine the full alteration of the nonlinear M-C curve (envelope), of the fracture plane angle $\theta_{fp}°$ and of R^{τ}. Just employing the SF mode F^{τ} cannot lead to a full course of the M-C curve and its quantities $\theta_{fp}°$, R^{τ}*
- ✓ *Due to the not locally full representing the course of the $\sigma_{III}(\sigma_{II})$ test data the mode F^{τ} is to correct by f_{σ} in order to simply obtain an approximation for a more realistic ('uni-axial') M-C curve*
- ✓ *Θ^{τ} must be considered, if the material is not ductile under compression. And ('bi-axially'), complete failure danger is the result of both the portions Eff^{NF} and Eff^{SF}, interaction is to consider*
- ✓ *For Normal Concrete it is the conclusion* that *R^{τ} is about 11 MPa and $\theta_{fp}°$ is approximately 70° at the cohesive strength point, compared to $\theta_{fp}° = 51°$ at the Touch point, representing R^{c} .*
- ✓ *Keep in mind: The presented results are averaged quantities and remind scatter!*

Applying - instead of the present Modal SFC - a so-called Global SFC, which globally maps by one single mathematical equation all test data with its two different modes, the same bottlenecks for the execution of this specific task would be found, too!

Note, please:

This is a good place to remind physics by stressing again the author's FMC-based failure mode thinking. It meets the action 'confining pressure' and the action 'bi-axial compressive stress':

Designing to hydraulic borehole fracturing 'Jaeger et al.' are still writing in 2007 (*cited in* [*You15*])

"*Tensile strengths predicted by both the Coulomb criterion (onset-of cracking, solid mechanics) and the Griffith criterion (cracked, fracture mechanics) are much higher than the measured magnitudes of almost all rocks, although the two criteria have clear physical backgrounds*".

This facts-neglecting citation is unbelievable for the author:

Each mode NF and SF is dominated by one technical strength R. And, it is also known that the cohesive (shear) strength is the result of two acting modes, namely SF with NF. Both these facts lead to the mechanics-based conclusion:

"*A Shear Failure-based criterion cannot give a prediction for a tensile strength* R^t".

22.8 Full UD-Mohr Envelope $\tau_{nt}(\sigma_n)$, Derivation of $\Theta_{fp}(\sigma_n)$ and of Cohesive shear Strength

Aim: *Unlocking the 'mystery' behind the shear quantities* R_{23}, R_{23}^{τ} and R_{23}^{A} *to be inserted in some UD SFC-linked analyses.*

Shear Strength Quantities in Analysis, Survey:

Fig.22-6 collects all figures which are necessary to understand the difference of applied shear quantities (*upper part figure*): The shear fracture stress R_{23}, R_{23}^{τ} (Tsai-Wu, Hashin), the so-called cohesive strength R_{23}^{τ} (UD construction material, rock mechanics) and the Action plane shear strength R_{23}^{A} (Puck).

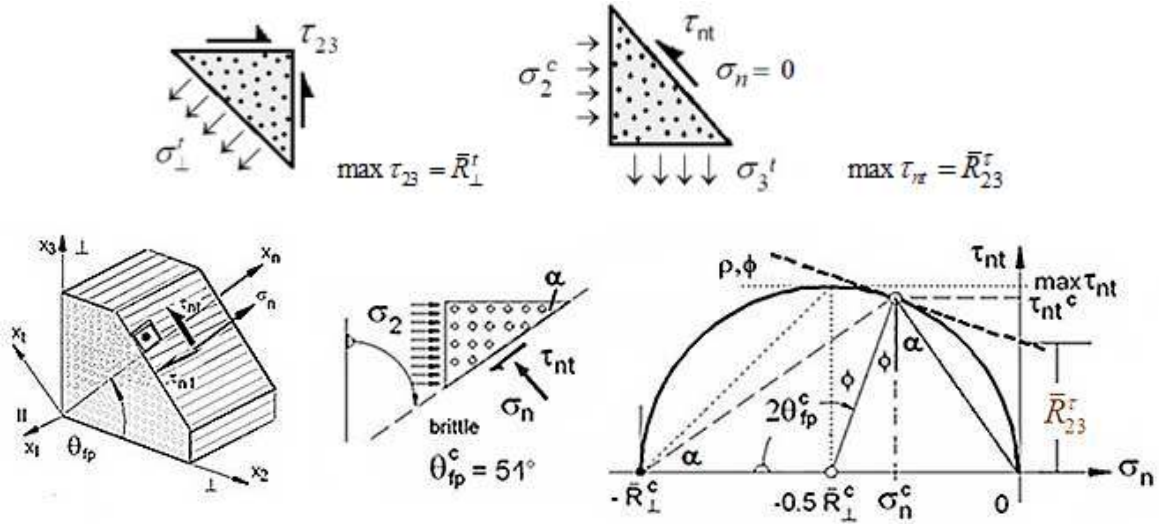

Fig. 22-6: Difference of transversal shear fracture stress and cohesive strength.

The dashed curve in *Fig.22-6* is the Linear Mohr-Coulomb (M-C) curve, ending at R_{23}^{τ}. This approach is a simple IFF2-extrapolation from the compressive strength point, keeping the *fracture angle measure* $C = C_{fp}^{c}$ constant, when estimating the so-called cohesive strength by

$$R_{23}^{\tau} = \tau_{nt}{}^{c} + \mu \cdot \sigma_n{}^{c} \text{ at } \sigma_n = 0 .$$

The letters $\rho = \phi$ in *Fig.22-6* address the so-called *friction* angle. The 3 sketches above demonstrate that the cohesive strength point $\bar{R}_{23}^{\tau}$ must be located in the mode's transition zone and cannot be reliably estimated just by an IFF2-Extrapolation, employing just SF! With M-C the parallel acting normal fracture part NF, namely IFF1, is neglected. But IFF1 may cause much more failure danger than the compression-linked shear mode IFF2 from the transition zone begin on.

The analytical determination of the M-C failure curve and of a value for the cohesive strength depends on the local quality of the used IFF2-model and the interaction in the transition zone. Therefore, in order to accurately determine $\tau_{nt}(\sigma_n)$ both the modes are to include in the derivation process of a realistic M-C curve, the determination of the fracture angle $\Theta_{fp}°$ and of the cohesive strength $\bar{R}_{23}^{\tau}$ at $(\tau_{nt}^{\text{fracture}}, \sigma_n = 0)$.

An improved treatment by a correction f_{corr} of the M-C curve has been effortful executed by the author

in [*Cun23b*]. Such a correction becomes necessary because any SFC has to be as simple as possible, which means that all presently applied SFCs will have a deficiency in the mode transition zones. The author has compensated for this with a correction (*compare fσ of the previous isotropic case*). The bottom figure in *Fig.22-1* displays, how the fracture angle increases, when approaching $\bar{R}_{\perp}^{t}$. Thereby the **bold** curve represents the optimum corrected mapping of the M-C curve in the transition zone around $\sigma_n = 0$. Now the steps of the tedious way to obtain *Fig.22-1* shall be presented.

22.8.1 Relations for a Transformation from a Test Fracture Curve $\sigma_3(\sigma_2)$ to Mohr's $\tau_{nt}(\sigma_n)$

The general stress state $\{\sigma\}$ in the material point of the lamina has to be transformed around the 1-axis to the arbitrary Mohr stress state $\{\sigma^{\theta}\} = [T_{\sigma}(\theta)]\cdot\{\sigma\}$, a fiber-parallel plane, by applying <u>*Fig.22-7*</u>, wherein *c*: = cos θ, *s* = sin θ and *n* is normal to the 'action plane' [*Cun22*]. Values of the parameters depend on the approach, whether it is a linear or a parabolic one.

$$\begin{matrix}\\ \rightarrow\\ \\ \rightarrow\\ \\ \rightarrow\end{matrix}\begin{bmatrix}\sigma_1\\ \sigma_n\\ \sigma_t\\ \tau_{nt}\\ \tau_{t1}\\ \tau_{n1}\end{bmatrix} = \left\{\sigma^{\theta}\right\} = \left[T_{\sigma}(\theta)\right]\{\sigma\} = \begin{bmatrix}1 & 0 & 0 & 0 & 0 & 0\\ 0 & c^2 & s^2 & 2sc & 0 & 0\\ 0 & s^2 & c^2 & -2sc & 0 & 0\\ 0 & -sc & +sc & c^2-s^2 & 0 & 0\\ 0 & 0 & 0 & 0 & c & -s\\ 0 & 0 & 0 & 0 & +s & c\end{bmatrix}\begin{bmatrix}\sigma_1\\ \sigma_2\\ \sigma_3\\ \tau_{23}\\ \tau_{31}\\ \tau_{21}\end{bmatrix}$$

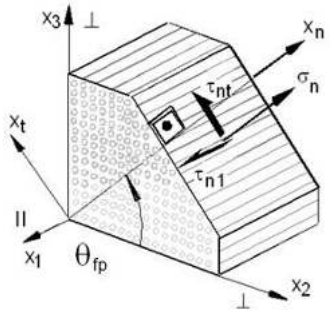

Fig. 22-7: Visualization of the transformation of lamina stresses into associated Mohr stresses. $\theta = \Theta_{fp}$ denotes the angle of the anti-clockwise transformation from the (1, 2, 3)-CoS to the (1, n, t)-CoS

According to

$\sigma_n^A(\theta) = c^2\cdot\sigma_2 + s^2\cdot\sigma_3 + 2\cdot s\cdot c\cdot\tau_{23}$, $\tau_{n1}^A(\theta) = c\cdot\tau_{21} + s\cdot\tau_{31}$, $\tau_{nt}^A(\theta) = -s\cdot c\cdot(\sigma_2-\sigma_3) + (c^2-s^2)\cdot\tau_{23}$ the transformed stresses $\sigma_n(\theta)$, $\sigma_t(\theta)$, $\tau_{nt}(\theta)$, which Puck termed 'Action Plane' Stresses, *Fig.22-1, <u>right</u>,* in the turned CoS depend on (σ_2, σ_3, τ_{23}) only, whereas τ_{t1}, τ_{n1} is linked to (τ_{31}, τ_{21}). They are acting in the potentially physical (fracture) failure 'plane' and are decisive for fracture. In case of normal stress-induced fracture (NF) σ_n will be responsible for fracture and in case of shear stress-induced fracture τ_{nt} will be the fracture dominating Mohr stress. The Mohr stress τ_{t1} has no impact but has to be considered in the derivations of the *Eff*-functions until it vanishes during the later transformation process.

Fracture plane will become that 'action plane' where the material stressing effort *Eff*($\sigma(\theta)$) will reach the value 1 = 100% at (maximum) failure loading and by that, where the theoretical material reserve factor f_{RF} will become a minimum.

22.8.2 Accuracy Problem of the IFF2-model in the transition zone IFF2 (SF) - IFF1 (NF)

In this subchapter the cohesion strength R_{23}^{τ}, activated by τ_{nt} in the quasi-isotropic plane of the UD material is envisaged. This quantity is located in the transition zone of the two modes IFF1 and IFF2. With isotropic materials the author learned that a transformation from UD lamina stresses into the desired Mohr stresses τ_{nt}, σ_n must be also possible. Thereby a closer look at R_{23}^{τ} and at the Mohr envelope $\tau_{nt}(\sigma_n)$ or M-C curve will be possible.

Here addressed is the <u>quasi-isotropic</u> UD plane (*works <u>similar</u> to isotropic concrete materials, using **available** multi-axially compression test-based data [Cun22]*). The compromise is on the 'safe Reserve Factor side'. This means: The engineering approach of above $Eff^{\perp\tau}$ (SF) is not problematic for Design

Verification, because *Eff* = 1 delivers conservative *RF*-values in the transition zone, since the curve runs more internally due to the generally *minimum value choice* of the interaction exponent *m*.

Focus here is the derivation of $\tau_{nt}(\sigma_n)$, $\theta_{fp}(\sigma_n)$ and R_{23}^{τ} from a measured fracture curve $\sigma_3(\sigma_2)$ and its course in the 2nd quadrant of $\sigma_3(\sigma_2)$. In *Table 22-7* all relations of the process steps necessary for the transformation are compiled and formulas for the searched entities τ_{nt} , σ_n , $\theta_{fp}°$ are presented. After transformation of the UD lamina (layer) stresses σ_2, σ_3, τ_{23} in the quasi-isotropic plane into the principal stresses σ^{pr} (*index pr means principal*), the shear stress τ_{23} vanishes. Therefore, with no loss of generality σ^{pr} can be simpler written in the further text, back again as plain letter σ, but thinking they might be principal stresses acting in the quasi-isotropic plane. In the addressed quasi-isotropic plane this transformation of the lamina stresses into Mohr stresses practically works via addition theorems and using $C(\Theta_{fp}°) = cos\Theta^2 - sin\Theta^2$, which is termed here 'fracture angle measure'.

As the author still found with isotropic materials, the interaction considering magenta curve (thinly-marked) in *Fig.22-8* cannot accurately map the course of test data. The improved **bold**-marked curve is physically more accurate and this local mapping shortcoming is to model more detailed as follows. *Fig 22-1* shows that with the IFF2-function the shear effort $Eff^{\perp\tau}$ cannot become zero in the M-C domain at $\sigma_2 = 0$. This numerical behavior is a shortcoming in the transition zone of the 'simple' engineering FMC-based IFF2 approach. An accurate alteration of the fracture angle $\Theta_{fp}°$ and of the associated Mohr stresses τ_{nt}, σ_n is not to achieve with the mathematical course of the given 'engineering' IFF2 function. The mapping quality of the given IFF2 is not fully sufficient if the alteration of the fracture angle Θ_{fp} in the transition zone is to determine. This bi-axially stressed transition zone between the normal fracture mode domain NF and the shear fracture mode domain SF is ruled by interaction and therefore requires both the Eff-modes to be inserted into the interaction equation *Eff* = 1. Specific points of the investigated M-C domain are: $(\sigma_2 = -\bar{R}_{\perp}^{c}, 0) \rightarrow (\sigma_2, \sigma_3 = -\sigma_2) \rightarrow (0, \sigma_3 = \bar{R}_{\perp}^{t})$. In order to sort out a better mapping description it is essential to know how the pure mode efforts of the activated modes IFF1 and IFF2 change its influence along the σ_2-axis, which is depicted in *Fig.22-8, too*. $Eff^{\perp\tau}$ firstly becomes zero at the equi-biaxial tensile 'strength' point $(\bar{R}_{\perp}^{tt}, \bar{R}_{\perp}^{tt}) < \bar{R}_{\perp}^{t}$. This zero point lies physically 'too late' for a more accurate revised local mode description. An improvement is to achieve.

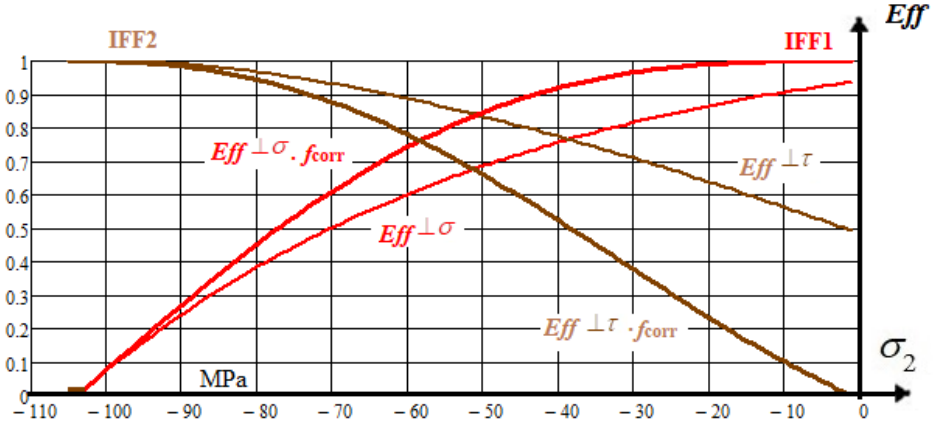

Fig.22.8: Course of the two efforts $Eff^{\perp\sigma}$, $Eff^{\perp\tau}$ *composing the fracture stress curve Eff =1= 100%.*

22.8.3 ***Improvement of the IFF2 Criterion in the Transition Zone,*** *Figs.22-8 and 22-9*

The required entities τ_{nt} , σ_n , $\Theta_{fp}°$ and $\bar{R}_{23}^{\tau}$ only become accurate if a physically necessary correction of $Eff^{\perp\tau}$ is considered by using a correctively acting decay function f_{corr} . In order to implement f_{corr} one just has to replace $a_{\perp\perp}$ by $f_{corr} \cdot a_{\perp\perp}$ and $b_{\perp\perp}$ by $f_{corr} \cdot b_{\perp\perp}$. For a realistic transformation of the test

curve, formulated in lamina stresses into a Mohr stress formulation, it is considered that $Eff^{\perp\tau}$ (SF) physically must become zero when reaching the pure NF domain at the point ($\sigma_3 = \bar{R}^t_\perp, \sigma_3 = 0$).

Table 22-7: IFF2-IFF1-interacted Derivation of $\tau_{nt}(\sigma_n), R^\tau_{23}, \theta_{fp}$ from a measured curve $\sigma_3{}^{fr}(\sigma_2)$

$$SF: Eff^{\perp\tau} = [a_{\perp\perp}\cdot(I_2) + b_{\perp\perp}\cdot\sqrt{I_4}]\ /\ \bar{R}^c_\perp = 1$$

$$= [a_{\perp\perp}\cdot(\sigma_2{}^{pr} + \sigma_3{}^{pr}) + b_{\perp\perp}\cdot\sqrt{(\sigma_2{}^{pr} - \sigma_3{}^{pr})^2 + 0^2}]\ /\ \bar{R}^c_\perp = 1 \text{ (lamina stresses)}$$

$$\equiv [a_{\perp\perp}\cdot(\sigma_n + \sigma_t) + b_{\perp\perp}\cdot\sqrt{(\sigma_n - \sigma_t)^2 + 4\tau_{nt}{}^2}]\ /\ \bar{R}^c_\perp = 1 \quad \text{(in Mohr stresses)}$$

$$NF: Eff^{\perp\sigma} = (\sigma_2{}^{pr} + \sigma_3{}^{pr}) + \sqrt{(\sigma_2{}^{pr} - \sigma_3{}^{pr})^2 + 0^2}]\ /\ 2\cdot\bar{R}^t_\perp = 1$$

$$\equiv [(\sigma_n + \sigma_t) + \sqrt{(\sigma_n - \sigma_t)^2 + 4\tau_{nt}{}^2}]\ /\ 2\cdot\bar{R}^t_\perp = 1.$$

Known: $\sigma_2{}^{pr}$, $\sigma_3{}^{pr}$. Searched is: σ_n, τ_{nt}, Θ_{fp} with $C = \cos(2\cdot\Theta_{fp}{}^\circ\cdot\pi/180°)$.

Use of addition theorems, $\sigma_\lambda = 0$. For lamina stresses ^{pr} now dropped for simplification

$$\sigma_n - \sigma_t = c^2\cdot(\sigma_2 - \sigma_3) - s^2\cdot(\sigma_2 - \sigma_3) = C\cdot(\sigma_2 - \sigma_3), \quad S = \sqrt{1 - C^2}$$

$$\sigma_t = \sigma_n - C\cdot(\sigma_2 - \sigma_3),\ C = c^2 - s^2 = 2c^2 - 1 = 1 - 2s^2,\ \sigma_n + \sigma_t = \sigma_2 + \sigma_3,$$

$$\tau_{nt} = -0.5\cdot S\cdot(\sigma_2 - \sigma_3) = -0.5\cdot\sqrt{1 - C^2}\cdot(\sigma_2 - \sigma_3),\ \sigma_n = (C+1)\cdot 0.5\cdot\sigma_2 + (1 - C)\cdot 0.5\cdot\sigma_3.$$

Differentiation of structural stresses-linked Mohr stresses delivers (minus due to implicit derivation)

$$\frac{d\tau_{nt}}{d\sigma_n} = \frac{(s^2 - c^2)\cdot(\sigma_2 - \sigma_3)}{-2\cdot s\cdot c\cdot(\sigma_2 - \sigma_3)} = \frac{C}{S}, \quad \text{valid } \textit{uni}\text{- and } \textit{bi}\text{-}\textit{axial} \text{ (like isotropic!).}$$

Fracture (interaction) equation ≡ mathematical equation of the fracture body

$$Eff = [(Eff^{NF})^m + (Eff^{SF})^m]^{m^{-1}} \quad \textit{or} \quad \text{computationally simpler}$$

$$(Eff^{NF})^m + (Eff^{SF})^m = 1 = 100\% \quad \text{total effort fracture curve}$$

From differentiation of the interaction equation (σ_t goes away)

$$\{[(\sigma_n + \sigma_n - C\cdot(\sigma_2 - \sigma_3)) + \sqrt{(\sigma_n - \sigma_n - C\cdot(\sigma_2 - \sigma_3))^2 + 4\tau_{nt}{}^2}]\ /\ 2\cdot\bar{R}^t_\perp\}^m +$$

$$+\{[a_{\perp\perp}\cdot(\sigma_n + \sigma_n - C\cdot(\sigma_2 - \sigma_3)) +$$

$$+ b_{\perp\perp}\cdot\sqrt{(\sigma_n - \sigma_n - C\cdot(\sigma_2 - \sigma_3))^2 + 4\tau_{nt}{}^2}]\ /\ \bar{R}^c_\perp\}^m = 1.$$

are obtained the two equations

$$d[(Eff^{NF})^m + (Eff^{SF})^m]/d\sigma_n =$$

$$m\cdot\{2\sigma_n - C\cdot(\sigma_2 - \sigma_3) + \sqrt{(C\cdot(\sigma_2 - \sigma_3))^2 + 4\tau_{nt}{}^2}]/2\bar{R}_\perp{}^t\}^{m-1}/\bar{R}_\perp{}^t +$$

$$+2a_{\perp\perp}\cdot\mathrm{m}\cdot\{a_{\perp\perp}(2\sigma_n - C\cdot(\sigma_2 - \sigma_3)) + b_{\perp\perp}\sqrt{(C\cdot(\sigma_2 - \sigma_3))^2 + 4\tau_{nt}{}^2}]\ /\ \bar{R}_\perp{}^c\}^{m-1}/\bar{R}_\perp{}^c,$$

$$d[(Eff^{NF})^m + (Eff^{SF})^m]/d\tau_{nt} =$$

$$\frac{2m\cdot\tau_{nt}\cdot\{2\sigma_n - C\cdot(\sigma_2 - \sigma_3) + \sqrt{(C\cdot(\sigma_2 - \sigma_3))^2 + 4\tau_{nt}{}^2}]/2\bar{R}_\perp{}^t\}^{m-1}}{\bar{R}_\perp{}^t\cdot\sqrt{(C\cdot(\sigma_2 - \sigma_3))^2 + 4\tau_{nt}{}^2}} +$$

$$+4b_{\perp\perp}\cdot\mathrm{m}\cdot\{a_{\perp\perp}(2\sigma_n - C\cdot(\sigma_2 - \sigma_3)) + b_{\perp\perp}\sqrt{(C\cdot(\sigma_2 - \sigma_3))^2 + 4\tau_{nt}{}^2}]\ /\ \bar{R}_\perp{}^c\}^{m-1}/\bar{R}_\perp{}^c.$$

Equating above two equations and replacing Mohr stresses by ply stresses

via $\sigma_n = (C+1)\cdot 0.5\cdot\sigma_2 + (1-C)\cdot 0.5\cdot\sigma_3$, $\tau_{nt} = -0.5\cdot\sqrt{1-C^2}\cdot(\sigma_2 - \sigma_3)$

yields an implicitely to solve equation for the fracture angle measure C

$$\frac{C(\sigma_2, \sigma_3)}{\sqrt{1-C^2}} = -\left[\frac{A}{\bar{R}_\perp{}^t} + \frac{2\cdot a_{\perp\perp}\cdot B}{\bar{R}_\perp{}^c}\right]/\left[\frac{2\cdot A}{\bar{R}_\perp{}^t\sqrt{(\cdot\sigma_2 - \sigma_3)^2}} + \frac{4\cdot b_{\perp\perp}\cdot\tau_{nt}(C)}{\bar{R}_\perp{}^c\sqrt{(\cdot\sigma_2 - \sigma_3)^2}}\right] \text{ with}$$

$$\mathrm{A} = \left[\frac{\sigma_2 + \sigma_3 + \sqrt{(\sigma_2 - \sigma_3)^2}}{2\cdot\bar{R}^t_\perp}\right]^{m-1}, \quad \mathrm{B} = \left[\frac{a_{\perp\perp}\cdot(\sigma_2 + \sigma_3) + b_{\perp\perp}\cdot\sqrt{(\sigma_2 - \sigma_3)^2}}{\bar{R}^c_\perp}\right]^{m-1}$$

and finally via $C = \cos(2\cdot\theta_{fp}) \rightarrow \theta_{fp} = 0.5\cdot\arccos\mathrm{C}$, $\theta_{fp}{}^\circ = \theta_{fp}\cdot 180°/\pi$.

By insertion of any stress state the associated 'running' C can be computed.

Cohesion strength $\bar{R}^\tau_{23}$ is determinable for $\tau^{fail}_{nt}(\sigma_n) = 0$

Similar to the isotropic case the bi-axial stress-ruled quasi-isotropic M-C curve, located in the quasi-isotropic plane, is oppositely dominated by two modes, IFF2 (SF) with IFF1 (NF). Therefore, attention was paid to the interaction of both these modes in the transition zone in order to finally obtain an 'accurate' fracture angle $\Theta_{fp}°$, being the pre-condition to determine the envisaged two Mohr stresses τ_{nt}, σ_n. the shear material stressing effort $Eff^{\tau} = Eff^{SF}$ must physically become zero at the tensile strength point (0, R^t). This specific shortcoming is brought about by a correction function that defines the decay of Eff^{τ} and is practically performed by setting $Eff^{\tau} = 0$ at $\sigma_{II} = 0$. As decay function the author often took (§10) an exponential one: $f_d = 1/(1+\exp(\frac{c_{1d}+\sigma_{II}}{c_{2d}})$, with c_{1d}, c_{2d} fixed at ($-\bar{R}^c$, 0.995) , (-0.01,+0.01).

Here it is sufficient to apply for the decay of $Eff^{\perp\tau}$: $f_{corr} = 1 + c_0 \cdot (\bar{R}^c_{\perp} + \sigma_2)^2$.

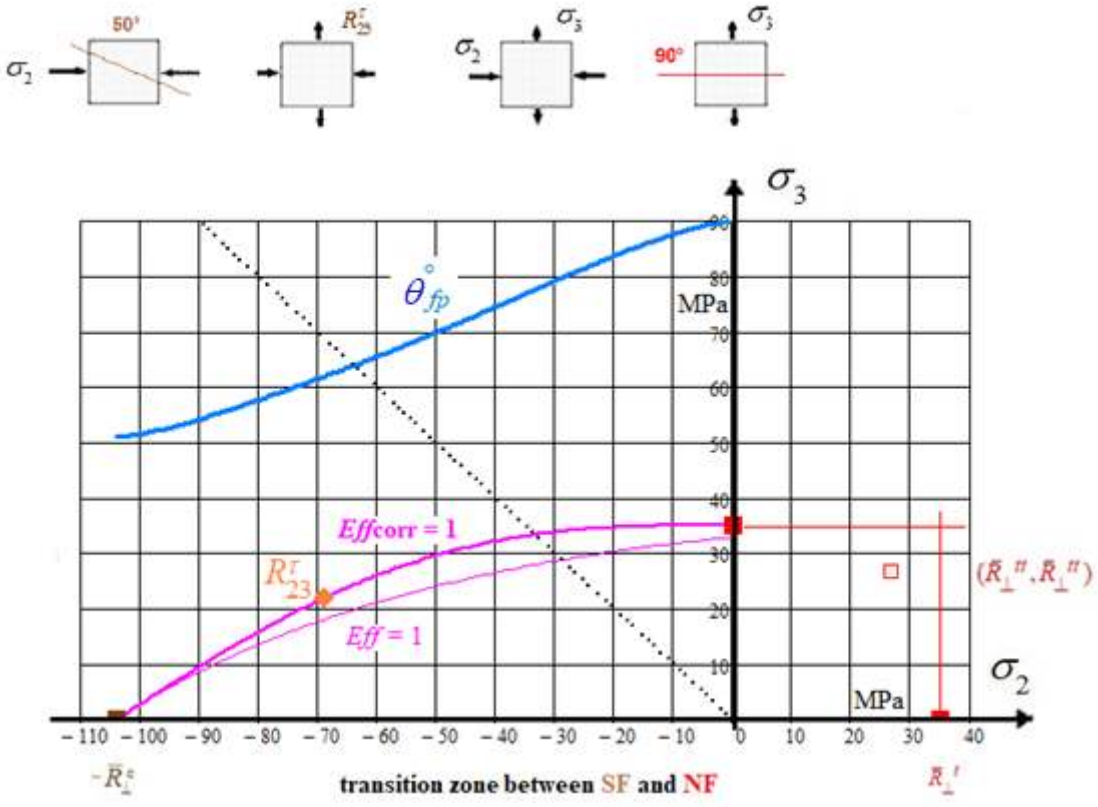

Fig. 22-9: Interaction curve $\sigma_3^{fracture}(\sigma_2)$ *with Eff = 1Failure stress curve* $\sigma_2(\sigma_3)$ *with alteration of fracture angle* $\theta_{fp}°$ *in the transition zone,. fracture angle measure* $C(\theta_{fp})$.

(Numerical example stems from a measurement of the fracture plane angle $\theta_{fp}°$ *in [VDI 97], square-marked bi-axial failure stress* $\bar{R}^{tt}_{\perp}$ *)*

Data set:

$\bar{R}^c_{\perp} = 104 MPa$, $\bar{R}^t_{\perp}$=35 MPa, $\Theta_{fp}° = 51°, C^c = -0.21 \leftrightarrow a_{\perp\perp} = 0.26$, $\mu_{\perp\perp} = 0.21$.

$f_{corr} = 1 + c_0 \cdot (\bar{R}^c_{\perp} + \sigma_2)^2$ with c_0 from inserting ($\sigma_2 = 0$, $\sigma_3 = \bar{R}^t_{\perp}$), $c_0 = 8.9 \cdot 10^{-5}$.

IFF1: $Eff^{\perp\sigma} = [(\sigma_2 + \sigma_3) + \sqrt{\sigma_2^2 - 2\sigma_2 \cdot \sigma_3 + \sigma_3^2}] / 2\bar{R}^t_{\perp}$,

IFF2: $Eff^{\perp\tau} = [a_{\perp\perp} \cdot f_{corr} \cdot (\sigma_2 + \sigma_3) + b_{\perp\perp} \cdot f_{corr} \sqrt{\sigma_2^2 - 2\sigma_2\sigma_3 + \sigma_3^2}] / \bar{R}^c_{\perp}$.

In *Fig. 22.9* are depicted:

► IFF2-IFF1- interacted fracture curve (*thin, original IFF2. With this 'simple' approach, the curve cannot run through* $\bar{R}_{\perp}^{t}$ = 35 MPa)

► IFF2-IFF1- interacted fracture curve *(bold, IFF2 decay function corrected, which better maps the course of measured fracture stress data)* and

► Course of the fracture plane angle θ_{fp}° (*bold, corrected*).

This correction changes the formula for the determination of the fracture angle measure *C* in *Table 22-8.* Therewith, after effortful MathCad programming and implicit numerical computations the desired accurate bi-axial fracture stress M-C-curve τ_{nt} (σ_n) could be derived in *Fig.22-10* by the refined IFF2 model and by re-transformation also ply stresses could be obtained. The fracture angle becomes now the realistic value of 90° instead 71°.

Table 22-8:

$$\frac{C}{\sqrt{1-C^2}} = -m\cdot\left[\frac{A}{\bar{R}_{\perp}^{t}}+\frac{2\cdot a_{\perp\perp}\cdot f_{corr}\cdot B}{\bar{R}_{\perp}^{c}}\right]/\left[\frac{2\cdot A}{\bar{R}_{\perp}^{t}\sqrt{(\cdot\sigma_2-\sigma_3)^2}}+\frac{4\cdot b_{\perp\perp}\cdot f_{corr}\cdot B\cdot\tau_{nt}}{\bar{R}_{\perp}^{c}\sqrt{(\cdot\sigma_2-\sigma_3)^2}}\right],$$

$$B_{corr}=\left[\frac{a_{\perp\perp}\cdot(\sigma_2+\sigma_3)+b_{\perp\perp}\cdot\sqrt{(\sigma_2-\sigma_3)^2}}{\bar{R}_{\perp}^{c}}\cdot f_{corr}\right]^{m-1} \quad \text{with} \quad f_{corr}=1+c_0\cdot(\bar{R}_{\perp}^{c}+\sigma_2)^2 .$$

22.8.4 Determination of Cohesive shear Strength R_{23}^{τ}

The interaction curve can be dedicated to the basic Mohr-Coulomb curve which runs from the compression strength point till the tensile strength point $\sigma_3=\bar{R}_{\perp}^{t}$. In order to find all relationships in one diagram the Mohr stresses are also inserted as functions of the lamina stresses σ_2 (σ_3) and not of σ_n alone, which is the usual diagram form. *Fig.22-4* includes the development of the fracture plane angle as function of the lamina stress σ_2. *Fig.23-1* still presented all MathCad-computed Mohr entities providing:

* Considering σ_2: '*linear Mohr'* $\bar{R}_{23}^{\tau}$

- Extrapolation from compressive strength point, straight IFF2-determined Mohr-Coulomb fracture curve

* Considering σ_2 and σ_3: *interaction*

- Full IFF2-IFF1-interacted Mohr-Coulomb fracture curve

- Course of the fracture plane angle θ_{fp}°/2 (thin, not decay function corrected) and corrected (bold).

The definition of the cohesive (shear) strength is $(\tau_{nt}^{fail}=\bar{R}_{23}^{\tau},\ \sigma_n=0)$. Searching $\bar{R}_{23}^{\tau}$(C), the derived formulation permits to continuously MathCad-compute the alternating fracture plane measure C with the associate fracture angle θ_{fp}°. The interpretation of the figures leads to the following conclusions:

- The general macro-mechanical IFF2 approach cannot offer a full accuracy of the realistically predicted Mohr-Coulomb curve. Just the *physically-based* decay function correction delivers the desired fidelity
- A SFC in lamina stresses can be transferred into a Mohr-Coulomb version
- The course of the fracture plane angle θ_{fp}° can be determined, too
- The idea of the FMC that IFF1 and IFF2 commonly add its *Eff* portions, which leads to the result that θ_{fp}° is in the sixty degrees ° at the cohesive strength point $\bar{R}_{23}^{\tau}$, with a degree value being the higher the higher the strength ratio $\bar{R}_{\perp}^{c}/\bar{R}_{\perp}^{t}$ is.

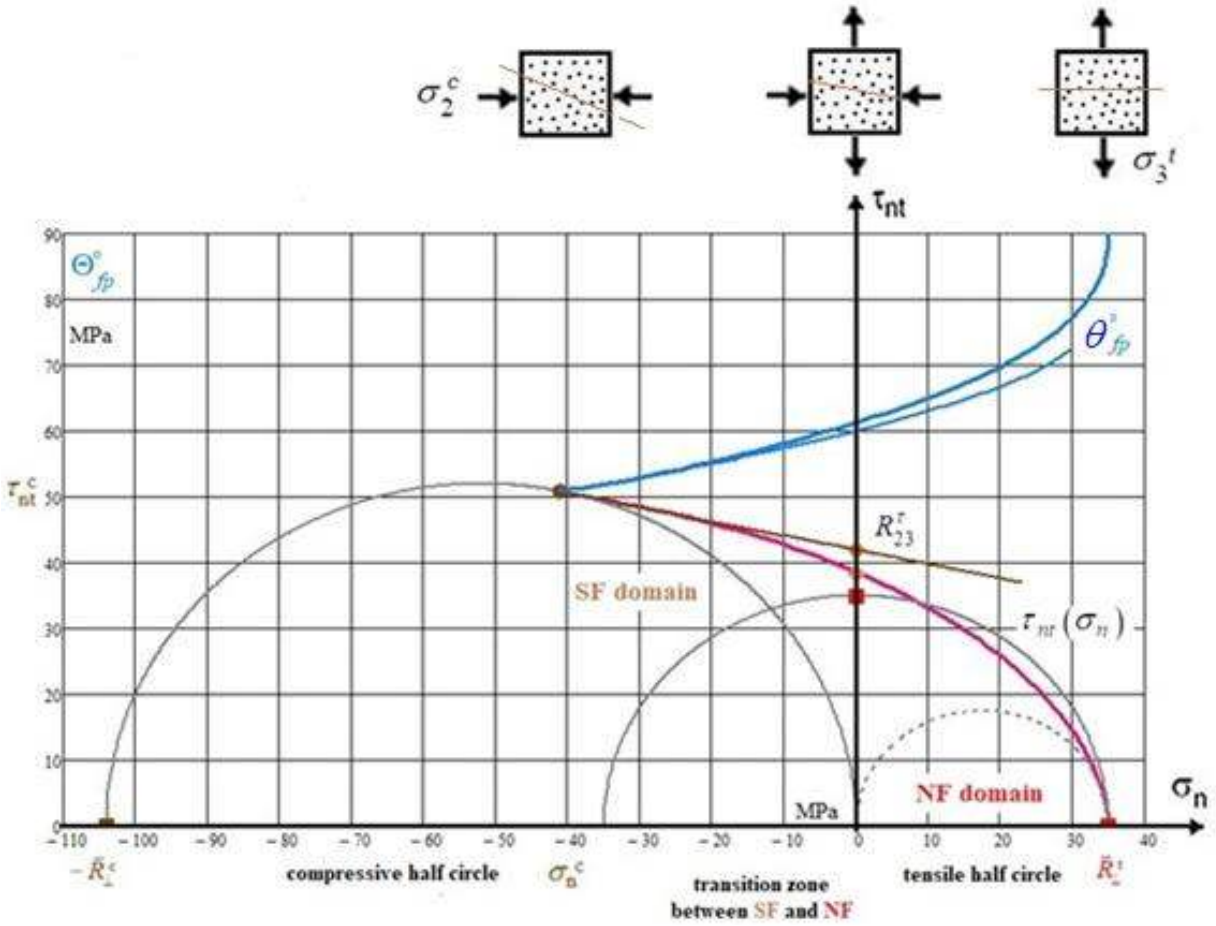

Fig. 22-10: Mohr-Coulomb curve characteristics, Mohr shear curves $\tau_{nt}(\sigma_n)$ with its special points and the 3 Mohr half-circles

LL:

- *Failure stress under pure shear* $\tau_{23}^{\text{fracture}} = max\,\tau_{23} > R_\perp^t$ *is a formalistically applied quantity*
- *Mohr-based approach linked so-called cohesive strength* $R_{23}^\tau = \tau_{nt}(\sigma_n = 0)$. *For the UD material a full derivation was possible because it was a 2-3plane problem and not spatial as with isotropicmaterials*
- *Puck's Action plane shear resistance* R_{23}^A*: Puck formulated a full IFF-SFC and could model-associated dedicate his not measurable action plane resistance a relation with the inclination model parameters p and the other strengths reading* $\bar{R}_{23}^A = \left[\bar{R}_{\perp\parallel} \cdot \sqrt{1 + 2 \cdot p_{\perp\parallel}^c \cdot \bar{R}_\perp^c / \bar{R}_{\perp\parallel}} - 1\right] / 2 \cdot p_{\perp\parallel}^c$.
- *Generally, assuming a transverse shear failure stress , which would be a sixth strength, will contradict material symmetry demands, which seem to require for UD materials a 'generic' number of 5, meaning 5 measurable strengths and 5 elasticity properties*
- *The ability for mobilizing friction processes depends on active compression stresses that cause via the friction value μ the necessary shear stress.*

Limits of R_{23}^τ and estimation

$$R_{23}^\tau = \tau_n^{Tp} + \mu \cdot \sigma_n^{Tp} \text{ (classical M-C)} > R_{23}^\tau = \tau_{nt}(\sigma_n = 0) > R_\perp^t ,$$

$$\sigma_n^{Tp} = c^2 \cdot \left(-R^c\right),\ \tau_n^{Tp} = -s \cdot c \cdot \left(-R^c\right) \text{ and } c = \cos\theta_{fp}^c = \cos\left(\theta_{fp}^c\,° \cdot \frac{\pi}{180°}\right),\ s = \sqrt{1 - c^2} ,$$

assuming fracture angle $\theta_{fp}^c\,°$ or friction value $\mu = -\cos(2 \cdot \theta_{fp}^c\,° \cdot \frac{\pi}{180°})$.

Estimation: $R_{23}^\tau \cong (R_{23}^\tau + R_\perp^t)/2$

23 Nonlinear Design Verification regarding MoS_{yield}, MoS_{ult} for Ductile Materials

Some specifications and standards (such as the ISO 14623) *even for ductile* behaving materials only require the determination of MoS_{ult}, as the design driving limit (*without rationale*). However, a realistic, nonlinearly computed MoS_{ult} is effortful to obtain when using ductile materials. In consequence of this requirement there are two demands: An efficient non-linear analysis and a procedure of how the Ultimate Strength Proof of Design has to be performed regarding MoS_{ult}.

Non-linear stress analysis and design verification at a too high-stressed so-called 'hot spot' requires a yield condition, which is usually the Mises yield condition. The limit of the validity of Mises-application may be exceeded in these 'hot spots', however, the material situation there is still capable of carrying load. Due to the fact that a non-linear design verification is very time consuming, the designer asks for a clear and practical engineering design procedure. This includes the non-linear analyses in order to predict the stress and deformation behavior and the Strength Design Verification which focuses on the assessment of the multi-axial state of stresses in the 'hot spot'. This stress state can be 2D and 3D. The latter loading can be exemplarily composed like $(\sigma_I, \sigma_{II}, p_{\text{at wall surface}})$.

In order to fully exploit the potential of a ductile material one has to distinguish two different types of such 'hot spots', the first is load-controlled and the second is strain-controlled.
The load-carrying limit of the latter is determined by the given redundancy or -in other words- by the remaining load carrying capacity of the lower stressed vicinity of the 'hot spot'. Here, redundancy means that the load locally changes its load path and generates a stress redistribution at this location. This stands for a load reserve. Hence, it is necessary to formulate a less effortful 'engineering approach'. This is to be verified by the company and accepted by the authority, of course.

ESA-specifications (ECCS) seem i. e. to rule out for ductile material the 'cheap' development way 'Pre-dimensioning structures to $MoS_{yield} = MoS_{0.2}$ (linear analyses only) instead to $MoS_{ult..}$ The reason for taking MS_{ult} probably comes from a typical linear analysis thinking: MoS_{ult} is just then the design driver if

$$f_{RF,ult} = R_m^t / j_{ult} < R_{p0.2}^t / j_{p0.2} \quad \text{with} \quad MoS = f_{RF} - 1.$$

This delivers for the example 'aluminum alloy AA2219':

(R_m^t = 390 MPa, $R_{p0.2}^t$ =290 MPa; $j_{p0.2}$=1.1, j_{ult}=1.25), R_m^t/1.25=312 MPa > $R_{p0.2}^t$/1.1 = 264 MPa

and proves, that MoS_{yield} is here the design driver but not MoS_{ult}!
And above that, this check is based on a linear analysis, only, which does not outline that the non-linear experience provides an additional reserve. As still mentioned: For brittle (behaving) materials MoS_{ult} is the essential *proof, whereas for ductile materials* (AA2219 for tanks or D6AC steel for the booster of the Ariane5) $MoS_{o.2}$ (< MoS_{ult}) is the more critical one.
Such considerations often will lead to the desired practical, simpler engineering design procedure.
On top it is to remind: f_{RF} is a material stress-linked, linearly simple to be computed value and *RF* a load-defined, nonlinearly to be computed value, $f_{RF} < RF = MoS + 1$.

23.1 Inelasticity topics of ductile and brittle materials

Some topics addressed in stress assessment read:

* A nonlinear computation ends at that *final load* level where numeric stops due to the fact that the load equilibrium is violated. This leads, at reaching *Eff* = 100%, to a margin

$$MoS_{ult} = \textit{final load} / (j_{ult} \cdot DLL) - 1.$$

* Viewing for instance the FE codes (about 2000) NASTRAN, MARC and Abaqus considering their nonlinear modules one has to require from them to deliver results that consistently remain on

engineering (σ,ε)-level or on true level. Design verification with the resulting higher true stresses compared to the engineering design allowable R_m^t is principally not accurate. In this context: Shell elements, which reflect *volume constancy* will provide *true stresses* in non-linear analysis. Why should in such cases *true stresses* not to be compared with *true strength values*?

* Residual stresses have to be respected on $\bar{R}_{p0.2}$-level for $MoS_{0.2}$. In the case of ductile behaving materials they are of vanishing influence on MoS_{ult} ($\bar{R}_m$-level) due to the stress redistribution in the non-linear domain. The higher the fracture strain the smaller the influence

* Engineering FEA stresses have to be assessed by engineering strengths

* Beyond $\bar{R}_m^t$: true $\sigma_{ax} \rightarrow$ trueσ_{eq} due to a 3D-stress state applying Bridgman modelling

* True stresses, computed by non-linear FEA, are higher than engineering stresses and therefore afford true strength assessment.

* Large strain non-linear analyses require the *true stress-true strain curve*.

Eventually the following formula set visualizes the difference in calculating linearly and non-linearly:

Linear analysis is sufficient (presumption): $\sigma \equiv \text{load} \quad \Rightarrow RF \equiv f_{RF} = 1 / Eff$

Material Reserve Factor $$f_{RF,\,ult} = \frac{\text{Strength Design Allowable } R}{\text{Stress at } j_{ult} \cdot \text{Design Limit Load}} > 1,$$

Non-linear analysis required: σ not proportional to load

Reserve Factor (load-defined) $$RF_{ult} = \frac{\text{Predicted Failure Load } \textit{for } \textit{Eff} = 100\%}{j_{ult} \cdot \text{Design Limit Load}} > 1.$$

Above formula let's assume how effortful it is to determine a value for the to be 'Predicted Failure Load' by a nonlinear structural analysis searching the critical location, where *Eff* becomes 100%.

***LL**:*

**Effortful non-linear analysis is required if a structural component is to save.*

**Before doing this formally check, whether $MoS_{0.2} < MoS_{ult}$ and thereby fulfill Design Verification.*

23.2 Thoughts before performing Linear Analysis and Non-linear analysis

- Load modelling: Average σ-ε-curve is to be utilized in stress and deformation analysis and for the load model computation in order to determining section forces and moments for the later structural dimensioning. This is a present topic in construction with our overloaded bridges!
- Material modelling: If a yield SFC is needed then an accurate choice is mandatory regarding whether the material is dense ('non-porous'), porous in the virgin material (*i.e.a foam*), or voids nucleated which grow under a tensile stress
- In the non-linear case three effects have to be considered: * non-linear stress-strain behavior of hardening (*metal below and beyond onset of necking ("post necking") or a lamina material below IFF*), *degradation caused softening (*smeared embedded lamina beyond IFF*), and *non-linear geometrical behavior concerning large strains and large deformations of the structural part
- Linear analysis is a convenient approximation which is sometimes still fully adequate for design. It has the advantage that the principle of superposition of load cases can be applied provided the boundary conditions are the same. A linear analysis is inadequate when the structure's stiffness

changes as it deforms or in other words if a part of deformation will remain after removing the load. Structures are very often inherently non-linear and statically indeterminate.

- Often only linear FE analyses are carried out. With the average curve and nominal wall thickness, an average stiffness is calculated in the component analysis and typical stresses are determined. The stresses calculated in this way are compared with minimum values (*design allowables*) in static or cyclic strength design verification. Considering the design limit strains when using structural materials: There is seldom a larger design limit strain than 1 % permitted.
- Non-linearity can take many forms such as geometric (*large deformation, instability*), material (*yielding & fracture*), and boundary/joint (*contact, joint non-linearity*). These different forms interact and increase the risk of failure! The principle of superposition is not valid anymore, results cannot be scaled, because the stress behavior is not anymore proportional to the loading applied. This makes realistic results expensive
- One must think in a practical case "Can the situation become critical if non-linearity is not enough respected"? A bolt for instance, bending in a connection, leads to a loss in structural part stiffness and probably to a change of the load distribution path. Then a question arises: Does the part still carry DUL if the bolt will only bend and not break? May then buckling be generated in any element of the structural part?
- Proportional loading causes sub-proportional stressing in non-linear case
- For initial IFF a linear analysis is sufficient in practice
- In case of well-designed, fiber-dominated laminates, very often, linear analysis is sufficient even for final failure because the embedded laminas are strain-controlled and experience no large operational strain (< 1% strain domain in the case of high-performance UD material)

***LL**:*

- *The dimensioning engineer is faced to decide „How much nonlinear analysis is required to solve a distinct task" or „Can the response of a load-carrying structure be assessed by using the simpler linear analysis, only". A decision on cost versus accuracy is required*
- *It is better to finish a linear analysis in time - after well-considering the physics behind the model - than perform a non-linear analysis that comes too late.*

23.3 General on the Stress-strain Curves to be used

Metal materials:

Fig.23-1 presents the tensile stress-strain curves for a variety of materials considering engineering and true stresses and strains. This figure offers some background for the following statements:

*If one wants to obtain the most reliable description of the physical structural behavior, the R/O equation of the real average stress-strain curve $\overline{\varepsilon\sigma}$ is to apply. Depending on nonlinearity and FEA code, average engineering or average true stresses are to use. In the case that a finite element analysis with large strains is to use, then – consistently – a true stress-strain curve must also be applied. See *§10.3.2*, too

*In a FE calculation with the $\min\sigma(\varepsilon)$-curve, the component behaves less stiff. This usually leads to the prediction of smaller stresses and greater strains than when calculating with the mean curve. Higher stresses can be predicted in some areas of the component and lower stresses in others. Depending on whether a strength criterion or a deformation criterion is used, this leads to either a non-conservative or a conservative assessment.

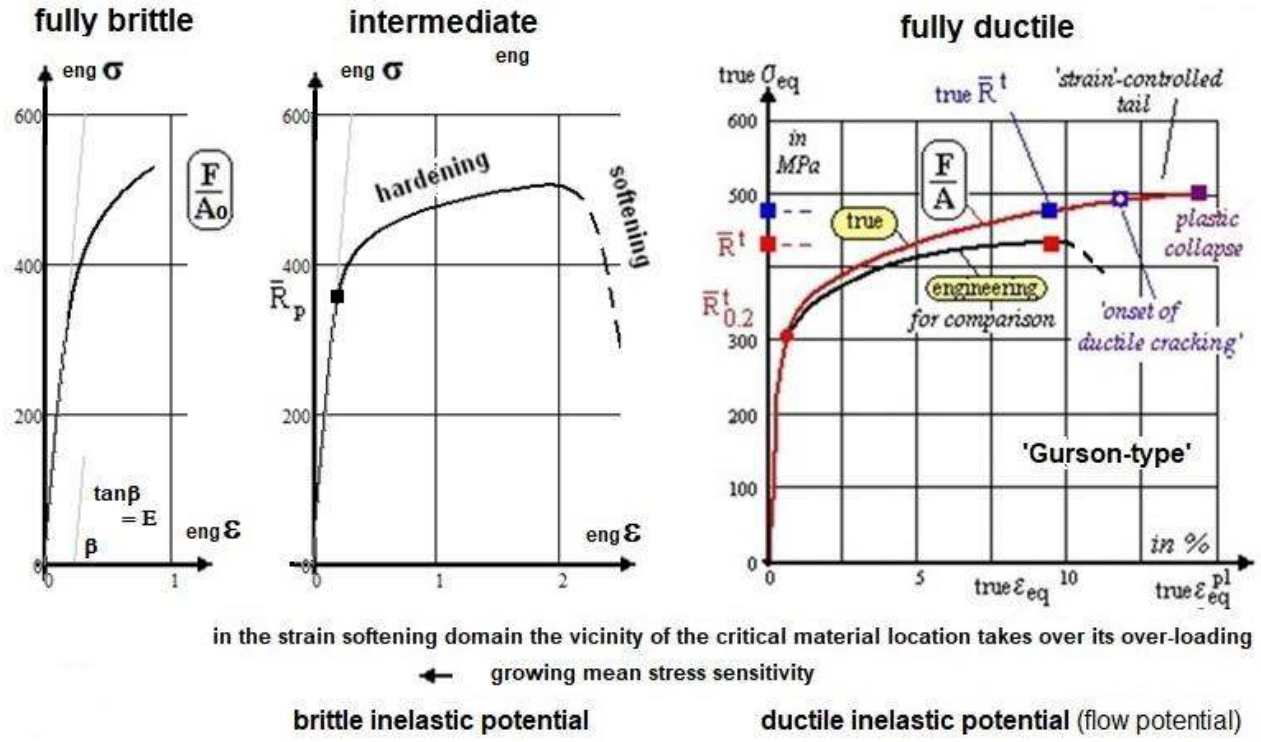

Fig.23-1: Tensile stress-strain curves addressing hardening and softening of brittle and ductile materials

*For certain stiffness cases, the application of a $\max\sigma(\varepsilon)$-curve for the FE calculation is also mandatory

*From above follows for a statically indeterminate structure, that the location of the critical point and of the associated stress state depends on the choice of the $\sigma(\varepsilon)$-curve

* One can conclude: Just for a 'one load path case' i.e. for the membrane area of a pressure vessel *(no redistribution possible, statically determined problem*), here, $\min\sigma(\varepsilon)$-curve can be used both, for design dimensioning and design verification of the final design

* For a nonlinear deformation analysis of a rotor at over-speed, the minimum value curve may be used. The proof of deformation is conservative because the 'softest' material was considered. The rotor does not bump into the housing. The use of the average curve would predict a typical and thus smaller deformation. Beside the ULS also the stronger SLS (*serviceability limit state*) is fulfilled

Depending on the evidence to be provided (of strength, stiffness, deformation), it would be necessary to check which calculation curve is to be used. Proof of deformation and proof of strength may have conflicting requirements. It is generally therefore recommended to calculate with average curves and to take into account required conservatisms by the assessment criteria (*design allowables, predetermined deformation limits, etc*.) during the design verification analyses.

***LL**:*

* A procedure, in which one wants to achieve a conservative design verification with a $\min\sigma(\varepsilon)$-curve is extremely problematic.

* For a reliable stress-strain analysis as a test result prediction the average curve is to apply.

UD materials:

The statements before are more addressing ductile and brittle isotropic materials. Therefore, a paragraph is added regarding the challenge of non-linear analysis of transversely-isotropic UD-materials, namely the progressive failure analysis of laminates (*this was an essential subject in WWFE-I and -II*). An accurate failure prediction firstly consists of a physically non-linear stress analysis if the

corresponding lamina stresses are high and of a geometrically non-linear analysis if the laminated structural part will extremely deform. If the computed lamina stresses do not consider this, strength and deformation analyses and thereby design verification are not acceptable. The prediction of the laminate behavior up to fracture is an effortful challenge. As procedure the so-called 'ply-by-ply' analysis method - based on Classical Laminate Theory (CLT) - is applied with the concern on the so-called First-Ply-Failure which is usual an Inter Fiber Failure (IFF).

To perform a non-linear stress analysis the relevant non-linear stress-strain curve is to be provided, which involves the so-called hardening and the softening. There are all 3 IFF–linked curves to consider. The 2 FFs always mean fracture for the high-performance UD materials. Strain hardening is the domain at the end of which the stress reaches a strength limit $\bar{R}_{\perp}^{t}, \bar{R}_{\perp}^{c}, \bar{R}_{\perp\|}$, which is addressed here as an initial failure level of IFF type. From that level on, that means for the further progressive failure or damage regime, the term softening is used. Of course, some micro-damage already begins with increased material hardening. Softening works for a lamina (ply), if it is embedded in a laminate and still contributes to the strength capacity and the stiffness capacity of the laminate. After the onset of micro-damage only so-called 'effective stresses' can be calculated for the micro-cracked lamina. The effective stresses are homogenized stresses, namely 'smeared' over a number of micro-cracks.

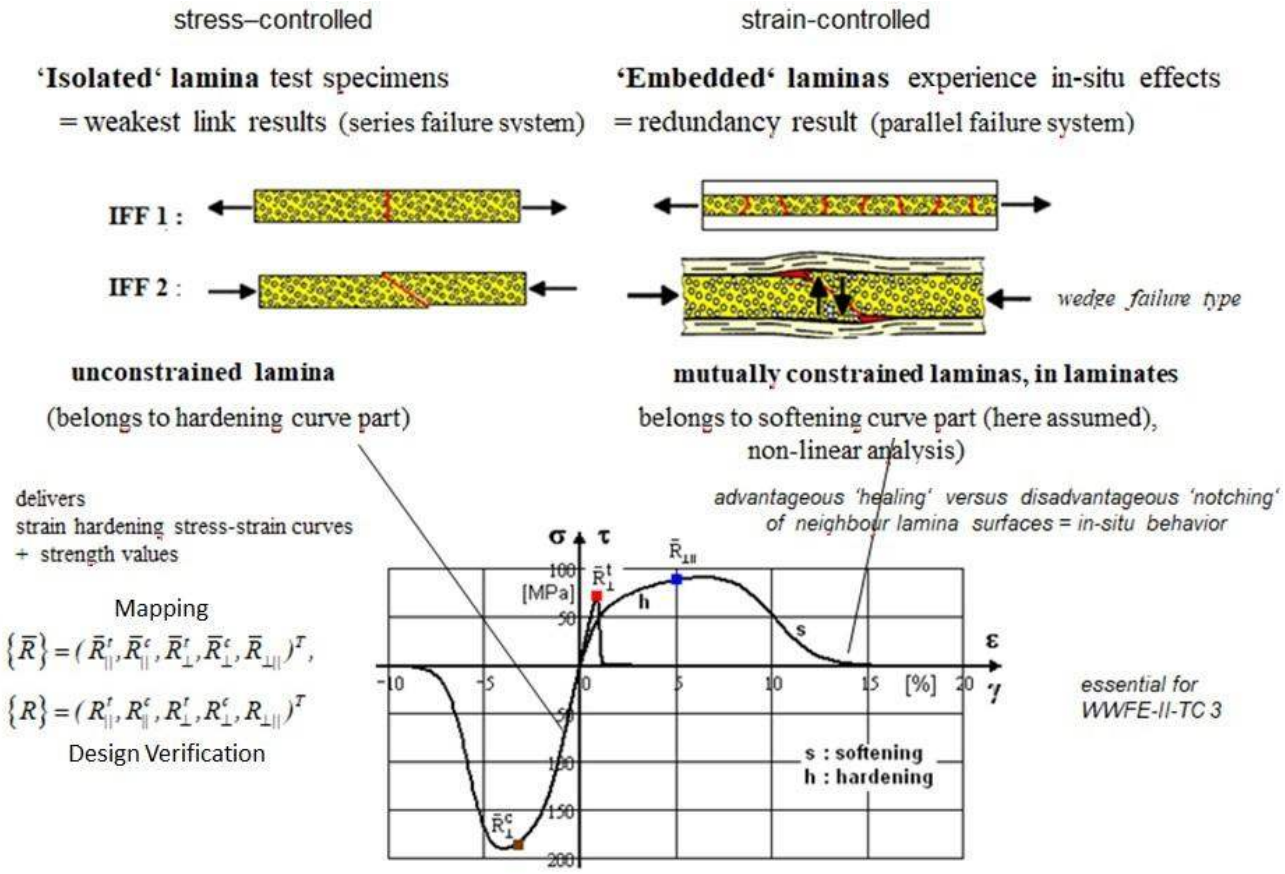

Fig.23-2: Stress-strain curves addressing strain-hardening and strain softening of brittle and ductile materials

Isolated test specimens deliver the values for the strength = failure stress, which represent the value at the end of the strain-hardening curve. Embedded laminas contribute further to the laminate stiffness and load carrying capacity as long as the microdamage-caused strain-softening curve is active.

The author proposes the following mapping functions [CUN

Strain-hardening:

For strain-hardening materials the classical Ramberg-Osgood (R-O) equation can be applied as mapping function

$\varepsilon_{hard} = \sigma / E_0^{mode} + 0.002\,(\sigma / \bar{R}_{0.2}^{mode})^n$, example $\gamma_{21} = \tau_{21} / G_{||\perp} + 0.002 \cdot (\tau_{21} / \bar{R}_{0.2\perp||})^n$.

Therein the R-O exponent (see Mil Hdbk 5, now MMPDS) reads

$$\bar{n} = \ell n\left(\varepsilon_{pl}(R_m)\right) / \ell n\left(\bar{R}_m^{mode} / \bar{R}_{p0.2}^{mode}\right)$$

and is estimated from the strength point $\left(\bar{R}_{\mathrm{m}}^{\mathrm{mode}},\ \varepsilon_{pl}(\bar{R}_{\mathrm{m}}^{\mathrm{mode}})\right)$ and a 'yield' point information. Of interest for analysis are the secant and the tangent E-modulus

$$\mathrm{E}_{sec} = \quad \sigma / \varepsilon \ = E_0 \ / [1 + 0.002 \cdot E_0 \ / \bar{R}_{0.2} \cdot (\sigma / \bar{R}_{0.2})^{\bar{n}-1}],$$

$$\mathrm{E}_{tan} = \ d\sigma / d\varepsilon = \ E_0 \ / [1 + 0.002 \cdot \bar{n} \cdot E_0 \ / \bar{R}_{0.2} \cdot (\sigma / \bar{R}_{0.2})^{\bar{n}-1}] \ .$$

For the design dimensioning analysis an average stress-strain curve should be applied in order to obtain the most probable state of the structure. This requires to map the desired average curve of a bunch of measured stress-strain curves. This will lead to a curve that might not run through the points $(\bar{R}_{0.2}^t,\ \varepsilon_{0.2}^t = 0.002)$ and $(\bar{R}^t,\ \bar{\varepsilon}_{fr}^t)$. Hence, the exponent $\bar{n}$ is also the result of the fitting process of the bunch of all measured stress-strain curves. An impressive example was WWFE-II, TC 2-4.

<u>Strain-softening:</u>

The full stress-strain curve consists of a hardening part which can be load-controlled measured and a softening part which is deformation-controlled by the structural vicinity. The associate two separate formulae are linked in the strength point.

The softening formula has to be assumed. This is due to the fact that the designer is generally lacking of experimental information for the degradation of the embedded lamina. An engineering modelling of this softening part or the post initial failure behavior of a laminate requires that assumptions have to be made regarding the decaying properties of the actually degrading lamina or laminas. The author's approach is based on the idea that the softening function is factorizing the Ramberg-Osgood hardening function. A simple function was used to map this softening in order to then derive the secant modulus for the full non-linear analysis. The equations for this effective curve (*smeared over the micro-cracks*) read:

$$\sigma_{soft} = \bar{R}_m / (1 + exp[(a_{soft} + \varepsilon) / b_{soft}]) = \bar{R}_m \cdot \eta \qquad \text{using} \quad exp[z] = e^z$$

where η is a degradation function and equals 1 in the hardening domain. The two curve parameters a_{soft}, b_{soft} are determined from two calibration points at least

$$(0.995 \cdot \bar{R}_m,\ \varepsilon(\bar{R}_m)) \qquad \text{and} \qquad (0.1 \cdot \bar{R}_m,\ \varepsilon(0.1 \cdot \bar{R}_m)) \qquad \text{or}$$

from curve fitting if enough test data is available in the softening domain. Applying $1.0 \cdot \bar{R}_m,\ \varepsilon(\bar{R}_m)$ as input is numerically not permitted. The moduli required for the non-linear analysis in the isotropic case read

$$E_{sec}^{hard} = \frac{\sigma}{\varepsilon} = \frac{\sigma}{\frac{\sigma}{E_0} + 0.002 \cdot (\frac{\sigma}{\bar{R}_{0.2}})^{\bar{n}}} = \frac{E_0}{1 + 0.002 \cdot \frac{E_0}{\bar{R}_{0.2}} \cdot (\frac{\sigma}{\bar{R}_{0.2}})^{\bar{n}-1}},$$

$$E_{sec}^{soft} = \frac{\sigma}{\varepsilon} = \frac{E_0}{1 + 0.002 \cdot \frac{E_0}{R_{0.2}} \cdot (\frac{\sigma \cdot \eta}{R_{0.2}})^{\bar{n}-1}} \quad \text{with} \quad \eta = \frac{1}{1 + exp(\frac{a_{soft} + \varepsilon}{b_{soft}})} \ .$$

By employing the equivalent stress reached in each failure mode the associated secant modulus of each mode can be determined for the hardening and the softening regime. For the various modes the same formula is valid, however, the mode parameters are different. Considering a consistent stress concept for all $\sigma_{\mathrm{eq}}^{\mathrm{modes}}$ an *explicit* dependency for $E_{sec}(\sigma_{\mathrm{eq}}^{\mathrm{modes}})$ is provided.

For UD material the *Onset-of-Failure* or *Initial Failure* level, respectively, an appropriate progressive failure analysis method has to be employed, also termed a *Successive Degradation Model* for the description of Post Initial failure, by using a failure mode condition that indicates failure type and micro-damage danger (level of *Eff* <= 100%). Final Failure occurs after the laminate (and thereby the structural part has experienced a stiffness reduction and has degraded to a level where it is no longer capable of carrying additional load.

Note, please: If R-O-material data sets are not provided for the hardening domain then instead of the R-O-approach a more mathematical formulation can be applied which should include both hardening and softening regime. This requires the application of the mathematical fitting function, that includes both domains , namely $\sigma = c1 \cdot c2 \cdot \varepsilon^{c1-1} \cdot exp(-c1 \cdot \varepsilon^{c2})$ [*Mathcad manual*]. Another formula from *A. Matzenmiller* reads $\sigma(\varepsilon) = \bar{R} \cdot exp\left[\frac{1}{c1 \cdot e} \cdot \left(\frac{\varepsilon}{\varepsilon_{fracture}}\right)^{c1}\right] \cdot \frac{\varepsilon}{\varepsilon_{fracture}}$.

For model validation, properties are not only needed for the pure failure mode domains but for the several 'mode-interaction domains' or Mixed Failure Domains (MiFD) too, where the actual stress state affects more than one mode. The influence of the stress state in a MiFD on the secant modulus of each affected mode was considered by the author in his simple "E_{sec}-approach" in the WWFEs by 'triggering'. This approach increases the *Eff* of the affected mode (*the secant modulus becomes smaller*) in the case of hardening and softening. After the onset of IFF 'smeared stresses' can be inserted into the SFCs only.

Some further aspects and tasks:

- The lamina is the general building brick or basic computational element for the prediction of laminate behavior
- To perform a reliable nonlinear analysis the clear identification of the design driving IFF mode is mandatory
- *Eff* = 100% remains valid throughout the analysis in the softening domain
- The high internal redundancy of a multi-layered laminate is better modelled by a probabilistic code. Probabilistic tools should be applied in order to gain some experience to practically understand and improve the deterministic procedures and to smooth (*due to joint failure probability*) the relatively sharp corners of a laminate's failure envelope. Deterministic failure path and probabilistic failure path may be not the same w.r.t. the different scatter of the design parameters effected, see [*Rac87*]
- The determination of effective mode softening curves for embedded laminas is future work. Appropriate test specimens and test evaluation have to be discussed. See a proposal in § 5.3.2
- In order to implement the multi-fold non-linearity approach into a commercial FEA code and taking advantage of a code's effective solution architecture an analogue procedure to '*yield* failure conditions + associated flow potential' of ductile materials has to be provided for the 3 IFF conditions '*fracture* failure condition (presented) + associated inelastic potential' for brittle UD materials, exemplarily.

23.4 Notes on Dimensioning and Verification concerning Stress and Deformation

Stress and strain, structural modeling and input

An analysis considers the external boundary conditions and internal restraints and converts the environmental loadings into internal forces, fluxes, stresses and strains for all the load cases, regarding:

- Use of adequate models to map the structural behavior
- Consideration of all relevant load cases

- Consideration of environmental influences such as temperature, humidity, radiation. They may have a substantial impact on the coefficient of thermal expansion, Young's modulus and strength design allowables.
- Use of adequate physical properties such as
  - average (typical) values of the stochastic design variables in order to end up with a structural behavior which meets real behavior best (which means with a 50% expectance value)
  - average stress-strain relationship (is to be seen as a physical quantity) in the applied models
- Utilized are average elasticity properties and nominal geometry (thickness, length) to represent average structural behavior.
- Physical properties to be used in analysis shall be adequate: Required are mean (typical, average) values of the stochastic design variables in order to end up with a structural behavior, which meets the real behavior best (*50% expectance value*). The stress-strain relationship is a feature of the applied physical models, and is to be seen as a physical quantity !
- Data input from a material handbook is to be carefully selected in order to match the real hardware (e.g. with respect to plate, sheet, extrusion, heat treatment).
- Stiffness Demonstration: Due to stiffness requirements upper and lower tolerance limits
- Strength Demonstration (*design verification*): One-sided tolerance bands (*for static and fatigue strength*) and two-sided tolerance bands (*for thickness, Young's modulus*) are considered.
- Application of statistically based A-value and B-value Design Allowables:
  - A-values: Application of the Safe Life Concept (single load path, where failure of a single element leads to the loss of structural integrity)
  - B-values: Application of the Damage Tolerance Concept (multiple load paths, redundancy).

If the structural analysis requires a non-linear treatment then some features are to keep in mind:

- Stressing is re-distributed to stiffer regimes (*in case of composites to the fibers*)
- In contrast to the linear model, an altered load path (*according to local weakening*) may be predicted by the non-linear model
- Large strains and large displacements may occur (*which in principle includes yielding of metals and micro-cracking caused quasi-yielding*)
- Change of shape of the loaded structure is possible
- Release of residual stresses according to degradation growth in case of monotonic and cyclic loading and in hygro-thermal environment
- The assessment of the critical stress state is performed with the obtained Eff and the strength design allowable. Global yielding is never permitted. If a critical strain state has to be assessed then a limit design strain needs to be defined.

Note: In statically indeterminate structures with its multiple load paths, loads are distributed according to the stiffness properties of the individual load paths. Therefore, it is essential to use average stiffness values (material and geometrical properties) to end up with typical load distributions. Otherwise it might happen that predicted load distributions are 'un-typical' with the result that stresses may be predicted too low and incorrect locations of critical points are assessed.

Strength Proof and its Strength Design Allowables

- Strength of a design is demonstrated, if 'No relevant SFC (*to be understood as the limit state of a failure mode*) is met or exceeded for all dimensioning load cases', resulting in a non-negative (positive) Margin of Safety MoS.
- Generally, strength analysis can be not performed in one shot together with stress-strain analysis

(*in fact, it is an iterative process*). Has to be performed separately as a 'post-processing work' to account for: Scatter of the design variables (e.g. upper or lower E-modulus), the strength design allowable (*statistical minimum values, and etc.).*

- Strength analysis can be separately performed as a 'post-processing work' to account for:
  - scatter of the design variables (*e.g. upper or lower Young's modulus in stiffness requirement cases, minimum local thickness values*),
  - strength design allowables (*statistical minimum values*).
- Essential in the strength analysis is the used SFC *F*. Its aim is to assess multi-axial stress states by just utilizing the basic uniaxial strength values, which are mandatory in design, anyway. Types of SFCs are the global and the modal ones (*see representative chapter*), namely

$$F(\{\sigma\},\{R\})=1 \quad \text{and} \quad F(\{\sigma\},\{R_{\text{mode}}\})=1 \rightarrow F(\{\sigma\},\{R_{\text{mode}},\mu_{\text{mode}}\})=1 \quad \text{with the FMC}.$$

Some Facts impacting strength analysis

It is too discriminate bi-axial fracture stress state and (uniaxial) strength, defined as technical strength in engineering. For practical reasons the term equi-bi-axial strength (R^{tt}, R^{cc}) is used for marking the bi-axial fracture stress state

- Multi-axial compression usually works as quasi-plasticizer
- Due to the redundancy effect ('healing', which causes an increase of the load carrying ability) found with 'dense' concrete and grey-cast iron under bi-axial compression (in contrast to porous foam and concrete stone) the dent in the negative I_1-domain is oriented outward, opposite to the tensile domain
- Flaw distribution effect: Activation of a critical fracture plane depends on the spatial distribution and orientation of the flaws
- Hoop Planes = deviatoric planes = π–planes are convex. Meridian planes are **not convex** at max I_1 (tension) and for UHPC in the high hydrostatic compression domain.
  Question arises: Is the traditional convexity condition linked to uniaxial stressing?
- The applicability of a SFC ends (example UD) when the driving mode stress σ^t (IFF1) or τ (IFF2) becomes zero and the associate *Eff* becomes negative. Therefore, the traditional use to just apply the so-called 'Proportional Loading (stressing)' concept in order to derive *Eff* from F must be checked whether the driving stress condition is fulfilled or not. In this context the concept of 'proportional loading' and the concept idea of 'driving stress' were presented. This invites for discussion regarding linear and non-linear stress analyses
- Limits of the applicability of the (material-linked) SFCs: Structural failure may occur which cannot be described by a SFC because it is not a material failure anymore like the UD example: Instability of a tube test specimen under compression; filament-upon-filament compression within an ultra-highly compressed stack, as in Test Case 12 of WWFE-II. This specific strength problem was inexplicably specified as a problem to be solved with an SFC, which is not right (see [*CUN22*]).

LL on modelling and results:

- ✓ *Physics has to be modelled accurately: A physically based strength model possesses a minimum number of model parameters. After proven demonstrations of a good mapping of the courses of accurate test data ('goodness of fit') such a model is able to even sort out false test data results of a successful qualification of a material model*
- ✓ *The choice of the task-corresponding stress-strain curve has to be carefully performed (min or mean or max values).*

- ✓ *Robust (tolerant) design or robustness to later changes of the design parameters with identification of the most sensitive design parameters is desired*
- ✓ *Basis of a good design is the modelling work of an experienced engineer. This requires an understanding of the full system supported by a basic technical knowledge such as mechanics.*
- ✓ *To proceed, we must improve the interdisciplinary work. System Engineering is mandatory.*
- ✓ *Again: Failure probability p_f does not dramatically increase if MoS turns slightly negative. A local safety measure MoS = -1 % is no problem in design development because the MoS value does not outline the risk or the failure probability!*
- ✓

Because tubes are many often used as test specimens a note on the evaluation of their yielding–driven failure tests shall be made:

- ➢ A non-linear analysis is to perform for non-brittle materials in order to capture the changing stress states over the wall of the internal surface and the outer surface
- ➢ The pressure on the inside surface drives yielding
- ➢ On the outside flaws might have a fracture-mechanical effect.

24 Finite Fracture Mechanics (FFM) for Investigating Statically-loaded Notches

Aim: *Giving the user some advices regarding the often used so-called 'Open Hole Panels'.*

Summary

Full Design Verification requires the verification of Strength and of Damage Tolerance in the case of potentially cracked (macro-damaged) statically-loaded structural components under sudden overloading.

The Strength Analysis (SA) requires that the effective multi-axial stress state is not above the given Strength Design Allowable and the Damage Tolerance Analysis (DTA) the same for the so-called residual strength of the structural component containing a pre-crack.

Lying between Strength analysis and Fracture Mechanics (FM) analysis 'Onset-of-Cracking' (OoC) is experienced at stress concentration sites such as notches like open holes in a panel of a sufficiently brittle material. In this context, Leguillon's Hypothesis [1] says

"*A (*generating*) crack is (*becomes*) critical when and only when both the released energy and the local stress reach critical values along an assumed finite crack".*

This novel hypothesis, 'Neuber'-improving, shall be presented here. It captures the prediction of the instantaneous OoC. The name of the tool is Finite Fracture Mechanics (FFM), see *Fig.24-1*. It predicts for notched components that loading level where the Strength Failure Criterion (SFC) equals the FM criterion or it determines as a coupled (hybrid) stress-energy criterion the critical loading that causes the finite crack size Δa_c. Because FM is one part of the FFM as introduction and for better understanding at first the well-known FM analysis tool R-curve shall be presented.

smooth structure	**notched structure** "transition domain"		**cracked structure**
no steep stress decay SFC	stress concentration Neuber method (up to now) K_t	'onset-of cracking' *assumed crack, FFM* (novel replacement)	stress intensity *real pre-cracks, FM* K_{Ic} *'no hole' and 'with hole'*

Fig. 24-1: Stress situations and methods in a structural component

Fig.24-2 visualizes the task to be solved. For practical application the concept of a linear-elastic stress intensity factor *K* may be sufficient and is usually applied. Coordinates used are depicted.

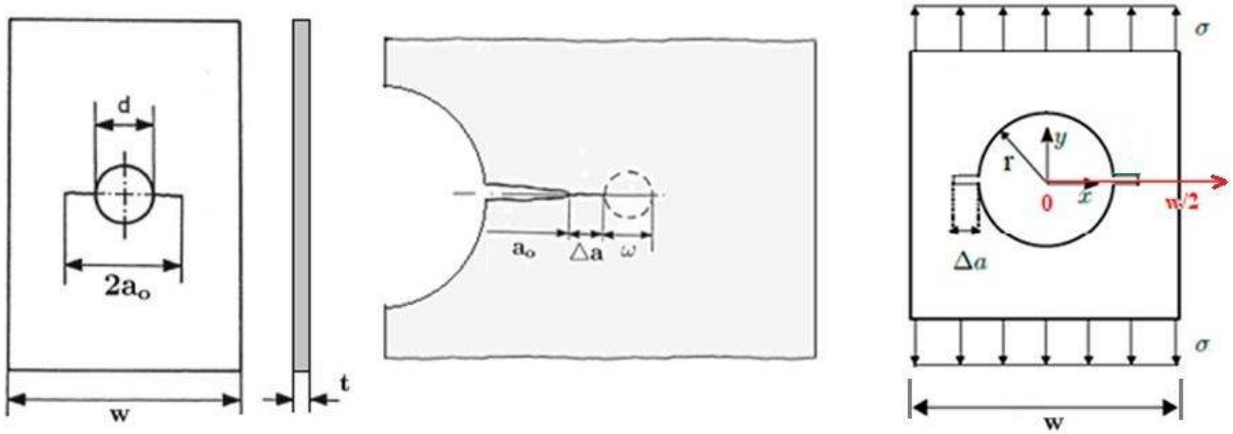

Fig.24-2: Plate strip with a central open hole and an existing through crack of the size $a = a_0 - r$.

(left) characterization of an open hole panel with existing crack , w= plate width, t = plate thickness, (center) crack growth details in the case of slight crack tip yielding ω of not fully brittle materials,

(right) σ = remote tensile stress, leading to cracking for $\sigma = \sigma_{fail}$, Δa = assumed FFM crack , d = 2r

(As member of the IASB this document is intentionally formatted similar to a HSB Airbus design sheet.)

Key Words: Residual strength, critical crack length, R-curve, Finite Fracture Mechanics, coupled criterion.

References

[1] Leguillon D: *Strength or toughness? A criterion for crack onset at a notch*. European Journal of Mechanics A, Solids 21(1), 61-72, 2002

[2] Weißgraeber P, Leguillon D and Becker W: *A review of Finite Fracture Mechanics: crack initiation at singular and non-singular stress raisers*. Archive of Applied Mechanics 86, 375-401, 2016

[3] HSB-draft, Nguyen-Hoang M and Becker W: *Finite Fracture Mechanics: A concept to assess structural integrity or failure in the case of stress concentrations*

[4] HSB 62232-02: *Evaluation of the residual strength and critical crack length using the R-Curve*, 1990

[5] HSB 62232-03: *Analytical model for the description of R-Curves*, 2006

[6] HSB 62232-05 *Application of R-curves*

[7] [Fla82] Flaggs D L and Kural M H*: Experimental Determination of the In Situ Transverse Lamina Strength in Graphite Epoxy Laminates*. J. Comp. Mat. Vol 16 (1982), S. 103-116

[8] HSB 34112-10: *Stress concentration and distribution in a finite pin-loaded plate under remote uniformly distributed tension*. Issue A, 2022

[9] Tada H, Paris P, and Irwin G: *The Stress Analysis of Cracks Handbook*. ASME Press, New York, 2000.

[10] HSB 63321-06: *Determination of the constants in the model describing the width dependency of the Feddersen-parameter*, 2009

[11] N.N.: *Standard Practice for R-Curve Determination*. ASTM E561-86, 1986

[12] Schwalbe K-H: *Bruchmechanik metallischer Werkstoffe*. Hanser-Verlag, München, 1980

[13] HSB 63203-03: *Experimental evaluation of fracture toughness of metallic materials.* 1993.

Luftfahrt-Technisches Handbuch (LTH): *HANDBUCH STRUKTUR BERECHNUNG* (HSB) *Fundamentals and Methods for Aeronautical Design and Analyses* issued by IASB (Industrie-Ausschuss für Struktur-Berechnung).

General

There are three approaches available to perform Design Verification (DV) for occurring static stress situations: Strength Failure Criteria (SFC), Continuum (micro-)Damage Mechanics (CDM, *not yet DV-capable*) criteria and Fracture Mechanics (FM) criteria for cracked (macro-damaged) components. A novel approach is the hybrid tool Finite Fracture Mechanics (FFM) which captures the ‘onset-of-cracking’ (OoC) at stress concentration (SC) points and at higher stress singularity points.

The FFM is a coupled (hybrid) criterion that fills a gap in FM by assuming an instantaneous formation of a crack of finite size [1, 2]. Intention is to initially show the classical application of FM, because FM provides one part tool of the FFM. *Fig.24-1* gave a survey on the situations faced.

Due to FFM, the Neuber method is now obsolete, but falls as a special case.

What Neuber called "support length" is precisely the crack length supplied by the FFM, without the need for acceptance or experimental identification!

The provided analyses are restricted to the 2D-case, 3D-extension will be a future task.

A SFC is a necessary condition but might not be a sufficient condition for the prediction of 'Onset-of-cracking', seen here as onset of failure:

*This is known for the author for about 50 years from the so-called 'thin layer effect' of UD-layer-composed laminates: *Due to being strain-controlled, the material flaws in a thin lamina (*transversely-isotropic material*) cannot grow freely up to micro-crack size in the thickness direction, because the neighboring laminas act as micro-crack-stoppers*. Considering fracture mechanics, the strain energy release rate, responsible for the development of damage energy in the 90° plies - from flaws into micro-cracks and larger -, increases with increasing ply thickness. Therefore, the actual absolute thickness of a lamina in a laminate is a driving parameter for initiation or onset of micro-cracks, i.e. [*Fla82*].
*Further and generally more known in metallic applications is the case of discontinuities of the here focused isotropic materials such as notch singularities with steep stress decays: only a *toughness + characteristic length-based energy balance condition* may form a sufficient set of two fracture conditions.

When applying SFCs usually ideal solids are considered which are assumed to be free of essential micro-crack-like flaws, whereas applying Fracture Mechanics the solid is considered to contain macro-cracks, respectively.

Since about 20 years Finite Fracture Mechanics (FFM) tries to fill a gap between the continuum mechanical strength analysis and the classical FM analysis. FFM is an approach to offer a criterion to predict the crack onset in brittle isotropic and UD materials.
This is a bridge that had to be built from the strength failure to the fracture mechanics failure ground. Attempts to link SFC-described 'onset of fracture' prediction methods and FM prediction methods for structural components have been performed. Best known is the still cited Hypothesis of Leguillon, where he assumes cracks of finite length Δa. Thus using FFM one obtains one more unknown but also a further equation to solve the equation system together with the SFC.
This coupled criterion does not refer to microscopic mechanisms to predict crack-*nucleation*!
Considering FFM it is referred to the literature [1, 2, 3].

Note on short Cracks according to citations in literature:

- In polycrystalline materials if short crack $a <$ grain diameter / 5
- Size of the cyclic plastic zone at the crack tip
- Different crack closure is faced due to the small crack and its flanks
- Notch surface quality is decisive.

24.1 List of Symbols

Symbol	Unit	Description
a	mm	crack length
a_0	mm	initial crack length (open hole panel: crack a + hole radius r)
a_c	mm	*critical* crack length
a_e	mm	*effective crack length* $a_e = a_p + \omega/2$
a_p	mm	*physical crack length* $a_p = a_0 + \Delta a$
c_{ij}		abbreviating functions and abbreviations
$f(a)$		correction function of the stress intensity factor (SIF)
f_d		correction function concerning the hole diameter d
f_w		correction function concerning the specimen width w
t; w	mm	panel specimen thickness; width of panel, test specimen
Δa	mm	stable increase of a due to static loading
Δa_e	mm	effective crack elongation (R-curve abscissa) $\Delta a_e = a - a_0$
A	mm	parameter of the R-curve model, cross-section
B	-	parameter of the R-curve model
E	MPa	Young's modulus (MPa = N/mm^2)
F	N	force
$\mathcal{G}_{Ic}$	MPa · m	Cracking resistance: potential strain energy release rate at failure. Under plane strain conditions (most critical case) $\mathcal{G}_{Ic} = K_{Ic}^2 \cdot (1-\nu^2) / E$, $\sqrt{\text{m}} = 31.6 \cdot \sqrt{\text{mm}}$
$K(\sigma,a)$	MPa · $\sqrt{\text{m}}$	Cracking action: stress intensity factor, (SIF) $K = \sigma \cdot \sqrt{\pi \cdot a} \cdot f(a)$,
K_{as}	MPa · $\sqrt{\text{m}}$	parameter of the R-Curve model (asymptotic value of R-curve)
K_b	MPa · $\sqrt{\text{m}}$	parameter of the R-Curve model (value at beginning of R-curve)
K_{app}	MPa · $\sqrt{\text{m}}$	apparent fracture toughness (general) = critical SIF (not the often used K_c)
K_p	MPa · $\sqrt{\text{m}}$	physical value of the SIF K: $K_p = \sigma \cdot \sqrt{\pi \cdot a_p} \cdot \sqrt{\sec\left(\pi \cdot a_p / w\right)}$, sec =1/cos
K_e	MPa · $\sqrt{\text{m}}$	Effective SIF: $K_e = \sigma \cdot \sqrt{\pi \cdot a_e} \cdot \sqrt{\sec\left(\pi \cdot a_e / w\right)}$, often termed K_R
K_{Ic}	MPa · $\sqrt{\text{m}}$	Cracking resistance: critical SIF (fracture mechanics Mode I testing) at onset of unstable sharp crack propagation in the plane strain state = most brittle condition, otherwise called K_c; or = fracture toughness of uni-axially tensile-loaded, minimum ductile (*brittle*) material specimens = material resistance to crack propagation $K_{Ic} = \sigma \cdot \sqrt{\pi \cdot a_c} \cdot f(w,d) = \sigma_c \cdot \sqrt{\pi \cdot a} \cdot f$
K_R	MPa · $\sqrt{\text{m}}$	Cracking resistance, R-curve ordinate
R-curve	MPa · $\sqrt{\text{m}}$	material *Resistance* to fracture curve in case of slow, stable crack propagation from a sharp notch, accompanied by growth of the plastic zone at the crack-tip (*unfortunately also the letter R was taken*)
R; R_{p02}	MPa	failure stress ≡ strength (*Resistance to stress action*); tensile yield strength
W	N·mm	Energy = $\int_0^{\Delta\ell} F \cdot d(\Delta\ell) = \int_0^{\Delta\ell} \sigma \cdot A \cdot d(\varepsilon \cdot \ell) = A \cdot \ell \cdot \int_0^{e} \sigma \cdot d\varepsilon = A \cdot \ell \cdot \int_0^{\sigma} \frac{\sigma}{E} \cdot d\varepsilon = V \cdot \frac{\sigma^2}{2 \cdot E}$
ν	-	Poisson's ratio
ω	mm	full plastic zone at the crack-tip
σ	MPa	Action: remote (far field) uniform tensile stress
σ_c	MPa	critical value of σ = residual strength

(In structural mechanics x is usually the length coordinate, however in fracture mechanics the net section direction)

The following sub-section represents an intended FM-introduction for the focused FFM-modelling.

24.2 Analysis using the Crack Growth Resistance curve = 'R-curve'

24.2.1 General on Fracture Mechanics quantities and R-curve Concept

Aim: *Chapter is helpful for better grasping the novel FFM, because FM is one part of the FFM.*

Basic assumption: Use of the largest crack size that can be expected, following the 'weakest link' failure model and regarding quality assurance measurement limits.

In the Damage Tolerance procedure of cracked (macro-damaged) structural components two basic questions are posed in analysis:

1. What is the static strength if a crack is present (residual strength problem)?
2. How is the propagation behavior of the present crack (large crack growth problem)?

In order to perform this for isotropic materials some different quantities are used to predict the stress state at the crack tip caused by a far-field stress or remote stress, respectively.

*The stress intensity factor (SIF) *K*, applied to homogeneous linear elastic materials. Its measured size depends on test specimen width w, the crack size *a*, the location of the present crack and the material. It can be written as $K = \sigma \cdot \sqrt{\pi \cdot a_0} \cdot f(a/w)$, where the SIF K_I of the fracture mechanics mode I is applied here, (*Fig. 24-4*).

*The strain energy release rate $\mathcal{G}$, defined as the instantaneous loss of total differential potential energy $\mathrm{d}\Pi$ per unit crack growth area (crack length Δa · plate thickness *t*) of the fresh surface S, by $\mathcal{G} = -d\Pi / dS$. In the case of brittle materials for its 'basic' Fracture Mode-I a relationship exists $\mathcal{G}_I = K_I^2$ /E' with E'= E/(1-ν^2) for plane strain.

*The J-integral *J* , characterizing the singular stress field at the crack tip in nonlinear elastic-plastic materials where the size of the plastic zone is small compared to the crack length. It is one way of determining the strain energy release rate $\mathcal{G}$. For brittle materials *J* corresponds to $\mathcal{G}$.

Macro-crack extension occurs when the stress intensity factor (SIF) *K* attains a critical value. Thereby the *Action-linked* SIF is entirely dependent on the structure geometry and loading condition, whilst the *Resistance-linked R*-curve is basically a material property dependent on temperature, environment, and loading rate as well the geometric test specimen range, etc.

Crack-growth resistance curves, the so-called *R*-Curves, are used here to predict:

- the residual strength of the structure for a given crack position and crack length,
- the critical length of an initial crack under given loadings.

These curves are conveniently plotted with crack extension Δa instead of crack size *a*, because the shape of the R-curve does not vary with the crack size.

* For very brittle materials with its flat *R*-curves, there is no stable crack extension and the initial crack size a_0 is the same as the critical crack size a_c. Then a single value of toughness characterizes the material, the cracking resistance K_{Ic}.

* For ductile materials (*such as low strength steels*) with a rising *R*-curve there is no single value of toughness that characterizes the material. Reason is that the plastic zone ω at the crack tip increases with crack growth and length, hence the energy dissipated to overcome plastic deformation will increase. In materials with a rising *R*-curve, stable crack growth occurs and the critical crack size will be larger than the initial crack size.

'Fatiguers', mind, please: "The R-curves (italic R letter) shall not be mixed up with the 'R-curves' in fatigue R = minσ/maxσ".

Fracture mechanics regards small scale ductility, usually described by its diameter ω, at the crack tip and multi-axial stressing, *Fig 25-2*.

In the case of a mixed-mode loading and opening of a crack, the energy release rate consists of the three parts $\mathcal{G}_I$, $\mathcal{G}_{II}$, $\mathcal{G}_{III}$ that correspond to the respective three fracture modes. The fracture-effective formulation then is $\mathcal{G} = \mathcal{G}_I + \mathcal{G}_{II} + \mathcal{G}_{III}$.
Crack extension occurs when above strain energy release rate $\mathcal{G}$ attains a critical value $\mathcal{G}_c$. In the case of fracture it becomes $\mathcal{G} \geq \mathcal{G}c$. $\mathcal{G}$ is directly related to the stress intensity factor K. It is associated in two-dimensional fracture mechanics with the loading modes (Mode-I, Mode-II, or Mode-III) the so-called Mixed-Mode Problem, applicable to cracks under plane stress, plane strain and anti-plane shear, see *Fig.24-4*. For the Fracture Mode-I, the energy release rate $\mathcal{G}$ is related to the Mode-I stress SIF K_I for a linearly-elastic material.

The two questions at the beginning of this sub-chapter can be answered using the analytical methods of fracture mechanics. For practical application the concept of the linear-elastic K is usually applied:
"*A structural component will fail in the case of static loading if the stress intensity factor (SIF) K of a brittle material reaches its critical value at K = K_c, termed fracture toughness, which depends on the material behavior*".
The determination of the K_c -values requires in the so-called K-concept the fulfilment of a geometric bound in order to achieve the real minimum K_{Ic}-value by a test specimen thickness of

$$t \; > \; 2.5 \cdot (K_{Ic} \,/\, R_{p0.2})^2 \;\rightarrow\; \sigma_c = K_{Ic} \,/\, (\sqrt{\pi \cdot a_0} \cdot f(a_0)\,.$$

Instead of the "Plain Strain Fracture Toughness" K_{Ic} (which is a material property but subject to certain minimum geometric requirements), an "Apparent Fracture Toughness" is inevitably to apply, adapted to the current geometric conditions.

A plot of strain energy release rate $\mathcal{G}$ versus crack extension Δa for a particular loading situation is termed driving force curve $\mathcal{G}(\Delta a)$. The driving force for crack propagation can be quantified by above characterizing parameters K, $\mathcal{G}$, or J. A plot of R versus crack extension Δa is a resistance curve, as still cited termed R-curve $R(\Delta a)$.

24.2.2 Models for R-curve (resistance) and for Stress Intensity Factor (SIF)-curve

Resistance: R-curve, ordinate $K_{R\,(}$*using a test data mapping function*)

For well mapping the test data course of the R-curve J. Broede in [2] proposed the mapping function

$$K_e(a) = K_{as} - (K_{as} - K_b) \cdot \frac{1 - B}{\exp\left(\dfrac{\Delta a_e}{A}\right) - B} \quad \text{with inverse} \quad \Delta a_e = A \cdot \ln\left(B + (1 - B) \cdot \frac{K_{as} - K_b}{K_{as} - K_e}\right)$$

$$\Rightarrow \quad \text{new } a_0 = a_0 + \Delta a_e = a_0 - A \cdot \ln\left(B + (1 - B) \cdot \frac{K_{as} - K_b}{K_{as} - K_e}\right)$$

including the effective quantities K_e and Δa_e. The plot $K_e(\Delta a_e)$ is termed effective R-curve. This mapping proposal addresses the usual structural materials which shall possess some ductility.

Action: *Stress Intensity Factor (SIF)-curve, K_{SIF}* (using a width correction function f_w)

With the so-called geometry correction functions f - *correcting the original infinite plate term* $\sqrt{\pi \cdot a}$ - concerning hole diameter (index d) and width (index w) of the centrally cracked panel ('plate strip') the SIF reads for the two cases:

* *Panel, version 'No hole'* $_{nh}$ *:*

$K_{nh} = \sigma \cdot \sqrt{\pi \cdot a} \cdot f_w(a)$ with $f_w(a) = \sqrt{\sec \frac{\pi \cdot a}{w}}$ capturing the panel width

$$K_{nh}(a) = \sigma \cdot \sqrt{\pi \cdot a} \cdot \sqrt{\sec \frac{\pi \cdot a}{w}} \quad , \qquad (\sec = 1/\cos).$$

* *Panel, version 'With hole'* $_{wh}$ *:* (Tada delivered in [9] a hole considering correction function *f(a)*):

$K = \sigma \cdot \sqrt{\pi \cdot a} \cdot f(a)$ with $f(a) = f_d(a) \cdot f_w(a)$ in the case of an open hole panel

$f_d(a) = \sqrt{1 - \frac{r}{a}} \cdot (1 + 0.358 \cdot \frac{r}{a} + 1.425 \cdot \left(\frac{r}{a}\right)^2 - 1.578 \cdot \left(\frac{r}{a}\right)^3 + 2.156 \cdot \left(\frac{r}{a}\right)^4)$, $f_w(a) = \sqrt{\sec(\frac{\pi \cdot r}{w}) \cdot \sec(\frac{\pi \cdot a}{w})}$.

$$K_{wh}(a) = \sigma \cdot \sqrt{\pi \cdot a} \cdot \sqrt{1 - \frac{r}{a}} \cdot (1 + 0.358 \cdot \frac{r}{a} + 1.425 \cdot \left(\frac{r}{a}\right)^2 - 1.578 \cdot \left(\frac{r}{a}\right)^3 + 2.156 \cdot \left(\frac{r}{a}\right)^4 \cdot \sqrt{\sec \frac{\pi \cdot r}{w} \cdot \sec \frac{\pi \cdot a}{w}}.$$

24.2.3 Conditions to Determine the unknown critical quantities σ_c , a_{ce}

'*Crack growth will occur when dG/da > dR/da and G ≥ R'.*

This corresponds to '*The SIF driving force curve is tangent with the R-curve'* as depicted in *Fig.24-3*. It can be interpreted as the critical condition when the energy available in the component for crack growth exceeds the maximum amount that the material can dissipate.

For fully brittle materials the *R*-curve is a horizontal constant line, a tangent-condition is not of interest.

In order to solve this task the following conditions must be met:

* $K_{SIF}(\sigma_c, a_{ce}) = K_e(a_{ce} - a_0)$ with $\Delta a_e = a - a_0$. This means, that:

firstly the coordinates of the touch point of SIF curve with R-curve are to determine.

$$K_e(a) = \sigma \cdot \sqrt{\pi \cdot a} \cdot f(a) = K_{as} - (K_{as} - K_b) \cdot \frac{1 - B}{\exp(\Delta a_e / A) - B} \quad \text{and}$$

* $dK_{SIF}(\sigma_c, a_{ce}) / da = dK_e(a_{ce} - a_0)/da$. This means, that:

secondly, the two slopes of both the curves must become the same at the touch point, task which requires a differentiation (*Mathcad 15 code,* symbolic *application*), delivering

$$\frac{dK_e}{da} \Rightarrow \sigma \cdot \frac{d}{da}\left(\sqrt{\pi \cdot a} \cdot f(a)\right) = K_{as} + \frac{(B-1) \cdot (K_b - K_{as})}{B - \exp(\frac{\Delta a_e}{A})} \Leftarrow \frac{dK_R}{da} .$$

For the SIF-curve holds for the two versions, SIF_{nh} no hole and SIF_{wh} with hole:

$$\text{SIF 'no hole'} : \frac{dK_{SIFnh}}{da} = \frac{d\left(\sigma \cdot \sqrt{\pi \cdot a} \cdot \sqrt{\cdot \sec \frac{\pi \cdot a}{w}}\right)}{da}$$

$$= \sigma \cdot \frac{\sqrt{\pi} / (2\sqrt{a} \cdot caw) + \pi^{1.5} \cdot \sqrt{a} \cdot saw / (w \cdot caw^2)}{2 \cdot \sqrt{\sqrt{\pi \cdot a} / caw}}, \; saw = \sin\left(\frac{\pi \cdot a}{w}\right), caw = \cos\left(\frac{\pi \cdot a}{w}\right).$$

SIF 'with hole' : (copied, Mathcad typing)

$$\frac{dK_{SIFwh}}{da} = \frac{d\left(\sigma\cdot\sqrt{\pi\cdot a}\cdot\sqrt{1-\frac{r}{a}}\cdot\left(1+0.358\cdot\frac{r}{a}+1.425\cdot\left(\frac{r}{a}\right)^2-1.578\cdot\left(\frac{r}{a}\right)^3+2.156\cdot\left(\frac{r}{a}\right)^4\bullet\sqrt{\sec\frac{\pi\cdot r}{w}\cdot\sec\frac{\pi\cdot a}{w}}\right)\right)}{da}$$

$$= \sigma\cdot\sqrt{\pi\cdot a}\cdot\left[c3\cdot\sqrt{1-\frac{r}{a}}\cdot(c1)+\frac{c3\cdot\sqrt{1-\frac{r}{a}}\cdot(c2)}{2\cdot a}+\frac{r\cdot c3\cdot(c2)}{2\cdot a^2\cdot\sqrt{1-\frac{r}{a}}}+\frac{\sin\left(\frac{\pi\cdot a}{w}\right)\cdot\sqrt{1-\frac{r}{a}}\cdot(c2)}{\sqrt{a}\cdot 2\cdot w\cdot\cos\left(\frac{\pi\cdot a}{w}\right)^2\cdot\cos\left(\frac{\pi\cdot r}{w}\right)\cdot c3}\right]$$

and the abbreviation functions

$$c1 = \frac{4.734\cdot r^3}{a^4}-\frac{8.624\cdot r^4}{a^5}-\frac{0.358\cdot r}{a^2}-\frac{2.85\cdot r^2}{a^3},\quad c2 = \frac{0.358\cdot r}{a}+\frac{2.156\cdot r^4}{a^4}+\frac{1.425\cdot r^2}{a^2}-\frac{1.578\cdot r^3}{a^3}+1,\quad c3 = \sqrt{\frac{1}{\cos\left(\frac{\pi\cdot a}{w}\right)\cdot\cos\left(\frac{\pi\cdot r}{w}\right)}}$$

* In the HSB sheet 62232-3 *J. Broede* mapped the *R*-curve by an appropriate analytical model, model parameters were determined there and finally $\sigma_c = R_{res}$ was derived by <u>iteratively</u> increasing the crack size up to a_c. This provides the failure stress for the maximally sustainable loading of the pre-cracked component.

* In <u>*Table 24-1*</u>, bottom, Cuntze delivers a <u>continuous</u> implicit mathematical computation.

*Table 24-1: Determination of the touch point = instability tangent point (*w width effect, no hole*)*

Vorgabe sigw = 11 a = 33

$$sigw\cdot\sqrt{\pi\cdot a}\cdot\sqrt{Sek\left(\frac{\pi\cdot a}{w}\right)} = Kas-(Kas-Kb)\cdot\frac{1-B}{\exp\left(\frac{a-a0}{A}\right)-B}\quad\textbf{(point)}$$

$$\frac{\pi\cdot sigw\cdot\left(\frac{\cos\left(\frac{\pi\cdot a}{w}\right)+\frac{\pi\cdot a}{w}\cdot\sin\left(\frac{\pi\cdot a}{w}\right)}{\cos\left(\frac{\pi\cdot a}{w}\right)^2}\right)}{2\cdot\sqrt{\frac{a\pi}{\cos\left(\frac{\pi\cdot a}{w}\right)}}} = \frac{e^{\frac{a-a0}{A}}\cdot(B-1)\cdot(Kb-Kas)}{A\cdot\left[B-e^{\frac{1}{A}\cdot(a-a0)}\right]^2}\quad\textbf{(slope)}$$

Aa := Suchen(sigw, a) $Aa = \begin{pmatrix}12.5\\55.4\end{pmatrix}$ sigw := Aa_0 sigw = 12.5 awc := Aa_1 awc = 55.4

$\sigma wc := sigw\cdot\frac{MPa\cdot\sqrt{m}}{\sqrt{mm}}$ $\sigma wc := sigw\cdot\sqrt{1000}$

$KSIFwc0 := sigwc\cdot\sqrt{\pi\cdot awc}\cdot\sqrt{Sek\left(\frac{\pi\cdot awc}{w}\right)}$ w = 300 KSIFwc0 = 180 $\sigma wc = 396$

24.2.4 Solution of the Equation set to Predict the Unknowns

The Mathcad computation delivers the searched quantities for the open hole panel. *Fig.25-3* provides the full data set. In the computation, the usually in $MPa\cdot\sqrt{m}$ given fracture toughness (= critical SIF) is taken, which however requires a final factorization of the obtained critical stress by $\sqrt{1000}$ to get into the MPa, mm system.

In *Fig.25-3*, for the envisaged panel, the *R*-curve is plotted together with two SIF-curves, one for an initially guessed reference stress of sig$_{wh}$=15 (dashed) and one for the computed critical reference value sig$_c$ =12.5 **(bold)**.

*For the 'no hole-panel' the critical SIF reads $K_c = 180\ \text{MPa}\cdot\sqrt{\text{m}} = 180\cdot\sqrt{1000}\ \text{MPa}\sqrt{\text{mm}}$ and the results are: $a_{ce} = 55.4$ mm, $\sigma_c = 12.5\cdot\sqrt{1000} = 396$ MPa.

*For the 'hole panel', in order to check any influence of the hole the associated rising **SIF-curve** was plotted, too. The same tangent point is obtained for this SIF-curve.

The computation of the 'no hole-panel' delivers as critical stress = residual strength, the value σ_{res} = 396 MPa (Mathcad computation scheme in *Table 24-1*).

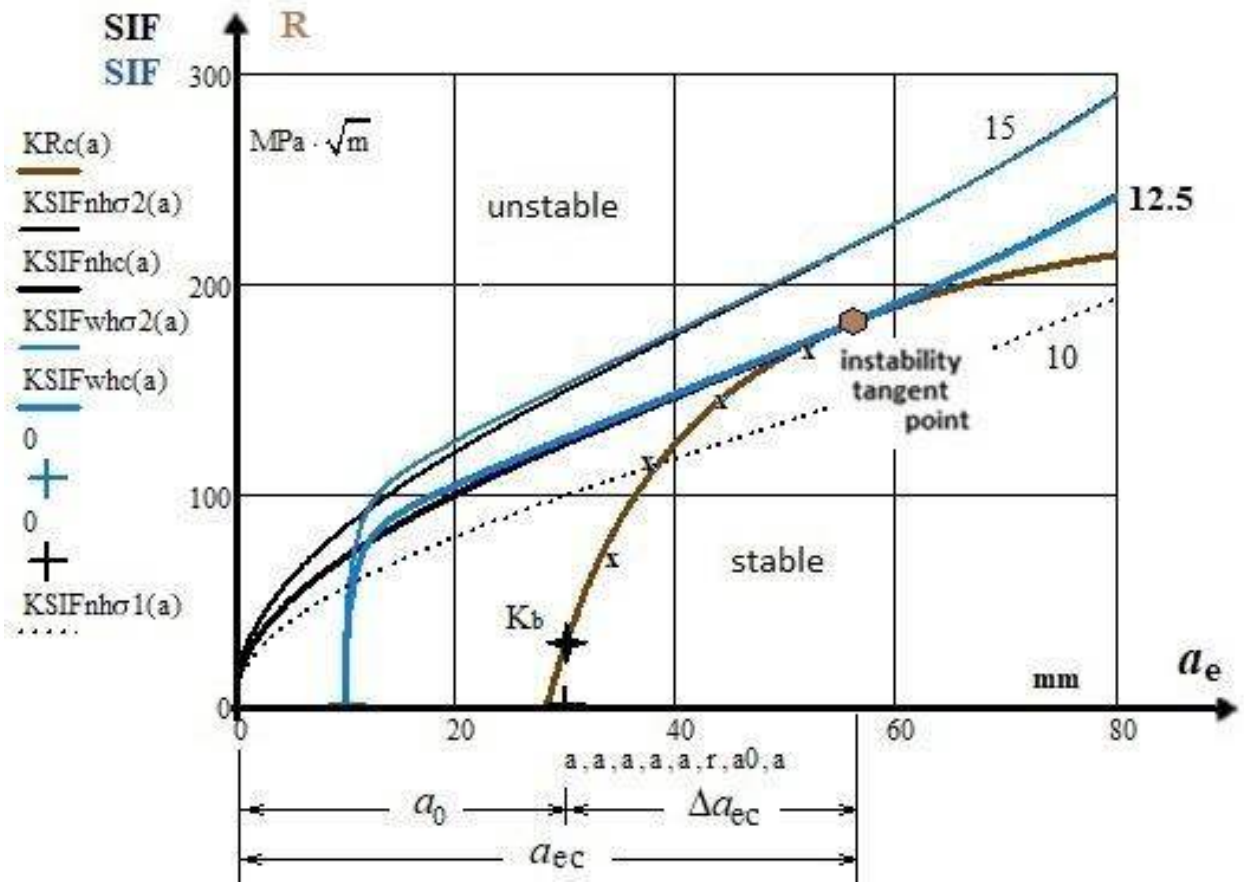

Fig.24-3: Wide panel example (HSB 62232-03) with w =300 mm, *t = 8*mm, a_0 *= 30* mm, *d =20* mm.
Aluminum Alloy 7475-T7351 in LT-direction: A =55.7 mm, *B = 0.75*, K_{as} *=246* $\text{MPa}\cdot\sqrt{\text{m}}$,
K_b *=29* $\text{MPa}\cdot\sqrt{\text{m}}$, R_{p02} *=425* MPa *(B-value for t = 6...38* mm*)*.
Instability point: K_e *= 180* $\text{MPa}\cdot\sqrt{\text{m}} = \text{MPa}\cdot\sqrt{\text{mm}}\cdot\sqrt{1000}$, a_{ce} *= 55.4* mm.
SIF-curve: reference stresses in MPa, to factor by $\sqrt{1000} = 31.6$: σ_2 =15 > σ_c =12.5 > σ_1=10, *Table* 1.
(For simplification the simple letter a was taken in the formulas instead of a_e*)*

Results:

The R-test curve (resistance, marked KR) captures all physical effects such as small scale yielding at the crack tip, marked by the letter ω! It is effective, therefore K_e*. Therefore, in order to be compatible the SIF-curve (action, marked KSIF) has to incorporate this effect. It does not depend on* a_0*, w.*

For information, however – no practical effect in *Fig.24-3* comparing the blue curve KSIF$_{wh}$ – the associated point condition with considering the hole is added below:

$$\text{sig}\cdot\sqrt{\pi\cdot a}\cdot\left(\text{c3}\cdot\sqrt{1-\frac{r}{a}}\cdot\text{c1}+\frac{\sqrt{\pi}\cdot\text{sig}\cdot\text{c3}\cdot\sqrt{1-\frac{r}{a}}\cdot\text{c2}}{2\cdot\sqrt{a}}+\frac{\sqrt{\pi}\cdot\text{sig}\cdot r\ \text{c3}\cdot\text{c2}}{2\cdot a^{1.5}\cdot\sqrt{1-\frac{r}{a}}}+\frac{\pi^{1.5}\cdot\sqrt{a}\cdot\text{sig}\cdot\sin\left(\frac{\pi\cdot a}{w}\right)\cdot\sqrt{1-\frac{r}{a}}\cdot\text{c2}}{2\cdot w\cdot\cos\left(\frac{\pi\cdot a}{w}\right)^2\cdot\cos\left(\frac{\pi\cdot r}{w}\right)\cdot\text{c3}}\right)$$

with the to be inserted abbreviation functions

c1, c2, c3

$$= \text{Kas}+\frac{(B-1)\cdot(\text{Kb}-\text{Kas})}{B-e^{\frac{1}{A}\cdot(a-a0)}}$$

The computation of the critical crack length a_c at the end of static loading is determined by the application of the formula below and there inserting K_{ec} (see application later). As K-values are usually given in $\text{MPa}\cdot\sqrt{\text{m}}$ this is intentionally widely followed here!

$$\text{new } a_0 = a_0 + \Delta a_{ec} = a_0 - A\cdot\ln\left(B+(1-B)\cdot\frac{K_{as}-K_b}{K_{as}-K_{ec}}\right) \quad .$$

Notes:

*The R-curve does not run out from a_0. This is caused because just the test data domain has to be fitted best. In the HSB sheet the beginning is therefore not sketched. The model point Kb lies on the a_0-line.

*Very brittle materials possess a horizontal *R*-curve.

► The test-based *R*-curve is essential for FFM to determine in future a more correct fracture toughness value K_{app} instead of the previous K_{Ic} for the usually FFM-treated very brittle material.

24.3 Analysis using Finite Fracture Mechanics (FFM)

24.3.1 General

To prove Structural Integrity several design verifications (DVs) must be performed for components having the following features: Smooth, notched (stress concentrations) and cracked (stress singularities), see *Fig.24-4, left.* Thereby, static and cyclic loadings must be taken into account focusing uni-axial and multi-axial stress states.
FFM-focus here is static loading under uni-axial stresses, which means Mode I-linked.

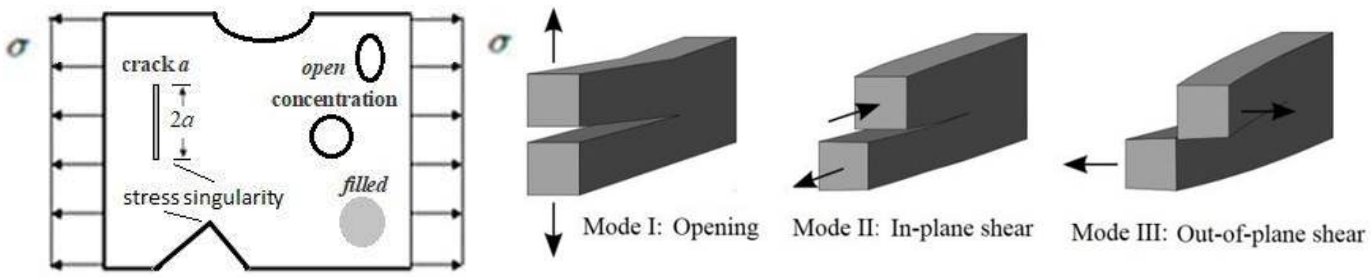

Fig. 24-4: (left) Stress concentrations and stress singularities under uni-axial stressing. (right) The 3 FM-modes, crack length a

The following levels are relevant when generating stress-related DV tools:

1. Stresses: *Strength Failure Conditions (SFC), as local design verifications* to predict onset-of-cracking (*several strength fracture failure modes and one yield mode,* practically just one for tension loading,)
2. Stress concentration: *Application of (local) stress concentration factors* K_t to predict onset-of-cracking (fracture)
3. Stress intensity (singularity): (*non-local*) *Fracture mechanics methods using stress intensity factors* $K = \sigma \cdot \sqrt{\pi \cdot a}$ *(SIFs) and fracture toughness (*representing the resistance of brittle materials to the propagation of flaws under an activated stress, assuming: the longer the flaw, the lower the bearable fracture stress) *being a critical* K_c *which is needed for a crack to grow under monotonic loading. For the usually envisaged tension loading* (pressure-linked geo-mechanics is not the focus*) there are three fracture mechanics modes to consider as depicted in Fig.4 above.*

All design verifications are required <u>in parallel</u> in accordance with the applicable regulations.

Tackling above three structural cases, then it can be attributed:

1. Stresses: *In the strength* fracture *failure criterion (SFC) strength values R (isotropic: here* $R^t \equiv R_m$*) are to insert, which capture any flaws and micro-cracks in the material data set of the test specimen. All effects are considered.*
2. Stress concentrations: *Experience tells that the application of a SFC with the application of a factor* K_t *is not sufficient. Here, a non-local DV method is required, which combines a strength fracture criterion and fracture mechanics criterion. This is the focus of FFM.*
3. Stress intensity: The necessary *('large') crack size value is identified by Quality Assurance or fixed as the minimum measurable crack size. The crack situation at hand is to model and toughness values* K_{Ic} *are to insert. A large crack analysis does not need a coupled DV in order to predict onset-of- further cracking, because the SFC is fulfilled.*

<u>Note</u>: There are stress-related and strain-related SFCs. Stress-related ones have the advantage, compared to strain-related ones that "*Residual stresses can be simply incorporated"*).

24.3.2 Introduction

Since about 20 years Finite Fracture Mechanics (FFM) intends to fill the gap between the continuum mechanical strength failure criteria (SFC) and the classical FM. FFM is an approach to offer a criterion to predict 'Onset-of-Cracking' in brittle isotropic and UD materials. This is a bridge that had to be built from strength failure to fracture mechanics failure.
Attempts to link SFC-described 'Onset-of-Cracking (OoC, fracture)' prediction methods and FM prediction methods for structural components have been performed. Best known is the still cited Hypothesis of Leguillon "*A crack is critical when and only when both the released energy and the local stress reach critical values along an assumed finite crack*". Within the FFM, Leguillon assumes instantaneous cracks of finite length Δa. Thus, using FFM one obtains one more unknown but also one more equation to solve together with the SFC the equation system.

Of the basic two previous FFM concept variants, the integral concept used here has proven to be the best. In this case, the stress curve is averaged over the fictitious, critical crack length for the SFC, i.e. converted into a locally evenly distributed stress curve averaged over this length.
As long as this is done over a comparatively small area, this is fine, but if it is a very large crack depth, where the crack extends far into an area of the stress profile where the stress peak has already been significantly reduced, the stress value averaged in this way becomes quite small. The question then is

whether this procedure can still lead to a valid SFC application. In the future therefore, it would make sense to limit the range over which the stress curve is averaged appropriately in such cases?

This coupled criterion does not refer to microscopic mechanisms to predict micro-crack nucleation.

Reasons to develop the FFM were some facts from studying 'Onset-of-Cracking':

- Isotropic material

The minor failure behavior of absolutely small holes compared to large holes, although the stress concentration factor K_t takes the same value, namely 3. With large holes, more material volume is highly stressed and thus physically-based the probability of failure due to more activated, material-inherent flaws is increased.

Further known is in the case of discontinuities such as notch singularities with steep stress decays: only a *toughness + characteristic length-based energy balance condition* may form a sufficient set of fracture conditions. Hence, a SFC is a necessary condition but might not be a sufficient condition for the prediction of 'Onset-of-Cracking'.

When applying SFCs usually ideal solids are viewed which are assumed to be free of essential micro-voids or microcrack-like flaws, whereas applying Fracture Mechanics tools the solid is considered to contain macro-cracks.

- Transversely-isotropic material

It is also known for a long time from the so-called 'Thin layer effect' of UD-layer-composed laminate that the SFC-application is not sufficient to understand failure: *Due to being strain-controlled, the material flaws in a thin lamina cannot grow freely up to micro-crack size in the thickness direction, because the neighboring laminas act as micro-crack-stoppers*. In other words: Thin plies, embedded in a laminate, fail at a higher loading level than thick ones.

Employing here fracture mechanics, the strain energy release rate, responsible for the development of damage energy in the 90° plies - *from flaws into micro-cracks and larger cracks* -, increases with increasing ply thickness. Therefore, the actual absolute thickness of a lamina in a laminate is a driving parameter for initiation of cracks, i.e. [*Fla82*].

For laminates - composed of different isotropic layers – such singularities occur, too and are effort fully treated!

24.3.3 FFM-model focusing isotropic dense material

The FFM concept is demonstrated here by the example "Uni-axially loaded symmetric open-hole plate strip". For this case, the coupled criterion can be simplified and can be analytically solved. Thereby no initial crack a_0 is to treat. Brittle fracture behavior is presumed.

*The SFC is given as the strength criterion for dense isotropic materials.

*The energy criterion postulates that the critical energy release rate $\mathcal{G}_{Ic} = K_{Ic}^{\ 2} \cdot (1-\nu^2) / E$, being proportional to the square of the fracture toughness, is met and that the stress criterion = SFC postulates that the concentrated stress within the net-section area, *averaged along the crack length* Δa, reaches a material strength value. This averaging is an assumption, which should to be checked.

From the differential FM strain energy release rate $\mathcal{G} = -d\Pi / dS$ → the FFM incremental one $-\Pi / S$.

Whereas the FM is more concerned about the full net section width, in the FFM the concern is basically just the net section length Δa, a portion of the width!

→ **SFC + FM build the *coupled FFM criterion.***

Goal of the coupled FFM criterion is to derive two fracture conditions, above strength R-related one and a fracture mechanical one assuming a crack of the size Δa. Finally the two conditions are combined and deliver an equation for the unknown critical crack Δa_c being the crack level at which OoC would occur under a critical stress and fracture mechanical condition, simultaneously.
The establishment of the coupled model is to perform on basis of average properties in order to obtain the optimally achievable reliability of 50 %. This means model validation, whereas in the DV statistically based Design Allowables are to apply.

The two parts of the coupled criterion can be expressed by equalities from a Fracture Mechanics (FM) criterion and a Strength Failure Criterion (SFC):

$$\text{FM:}\quad \frac{1}{\Delta a}\cdot\int_{r}^{r+\Delta a} K_1^2(x)\cdot dx = K_{1c}^{\,2} \qquad \text{and} \qquad \text{SFC:}\quad \frac{1}{\Delta a}\cdot\int_{r}^{r+\Delta a} \sigma(x, y=0)\cdot dx = R_{\mathrm{m}}.$$

For a simpler comparison, for the SFC the square usually is taken, whereby – advantageously - the remote stress σ cancels out in the coupled equation. Fracture failure occurs if both these criteria are simultaneously fulfilled. This leads to the required equation for the determination of

the generated critical crack size Δa_{c} via

$$\frac{\frac{1}{\Delta a}\cdot\int_{r}^{r+\Delta a} K_I^2(x)\cdot dx}{\left(\frac{1}{\Delta a}\cdot\int_{r}^{r+\Delta a} \sigma_y(x)\cdot dx\right)^2} = \frac{K_{Ic}^{\,2}}{R_m^{\,2}} = c_{KR}\ , \quad \mathrm{r} = \mathrm{d}/2\ ,$$

which is to be integrated in the Δa-process zone.

Later, the author will use the upper, two single versions, because this better displays the parallel working conditions of FM with SFC.

As the two required resistance quantities are not fully clear and not given, it is sufficient for the following first numerical application of the FFM to apply the available values '*Plain Strain Fracture Toughness'* K_{Ic} (*the inherent lowest material property, subject to certain minimum geometric test specimens requirements to achieve a plain strain condition*), and tensile strength R_{m}. This will mean the application to a brittle metal. In general, the real critical fracture toughness should be termed '*Apparent Fracture Toughness'* K_{app} (to be understood as a component property, adapted to the current geometrical conditions). For K_{app} seldom a value is available. Hence, K_{Ic} will be used for the FFM here, despite of the necessity to consider small scale yielding at the crack tip when using structural metal materials, like shown in the chapter R-curve.

Validation of the FFM model is effort-fully to be performed by running isotropic test series for different w/d-ratios of panels.

24.4 Design Verification of a 'Through center cracked Open hole Panel'

Presumptions and given data for geometry, loading from testing

Presumptions:

- Linear Structural Analysis permitted
- Not fully brittle materials which generate small scale yielding at the crack tip
- Worst case loading situation, no residual *stresses.*

Material resistance: Aluminum alloy 7475-T7351 in L(ength)-T(ransverse) direction,

example from [3]

- *R*-curve: A = 55.7 mm, B = 0.75, K_{as} = 246 MPa $\cdot\sqrt{\text{m}}$, K_b =29 MPa $\cdot\sqrt{\text{m}}$. R_{m} = 850 MPa
- Yield strength: R_{p02} = 425 MPa (B-value, for t = 6...38 mm), HSB 62232-03,
  concluding the 445 MPa, as used in HSB 62232-01, can be seen an average value.
- K_{Ic} = 48 MPa $\cdot\sqrt{\text{m}}$ = 1518 MPa $\cdot\sqrt{\text{mm}}$, $(K_{\text{Ic}} / R_{\text{m}})^2$ = 3.23 mm.

Panel dimensions

- Width w =300 mm, thickness t = 8 mm, open hole radius d = 25 mm
- Initial crack size a_0 = 30 mm.

Loading Action with Design Factor of Safety (FoS)

- j =1, Design Limit Load representative
- Uni-axial stress state $\{\sigma\}_{\text{design}} = \{\sigma_{\text{L}}\} \cdot j$ with $\{\sigma\}_{\text{L}} = (\sigma_x, \sigma_y, \tau_{xy})^T \cdot j = (0,\ 250,\ 0)^T$ MPa.

24.4.1 Application of FM, R-curve, concerning 'Open hole panel fracture', pre-crack a_0

See *Fig.25-3* with the procedure attached. a_0 = 30 mm, d = 25 mm, w = 300 mm.

Design case: Remote loading stress σ_{design} = 250 MPa $\equiv \sigma_{\text{I}}$.

Determination of the residual strength, [HSB 62232-03], with the R-curve

The computation in *Table 25- 1* delivers the following values in the instability point (touch point)

FM-resistance: $K_{\text{ec}} = 180$ MPa $\cdot\sqrt{\text{m}} = 180 \cdot \sqrt{1000}$ MPa $\cdot\sqrt{\text{mm}}$, proof in *Fig.3*

and further residual strength σ_c = 396 MPa and critical crack length a_{ec} = 55 mm.

Above remote failure stress = structural residual strength of the panel (plate strip) reads

$$\sigma_{\text{fail}} = R_{\text{res}} = R_{\text{struct}} = \sigma_c .$$

For comparison, the following analyses deliver the satisfactory information:

* Stress concentration: $\sigma_{\text{fail}} = R_{\text{m}} / K_{\text{t}}(d = \infty) = 850 / 3 = 283$ MPa $> \sigma_I$ = 250 MPa.

* Fracture Mechanics: for a Quality Assurance-defined crack size such as $a_{\text{defined}} = 33$ mm,

$$\sigma_{\text{fail}}(33) > \sigma_{\text{fail}}(55) .$$

Results for σ_{design} = 250 MPa = *sig3:*

The crack grew under the design stress by $\Delta a_{\text{design loading}}$ = *3 mm.*

→ *new* $a_0 = a_0 + \Delta a_{\text{design loading}}$ = *30 +3 = 33 mm.*

► *Computation of the Reserve Factor for Design Limit load level*, Design Load case j =1

Linear analysis is sufficient (presumption of FFM model at hand): then $\sigma \sim$ load.

$$RF = \frac{\text{Structural strength Design Allowable } R_{\text{struct}}}{\text{Stress } \sigma \text{ at } j \cdot \text{Design Limit Loading}} = \frac{R_{\text{struct}}}{\sigma_{\text{design}}} = \frac{396}{250} = 1.58 > 1.$$

According to the regulations, R_{struct} has to be a Design Allowable too, which is assumed here due to R_{m} being a strength Design Allowable and K_{Ic} being statistically–based, too.

Yielding Check in the net-section: as a limit-of-usage check. One obtains:

$$\sigma_{\text{fail}} = \sigma_{\text{netyield}} = R_{\text{p02}} \cdot \left(1 - \frac{2 \cdot a_{\text{ec}}}{w}\right) = 425 \cdot \left(1 - \frac{2 \cdot 55}{300}\right) = 267 \text{ MPa} \rightarrow RF = \frac{267}{250} = 1.14 > 1.$$

Result: Due to the requirement $\sigma_{netyield} < \sigma_c$ net section yielding limits the loading here.

Determination of the critical crack length, touch point, considering 'no hole, 'with hole'

In the effective curve (*index e is written*) defined by $K_{ec} = 180\ \text{MPa} \cdot \sqrt{\text{m}}$ the plastic zone ω and the hole diameter are included.

The computation of the critical data set had to be still performed for the establishment of *Fig.25-3*.

► Computation of the design stress-linked Touch Point + generated crack growth $\Delta a_{\text{design loading}}$

After employing both the SIF functions, from *§ 24.3.1*,

$$KSIF_{nh}(a) = \sigma \cdot \sqrt{\pi \cdot a} \cdot \sqrt{\sec\frac{\pi \cdot a}{w}} \quad , \qquad \text{and}$$

$$KSIF_{wh}(a) = \sigma \cdot \sqrt{\pi \cdot a} \cdot \sqrt{1 - \frac{r}{a}} \cdot \left(1 + 0.358 \cdot \frac{r}{a} + 1.425 \cdot \left(\frac{r}{a}\right)^2 - 1.578 \cdot \left(\frac{r}{a}\right)^3 + 2.156 \cdot \left(\frac{r}{a}\right)^4\right) \cdot \sqrt{\sec\frac{\pi \cdot r}{w} \cdot \sec\frac{\pi \cdot a}{w}}$$

the Mathcad computation in *Table 24-2* was executed, (see [3]).

Table 24-2 Derivation of a ductility-considering SIF K with improved associate crack a

Kec = 180 Kas = 246 Kb = 29 A = 34.682 B = 0.75 a0 = 30 w = 300 Rp02 = 425

Vorgabe a := 33

Crack, no hole

$$sig3 \cdot \sqrt{\pi \cdot a} \cdot \sqrt{Sek\left(\frac{\pi \cdot a}{w}\right)} = Kas - (Kas - Kb) \cdot \frac{1 - B}{\exp\left(\frac{a - a0}{A}\right) - B}$$

Aa := Suchen(a) Aa = 32.734 a := Aa a = 32.7

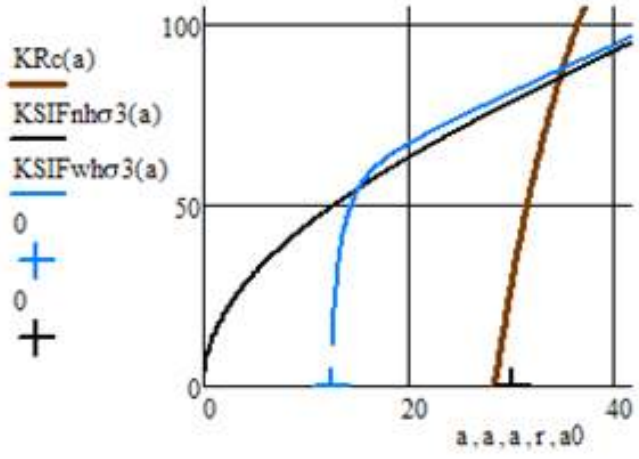

Additional information: Determination of the (physical) K_P from the effective values a_e

There are two methods to determine data of a R-curve The Potential method is used to determine physical data and the Compliance-Method (*applied here*) effective data for the given initial crack length a_0 and the loading stress σ [13, 12, 11].

If necessary, physical data can be derived from effective data by inserting

$a_p = a_e - 0.5 \cdot \omega, \quad \omega = \frac{1}{\pi} \cdot \left(\frac{K_p}{R_{p0.2}} \right)^2$ into $K_p = \sigma \cdot \sqrt{\pi \cdot a_p} \cdot \sqrt{\sec\left(\pi \cdot a_p / w \right)}$ solving the generated implicit equation via

Vorgabe Kp := 180

$$Kp = \sigma \cdot \sqrt{\pi \cdot \left[ae - 0.5 \left[\frac{1}{\pi} \cdot \left(\frac{Kp}{Rp02} \right)^2 \right] \right]} \cdot \sqrt{\frac{1}{\cos\left[\pi \cdot \frac{ae - 0.5 \left[\frac{1}{\pi} \cdot \left(\frac{Kp}{Rp02} \right)^2 \right]}{w} \right]}}$$

D := Suchen(Kp)

.

Whether this might be important could be checked by inserting Kpc through Kec calculating

$$\omega_{Kec} = \frac{1}{\pi} \cdot \left(\frac{K_{ec}}{R_{p0.2}} \right)^2 .$$

In order to present a good feeling for the difference between Kp and Ke the respective values shall be computed in *Table 24-3* below for the critical case, indexed c :

Table 24-3: Difference of the critical values of physical K_p and effective K_e

σfail := 12.5 σ := σfail·√1000 σ = 395 Rp02 := 425 w := 300 a0 := 30 Kec := 180·(√1000)

aec := 55.4 Δaec := aec − a0 Δaec = 25.4 mm Kec = 5692

Vorgabe Kpc := 5555

$$Kpc = \sigma \cdot \sqrt{\pi \cdot \left[aec - 0.5 \left[\frac{1}{\pi} \cdot \left(\frac{Kpc}{Rp02} \right)^2 \right] \right]} \cdot \sqrt{\frac{1}{\cos\left[\pi \cdot \frac{aec - 0.5 \left[\frac{1}{\pi} \cdot \left(\frac{Kpc}{Rp02} \right)^2 \right]}{w} \right]}}$$

D := Suchen(Kpc) D = 4479

$$\omega ec := 0.5 \left[\frac{1}{\pi} \cdot \left(\frac{Kec}{Rp02} \right)^2 \right] \qquad \omega pc := 0.5 \left[\frac{1}{\pi} \cdot \left(\frac{Kpc}{Rp02} \right)^2 \right]$$

apc := aec − 0.5·(ωec)

ωec = 28.5 ωpc = 27.2 mm apc = 41.1

24.4.2 Application of FFM, concerning 'Onset-of-Cracking' at a non-cracked Open Hole edge

Determination of finite crack length *Δa* and failure stress of the panel: *Mathcad 15 application*

In this sub-chapter the 'classical' FFM-procedure with the square will be presented.

- The FM-linked failure portion: The equation reads:

$$\frac{1}{\Delta a} \cdot \int_r^{r+\Delta a} \left[K_I^2(x) \right] \cdot dx =$$

$$\frac{1}{\Delta a} \cdot \left[\int_r^{r+\Delta a} \left(\sigma \cdot \sqrt{\pi \cdot r} \cdot \sqrt{1 - \frac{r}{x}} \cdot \left(1 + 0.358 \cdot \frac{r}{x} + 1.425 \cdot \left(\frac{r}{x} \right)^2 - 1.578 \cdot \left(\frac{r}{x} \right)^3 + 2.156 \cdot \left(\frac{r}{x} \right)^4 \cdot \sqrt{\sec \frac{\pi \cdot r}{w} \cdot \sec \frac{\pi \cdot x}{w}} \right]^2 \cdot dx \right.$$

- The SFC-linked failure portion: For details see *Annex1*
  For this portion a model for the stress distribution along the net section is to provide, namely,

$$\sigma_{\text{netsec}}(x) = \sigma \cdot c_{\text{wd}} \cdot [0.335 + 0.665 \cdot (1 + c_{11} \cdot \frac{x-r}{0.5 \cdot w - r})^{c_{12}} + c_{13} \cdot (\frac{x-r}{0.5 \cdot w - r})^4 \ , \ [8]$$

with the abbreviation functions $c_{\text{wd}} = 3.215 - (\frac{w}{d})^{-0.5} + 4.294 \cdot (\frac{w}{d})^{-1.5}$ and

$c_{11} = -3.765 + 2.148 \cdot (\frac{w}{d})^{0.879}$, $c_{12} = -2.552 - 42.894 \cdot (\frac{w}{d})^{-3.17}$, $c_{13} = -0.7497 \cdot (\frac{w}{d})^{-1.858}$.

The equilibrium equation of the SFC-portion reads

$$\frac{1}{\Delta a} \cdot \int_r^{r+\Delta a} \sigma(x, y=0) \cdot dx = \frac{1}{\Delta a} \cdot \int_r^{r+\Delta a} \sigma_{\text{netsec}}(x) \cdot dx =$$

$$\frac{1}{\Delta a} \cdot \int_r^{r+\Delta a} \sigma \cdot c_{\text{wd}} \cdot [0.335 + 0.665 \cdot (1 + c_{11} \cdot \frac{x-r}{0.5 \cdot w - r})^{c_{12}} + c_{13} \cdot (\frac{x-r}{0.5 \cdot w - r})^4 \cdot dx$$

.

The implicit FFM-solution procedure of the Mathcad software in standard FFM-formulation is shown below in *Table 24-4* (Mathcad font):

Table 24-4: Implicit solution process of the two unknowns Δa_c and σ_{fail}

Vorgabe

$\Delta a := 1$ $\sigma := 11$

$$\left[\frac{1}{\Delta a}\cdot\int_r^{r+\Delta a}\left[\left[\sigma\cdot\sqrt{\pi\cdot x}\cdot\left[\sqrt{1-\frac{r}{x}}\cdot\left[1+0.358\cdot\frac{r}{x}+1.425\cdot\left(\frac{r}{x}\right)^2-1.578\cdot\left(\frac{r}{x}\right)^3+2.156\cdot\left(\frac{r}{x}\right)^4\right]\right]\cdot\sqrt{\text{Sek}\left(\frac{\pi\cdot r}{w}\right)\cdot\text{Sek}\left(\frac{\pi\cdot x}{w}\right)}\right]\right]^2 dx\right] = \frac{KIc^2}{Rm}$$

$$\frac{1}{\Delta a}\cdot\int_r^{r+\Delta a}\left[\sigma\cdot crw\cdot\left[0.335+0.665\cdot\left(1+c11\cdot\frac{x-r}{0.5\cdot w-r}\right)^{c12}+c13\cdot\left(\frac{x-r}{0.5\cdot w-r}\right)^4\right]dx\right]$$

$$\frac{1}{\Delta a}\cdot\int_r^{r+\Delta a}\sigma\cdot crw\cdot\left[0.335+0.665\cdot\left(1+c11\cdot\frac{x-r}{0.5\cdot w-r}\right)^{c12}+c13\cdot\left(\frac{x-r}{0.5\cdot w-r}\right)^4\right]dx = Rm$$

$A := \text{Suchen}(\Delta a, \sigma)$ $A = \begin{pmatrix} 1.77 \\ 420.83 \end{pmatrix}$ $\Delta a := A_0$ $\Delta ac := \Delta a$ $\sigma := A_1$ $\sigma fail := \sigma$

$\Delta ac = 1.77$ $\sigma fail = 421$

Result: Within the FFM, the two models from FM and from strength analysis are commonly employed to predict the failure event 'Onset-of-Cracking' at a non-cracked hole. In the case above the instantaneously generated finite crack length reads $\Delta a_c = 1.77$ mm *and the associated remote average structural failure stress of the panel* σ_{struc} *reads* σ_{fail} *= 421 MPa.*

Fig.24-5 finally tries to illustrate the FFM hypothesis "*Both the conditions must be fulfilled*". It points out the failure-causing relationship and the dominated domains, where stress states may happen to be.

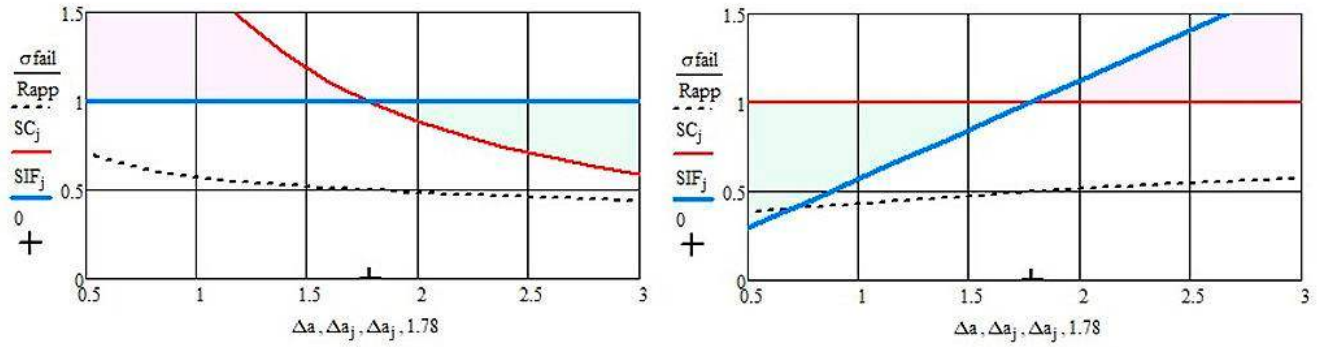

Fig. 24-5, w=36mm , a_0 = 30 mm, d =6 mm: $\Delta a_c = 1.77$ mm

(left) 'SIF' is assumed to be 100% with the question "When does the 'SC' not show failure?
Vice versa: (right) SC assumed to be 100% with the question "When does the 'SIF' not show failure?

One basic interest is how a varying resistance ratio $c_{KR} = K_{Ic}^2/R_m^2$ affects critical **crack length** and **failure stress**. *Fig.24-6* shows the mapped numerical results for a number of ratios.

Result: With increasing resistance ratio both critical crack size and failure stress naturally grow.

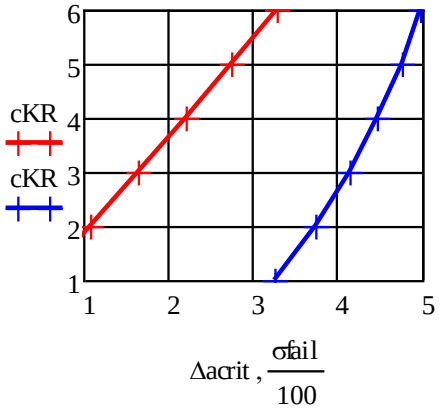

Fig.24-6, w=36mm , a_0 = 30 mm, d =6 mm:
Effect of varying resistance ratio c_{KR}, measured in mm,
on Δa_c (left) and σ_{fail} (on the abscissa)

AA 7475-T7351:
$c_{KR0} = (K_{Ic} / R_m)^2 = 3.23$ mm, $\Delta a_c = 1.77$ mm

Of further interest might be how the FM-linked and the SC-linked portions change with the crack length. *Fig.24-7* depicts these courses after employing the two integrals, termed 'SIF' and SC, below.

$$\frac{\frac{1}{\Delta a}\cdot\int_r^a K_I^2(x)\cdot dx}{\left(\frac{1}{\Delta a}\cdot\int_r^a \sigma_y(x)\cdot dx\right)^2} = \frac{K_{Ic}^2}{(R_m)^2} = c_{KR} \quad \Rightarrow \quad \frac{\frac{1}{\Delta a}\cdot\int_r^a K_1^2(x)\cdot dx / K_{1c}^2}{\left(\frac{1}{\Delta a}\cdot\int_r^a \sigma_y(x)\cdot dx\right)^2 / R_m^2} = \frac{\text{'SIF'}}{\text{SC}} \quad \text{with}$$

$$SIF_i := \frac{\frac{1}{\Delta a_i}\cdot\int_r^{r+\Delta a_i}\left[\sigma\cdot\sqrt{\pi\cdot x}\cdot\left[\sqrt{1-\frac{r}{x}}\cdot\left[1+0.358\cdot\frac{r}{x}+1.425\cdot\left(\frac{r}{x}\right)^2-1.578\cdot\left(\frac{r}{x}\right)^3+2.156\cdot\left(\frac{r}{x}\right)^4\right]\right]\cdot\sqrt{Sek\left(\frac{\pi\cdot r}{w}\right)\cdot Sek\left(\frac{\pi\cdot x}{w}\right)}\right]^2 dx}{KIc^2}$$

$$SC_i := \frac{\frac{1}{(\Delta a_i)^2}\cdot\left[\int_r^{r+\Delta a_i}\sigma\cdot crw\cdot\left[0.335+0.665\cdot\left(1+c11\cdot\frac{x-r}{0.5\cdot w-r}\right)^{c12}+c13\cdot\left(\frac{x-r}{0.5\cdot w-r}\right)^4\right]dx\right]^2}{Rm^2}$$

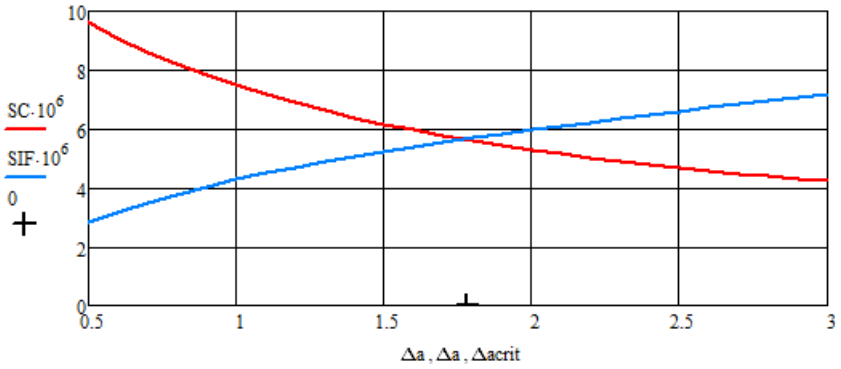

Fig.24-7, w =36mm, a_0 = 30 mm, d =6 mm: Course of growing FM-portion (SIF) and decaying Strength Mechanics portion (SC) over the finite crack size Δa

Result: The critical point at a_c = 1.78 mm is clearly marked at 'SIF' = SC.

After having depicted the influence of the resistance ratio $c_{KR} = K_{Ic}^2/R_m^2$ in *Fig.6* the effect of a fixed ratio 'panel width/hole diameter' w/d shall be displayed for two widths in *Fig.24-8* presenting how the remote failure stress σ_{fail} of the panel changes with Δa.

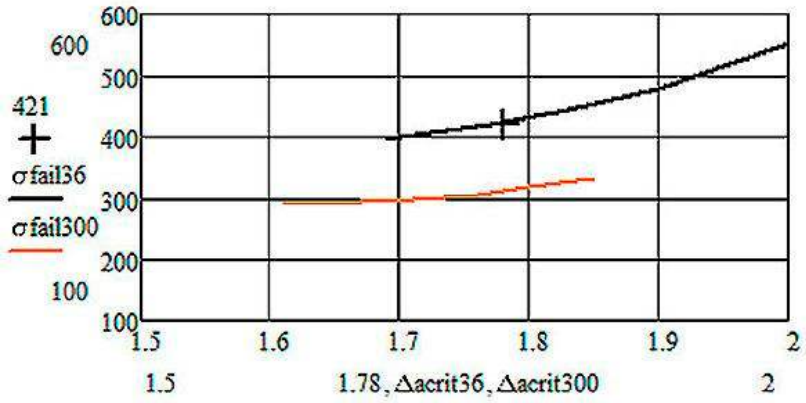

Fig.24-8, w=36mm, w = 300mm: Effect of different panel geometry, ratios w/d = 6.

Result:
For a given resistance ratio c_{KR}, for two panel widths, above stress failure curves are plotted as functions of the individually given critical crack size. The wider panel allows a lower stress only, because more volume is highly stressed.

► Computation of the *Reserve Factor* for Design Limit load level, j =1

Remote loading stress $\sigma = \sigma_I$ = 250 MPa, a_0 = 30 mm, d =25 mm.

Linear analysis is sufficient (presumption of FFM model): then $\sigma \sim$ load

Assumed σ_{fail}, to be a Design Allowable, the Reserve Factor against 'Onset-of-Cracking' at the hole edge is

$$RF = \frac{\sigma_{struct}}{\sigma_{design}} = \frac{421\ \text{MPa}}{250\ \text{MPa}} = 1.7\ .$$

According to the regulations, a Design Allowable has to be applied, too, which is assumed here, because R_m is a Strength Design Allowable and K_{Ic} is assumed to be statistically based.

Yielding Check in the net-section:, as a limit-of-usage check. One obtains:

$$\sigma_{fail} = \sigma_{netyield} = R_{p02} \cdot \left(1 - \frac{2 \cdot a_{ce}}{w}\right) = 425 \cdot \left(1 - \frac{2 \cdot 55.4}{300}\right) = 268 \text{ MPa}.$$

$$RF = \frac{268}{250} = 1.14 \ > \ 1.$$

Result: Due to the requirement $\sigma_{netyield} < \sigma_c$ *net section yielding limits the loading here.*

24.5 Application of the FFM to a Test Data-based HSB-example

Task: Mapping of the critical stress 'σ_c-curve' as function of the running crack size *a*.

The course of just 3 test points of a fixed open hole panel (from HSB 62232-01 on '*Width dependency of the so-called Feddersen-parameter'*, [10], is to map. These fracture values are given for the original $a_0 = a$ + r, also depicted in the plot.

Note, please, when assessing the test data set: The 3 test points with the different crack sizes are assumed average values. (1) In this context, in the HSB sheet the sample size number of tests belonging to one 'average' point was not given. (2) Further, an additional fitting process of the foreseen correction function was performed.

Fig.24-9, left, displays the geometry and the loading of the envisaged HSB-panel. The coordinate x has its origin in the hole center.
Fig.24-9 right, presents the course of the SIF *K* and of the net section stress along x together with the three average test points at the abscissa x with the coordinate points $r + a = a_0$.

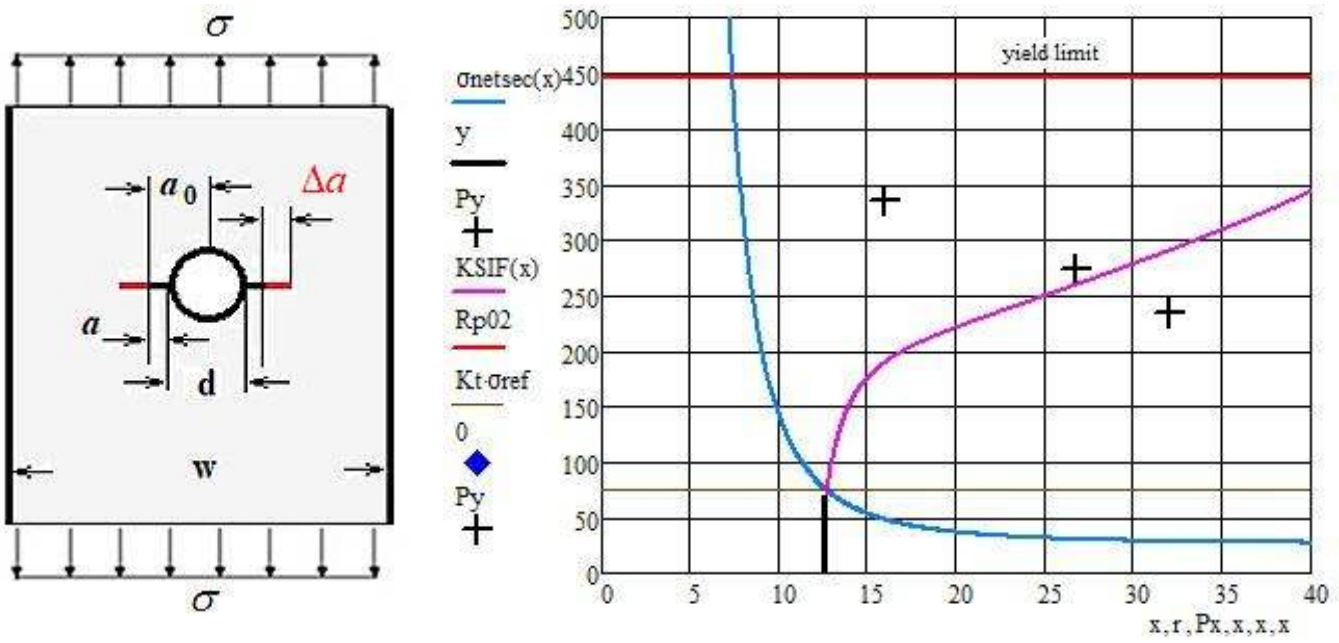

Fig.24-9: (left) Geometry of the fixed Open Hole Panel and its uniaxial loading.
(right) Test points with the courses of the 'SIF' and the net section stress in width x-direction
w =160 mm, *t* =2 mm, *d* =25 mm. *AA 7475-7761:* R_{p02}= 445 *MPa,* $K_{c,\infty} = 2500 \text{ MPa} \cdot \sqrt{\text{m}}$ ·
Abscissa points in mm: x = r = 12.5; a_0 =16, 26.7, 32

Result:
Shifting the FFM failure stress point by Δa gives a point a little far from the derived FM-curve, This crack size Δa defines the a_0 *when analyzing future loading and crack growth.*

In *Fig.24-10* for the given hole, d = 2·r, the computed FFM-linked failure stress point σ_{fail} (bold) is depicted with the generated crack size Δa. The Mathcad computations were presented in *Table 24-3*, which presents a mixture of FFM and FM results.
In order to map the FM-data course optimal two different K-values have been applied with a physically logic higher value for the higher a_0-values of $K_{upper} = 2700\ \text{MPa}\cdot\sqrt{\text{m}}$ than the mean value 2500.

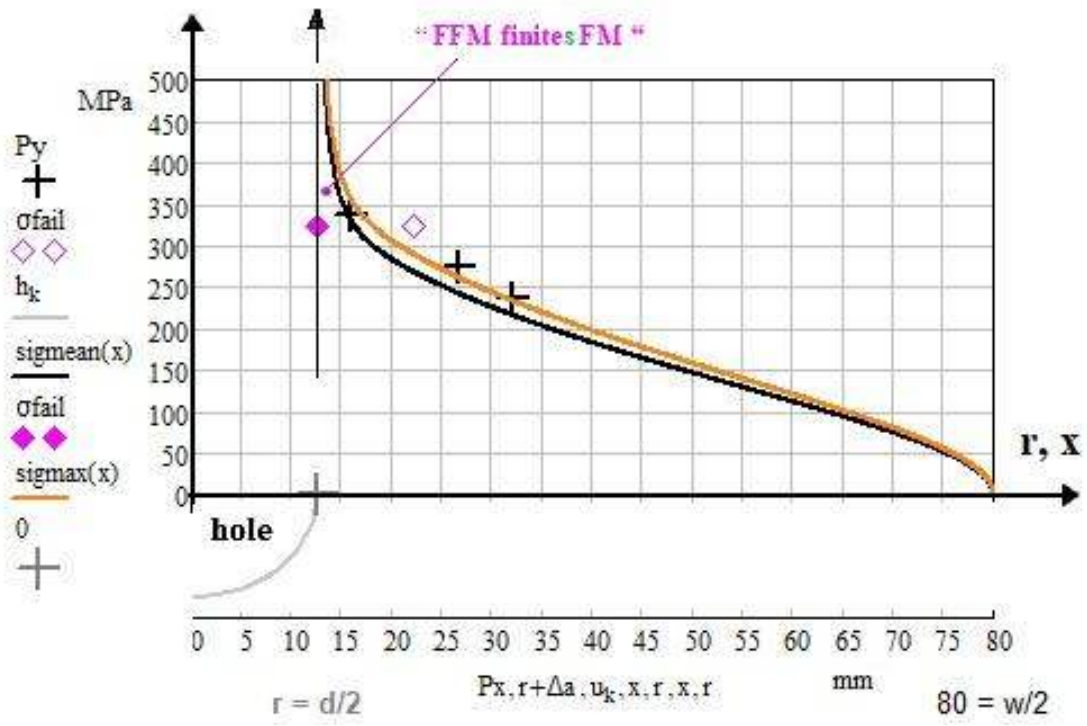

Fig.24-10, 80 mm= w/2, t =2 mm, r =25/2 = 12.5mm hole:

Depiction of the FFM-based failure stress at 'Onset-of-Cracking' for generating Δa = 9.6 mm and of the FM-based mapping of the course of the three test points with its associate initial different crack size a_0. For this mapping two different K-values are applied 2500 and 2700 (upper)

Result:

For the identical hole radius 12.5 mm the FFM-based failure stress (a_0 = 0) lies in the vicinity of the first FM-based failure stress (a = 16.0 - 12.5=3.5 mm) point +.

► ***In the frame of the scatter:***

the* FM-curve tendency of small initial cracks *a*→ 0 *matches well with the FFM!

The Mathcad computation is presented in *Table 24-4*.
The upper part depicts the classical FFM procedure and the center the Cuntze procedure with directly using the single equations.

Result: Both, the procedures end with the same numbers.

Also a FM-linked mapping of the three test point examples with its initial crack sizes a_0 was successfully performed, see the bottom of *Table 24-4*. Thereby the SIF *K* was varied, the above mentioned mean and the higher assumed value was applied.
This might be of interest for a rework of the 'Feddersen parameter sheet' HSB 63321-06.

Result:
Mapping was successful. The difference of the two K-values vanishes at both the ends.

Table 24-4, Mathcad computations:

*(up) Standard FFM procedure (*using the square*), however solved without necessary iterations, $a_0 = 0$*
(center) Cuntze's procedure: separate FFM- and SFC-equation, $a_0 = 0$
(down) FM-based mapping of the three test points with its individual initial cracks a_0

Vorgabe $\Delta a := 11$ $\sigma := 111$

$$\left[\frac{1}{\Delta a}\cdot\left[\int_{r}^{r+\Delta a}\left[\left[\sigma\cdot\sqrt{\pi\cdot x}\cdot\left[\sqrt{1-\frac{r}{x}}\cdot\left[1+0.358\cdot\frac{r}{x}+1.425\cdot\left(\frac{r}{x}\right)^2-1.578\cdot\left(\frac{r}{x}\right)^3+2.156\cdot\left(\frac{r}{x}\right)^4\right]\right]\cdot\sqrt{\mathrm{Sek}\left(\frac{\pi\cdot r}{w}\right)\cdot\mathrm{Sek}\left(\frac{\pi\cdot x}{w}\right)}\right]\right]^2 dx\right]\right] = \frac{Kc^2}{Rp02^2}$$

$$\left[\frac{1}{\Delta a}\cdot\int_{r}^{r+\Delta a}\sigma\cdot crw\cdot\left[0.335+0.665\cdot\left(1+c11\cdot\frac{x-r}{0.5\cdot w-r}\right)^{c12}+c13\cdot\left(\frac{x-r}{0.5\cdot w-r}\right)^4\right]dx\right]^2$$

$$\frac{1}{\Delta a}\cdot\left[\int_{r}^{r+\Delta a}\sigma\cdot crw\cdot\left[0.335+0.665\cdot\left(1+c11\cdot\frac{x-r}{0.5\cdot w-r}\right)^{c12}+c13\cdot\left(\frac{x-r}{0.5\cdot w-r}\right)^4\right]dx\right] = Rp02$$

$A := \mathrm{Suchen}(\Delta a,\sigma)$ $A = \begin{pmatrix} 9.6 \\ 322.28 \end{pmatrix}$ $\Delta a := A_0$ $\sigma := A_1$ $\Delta a = 9.6$ $\sigma = 322$

Vorgabe $\Delta a := 11$ $\sigma := 111$

$$\left[\frac{1}{\Delta a}\cdot\left[\int_{r}^{r+\Delta a}\left[\left[\sigma\cdot\sqrt{\pi\cdot x}\cdot\left[\sqrt{1-\frac{r}{x}}\cdot\left[1+0.358\cdot\frac{r}{x}+1.425\cdot\left(\frac{r}{x}\right)^2-1.578\cdot\left(\frac{r}{x}\right)^3+2.156\cdot\left(\frac{r}{x}\right)^4\right]\right]\cdot\sqrt{\mathrm{Sek}\left(\frac{\pi\cdot r}{w}\right)\cdot\mathrm{Sek}\left(\frac{\pi\cdot x}{w}\right)}\right]\right]^2 dx\right]\right] = 1$$

$$Kc^2$$

$$\frac{\frac{1}{\Delta a}\cdot\int_{r}^{r+\Delta a}\sigma\cdot crw\cdot\left[0.335+0.665\cdot\left(1+c11\cdot\frac{x-r}{0.5\cdot w-r}\right)^{c12}+c13\cdot\left(\frac{x-r}{0.5\cdot w-r}\right)^4\right]dx}{Rp02} = 1$$

$A := \mathrm{Suchen}(\Delta a,\sigma)$ $A = \begin{pmatrix} 9.6 \\ 322.3 \end{pmatrix}$ $\Delta a := A_0$ $\sigma := A_1$ $\Delta a = 9.6$ $\sigma = 322$

$$\mathrm{sigmean}(x) := \frac{2500}{\left[\sqrt{\pi\cdot x}\cdot\left[\sqrt{1-\frac{r}{x}}\cdot\left[1+0.358\cdot\frac{r}{x}+1.425\cdot\left(\frac{r}{x}\right)^2-1.578\cdot\left(\frac{r}{x}\right)^3+2.156\cdot\left(\frac{r}{x}\right)^4\right]\right]\cdot\sqrt{\mathrm{Sek}\left(\frac{\pi\cdot r}{w}\right)\cdot\mathrm{Sek}\left(\frac{\pi\cdot x}{w}\right)}\right]}$$

;Kc – Variants

$$\mathrm{sigmax}(x) := \frac{2700}{\left[\sqrt{\pi\cdot x}\cdot\left[\sqrt{1-\frac{r}{x}}\cdot\left[1+0.358\cdot\frac{r}{x}+1.425\cdot\left(\frac{r}{x}\right)^2-1.578\cdot\left(\frac{r}{x}\right)^3+2.156\cdot\left(\frac{r}{x}\right)^4\right]\right]\cdot\sqrt{\mathrm{Sek}\left(\frac{\pi\cdot r}{w}\right)\cdot\mathrm{Sek}\left(\frac{\pi\cdot x}{w}\right)}\right]}$$

24.6 Some Conclusions

Strength criteria alone or energy-based fracture mechanical criteria alone cannot always lead to a reliable fracture failure prediction. Design Verification (DV) by using a coupled criterion will improve the situation and be an aid for understanding the stress state-depending Onset-of-Cracking.
The so-called FFM concept should bring a solution to close the gap. It assumes the formation of cracks of finite size Δa at Onset-of-Cracking.

Fracture Mechanics

The crack-linked residual strength R_{res} is the gross-sectional tensile stress σ at failure of a structural component containing a crack. *(for fatiguers: R* of the last fatigue phase is to discriminate from R_{res} in the previous fatigue phase. Thereby, the crack length a_0 at the beginning of the static up-loading will increase to its critical value a_c in general).
A structural component will fail in the case of static loading if the SIF *K* of a brittle material reaches its critical value at $K = K_c$, termed fracture toughness, which depends on the material behavior. The determination of the K_c values requires in the so-called *K*-concept used above the fulfilment of a geometric bound in order to achieve a real minimum value by taking a minimum test specimen thickness of

$$t > 2.5 \cdot (K_{Ic} / R^t_{0.2})^2 \rightarrow \sigma_c = K_{Ic} / (\sqrt{\pi \cdot a_0} \cdot f(a_0)).$$

In the less brittle material case the limit reads $\mathcal{G} = \mathcal{G}c$.
The influence of the geometry factor *f* decreases with the specimen thickness, resulting in fracture toughness independent of the specimen dimensions. For the same materials, the fracture toughness decreases with an increasing yield strength of 0.2 %.

Fig.24-11 shall illustrate how the failure stress is governed by the crack size. Plastic deformation plays a significant role.

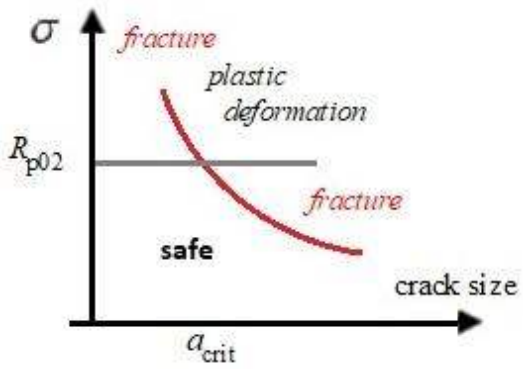

Fig.24-11: Illustration of the example with the concern plastic yielding

Strength

Dependent on the design requirements the average, the upper or a lower value of the property is used for the various physical properties.
In the case of the resistance property strength a statistically reduced value *R* is to apply and in order to achieve a reliable design a so-called Strength Design Allowable has to be applied. It is a value, beyond which at least 99% ("A"-value) or 90% ("B"-value) of the population of values is expected to fall, with a 95% confidence (*on test data achievement*) level, see MIL-HDBK 17.

> In this context, note please: Measurement data sets are the result of a Test Agreement (norm or standard), that serve the desire to make a comparability of different test procedure results possible. The Test Agreement consists of test rig, test specification, test specimen, test procedure and the test data evaluation

method. Therefore, one could only speak about '*exact test results and properties in the frame of the obtained test quality'*.
Test specimens shall be manufactured like the structure, 'as-built'.

Bearable load(ing)

The provision of bearable load(ing)s requires series tests of the distinctive structural component with statistical evaluation in order to determine a structural 'load-resistance design allowable'. This is valid for the FFM applications. See the 3 average open-hole dots in *Fig.24-10*.

Load-defined Reserve Factor *RF* and design Factor-of-Safety *FoS j*

* A *RF* is usually the result of worst case assumptions that does not take care of the joint actions of the stochastic design parameters and thereby cannot take care of their joint failure action and probability.
* The *RF* value does not outline a failure probability, and failure probability p_f does not dramatically increase if *RF* turns slightly below 1.
* A *FoS* is given and not to calculate such as a the Reserve Factor *RF* .

Application limits linked to FFM

In Design, as with each criterion, validity limits are faced, such as

- Application-extension of linear structural analysis and high brittleness
- Future task to capture small scale yielding at the crack tip which requires the provision of the associate statistically-based toughness K_c-values in order to master Design Verification
- The stress in the net-section of the panel should not exceed the tensile yield strength R_{p02}.
- 3D-application.

Many thanks to my friends, Prof. Dr.-Ing. habil. Wilfried Becker and Dr.-Ing. Jürgen Broede for the excellent exchange on this difficult novel topic FFM

24.7 Annexes

1. Course of net-section stress

In the context above and because it is necessary for understanding the FFM an illustration of the stress distribution along the net-section is to provide. In *Fig.24-12* the curves are depicted for the x- and an integration-simplifying normalized ξ-coordinate, proposed in HSB 34112-11. The relationship reads

$x = d/2$: $\xi = \dfrac{2 \cdot x/d - 1}{w/d - 1} = \dfrac{x - r}{0.5 \cdot w - r} = 0$ (hole edge)

and $x = a = d/2 + \Delta a$: $\xi = \dfrac{2 \cdot x/d - 1}{w/d - 1} = \dfrac{2 \cdot \Delta a/d}{w/d - 1} = \Delta\alpha$, abbreviated .

In [10] was given $\sigma_y = \sigma_{netsec}(\xi) = \sigma \cdot K_{t,wd} \cdot [0.335 + 0.665 \cdot (1 + c_{11} \cdot \xi)^{c_{12}} + c_{13} \cdot \xi^4$

with the geometry-dependent stress concentration factor K_t (w, d)

$$K_t(w,d) = 3.215 - (\frac{w}{d})^{-0.5} + 4.294 \cdot (\frac{w}{d})^{-1.5} \equiv c_{dw}$$

and the abbreviation functions

$$c_{11} = -3.765 + 2.148 \cdot (\frac{w}{d})^{0.879}, \quad c_{12} = -2.552 - 42.894 \cdot (\frac{w}{d})^{-3.17}, \quad c_{13} = -0.7497 \cdot (\frac{w}{d})^{-1.858}.$$

For the example w = 300 mm, d = 25 mm, c_{dw} = 3.03, c_{11} = 19.5, c_{12} = -2.56, c_{13} = -4.9· 10^{-3} follow after normalization by $K_{t,\infty}(w=\infty)$=3, and setting a reference stress σ = 100 MPa the following plots:

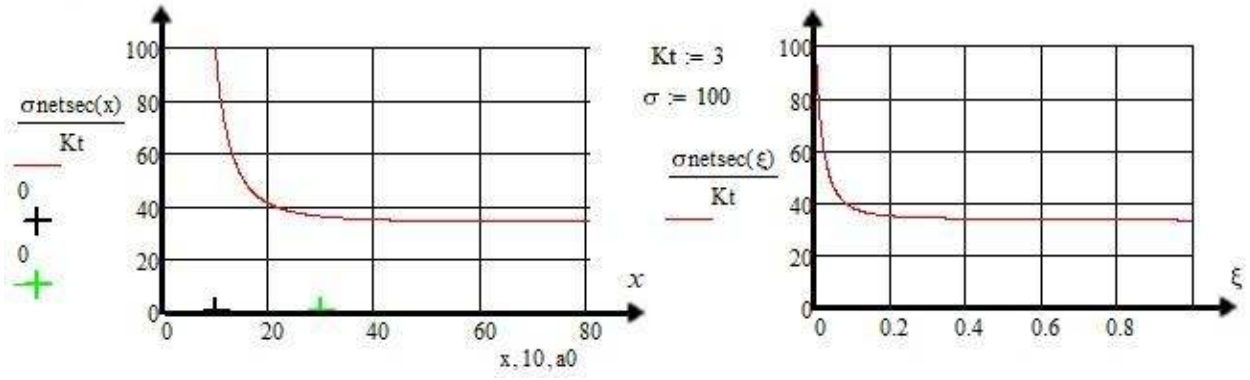

Fig.24-12: Contour of the stress along the net-section of the panel considering the coordinates x and ξ.
*σ_{ref} = 100*MPa, *r =12.5* mm, *a_0= 30*mm, *$K_{t,\infty}$ =3, x width coordinate (ligament), $\xi = (x-r)/(0.5\cdot w-r)$*

<u>*Results*</u>:
With increasing distance to the hole edge the stresses are monotonically descending whereas the incremental energy release rate $\mathcal{G}$ is monotonically ascending (see *Fig.12).*

2. Integration of net-section stress

* <u>HSB 34112-11</u> computation, retraced:
Applying the afore mentioned coordinate transformation x → ξ enables the following symbolic integration

$$\frac{1}{\Delta a}\cdot\int_{r}^{r+\Delta a}\sigma_y\cdot dx = \frac{\sigma\cdot c_{wd}}{\Delta\alpha}\cdot\int_{0}^{\Delta\alpha}[0.335+0.665\cdot(1+c_{11}\cdot\xi)^{c_{12}}+c_{13}\cdot\xi^4]\cdot d\xi$$

$$=\frac{\sigma\cdot c_{wd}}{\Delta\alpha}\cdot\left[0.335+c_{14}\cdot\frac{(1+c_{11}\cdot\Delta\alpha)^{c15}-1}{\Delta\alpha}+c_{16}\cdot\Delta\alpha^4\right]$$

$$\text{with}\qquad c_{14}=\frac{0.665}{c_{11}\cdot(c_{12}+1)},\quad c_{15}=c_{12}+1,\quad c_{16}=\frac{c_{13}}{3}.$$

* <u>Variant Cuntze</u>:
Despite of the more complicate integration limit $r+\Delta a$ instead of $\Delta\alpha$, the Mathcad solution process allows to stick to the x coordinate, avoiding a mixture of α with a within the solution process. Inserting into the equation above the relationship $\xi = (x-r)/(0.5\cdot w-r)$ leads to

$$\frac{1}{\Delta a}\cdot\int_{r}^{r+\Delta a}\sigma_y\cdot dx=\frac{1}{\Delta a}\cdot\int_{r}^{r+\Delta a}\sigma\cdot c_{wd}\cdot[0.335+0.665\cdot(1+c_{11}\cdot\xi)^{c_{12}}+c_{13}\cdot\xi^4]\cdot dx$$

$$=\frac{1}{\Delta a}\cdot\int_{r}^{r+\Delta a}\sigma\cdot c_{wd}\cdot[0.335+0.665\cdot(1+c_{11}\cdot\frac{x-r}{0.5\cdot w-r})^{c_{12}}+c_{13}\cdot\left(\frac{x-r}{0.5\cdot w-r}\right)^4\cdot dx.$$

<u>*Result*</u>:
The solution of the coupled equation delivers the remote failure stress with its associated crack length size Δa , see Table 3, too.

Of interest could be the effect of a varying panel width geometry. *Finally Fig.24-13 plots the influence of the resistance ratio c_{KR}= K_{app}^2/R_{app}^2 on the critical crack size Δa_c . The c_{ik} are the variables:*

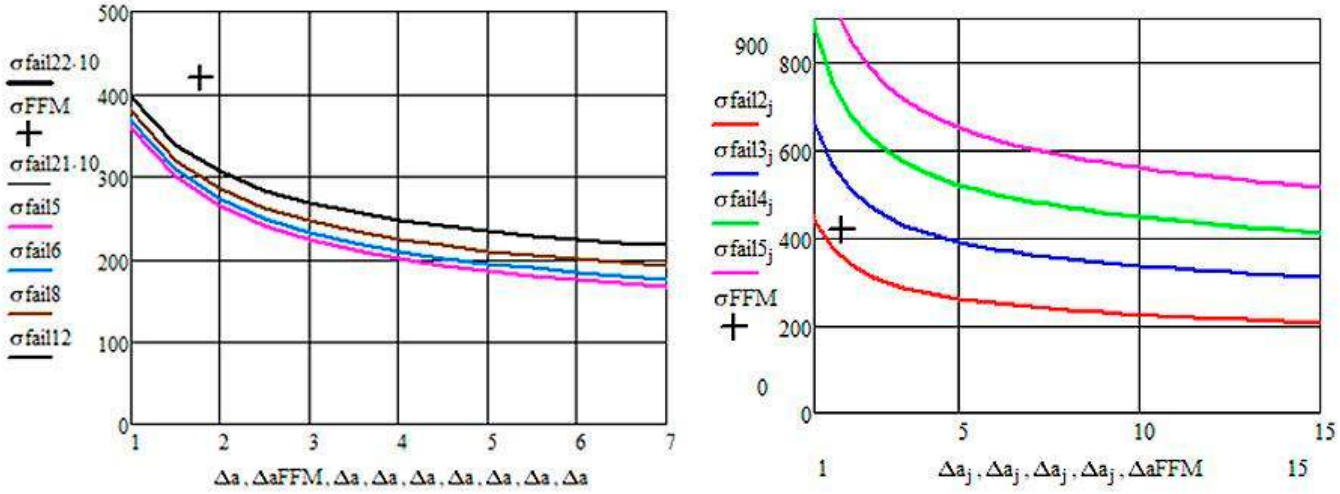

Fig.24-13 (l eft), general, w = 300mm: Effect of different panel geometry, ratios w/d=5, 6, 8, 12 as variables.
Fig.24-13 (right), general, w = 300mm: Effect of different resistance ratios KIc^2/Rm^2 = 2, 3, 4, 5

Lessons Learned on FFM and its two parts

FFM: ► FFM finites FM!

- *In the case of plain structural parts 'Onset-of-Cracking' in brittle and semi-brittle materials cannot be fully captured by the SFCs, because both a critical energy and a critical stress state must be fulfilled. Therefore, SFCs are 'just' necessary but not sufficient for the prediction of strength failure, onset of cracking. Also due to significant internal flaws an energy criterion is to apply*
- *The novel approach 'Finite Fracture Mechanics (FFM)' offers a 2D hybrid criterion to more realistically predict the stress-based 'Onset-of-Cracking' in brittle isotropic (the focus here) and UD materials.*
- *FFM enables to predict a hybrid (coupled) failure stress being assumed to be a resistance quantity on basis of the chosen statistically reduced resistances of the FFM-parts fracture mechanics (FM) and structural strength (SFC), the strength design allowables*
- *FFM is advantageous for the analysis of notched structural parts and captures applications usually treated by the well-known Neuber theory. The coupled FFM-criterion 'SFC-FM' can be used with some confidence to predict onset of cracking (failure) in brittle materials in design situations as never could be done before.*
- *Unfortunately there is still a lack of test data sets for the validation of FFM*
- *Multi-axial stress states are captured by the principal stress σ_I*
- *Using the chosen locally evenly distributed stress curve averaged over the finite length Δa is principally to check*
- *In the frame of the scatter the FM-curve tendency matches well with the FFM result. The FMC-application looks successful for the 'open hole panel' example, a realistic failure stress can be estimated, qualifying the Feddersen concept.*

FM (R-curve):

- *It is to regard, when considering the formulations to be applied: Short Cracks behave differently to Large Cracks*
- *It is unbelievable (see the treated HSB example Feddersen concept) that no test results can be found in literature concerning panels with different ratios 'width/hole radius'. Such tests should have been performed when investigating the Neuber theory (Where are these?)*
- *Notch surface quality and the metal homogeneity faced naturally have its impacts on the results.*
- *The R-curve does not depend on a_0 and w.*
- *The fracture stress is to base on $a_e = a + \Delta a + \omega$ (ductile notch tip yielding).*
- *Principal stress-linked procedure.*

Considering the up-coming AI age

For the author the valuability of Design Sheets will be growing. Therefore the structure of such a Design Sheet – structured as before - shall be included:

The **HSB design sheet** shall give the user a guide enabling an easy and correct use of it.

Its content should be divided into sections as follows:

1 General *addressing the following items*

• What is the purpose of the sheet? • Which requirements are valid for the sheet?

• Which presumptions are valid? • Which is the content of the sheet?

• For which materials, product forms, components is the sheet applicable?

• Is it possible to use the method for modified conditions (geometry, material, loading, . . .)?

• What are the restrictions of the application? • Which application cases have to be avoided?

2 List of Symbols *giving* Symbols, SI units and descriptions

3 Analysis *describing*

• The different steps should be unambiguous and appear in a correct order.

• Equations in a form that units are unambiguous

• Tables and figures in a clear, easily readable form

• The analytical method that it can be applied without any additional references.

4 Examples *chosen*

• to demonstrate the application of the analytical method for all real cases in a way allowing the user to follow easily and clearly all steps of the analytical method

5 Application *answering*

• What requirements have to be fulfilled? • Which units are mandatory?

• Where are the limitations of the analytical method?

• Are interpolation/extrapolations possible and/or allowed? If so, how?

• How accurate is the analytical method?

• What are the influences of deviations from the presumptions?

References *(minimum, necessary ones)*

25 Influence of low Cross-sectional Shear Rigidity and Rotatory Inertia on the Critical Speeds of Shafts

***Aim**: Presentation of a paper on understanding the critical critical speeds of rotating shafts under consideration of shear rigidity and rotatory.*

25.1 Introduction to this Gas-Ultra-Centrifuge-driven Elaboration

The influence of low shear rigidity and rotational inertia of the cross-section is usually only to be taken into account in the case of shafts at higher vibration modes. However, if the shafts are made of fiber composite material the ratios (elasticities: *G/E* and stiffnesses: *A/I become small*) or, for example, if the shafts are built of thin steel tubes the influences are often important even with the low vibration modes. Timoshenko's theory must then be used in order to be able to calculate the critical speeds accordingly.

A detailed derivation of the influence of shear elasticity and rotational inertia on the bending natural frequencies of the beam with a hinge at the ends can be found in [1], where a frequency ratio over the degree of the slenderness grade of the beam is depicted. Based on this, bending natural frequencies for the remaining bearing cases are calculated in [2]. The beam rotating around a transverse axis has been investigated in [3] taking into account rotational inertia and shear elasticity and classical boundary conditions. Timoshenko's theory has also been used for the rotating shaft in various publications [4-6], although a comparison with results from classical theory is missing. Only in [7] such a comparison appears to some extent. For the main support (*boundary*) cases, a compiling calculation with comparison of the bending-critical speeds of the classic model and the Timoshenko model is therefore missing.

As a result of the investigations, the physical background is presented in a concise form and the influences are further plotted in the form of diagrams. This enables the user to carry out a rapid estimation of the natural frequency f_{SD} of the shaft via the bending natural frequency f_0 of the shear-rigid and rotation-free beam of the classical beam theory as a reference frequency. As a critical rotational frequency of the shaft under shear and rotational inertia influence can then be determined very easily after insertion of the corresponding bending eigenvalues α_o

$$f_{SD} = K_{SD} \cdot f_0 = K_{SD} \cdot \alpha_0^2 \, [(E \cdot I / \rho \cdot A) / l^4]^{0.5} / 2\pi \, .$$

The parameters for the shaft are: E = modulus of elasticity, I = moment of inertia, A = cross-sectional area, l = length of the shaft, ρ = density, α_0 = frequency parameter.

The curve for the correction coefficient K_{SD} will directly represent the percentage influencing factor. The dependence of the correction coefficient on the excitation frequency f is taken into account by the fact that it is specified for the absolutely necessary frequency ratios $f / f_{SD} = \Omega/\omega = 1/2$ indirectly and +1 of the (*Gleichlaufkritische*) synchronization angular frequency where excitation angular frequency Ω and natural angular frequency ω are the same. The specification of the calculation results for the synchronous frequency ratio Ω/ω = -1 was omitted due to the low practical importance for the design of a shaft.

25.2 Theoretical Relations , Shaft with Uniformly Distributed Mass

The equilibrium conditions already known from [8] on the oscillating, rotating shaft element are for the plane x-z, see [Cun84]:

$$-\frac{\partial M_y}{\partial x} + Q_z = \varrho I \frac{\partial^2 \theta_y}{\partial t^2} + 2\varrho I \Omega \frac{\partial \theta_z}{\partial t}; \qquad \frac{\partial \theta_z}{\partial x} = \varrho A \frac{\partial^2 w_z}{\partial t^2}; \qquad M_y = -EI\theta_y'; \quad Q_z = GA_S(w_z' - \theta_y)$$

and for the plane x-y with $\partial(\partial t) = \dot{}$, $\partial(\partial x) = '$

$$-M_z' + Q_y = \varrho I\ddot{\theta}_z - 2\varrho I\Omega\dot{\theta}_y; \qquad Q_y' = \varrho A\ddot{w}_y; \quad M_z = -EI\dot{\theta}_z; \qquad Q_y = GA_S(w_y' - \theta_z);$$

$M_z,\ M_y,\ Q_z,\ Q_z$ bending moments and shear forces in the planes xz and xy

$w_z,\ w_z,\ w_z,\ w_z$ deflections and bending angle referred to the elastic line of these planes

$2\rho \cdot I \cdot \Omega \cdot \dot{\Theta}_z, 2\rho \cdot I \cdot \Omega \cdot \dot{\Theta}_y$ gyroscopic moments

G shear modulus, A_s *e*ffective shear area .

After appropriate summary with elimination of the bending angles θ_y and θ_z of the equations above to a single equation each, the two remaining equations can be represented by a single equation via the approach $w_0 = w_z + i \cdot w_y$ with $i = \sqrt{-1}$. Applying the natural oscillation approach $w_0 = w \cdot e^{i \cdot \varpi \cdot t}$ this oscillation differential equation is finally called

$$w^{IV} + \frac{\alpha_{SD}^4}{l^2}(\delta + \bar{\vartheta})\, w^{II} - \frac{\alpha_{SD}^4}{l^4}(1 - \alpha_{SD}^4 \delta\bar{\vartheta})\, w = 0;$$

$$\delta = \frac{EI}{GA_S}\frac{1}{l^2} = \frac{(EI)}{(GA)}\frac{\varkappa}{l^2}; \quad \vartheta = \frac{(\varrho I)}{(\varrho A)}\frac{1}{l^2};$$

with $x = A/A_s$ as the so-called shear distribution number, and the further abbreviations

$$\bar{\vartheta} = \vartheta \cdot (1\text{-}2\frac{\Omega}{\varpi}), \quad \alpha_{SD}^2 = \varpi_{SD} / \sqrt{\frac{E \cdot I}{\rho \cdot A} \cdot \frac{1}{l^4}}, \quad \varpi_{SD} = 2\pi \cdot f_{SD} .$$

As parameters, δ stands for the shear influence, ϑ for the influence of the rotational inertia and Ω/ω for the influence of the gyroscopic effect.

The approach $w = \tilde{C} \cdot exp(\lambda \cdot x / l)$ provides the characteristic equation with 4 solutions

$$\lambda^4 + \alpha_{SD}^4(\delta + \bar{\vartheta})\,\lambda^2 - \alpha_{SD}^4(1 - \alpha_{SD}^4\delta\bar{\vartheta}) = 0; \quad \begin{pmatrix}\Lambda_1\\ \Lambda_2\end{pmatrix} = \alpha_{SD}\sqrt{\pm\frac{\alpha_{SD}^2}{2}(\delta + \bar{\vartheta}) + \sqrt{1 + \frac{\alpha_{SD}^4}{4}(\delta - \bar{\vartheta})^2}}.$$

In the case of classical beam theory $\Lambda_1 = \Lambda_2 = \alpha_{SD} = \alpha_0$ holds.

As a solution function, after conversion of the traditional e-function approach, is obtained

$$w_I = \bar{C}_1 \cosh \Lambda_1 \frac{x}{l} + \bar{C}_2 \sinh \Lambda_1 \frac{x}{l} + \bar{C}_3 \cos \Lambda_2 \frac{x}{l} + \bar{C}_4 \sin \Lambda_2 \frac{x}{l}$$

While Λ_2 is always positive, Λ_1 changes the sign, if $\alpha_{SD}^4 \cdot \delta \cdot \vartheta > 1$. In this solution area, the solution part with the hyperbolic functions will change to a form with trigonometric functions.

For five support cases, the free constants $\bar{C}_i$ for the beam were determined and compiled in [10]. They also remain valid for the shaft if one replaces ϑ by $\bar{\vartheta}$.

After determining the zeros of the frequency equation as a function of δ, ϑ, frequency ratio Ω/ω with rotational frequency Ω, and of the frequency parameter α_{SD}, the corresponding correction coefficient

$$K_{SD} = \frac{\alpha_{SD}^2}{\alpha_0^2} = \frac{\varpi}{\varpi_0} = \frac{f_{SD}}{f_0} .$$

can be computed.

The results are presented as correction curves with shear and rotatory inertia as parameters. It can be

shown, that descending shear stiffness causes a decrease in the critical speeds while the effect of rotatory inertia is vanishing. Beside this, the influence of gyroscopic effects on the critical speeds reduces with increasing degree of boundary constraint.

25.3 Range and Limit Value considerations

Each eigenvalue curve can pass through two solution areas. However, if one sets only one of the two influences δ or ϑ equal to zero in the characteristic equation, one does not get into the second solution range. The same applies if $\bar{\vartheta} = 0$ or $\Omega/\omega = +1 / 2$.

In *Fig.25-1* natural frequency curves f_{SD} are represented as a function of the rotational frequency Ω of the shaft. Parameter is the ordinal number *n* of the tone. It can be seen here, analogous to the bending eigenvalues, that two solutions are now obtained for each tone instead of an eigenvalue curve, as in classical beam theory. So it is better to no longer speak of a mode, but of a mode (tone) family that physically has a higher ω_{n2} and a lower frequency ω_{n1} vibration shape.

The right side of *Fig.25-1* belongs to a synchronous critical frequency (forward precession, Gleichlauf) and the left side to the so-called counter-critical rotation ones (backward precession, Gegenlauf).

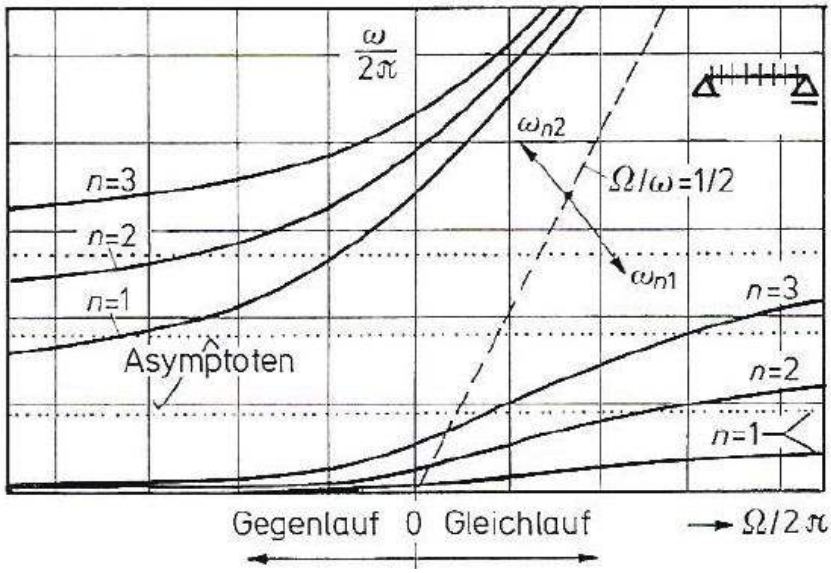

Fig.25-1. Natural frequency value curves for the double hinge-supported rotating shaft (Special example according to [8])

We do not want to consider the higher frequency oscillation form (upper eigenvalue curve), as we limit ourselves here to the two lowest and usually technically most important natural frequencies ω_{11} and ω_{21} of the whole spectrum. The eigenvalues ω_{12}, ω_{22}, ω_{32} are already higher than ω_{21}.

25.4 Results

25.4.1 General information on the evaluation of results

According to *Fig.25-1* and *Fig.25-2* prominent points of each natural frequency curve are synchronous critical rotation frequency $f = f_{SD}$ ($\Omega/\omega = 1$), the bending natural frequency f_{SD} ($\Omega/\omega = 0$), f_{SD}(O) and the counter-critical rotation frequency f_{SD} ($\Omega/\omega = -1$).

Rotational frequencies of the shaft of the synchronous critical frequency are dangerous, since then the always existing residual imbalances lead to resonance. Counter-critical rotational frequencies are less important, as they can only lead to resonance in the ideal case of perfect rotor symmetry, which is

hardly ever available. The counter-rotation area is therefore no longer listed in *Fig. 26-2.*

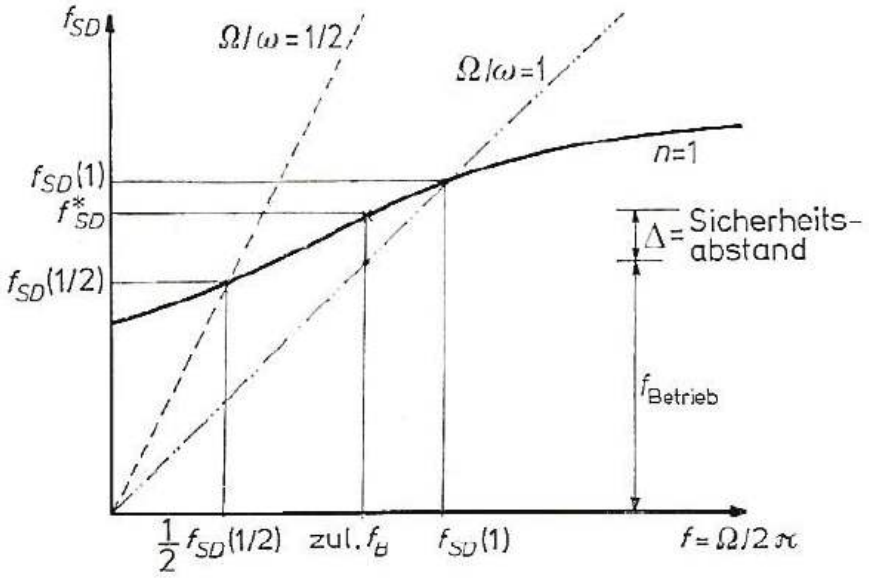

Fig.25-2. Definition of the different frequency values, Λ is the safety distance

Fig.25-2 also shows that for a certain operating (*Index $_B$ for Betrieb = operation*) frequency f_B an associated natural frequency value belongs, e.g f^*_{SD} in the synchronous range, which is below the synchronous critical rotation frequency. A safety distance of 15 to 25 % is to be strived for against f^*_{SD} and not towards $f_{SD}(1)$, depending on the balancing quality. In the important application that in operation - as shown above - subcritical, namely below the lowest synchronous critical rotation frequency the shaft is run, the associated natural frequency value can be estimated quite accurately by straight interpolation between the support points Ω/ω = 1/2 and Ω/ω = 1. The determination equation for the permissible operating frequency is then at Δ percent safety distance, taking into account permissible $f_B = f^*_{SD} \cdot (100\text{-}\Delta) / 100$,

$$\text{zul } f_B = \frac{100 - \Delta}{100} \frac{(2 - \bar{K}) f_{SD}\left(\frac{1}{2}\right)}{2\left(1 - \frac{100 - \Delta}{100} \bar{K}\right)} \quad \text{mit} \quad \bar{K} = \frac{f_{SD}(1) - f_{SD}\left(\frac{1}{2}\right)}{f_{SD}(1) - \frac{1}{2} f_{SD}\left(\frac{1}{2}\right)}.$$

The quantity K characterizes the influence of the gyroscopic effect. For $f_{SD}(1) = f_{SD}(1/2)$ the gyroscopic effect is zero.

25.4.2 Presentation of the Correction Coefficient curves

In the *Figs. 25-3* trough *-5*, the correction coefficient KSD for Ω/ω = 1 is plotted as a function of the shear influence number δ and the rotational inertia influence value θ as a parameters. For large values of δ was chosen θ = 0; 0.01; 0.05 and 0.1, for small values δ the row θ = 0; 0.01; 0.02; 0.04; 0.06; 0.08.

For the five most important boundary cases, the results are displayed graphically. To each case, two pictures belong since the application for small and large shear influence values had to be done separately.

Comments on the individual figures in the order of numbering:

*The free-free beam has the lowest degree of fixation and thus represents a limit value with which other boundary cases can be compared. Striking here is a strong increase in K_{SD} against small values of δ; the influence of the gyroscopic effect increases sharply below δ = 0.01. At a large δ, on

the other hand, this influence disappears.

*As can be seen in the other figures, an increase in the influence of rotational inertia ϑ causes K_{SD} to grow, i.e. the K_{SD} curve with the largest parameter value ϑ is the top curve of bundle. In 3.2, however, the curves for ϑ = 0.1 for the 1st and 2nd tone are well below the rest of the curves. A physical explanation could not be found at that time, not even the confirmation that the cause of the unexpected curve lies in the numeric. So be careful when using these two curves.

*The next boundary case in the 4.1 and 4.2 is the double hinge-supported and the one side hinged, one side clamped shaft. Less than in the previously discussed case, K_{SD} increases at low ϑ values; the less influence of ϑ makes the group of curves to get more densely together.

*Finally, in the case of clamped-free 5.1, 5.2, the ϑ-influence almost disappears at least in the 1st mode (tone), only the second tone still shows the natural frequency-increasing gyroscopic influence in the range of smaller δ.

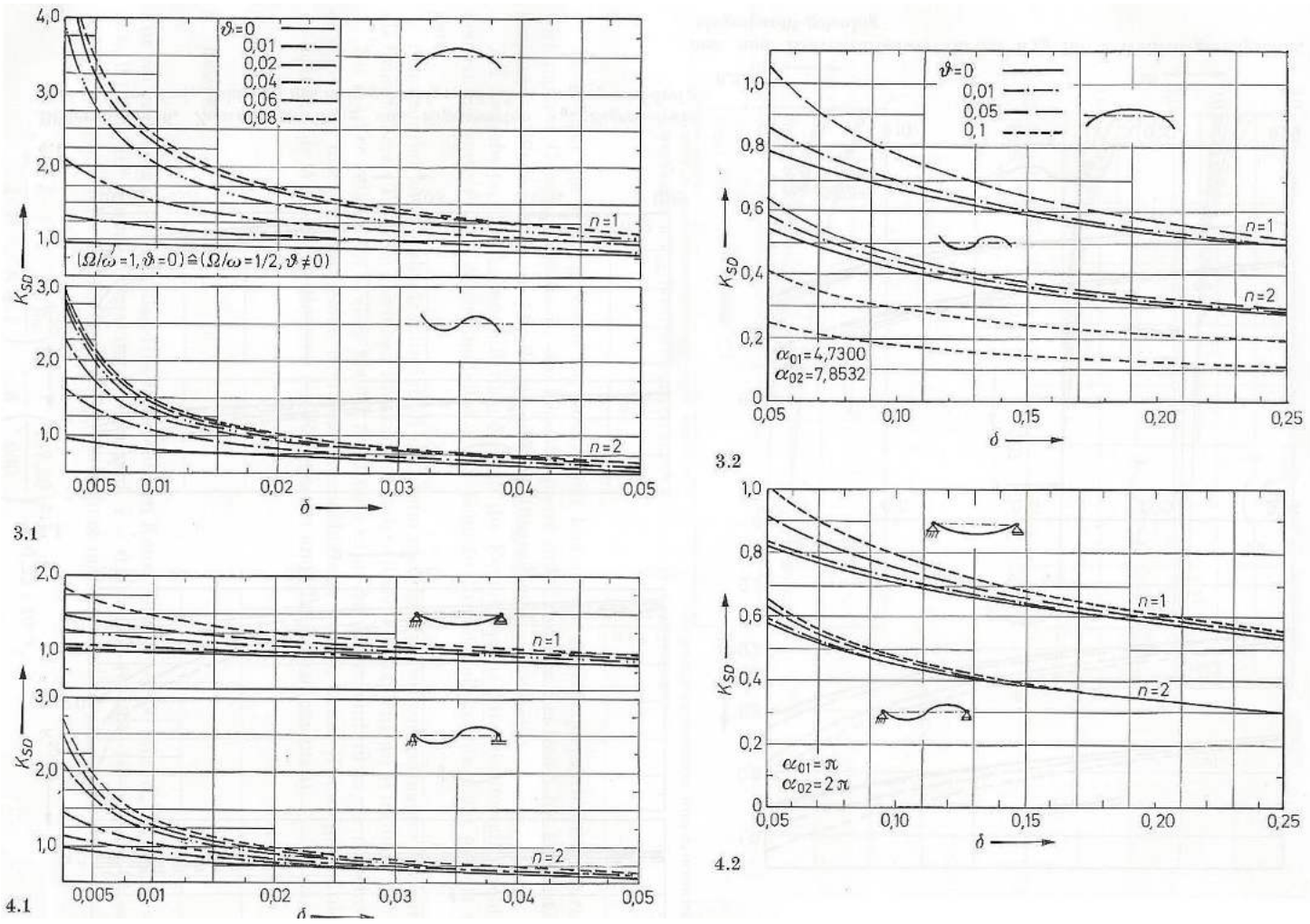

Fig.25-3: Eigenvalues α_0, natural mode shapes and correction value K_{SD} curves
3-1: Free-free beam; 3-2: Detail of 3-1
.4-1: Double hinge supported beam; .4-2: Detail of .4-1

*There remain 2 boundary cases 6.1, 6.2 with strong constraints (clamped), in which the influence of ϑ largely no longer plays a role.

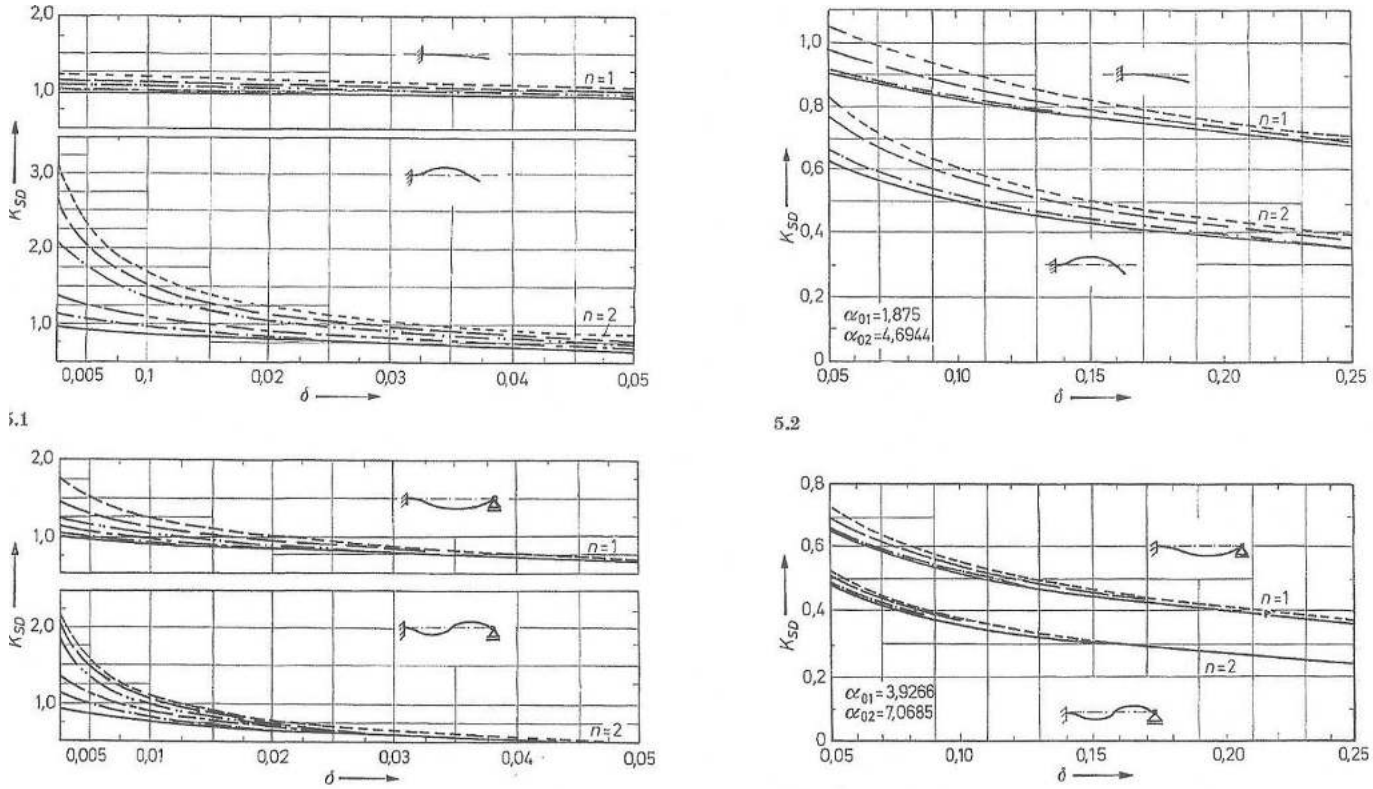

Fig.25-4: Further eigenvalues α_0, natural mode shapes and correction value K_{SD} curves
5-1: Cantilever beam; 5-2: Detail of 5-1
6-1: Beam, one side hinged, one side clamped; 6-2: Detail of 6-1

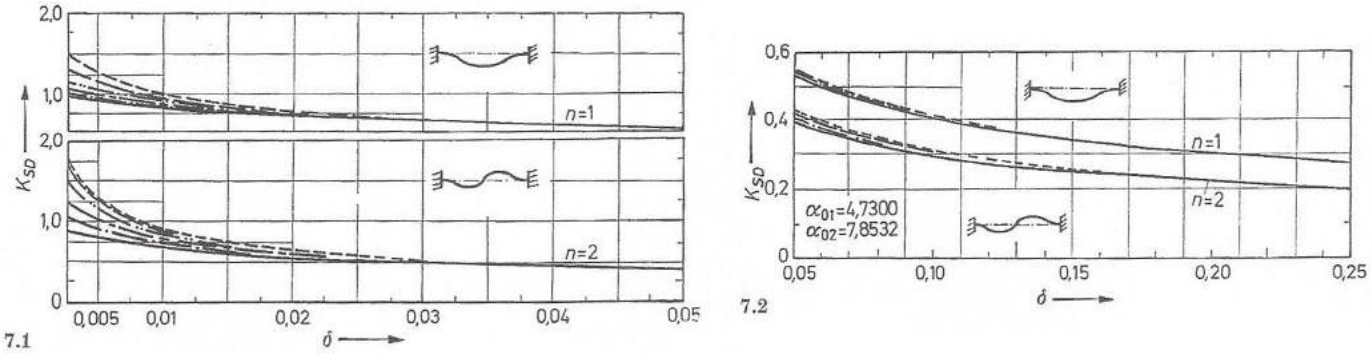

Fig.25-5: Further eigenvalues α_0, natural mode shapes and correction value K_{SD} curves
7-1: Beam, clamped at both ends; 7-2: Detail of 7-1

LL: for all five types of boundaries.

- *With decreasing shear stiffness δ, the K_{SD} value decreases or the synchronous critical rotation frequency decreases*
- *For small shear stiffness values δ, the rotatory inertia influence disappears compared to the shear influence. All ϑ-curves approach ϑ = 0*
- *The less the shaft is bound, the more the natural frequency-increasing gyroscopic effect comes into its own, i.e. the natural frequency decreases from the free-free to the firmly clamped shaft relative to the respective bending natural frequency $f_{SD}(0)$.*
- *With fixed shear influence variable δ, the natural frequency increases for increasing inertial influence values ϑ. (The exception case ϑ = 0.1 in the free-free case could not be clarified).*
- *The influences of shear and inertia are less important for the lower tone than for the higher*

tone. They gain in effect with increasing synchronization frequency.

- *In the case of more strongly bound tube shafts than the free-free ones, the gyro influence can be so small that it can be neglected compared to the other two influences.*

Of course, this no longer applies to shafts or rotors with final masses and moments of inertia.

25.5 Numerical Example

A tube, shaft-mounted on both sides - with the parameters l = 660 mm ; d_m = 147,25 mm ; E = $185.5 \cdot 10^3$ N/mm^2; Poisson ratio ν = 0.30; G = $71.3 \cdot 10^3$ N/mm^2; ρ = $8.0 \cdot 10^{-9}$ Ns^2/mm^4 und κ = 1,89 (see *Table 26-1*) at first the parameter values are determined:

Table 25-1. Schubverteilungszahlen κ (from [11])

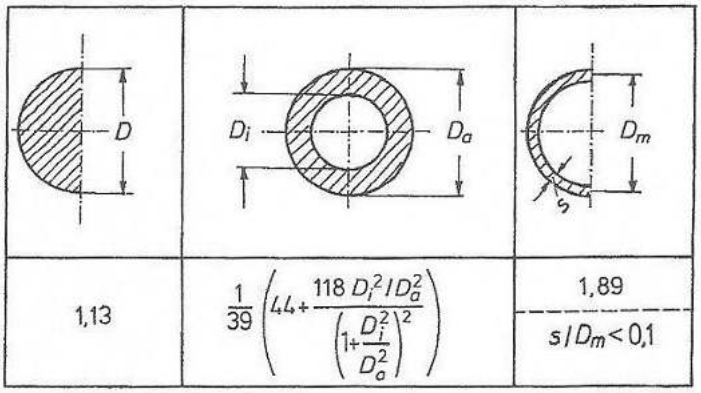

$$\frac{1}{2\pi}\sqrt{\frac{EI}{\varrho A}\frac{1}{l^4}}=\frac{1}{2\pi}\sqrt{\frac{E}{\varrho l^2}}\vartheta=\frac{1}{2\pi}\sqrt{\frac{0{,}1855\cdot 10^6\cdot 6{,}22\cdot 10^{-3}}{8{,}0\cdot 10^{-9}\cdot 660^2}}=91{,}58\ \mathrm{s}^{-1}.$$

For the first tone, one obtains as the bending natural frequency according to the classical beam theory $\alpha_{01}=\pi \qquad f_0=f_0(0)=\pi^2\cdot 91{,}58=904\ \mathrm{Hz}.$

A list of the essential natural frequency values for $\Omega/\omega=0$ and 1 in different combinations of influences is given in *Table 25-2*.

Table 25-2: Some essential natural frequency values of the numerical example

Ω/w	δ	ϑ	K		
0	0	0	1		f_0 = 904 Hz
0	0	0,00622	0,97	aus	f_D = 876 Hz
0	0,0306	0,00622	0,86	[3]	f_{SD} = 777 Hz
1	0	0	1		f_0 = 904 Hz
1	0	0,00622	1,03	aus	f_D = 932 Hz
1	0,0306	0,00622	0,96	Bild 3	f_{SD} = 806 Hz

Fig.25-6 shows the variability of the two lowest natural frequencies as a function of the rotational frequency *f* in the case of rotatory inertia influence alone(f_D dashed line) and for the case of shear and rotatory inertia influence together (f_{SD} **solid line**).

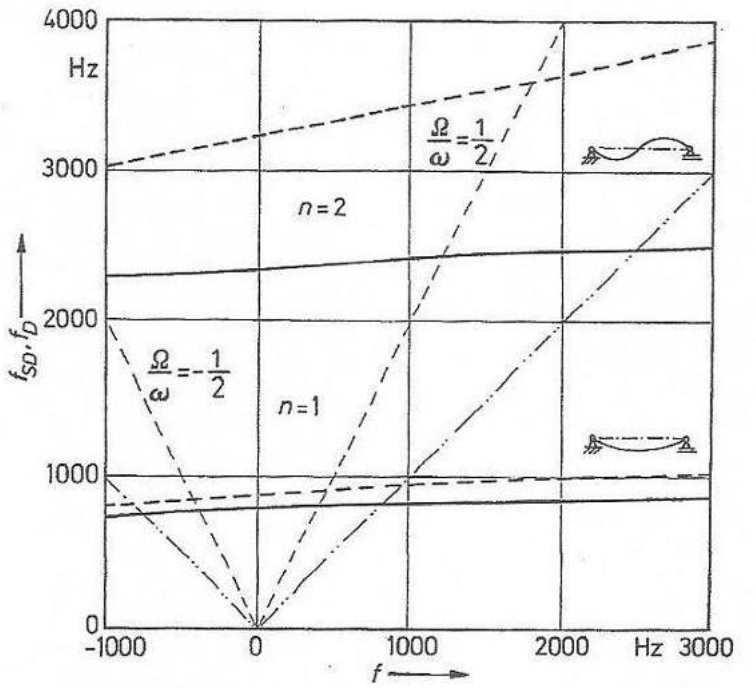

Fig.25-6: Display of natural frequency curves for the parameters ϑ =0.00622, δ =0.0306.
(solid) f_{SD} shear rigidity and rotatory inertia, (- - - dashed) f_D with rotatory inertia, f_0 (.....) without

Finally, *Fig.25-7* uses the chosen example to illustrate the numerical significance of shear, rotational and gyroscopic influence. However, the exact figures were of course no longer read in *Fig.26-3*. They were taken from a control calculation with another calculation program.

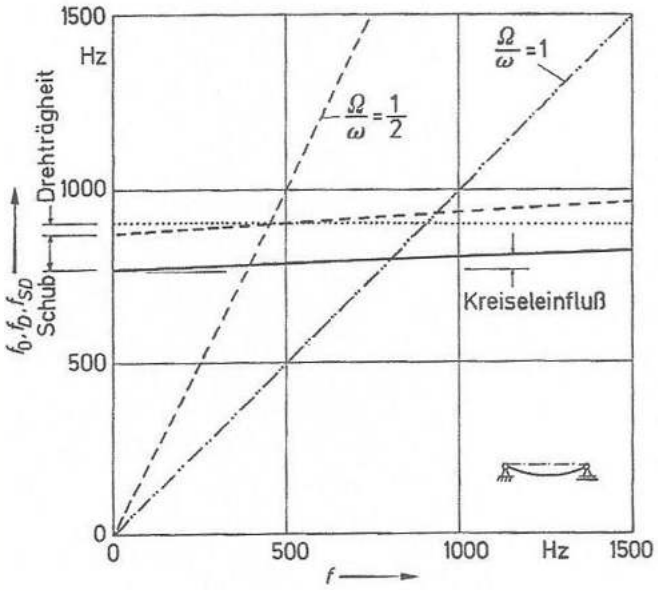

Fig.25-7: Splitting of the lowest natural frequency value curve of the number example into the individual influences (- - - is without shear rigidity and rotatory inertia influences (= Kreiseleinfluß))

***LL**:*
As in other disciplines like buckling or like strength, also in vibration it is similarly experienced: Two narrow-located neighboring modes (natural frequency = eigenfrequency) interact, which leads to a lower combined frequency!

1. Shames, I. H.; Dym, C. L.: Solid mechanics: A variational approach. London: McGraw Hill 1973, Kap. 7.7
2. Bohdaschewskij, W.: Biegeschwingungen von elastischen Balken. Diplomarbeit, Lehrstuhl B für Mechanik, TU München, Sept. 1979
3. Nachmann, A.; Lakin, W. D.: Transverse buckling of a rotating Timoshenko beam. J. Eng. Math. 16 (1982) 181—195
4. Pederson, P. T.: On forward and backward precession of rotors. Ing. Arch. 42 (1972) 26—41
5. Pederson, P. T.: On selfexcited whirl of rotors. Ing.-Arch. 4 (1973) 267—284
6. Buckens, F.: The importance of shear deformation in the calculation of critical speeds of rotating shafts. In: P. Y. Willems (ed.): Gyrodynamics. Berlin, Heidelberg, New York: Springer 1974, S. 71—78
7. Gronbach, W.: Zur Dynamik der fliegenden Welle. Diplomarbeit, Lehrstuhl B für Mechanik, TU München, Mai 1979
8. Dimentberg, F. M.: Flexural vibrations of rotating shafts. London: Butterworths 1961
9. Fuhrke, H.: Bestimmung von Balkenschwingungen mit Hilfe des Matrizenkalküls. Ing. Archiv 23 (1955) 329—348
10. Cuntze, R.; Eder, J.: Diagramme für den Einfluß von Schubelastizität und Drehträgheit auf die Biegeeigenfrequenz gleichförmig massebelegter Einfeldbalken. Bericht NT 5-82. MAN-München (1982), Dachauer Str. 667, Abt. EGS
11. Cowper, G. P.: The shear coefficient in Timoshenko's beam theory J. Appl. Mech. 33 (1966) 335—340

26 Note on Application of Shell-Tensor-Analysis to Filament Winding

Aim: *Forwarding, that tensor analysis helped me to understand MAN-applied winding technology.*

26.1 Introduction

Excerpt from Habilitation work, 1978, "Grundlagen für die Berechnung von Rotationsschalen aus Faserverbundwerkstoff (Fundamentals for the calculation of rotational shells made of fiber composites)". Above private investigations were partly executed at that time for a better design understanding of the high pressure vessels (tanks) wound at MAN Technology.

In the first section of the habilitation thesis, the shell parameters essential for wound shells are determined tensorially, namely the radii of curvature and the so-called geodesic condition for the placing of the winding thread, which shall be the sole focus below. Adherence to the geodesic condition means that the thread is laid on a surface along the shortest path between two points. This eliminates the need for friction to prevent the thread from slipping.

The second section first presents a compilation of the equilibrium conditions and deformation relationships for the slightly curved continuum shell made of fiber-reinforced composite material, as well as the fiber mesh shell of the wound body, along with assumptions and prerequisites. This is followed by a proof of identity demonstrating that the requirement for geodesic thread laying and constant winding thread tension lead to the same base contour; they are therefore identical.

The third section presents the base contours of wound containers: for the two application cases of internally pressurized fiber mesh shells with a load-bearing liner (high-pressure tanks) and, presumably for the first time, for fiber mesh shells under centrifugal force (flywheels). For internal pressure, it is possible – at least theoretically – to produce so-called isotensoids, i.e., wound bodies with the same fiber stress. For the model of a biaxially stressed fiber net shell with up to three layers, the following assumptions apply: *the matrix does not participate in force capture, $*\sigma_2 = 0,\ *\tau_{21} = 0$. This characterizes the so-called fiber net theory.

26.2 Tensorial Derivation of Clairaut's Condition for Geodesic Lines on bodies of revolution

According to E. Klingbeil (p.118), the following differential equations apply using the arc length coordinate s (= fiber winding direction) of the geodesic line.

$$\ddot{\Theta}^{\mu} + \Gamma^{\mu}_{\alpha\beta} \cdot \dot{\Theta}^{\alpha} \cdot \dot{\Theta}^{\beta} \quad \text{with} \quad \dot{\Theta} = d\Theta/ds .$$

The execution of the above rule yields the following conditions for geodetic lines on bodies of revolution

$$\dot{\Theta}^1 + \Gamma^1_{22}(\dot{\Theta}^2)^2 = 0 \quad \text{and} \quad \ddot{\Theta}^2 + 2 \cdot \Gamma^2_{12} \dot{\Theta}^1 \dot{\Theta}^2 = 0 \quad \text{or} \quad \text{inserted}$$

With the coordinate of the generating axial surface line ℓ it reads

$$\frac{\ddot{\ell}}{\bar{L}} - \frac{r r'}{\bar{L}}(\dot{\vartheta})^2 = 0 \quad \text{and} \quad \ddot{\vartheta} + 2 \cdot \frac{r'}{r} \frac{\dot{\bar{L}}}{\bar{L}} \dot{\vartheta} = 0 \quad \text{with} \quad \dot{\ell} = d\ell/ds = \cos\alpha(\ell),\ \dot{\vartheta} = d\vartheta/ds = \sin\alpha(\ell)/r(s).$$

Writing $r' = dr/d\ell = dr/ds \cdot ds/d\ell = \dot{r}/\dot{\ell}$ leads to the final differential equation systems

$$\dot{\ell} \cdot \ddot{\ell} - r \cdot \dot{r} \cdot \dot{\vartheta}^2 = 0 \quad \text{and} \quad \ddot{\vartheta} + 2 \cdot \frac{\dot{r}}{r} \cdot \dot{\vartheta} = 0 \rightarrow \frac{1}{r^2} + \frac{d(r^2 \dot{\vartheta})}{ds} = 0.$$

The last equation represents the so-called 'Clairaut condition' for geodesic lines on bodies of revolution, which, after substitution of the pressure vessel pole condition $\alpha = 90°,\ r = e$ reads

$$r^2 \dot{\vartheta} = r^2 \frac{\sin\alpha}{r} = r \bullet \sin\alpha = \text{constant} = e .$$

This second solution is the only solution of the system if the first differential equation leads to an identity. This shall be proven:

Because the relationships $\frac{1}{2}\cdot\frac{d(\dot{\ell}^2)}{ds}=\dot{\ell}\cdot\ddot{\ell}$, $\frac{1}{2}\cdot\frac{d(1/r^2)}{ds}=-\frac{\dot{r}}{r^3}$, $r^2\cdot\dot{\vartheta}=e$ are given, the first equation simplifies to $\frac{1}{2}\cdot\frac{d(\dot{\ell}^2)}{ds}-r\cdot\dot{r}\cdot\frac{e^2}{r^4}=\frac{1}{2}\cdot\frac{d(\dot{\ell}^2+e^2/r^2)}{ds}=0$.

Hence after integration follows for $\alpha=90°,\ r=e$

$\rightarrow\ \dot{\ell}^2+e^2/r^2=cos^2\alpha+e^2/r^2=cos^2\alpha+sin^2\alpha=1$ an identical fulfillment, see <u>*Fig.26-1*</u>.

Geodesic lines of unwinding (*abwickelbar in German*) surfaces such as cylinders and cones appear as straight lines in the plane unwinding.

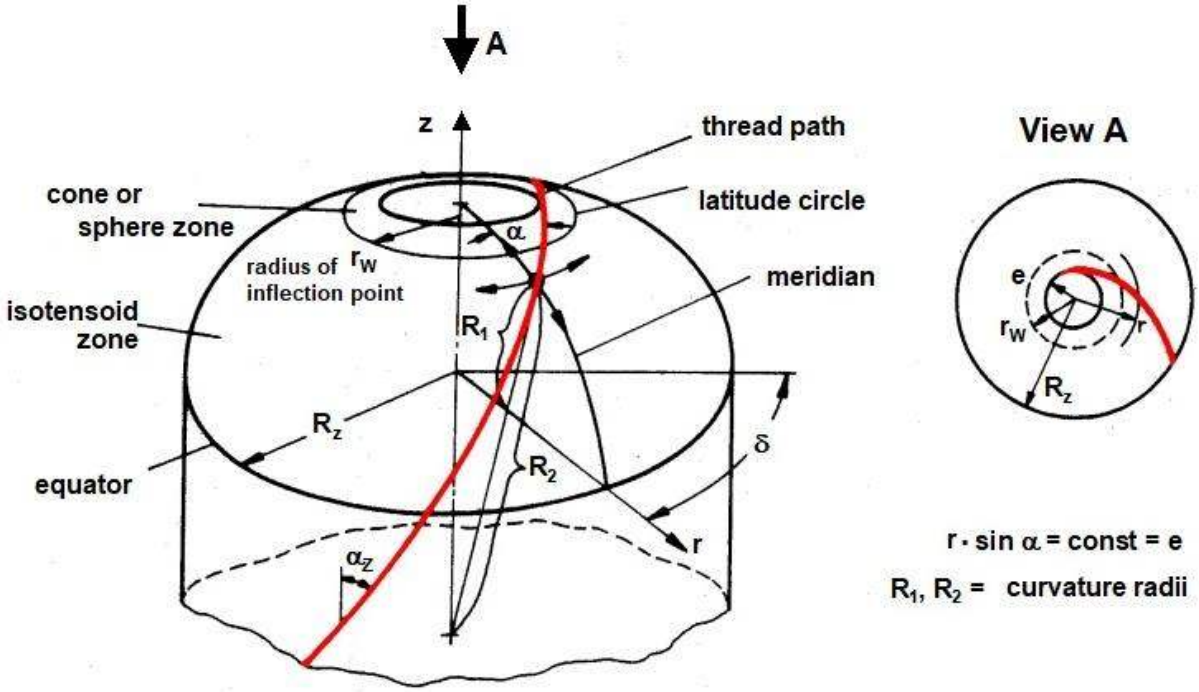

Fig.26-1: Geodesically wound geodesically-generated vessel shape

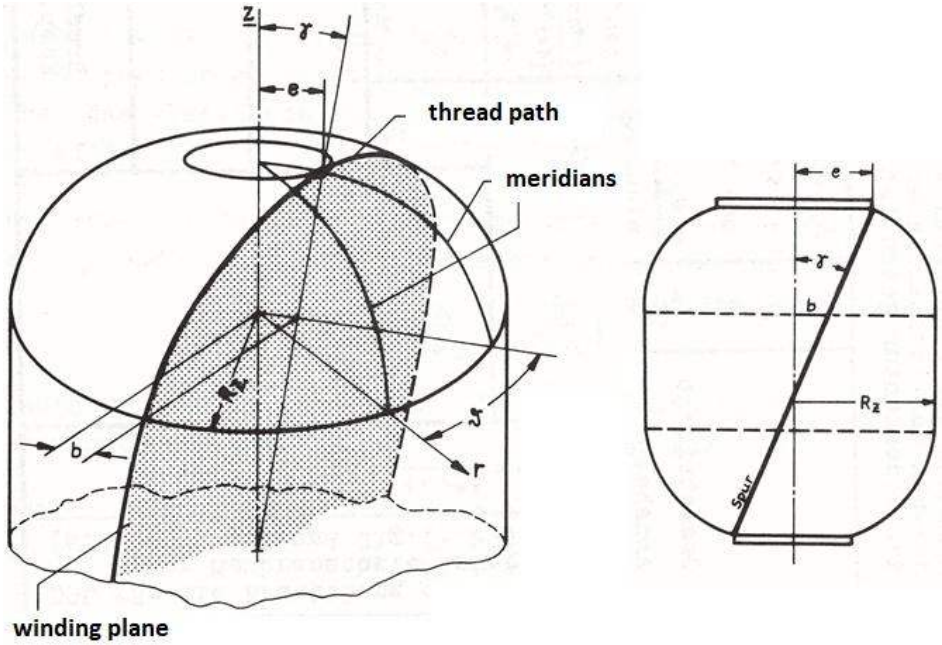

Fig.26-2: Planar wound vessel

<u>*Fig.26-2*</u> illustrates planar winding. The bottom shape may be determined geodesic (= isotensoid), planar and different to these.

Thread crossings affect the strength of vessels. Therefore, the winding patterns of vessels with different ratios of length to diameter shall be presented in *Fig.26-3*.

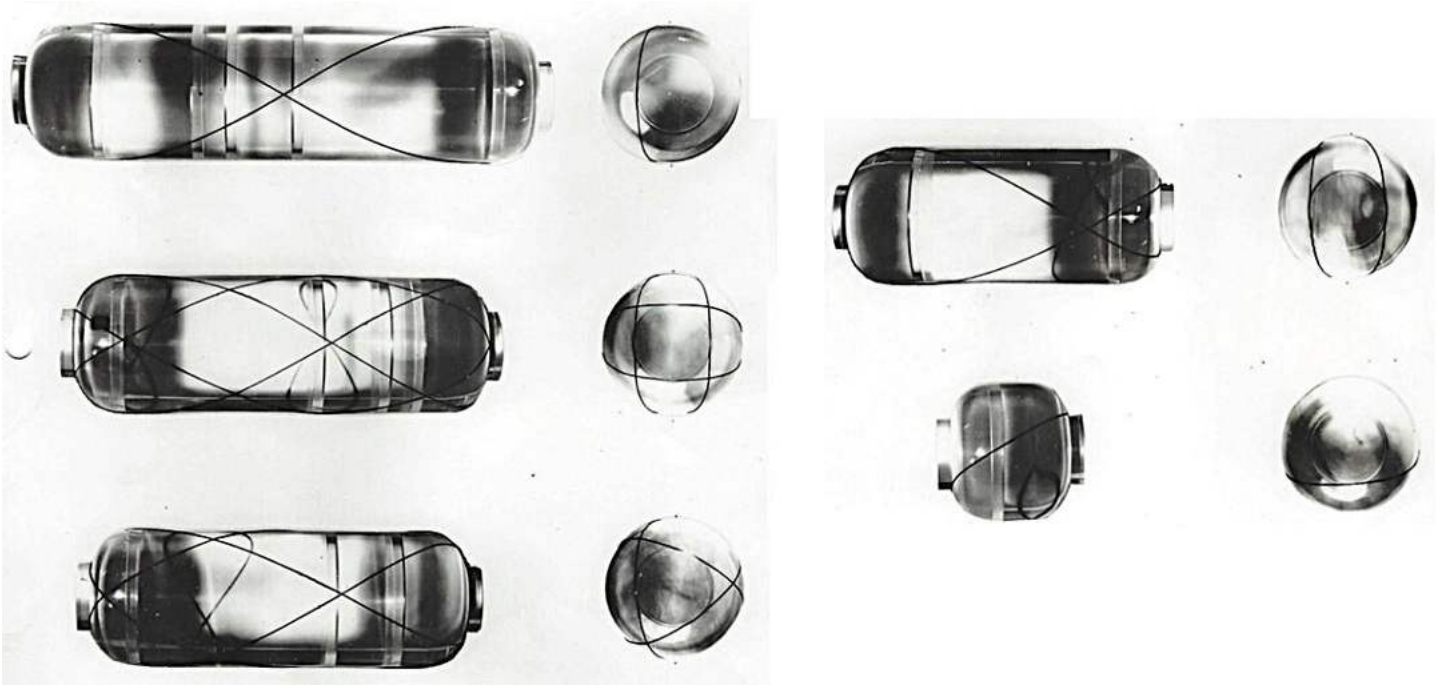

Fig.26-3: Helix layers, winding patterns for different ratios of length/diameter

26.3 Filament Wound Pressure Vessels and some Practice at MAN Technologie (> 1971)

Fig.26-4 shows some details of the pressure vessel bottom including essential quantuties.

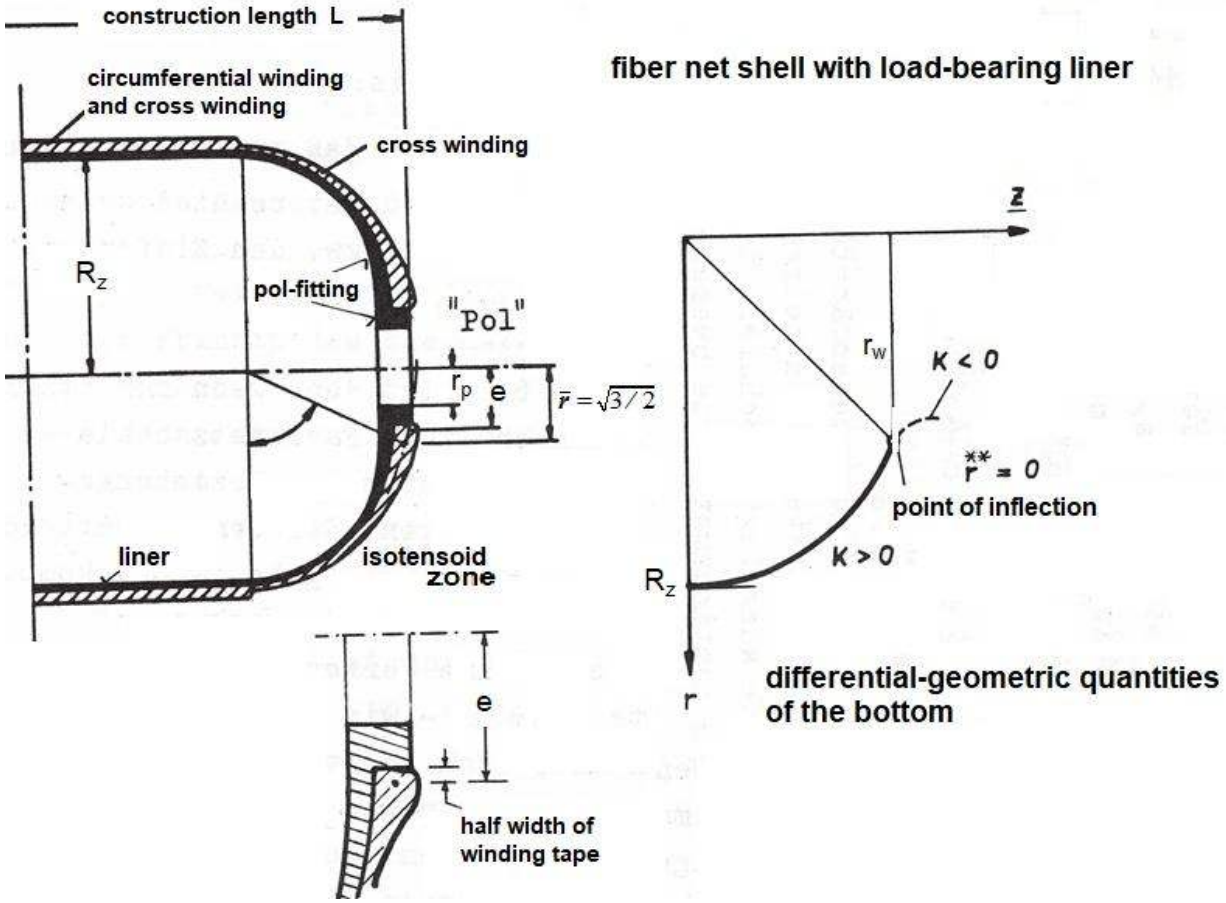

Fig.26-4:Essential quantities of the dome area (picture 1972)

There are one shell vessels (tanks here, *Fig.26-4* and -5) and high pressure multishell vessels (Fig.26-7) affording a complicate winding procedure. For the latter the design dimensioning tool ‘net theory’ can here just be a predesign tool.

Length measurement of a high pressure vessel showed that uploading initially led to a length reduction. After measurement of the associated relevant quantities a nonlinear FE-csimulation of this initial behavior gave the basis for a full nonlinear internal pressure load analysis. Essential was the stress situation in the equator domain with the acting residual stresses.
Basically responsible for this effect are *chemical* shrinkage (Schwindung) and (*hygro-*)*thermal* shrinkage (Schrumpfung) of the matrix (= resin system). In the case of non-tightly crosslinked matrix systems such as thermoplastics, the undesirable residual stresses can be reduced by annealing (Tempern). In the case of epoxy thermoset matrices, it is well known that no reduction of residual stresses caused by production can be achieved by annealing. Residual stresses are generated at the micro-mechanical and the macro-mechanical level. Those at the micro-mechanical level (filament, matrix) are regarded as considered in the measured macro-mechanical material characteristics.

Important for their assessment is the knowledge of the variable thread tension during winding, the winding core, the winding pattern with its not so favorable crossing points in terms of strength and this the more for multi-shell vessels with their partial shells. During the hardening of the partial shell, a first residual stress state is generated. As a result of the intermediate hardening of the partial shells, the respective associated residual stress state in the partial shell is not so large with optimal, decreasing variable winding pretension thread. By joining the partial shells in the further winding process, a second residual stress state is then superimposed. Both states are then responsible for the deformation behavior.

To address is the equilibrium system of circumferential residual stresses over the wall thickness. The load stress state includes the shear and tensile stresses in the ω-cross layer. Critical for the formation of micro-cracks are the stress states between the 90°- layer and the ω° cross- layer, the more internal 90° layer remains 'behind'.

The quantification of the residual stress is pretty difficult. A ring test specimen may give some information. For the estimation of the occurring residual stress state, previously unloaded, virgin rings are to provide. Such a frozen residual stress state is released by cutting (‘open’) the ring test specimen. The cut ring deforms both in the virgin state and in the already damaged by corresponding loadings. Thereby the occurring micro-cracks will reduce the residual stress state because it can partially relax. In the final fracture state, net theory would be applicable (used in an WWFE-II Test Case) instead of continuum theory and the residual stress state would have disappeared. In the rings, the deformations occurring during cutting become smaller with increasing thickness. Simulation of the deformation states delivers the residual stress information.

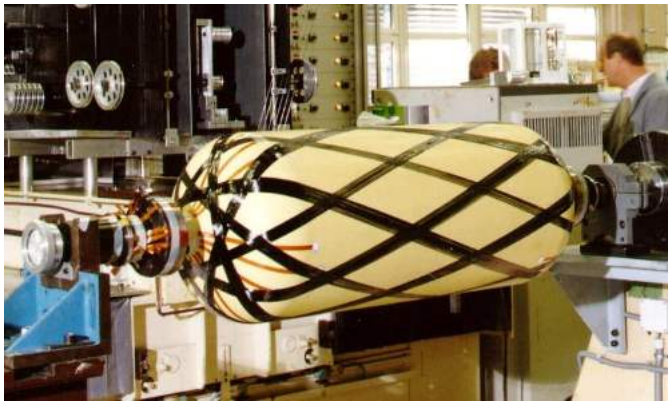

Fig.26-5: Pattern of a GFRP Disc and a CFRP filament wound pressure tank on a lathe (about 1982)

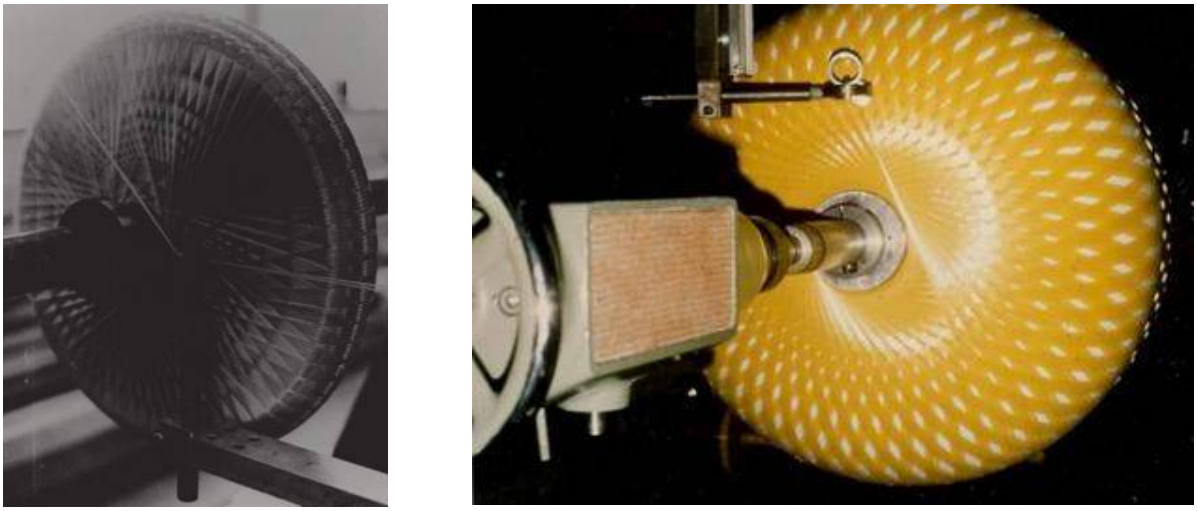

Fig.26-6: Pattern of a CFRP and of a AFRP fly wheel at MAN Technologie

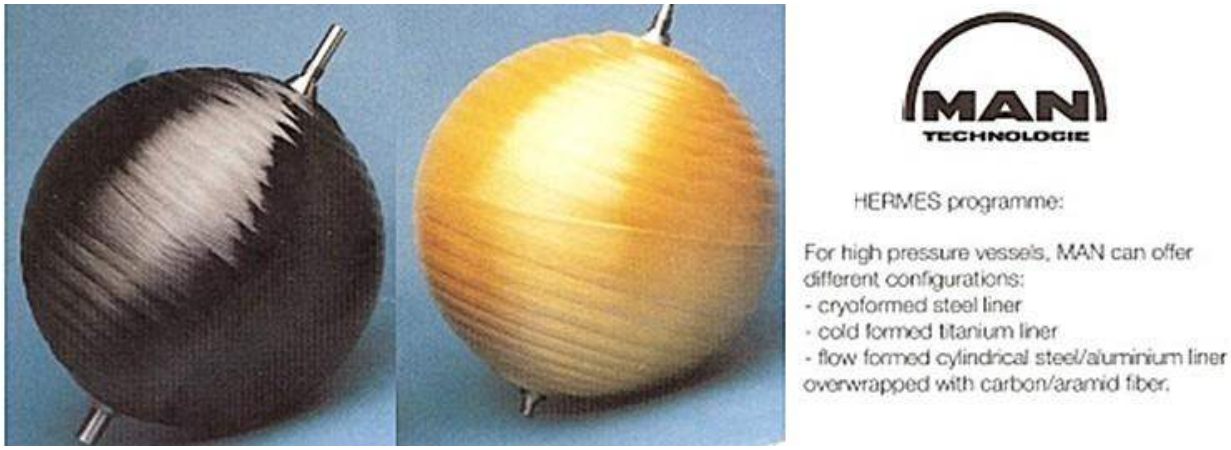

Fig. 26-7: Spherical HighPressureTank, CFRP and AFRP
CFRP-HighPressureTanks for METEOSAT (1977), AFRP for ITALSAT

***LL**:*

- *A geodesically generated shape, when further geodesically wound using fiber net theory (shortly net theory) only becomes an isotensoid, a body of uniform strength*
- *If one mathematically adheres consistently to network theory, replacing the geodetic shape condition with, for example, a planar condition will result in a different contour*
- *One could lay threads planarly on geodesically generated dome shapes*
- *Planar thread laying of a winding machine, even on a geodesically determined contour, does not lead to a isotensoid.*
- *The difference between the inner contour and the calculated center contour must be considered in the design.*
- *Fiber net shells are much shallower than half-spheres.*
- *If a winding machine cannot be laid geodesically, or if different pole openings are present, an isotensoid cannot be achieved.*
- *For practical winding applications, the validity of the curve ends at the curve's inflection point, i.e., in the collar section of the base (Fig. 26-2). From this point onward, the winding thread lifts off under the winding tension.*
- *No-geodesically winding requires friction, which is to be provided by an adequate resin system.*

26.4 Application of winding technology, re-calculation of a Kevlar tank

1 Task

For a wound internal pressure vessel made of Aramid (Kevlar) fibers for Meteosat and an epoxy resin system, the dimensioning according to the net (mesh) theory and the calculation according to the continuum theory is to demonstrate, see *Fig.26-8*.

2 Input

- Loading: MEOP = maximum operational pressure (*DLL* level) p_{int} = 51 bar (*short time stressing*)
- Design safety factor: j_{ult} = 1,5 → $p_{DUL} = j_{ult} \cdot MEOP$
- Internal radius at equator r_{in} = 377 mm; pole-openings e = 124 mm; volume 260 dm^3
- Properties:
  Strength Kevlar-Fiber: R_f > 1950 N/mm^2, Elasticity moduli: E_f = 1.4·105 N/mm^2 , $E_m = 3 \cdot 10^3$ N/mm^2
  UD properties for $\varphi_{ax} = \varphi_{90} = \varphi = V_f = 0.60$ and resin 0502/hardener (HT 972) in mix 100/34:
  $E_{||} = 85 \cdot 10^3$ N/mm^2; $E_{\perp} = 5.6 \cdot 10^3$ N/mm^2; $G_{\perp||} = 2.1 \cdot 10^3$ N/mm^2; $\nu_{\perp||} = 0.34$; $\rho_{||} = 1.39$ g/cm^3
  Strength Design Allowables, short time, for loading:
  $$\{R\} = (R_{||}^t,\ R_{||}^c,\ R_{\perp}^t,\ R_{\perp}^c,\ R_{\perp||})^T = (1250,\ -,\ 10,\ -,\ 50)^T \text{ MPa}\ .$$
- Production:
  Use of a winding tape consisting of two rovings with each 4·768 filaments
  with the filament cross-section of the aramide filament of 12 µm
  $A_2 = 2 \cdot 0.35 = 0.70$ mm^2 → $A = A_2/\varphi = 1.17$ mm^2.
  As tape- (band-)widths were measured for two rovings W_{90} = 6.0 mm (wider placed) und W_{α} = 3.75 mm .
  Pull-off speed of the winding tape 0.2 m/s. Winding tension per tape: F^t = 30 N
  Processing temperature of the resin: 50°C. Curing: 19 h at 60°C, 5h at 80°C and 10 h at 110°C.
  Layers: Hoop (90°) and helix (α).

3 Design dimensioning using net theory

- Winding angle, winding pattern and contour:
  For most tank designs, the volume is fixed. Since the pole openings are generally fixed for design requirements, e in *Fig.26-4* is still known. If the tank shape is still roughly prescribed, the pattern can be found with known e and r_{cyl}. For the geodetic winding type, the winding angle can then be calculated from
  $r_{cyl} = r_{in} + \approx 1$ = 378 mm of mid plane, $\mathbf{r_{cyl}} \cdot \sin \alpha_{cyl} = e = 122 + 3.75/2 = 124$ mm → $a_{cyl} = 19.2°$.
  For a possible 'winding pitch number' T = 1 causing the pattern, a cylindrical length results after integration of the contour differential equation (CDE) and the volume content of the bottom of L_{cyl} = 250 mm. For the production of the construction drawing, the inner and outer liner contour of the bottom must now be determined and the coordinates of these contours must be recorded for production. For this purpose, the contour in the validity area of the CDE (α < 54.75°) is applied to the extent that a meaningful final contour can be designed up to the pole.

  In the present case, the liner's outer contour including fitting area from α = 45° is continued with the meridian curvature radius R_2 = R(45°) present at α = 45°. The difference to a conical end is very small. The liner contour including fitting area is found by simple geometric relationships with the help of the outer contour.
- Wall thickness:
  The following equations are used to determine the total composite thickness
  $$erf\ t_{\alpha\ cyl} = p_{DUL} \frac{1/2\ R_{cyl}}{R_{||}^t \cdot \cos^2 \alpha_{cyl}} = 7.65\,\text{mm} \qquad \frac{378}{2 \cdot 1250 \cdot \cos^2 19{,}2^{\circ}} = 1.30\,\text{mm} \quad \text{and}$$

$$erf\ t_{90} = p_{DUL} \cdot \frac{R_{cyl} \cdot \left(1 - 0.5 tan^2\ \alpha_{cyl}\right)}{R_{\parallel}^{t}} = 7.5 \cdot \frac{378 \cdot \left(1 - 0{,}5\ tan^2\ 19.2^{\circ}\right)}{2 \cdot 1250 \cdot cos^2\ 19.2^{\circ}} = 2{,}17\,\text{mm} \rightarrow \text{Chosen: 2.35 mm.}$$

For $V_f = \varphi = 0.60$, these composite thicknesses correspond to pure fiber thicknesses of $t_{\alpha f} = 0.60 \cdot 1.30 = 0.78$ mm and $t_{90f} = 1.41$ mm.

As wall thicknesses are thus present in the cylinder area $t = 1.30 + 2.35 = 3.65$ mm.

The wall thicknesses of the individual layers are thus calculated from ($\alpha = +\omega, -\omega$)

$$t_{90}^{(1)} = \frac{A}{W_{90}} = \frac{1.17}{6.0} = 0.195 \quad \text{and} \quad \frac{A}{W_{\alpha}} = \frac{1.17}{3.75} = 0.312\ ,$$

where A is the cross-section of the winding tape. W_{90} and W_{α} are the laying widths of the winding tape during hoop and helix winding.

The winding provides an orthotropic, asymmetrically constructed laminate [$\pm\omega$/ $\pm\omega$/ 90/ 90/ 90/ 90/ 90/90], which means 2 cross layers $\alpha = \pm\omega$, plus the hoop layers in the cylindrical area.

4 Design Verification using continuum theory

The determination of the stresses and deformations of the present orthotropic composite in the operating state is carried out according to the continuum theory. Therefore it is assumed, that the laminate of the cylinder is non-cracked. The calculation takes into account shell bending and non-symmetrical laminate lay-up.

Provided is the vector of laminate mean stresses $\{\hat{\sigma}\} = j_{ult} \cdot (1/2\ p_{DLL} \cdot R_{cyl},\ p_{DLL} \cdot R_{cyl},\ 0)^T$

and the elasticity matrix of the layer $[Q] = \begin{bmatrix} 85650 & 1919 & 0 \\ 1919 & 5643 & 0 \\ 0 & 0 & 2100 \end{bmatrix}$ in N / mm^2 .

From the elasticity matrix of the single layer we come to the sizes of the laminate, which has a layer structure in the cylinder area - from the inside to the outside - of [19.2/-19.2//19.2/-19.2/90/90/90/90/90/90]. The reference plane (*Bezugsebene*) lies between the helix layers, (*Fig.12*).. This results in the stiffness matrices (N and mm are used as units)

$$[D] = \begin{bmatrix} 764300 & 18840 & 0 \\ 18840 & 62980 & 0 \\ 0 & 0 & 20480 \end{bmatrix}, \quad [B] = \begin{bmatrix} 367300 & 8228 & 584 \\ 8228 & 24200 & 4652 \\ 589 & 4652 & 9006 \end{bmatrix}$$

For the preceding matrices, [B] and [D] show how asymmetrical the present stratification is. Due to this asymmetrical stack, bending stresses are present during operation (42 bar). They are based on the in reality greater widening (according to the net theory is the same widening) of the cylinder compared to the bottom side at the equator. Here they amount to up to 15 % of the membrane calculation value In order to reduce the bending stresses, reinforcements can be applied in the cylinder area and the equatorial points, if possible and can be produced, compared to the net theory design.

When compared with test results, although only a very similar tank design was tested, a linear increase in strain was observed in the fiber direction at all measuring points up to $\varepsilon = 1$ %. Furthermore, with proper production, the burst pressure calculated according to the net theory was in the tolerance range +5% of the actually achieved, average burst value.

Note:

In the following years the application of FE analysis - linear and later nonlinear - of such tanks became standard at MAN-Technologie.

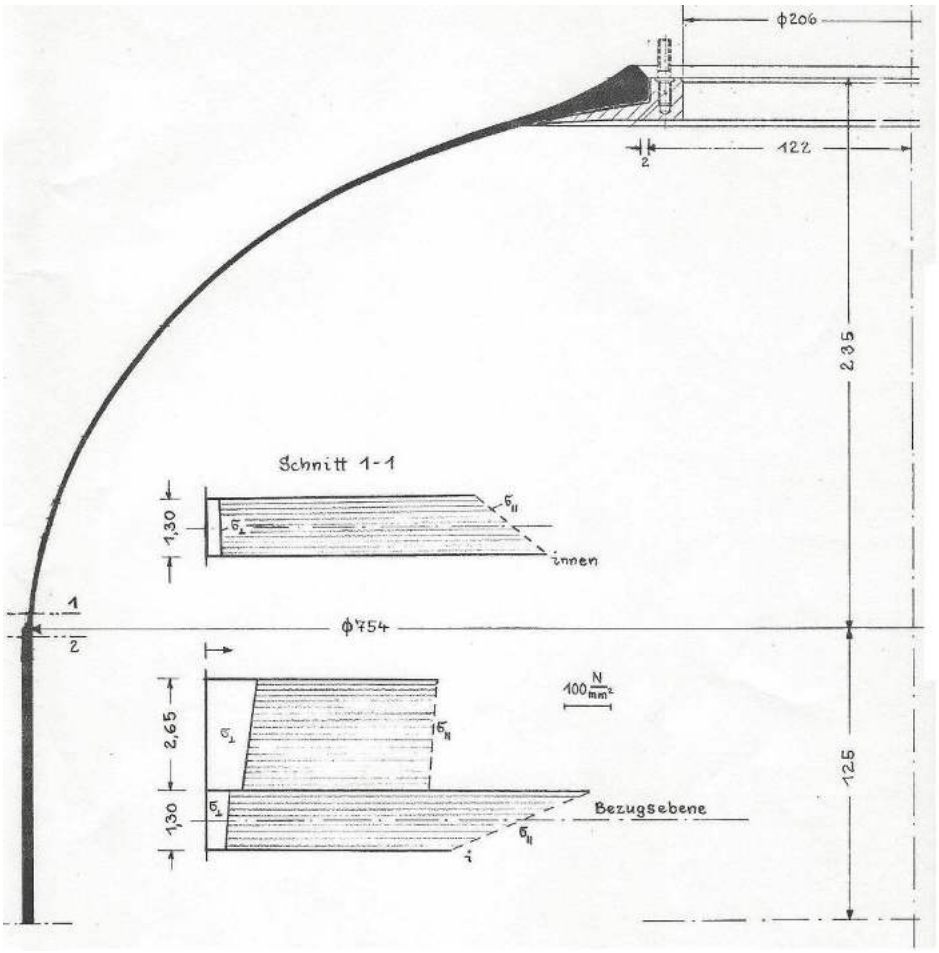

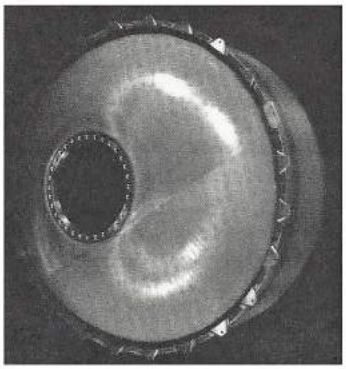

Fig.26-8: Vessel (one shell tank) dimensions and some layer (ply) stresses. Wound with Kevlar fibers

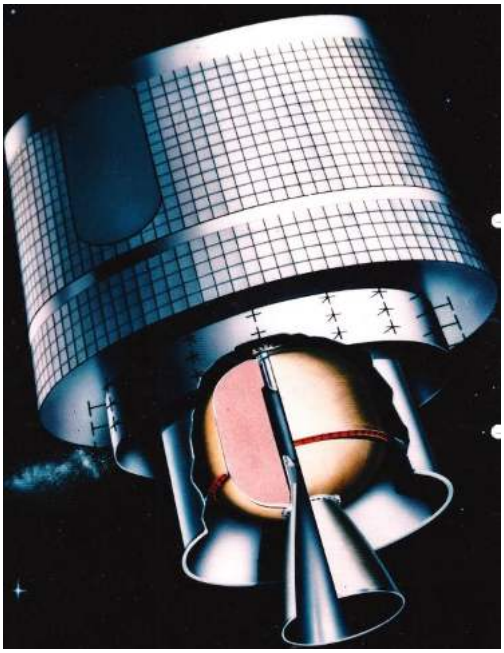

Fig. 26.9: Modern tape-wound tank (left up).

Fig.26.10: Kevlar tank as apogee motor in satellite MAGE

(up and left)

27 References, Papers, Presentations & MAN reports

27.1 References

[Arg73] Argo A S: *Physical basis of distortional and dilatational plastic flow in glassy polymers.* J. Macromol. Sci. Phys B8 (1973), 573-596

[Awa78] Awaji H and Sato S: *A Statistical Theory for the Fracture of Brittle Solids under Multiaxial Stresses*. Int. J. of Fracture 14 (1978), R 13-16

[Bec94] Becker W. and Kress G: *Stiffness Reduction in Laminate Coupons due to the Free-edge Effect*. Comp.Science and Technology 52 (1994), 109-115

[Bir38] Birch R.: *The Effect of Pressure Upon the Elastic Parameters of Isotropic Solids, according to Murnaaghan's Theory of Finite Strains*. Journal of Applied Physics 9 (4), 279-288.

[Boe0?] Böhm R: *Bruchmodebezogene Beschreibung des Degradationsverhaltens textilverstärkter Verbundwerkstoffe*. Dissertation, TU Dresden, 2008

[Boer89] de Boer, R. and Dresenkamp, H.T.: *Constitutive Equations for concrete in failure state*. J. Eng. 115 (8), 1989, 1591-1608

[Boe85] Boehler, J.P.: *Failure criteria for glass-fiber reinforced composites under confining pressure*. J. Struct. Mechanics 13, 371-393

[Boe87] Boehler J P : *Introduction to the invariant formulation of anisotropic constitutive equations*. 1987. In: Boehler J.P. (Ed.) *Applications of Tensor Functions in Solid Mechanics*. CISM Course no.292. Springer-Verlag. In addition a personal note from J. Boehler on UD invariants which were later applied by the author in his FMC

[Bre79] Breuer H und Stabenow J: *Schädigungskriterien glasiger Polymere im Hinblick auf deren Schlagzäh-modifizierung*. Die Angewandte Makromolekulare Chemie 78 (1979), 45-65. SF-shape is SY-shape

[Bri52] Bridgeman P.W.: *Studies in Large Plastic Flow and Fracture*. McGraw-Hill, New York, 1952

[Bro18] Brocks W: *Plasticity and Fracture.* Springer, Series Solid Mechanics, Applications.

[Bus06] Busse G, Kröplin B and Wittel F K: *Damage and its Evolution in Fiber-Composite Materials: Simulation and Non-Destructive Evaluation.* SFB 381, Stuttgart, ISBN 3-930681-90-3

[Car93] Carpinteri A, Valente S, Ferrara G and Melchiorri G: *Is mode II Fracture Energy a real Material Property*? Computers & Structures 48 (1993), No3, 397-413

[Che11] Cherif Ch: *Textile Werkstoffe für den Leichtbau*. Springer-Verlag, 2011

[Che13] Cherif, editor: *Leichtbau mit Textilverstärkung für Serienanwendungen: Bindermaterialien – Textile Preforms – Verbundbauteile; Buch zum DFG-AiF-Clustervorhaben – Leichtbau und Textilien.* Verlag Wissenschaftliche Skripten, 2013, ISBN 978-3-942267-81-6

[Chr97] Christensen R M: *Yield Functions/Failure Criteria for Isotropic Materials*. Proc. R. Soc. Lond. A (1997) 453, 1473-1491. *Yield Functions/Failure Criteria for Isotropic Materials*. Proc. R. Soc. Lond. A (1997) 453.

[Chr98] Christensen R M: *The Numbers of Elastic Properties and Failure Parameters for Fiber Composites.* Transactions of the ASME, Vol. 120 (1998), 110-113

[**CUN85**] Buchmanuskript "*Auslegung von Bauteilen aus Faserverbundwerkstoff*", 1975, private document at MAN - Neue Technologie, 600 pages*

[Cun85] Cuntze R and Löbel G.: *Evaluation of Stress Strain Test Results for Effective Use in Computational Analysis and Adequate Statistical Quantities*. ICOSSAR 85, III-664-668. 4th Intern. Conf. on Structural Safety and Reliability. Kobe, Japan

[Cun87] Cuntze R: *Failure Path Analysis of Multi-layered Fiber Reinforced Plastic Components with the Reliability Calculation Programme FRPREL*. ESA/ESTEC conference Noordwijk, Oct. 1987

[Cun93] Cuntze R: *Deterministic and Probabilistic Prediction of the Distribution of Inter-Fiber Failure Test Data of Pre-strained CFRP Tubes composed of Thin Layers and loaded by radial pressure*. Wollongong. *Advanced Composites ,93, 579-585. The Minerals, Metals & Materials Society, 1993*

[Cun96a] *Bruchtypbezogene Auswertung mehrachsiger Bruchtestdaten und Anwendung im Festigkeits-nachweis sowie daraus ableitbare Schwingfestigkeits- und Bruchmechanik-Aspekte*. DGLR-Kongreß 1996, Dresden. Band 3

[Cun96b] *Fracture-type Strength Criteria - formulated by Invariants which consider the Materials Symmetries of the Isotropic/Anisotropic Material used*. Conf. on Spacecraft Structures, Materials and Mechanical Testing. ESA-CNES-DARA: Noordwijk, March 1996 (Conf. Hdbk)

[Cun97] Cuntze R: Evaluation of Multi-axial Test Data of UD laminas by so-called "Fracture-type Strength criteria" and by supporting probabilistic means, ICCM 1997, 14 pages*

[Cun98a] Cuntze R: *Strength Prediction for Multi-axially Loaded CMC-Materials*. 3rd European Workshop on thermal Protection Systems. ESA-ESTEC: Noordwijk, March 1998, WP P141

[Cun98b] Cuntze R: *Application of 3D-strength criteria, based on the so-called "Failure Mode Concept", to multi-axial test data of sandwich foam, concrete, epoxy, CFRP-UD lamina, CMC-Fabric Lamina*. ICCE/5, Las Vegas, July 1998 (presentation)

[Cun98c] Cuntze R and Sukarie G.: *Effective Dimensioning of 3D-stressed UD-laminas on Basis of Fracture-type Strength Criteria. Int. conf. on Mechanics of Composite Materials*. Riga, April 20-23, 1998. *Conference handbook*, presentation

[Cun98d] Cuntze R: *The Failure Mode Concept- a new comprehensive 3D-sterength Analysis Concept for any Brittle and Ductile behaving Material*. European Conference on Spacecraft and Structures, Materials and Mechanical Testing. ESA-CNES-DGLR-DLR, Braunschweig, Nov.4-6 1998

[Cun99] *The Failure Mode Concept - A new comprehensive 3D-strength Analysis Concept for Any Brittle and Ductile behaving Material*. Europ. Conf. on Spacecraft Structures, Materials and Mechanical Testing. ESA-CNES-DGLR-DLR; Braunschweig, Nov. 1998, ESA SP-428, 269-287

[Cun99] *Progressive Failure of 3D-stressed Laminates: Multiple Non-linearity treated by the Failure Mode Concept* (FMC). DURACOSYS99, Brussels, July 1999. Balkema, Rotterdam, 2000

[Cun00a] *Static Design and Strength 'Proof of Design' of Pressure Vessels, built from Ductile or Brittle Materials*. Problems of the North; Yakutsk 2000

[Cun00b] *Are there Cost Drivers in the Structural Analysis of the ARIANE 5-Development*? Noordwijk, 29. Nov./1. Dec. 2000.

[Cun01] *Assessment of Load- and Strain-controlled States of Stress in 'hot Spots' – On the way to an Industrial Approach for Gurson Materials*. 3rd European Conference on Launcher Technology. CNES, DLR, ESA-ESTEC, ISU: Strasbourg, Dec. 11-14, 2001.

[Cun03] Cuntze R and Memhard D*: Evaluation of the Tension Rod Test for Ductile Material Behavior*. European Conference on Spacecraft Structures, Materials & Mechanical Testing CNES, DLR; ESA, ISU: Toulouse, 11-13 December, 2002. Conference Proceedings

[Cun04] Cuntze R.: *Should we consider Matrix Yielding when investigating the Deformation Behavior?* 9th European-Japanese Symposium on Composite Materials.. Technical University of Hamburg –Harburg, May 2014

[Cun04] Cuntze R: *Non-linear Failure Analysis of FRP Laminates composed of UD laminas – a comparison of the author's predictions with test results within the worldwide Failure Exercise in the UK*. FDM, Paderborn, 2004

[Cun14] *The World-Wide-Failure-Exercises I and II for UD MATERIALS – valuable attempts to validate failure theories on basis of more or less applicable test data*. Europ. Conf. on Spacecraft Structures, Materials and Environmental Testing. Braunschweig. SSMET 201

[Cun04a] Cuntze R and Freund A: *The predictive capability of failure-mode-concept-based strength criteria for multidirectional laminates*. WWFE-I, Part A. Comp. Science Technology 2004 , pp 343-377

[Cun04b] Cuntze R: *The Predictive Capability of Failure Mode Concept-based Strength Criteria for Multidirectional Laminates*. WWFE-I, Part B. Comp. Science and Technology 64 (2004), 487-516

[Cun05] Cuntze R: *Is a Costly Re-design really justified if slightly negative margins are encountered? Konstruktion*, März 2005, 77-82 and April 2005, 93-98 (*reliability treatment of the problem*)*

[Cun05] Cuntze R: *Efficient 3D and 2D failure conditions for UD laminas and their applications within the verification of the laminate design*. Comp. Sci and Technology 66 (2006), 1081-1096

[Cun06] *Failure Conditions for Isotropic Materials, Unidirectional Composites, Woven Fabrics - their Visualization and Links*. https://www.ndt.net › cdcm2006 › papers › cuntze, PDF

[Cun08] Cuntze R.: *Strength Failure Conditions of the Various Structural Materials: Is there some Common Basis existing*?. SDHM, vol.074, no.1, pp.1-19, 2008

[Cun11] Cuntze R: *Lessons Learnt from the World-Wide-Failure-Exercise Contributions when validating 2D (WWFE-I) and 3D (-II) FMC-based UD Failure Conditions*. Conference Proceedings Composites 2011, 3rd ECCOMAS Thematic Conference on the Mechanical Response of Composites, Hannover

[Cun12] Cuntze R: *The predictive capability of Failure Mode Concept-based Strength Conditions for Laminates composed of UD Laminas under Static Tri-axial Stress States*. WWFE-II, Part A. Journal of Composite Materials 46 (2012), 2563-2594

[Cun12] HSB 02000-01. Cuntze R: *Essential topics in the determination of a reliable reserve factor*. 2012, HSB sheet, 20 pages. HSB = (luftfahrttechnisches) Handbuch für Strukturberechnung (*German aerospace handbook*). Edited by the industrial committee (*working group*!) IASB = IndustrieAusschuss für StrukturBerechnung

[Cun13a] Cuntze R: *Comparison between Experimental and Theoretical Results using Cuntze's Failure Mode Concept model for Composites under Tri-axial Loadings* – Part B of the WWFE-II. Journal of Composite Materials, Vol.47 (2013), 893-924

[Cun13b] Cuntze R.: *Tackling Uncertainties in Design – uncertain design parameters, safety concept, modelling and analysis*. Verbundwerkstoffe, GDM, 18. Symposium, Chemnitz 30.3. – 1.4. 2011

[Cun14a] *The World-Wide-Failure-Exercises I and II for UD materials – valuable attempts to validate failure theories on basis of more or less applicable test data*. Europ. Conf. on Spacecraft Structures, Materials and Environmental Testing. Braunschweig. SSMET 2014, 1. - 4. April, 8 pages

[Cun14b] Cuntze R: *The Fracture Failure Surface of Foams, derived on basis of the author's Failure Mode Concept*. PPT presentation, Carbon Composites e.V. (CCeV), meeting of the working group 'Engineering', July 11, 2014*

[Cun14c] HSB 01501-01: *Essential Topics in the Determination of a Reliable Reserve Factor*. IASB, Issue A, 2014 (Cuntze author) TIB Hannover, 20 pages,

[Cun15a] Cuntze R: *Static & Fatigue Failure of UD-Ply-laminated Parts – a personal view and more*. ESI Group, Composites Expert Seminar, Uni-Stuttgart, January 2015, 27-28, keynote presentation*

[Cun15b] Cuntze, R: *Reliable Strength Design Veriftcation – fundamentals, requirements and some hints*. 3rd. Int. Conf. on Buckling and Postbuckling Behavior of Composite Laminated Shell Structures, DESICOS 2015, Braunschweig, March 26 ~27, Extended Abstract, Conf. Handbook, 8 pages

[Cun15c] Cuntze R: *Basis Document, Update ComPoLyX Manual chapter Cuntze and Relationship of Cuntze's UD friction parameters b with Mohr's friction coefficients.* CCeV website, May 4, 2015 *

[Cun16a] Cuntze R: *Fracture failure surface of the foam Rohacell 71G*. 3. NAFEMS Regionalkonferenz, 25.-27. April, 2016. Berechnung und Simulation, 35 slides *

[Cun16b] Cuntze R: *Introduction to the Workshop – from Design Dimensioning via Design Verification to Product Certification*. Experience Composites 16 (EC16), September 21 – 23, 2016, Augsburg. Extended Abstract in the Symposium Abstracts. 10 pages*

[Cun16c] Cuntze R: *Progress reached, in Static Design and Lifetime Estimation*? Mechanik-Kolloquium, TU-Darmstadt, December 21, 2016 (UD and isotropic materials, Extended Presentation, 150 slides) *

[Cun17] Cuntze R: *Fracture Failure Bodies of Porous Concrete Stone (isotropic foam-like), Normal Concrete, Ultra-High-Performance-Concrete and of the Lamella (sheet) – generated on basis of Cuntze's Failure-Mode-Concept (FMC).* NWC 2017, June 11-14 Stockholm. Extended Abstract, Symposium Handbook, 13 pages *

[Cun19a] Cuntze R: presentation in the author's working group CU AG "Engineering" on *3D-Festigkeitsbedingungen für spröde Werkstoffe isotrop, transversal–isotrope UD-Schicht und orthotropes Gewebe – ermittelt auf Basis des Failure-Mode-Concepts (FMC) von Cuntze*. June 25, 2019 Basel (English slides) *

[**CUN19**] Cuntze R: *Technical terms for composite components in civil engineering and mechanical engineering*. Fachbegriffe mit Erklärung und Definition. In: *Fachbegriffe für Kompositbauteile – Technical terms for composite parts.* Springer Vieweg, Wiesbaden, 2019, 171 pages * Pre-print downloadable

[Cun20a] Cuntze R: Einführungsvortrag des Autors als Leiter der AG „Bemessung und Nachweis“ zum CU-Thementag „*Richtlinien, bauaufsichtliche Zulassungen und Bauartgenehmigungen für die potentiellen Anwender Architekten, Tragwerksplaner und Bauherrn“*. Zoom conference, 19. Nov. 2020. 40 slides (English and German) *

[Cun20b] Cuntze R: *Normal Yielding NY and Compression-induced Critical Stress Intensity Factor $K_{IIcr}{}^{c}$- Missing Links in an Isotropic ‘Closed’ Macro-Mechanics Building*. 30 pages *

[Cun21] Cuntze R: *Strength capacity of bi-axially compressed UD strands at turning points of rotor blade loops and of hangers of network arch bridges.* CU-AG “Engineering”, May 20. *

[Cun21b] Cuntze R: *The Mohr Coulomb Fracture Failure Curve $\tau_{nt}(\sigma_n)$ and Associated Topics*. Jun 21, pp 59*

[**CUN22, 23**] *Life-Work Cuntze - a compilation*. 2022/2023. *The Failure-Mode-Concept FMC, a physical and theoretical Material Symmetry-driven basis to generate Strength Criteria, that gave a reason to look after a ‘more closed’ Strength Mechanics Building, and in addition Very Much on Structural Materials, Techniques and Design including work-life experiences of the author in many engineering fields*. (about 850 pages), downloadable from https://www.carbon-connected.de/Group/Prof.Ralf.Cuntze

[Cun23a] *Design of Composites using Failure-Mode-Concept-based tools— from Failure Model Validation to Design Verification.* Mechanics of Composite Materials, Vol. 59, No. 2, May, 2023, pp. 263-282*

[Cun23b] *Minimum Test Effort-based Derivation of Constant-Fatigue-Life curves - displayed for the brittle UD composite materials.* Springer, Advanced Structured Materials, Vol.199, 107–146, draft in*

[Cun23c] *Comparative Characterization of Four Significant UD Strength Failure Criteria (SFC) with focusing a direct use of Friction Values, use of ‘Strength’ and ‘Proportional Loading’. 54 pages**

[Cun23d] *Gedanken eines faseranwendungserfahrenen Ingenieurs zum Umgang mit Faser-Mikro-bruchstücken und Feinstäuben bei Herstellung und Recycling faserverstärkter Bauteile*. Composites United construction (CU Bau) *

[Cun23e] *Strength Model Validation and Design Verification of Ceramic Structural Components*, 13jul23 * 32pages

[Cun24a] Cuntze R and Kappel E: *Why not designing multidirectional laminates with in-plane Strength Design Sheets applying the UD criteria of Tsai-Wu and Cuntze*? Part 1, Analytical foundation in Mechanics of Composite Materials (MCM), Vol. 60, No. 5, November, 2024; Part 2 , Application in MCM , November 2024

[Cun24b] *Ceramic Strength Models for Monolithic (isotropic), Transversely-isotropic UD and Fabric Materials**

[Cun24c] Cuntze R and Kappel E: *Benefits, applying Tsai’s Ideas ‘Trace’, ‘Double-Double’ and ‘Omni Failure Envelope’ to Multiply UD-ply composed Laminates.* 60 pages *

[Cun25] *UD-composites Strength Failure Criteria – However, which one should I take* ? Presentation at the 12. Landshuter Leichtbau-Kolloquium, 26./27. Februar 2025 * (published by Springer)

[**CUN25**] *Curriculum Vitae of Ralf Cuntze comprising Family, a bit of history, Career with professional employment, participation in working groups, Essential Scientific Findings & Pictures from the hobby photographer*. https://www.carbon-connected.de/Group/Prof.Ralf.Cuntze [CV Ralf Cuntze]

[DeTer99] De Teresa S.J.: *Failure of a composite lamina under three-dimensional stresses*. UCRL-JC-135664

[DeTer04] DeTeresa S J, Dennis C, Freeman O C, and Groves S E: *The Effects of Through-thickness Compression on the Interlaminar Shear Response of Laminated Fiber Composites*. J. Compos Mater, V 38, No. 8, pp681-697, 2004

[Dru52] Drucker D C and Prager W: *Soil mechanics and plastic analysis for limit design*. Quarterly of Applied Mathematics, 1952, vol. 10, no. 2, pp. 157–165

[Ern07] Ernst G., Vogler M, Hühne C. and Rolfes R.: *Multi-scale Simulation for Stiffnesses and Strengths of Textile Composites*. NAFEMS Seminar, Simulating Composite Materials and Structures. Bad Kissingen, Nov. 2007

[Fla82] Flaggs D L and Kural M H*: Experimental Determination of the In Situ Transverse Lamina Strength in Graphite Epoxy Laminates*. J. Comp. Mat. Vol 16 (1982), S. 103-116

[Gai19] Gaier C and Dannbauer H: *Eine Software-basierte Methode zur Betriebsfestigkeitsanalyse von Strukturbauteilen aus CFK*. Engineering Center Steyr, Magna, J. Maier, G. Pinter, Montanuniversität Leoben

[Gei97] Geiwitz W, Theuer A and Ahrends F J: *Experimentelle Bestimmung eines Versagenskriteriums für faserverstärkte Keramik*. Tagungband "Verbundwerkstoffe und Werkstoffverbunde", Kaiserslautern september 1997

[Gie94] Gierlinski J T and Smith M (WS Atkins, UK); Thoft-Cristensen P (CSR Denmark); Santos J L T (IST Portugal); Cuntze R (MAN) & Gollwitzer S (RCP), Germany: *Reliability–based Design of structural components.* Proc. Symp. On Advanced Materials for Lightweight Structures at ESTEC Noordwijk, March 1994, ESA –WPP-070, pp 121 -125

[Gol66] Goldenblat I I and Kopnov,V A*: Strength of Glass-Reinforced Plastics in the complex stress state*. Polymer Mechanics of Mechanical Polimerov, Vol. 1 1966, 54-59

[Gur77] Gurson A L: *Continuum Theory of Ductile Rupture by Void Nucleation and Growth. Part 1:Yield criteria and flow rules for porous ductile media*. J.Eng. Mater. Techn.99 (1977), 2-15

[Gri21] Griffith, A.A.: *The phenomena of rupture and flow in solids*. Philosophical Transactions of the Royal Society of London, 1921, A 221: 163–198

[Gur77] Gurson A L: *Continuum Theory of Ductile Rupture by Void Nucleation and Growth. Part 1:Yield criteria and flow rules for porous ductile media*. J. Eng. Mater. Techn.99 (1977), 2-15

[Hah15] Hahne C: *Zur Festigkeitsbewertung von Strukturbauteilen aus Kohlenstofffaser-Kunststoff-Verbunden unter PKW-Betriebslasten*. Shaker Verlag, Dissertation 2015, TU-Darmstadt, Schriftenreihe Konstruktiver Leichtbau mit Faser-Kunststoff-Verbunden, Herausgeber Prof. Dr.-Ing Helmut Schürmann

[Har93b] Hart-Smith L J: *An Inherent Fallacy in Composite Interaction Failure Curves*. Designers Corner, Composites 24 (1993), 523-524 [Has80] Hashin Z: *Failure Criteria for Unidirectional Fiber Composites*. J. of Appl. Mech. 47 (1980), 329-334

[Has80] Hashin Z: *Failure Criteria for Unidirectional Fiber Composites*. J. of Appl. Mech. 47 (1980), 329-334

[Hin02] Hinton M J , Kaddour A S and P.D. Soden P D: *A comparison of the predictive capabilities of current failure theories for composite laminates, judged against experimental* ***evidence*** (it would have been very nice). Composites Science and Technology 2002 (62), 1725-97

[Hin04] Hinton M J, Soden, P D and Kaddour A S: *Failure criteria of fiber reinforced polymer composites*. The World-Wide Failure Exercise. Elsevier, 2004, ISBN 0-08-044475-X, 700 pages

[Hin05] Hine PJ, Duckett RA and Kaddour AS, et al.: The effect of hydrostatic pressure on the mechanical properties of glass fiber/epoxy unidirectional composites. Compos Pt A: Applied Science and Manufacturing 2005; 36(2): 279–289

[Hop95] Hoppel C.R.R., Bogetti T.A. and Gillespie J.W.jr.: *Literature review – Effects of hydrostatic pressure on the Mechanical Behavior of Composite Materials*. J. of Thermoplastic Composite Materials 8 (1995), 375-409

[Hoek14] Hoek E and Martin C D: *Fracture initiation and propagation in intact rock – A review*. Journal of Rock Mechanics and Geotechnical Engineering 6 (2014) 287-300

[Hol19] Holschemacherk (editor) et al.:*Entwurfs-und Berechnungstafeln für Bauingenieure*. 8.Auflage, Beuth Verlag GmbH

[HSB] German Aeronautical Technical Handbook '*Handbuch für Strukturberechnung*', issued by Industrie-Ausschuss-Struktur-Berechnungsunterlagen. TIB Hannover

[Irw57] Irwin, G: *Analysis of stresses and strains near the end of a crack traversing a plate.* Journal of Applied Mechanics 24 (1957), 361–364.

[Jai20] Jain N and Koch D: *Prediction of Failure in Ceramic Matrix Composites Using Damage-Based Failure Criterion*. J. Compos. Sci. 2020, 4, 183; doi:10.3390/jcs4040183

[Kad13] Kaddour A and Hinton M: *Maturity of 3D failure criteria for fiber-reinforced composites: Comparison between theories and experiments*. Part B of WWFE-II, J. Compos. Mater. 47 (6-7) (2013) 925–966.

[Kaw04] Kawai M: *A phenomenological model for off-axis fatigue behavior of uni-directional polymer matrix composites under different stress ratios*. Composites Part A 35 (2004), 955-963

[Kaw88] Kawagoe M and Kitagawa M: *On criteria for craze initiation in glassy polymers*. J. of Materials Science 23 (1988), 3927-3932

[Kli66] Klingbeil E: *Tensorrechnung für Ingenieure*. BI-Hochschultaschenbuch 197/197a, 1966

[Kno03] Knops M.: *Sukzessives Bruchgeschehen in Faserverbundlaminaten*. Diss. 2003. Aachen, Institut für Kunststoffverarbeitung

[Kol12] Kolupaev V A, Bolchoun A and Altenbach H: *Unified Representation and Evaluation of the Strength Hypotheses.* 2012

[Kol17] Kolupaev V A: *Equivalent stress concept for limit state analysis*. Springer, Vol 86 in Advanced Structured Materials

[Kow83] Kowaltschuk B.I. and Giginjak F.F.: ..in Russian, Kiew, Naikowa Dumka 1983

[Kup73] Kupfer H: *Das Verhalten des Betons unter mehrachsiger Kurzzeitbelastung unter besonderer Berücksichtigung der zweiachsigen Beanspruchung*. In Deutscher Ausschuss für Stahlbeton, Band 229, 1973

[Laf 12] Laffan M.J., Pinho S.T., Robinson P., McMillan A.J., *Translaminar fracture toughness testing of composites: A review*, Polymer Testing (31) 2012, 481-489.

[Laf 12] Laffan M. J., Pinho S. T., Robinson P., Iannucci L., McMillan A. J., *Measurement of the fracture toughness associated with the longitudinal fiber compressive failure mode of laminated composites*, Composites Part A: Applied science and manufacturing (43) 2012, 1930-1938.

[Lan19] Hengxing Lan, Junhui Chen & Renato Macciotta: *Universal confined tensile strength of intact rock*. Scientific Reports | (2019) 9:6170 | https://doi.org/10.1038/s41598-019-42698-6

[Leg02] Leguillon D: *Strength or Toughness? –A criterion for crack onset at a notch.* Europ. J. of Mechanics A/Solids 21 (2002), 61 – 72 end. Ist. D. sci. Lett., Cl. Mat. Nat.18, 705-714 (1885

[Lem08] Lemnitzer L, Eckfeld L, Lindorf A and Curbach M (IfM TU Dresden): *Bi-axial tensile strength of concrete – Answers from statistics*. In: Walraven, J. C.; Stoelhorst, D. (Hrsg.): Tailor made concrete structures. New solutions for our society. Amsterdam, The Netherlands: CRC Press / Balkema, 2008, S. 1101-1102

[Li24] Li H, Pel L, You Z and Smeulders D: *Stress-dependent Mohr-Coulomb shear strength parameters for intact rock*. Nature.com/scientific reports

[Liu14] Liu J, Zhu Z and Wang B: *The fracture characteristic of three collinear cracks under true tri-axial compression.* The scientific World Journal, V 2014, article ID459025, 5 pages

[Lod26] Lode Walter.: *Versuche über den Einfluß der mittleren Hauptspannung auf das Fließen der Metalle Eisen, Kupfer und Nickel*. Z Phys 36:913–939 66.1926

[Lut06] Lutz G: *The Puck theory of failure in laminates in the context of the new guideline VDI 2014, Part* 3. NDT.net https://www.ndt.net › cdcm2006 › papers › lutzii, PDF

[Mas94] Masters J.: *Fractography of Modern Engineering Materials*. Composites and Metals. 2nd volume. ASTM STP1203,1994

[Mat75] Matsushige K, Radcliffe S V and Baer E: *The mechanical behavior of polystyrene under pressure*. J. of Material Science 10 (1975), 833-845

[Mathcad 13 and 15]: *PTC mathematical programs*, used by the author

[Mat95] Matzenmiller A, Lubliner J and Taylor R L: *A constitutive model for anisotropic damage in fiber-composites*. Mechanics of Materials 20 (1995), 125-152

[Mat07] Matzenmiller A and Koester B: *Consistently Linearized Constitutive Equations of Micro-mechanical Models for Fiber Composites with Evolving Damage*. Int. Solids and Structures 44 (2007), 2244-2268

[Mec21] Mechtcherine V: *Klassifizierverfahren digitalerFertigungsvefafahren im Betonbau*. March 2012. Cu Bau AG. 4. Thementag (lead by the author) ‚Automatisierte Fertigung im Bauwesen inklusive Serielles Bauen‘.

[Mel77] Melville PH: *Fracture mechanics of brittle materials in compression*. Int. J. Frac.13, 532-534 (cited in Liu 14)

[MIL17] MIL-HDBK 17 “*Polymer Matrix Composites*”: Vol I “Guidelines for Characterization of Structural Materials”; Vol II “Material Properties”; Vol. III “Utilization of Data”. Dep. Of Defence (DOD), Technomic Publishing USA

[Moh00] Mohr O.: *Welche Umstände bedingen die Elastizitätsgrenze und den Bruch eines Materials*? Civilingenieur XXXXIV (1900), 1524-1530, 1572-1577

[Mul67] Mulhern J F, Rogers T G and Spencer A J M: *A Continuum Model for Fiber-Reinforced Plastic Materials*. Proceedings of the Royal So ciety, Series A, Vol. 301,1967, p. 473

Mur09] Murthy A R, Ch, Palani G S and Iyer N: *State-of-the-art review on fracture analysis of concrete structural components*. Sadhana Vol.34, Part 2, April 2004, 345-367

[Nem90] Nemeth, N.N., Manderscheid, J.M. and Gyekenyesi, J.P.: *CARES (Ceramic Analysis and Reliability Evaluation of Structures) users and Programmers Manual*. NASA Technical Paper 2916, August 1990

[Ott77] Ottosen N S: *A failure criterion for concrete*. Journal of the Engineering Mechanics. ASCE, 103(EM4):527–535, August 1977

[Oro68] Orowan E: *Fracture and strength of solids*. Reports on Progress in Physics XII, 1948, 185–232

[Pae96] Pae K D: *Influence of Hydrostatic Pressure on the Mechanical Behavior and Properties of Uni-directional, Laminated, Graphitefiber/Epoxy matrix Thick Composites*. Composites Part B 27B (1996), 599-611

[Pag81) Page A W: *The biaxial compressive strength of brick masonry*. Proc. Inst.Civil Engrs.; 71(2) (1981)., pp. 893–906.

[Pag83] Page A W: *The strength of brick masonry under biaxial tension–compression.* International Journal of masonry constructions; 3 (1), (1983),pp. 26-31.

[Pap96] Papa E : *A unilateral damage model for masonry based on a homogenization procedure*. Wiley online library, Volume1, Issue4, October 1996. Pages 349-366

[Par85] Parry TV and Wronski AS: The effect of hydrostatic pressure on the tensile properties of pultruded CFRP. J Mater Sci 1985; 20(6): 2141–2147

[Par90] Parry T V and Wronski A S : The effect of hydrostatic pressure on the transverse strength of glass and carbon fiber epoxy composites. J Mater Sci 1990; 25: 3162–3166

[Pau61] Paul, B.: *A Modification of the Coulomb Mohr Theory of Fracture*. J. of Appl. Mech. (1961), 259-268

[Pet15] Petersen E, Cuntze R and Huehne C: *Experimental Determination of Material Parameters in Cuntze's Failure-Mode-Concept-based UD Strength Failure Conditions.* Composite Science and Technology 134, (2016), 12-25 *

[Pin06] Pinho S T, Robinson P, Iannucci L, *Fracture toughness of the tensile and compressive fiber failure modes in laminated composites*, Composites Science and Technology 66 (2006), 2069–2079.

[Pha03] Phan A V, Napier J A L , Gray L J and Kaplan T: *Stress intensity factor analysis of friction sliding at discontinuity interfaces and junctions*. Computational Mechanics 32 (2003), 392 -400

[Puc96] Puck A: *Festigkeitsanalyse von Faser-Matrix-Laminaten - Modelle für die Praxis.* München, Carl Hanser Verlag, 1996

[Puc02] Puck A and Schürmann H: *Failure Analysis of FRP Laminates by Means of Physically-based Phenomenological Models.* Composites Science and Technology 62 (2002), 1633-1662

[Puc02a] Puck A, Knops M and Kopp J: Guidelines for the determination of the parameters in Puck's action plane strength criterion. Comp. Science and Technology 62 (3) (2002) 371–378

[Rac87] Rackwitz R and Cuntze R: *System Reliability Aspects in Composite Structures*. Eng. Opt. 11 (1987), 69-76

[Ric68] Rice J R: *A path independent integral and the approximate analysis of strain concentration by notches and cracks*. Journal of Applied Mechanics 35 (1968), 379–386

[Ric13] Richard H., Eberlein A. and Schirmeisen N-H.: *Experiments on Cracks under Spatial Loading*. 13th Int. Conf. On Fracture, Beijing June 16-21 2013

[Ren38] Rendulic, L.: Eine *Betrachtung zur Frage der plastischen Grenzzustände.* Der Bauingenieur, 19 (1938), 159-164

[Rou87] Rousselier G:, *Ductile fracture models and their potential in local approach of fracture*. Nucl. Eng. Design. 105: 97-111, 1987.

[Ric69] Rice J R and Tracey D M: *On the Ductile Enlargements of Voids in Triaxial Stress Fields*. J. Mech. Phys. Solids (17), 1969, pp. 201-217

[Roh14] Rohwer K.: *Predicting Fiber Composite Damage and Failure*. Journal of Composite Materials, published online 26 Sept. 2014 (online version of this article can be found at: http://jcm.sagepub.com/content/early/2014/09/26/0021998314553885)

[Sch05] Schürmann H.: *Konstruieren mit Faser-Kunststoff-Verbunden*. Springer-Verlag 2005

[Ste97] Steglich D and Brocks W: *Micromechanical Modelling of the Behavior of Ductile Materials including Particles.* Comp. Mat. Science 9 (1997), 7-17

[Ste73] Sternstein S S and Myers F A: *Yielding of glassy polymers in the second quadrant of principal stress space.* J. Macromol. Sci, Phys. B 8 (1973), 539-571

[Tal94] Talreja R (Hrsg.): *Damage Mechanics of Composite Materials*. Elsevier, Amsterdam/ London/New York/Tokyo 1994

[Tay02] Taylor D: *The Theory of Critical Distances – a new perspective in fracture mechanics.* Elsevier, Oxford, UK, 2000

[The96] Theuer A: *Experimentelle Untersuchungen zum thermomechanischen Verhalten von Faserkeramik. Dissertation*. Univ. Stuttgart, 1996

[Thi07] Thielicke B: *Die Ermittlung der interlaminaren Scherfestigkeit von kohlenstoff-faserverstärkten Kohlenstoffen mit dem Druckscherversuch im Temperaturbereich zwischen Raumtemperatur und 2000°C*. Dissertation, Uni Karlsruhe, 1997

[Tsa71] Tsai S W and Wu E M: *A General Theory of Strength for An-isotropic Materials*. Journal Comp. Materials 5 (1971), 58-80

[Tsa15] Tsai S W and Melo J D: *Composite Materials design and Testing* (*unlocking mystery with invariants). ISBN 978-0-9860845-1-5*

[Tve81] Tvergaard V: *Influence of Voids on Shear Band Instabilities under Plane Strain Conditions.* Int. J. Fracture 17 (1981) 389-407

[Kaw88] Kawagoe M and Kitagawa M: *On criteria for craze initiation in glassy polymers*. J. of Materials Science 23 (1988), 3927-3932

[Vas10] Vassilopoulos A P: *Methods for fatigue life prediction of composite materials and bonded composite joints*. Composite Construction Laboratory Lausanne

[VDI 97] Cuntze R, Deska R, Szelinski B, Jeltsch-Fricker R, Meckbach S, Huybrechts D, Kopp J, Kroll L, Gollwitzer S, and Rackwitz R: *Neue Bruchkriterien und Festigkeitsnachweise für unidirektionalen Faserkunststoffverbund unter mehrachsiger Beanspruchung –Modellbildung und Experimente –*.VDI-Fortschrittbericht, Reihe 5, Nr. 506 (1997), 250 pages. (*New fracture criteria (Puck's criteria) and Strength 'Proof of Design' for Uni-directional FRPs subjected to Multi-axial States of Stress –model development and experiments*-. In German) * BMBF-Vorhaben 03N8002 (A. Puck, adviser 1995)

[VDI 2014] VDI 2014: German Guideline, Sheet 3 *Development of Fiber-Reinforced Plastic Components, Analysis*. Beuth Verlag, 2006. (in German and English, author was convenor)

[Wei15] Weißgräber P, Leguillon D and Becker W: *A review of Finite Fracture Mechanics: crack initiation at singular and non-singular stress raisers*. Arch. Appl. Mech. DOI 10.1007/s00419-015-1091-7, Springer-Verlag Berlin Heidelberg 2015

[You15] You M: *Strength criterion for rocks under compressive-tensile stresses and its application*. J. of Rock Mechanics and Geotechnical Engineering 7 (2015), 434-439

[Yu02] Yu M: *Advances in Strength Theories for Materials under Complex Stress States in the 20th Century*. Appl. Mech. Rev, vol 55, no3, May 2002

[ZTL 80] Dornier, Fokker, MBB, DLR: *Investigations of Fracture Criteria for Laminas* (in German). 1975-1980, Grant from Ministry of Defence, BMVg, Koblenz

27.2 Some further works, presentations of the author and MAN reports

1. Dissertation, TH Hannover 1968, *Ermittlung von Eigenfrequenzen dünner, schiefwinkliger isotroper Platten*. ZAMM 49 (1969)
2. *Ermittlung transversaler Eigenfrequenzen dünner Rechteckscheiben und Vergleich mit der Näherung von Timoshenko*. Acta Mechanica (1969)
3. *Theoretische Ermittlung der dreidimensionalen Spannungsverteilung in Radialver-dichterrädern*. DLR-FB-70-16 (1970), 73Seiten
4. *Der Einfluß von Eigengewicht und elastischer Einspannung auf die Biegeeigenfrequenzen eines schlanken Stabes von linear veränderlicher Dicke*. Der Bauingenieur (1971)
5. Meinke, Celep, Cuntze: *Eigenverhalten und Umwuchteinflüsse eines zweigliedrigen Rotors mit elastischem Gelenk*. MAN-NT 71 (1971)
6. Meinke P und Cuntze R: *Bewegungsgleichungen eines starren zweigliedrigen Sickenrotors*. NT 6/71

7. *Reduktion der Randstörungen von Rotationsschalen durch gezielte Formgebung des Randauflagerung*. NT 25/71, 19 Seiten
8. *Vergleich faserverstärkter und fasergewickelter Behälter mit Metallbehältern*. MAN-FB-72002 (1972)
9. Cuntze R und Celep Z: *Freie Bewegungen 2- und 3-stöckiger Rotoren*. NT 39/71
10. Kreft, Wolf, Cuntze: *Investigation of Fibers and Composites Applicable to the Design of High Pressure Vessels for Satellites*. ESTEC Contract No. 1485/7111, ESRO-Bericht (1972)
11. *Festigkeitsqualifikation der G2-Zentrifuge zur Urananreicherung*. NT 20/72
12. *Eine Bemerkung zur Anwendung des Finite-Element-Verfahrens in der Strukturmechanik*. Die Konstruktion (1973)
13. *Gehäuse-Auslegungsstudie zur Definition eines Standard-Feststoff-Apogäumsmotors*. NT 11/74
14. MAN-Beitrag zur Entwicklungsstudie „CFK-Bauteile für Spacelab“. NT 30/74
15. *Compendium über Auslegung von Bauteilen aus Faserverbundwerkstoff (design of structures built from FRP***).** M.A.N.-Neue Technologie (1975), 600 Seiten. Eigendruck MAN
16. Cuntze R und Thiele H-M: *Vorstudie über Möglichkeiten einer experimentellen und rechnerischen Lebensdauerbestimmung eines Nutzfahrzeugs und seiner Strukturteile. NT 9/77*
17. *Schwierigkeiten bei der Ermittlung von genauen Spannungen und Verformungen an Rotationsschalen aus Faserverbundwerkstoffen*. Strukturmechaniktagung 1.6./2.6.1977 in Ottobrunn über Probleme der Festigkeitsforschung im Flugzeugbau und Bauingenieurwesen. Sonderheft der DFVLR (1977).
18. Cuntze R and Zaun J: *Calculation of the Natural Frequencies of the braced GROWIAN tower with dead head mass* (1978). KFA-Jül. Spez-28, Jan.79. ISSN 0343-7639
19. *Entwurf und Festigkeitsanalysen fließgedrückter Rohre*. NT 29/78
20. Habilitationsschrift, TU München, 1978: *Grundlagen für die Berechnung von Rotationsschalen aus Faserverbundwerkstoff*
21. ROTTSCHWIMM 32- *Einsatz eines 5 t schweren Energiespeicherrades bei einem Schwinmm-kran – Auslegung und bruchmechanischer Nachweis*. NT 4/82 (*viele Jahre in Betrieb*)
22. Cuntze R. und Eder J: *Einfluß von Schubelastizität auf Drehträgheit und Biegeeigenfrequenz gleichförmig massebelegter Einfeldbalken*. Die Konstruktion 35 (1983), H.5, S 183-186
23. *Der Einfluß von Schubelastizität und Drehträgheit auf die kritischen Drehzahlen gleichförmig massebelegter, einfeldriger Wellen***.** Ing.-Archiv (1984)
24. Cuntze R und Wein J: *Strukturauslegung und –nachweis in Einbindung leistungsfähiger Pre- und Postprozessorsysteme*. DGLR-Fachausschuß „Festigkeit und Bauweisen“. Neubiberg, 5.7.1984. Tagungshandbuch
25. *Probleme bei der Übertragung eines Zwischenfaserbruchkriteriums von einem UD-Probekörper auf einen Mehrschichtenverbund*. DGLR-Symposium „Entwicklung und Anwendung von CFK-Strukturen“. TU, Berlin. 8./9.11.1984
26. *CAE-Einsatz beim Projekt ARIANE. Ein Anwenderbericht.* CAE-Journal, Heft 6 (1984), 24-31
27. *Bruchverhalten von kohlenstoffaserverstärkten Kunststofflaminaten. – Theor. Untersuchungen* – Bericht: MAN-NT 44/83 (20.12.84). BMFT-Forschungsvorhaben 01ZA 029-/K/NT/NTS 1022
28. *Strukturberechnung. Teil der Bauteilentwicklung – ein Überblick*. Konferenzbericht der Tagung Mechanik und Industrie. IGLS, Österreich. 26./27. Februar 1985. Herausgeber: Institut für Mechanik, Universität Innsbruck. Springer, Wien 1986
29. Cuntze R und Hajek M.: *Eigenfrequenz eines angerissenen Kragträgers*. Ing. Arch. 55 (1985), S. 237-241
30. Crostack H.A., Nolte F., Zeilinger H. und Cuntze R.: *Untersuchung des Schädigungsablaufes in kohlenstoff-faserverstärkten Kunststoffen.* Zeitschrift für Werkstofftechnik 16 (1985) 366-372
31. Rackwitz, R. and Cuntze, R.: *Formulations of Reliability-oriented Optimization with Application*. NATO Advanced Study Institute. Conference on Computer Aided Optimal Design, Troia, Portugal. June 29-July 11, 1986. Springer
32. Cuntze R and Grimmelt M: *Influence of the Variation of Structural Properties on the Probability of a Composite Plate to meet a Target Eigenfrequency*. EUROMECH Coll. 219, Sept. 23-25, 1986, Kassel

33. Cuntze R und Schuelein R.: *Einsatz der Bruchmechanik bei der Entwicklung von Struktur-Bauteilen aus Faserkunststoffverbund (FKV).* Vortragsveranstaltung „Bruchmechanik bei Verbund-werkstoffen“ bei der Dechema. Frankfurt, 19.02.1987
34. Rackwitz R and Cuntze R: *System Reliability Aspects in Composite Structures*. Eng.’ Opt., 1987, Vol. 11, pp. 69-76
35. Cuntze R: *Failure Path Analysis of Multilayered Fiber Reinforced Plastic Components with the Reliability Calculation Programme FRPREL*. Noordwijk, Oct. 1987
36. Cuntze R: *Influence of the Stochastic Behavior of Design Parameters on the First Ply Failure (FPF) in Pressurized CFRP-Tubes*. ESA/ESTEC, Noordwijk, March 1988
37. Scharringhausen J. and Cuntze,R: *FEM-Calculations on the Domes of Fiber Reinforced Plastic Cases for Solid Propellant Motors.* ESA/ESTEC Workshop, Noordwijk, March 23-25, 1988
38. Cuntze R and Zaun J: *Delamination Optimization of Hoop-Wound Composite Fly-wheels*. ICCM 7, Beijing, August 1 – 4, 1989
39. Cuntze R and Schuelein R: ***Werkstoffdatenbanken*** *im industriellen Einsatz (material data banks in industrial use) – aus der Sicht eines Anwenders*. MAN Technologie GmbH, München. Bericht und Vortrag MAN-intern (Febr. 23, 1989). Fachgespräch bzgl. MAN Werkstoff-Informations-System
40. Grimmelt M and Cuntze R: *Probabilistic Prediction of Structural Test Results as a Tool for the Performance Estimation in Composite Structures Design.* . VDI-Bericht 771 (1989), 191-200
41. Dr. med. Stock W und Dr.-Ing. Cuntze R: *Computergestützte biomechanische Untersuchungen zur Knochen-transplantation.* Vortrag, BMFT Seminar. Hamburg, 1988
42. Cuntze R und Schuelein R: *Werkstoffdatenbank: Qualitätswerkzeug für die Entwicklung zuverläs-siger Bauteile. VMPA-Tagung „Qualität und Zuverlässigkeit durch Materialprüfung*“, München, April 1990
43. *Auslegung, Nachweis und Zuverlässigkeitsoptimierung von Faserkunststoffverbund-Bauteilen. Fachtagung „Rechnereinsatz beim Konstruieren von Kunststoff-Formteilen“.* Süddeutsches Kunststoffzentrum, Mannheim, Mai 1990
44. Cuntze R: *Influence of the Stochastic Behavior of Design Parameters on the First Ply Failure (FPF) in Pressurized CFRP-Tubes*. ESA/ESTEC, Noordwijk, March 1988
45. *Structural Design, Optimization and Reliability Justification – a comparative survey related to the example: Axially compressed strut*. GAMM/IFIP-Workshop “Stochastic Optimization”, Neubiberg, May 1990 (not published)
46. Cuntze R. and Heibel R: *Increasing the Limit of Usability of CFRP Tubes by Built-in Stresses*. X. Int. Herman F. Mark-Symposium. Wien, 1991
47. *Prediction of the Distribution of Inter-Fiber-Failure Test Data of Radial Loaded, Pre-strained CFRP Tubes composed of Thin Layers*. 5th Workshop “Composite-Forschung in der Mechanik”, Paderborn, October 1992
48. Gollwitzer S, Cuntze R, Grimmelt M and Zwerev A.: *Structural Reliability Applications in Aerospace Engineering.* ICOSSAR 93, Innsbruck, 1993
49. *Deterministic and Probabilistic Prediction of the Distribution of Inter-Fiber-Failure Test Data of Pre-strained CFRP Tubes composed of Thin layers and loaded by radial pressure*. Wollongong, Advanced Composites ‘93. The Minerals, Metals & Materials Society, 1993
50. *Evaluation and Application of a New Physically Based 2D/3D-Inter-Fiber-Fracture (IFF) Strength Criterion*. Proceedings of International Symposium on Advanced Materials for Lightweight Structures, Noordwijk, März 1994, ESTEC, 133-139
51. Gierlinski, Smith, Thoft-Christensen, Santos, Cuntze, Gollwitzer: *Reliability-based Design of Structural Components*. Proceeding of the Int. Symp. On Advanced Materials for Light weight structures, ESTEC, Noordwijk, March 1994 (ESA-WPP-070), 121-125
52. „*Quick Design“, Entwurfsregeln und Normen zur Strukturberechnung.* Kolloquium „Ausgewählte Probleme der Strukturmechanik“, 11.5.95, zu Ehren von Dr.-Ing. B. Geier. IB 131-95-13, DLR-Braunschweig
53. *Festigkeitskriterien für Werkstoffe aus Faserkunststoffverbund (FKV).* Symposium „Berechnungen von Faserverbundstrukturen unter Anwendung numerischer Verfahren“. München, Techn. Uni, 13/14. März 1996

54. *"Fracture-type Strength Criteria" formulated by Invariants which consider the Material Symmetries of the Isotropic/Anisotropic Material used*. Conf. on Spacecraft Structures, Materials and Mechanical Testing. ESA-CNES-DARA: Noordwijk, 27-29 March 1996, pp. 399-409
55. *Zum verbesserten Festigkeitsnachweis von FKV-Bauteilen*. Werkstoffwoche 96, Stuttgart 28.- 31. Mai 1996. Projektberichterstattung
56. *Bruchtypbezogene Auswertung mehrachsiger Bruchtestdaten und Anwendung im Festigkeitsnachweis sowie daraus ableitbare Schwingfestigkeits- und Bruchmechanikaspekte*. DGLR-Kongreß 1996 Dresden, Kongreß-Band
57. *Evaluation of Multiaxial Test Data of UD-laminas by so-called "Fracture-type Strength Criteria" and by supporting Probabilistic Means*. ICCM-11, Gold Coast, 1997
58. Cuntze R et.al.: *Neue Bruchkriterien und Festigkeitsnachweise für unidirektionalen Faserkunststoffverbund unter mehrachsiger Beanspruchung – Modellbildung und Experimente*. VDI-Fortschrittbericht, Reihe 5, Nr. 506 (1997), 250 pages. [New fracture criteria (Puck's criteria) and Strength 'proof of Design' for Unidirectional FRPs subjected to Multi-axial States –model development and experiments-, in German]
59. *Stand von Auslegung und Nachweis von Bauteilen aus Faserkunststoffverbund nebst einigen Ausblicken*. Plenarvortrag, DGM-Tagung "Verbundwerkstoffe und Werkstoffverbunde", Kaiserslautern, Sept. 1997
60. *Strength Prediction* ***for Multi-axially Loaded CMC-Materials*****.** 3rd European Workshop on Thermal Protection Systems. Conf. on Spacecraft Structures, Materials and Mech. Testing. ESA-ESTEC: Noordwijk, March 1998, WP P141
61. *Application of 3D-strength criteria, based on the so-called "Failure Mode Concept", to multi-axial test data of sandwich foam, concrete, epoxy, CFRP-UD lamina, CMC-Fabric Lamina*. ICCE/5, Las Vegas, July 1998 (presentation)
62. *The Failure Mode Concept - a new comprehensive 3D-strength Analysis Concept for Any Brittle and Ductile behaving Material*. Europ. Conf. on Spacecraft Structures, Materials and Mechanical Testing. ESA-CNES-DGLR-DLR; Braunschweig, Nov. 1998, ESA SP-428, 269-287
63. *Progressive Failure of 3D-stressed Laminates: Multiple Non-linearity treated by the Failure Mode Concept (FMC).* DURACOSYS99, Brussels, July 1999. Balkema, Rotterdam, 2000
64. *Static Design and Strength 'Proof of Design' of Pressure Vessels, built from Ductile or Brittle Materials*. Problems of the North; Yakutsk 2000
65. *Are there Cost Drivers in the Structural Analysis of the ARIANE 5-Development?* Noordwijk, 29. Nov./1. Dec. 2000
66. *Assessment of Load- and Strain-controlled States of Stress in 'hot Spots' – on the way to an Industrial Approach for Gurson Materials*. 3rd European Conference on Launcher Technology. CNES, DLR, ESA-ESTEC, ISU: Strasbourg, Dec. 11-14, 2001
67. Huybrechts D, Cuntze R., Druwen S, and Lutz G.: *VDI-Ri 2014, Blatt3, Berechnungen*. SAMPE 2002.
68. Cuntze R: *Non-linear Failure Analysis of FRP Laminates composed of UD Laminas – a comparison of the author's predictions with test results within the Failure Exercise in the UK*. 3rd Int. Conf. on Fracture and Damage Materials; Paderborn, September 2-4, 2003.

Born in the Chinese Year of the Earth Rabbit,
which is considered vigilant, witty, and resourceful.

***Did this have any significance in my life*?**

Some Notes on AI considering qualified available data sources and sound theories:

"My test-validated SFCs are underutilized; instead, fewer validated SFCs continue to be used. This makes to think as structural engineer about present and future AI results in engineering".

Following [Wikipedia]

Artificial intelligence (AI): Capability of computational systems to perform tasks typically associated with human intelligence, such as learning, reasoning, problem-solving, perception, and decision-making. AI models process this.

Algorithm: A step-by-step instruction that performs a task by transforming a specific input into a desired output, like a cooking recipe. This principally is similar to the presented material models with manually searching the necessary data base, however, instead of using an AI search algorithm fed by a vast digital data basis.

AI model versus Agorithm: The model is used to make predictions or decisions and an algorithm is the logic by which that AI model operates.

AI task: an entity, to be formulated carefully.

My comments on AI:

* Mechanics remains one very essential basis when developing light-weight structural components and Artificial Intelligence (AI) with its algorithms is a helpful supporting tool
* The valuable tool AI, sensibly applied, helps us to get suggestions for solutions. But who is supposed to judge them without corresponding knowledge of mechanics?
* Only System Engineering with experienced engineers using mechanics and the necessary other disciplines - together with AI - enables to produce qualified products**. At the end always an experienced engineer will have to sign that the structure will work.**
* It can already be said: The quality of the results of the algorithms-using AI models will decline, if more unverified, AI-generated content (fakes?) will form the growing information basis for the AI models' learning. Therefore, I hope that at least researched content will be loaded at least on the technical side. This costs money, but otherwise designed sky scrapers and mechanical machines for instance will collapse. AI apps are based on models, statistics and probabilistics. Their electric power and water consumption is gigantic, which we do not want to hear during the current hype.
* AI models are good at calculating probabilities based on massive amounts of data and using them to inform their predictions. The models break down information into its smallest units and then reassemble it as needed due to how the algorithm interprets the inquiry. However, there's no guarantee that they do this reliably or accurately. A recent example, using an AI-assisted translation tool, was pretty disappointing and dangerous: "*I've found twice that a translation German into English expressed the exact opposite of what I not bad formulated and meant".*

<u>In AI context</u>:

Data-Driven Engineering should be a *real* data driven one, using a 'simple' Data Exchange.

One should always understand the basics of the delivered AI results. It should not be like below:

The farther apart galaxies are, the faster they are moving away from each other. According to the so-called Hubble constant, for example, two galaxies only 3 million light-years apart are moving away at about 70 km/s. *Where to?*

<u>Upcoming Necessity</u>:

Learning to Learn and elaborating a novel Teaching Scheme has to come up regarding the not filled lecture halls in essential, but difficult disciplines like basic mechanics. Consequence: Germany will no

longer be able to build and sell good constructions in the future. In Munich we try to improve this situation by a WG consisting of university with industry members.

Nice picture shot in Columbia

Sometimes you can and should let yourself be carried along.
The little monkey cleverly used its innate intelligence and let the large Ara parrot carry him upstairs.
I don't think the monkey will stay there for long.

The same applies to us when using artificial intelligence. We enjoy its use.
However, without also utilizing our innate intelligence and experience, the benefits of artificial intelligence will diminish.

An Orang-Utan

handing over a '*small plan for further evolution*'

to a homo sapiens sapiens

(*the knowing, knowing human !!??*).

Orangutans, along with gorillas, chimpanzees, and humans, belong to the family of great apes (Hominidae).
The DNA sequence of orangutans and humans is 99 percent identical.

Acknowledgement (see details in [CUN25]*)

- To my wife Maria: "*My heartfelt thanks for allowing me to devote so much time of 'our time together' to my time-consuming hobby*".
- Dedication to all the people who have guided me to the wide variety of technical fields during my over 60-years of working life.